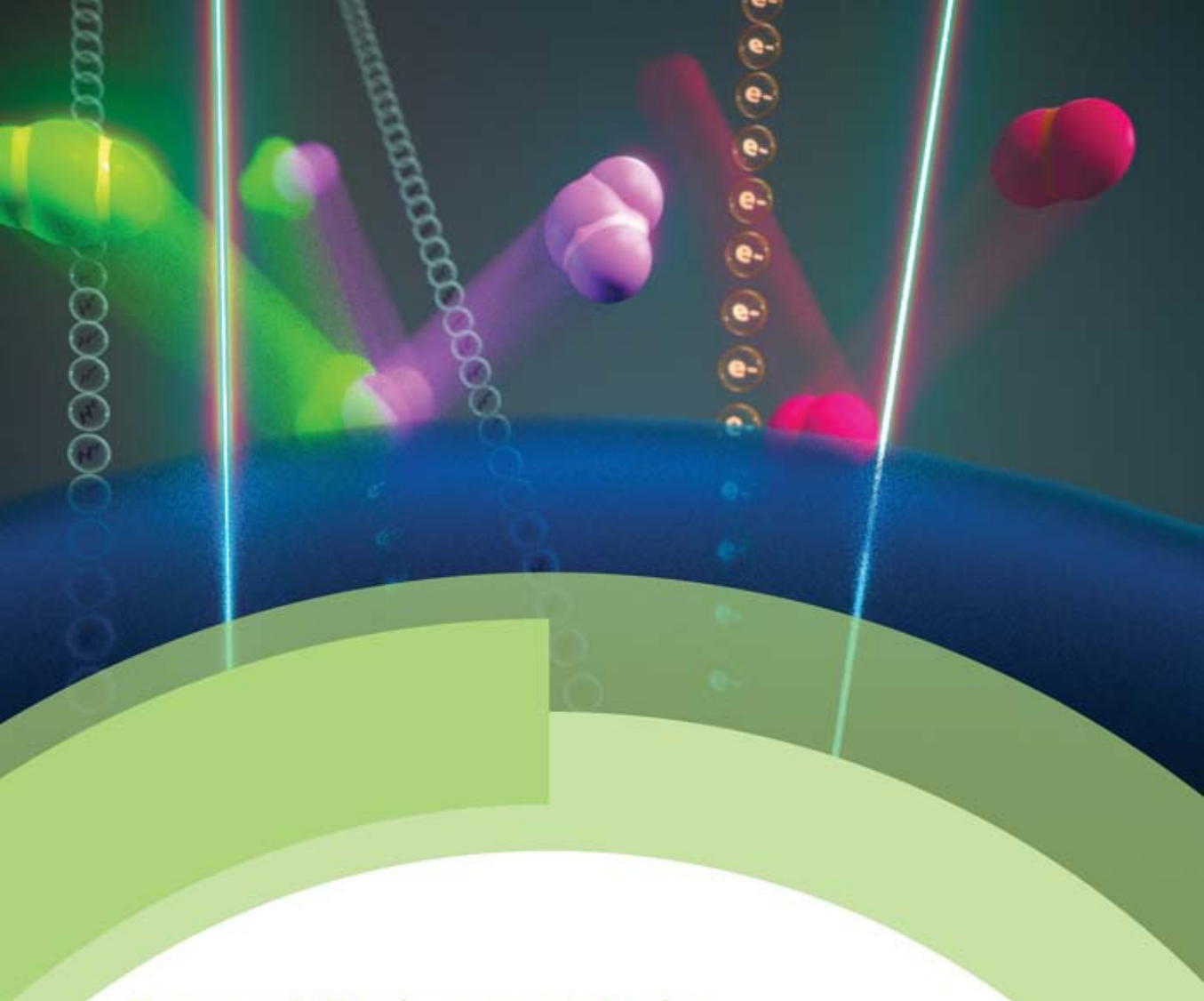

Energy & Environment Series

# Ultrathin Oxide Layers for Solar and Electrocatalytic Systems

Edited by Heinz Frei and Daniel V. Esposito

ROYAL SOCIETY OF CHEMISTRY

Ultrathin Oxide Layers for Solar and Electrocatalytic Systems

**Energy and Environment Series**

*Series editors:*
Nigel Brandon OBE FREng, *Imperial College London, UK*
Roberto Rinaldi, *Imperial College London, UK*
Vivian Wing-Wah Yam, *University of Hong Kong, Hong Kong*

*Titles in the series:*
1: Thermochemical Conversion of Biomass to Liquid Fuels and Chemicals
2: Innovations in Fuel Cell Technologies
3: Energy Crops
4: Chemical and Biochemical Catalysis for Next Generation Biofuels
5: Molecular Solar Fuels
6: Catalysts for Alcohol-Fuelled Direct Oxidation Fuel Cells
7: Solid Oxide Fuel Cells: From Materials to System Modeling
8: Solar Energy Conversion: Dynamics of Interfacial Electron and Excitation Transfer
9: Photoelectrochemical Water Splitting: Materials, Processes and Architectures
10: Biological Conversion of Biomass for Fuels and Chemicals: Explorations from Natural Utilization Systems
11: Advanced Concepts in Photovoltaics
12: Materials Challenges: Inorganic Photovoltaic Solar Energy
13: Catalytic Hydrogenation for Biomass Valorization
14: Photocatalysis: Fundamentals and Perspectives
15: Photocatalysis: Applications
16: Unconventional Thin Film Photovoltaics
17: Thermoelectric Materials and Devices
18: X-Ray Free Electron Lasers: Applications in Materials, Chemistry and Biology
19: Lignin Valorization: Emerging Approaches
20: Advances in Photoelectrochemical Water Splitting: Theory, Experiment and Systems Analysis
21: Electrochemical Reduction of Carbon Dioxide: Overcoming the Limitations of Photosynthesis
22: Integrated Solar Fuel Generators
23: Magnesium Batteries: Research and Applications
24: Organic Thermoelectric Materials

25: Electrochemical Methods for Hydrogen Production
26: Carbon Capture and Storage
27: Heterogeneous Catalysis for Energy Applications
28: Carbon Dioxide Electrochemistry: Homogeneous and Heterogeneous Catalysis
29: Thermal Energy Storage
30: Ultrathin Oxide Layers for Solar and Electrocatalytic Systems

*How to obtain future titles on publication:*
A standing order plan is available for this series. A standing order will bring delivery of each new volume immediately on publication.

*For further information please contact:*
Book Sales Department, Royal Society of Chemistry, Thomas Graham House, Science Park, Milton Road, Cambridge CB4 0WF, UK
Telephone: +44 (0)1223 420066, Fax: +44 (0)1223 420247
Email: booksales@rsc.org
Visit our website at www.rsc.org/books

# *Ultrathin Oxide Layers for Solar and Electrocatalytic Systems*

Edited by

**Heinz Frei**
*Lawrence Berkeley National Laboratory, USA*
*Email: hmfrei@lbl.gov*

and

**Daniel V. Esposito**
*Columbia University, USA*
*Email: de2300@columbia.edu*

ROYAL SOCIETY OF CHEMISTRY

Energy and Environment Series No. 30

Print ISBN: 978-1-83916-179-7
PDF ISBN: 978-1-83916-370-8
EPUB ISBN: 978-1-83916-371-5
Print ISSN: 2044-0774
Electronic ISSN: 2044-0782

A catalogue record for this book is available from the British Library



The Royal Society of Chemistry is a charity, registered in England and Wales, Number 207890, and a company incorporated in England by Royal Charter (Registered No. RC000524), registered office: Burlington House, Piccadilly, London W1J 0BA, UK, Telephone: +44 (0) 20 7437 8656.

For further information see our website at www.rsc.org

Printed in the United Kingdom by CPI Group (UK) Ltd, Croydon CR0 4YY, UK

# *Contents*




Energy and Environment Series No. 30
Ultrathin Oxide Layers for Solar and Electrocatalytic Systems
Edited by Heinz Frei and Daniel V. Esposito



Published by the Royal Society of Chemistry, www.rsc.org

CHAPTER 1

# *Introduction*

H. FREI*[a] AND D. V. ESPOSITO*[b]

[a] Molecular Biophysics and Integrated Bioimaging Division, Lawrence Berkeley National Laboratory, University of California, Berkeley, CA 94720, USA; [b] Department of Chemical Engineering, Columbia University, New York, NY 10032, USA
*Emails: hmfrei@lbl.gov; de2300@columbia.edu

If there is a single most important factor that enabled the development of ultrathin oxide layers for advancing photo-, electro-, and thermal catalytic systems for energy, it is the birth of and explosive growth in the field of nanoscience starting in the 1990s. This opened up the capability of synthesizing and manipulating inorganic matter on a length scale of nanometers, which is the scale on which charge transfer, ion transport, and chemical transformations need to be controlled for designing and optimizing catalytic systems for energy conversion applications. The concurrent emergence of an array of new characterization tools, from advanced electron and tunneling microscopies to X-ray spectroscopy and super-resolution optical microscopy, has allowed researchers to characterize nanosized structures at atomic resolution and accelerate the understanding of the fundamental physics and chemistry that underlie nanoscience and nanotechnologies. Breakthroughs over the past two decades in solar cells, batteries, catalysis for the manufacture of chemicals, and sensors, to name just a few, have led to dramatic performance improvements and the implementation of new technological concepts that could not have been contemplated before the advent of the nanoscience revolution.

The special interest in nanoscale components made of metal oxide materials for technological applications should not come as a surprise given the role and impact of thin metal oxide layers that have been part of civilization's

Energy and Environment Series No. 30
Ultrathin Oxide Layers for Solar and Electrocatalytic Systems
Edited by Heinz Frei and Daniel V. Esposito

Published by the Royal Society of Chemistry, www.rsc.org

infrastructure and technological advances for millennia. For example, metals such as iron and copper that are ubiquitous in bridges, vehicles, ships, tools, electronics and more are in many cases irreplaceable in their role(s), yet their robustness and durability under use in harsh environmental conditions are often reliant on the presence of thin metal oxide layers that protect the metal from corrosion. A house roof made of copper is a prime example of the enormous practical importance of metal oxide layers in everyday life. Famously, the copper sheets of the Statue of Liberty in New York harbor are only 2.5 mm thick, yet since 1886 have only lost 0.1 mm thickness thanks to protection by copper patina, as illustrated in Figure 1.1a,b.[1] Many metals would not be technologically viable under working conditions were it not for the spontaneous formation of oxide protection layers driven by the high stability of the metal–oxygen chemical bond. In modern societies, nanosized metal oxides find their main importance in the manufacture of everyday chemicals where heterogeneous

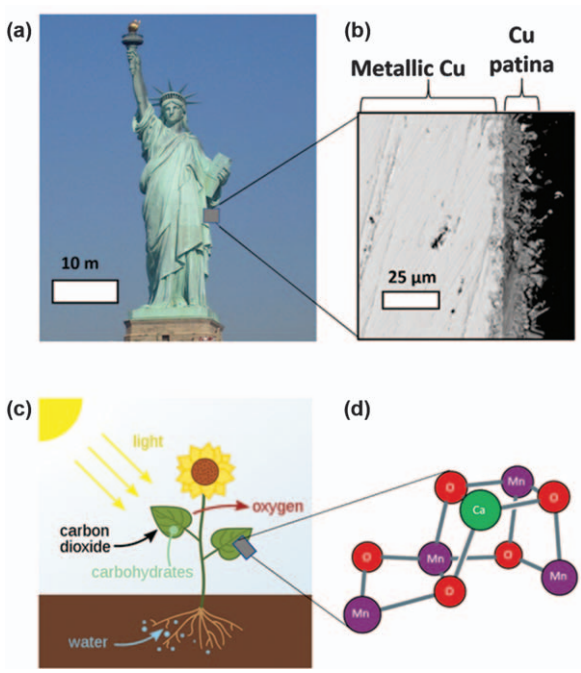


**Figure 1.1** (a) Statue of Liberty, New York harbor. Reproduced from https://commons.wikimedia.org/wiki/Statue_of_Liberty#/media/File:Statue-de-la-liberte-new-york.jpg, under the terms of the CC BY-SA 2.0 license, https://creativecommons.org/licenses/by-sa/2.0/deed.en. (b) Cu patina preventing further oxidation. Reproduced from ref. 1 with permission from Springer Nature, Copyright 2012. (c) Plant photosynthesis. Reproduced from https://commons.wikimedia.org/wiki/File:Photosynthesis_en.svg, under the terms of the CC BY-SA 4.0 license, https://creativecommons.org/licenses/by-sa/4.0/deed.en. (d) $Mn_4CaO_5$ catalyst for water oxidation in photosystem II. Reproduced from ref. 2 with permission from Springer Nature, Copyright 2018.

processes play a dominant role, whether as robust catalysts or as supports. Zeolites, which are microporous aluminosilicates featuring oxide nanowalls, play a huge role as acid catalysts in the preparation of transportation fuel from petroleum resources, or as supports for nanoparticle or organometallic catalysts for the manufacture of specialty chemicals. The role of metal oxide nanolayers in renewable energy technologies is currently nowhere more prominent than in advanced solar cells, and the multitude of physical properties of metal oxides and their diverse chemistry are what drives their expanding use in emerging technologies. Beyond imparting chemical stability, many classes of metal oxide materials possess tunable electronic and/or optical properties that can be manipulated by varying the identity of the metal(s), the metal-to-oxygen stoichiometry, structural phases and morphologies, and dopant species. As a prime example, the electronic conductivity of a number of metal oxides can be varied from metal-like to insulator-like through the selection and control of the concentrations of various dopant elements. Similar control knobs can be used to tailor the optical properties of oxides to vary from completely transparent to completely opaque across the visible spectrum, while the ability to tune the structural characteristics of oxides, such as their microporosity, can give them built-in molecular sieving capabilities that can be leveraged to enable selective transport of molecules and ions while blocking others to control reactant and intermediate concentrations at active sites in catalytic, electrocatalytic, and photocatalytic systems.

Humans are not the only species on Earth to have taken advantage of the unique and tunable properties of metal oxides, as evidenced by their use in Nature. The most prominent nanoscale metal oxide component in the living world is the $Mn_4CaO_5$ cluster catalyst for oxygen evolution from water, whose function in photosystem II is essential for life of Earth (Figure 1.1c,d).[2] While biological function relies overwhelmingly on the assembly and control of soft matter components, Nature's design features at the nanoscale for accomplishing unparalleled selectivity and specificity of highly complex processes of charge, ion, and molecule transport and of chemical transformations are a great source of principles and inspiration for guiding new or improved engineered function. Ultrathin oxide layers have emerged as particularly useful components for engineering systems and devices that strive to implement this level of control and efficiency using the methods and tools of nanoscience.

Thanks to advances in nanofabrication and characterization over the past 20–30 years, ultrathin oxide layers with tunable properties have enabled new approaches and methods for enhancing the activity and selectivity of catalytic materials to be developed, dramatically improving the durability of semiconductor light absorbers, photocatalysts, and heterogeneous thermal catalysts and facilitating integration of functional components at the nanoscale. As a result, the use of ultrathin layers has been rapidly expanding in the areas of solar, catalytic, and (photo)electrocatalytic energy conversion technologies. However, much of the emerging knowledge in this area is scattered across the literature of disparate fields of specialization, making it difficult to gain familiarity and take advantage of these developments for

new applications. This motivated the overall purpose of this book, which is to describe in a single place the fundamentals and emerging applications that may accelerate the use and benefits of ultrathin oxide layer materials.

Following this introductory chapter, the book covers two main areas of focus and ends with a forward-looking closing chapter. In the first focus area, which contains Chapters 2–5, recent breakthroughs in improving the stability and efficiency of semiconductor light absorbers in photovoltaic (PV) cells for electricity generation and photoelectrochemical (PEC) cells for solar fuel generation are described. In *Chapter 2*, Davis, Garland, and Strandwitz lay out recent advances in synthesis techniques for metal oxide nanolayers for PV and PEC devices, and introduce the basic physical and chemical processes by which these coatings enhance the performance of the light absorber. These include electronic passivation of semiconductor surfaces for enhancing the productive use of separated charges, chemical protection that improves durability, and the introduction of selective electrical contacts. Although the main focus of this chapter is on crystalline Si, the techniques are equally effective for III–V semiconductors where they have led to dramatic stability increases, even allowing the revival of materials with highly favorable electronic properties that previously were found unsuitable for applications owing to a lack of chemical stability. In *Chapter 3*, Palmstrom and Reese explain in depth the full range of diverse functional roles of ultrathin oxide layers for PV technologies, often with more than one role being played by a single metal oxide layer. Examples focus on thin-film PV technologies and range from next-generation materials to commercially established PV devices. Among the ultrathin coatings, blocking layers permit directional control of charge flow by functioning as a tunneling barrier, or serving as part of an energy cascade. Next, the mechanisms by which oxide blocking layers impose directionality on visible light-driven electron transfer and how they can be leveraged to optimize performance are investigated by ultrafast THz and transient optical absorption spectroscopy in *Chapter 4* by Swierk. For the systems discussed in this chapter, the light harvesting is accomplished by dye molecules attached to the oxide layer. Through the use of advanced electrochemical and spectroscopic methods, Swierk describes how ultrathin oxide blocking layers incorporated into dye-sensitized solar cells or photoelectrochemical cells for water splitting can lead to substantial improvements in the performance of these devices. In *Chapter 5*, Wang and Cronin discuss the recent burst of efforts in the exploration and understanding of the remarkable effects of $TiO_2$ nanolayers on the photoelectrochemical performance of III–V semiconductor-based systems. Ultrathin titania layers inserted between semiconductor light absorber and metal catalyst films or nanoparticles, including those with plasmonic properties, are shown to enhance photoelectrocatalytic $H_2O$ splitting or $CO_2$ reduction efficiency, dramatically in some cases, by selecting the appropriate structural phase and thickness of the titania layers, by the generation of defects, through the influence of built-in electric fields at the $TiO_2$/III–V semiconductor interface, or by plasmonic effects. Elucidation of the underlying

mechanisms using advanced microscopy, spatially resolved electron spectroscopy, and photoelectrochemical methods reveals the atomic and electronic structural factors responsible for the substantial improvements in stability, charge separation and transport efficiency, and lowering of overpotentials for reactant activation.

While Chapters 2–5 are primarily focused on the solid-state physics associated with the use of oxide layers deposited on semiconductor light absorbers, Chapters 6–11 place greater emphasis on applications in which ultrathin oxides are also intimately involved with electrocatalytic or catalytic processes. As a bridge between these two areas of emphasis, the topic of *Chapter 6* is the study of oxide-based co-catalyst layers that are deposited directly on photoelectrodes where their function extends beyond those discussed in Chapters 2–5 to also directly participate in electrocatalytic reactions. Transient optical spectroscopy has recently revealed that the mechanistic roles of such ultrathin co-catalyst layers in many photoanode materials such as $Fe_2O_3$, $BiVO_4$, $TiO_2$, and Si is highly complex. Motivated by the need to pin down the precise roles of co-catalyst layers and how they depend on the details of the photoanode/co-catalyst interfacial properties and experimental conditions, Qiu, Nellist, and Boettcher present results from recent studies using dual working electrode and potential-sensing electrochemical–atomic force microscopy techniques of several photoanode–co-catalyst assemblies.

Ultrathin oxide layers have similarly resulted in big leaps in the performance of heterogeneous catalysts and photocatalysts. Here, additional properties of oxide nanolayers beyond optimization of photoinduced charge transport and chemical protection discussed in the earlier chapters come into play, namely the ability to design microporous structures for controlling catalytic activity and/or selectivity by providing selective access of reactant species to active sites located at buried interfaces between the oxide overlayer and underlying catalyst. In the next five chapters, the relevant physicochemical phenomena and models for species transport through oxide layers are introduced, and synthetic methods and applications in heterogeneous thermal catalysis, electrocatalysis, photocatalysis, and ultrathin separation membranes for artificial photosynthesis are described. To provide guidance for designing oxide overlayers for electrocatalysts, *Chapter 7* by Esposito, Guilimondi, Vos, and Koper presents the principles of species transport through metal oxide nanolayers and reaction kinetics at the buried interface that govern the operation of electrocatalysts encapsulated by semipermeable oxide nanolayers, in addition to a brief overview of experimental methods for the quantitative performance assessment of oxide-encapsulated electrocatalysts. The design principles introduced in this chapter provide guidance for the design of nanoscale oxide overlayers to optimize catalytic activity and product selectivity. The practical importance of improved chemical stability and prolonged activity of heterogeneous catalysts imparted by ultrathin metal oxide coatings cannot be overstated in light of the dominant role of heterogeneous catalysis in the manufacture of

chemicals. In *Chapter 8*, Lu and Elam present a suite of strategies to encapsulate heterogeneous thermal catalysts with emphasis on atomic layer deposition (ALD), with the goals of inhibiting catalyst poisoning, coking, sintering, and other degradation mechanisms in industrially important chemical processes. Central to the discussion are specialized ALD reactor designs and deposition protocols for achieving uniform encapsulation of catalyst nanoparticles on high surface area supports, and methods for deposition on selected areas of the supported nanocatalyst sample that can allow spatial and compositional control of catalyst nanoparticles for enhancing product selectivity. Solution-based chemical processes for ultrathin metal oxide encapsulation of industrial electrocatalysts, with focus on oxygen reduction under acidic conditions, are the topic of *Chapter 9* by Xing. Focus is placed on recent developments in sol–gel and condensed layer deposition methods that afford extraordinary thickness control of oxide nanocoatings for high surface area supported electrocatalysts. The interactions between highly conformal coatings and noble metal catalysts result in a remarkable increase in the longevity of these electrodes and, in some cases, increases in their electrocatalytic activity towards oxygen reduction.

Recent advances in the development of systems comprised of composite materials for solar fuels production have been assisted by an additional unique property of certain ultrathin, pore-free oxide layers, namely the ability to transmit protons while blocking molecules as small as oxygen. Proton permeability of solid oxide barriers that are part of any solar fuel system involving water oxidation is essential because $H^+$ ions, which are generated upon oxidation of water at anodic sites, need to reach cathodic sites for reduction in order to close the photocatalytic cycle. In *Chapter 10*, Pan, Hisatomi, and Domen present ultrathin dense metal oxide overlayers that are coated on nanoparticle photocatalysts. Within these composite architectures, the oxide overlayers transmit protons but block oxygen transport, thereby preventing the undesirable $O_2$ reduction reaction from taking place at co-catalyst active sites buried beneath the overlayer. The rich materials chemistry of oxides affords tailored nanolayers of various metals or metal combinations, some in a hydrated state, which permits additional activity-enhancing properties for semiconductor nanoparticle photocatalysts. Specific examples highlighting the ability to control the hydrophilic character and redox selectivity of encapsulated photocatalysts are presented that demonstrate functionality that goes beyond passivation and prevention of photocorrosion. In order to develop ultrathin oxide layers that can serve as membranes separating incompatible redox catalysis environments such as $H_2O$ oxidation and $CO_2$ reduction, independent optimization of charge transfer, proton transport, and chemical separation properties is required. This task may be achieved by embedding organic molecular wires, which offer precise fine tuning of the charge transport energetics in ultrathin oxide layers. This approach affords independent optimization of charge transfer from proton transport and chemical separation properties. In *Chapter 11* by Jo, Zhang, Katsoukis, and Frei, few nanometer thick silica

layers deposited by ALD are shown to provide high proton conductivity and complete blocking of oxygen and other small molecules, and allow encapsulation of electron- or hole-conducting molecular wires that can be energetically tuned for optimal energy level alignment with light absorbers and catalysts. These ultrathin separation membranes permit the integration of incompatible catalytic environments for the development of complete nanoscale photosynthetic systems, cascade catalysis systems, or nanoscale inorganic/microbial systems (biohybrids), with the short length scale minimizing the major efficiency-degrading processes that are inevitable at the macroscale.

The final *Chapter 12* by Esposito and Frei describes major challenges and opportunities for deepening our understanding of the fundamental physical and chemical processes that occur at the buried interfaces and exposed surfaces of ultrathin oxide layers. With significant continued progress in fundamental research activities that are well aligned with these key challenges and opportunities, we anticipate that the uses and functionalities of ultrathin oxides within modern clean energy technologies will only accelerate in the coming years.

## References

1. M. M. Mennucci, M. Sanchez-Moreno, I. V. Aoki, M. C. Bernard, H. G. de Melo, S. Joiret and V. Vivier, *J. Solid State Electrochem.*, 2012, **16**, 109–116.
2. J. Kern, R. Chatterjee, I. D. Young, F. D. Fuller and L. Lassalle, *et al.*, *Nature*, 2018, **563**, 421–425.

CHAPTER 2

# *Oxide Coatings for Semiconductor Light Absorbers: Advanced Synthesis and Applications*

B. E. DAVIS, B. M. GARLAND AND N. C. STRANDWITZ*

Department of Materials Science and Engineering, Lehigh University, 5 East Packer Avenue, Bethlehem, PA 18015, USA
*Email: nis212@lehigh.edu

## 2.1 Context and Introduction

This chapter provides an overview of various techniques for the formation of ultrathin oxide layers for applications in solid-state, inorganic photovoltaic (PV) and photoelectrochemical (PEC) devices. After first motivating the use of ultrathin oxides in PV and PEC devices, we explain some of their specific functionalities that are used to improve the performance of these technologies. We then highlight various synthetic methods for film growth and key property measurements. Finally, we discuss three case studies involving corrosion prevention, surface (electronic) passivation, and selective carrier contacts.

### 2.1.1 Silicon and III–V Photovoltaics and Photoelectrochemistry

This chapter focuses on the intersection of ultrathin oxide films and applications in PV and PEC devices that utilize Si or III–V semiconductors.

Energy and Environment Series No. 30
Ultrathin Oxide Layers for Solar and Electrocatalytic Systems
Edited by Heinz Frei and Daniel V. Esposito

Published by the Royal Society of Chemistry, www.rsc.org

The focus on Si and III–V materials is due to the content of other chapters and the large body of work on Si and III–V materials for this application. Further, PV and PEC devices based on these materials rely almost solely on single crystals and the materials are subject to (generally unfavorable) oxidation and corrosion, such as the formation of silicon oxides, or gallium oxides for Si and Ga–group V-based devices. Finally, Si and many III–V semiconductors possess similar crystal structures and are widely available as commercial single crystals. Thus, a significant body of work exists on the employment of thin oxide films on these semiconductors.

### 2.1.2 Functionalities of Ultrathin Films in PV and PEC Devices

Ultrathin oxide films can play a number of roles in PV and PEC devices. Here we define the vocabulary and basic idea of these roles (Figure 2.1). First, films can offer *chemical protection*, which inhibits chemical (corrosion or otherwise) reactions of the underlying material. This functionality is important for both PV and PEC devices, but has a central role in the latter, since semiconductors are often immersed in aqueous solutions, which sometimes have extreme pH values. Second, films may offer *electrical passivation*, which generally slows carrier recombination at the interface between the film and semiconductor relative to an unpassivated surface. This passivation functionality is essential for PV and PEC systems because recombination at material interfaces and surfaces will, in general, lower efficiencies. Electrical passivation can result from net charge at the interface and/or changes in chemical bonding that remove or alter interfacial electrical traps that aid recombination. Since PV and PEC applications require the generation of a net potential difference between two electrodes, there needs to be some asymmetry in the device. Films can introduce an asymmetry by modifying the space charge layer at a surface or by allowing for *selective transport* of one carrier, such as the selective uptake and extraction of valence band holes

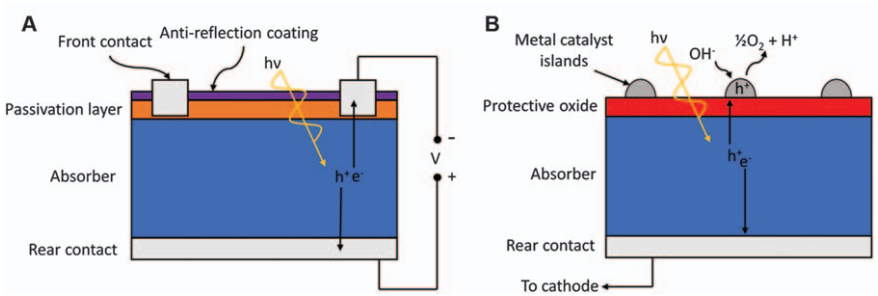


**Figure 2.1** Schematic cross-sections of (A) a potential photovoltaic (PV) configuration, where oxide thin films can be used as passivation layers, tunnel layers, and anti-reflective coatings, and (B) a potential photoelectrochemical (PEC) configuration, where protective oxide films can be used to prevent corrosion of the absorber in addition to providing many of the same benefits as oxide coatings in PV cells.

(*i.e.* a hole-selective contact). Finally, both PV and PEC systems rely on photoexcitation as a source of generating a chemical potential difference, so thin films can have *antireflective properties* or other optical effects that maximize photon absorption in the desired region.

### 2.1.3 Why Oxides for These Applications?

One might ask, "Why use oxides for these applications to achieve these desired effects?". Surely, it is not only oxides that can achieve these functionalities; for example, hydrogenated amorphous silicon (a-Si : H) thin films provide excellent passivation of crystalline silicon.[1] As discussed in Chapter 1, there are several key reasons for the use of oxides, including their ease of synthesis, stability, optical transparency, and, in some cases, amorphous structure. As we shall see in the next section, there are a host of methods for the synthesis of oxide thin films, including some that are not generally transferable to non-oxides, such as solution processing. This ease of synthesis is directly tied to another common advantage of oxide materials: their high degree of stability. For PV and PEC applications, materials are subject to illumination, mild temperatures, and atmospheric and/or aqueous conditions. These situations generally favor oxides from a thermodynamic stability point of view. Therefore, by applying oxide thin films that may already be in their lowest thermodynamic energy states in terms of composition (as opposed to composition *and* structure), chemical stability may be enhanced. Oxides are generally transparent to much or all of the visible light spectrum, further making them useful in photon-absorbing systems described here. Finally, the high energy for bond rearrangement in many oxides (particularly aluminum oxide) often results in amorphous structures, which have the advantages of (1) avoiding the need for lattice matching to crystalline substrates and (2) excellent diffusion barrier properties.[2,3]

## 2.2 Recent Developments in the Synthesis of Ultrathin Oxide Layers

This section provides an overview of methods for the synthesis of oxide thin films while highlighting their applicability, advantages, and disadvantages for PV and PEC applications, primarily as applied to Si and III–V semiconductor absorbers. This section is not meant to be all-encompassing, and additional emphasis is placed on *newer* techniques and variations, and also techniques that are particularly well suited to PV and PEC applications. For additional information, the reader is referred to the several texts on the subject of film growth.[4,5]

### 2.2.1 Physical Vapor Deposition

First, we discuss physical vapor deposition (PVD) techniques, the simplest of which is thermal evaporation. Oxide films can be grown by thermal

evaporation; however, several issues can arise, including loss of oxygen from the source material as it is heated, and involatility of the oxide source material. To address the former issue, small amounts of oxygen can be introduced into a vacuum evaporation chamber ($1\times10^{-4}$–$1\times10^{-5}$ Torr) to provide a constant background of oxygen that will become incorporated into the film. There are a few notable compositions that appear to be well suited for vacuum evaporation, including $MoO_x$, which is relevant for hole collection/injection layers.[6] This technique has the advantage of being fairly simple and imposes little or no damage to the substrate, aside from being exposed to the radiative heating of the evaporation source. Electron beam evaporation also vaporizes material thermally, but provides more localized heating than thermal evaporation. The electron beam can ionize species in the vapor phase, and will often cause X-ray emission from the source material that impinges on the substrate. As with all vacuum techniques, there is a cost associated with equipment and limitations on throughput. Additionally, transport of source material in PVD processes occurring at high-vacuum pressures ($1\times10^{-6}$ Torr) and below is *line of sight*, which does not easily allow for conformal growth on non-planar surfaces.

Closely related to vacuum evaporation is molecular beam epitaxy (MBE), in which ultrahigh vacuum conditions are accessed and often supplemented with vapor-phase $O_2$, $O_3$, or O plasma.[6,7] Highly controlled fluxes of pure metals, or in some cases molecular precursors,[6] are directed at a sample surface. Typically, in MBE, samples are heated to modest or high temperatures for the purpose of achieving surface atom diffusion rates high enough to achieve epitaxy. Oxide-based MBE has attracted a massive amount of attention in recent years owing to various emergent physical properties (correlated electron effects, ferroelectrics, *etc.*), and the unit cell level of specificity that allows the creation of complex superlattices.[8] Oxide-based MBE has not been widely used in PV and PEC applications based on Si and III–V semiconductors, possibly owing to high system costs and the generally high substrate temperatures used. In one example, $SrTiO_3$ was grown epitaxially *via* MBE on Si for a stabilized photocathode.[6] Certain advantages of MBE may exist in these applications, including the ability to grow single-crystal epitaxial films with appropriately lattice-matched oxides, which may provide a high degree of chemical protection and a low density of interfacial structural and electronic defects.

### 2.2.2 Chemical Vapor and Atomic Layer Deposition

The use of chemical vapor deposition (CVD) and related techniques, such as atomic layer deposition (ALD), has received considerable attention with respect to the growth of oxide films for PV and PEC applications. In chemical vapor-based techniques, one or more precursors are dosed on a sample surface and vapor–surface (ALD and CVD) and/or vapor–vapor (CVD) chemical reactions occur. Typically, CVD techniques operate at higher pressure than vacuum evaporation, often using an inert carrier gas.

Thus, CVD techniques are capable of coating non-planar surfaces with better uniformity than line-of-sight techniques.

ALD has attracted increasing attention as a versatile approach for growing ultrathin oxide films in recent years. In ALD, two or more self-limiting surface chemical reactions result in thin-film growth.[9,10] For example, the growth of aluminum oxide, a commonly considered oxide for PV and PEC applications, can be achieved by the following method (Figure 2.2): (1) flowing trimethylaluminum vapor in an inert carrier gas over a substrate, resulting in approximately one monolayer of chemisorbed TMA molecules; (2) purging out remaining unreacted TMA molecules; (3) flowing water vapor (or another O source) over the substrate, generating OH-terminated surfaces; and (4) purging out remaining O precursor. This process is then repeated, and typically results in the addition of ~1 Å of material for each cycle of steps 1–4. Currently, almost any metal oxide can be grown using ALD, and in many cases a variety of precursors are available, which may impact the structure, chemistry, and properties of the grown film.[11]

### 2.2.2.1 *Advantages of ALD*

ALD boasts several advantages that explain the recent flurry of interest in the technique. Because each ALD cycle deposits a (generally) known and consistent amount of material, films of precise thickness can be deposited, even on the

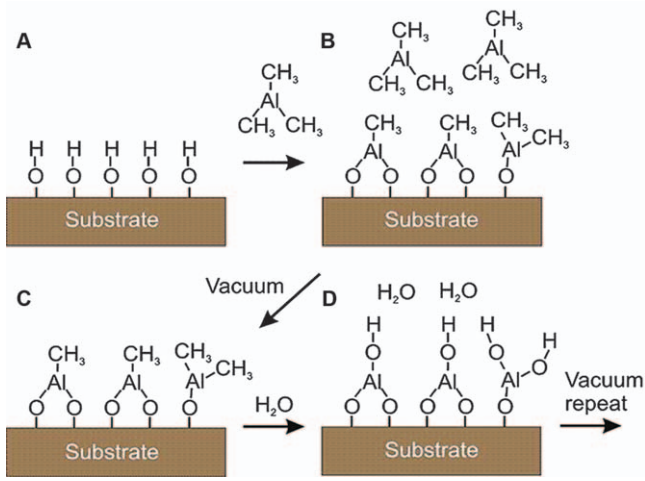


**Figure 2.2** Schematic of the ALD process showing (A) initially OH-terminated substrate, (B) exposure to trimethylaluminum vapor, resulting in an approximate self-limited monolayer, (C) removal of non-bound trimethylaluminum species, and (D) exposure to water to hydrolyze remaining methyl groups, reproducing a similar OH surface to (A). The key differentiating feature of ALD over CVD is the sequential exposure to one or more reactants that form self-limiting monolayers. Thus, the trimethylaluminum and water can be substituted for other precursors to modify the film composition and structure.

sub-nanometer scale.[9] While MBE can achieve similar precision, MBE utilizes *flux* control whereas ALD utilizes *self-limiting chemical reactions* for control of film thickness. The fact that only surface chemical reactions occur in ALD allows for conformal deposition on high aspect ratio substrates, provided that there is sufficient time for precursor diffusion into and out of openings.[12] Finally, low-vacuum conditions are often used along with a carrier gas, so pumping requirements and tool costs are not as high as in (for example) MBE. Precursor decomposition must be avoided, however, which places an upper limit on the sample temperature during growth that corresponds to the decomposition temperature of the metal precursor, or desorption of the film, whichever is lower. A lower temperature limit also exists where insufficient thermal energy or precursor condensation occurs, disrupting the ideal ALD process. Finally, in the case of thermal ALD, generally little damage is done to the substrate owing to the low energy of incoming precursors. A potential concern with the growth of oxides is the use of reactive oxidizing species, including water and ozone, which may oxidize the substrate during growth.

#### *2.2.2.2 Spatial ALD*

Two different techniques within ALD have emerged for deposition on non-powder, monolithic substrates: temporal and spatial ALD. Temporal ALD is the most common subset, where the sample is stationary and each reactant flows through the chamber at a different time (hence *temporal*). An example of this is a fixed tubular reactor.[13] More recently, partly in an effort to speed up deposition processes, spatial ALD has emerged, in which the sample is moved through different *spatial* zones where it is exposed to different precursors.[14,15] One scenario for spatial ALD consists of a sample that is on a circular chuck, which is rotated between different zones that consist of either precursor vapors or inert gas purges.[16] Thus the sample can be quickly rotated, resulting in higher deposition rates (thickness per unit time) even if the growth per cycle (thickness per cycle) is the same as for a similar chemistry in temporal ALD. Spatial ALD is of particular interest where thicker films are needed or where short deposition times are desirable.

#### *2.2.2.3 Area-selective ALD*

Another recent development within the ALD community is area-selective ALD.[16] This development parallels other selective area growths where film species do not nucleate on one surface but do nucleate on another surface, owing to some differences in surface chemistry. Hence, by patterning the surface chemistry, the ALD film can be placed just ''where you want it''. This may be useful for applying protective films selectively on certain regions, or for limiting the thickness of an ALD film on regions that require low resistance to electron transfer. It should be noted that area-selective deposition has not been widely explored for use in semiconductor light absorbers so far, but it has been of high interest for nanoelectronics.[16]

#### 2.2.2.4 Plasma-enhanced ALD

In ALD,[17,18] CVD, and PVD in general, it is possible to provide a non-thermal energy input during film growth in the form of a plasma-enhanced (PE) process. An oxygen plasma, for example, will increase the chemical reactivity of oxygen and can be useful in eliminating carbon and other precursor by-products and will increase the overall reaction rate. In PE-CVD, generally the plasma is active during the entire deposition process, whereas in PE-ALD, the plasma is applied during only the oxygen (or non-metal) precursor exposure step. This process flow prevents the metal precursor from being exposed to the plasma, which would result in decomposition and CVD-like growth. As in sputtering, the reactor geometry, plasma power, system pressure, and substrate bias play a large role in the interaction of the plasma with the growing film.

Recently, the use of RF biasing, which is common in sputtering systems, has been studied in PE-ALD and has proven to be a useful parameter that can be tuned to change film properties, such as density and crystal structure. For example, increasing RF bias can have the effect of initially increasing film density and refractive index and subsequently, at sufficiently high bias, can decrease these parameters. Further, RF bias can change the phase of the film from the unbiased case, such as from anatase (0 V) to rutile (>200 V) for $TiO_2$ ALD.[19]

### 2.2.3 Wet Chemical Deposition and Substrate Oxidation

#### 2.2.3.1 Electrochemical Oxidation/Anodization

A variety of oxide growth techniques do not fall into the vacuum deposition category and may boast advantages of lower cost and easier scalability. Here we differentiate from earlier deposition techniques because the following involve oxide formation *via* substrate oxidation or solution (wet chemical) methods for deposition.

Anodization of metals and semiconductors can create insoluble films or soluble corrosion products. In the former case, the insoluble films can passivate the surface and prevent continual corrosion. Well-known cases include the anodization of aluminum, which generally results in the formation of nanoporous aluminum oxide.[20] Since aluminum oxide is a common passivating layer in Si PV studies, anodization of aluminum has been explored for the formation of passivating alumina layers.[21] However, anodization of other metals such as tin[22] has been explored for the formation of a semiconductor oxide.

The most frequently employed absorber, silicon, also has a long history of anodization studies. For example, anodization of hydrogen-terminated silicon in HF-containing solutions can result in an Si monohydride surface[23] which presents a low density of electronic defects. Although also resulting in some oxidic film formation, anodization of silicon can be used to create porous silicon, similarly to the case of anodization of aluminum.[24] Additionally, electrochemical anodization of Si can form a passivating oxide with pinholes similar to those in anodic alumina. Metals can then be

electrodeposited within the pinholes for the deposition of catalyst or Schottky barrier-forming metals.[25,26] Despite the ability to anodize semiconductors to create thin films of oxides or porous layers, passivation and protection using such techniques are not frequently employed.

#### *2.2.3.2 Thermal and Wet Chemical Oxidation*

Thermal and wet chemical oxidation of substrates (here semiconductors) are other routes to forming thin oxide films. Wet chemical oxide growth of thin 1–2 nm silicon oxide ($SiO_x$) layers on silicon substrates can be achieved by contact with ammonium hydroxide, hydrogen peroxide, nitric acid, and other species at room temperature or slightly elevated temperatures. Thermal oxidation of silicon is an extremely well-developed process stemming from the use of oxide films as oxide barriers for dopant diffusion in the integrated circuit industry. Although a thin native $SiO_x$ layer forms spontaneously in air on freshly exposed Si surfaces, thermal oxidation[27] and nitric acid[28] treatment have been exploited for the purposeful creation of slightly thicker, and likely more stoichiometric, $SiO_x$ films as tunnel layers to passivate electrical contacts. Even focusing strictly on passivation, various wet chemical and thermal preparations of $SiO_x$ layers were shown to have a large effect on the retained fixed negative charge after capping the $SiO_x$ layers with alumina.[29] In particular, it was found that thermal oxides sandwiched between Si and alumina resulted in a smaller magnitude of fixed negative charge, relative to various wet chemical approaches to silicon oxide formation.

#### *2.2.3.3 Spin Coating, Solution Deposition*

Thin oxide films can be created using solution-based deposition, such as spin coating or dip coating, and may make use of metal oxide clusters[30] or metal alkoxides as precursors.[28] Sol–gel techniques can even be conducted in a layer-by-layer fashion similar to ALD, although conducted using liquid solutions rather than vapor-phase precursors.[31] These methods have the advantage of not requiring vacuum chambers or expensive film growth tools. For a detailed description of these methods, the reader is referred to Chapter 9, which provides a comprehensive overview of sol–gel and condensed layer deposition methods for fabricating ultrathin oxide coatings.

## 2.3 Case Studies of Thin Oxide Layers

### 2.3.1 Thin Oxide Protective Films for Semiconductor Photoelectrochemistry

Although most current applications of semiconductors, such as in microelectronics, power electronics, and even photovoltaics, do not expose the semiconducting material to chemically corrosive environments, there are

emerging applications in which semiconductor corrosion is a significant problem. For example, photoelectrochemical devices, such as solar fuel generators,[32] and electrochemical sensors[33] operate in an environment where the semiconductor is in contact or nearly in contact with aqueous or otherwise corrosive media. For example, exposure of silicon to aqueous solutions can result in the formation of insulating silicon oxides and/or dissolution of Si oxidation products, both of which can degrade the performance of a device or damage it. Therefore, many different coating strategies have been employed, with varied success, to prevent chemical corrosion of silicon and other semiconductor surfaces. We summarize some of the particularly notable examples here, but also point the reader to several reviews on this topic.[34–39]

Some of the first reports of attempts to stabilize semiconductor photoelectrodes involved the use of metal films that were thin enough be partially transparent. These reports were followed by the use of oxide layers that were typically created using sputtering, thermal or electron beam evaporation, or electrodeposition, and achieved mild success. However, the need for pinhole-free films of highly chemically stable oxides was still apparent.

In 2011, McIntyre and co-workers reported the use of ALD-grown $TiO_2$ films to protect n-Si photoanodes.[40] $TiO_2$ in this case was used as a tunneling protective layer, which almost necessitated the use of ALD to control the film thickness in the ~2 nm region. The chosen composition of $TiO_2$ was also important owing to the wide window of stability of $TiO_2$ (solid) in aqueous media.[41] Following the highly promising results with $TiO_2$ tunnel layers, Hu *et al.* demonstrated highly stable photoanodes using $TiO_2$ grown by ALD but in a much wider thickness range that precluded direct tunneling from the semiconductor to the surface-bound Ni catalyst.[42] In this case, a defect-mediated transport was active that allowed the use of thicker, and thus possibly more protective, layers of $TiO_2$ (Figure 2.3). The mechanisms of charge carrier transport may be due to conduction band electrons[43] or

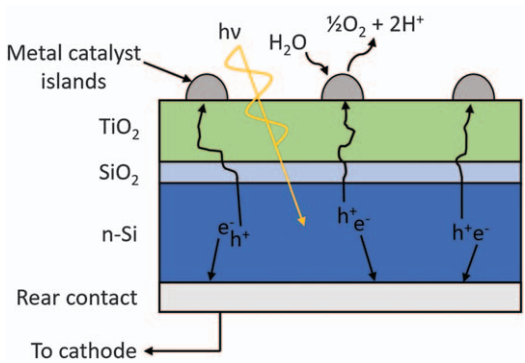


**Figure 2.3** Schematic cross-section of a $TiO_2$-protected photoanode that collects holes within the $TiO_2$ layer and transports them to a surface-bound metallic co-catalyst that carries out the oxygen evolution reaction.

involve a defect-mediated process.[44,45] Further work has shown the importance of the thickness of the $SiO_2$ interfacial layer and the $TiO_2$ protective film, and also incorporation of Ir into the $TiO_2$ layer.[46,47] Other oxides have also been explored as protective films using ALD and sputtering that were successful in providing enhanced stability, including NiO, MnO, $CoO_x$, and FeOOH.[48–51]

ALD has proven to be an important technique for semiconductor photoelectrode stability enhancement owing to its ability to control thickness on the sub-nanometer scale, the mild conditions of the deposition technique (typically low-temperature thermochemical reactions), the diversity of oxides that can be grown, and the conformality of the grown films even on high aspect ratio substrates, as evidenced by work on nanopillars and anodic alumina.[12,52] The aspect of conformal growth is particularly important when considering structured semiconductor electrodes such as nanowires and nanoporous semiconductors.[53,54]

Remaining challenges mostly relate to failure of these films, which may include permeation of the electrolyte through defects, such as pinholes, that eventually corrode the underlying semiconductor layer, slow dissolution of the protective film, or permeation of solution species through the bulk of the film. Further, control of the interfacial chemistry between the semiconductor absorber and protective film is important in controlling interface recombination and band alignments and should also be carefully considered. Nonetheless, the use of thin oxide coatings, and especially using ALD, have led to enormous increases in semiconductor photoelectrode stability in contact with aqueous media, in some cases showing >2200 h stability during the water oxidation reaction.[52]

### 2.3.2 Surface Passivation of Silicon

Surface passivation, defined here as the decrease in electron–hole recombination rates at interfaces, is a key aspect to achieving high efficiency in photovoltaics. The use of the term *passivation* is to be distinguished from that of *protection*, although passivation is sometimes used to mean protection in other texts. Surfaces and interfaces are two-dimensional defects and generally create electronic states within the energy band gap that can increase recombination rates relative to the bulk. The chemistry and structure of the interface will dictate the precise extent to which electron–hole recombination will occur there. Generally, the passivation of dangling bonds by reaction of the bonds with an oxide or hydrogen results in the elimination or suppression of defect levels located within the band gap and decreases recombination rates.[55] A key example that is useful for passivation of Si surfaces and in the bulk of amorphous silicon is the use of hydrogen.[56] Hydride-terminated Si crystalline surfaces are known to have lower surface recombination rates than Si surfaces with a native $SiO_x$ layer.[57] Another widely used technology for Si is the use of heterostructures between amorphous silicon and crystalline silicon. In these structures, the

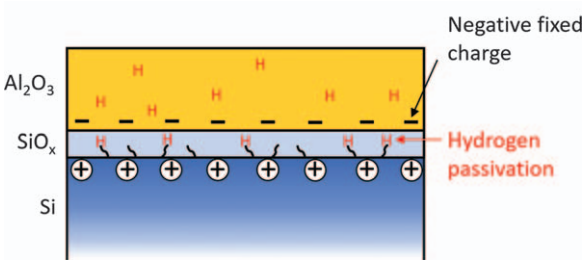


**Figure 2.4** Schematic cross-section of ALD alumina film on a silicon substrate. Notable elements in the heterostructure include the large negative fixed charge at the interface and the presence of H that passivate dangling Si bonds.

hydrogenated amorphous Si provides hydrogen to passivate the interface between amorphous and crystalline silicon.

Owing to their optical transparency and often simple deposition, ultrathin metal oxide films have seen increasing use as surface passivation layers, with aluminum oxide as a notable example (Figure 2.4).[58,59] ALD alumina often retains some H, largely through the incorporation of OH groups from water (thermal ALD)[60] or decomposed $CH_3$ species (plasma ALD). Upon annealing, the H present can migrate to the $Si/SiO_x$ surface and passivate electronic defects; this process is referred to as ''chemical passivation''. Evidence for the presence of H supplied by ALD aluminum oxide has been observed in effusion studies[61] and also time-of-flight secondary ion mass spectrometry.[62]

Another important aspect of aluminum oxide passivation layers is the ability of the alumina/silicon interface to retain a large amount of fixed negative charge ($\sim 5 \times 10^{12}\,cm^{-2}$).[63–66] This large amount of interface charge can induce band bending by repelling electrons from the surface, thus decreasing interface recombination purely through an electrostatic effect; this phenomenon is referred to as ''field effect'' passivation. The precise physical origin of the fixed negative charge has not been identified. However, it is known that the charge lies at the alumina/silicon interface,[63] exists in ultrathin (1 nm) alumina layers,[67] and is diminished when the alumina layer is separated from the silicon by more than a few nanometers of $SiO_2$ or $HfO_2$.[68,69] Evidence for the formation of a fixed charge even during the first exposure of the surface to trimethylaluminum during growth was shown by *in situ* transconductance measurements.[70] Despite the dominance of ALD alumina as a passivating film for silicon, a wide array of other metal oxides have been examined with various degrees of success, including $TiO_2$, $Nb_2O_5$, and $HfO_2$.[71–73]

### 2.3.3 Selective Contact (Charge-extracting) Layers as Applied to Silicon

The use of metal oxide thin films as carrier-selective contacts has the potential to increase the cost-effectiveness of silicon and other photovoltaic technologies.

Selective contacts extract one type of charge carrier (either electrons or holes) from the absorber layer while blocking the other. Traditionally, this carrier separation has been accomplished by diffused p–n junctions within the absorber layer. The high temperatures required for dopant drive-in necessitate processing in highly clean environments, which are expensive to maintain. Cost reduction, while maintaining high efficiency, thus motivates the development of alternative cell technologies to diffused p–n junctions. With regard to efficiency, significant electron–hole recombination occurs at the interfaces between metal contacts and crystalline silicon absorbers. Creation of a heterojunction with a thin film can serve to passivate defects at the semiconductor surface, reducing this recombination and improving cell efficiency.

While intrinsic hydrogenated amorphous silicon, a-Si : H(i), is used as a passivating layer, p- and n-type a-Si : H layers are often deposited as hole- and electron-selective contacts, respectively. In 2017, the efficiency record for a single-junction c-Si cell was broken using p- and n-type a-Si : H contacts, each passivated with a-Si : H(i) interlayers.[74] These materials are not without their drawbacks, however. Owing to the relatively small band gap of a-Si, such layers are well known to absorb light parasitically, decreasing the amount of charge carrier generation in the c-Si absorber. Therefore, in order to create higher efficiency PV devices, it is desirable to replace a-Si with wider band gap-selective contacts, and several oxide thin films have emerged as promising candidates.

Selectivity in oxides (usually transition metal oxides) originates from relative band offsets between the oxide material and the semiconductor absorber. Electron-selective contacts such as $TiO_2$ exhibit a small conduction band offset from Si while maintaining a large valence band offset (Figure 2.5).[75] The oxide therefore easily extracts photogenerated electrons in the conduction band while blocking the corresponding holes in the valence band. Similarly, certain hole-selective contacts such as NiO maintain a small valence band offset with Si and a large conduction band offset.[76]

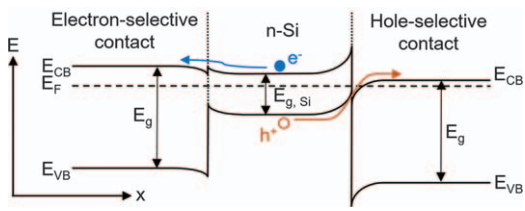


**Figure 2.5** Energy band diagram of a possible configuration of selective contacts to an Si light absorber. On the left, a nearly continuous conduction band between the electron-selective contact and Si allows for electron collection, but presents a large barrier to hole transfer from the Si valence band. This configuration is typical of $TiO_2$, which has a similar electron affinity to that of Si. On the right, holes are collected by recombination with electrons in the conduction band of a high work function and wide band gap n-type semiconductor. This configuration is similar to the proposed model for $MoO_x$ contacts to Si.

Molybdenum oxide is an example of a material that possesses hole selectivity because of its large work function.[77] Such oxides establish the Fermi level near the valence band maximum of silicon, inducing band bending and hole accumulation at the interface. The holes are then able to be extracted through the oxide conduction band (Figure 2.5). Vapor-phase deposition of these materials results in oxygen vacancies, hence in this context molybdenum oxide is often referred to as $MoO_x$ instead of $MoO_3$ (where $x<3$). These vacancies act as electron donors, giving the oxide an n-type characteristic and creating a defect band that assists hole transport through trap-assisted tunneling. However, a sufficiently high density of oxygen vacancies will reduce the material's work function[74] and inhibit carrier selectivity.[78]

Transition metal oxide contacts provide various degrees of passivation at Si interfaces. Low recombination rates have been observed at direct contacts between Si and ALD $TiO_2$.[79] $MoO_x$, on the other hand, exhibits a low charge carrier lifetime (high recombination rates) in direct contact with Si.[80] For this reason, a-Si : H(i) interlayers have been introduced to reduce recombination at $MoO_x$ contacts. In addition to the parasitic absorption mentioned previously, degradation of $MoO_x$ with annealing has been linked to the a-Si : H buffer.[81] Without n- or p-type capping layers, a-Si : H(i) passivating layers are also known to undergo light-induced degradation.[82] Thus, $Al_2O_3$ layers thin enough to support tunneling (<2 nm) have recently been introduced as an alternative passivating interlayer for $MoO_x$ contacts.[83,84] $Al_2O_3$ tunnel layers have also been used to improve the passivation of $TiO_2$ and other types of contacts such as polycrystalline Si.[85,86] It has been suggested that, in the case of hole-selective contacts, the high density of fixed negative charges in annealed $Al_2O_3$ may enhance band bending and hole selectivity in its repulsion of electrons from the interface.

In addition to Mo, Ti, and Ni oxides, several other metal oxides have shown promise as selective contacts, including tantalum oxide[87] and niobium oxide[88] as electron-selective contacts and copper oxide,[89] tungsten oxide,[90] and vanadium oxide[90] as hole-selective contacts. Regardless of which materials ultimately yield the best-performing devices, transition metal oxide selective contacts represent a promising technology for next-generation solar cells.

## 2.4 Future Outlook

Ultrathin metal oxide films have many important roles in photovoltaic and photoelectrochemical systems and these roles are likely to expand further in the coming years. The fact that many metal oxides are chemically stable in air and in many aqueous media alone makes them desirable. Having a component of a system that is highly non-reactive can lead to a long lifetime, similar to that of silicate window glass or oxide-based rocks. This stability also presents the argument that *making* these materials should be low cost and accessible. Indeed, simply the use of metal salts and their decomposition into oxide films requires little expertise or equipment.

With regard to techniques, numerous processes for growing or depositing thin oxide films have been developed. Although many are still used today, ALD, MBE, and pulsed laser deposition are most often employed, possibly owing to the large degree of thickness control characteristic of these techniques. Although they are fairly well-developed techniques, it can be expected that they will enjoy considerably more development over the coming years, in terms of their capabilities and the understanding of the processes.

The stability aspect of many metal oxide films has been a crucial determinant in their adoption as protective films. Not only do they tend to be resistant to further oxidation, but in the case of aluminum oxide and several others they are thermodynamically stable when placed in contact with Si and other non-oxide semiconductors. If PEC devices are to provide us with solar-derived chemical fuels, the stability of these films must be evaluated on a time frame of tens of years, rather than hundreds or thousands of hours. In PEC devices in particular, the challenge of simultaneously maintaining protection, stability, optical transparency, and carrier conductivity can be daunting, yet several compositions outlined above have satisfied these criteria for time frames of 100 + h. Future efforts will likely be focused on improving these figures of merit over longer time periods, and on developing a more detailed understanding of failure mechanisms.

Regarding passivation and selective contacts for silicon photovoltaics, oxide films have moved to replace non-oxide components, such as silicon nitride passivation layers, amorphous silicon heterostructures, and crystalline silicon p–n homojunctions. Aluminum oxide has become a key material for passivation and it has been making its way into commercial PV systems. Selective contact materials still present some challenges in understanding their precise modes of operation, and how they are best integrated with crystalline silicon absorbers.

Finally, a notable aspect of many of the thin oxide films discussed in this chapter is that they are structurally amorphous and lack order beyond 5–10 Å. Although their amorphous structures do not preclude their use in applications, they do present challenges to detailed understanding at the atomic level. For example, although first-principles (quantum-chemical) calculations are routinely used to obtain accurate information about bonding, defect levels, band structures, *etc.*, in crystalline materials, such calculations are difficult in amorphous systems because of their intrinsically ill-defined structure and heterogeneity at the atomic scale. If structural models do exist, they are generally large in order to capture the diversity of structural/bonding motifs within a real amorphous solid. Therefore, the first-principles calculations involve more atoms than in a typical crystal, hence they are more expensive and time consuming. Further understanding of the details of structure within these amorphous metal oxide films and translating that structural knowledge into detailed physical understanding are critical.

## Acknowledgements

The authors gratefully acknowledge funding from the National Science Foundation (NSF 1605129). The material in this chapter is based upon work supported by the US Department of Energy Solar Energy Technology Office program under Award Number DE-EE0008743. We thank Connor Leach for assistance with the production of the figures.

## References

1. J. I. Pankove and M. L. Tarng, *Appl. Phys. Lett.*, 1979, **34**, 156–157.
2. P. F. Carcia, R. S. McLean, M. H. Reilly, M. D. Groner and S. M. George, *Appl. Phys. Lett.*, 2006, **89**, 031915.
3. M. D. Groner, F. H. Fabreguette, J. W. Elam and S. M. George, *Chem. Mater.*, 2004, **16**, 639–645.
4. D. L. Smith, *Thin-Film Deposition: Principles and Practice*, 1st edn, 1995.
5. M. Ohring, *Materials Science of Thin Films*, Elsevier, 2002.
6. C. Battaglia, X. Yin, M. Zheng, I. D. Sharp, T. Chen, S. Mcdonnell, A. Azcatl, C. Carraro, B. Ma, R. Maboudian, R. M. Wallace and A. Javey, *Nano Lett.*, 2014, **14**, 967–971.
7. Y. E. Suyolcu, G. Christiani, P. A. van Aken and G. Logvenov, *J. Supercond. Novel Magn.*, 2020, **33**, 107–120.
8. R. Ramesh and D. G. Schlom, *Nat. Rev. Mater.*, 2019, **4**, 257–268.
9. S. M. George, *Chem. Rev.*, 2010, **110**, 111–131.
10. A. W. Ott, J. W. Klaus, J. M. Johnson and S. M. George, *Thin Solid Films*, 1997, **292**, 135–144.
11. V. Miikkulainen, M. Leskelä, M. Ritala and R. L. Puurunen, *J. Appl. Phys.*, 2013, 021301.
12. J. W. Elam, D. Routkevitch, P. P. Mardilovich and S. M. George, *Chem. Mater.*, 2003, **15**, 3507–3517.
13. J. W. Elam, M. D. Groner and S. M. George, *Rev. Sci. Instrum.*, 2002, **73**, 2981.
14. D. Muñoz-Rojas and J. Macmanus-Driscoll, *Mater. Horizons*, 2014, **1**, 314–320.
15. P. Poodt, D. C. Cameron, E. Dickey, S. M. George, V. Kuznetsov, G. N. Parsons, F. Roozeboom, G. Sundaram and A. Vermeer, *J. Vac. Sci. Technol., A*, 2012, **30**, 010802.
16. P. Poodt, A. Lankhorst, F. Roozeboom, K. Spee, D. Maas and A. Vermeer, *Adv. Mater.*, 2010, **22**, 3564–3567.
17. H. Kim and I. K. Oh, *Jpn. J. Appl. Phys.*, 2014, **53**, 3–4.
18. H. B. Profijt, S. E. Potts, M. C. M. van de Sanden and W. M. M. Kessels, *J. Vac. Sci. Technol., A*, 2011, **29**, 050801.
19. T. Faraz, H. C. M. Knoops, M. A. Verheijen, C. A. A. van Helvoirt, S. Karwal, A. Sharma, V. Beladiya, A. Szeghalmi, D. M. Hausmann, J. Henri, M. Creatore and W. M. M. Kessels, *ACS Appl. Mater. Interfaces*, 2018, **10**, 13158–13180.

20. A. Ruiz-Clavijo, O. Caballero-Calero and M. S. Martín-González, *Nanoscale*, 2021, **13**, 2227–2265.
21. P. H. Lu, K. Wang, Z. Lu, A. J. Lennon and S. R. Wenham, *IEEE J. Photovoltaics*, 2013, **3**, 143–151.
22. D. A. Afanasyev, N. K. Ibrayev, G. S. Omarova and Z. K. Smagulov, in *IOP Conference Series: Materials Science and Engineering*, Institute of Physics Publishing, 2015, vol. 81, p. 012118.
23. Z. Yamani, W. H. Thompson, L. AbuHassan and M. H. Nayfeh, *Appl. Phys. Lett.*, 1997, **70**, 3404–3406.
24. T. Unagami, *J. Electrochem. Soc.*, 1980, **127**, 476–483.
25. M. Aggour, K. Skorupska, T. Stempel Pereira, H. Jungblut, J. Grzanna and H. J. Lewerenz, *J. Electrochem. Soc.*, 2007, **154**, H794.
26. H. J. Lewerenz, C. Heine, K. Skorupska, N. Szabo, T. Hannappel, T. Vo-Dinh, S. A. Campbell, H. W. Klemm and A. G. Muñoz, *Energy Environ. Sci.*, 2010, **3**, 748–760.
27. A. S. Kale, W. Nemeth, S. P. Harvey, M. Page, D. L. Young, S. Agarwal and P. Stradins, *Sol. Energy Mater. Sol. Cells*, 2018, **185**, 270–276.
28. C. J. Brinker, A. J. Hurd, P. R. Schunk, G. C. Frye and C. S. Ashley, *J. Non. Cryst. Solids*, 1992, **147–148**, 424–436.
29. B. Nemeth, S. P. Harvey, J. V. Li, D. L. Young, A. Upadhyaya, V. LaSalvia, B. G. Lee, M. R. Page and P. Stradins, in *Energy Procedia*, Elsevier Ltd, 2017, vol. 124, pp. 295–301.
30. Z. L. Mensinger, J. T. Gatlin, S. T. Meyers, L. N. Zakharov, D. A. Keszler and D. W. Johnson, *Angew. Chemie Int. Ed.*, 2008, **47**, 9484–9486.
31. I. Ichinose, H. Senzu and T. Kunitake, *Chem. Mater.*, 1997, **9**, 1296–1298.
32. *Integrated Solar Fuel Generators*, ed. I. D. Sharp, H. A. Atwater and H.-J. Lewerenz, Royal Society of Chemistry, Cambridge, 2018.
33. N. Chaniotakis and N. Sofikiti, *Anal. Chim. Acta*, 2008, **615**, 1–9.
34. M. F. Lichterman, K. Sun, S. Hu, X. Zhou, M. T. McDowell, M. R. Shaner, M. H. Richter, E. J. Crumlin, A. I. Carim, F. H. Saadi, B. S. Brunschwig and N. S. Lewis, *Catal. Today*, 2016, **262**, 11–23.
35. F. Nandjou and S. Haussener, *J. Phys. D: Appl. Phys.*, 2017, **50**, 124002.
36. S. D. Tilley, *Adv. Energy Mater.*, 2019, **9**, 1802877.
37. Y. He, T. Hamann and D. Wang, *Chem. Soc. Rev.*, 2019, **48**, 2182–2215.
38. C. Ros, T. Andreu and J. R. Morante, *J. Mater. Chem. A*, 2020, **8**, 10625–10669.
39. S. Hu, N. S. Lewis, J. W. Ager, J. Yang, J. R. McKone and N. C. Strandwitz, *J. Phys. Chem. C*, 2015, **119**, 24201–24228.
40. Y. W. Chen, J. D. Prange, S. Dühnen, Y. Park, M. Gunji, C. E. D. Chidsey and P. C. McIntyre, *Nat. Mater.*, 2011, **10**, 539–544.
41. G. C. Correa, B. Bao and N. C. Strandwitz, *ACS Appl. Mater. Interfaces*, 2015, **7**, 14816–14821.
42. S. Hu, M. R. Shaner, J. A. Beardslee, M. Lichterman, B. S. Brunschwig and N. S. Lewis, *Science*, 2014, **344**, 1005–1009.

43. W. Cui, T. Moehl, S. Siol and S. D. Tilley, *Sustainable Energy Fuels*, 2019, **3**, 3085–3092.
44. S. Hu, N. S. Lewis, J. W. Ager, J. Yang, J. R. McKone and N. C. Strandwitz, *J. Phys. Chem. C*, 2015, **119**(43), 24201–24228.
45. P. Nunez, M. H. Richter, B. D. Piercy, C. W. Roske, M. Cabán-Acevedo, M. D. Losego, S. J. Konezny, D. J. Fermin, S. Hu, B. S. Brunschwig and N. S. Lewis, *J. Phys. Chem. C*, 2019, **123**, 20116–20129.
46. A. G. Scheuermann, J. P. Lawrence, K. W. Kemp, T. Ito, A. Walsh, C. E. D. Chidsey, P. K. Hurley and P. C. McIntyre, *Nat. Mater.*, 2016, **15**, 99–105.
47. O. L. Hendricks, R. Tang-Kong, A. S. Babadi, P. C. McIntyre and C. E. D. Chidsey, *Chem. Mater.*, 2019, **31**, 90–100.
48. K. Sun, M. T. McDowell, A. C. Nielander, S. Hu, M. R. Shaner, F. Yang, B. S. Brunschwig and N. S. Lewis, *J. Phys. Chem. Lett.*, 2015, **6**, 592–598.
49. J. Yang, K. Walczak, E. Anzenberg, F. M. Toma, G. Yuan, J. Beeman, A. Schwartzberg, Y. Lin, M. Hettick, A. Javey, J. W. Ager, J. Yano, H. Frei and I. D. Sharp, *J. Am. Chem. Soc.*, 2014, **136**, 6191–6194.
50. H. Morisaki, H. Ono, H. Dohkoshi and K. Yazawa, *Jpn. J. Appl. Phys.*, 1980, **19**, L148–L150.
51. N. C. Strandwitz, D. J. Comstock, R. L. Grimm, A. C. Nichols-Nielander, J. Elam and N. S. Lewis, *J. Phys. Chem. C*, 2013, **117**, 4931–4936.
52. M. R. Shaner, S. Hu, K. Sun and N. S. Lewis, *Energy Environ. Sci.*, 2015, **8**, 203–207.
53. M. T. Mayer, C. Du and D. Wang, *J. Am. Chem. Soc.*, 2012, **134**, 12406–12409.
54. N. P. Dasgupta, C. Liu, S. Andrews, F. B. Prinz and P. Yang, *J. Am. Chem. Soc.*, 2013, **135**, 12932–12935.
55. R. S. Bonilla, B. Hoex, P. Hamer and P. R. Wilshaw, *Phys. Status Solidi*, 2017, **214**, 1700293.
56. J. L. Benton, C. J. Doherty, S. D. Ferris, D. L. Flamm, L. C. Kimerling and H. J. Leamy, *Appl. Phys. Lett.*, 1980, **36**, 670–671.
57. E. Yablonovitch, D. L. Allara, C. C. Chang, T. Gmitter and T. B. Bright, *Phys. Rev. Lett.*, 1986, **57**, 249–252.
58. B. Hoex, J. J. H. Gielis, M. C. M. Van De Sanden and W. M. M. Kessels, 2008, **104**, 113703.
59. B. Hoex, S. B. S. Heil, E. Langereis, M. C. M. Van De Banden and W. M. M. Kessels, *Appl. Phys. Lett.*, 2006, **89**, 9–12.
60. C. Guerra-Nuñez, M. Döbeli, J. Michler and I. Utke, *Chem. Mater.*, 2017, **29**, 8690–8703.
61. G. Dingemans, F. Einsele, W. Beyer, M. C. M. Van De Sanden and W. M. M. Kessels, *J. Appl. Phys.*, 2012, **111**, 093713.
62. S. Jakschik, U. Schroeder, T. Hecht, D. Krueger, G. Dollinger, A. Bergmaier, C. Luhmann and J. W. Bartha, *Appl. Surf. Sci.*, 2003, **211**, 352–359.
63. J. a. Aboaf, D. R. Kerr and E. Bassous, *J. Electrochem. Soc.*, 1973, **120**, 1103.

64. Y. N. Dou, Y. He, C. Y. Huang, C. L. Zhou, X. G. Ma, R. Chen and J. H. Chu, *Appl. Phys. A: Mater. Sci. Process.*, 2012, **109**, 673–677.
65. G. Dingemans and W. M. M. Kessels, *J. Vac. Sci. Technol., A*, 2012, **30**, 040802.
66. J. Schmidt, A. Merkle, B. Hoex, M. C. M. van de Sanden, W. M. M. Kessels and R. Brendel, *2008 33rd IEEE Photovolatic Spec. Conf.*, 2008, 1–5.
67. F. Werner, B. Veith, D. Zielke, L. Kühnemund, C. Tegenkamp, M. Seibt, R. Brendel and J. Schmidt, *J. Appl. Phys.*, 2011, **109**, 2–8.
68. N. M. Terlinden, G. Dingemans, V. Vandalon, R. H. E. C. Bosch and W. M. M. Kessels, *J. Appl. Phys.*, 2014, **115**, 033708.
69. D. K. Simon, P. M. Jordan, T. Mikolajick and I. Dirnstorfer, *ACS Appl. Mater. Interfaces*, 2015, **7**, 28215–28222.
70. L. Ju, M. R. Watt and N. C. Strandwitz, *Appl. Phys. Lett.*, 2015, **106**, 61603.
71. J. Cui, T. Allen, Y. Wan, J. Mckeon, C. Samundsett, D. Yan, X. Zhang, Y. Cui, Y. Chen, P. Verlinden and A. Cuevas, *Sol. Energy Mater. Sol. Cells*, 2016, **158**, 115–121.
72. B. Macco, M. Bivour, J. H. Deijkers, S. B. Basuvalingam, L. E. Black, J. Melskens, B. W. H. Van De Loo, W. J. H. Berghuis, M. Hermle and W. M. M. Kessels, *Appl. Phys. Lett.*, 2018, **112**, 242105.
73. J. Gope, Vandana, N. Batra, J. Panigrahi, R. Singh, K. K. Maurya, R. Srivastava and P. K. Singh, *Appl. Surf. Sci.*, 2015, **357**, 635–642.
74. K. Yoshikawa, W. Yoshida, T. Irie, H. Kawasaki, K. Konishi, H. Ishibashi, T. Asatani, D. Adachi, M. Kanematsu, H. Uzu and K. Yamamoto, *Sol. Energy Mater. Sol. Cells*, 2017, **173**, 37–42.
75. S. Avasthi, W. E. Mcclain, G. Man, A. Kahn, J. Schwartz and J. C. Sturm, *Appl. Phys. Lett.*, 2013, **203901**, 1–4.
76. R. Islam, P. Ramesh, J. H. Nam and K. C. Saraswat, in *2015 IEEE 42nd Photovoltaic Specialist Conference, PVSC 2015*, Institute of Electrical and Electronics Engineers Inc., 2015.
77. C. Battaglia, X. Yin, M. Zheng, I. D. Sharp, T. Chen, S. McDonnell, A. Azcatl, C. Carraro, B. Ma, R. Maboudian, R. M. Wallace and A. Javey, *Nano Lett.*, 2014, **14**, 967–971.
78. C. Messmer, M. Bivour, J. Schön and M. Hermle, *Cit. J. Appl. Phys.*, 2018, **124**, 85702.
79. V. Titova, B. Veith-Wolf, D. Startsev and J. Schmidt, in *Energy Procedia*, Elsevier Ltd, 2017, vol. 124, pp. 441–447.
80. T. Zhang, C.-Y. Lee, Y. Wan, S. Lim and B. Hoex, *J. Appl. Phys.*, 2018, **124**, 73106.
81. L. Neusel, M. Bivour and M. Hermle, *Energy Procedia*, 2017, **124**, 425–434.
82. H. Plagwitz, B. Terheiden and R. Brendel, *J. Appl. Phys.*, 2008, **103**, 094506.
83. G. Gregory, C. Feit, Z. Gao, P. Banerjee, T. Jurca and K. O. Davis, *Phys. Status Solidi*, 2020, **217**, 2000093.
84. B. E. Davis and N. C. Strandwitz, *IEEE J. Photovoltaics*, 2020, **10**, 722–728.

85. G. Masmitjà, P. Ortega, J. Puigdollers, L. G. Gerling, I. Martín, C. Voz and R. Alcubilla, *J. Mater. Chem. A*, 2018, **6**, 3977–3985.
86. Z. Xin, Z. P. Ling, P. Wang, J. Ge, C. Ke, K. B. Choi, A. G. Aberle and R. Stangl, *Sol. Energy Mater. Sol. Cells*, 2019, **191**, 164–174.
87. Y. Wan, S. K. Karuturi, C. Samundsett, J. Bullock, M. Hettick, D. Yan, J. Peng, P. R. Narangari, S. Mokkapati, H. H. Tan, C. Jagadish, A. Javey and A. Cuevas, *ACS Energy Lett.*, 2018, **3**, 125–131.
88. B. Macco, L. E. Black, J. Melskens, B. W. H. van de Loo, W. J. H. Berghuis, M. A. Verheijen and W. M. M. Kessels, *Sol. Energy Mater. Sol. Cells*, 2018, **184**, 98–104.
89. X. Zhang, Y. Wan, J. Bullock, T. Allen and A. Cuevas, *Appl. Phys. Lett.*, 2016, **109**, 052102.
90. L. G. Gerling, S. Mahato, A. Morales-Vilches, G. Masmitja, P. Ortega, C. Voz, R. Alcubilla and J. Puigdollers, *Sol. Energy Mater. Sol. Cells*, 2016, **145**, 109–115.

CHAPTER 3

# *Ultrathin Oxides for Solar Cells*

A. F. PALMSTROM* AND M. O. REESE*

National Renewable Energy Laboratory, Denver West Parkway, Golden, CO 80401, USA
*Emails: axel.palmstrom@nrel.gov; matthew.reese@nrel.gov

## 3.1 Passivation Layers

### 3.1.1 Function

The motivation for passivation layers in photovoltaic (PV) devices is derived directly from the fundamental efficiency limit of p–n junction solar cells as originally outlined by the detailed balance limit in 1961.[1] In this detailed balance limit, the maximum theoretical photon conversion efficiency that can be achieved occurs when all recombination within a PV device is radiative. The primary types of recombination in PV devices are classified as radiative (band-to-band) recombination, Auger recombination (three-particle interaction), and Shockley–Read–Hall recombination (through defect levels).[2–5]

Radiative recombination is fundamental to semiconductors and is the opposite of photon absorption. Radiative recombination rates depend on the excess carrier concentration, the band gap, and whether the band gap is direct or indirect. Auger recombination is non-radiative and requires the simultaneous interaction of two electrons and one hole and, therefore, becomes significant only at high carrier densities. Shockley–Read–Hall (SRH) recombination, also known as trap-mediated recombination, is also a form of non-radiative carrier recombination and occurs at electronic defect states that exist within the band gap of a semiconductor. Non-radiative recombination processes are depicted in Figure 3.1a. Trap states are often

Energy and Environment Series No. 30
Ultrathin Oxide Layers for Solar and Electrocatalytic Systems
Edited by Heinz Frei and Daniel V. Esposito

Published by the Royal Society of Chemistry, www.rsc.org

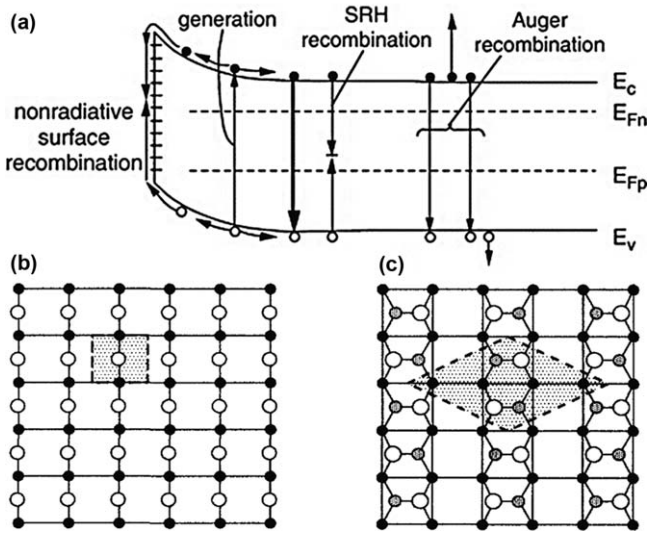


**Figure 3.1** (a) Recombination processes in a semiconductor material. Surface trap states provide recombination centers for non-radiative surface recombination. Reproduced from ref. 6 with permission from Elsevier, Copyright 2006. The Si(001) surface and unit cell are depicted (b) as an ideal $p(1\times1)$ termination (no reconstruction) and (c) as a lower-energy $c(4\times2)$ surface reconstruction. Black circles represent a layer of atoms below the surface and white and gray circles represent surface atoms with the white circles protruding further from the surface than the gray circles. Reproduced from ref. 7 with permission from American Physical Society, Copyright 1995.

formed by impurities, defects in the crystal lattice (*e.g.* vacancies, interstitials, dislocations), dangling or heterogeneous bonds at the semiconductor surface, and adsorbed surface species (*e.g.* $O_2$ or $H_2O$). Bulk trap states are typically addressed by increasing the semiconductor purity and decreasing the defect density within the semiconductor crystal. SRH recombination that occurs at surfaces and interfaces is referred to as surface recombination. Increasing the crystalline grain size (with the limit being bulk single crystals) can reduce the area for surface states; however, even a perfect single crystal may have surface trap states as crystal termination is inherently a discontinuity in the lattice. Clean surface terminations at a minimum will have dangling bonds, which may create states within the band gap, but may also rearrange to form a lower energy configuration, as depicted in Figure 3.1b,c. The minority carrier lifetime is dependent on both the bulk and surface recombination, as shown in eqn (3.1), where $\tau_{\text{eff}}$, $\tau_{\text{bulk}}$, and $\tau_{\text{surface}}$ are the effective, bulk, and surface lifetimes, respectively. Surface lifetime can be defined from a surface recombination velocity, $S$ cm s$^{-1}$, as shown in eqn (3.2) (assuming two surfaces with equal surface recombination velocity), where $W$ is the thickness of the semiconductor and $D$ is the

diffusivity ($cm^2\,s^{-1}$) of the minority carrier. Passivation layers in PV devices are specifically designed to reduce the surface recombination velocity.

$$\frac{1}{\tau_{\text{eff}}} = \frac{1}{\tau_{\text{bulk}}} + \frac{1}{\tau_{\text{surface}}} \tag{3.1}$$

$$\tau_{\text{surface}} = \frac{W}{2S} + \frac{4}{D}\left(\frac{W}{\pi}\right)^2 \tag{3.2}$$

### 3.1.2 Mechanisms

Electrons of a single, isolated atom exist in discrete energy levels called atomic orbitals. When two atoms are brought together, their atomic orbitals overlap to form a molecular orbital. When many atoms are brought together, the molecular orbitals form effectively continuous energy bands. These bands form the conduction and valence bands in a semiconductor. By definition, the conduction and valence bands in a semiconductor will be separated by a region that is void of electronic states. The energy differential across this gap is called the band gap. In real materials, there are always defects. Defects disrupt the local order within the lattice and may result in electronic states that reside within the band gap.

In the context of passivation, defects can occur both in the bulk and at the surface. Here, we are primarily interested in the electronic states that exist at the surfaces of a semiconductor, where the lattice abruptly ends. At a minimum, there will be lone, unbound electrons, sometimes referred to as dangling bonds. In many cases, the crystalline surface will rearrange to a lower energy state. A classic example of surface rearrangement is the Si(111)-(7×7) surface reconstruction, which has been carefully observed by scanning tunneling microscopy.[8] Exactly how the disruption of a crystalline lattice affects the band structure and surface recombination velocity in the semiconductor is dependent upon the material system and preparation.

Passivation broadly means some sort of treatment to reduce defective electronic states. This includes interfacing with a bulk material, the deposition of a thin film, the application of an adsorbed monolayer (*i.e.* molecular or atomic species), or even partial coverage of the semiconductor surface (*e.g.* selectively passivating specific facets in a polycrystalline film). There are two primary strategies that have been applied to solar cells to passivate surfaces, generally referred to as chemical passivation and field-effect passivation. Chemical passivation is the reduction/elimination of dangling and heterogeneous bonds in order to remove surface states. Interactions with a passivation layer may also alter the surface energy and modify or eliminate surface reconstruction. Chemical passivation may include processes to alter surface states (*e.g.* thermal treatment) without adding a new material. Ideally, any new states formed at the interface lie outside the band gap.

Field-effect passivation is achieved by creating a near-surface dipole or electric field. With this strategy, the field will selectively inhibit one carrier

type from reaching the surface traps. In doing so, the surface recombination velocity is reduced because both carrier types are required for a recombination event. A passivation material may have both chemical (reduced trap state density) and field passivation (reduced minority carrier density) effects.

The requirements of a passivation layer in a solar cell are dependent upon the device architecture. Some considerations include optical transparency, electrical conductivity, thermal budget for subsequent processes, mechanical robustness, stability, and cost. Ultrathin oxides are a suitable choice to serve as passivation layers. First, ultrathin passivation layers are desirable because passivation layers are not designed for lateral transport of charge carriers, but rather solely to optimize the interface. The thinner a passivation layer is, the less it will increase series resistance (out-of-plane charge transport) and the less it will contribute to optical absorption. As an aside, it should be noted that the thicknesses and refractive indices of passivation layers sometimes need to be engineered to reduce reflective losses, for which reason the passivation layer should be included when modeling the optical properties of a PV device. There are numerous methods for depositing ultrathin oxide materials, including atomic layer deposition, chemical vapor deposition, sputtering, molecular beam epitaxy, native formation or oxidation processes, *etc.*, at both low and high temperatures. More information on deposition methods for ultrathin oxides can be found in Chapter 2, which focuses on atomic layer deposition (ALD), and Chapter 9, which focuses on wet chemical processes. Second, oxides have a wide range of electrical properties, including insulators, n- and p-type semiconductors, and transparent conductors. In these materials, the optoelectronic properties can be controlled through crystallinity (amorphous or various crystalline phases), oxygen vacancy doping, substitutional doping, and interstitial doping. Finally, oxides can form high-quality barriers to diffusion (Chapter 3, Section 3.4) and are often very stable. We will next look at some examples of how ultrathin oxide layers have been used as passivation layers in PV devices.

### 3.1.3 Examples

Silicon solar cells dominate the international PV market, with about 95% of total production in 2019.[9] The silicon PV market can be further divided, with the most common silicon technologies described by crystallinity (monocrystalline, multicrystalline, or amorphous) and architecture [*e.g.* aluminum back surface field (Al-BSF), passivated emitter and rear cell (PERC), and silicon heterostructures (HIT)]. Silicon surface passivation is a large field and has a rich history going back decades that has enabled the success of silicon PV today. An investigation of this field is beyond the scope of this chapter, but more information can be found in reviews.[10,11]

In this section, we focus on the development of ultrathin aluminum oxide passivation layers used in the highest efficiency silicon PERC modules today. These monocrystalline silicon PERC cells have a record module efficiency of 24.4%,[12] and are expected to be favored over Al-BSF for future added

production capacity owing to a lower balance of systems cost and a shift towards bifacial silicon modules.[13,14] The success of silicon PERC cells is due to the development of high-quality passivation layers, which are most commonly bilayers composed of ultrathin $AlO_x$ and a capping layer (*e.g.* $SiN_y$). $AlO_x$ is deposited by atomic layer deposition (ALD) or plasma-enhanced chemical vapor deposition (PECVD). ALD typically offers better step coverage and conformality whereas PECVD has faster growth rates and lower costs; both ALD and PECVD are used commercially for PERC cells, but PECVD is more prevalent.

Hezel and Jaeger reported aluminum oxide front surface passivation of silicon by pyrolysis of aluminum triisopropoxide in 1989.[16] Although at the time this was not as effective as the hydrogen-passivated $SiO_2$ obtained through the "*alneal*" process, this work permitted silicon passivation at significantly lower temperatures, 290–510 °C, compared with 950–1100 °C for the alneal process. A high-performance demonstration of $Al_2O_3$ on Si was later reported by Hoex *et al.* in 2006 through plasma-enhanced ALD at 200 °C with a 425 °C post-anneal.[15] In that work, $Al_2O_3$ was demonstrated on both n- and p-type silicon with effective surface recombination velocities of 2 and 13 cm $s^{-1}$, respectively, which was on a par with alneal-produced silicon dioxide.[17] A high-resolution cross-sectional transmission electron microscopy (TEM) image of an $Al_2O_3$/Si interface is shown in Figure 3.2.

There are two important factors that contribute to the success of $Al_2O_3$ silicon passivation. First, during alumina deposition, an ultrathin (~1.5 nm) layer of $SiO_2$ forms at the interface between Si and $Al_2O_3$. Aluminum atoms from the alumina are capable of tetrahedral or octahedral coordination to

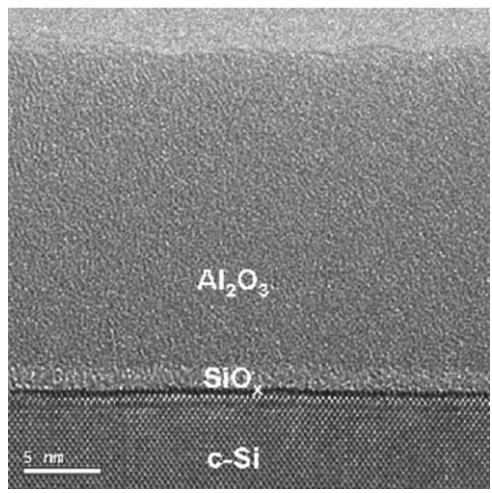


**Figure 3.2** High-resolution TEM image of a 20 nm thick passivating $Al_2O_3$ film on crystalline silicon.
Reproduced from ref. 15 with permission from AIP Publishing, Copyright 2006.

the oxygen in $SiO_2$; it is this tetrahedral bonding environment that is reported to form a negative interfacial charge.[16,18] The post-anneal is critical for high-performance passivation because it results in a localized reconstruction at the interface, resulting in more tetrahedrally coordinated Al sites and a large built-in negative interfacial charge.[19] The formation of a built-in negative charge specifically passivates p-type silicon by repelling minority carriers (electrons) from the passivated surface and, therefore, minimizing surface recombination through field-effect passivation. Second, another proposed effect of thermal annealing is (chemical) hydrogen passivation of the $Si/SiO_2/Al_2O_3$ interface.[15] Hydrogen is a well-known passivant for silicon and is relied on in the alneal process and other passivation schemes. In this scenario, residual hydrogen from the deposited alumina film diffuses to the interface. Residual ligand is common in lower temperature CVD and ALD processes. Often this is undesirable because incomplete reactions result in higher defect densities within the grown thin film, but occasionally residual ligand can become beneficial, leading to ligand passivation effects.

These approaches are not restricted to silicon systems. Chemical and field-effect passivation are used in nearly every absorber interface (whether intentionally or incidentally) across solar technologies. For example, alumina has also been studied as a passivation layer for CdTe. Perkins *et al.*[20] investigated the interfaces between CdTe and ALD $Al_2O_3$, and showed that growth of $Al_2O_3$ by trimethylaluminum and water eliminated tellurium oxides, native oxides formed on the CdTe surface. $CdCl_2$ post-treatment led to the regrowth of tellurium oxides at the $Al_2O_3$ interface, which was necessary for successful passivation. $Al_2O_3$ passivation in this case was attributed to chemical passivation rather than field-effect passivation. Unlike Si, the use of CdTe is a direct band-gap thin-film technology with shorter diffusion lengths than silicon. Therefore, both top and bottom absorber surfaces are usually used for charge carrier collection, meaning that insulating materials, such as $Al_2O_3$, present a challenge to charge transport. One strategy that enables charge collection through $Al_2O_3$ passivation layers is the use of point contacts. This was investigated with partial success in the CdTe–$Al_2O_3$ system by Kephart *et al.*,[21] where the $Al_2O_3$ passivation layer was patterned with a series of 2 μm holes by photolithography and an etch process. A magnesium zinc oxide window layer was deposited on top of the $Al_2O_3$ passivation layer and made direct contact with the CdTe through the patterned holes while the majority of the absorber surface remained passivated. This particular study demonstrated improved carrier lifetimes, but was unsuccessful at increasing the device voltage. Point contacts have been applied more successfully in Cu(In,Ga)$Se_2$ (CIGS),[22] but tend to trade increased open-circuit voltage ($V_{oc}$) for a reduced fill factor (*FF*).

Ligand passivation effects are usually restricted to CVD-type depositions methods, where the precursor ligand or counter reagent (water) provides passivation, typically by a chemical passivation mechanism. Hydrogen passivation of Si through residual ligands by ALD/CVD of $Al_2O_3$, mentioned

above, is not an isolated example. Recent reports have suggested that ligand passivation effects play a role in the success of ALD tin oxide electron-selective contacts for metal halide perovskite (MHP) solar cells (discussed further in Section 3.2.3). In this system, there are varying amounts of residual dimethylamine ligand from tetrakis(dimethylamino)tin(IV) precursor in the tin oxide thin film as a result of the processing temperature and post-annealing.[23] This effect, along with perovskite-compatible processing conditions, may be one reason why low-temperature, ultrathin oxide contacts obtained by ALD have been highly effective in MHPs.[24–27]

There are numerous other demonstrations of surface passivation with oxides in PV devices, but most of them can be related to the concepts discussed in this section.

## 3.2 Contact Layers/Buffer Layers

### 3.2.1 Function

Two additional roles that oxides can serve when adjacent to a semiconductor absorber material in a PV device are contact layers and buffer layers. A contact layer is a general term that can have different meanings depending on the context/architecture of the solar cell. Broadly speaking, a contact layer is defined as a charge-conductive material in electrical contact with the absorber; a contact layer does not generate appreciable photocurrent itself. In silicon devices, the contact typically refers to a charge collector (*e.g.* a metal or transparent conducting oxide) designed to collect and transport all of the photogenerated current from the device. Charge collector contacts can have carrier selectivity through the formation of a Schottky junction (which is critical in many devices), but the primary role is to reduce series resistance. In thin-film solar cells, there often is no p–n homojunction and instead a heterojunction is made of two dissimilar materials. A contact layer in this thin-film example is typically another semiconductor that selectively accepts a single carrier type. In this context, a contact layer is more precisely described as a selective contact layer and requires through-plane charge transport to a charge collector, but not in-plane charge transport. A selective contact is often multifunctional and provides surface passivation, charge carrier selectivity, optical transmissivity, and various barrier properties. As such, selective contact materials are often much thinner and less conducting than metallic contacts used for in-plane charge transport. This makes ultrathin oxides a common choice of material for selective contact layers.

A buffer layer can also have multiple meanings in photovoltaics. Traditionally, the term ''buffer layer'' referred to a layer that enabled the epitaxial growth of one material on top of a substrate with a dissimilar lattice constant. In the context of epitaxial growth (*e.g.* III–V materials), this is almost certainly the meaning, although oxides are typically not used as buffer layers for III–V applications. In a looser definition, a buffer layer can also refer to a

layer that improves the mechanical robustness at an interface and/or seeds the growth of another layer, even if non-epitaxial. Many solar applications for oxides fall into the latter definition of buffer layers.

As is a theme of this chapter, a single material is not limited to one function, but rather could be a contact layer, buffer layer, and passivation layer. This has led some PV fields to use contact layer, buffer layer, and window layer almost interchangeably. For the purposes of this chapter, we shall use the above descriptions where contact layer properties are more electronic in nature and buffer layers are designed for mechanical properties or the seeding of thin-film growth. In this section, we will look at ultrathin oxides used as selective contact layers and buffer layers.

### 3.2.2 Mechanisms

Band bending will occur when two different semiconductors are brought into electrical contact. When band bending occurs, an electric field is created, which can collect or repel charge carriers of a specific type. A traditional p–n junction band diagram is shown in Figure 3.3a; p–n junctions are the basis for charge separation in most solar cell technologies. A variation on a p–n junction is a p–i–n device, shown in Figure 3.3b, where the semiconductor is only slightly doped and selective n- and p-type contacts are used on opposite sides of the device. Perovskite solar cells are often fabricated in a p–i–n configuration. The electron-selective contact accepts electrons and repels holes, whereas the hole-selective contact accepts holes and repels electrons as a result of the band bending and band offsets near the respective interfaces. The majority of oxides are n-type (*e.g.* tin oxide, titanium dioxide, and zinc oxide); however, some oxides can be p-type (*e.g.* nickel oxide and cupric oxide) or exhibit facile hole transport through defect levels (*e.g.* molybdenum oxide and vanadium oxide); both n- and p-type oxides are used as selective contacts in solar cells.

Oxide contact layers are typically thin and transparent and have sufficiently high doping to extend the depletion region into the absorber. Electronic effects are controlled by the electronic band structure of the contact layer material. When two semiconductors with different Fermi levels are brought into electrical contact, the Fermi levels will equilibrate through charge transfer, resulting in an electric field and band bending near the interface. Charge transport occurs between one semiconductor and another through the transport of holes (in the valence band) and electrons (in the conduction band). Solar cell operation results in the photogeneration of equal numbers of electrons and holes that must be extracted to generate photocurrent. The alignment of the conduction/valence band between the selective contact and absorber will dictate electron/hole transport with the selective contact.

The Fermi level is a function of doping and is most often modulated in oxides through the density of oxygen vacancies or by alloying interstitial metals. Oxygen vacancy tuning can be accomplished through processing,

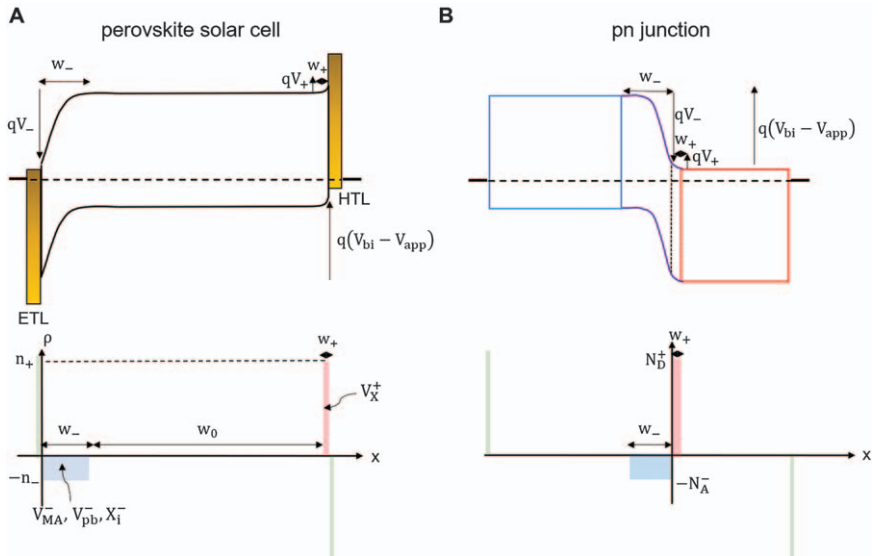


**Figure 3.3** (A) Band diagram of a p–n junction. Charge transfer is required to equilibrate the Fermi level of the n- and p-type semiconductors, which results in depletion near the interface on the formation of an electric field. (B) Band diagram of a metal halide perovskite p–i–n solar cell. Reproduced from ref. 29 with permission from Elsevier, Copyright 2020. $V_{bi}$ and $V_{app}$ are the built-in and applied potentials, respectively; $q$ is the elemental charge. $V_-$ and $w_-$ are the voltage drop and depletion width, respectively, across the electron-selective contact–perovskite junction, and $V_+$ and $w_+$ are the voltage drop and depletion width, respectively, across the perovskite junction–hole-selective contact junction. MHPs exhibit ionic mobility in addition to electronic mobility. Halide vacancies (positively charged) are believed to be the dominant ionic carrier and can drift in electric fields where halide vacancies accumulate in the $w_+$ region and are depleted in the $w_-$ region.

such as manipulating the oxygen partial pressure during evaporation or sputtering. In addition to modulating the Fermi level, doping will also affect the oxide mobility and carrier density, which in turn affects the conductivity and transparency. All other parameters being equal (*e.g.* crystal structure), oxides with low concentrations of oxygen vacancies will have high mobility, high transparency, and low carrier density. Beyond direct oxygen vacancy control, transport properties can be modulated during deposition in numerous ways, including varying the deposition temperature, post-annealing under an oxidizing or reducing atmosphere, diffusion of ions from substrates (*e.g.* alkali metal ions from glass, especially during annealing), control over crystalline defects and grain boundaries, incorporation of dopants, or even unintentional doping (*e.g.* chlorine ligands from metal halide CVD precursors). The textbook *Semiconducting Transparent Thin Films* by Hartnagel, Dawar, Jain, and Jagadish is a useful reference for understanding how electrical properties can be manipulated in oxide thin films.[28]

Epitaxial buffer layers are used to grow single-crystal thin films on substrates with a lattice mismatch or "*misfit*", as defined in eqn (3.3). The rule of thumb for epitaxial growth is that the critical thickness ($t_{crit}$) at which lattice strain begins to cause crystalline defects (*e.g.* dislocations) in a film with lattice constant $a_{film}$ grown on a substrate with lattice constant $a_{substrate}$ is defined as in eqn (3.4). The buffer is designed to have an intermediate lattice constant to minimize stress and defects in the epitaxial film. Amorphous buffer layers have also been used to enable epitaxial growth. This is an important concept, but is not a focus in this chapter.

$$misfit = \frac{a_{film} - a_{substrate}}{a_{substrate}} \tag{3.3}$$

$$t_{crit} = 0.1\left(\frac{a_{film}}{misfit}\right) \tag{3.4}$$

Protective buffer layers (*e.g.* a sputter buffer layer to protect from sputter damage) are used after absorber growth as a barrier to stop energetic ion penetration and/or oxidative reactions with an underlying layer during subsequent depositions. This type of buffer layer is inorganic and is used to protect sensitive materials or interfaces, such as with organic and metal halide perovskite photovoltaics. Buffer layers used in this way must be electronically compatible with the selective contact/conductor for efficient carrier collection, with the exception of all-back-contact or point contact architectures. This is one reason why the terminology is often used inconsistently. We will next discuss a few examples of oxide contact/buffer layers used across various PV technologies.

### 3.2.3 Examples

Nickel oxide ($NiO_x$) is an interesting p-type oxide owing to its tendency to form a higher proportion of metal vacancies with respect to oxygen vacancies, a phenomenon known as defect asymmetry.[30] $NiO_x$ also has a high conductivity and a broad range of uses, such as in catalytic materials, batteries, capacitors, and photovoltaics. For PV applications, nickel oxide is often applied as a hole-selective contact. Nickel oxide can be processed in a variety of ways, including sputtering, e-beam evaporation, nanoparticle solution processing, and sol–gel synthesis. The electronic properties of nickel oxide are sensitive to the surface oxidation state and can be manipulated through processing changes and post-treatment (Figure 3.4).

The use of $NiO_x$ has been demonstrated in numerous PV technologies, but it is most prevalent in the fields of organic photovoltaics (OPVs) and MHPs. Irwin *et al.* reported one of the earliest studies of high-efficiency PV devices using nickel oxide as a hole-selective contact in OPV devices.[31] In this work, $NiO_x$ was deposited by pulsed-laser deposition on an indium

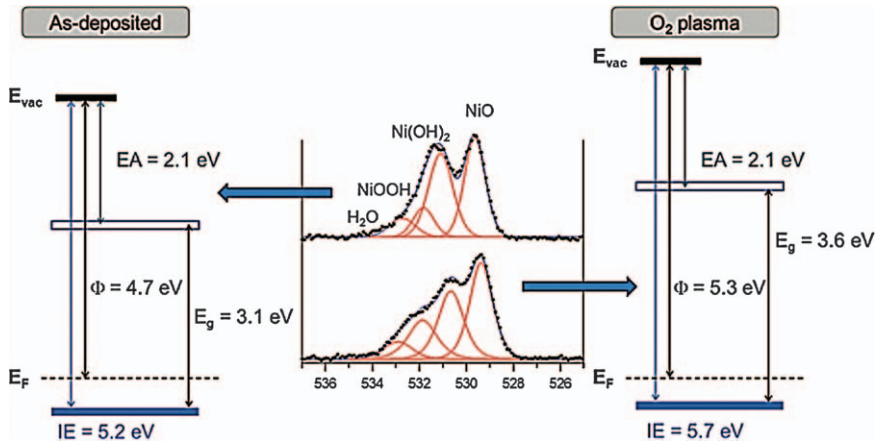


**Figure 3.4** Surface states of solution-processed $NiO_x$ films measured by X-ray photoelectron spectroscopy. $NiO_x$ surface states are sensitive to processing and post-treatments (*e.g.* $O_2$ plasma) and will affect the electronic properties of the film and the resulting device interface when processed with another semiconductor. EA, electron affinity; IE, ionization energy; Φ, work function; $E_F$, Fermi level; $E_{vac}$, vacuum level; $E_g$, band gap.
Reproduced from ref. 32 with permission from American Chemical Society, Copyright 2011.

tin oxide (ITO) (tin-doped indium oxide) substrate. The nickel oxide worked to conduct holes and repel electrons at the ITO interface and boosted efficiencies in an organic bulk heterojunction device consisting of the architecture ITO/$NiO_x$/P3HT:PCBM/LiF/Al, where P3HT is poly(3-hexylthiophene) and PCBM is [6,6]-phenyl-$C_{61}$-butyric acid methyl ester. $NiO_x$ has a relatively high optical absorption and must be thin to minimize optical losses. An $O_2$ partial pressure of $7.0\times10^{-4}$ Torr and a thickness of 5–10 nm provided the optimal results. In later work, Ratcliff *et al.* studied the complexity of the nickel oxide surface and the effects of processing on the band structure.[32] Here, it was clearly shown that not all nickel oxide films are equivalent. The numerous $NiO_x$ surface states and device performance are sensitive to processing.

Metal halide perovskites adapted the early OPV work on nickel oxide to perovskite device stacks (*e.g.* p–i–n superstrate structure: glass/transparent conducting oxide/$NiO_x$/perovskite/electron-selective contact/metal). This has the benefit of replacing organic hole-selective contacts, which are often doped with mobile dopants that create stability issues, with an inorganic oxide with higher thermal stability and improved optical transparency (IR transmission is of particular importance for tandem solar cells). It is easier to work with nickel oxide in the perovskite p–i–n superstrate architecture because the nickel oxide is deposited before the perovskite and therefore the processing conditions are not constrained by the stability of the perovskite. However, high-efficiency n–i–p superstrate devices have been

reported with nickel oxide hole-selective contacts deposited on top of the perovskite through solution processing with nanocrystalline inks. As with the OPV field, the perovskite devices are sensitive to the nickel oxide surface, making process development somewhat difficult. Furthermore, it has been shown that the nickel oxide surface is not chemically inert to perovskite inks and can undergo redox reactions that deprotonate organic A-site cations (*e.g.* methylammonium or formamidinium). Boyd *et al.* showed that this redox pathway led to the formation of an interfacial $PbI_2$, which limited device voltages, but could be mitigated by adding excess organic cations to the perovskite ink.[33] Although the complexities of nickel oxide can make it a challenging material to use in OPV and MHP selective contact layers, it has been highly successful at the research scale.

Oxides also make excellent electron-selective contacts. CdS is a traditional electron-selective contact layer/buffer for CdTe and CIGS solar cells that is often referred to as a CdS buffer or window layer in the literature and is used for both sputter protection and interfacial electronic properties. CdS was popular because it is easy to form by chemical bath deposition, has a band gap of 2.4 eV (mostly transparent, but must be thin to avoid optical losses), and possesses proper energy alignment with respect to CdTe and CIGS for electron collection, hole repulsion, and field-effect passivation. Unfortunately, cadmium is highly toxic and its use had been banned in several countries for PV applications. Today, these regulations have largely been relaxed for solar cells with a specific exception for PV in the European Union's Restriction of Hazardous Substances Directive (RoHS) with life-cycle management and manufacturer-led recycling programs, enabling the spread of CdTe PV. It should be noted that CdTe is a very stable cadmium-containing compound that will not easily leach out of a solar cell. However, in the early 2000s, it was critical to replace the CdS-selective contact from CIGS with a more efficient and cadmium-free material in order to open up additional markets to the technology (*e.g.* Japan). One successful strategy was the development of Zn(O,S) (zinc oxysulfide).

A common superstrate structure for CIGS solar cells is soda-lime glass/Mo/CIGS/CdS/ZnO/ZnO:Al. In an effort to remove CdS from the device stack, ZnO and ZnS were tried as electron-selective contacts. Neither material worked well owing to poor conduction band alignment. However, solution-processed ZnS with residual oxygen, forming Zn(S,OH), was found to be a promising replacement.[34] Platzer-Björkman *et al.* combined ALD processes for ZnO and ZnS to tune controllably the S : O ratio in Zn(O,S) ultrathin contact layers.[35] This approach allowed the successful modulation of the Zn(O,S) conduction band around that of the CIGS absorber, demonstrating that a low sulfur content resulted in devices with a negative conduction band offset and low open-circuit voltages, while higher sulfur contents created a positive conduction band offset and low photocurrent. Efficiency improvements over CdS were achieved through proper compositional tuning of ultrathin (~30 nm) Zn(O,S)-selective contacts.

Finally, we will discuss sputter buffer layers that serve as barriers to protect underlying absorber layers from sputter damage in MHPs. Most single-junction perovskite devices use metallic back contacts. Metallic contacts are successful because metals can be easily evaporated onto organic contact layers without interfacial damage. However, metals are optically opaque and will not transmit longer wavelength photons to underlying low-gap absorbers in tandem or multijunction solar cells, prevent back-side transmission in bifacial devices, and are a stability concern through reactions with free halogens. Transparent conducting oxides (TCOs) can be used instead as a transparent charge-collecting contact. TCOs are common in thin-film solar cells (*e.g.* First Solar CdTe modules); however, they are deposited by sputtering or CVD processes that are not directly compatible with perovskites and/or organic contact layers. In order to solve this problem, ultrathin, inorganic, sputter buffer layers deposited by soft deposition techniques (*e.g.* thermal evaporation or ALD) are used between organic charge-selective contacts and TCOs. Currently, the most prevalent sputter buffer layer for MHPs is tin oxide grown by ALD.

The first demonstrations of tin oxide sputter buffer layers were in perovskite/perovskite[36] and silicon/perovskite tandems.[24] In these studies, the sputter buffer layers were applied to wide-gap (>1.6 eV) perovskite stacks based off the p–i–n superstrate architecture: ITO/$NiO_x$/perovskite/$C_{60}$/$SnO_x$ sputter buffer layer/ITO. Here, fullerenes ($C_{60}$) act as the charge-selective contact and mitigate chemical reactions between the organometallic tin (used in ALD) and the organic cations in the perovskite.[27] Conformal, amorphous $SnO_x$ layers ~8–20 nm thick deposited at ~80–100 °C have negligible impact on the device series resistance and optical losses while providing sufficient protection to TCO sputter processing. Tin oxide itself is frequently used as an electron-selective contact in n–i–p superstrate devices, but so far there has not been a successful demonstration of thin-film oxides deposited directly on top of perovskite absorbers without an organic interlayer. Some reported alternative sputter buffer layers are molybdenum oxide,[37] vanadium oxide,[38] and aluminum-doped zinc oxide[26] and these can be used in combination with alternative organic selective contact layers, such as PCBM, Spiro-OMeTAD (2,2′,7,7′-tetrakis(*N*,*N*-di-*p*-methoxyphenylamine)-9,9′-spirobifluorene), and PTAA (poly[bis(4-phenyl)(2,4,6-trimethylphenyl)amine]). While these oxides must be electronically compatible with the device stack for efficient photogenerated carrier extraction, the sensitivity to defects and energy level misalignment in the oxides are almost certainly reduced when used in conjunction with an organic-selective contact, leading to the success of a wide range of low-temperature processed oxide buffers.

## 3.3 Recombination Layers

### 3.3.1 Function

The detailed balance limit for photovoltaic conversion efficiency (PCE) was briefly discussed in Section 3.1. The theoretical efficiency limit changes

based on the number of complementary absorbers used within a solar cell device stack. This occurs because a multijunction solar cell can (i) more closely match the absorber band gap to the absorbed photon energy, thereby reducing thermalization losses in the solar cell, and (ii) utilize lower energy photons that are not collected by single-absorber solar cells. Increasing the number of absorbers in a solar cell raises the one-sun theoretical efficiency from ~30% for a single absorber to 42% for two absorbers, and up to 62% for an infinite number of absorbers.[39] Several strategies have been proposed to break the detailed balance limit, such as hot carriers, multiple exciton generation, or an upconverting layer.[40] However, to date, the only demonstrated strategies to achieve PCEs beyond the 30% single-junction, one-sun detailed balance limit are solar concentration and pairing multiple absorbers in multijunction architectures. The most efficient technologies use both approaches. Note the clarifiers on the 30% limit. Multijunction and concentration strategies do not *break* the detailed balance limit, but rather change the calculation, *i.e.* a multijunction cell with light concentration may be above 30%, but the detailed balance limit efficiency is no longer 30% for that architecture; no device has surpassed its own detailed balance limit.

Power conversion efficiency is the primary module figure of merit for designing a solar installation. The PCE has a direct impact on the number of panels and installed area required to meet a given power specification. With module costs accounting for less than 50% of the total installed cost for most residential and utility PV installations,[41] there is considerable opportunity to bring down the levelized cost of electricity through the development of higher efficiency solar panels and reduction of installation costs/land use; this can be true even at a modest increase in module cost ($\$\,W^{-1}$). Furthermore, many ''niche'' PV applications that value high efficiency, such as electric vehicles, high-altitude drones, and satellites, are becoming high-value markets in the PV industry.[42] These applications have a limited surface area and often strict weight restrictions and can pay a premium for technologies with high power density ($W\,m^{-2}$) and/or high specific power ($W\,g^{-1}$). In a thin-film solar cell, the majority of the mass comes from the substrate and packaging. Adding additional absorber layers to form a tandem or multijunction cell can increase the power density of the device with negligible impact on the overall weight.

In order to realize the potential of multijunction solar cells, the individual subcells must be electrically connected. Individual subcells are most often connected in series, which is done through recombination layers. Recombination layers are the transparent interconnects between monolithically integrated absorbers and allow the pairing of more than one semiconductor in tandem or multijunction solar cells.

### 3.3.2 Mechanisms

The role of a recombination layer is simple: it allows electrons from one subcell (absorber 1) to recombine with the holes of another subcell (absorber 2).

By this process, the electron quasi-Fermi level of absorber 1 will align with the hole quasi-Fermi level of absorber 2, permitting voltage addition of the two subcells, as shown in Figure 3.5. Another requirement of a recombination layer is that it is optically transparent. Tandem and multijunction subcells are engineered to absorb a fixed range of the solar spectrum and transmit the remainder. Any absorption within the recombination layer(s) will result in efficiency losses. The interconnection of subcells with recombination layers is analogous to wiring two solar cells in series, except that the subcells are monolithically stacked and the "wire" is a transparent thin film.

A recombination layer can be either a material that behaves electronically as a metal (*e.g.* a TCO), an ultrathin and nearly transparent metal (*e.g.* metal nanoparticles or ultrathin layer), or an ultrathin, highly doped $n^+/p^+$ bilayer, such that tunneling of charge carriers can occur between the conduction band of the $n^+$ layer and the valence band of the $p^+$ layer. The latter is referred to as a tunnel junction (TJ) and is used primarily in highly crystalline PV systems when lattice matching is required and doping can be tightly controlled. Tunneling can also occur between two adjacent quantum wells in a quantum well tunnel junction.[43] TCOs or ultrathin metals are used when lattice matching is not required and/or doping levels cannot be precisely controlled; TCOs or ultrathin metals tend to be used in thin-film technologies involving CIGS, CdTe, OPVs, and MHPs. We will explain why later in this section.

The majority of research on recombination layers has been focused on increasing the efficiency limits of III–V multijunction systems. The first demonstration was a TJ reported by Bedair *et al.* in 1979.[44] In that work, a TJ

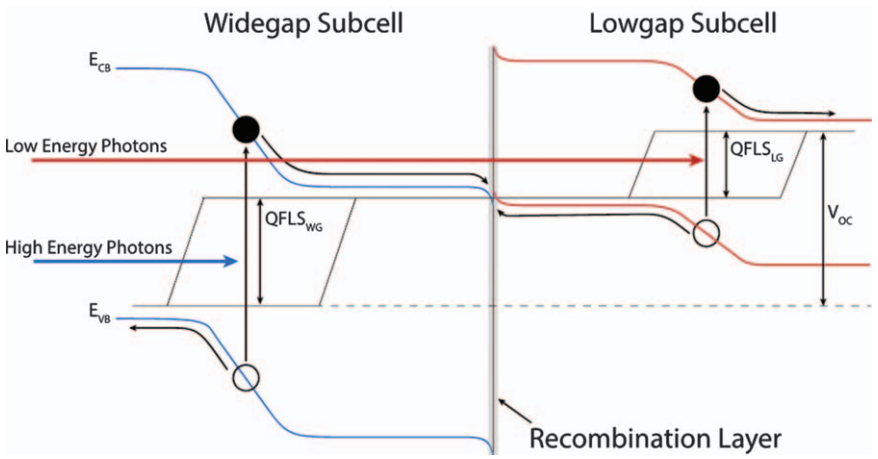


**Figure 3.5** Band diagram of a monolithically integrated tandem solar cell. High-energy photons are absorbed by the wide-gap subcell and low-energy photons by the low-gap subcell. Voltage stacking of two subcells is enabled by a recombination layer. QFLS, quasi-Fermi-level splitting.

was created with $p^+/n^+$ AlGaAs to connect a GaAs and a AlGaAs subcell and allowed an open-circuit voltage of 2.0 V, greater than the band gap of either subcell. Today, most III–V multijunction cells use AlGaAs $p^+$ (carbon doping)/GaAs $n^+$ (Te doping) as a TJ, although optical transmission can be improved with AlGaAs/InGaP or quantum well TJs. The record efficient solar cell to date is a six-junction III–V cell with 47.1% conversion efficiency under 143 suns solar concentration.[45] These nearly ideal semiconductors push the limits of what is possible in a PV device. However, owing to the high fabrication cost of multijunction III–V solar cells, they are used for very specific applications (*e.g.* PV for space or concentrator PV systems) with strict requirements on the properties in the TJ. These requirements include lattice matching for epitaxial absorber deposition, carrier conduction on the order of tens of $A\,cm^{-2}$ (for concentrator systems), and ultralow resistance with ultrahigh transparency (five TJs in a six-junction device).

No other PV system is as tunable and controllable as III–V semiconductors, and as such, six-junction devices are not practical for Si, CIGS, CdTe, or MHPs; however, these emerging systems can benefit from pairing in two- or three-junction configurations and are projected to do so with manufacturing costs practical for one-sun applications.[46] The needs of recombination layers in emerging PV include (i) voltage stacking of subcells, (ii) high optical transmission, (iii) low through-plane resistance, (iv) low fabrication cost, (v) high stability, and (vi) diffusion barrier properties (*e.g.* solvent, ions). These requirements have led to the application of amorphous or polycrystalline transparent conducting oxides as recombination layer materials.

### 3.3.3 Examples

Most PV material systems of compatible band gaps cannot be easily fabricated monolithically, whether due to thermal budget, surface roughness/lattice mismatch, cell patterning, or otherwise. Wafer bonding has been used but requires highly polished and clean surfaces, which is expensive and may not always be possible in thin-film technologies. An interesting approach reported by Klein *et al.*[47] is to use a transparent conductive adhesive (TCA) to mechanically bond and electrically connect two subcells. The TCA is an ethylene vinyl acetate (standard encapsulant) with blended silver-coated poly(methyl methacrylate) (PMMA) microparticles.

The recombination layer stack is TCO/TCA/TCO, where two thin-film TCO layers on either side of the TCA allow low silver–PMMA microparticle loading and >92% optical transparency (local lateral charge collection allows distributed silver–PMMA microparticles to act as point contacts). The PMMA particles can be deformed to bond two non-planar surfaces. The versatility of this approach allows the integration of almost any two subcells. Follow-on studies from this work demonstrated three-terminal operation of a GaInP/Si monolithic tandem by utilizing the TCO/TCA/TCO recombination layer as a third contact.[48] The three-terminal operation approach reduces the

performance sensitivity to the band gap matching of the two subcells, permitting higher theoretical performance for two non-ideally matched absorbers (as is the case when pairing most established PV technologies).[49]

Barrier properties of the recombination layer can also provide benefit as a "functional barrier" in a device stack that also provides additional stability benefits during fabrication or operation through barrier properties. Furthermore, similarly to selective contact layers, recombination layers only require through-plane charge transport and therefore do not require high lateral conductivity (Figure 3.6). Poor conductors can make excellent recombination layers (at least in one-sun applications) provided that they are thin enough that they do not add too much resistance for through-plane charge transport. For example, a 10 nm thick recombination layer with a resistivity of $10^4$ Ω cm (typical conducting metals have resistivities on the order of $10^{-5}$–$10^{-6}$ Ω cm) would contribute only 0.01 Ω $cm^2$ to the solar cell series resistance. In fact, recombination layers with low lateral conductivity can improve the device yield, because a laterally conductive recombination layer can electrically connect shunt pathways in the two connected subcells.

Series resistance is calculated using eqn (3.5), where $R_{series}$ is the series resistance, $\rho$ is the resistivity, and $t$ is the film thickness. Resistivity is related to the sheet resistance, $R_{sheet}$, as shown in eqn (3.6).

$$R_{series} = \rho t \tag{3.5}$$

$$\rho = R_{sheet} t \tag{3.6}$$

In eqn (3.6), bulk resistivity (Ω cm) is often estimated from measurements of in-plane sheet resistance; this is an isotropic approximation of the material resistivity, which may not be valid in many ultrathin films – especially when the thickness of the layer is on the order of the grain size of the film.

Recent work on all-perovskite tandem solar cells[26] focused on recombination layer development with the two concepts of functional barriers and reduction of in-plane conductivity in mind. Here, a 25 nm aluminum-doped zinc oxide (AZO) recombination layer grown by ALD was used as a

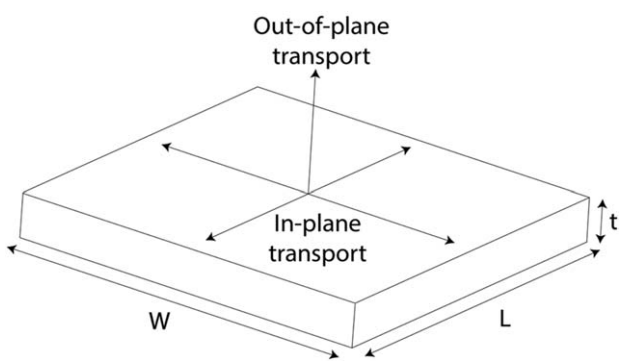


**Figure 3.6** Geometry of contact layer with in-plane and through-plane charge transport depicted.

recombination layer between wide-gap and low-gap MHP subcells in both rigid and flexible architectures. The AZO layer was grown on top of fullerenes (n-type selective contact). Under normal conditions, fullerenes are susceptible to subsurface diffusion of the organometallic tin, resulting in subsurface growth. Subsurface chemical reactions are exothermic and cause the expansion and contraction of the oxide film throughout the ALD growth cycle and have been reported to form a diffuse interface with non-functionalized polymers.[50] This type of growth mode was found to result in poor AZO barriers when grown on top of fullerenes in perovskite stacks. Nucleation on the fullerene layer was improved by a surface treatment with hydroxyl-containing polyethylenimine ethoxylated (PEIE), which provided a surface growth site for ALD. This led to AZO films with about an order of magnitude lower water vapor transmission rate and decreased permeability to dimethylformamide (a metal halide perovskite processing solvent), permitting subsequent solution processing of the low-gap perovskite film on top of the AZO layer. The 25 nm thick AZO layer had a high sheet resistance of $\sim 10^9\ \Omega\,\mathrm{sq}^{-1}$ (“ohms per square”) when processed at 90 °C. This corresponds to a resistivity of $\sim 2.5 \times 10^3\ \Omega\,\mathrm{cm}$ and a series resistance contribution of $\sim 0.006\ \Omega\,\mathrm{cm}^2$. Incorporating the AZO interconnect layer, the perovskite subcells in this work current matched under one sun at 16.0 $\mathrm{mA\,cm}^{-2}$ with a tandem PCE of 23.1% on rigid glass superstrates and also in flexible tandem solar cells with a PCE of 21.3%.

Tandem and multijunction PV devices are now moving beyond III–V materials to pairing established single-junction technologies (Si, CdTe, CIGS, *etc.*) and emerging technologies (OPVs, MHPs) where traditional tunnel junctions cannot be easily implemented and where solar concentration is not required to enable the economics of terrestrial multijunction systems. This has shifted the critical material design properties of recombination layers. In emerging applications, the capability to integrate to dissimilar materials, optical transparency, and additional functionality (*e.g.* barrier properties and reduction of in-plane conductivity) are of high importance. Ultrathin oxides have found a role in this area owing to their highly tunable electronic and optical properties and also a wide range of deposition conditions.

## 3.4 Barrier Layers

### 3.4.1 Function

PV devices are among the few electronic devices produced today for intended use outdoors. They are subjected to intense ultraviolet radiation, damp heat, freeze–thaw cycling, wind load, and hail storms – with warranties of at least 25 years and a community studying how to realize 50 year reliability with lower initial costs than today’s devices. This is an unparalleled level of reliability compared with commercial electronics and even cars which expect constant maintenance, and also relatively “low-tech” non-electronic devices such as roofs and roads. A key component facilitating this long-lived

performance is the device packaging. Barriers that can minimize oxygen and moisture ingress have long been viewed as critical for existing [Cu(In,Ga)$Se_2$ and CdTe] and emerging (metal halide perovskites, quantum dots, dye-sensitized solar cells, organic photovoltaics) thin-film technologies. In the case of metal halide perovskites, limiting the egress of components such as organics is also being considered. As photovoltaics have matured, they have been deployed at increasingly high system voltages as a cost-saving measure (more modules in series per string allows fewer inverters); previously 600 V DC, then 1000 V DC and now 1500 V DC is a typical rating for strings of modules, with 2000 V DC being contemplated. Pushing systems to these increasingly high voltages has made potential-induced degradation (PID) an industry-wide concern as ions (*e.g.* $Na^+$) are pulled from the glass and find their way into the cells.[51] While careful control of grounding a module relative to the system voltage can somewhat mitigate this, ion diffusion barriers are also used and are currently being researched to enhance the tolerance of devices to this.

### 3.4.2 Mechanisms

Both moisture and ionic diffusion barriers have similar requirements, and mechanistically behave in a similar manner. Both concentration gradients (diffusion) and voltage (migration) can serve as a driving force for species transport, with ions typically driven by voltage and moisture by concentration gradients. This can be described by the Nernst–Planck equation:

$$J = -D\left(\nabla\varphi + \frac{ze}{k_B T}\right)\varphi\nabla\phi \tag{3.7}$$

where $J$ is the flux, $D$ the diffusion constant, $\varphi$ the concentration, $T$ the temperature, $\phi$ the electric potential, $z$ the valence, $k_B$ Boltzmann's constant, and $e$ the electron charge. In cases where voltage-driven migration is negligible (*e.g.* neutral species such as $H_2O$ or low voltages), this simplifies to Fick's first law of diffusion, which states that the permeant will move from the region of high concentration to that of low concentration proportional to the spatial gradient:

$$J = -D\nabla\varphi \tag{3.8}$$

Fick's second law combines conservation of mass with Fick's first law to predict the time dependence of a concentration, which is expressed as

$$\frac{\partial\varphi}{\partial t} = D\nabla^2\varphi \tag{3.9}$$

Some well-behaved materials are described as ''Fickian'', in that they obey Fick's laws of diffusion. These diffusion equations present a good initial description of how a barrier might behave, although ''non-Fickian'' diffusion

is not uncommon. This merely means that a diffusion process does not obey the simplest form of these equations. The diffusion process can be complicated in many ways. For instance, multiple diffusion pathways or chemical reactions can affect the conservation of mass assumption. The permeant can travel along the surface – this leads to grain boundary diffusion in polycrystalline materials. The permeant can also become dissolved in the bulk of a material up to the maximum solubility concentration limit and diffuse at a different bulk diffusion rate. Grain boundary diffusion typically presents as a faster diffusion process than bulk diffusion.

Ionic, moisture, and oxygen barriers are all fundamentally governed by similar material limitations. For this reason, a fairly good correlation has been observed for oxygen and moisture permeation rates in the absence of a selective reactive component (*e.g.* a desiccant that targets $H_2O$ rather than $O_2$).

Most inorganic materials are better diffusion barriers than organic materials. For instance, the diffusivity of water through polymers at 85 °C is typically in the range $10^{-8}$–$10^{-6}$ $cm^2\,s^{-1}$, whereas its diffusivity in an inorganic material such as alumina is usually orders of magnitude lower (>20 orders of magnitude).[52] This means that organic compounds such as polymers have permeabilities (permeability = diffusivity × solubility) that are orders of magnitude too high to serve the demands of photovoltaics. Figure 3.7 may be useful in helping the reader understand water vapor transmission rate (WVTR) levels, barrier requirements, and even the challenges associated with measuring these properties. Food packaging tends to have WVTR levels in the range 0.1–100 $g\,m^{-2}$ per day. The most impermeable polymers (*e.g.* Aclar® and Vectran®) can have WVTR values for ~100 μm thick films in the region of $10^{-2}$ $g\,m^{-2}$ per day, but most polymers, such as poly(ethylene terephthalate) (PET), have values >1 $g\,m^{-2}$ per day (Figure 3.8).

To be a ''PV-quality'' moisture barrier requires a WVTR below $10^{-4}$ $g\,m^{-2}$ per day. This can be understood in a straightforward manner. The WVTR indicates how many grams of moisture permeate through a unit area in a specified amount of time. A 1 g amount of water takes up 1 $cm^3$, and when spread across 1 $m^2$ this becomes a 1 μm thick layer. While the sensitivity of a PV technology to a particular species such as moisture can be determined experimentally,[53,54] a rough estimate can be made based on a series of factors such as the thickness of the most sensitive layers in the device. Thin-film PV tends to have layers that are from tens of nanometers to a few microns thick in the active device. If a chemical reaction were to occur in the presence of moisture, it can be expected that significant degradation will occur if the device is exposed to the same order of magnitude of moisture as the thickest device layers. If a warranty of 30 years is considered, which corresponds to nearly 11 000 days (~$10^4$ days), then a WVTR of $10^{-4}$ $g\,m^{-2}$ per day is the *minimum* level required for a ''PV-quality'' barrier. It is expected that some technologies such as organic photovoltaics and metal halide perovskites might require barriers in the range $10^{-5}$–$10^{-6}$ $g\,m^{-2}$ per day. This is already the range that is typically specified for organic light-emitting diodes, which are used in milder temperature ranges and with shorter lifetimes associated

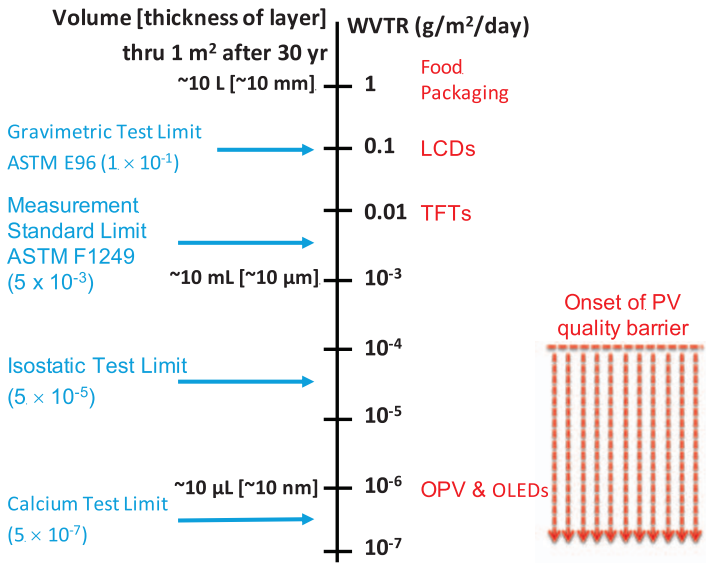


**Figure 3.7** Illustration of water vapor transmission rate values relative to some typical test method limits (left side, blue), relative to the cumulative amount of moisture transmitted after 30 years in terms of thickness and volume (left axis), and relative to the water vapor transmission rate (WVTR) in $g\,m^{-2}$ per day (right axis). Some applications are placed roughly near their WVTR needs (right side, red). "PV quality" barriers do not begin until $10^{-4}$ $g\,m^{-2}$ per day. ASTM, American Society for Testing and Materials; LCD, liquid crystal display; TFT, thin-film transistor; OPV, organic photovoltaic; OLED, organic light-emitting diode.

with consumer electronics. Certain packaging architectures can lessen the sensitivity of moisture by effectively introducing a sorbent encapsulation layer between the expected point of ingress to effectively extend the life of the active layers of the device. Similarly, there are niche applications that do not demand a 30 year operational lifetime – most of these are for lightweight, high specific power (power-to-weight ratio) applications such as person-portable, vehicle-integrated, and aerospace.[42] Achieving these lightweight flexible packages may still require some level of barrier integration. Although some flexible, lightweight, non-polymeric substrates/packages such as zirconia ribbon ceramics and flexible glasses (*e.g.* Corning® Willow® glass, NEG G-Leaf™, Asahi glass SPOOL™, and Schott AG) exist and should all be effectively impermeable to moisture as far as PV is concerned, many of these materials are fragile compared with their organic counterparts.

It is worth noting that although most people discuss the WVTR as a single number, there are a variety of details that cause it to be less precise. First and foremost, permeation generally presents itself as a temperature-activated process. Spanning the temperature range that PV modules are generally expected to experience (–40 to 85 °C) leads to significant deviations of

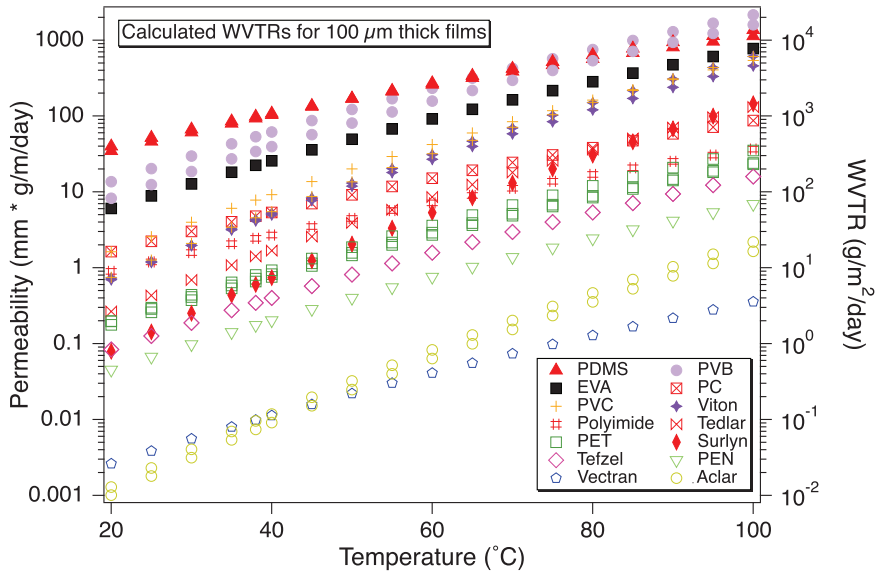


**Figure 3.8** Temperature dependence of permeability (left axis) and WVTR calculated for 100 μm thick films (right axis) of a variety of polymers, many typical of PV applications, including polydimethylsiloxane (PDMS), ethylene vinyl acetate (EVA), poly(vinyl chloride) (PVC), poly(ethylene terephthalate) (PET), polyvinylbutylene (PVB), and poly(ethylene naphthalate) (PEN).

permeation rates. WVTR values are mostly quoted as standard at either 25 or 38 °C. Using PET as an example, the change from 25 to 38 to 85 °C results in the WVTR of a 100 μm film increasing from 3 to 7 to 115 $g\,m^{-2}$ per day (Figure 3.8). Although diffusion through an inorganic moisture barrier film is generally non-Fickian, some level of temperature activation is still observed. Another consideration associated with permeation is that people often want to consider the steady-state WVTR value, but if packages are assembled in a dry manner, there can be considerable lag times to reach the steady state. It is also worth noting that depending on how a barrier is fabricated, there can be unreacted species that effectively serve as a desiccant. Owing to the challenges in measuring WVTR at ultralow values, this can sometimes lead to artificially low steady-state WVTR values.

Although there are methods (*e.g.* the cup test and isostatic method) with standards associated with them to measure WVTR values above $0.5\times10^{-2}\,g\,m^{-2}$ per day, measuring WVTR in the range $10^{-4}$–$10^{-7}\,g\,m^{-2}$ per day is possible but challenging. The methods used for this, in order of reported sensitivity from least to most sensitive, include the isostatic method with coulometric detection ($\sim5\times10^{-5}\,g\,m^{-2}$ per day), laser adsorption spectroscopy ($\sim10^{-5}\,g\,m^{-2}$ per day), calcium test ($\sim10^{-7}\,g\,m^{-2}$ per day), mass spectrometry ($\sim10^{-7}\,g\,m^{-2}$ per day), and the tritium test ($\sim10^{-8}\,g\,m^{-2}$ per day).[55] The main challenge in measuring in this range is the limited number of water molecules

expected to pass through a barrier in a reasonable amount of time. A WVTR of $10^{-6}$ g m$^{-2}$ per day would accumulate a uniform layer (area equivalent to the barrier) of ~0.3 nm of water over 1 year. Using larger barrier test samples (*e.g.* 50 cm$^2$) and concentrating the permeant onto a detector helps shorten the test time and increase the sensitivity. Obtaining reliable information on WVTR in this range tends to require a minimum of 200–1000 h.

Measuring the diffusion of ions such as $Na^+$ is typically carried out using a technique with good sensitivity to impurities with spatial resolution, such as secondary ion mass spectrometry (SIMS). This is not done for moisture owing to the inherent difficulty in measuring hydrogen. Measuring oxygen permeation is similarly challenging with SIMS, especially through an oxide.

### 3.4.3 Examples

In the pursuit of flexible electronics opportunities, numerous companies and academic researchers have developed multilayer moisture/oxygen barriers based on polymer films. These might be multifunctional, with the exterior layers providing some level of anti-reflection, anti-soiling, and abrasion resistance. Poly(ethylene terephthalate) (PET) and poly(ethylene naphthalate) (PEN) are two of the most common polymer supports used in barrier films owing to tradeoffs associated with cost, durability, transparency, and temperature. PET is cheaper, but its dimensional stability is significantly reduced when temperatures exceed ~120 °C. Heat-stabilized PEN can extend operating temperatures to ~160 °C, with low shrinkage for short durations up to ~190 °C. Operating temperature ranges and cost are of major interest to the PV community. Temperature is important not only in later substrate growth and lamination processes, but also in the methods used to construct barrier layers.

Moisture barrier layers require inorganic layers, owing to the aforementioned high permeability of organics. Although nitrides such as SiN are occasionally used, ultrathin oxides are the most common layers considered, with $Al_2O_3$ and $SiO_x$ the most popular. Although electronic materials often benefit from being crystalline, there may be an intrinsic advantage in keeping a barrier layer amorphous in nature since it minimizes the grain structure and hence grain boundary diffusion.

A variety of deposition methods have been explored to generate these thin barrier layers, including ALD,[56] sputtering,[57] CVD,[58] solution processing,[59] and evaporation.[60] Although ALD is well known to give good conformal coatings, which may lead to more robust pinhole-free layers even in the presence of particulates, it has yet to establish itself in industry as a high-throughput deposition method. Sputtering and CVD are generally the most popular techniques at scale, although keeping their films free of pinholes is inherently challenging.

Although inorganic materials seem to have near-zero moisture permeabilities, this does not mean that merely depositing a layer will lead to the same value as observed in the bulk. $Al_2O_3$, $SiO_x$, and Al layers, for instance, are

commonly used in the food industry (think about the inside of a bag of chips/crisps) to decrease barrier levels down towards $10^{-2}$ g m$^{-2}$ per day. These barriers tend to be defect limited. Mitigating the presence of these defects is critical in the lowering of permeation as grain boundaries and pinholes are the main source of diffusion. Although careful control of particulates and clean surfaces with appropriate treatments to lower the surface energy prior to deposition are an obvious means to minimize pinholes, defects are unavoidable at sufficiently large scale. To deal with this, the concept of a ''tortuous path'' was identified as a way to decouple the defects through the use of multilayer stacks. Some of the earlier work in this area sought to decouple defects in one inorganic layer with another, by depositing a thin organic layer between inorganic layers.[61] Other work has shown reduced permeation with inorganic layers in direct contact with one another.[62] There is a distinct decrease in the permeation of two compositionally distinct thin layers compared with a layer of a single composition that is twice as thick. Although there is some thickness dependence of pinholes, with the ability to close off pinholes or reduce their diameter with increasing film thickness, once a film has fully formed and reached a critical thickness there is generally limited benefit in increasing the thickness of an individual layer with respect to the elimination of defects.

Allowing for thinner films has multiple benefits, including improved transparency, shortened deposition time, and improved flexibility. Moisture barriers are most often considered for flexible applications, making it important to recognize that flexibility is critically linked to the thickness, with reasonable flexibility for films in the 10–100 nm range. Although oxides and inorganic materials in general are often considered brittle, thinning down a layer makes it inherently more flexible, with an inverse relation between the film thickness and yield strength. This is intuitively obvious when considering something like glass, which is generally considered brittle in thick sheets but flexible when thinned down to <100 μm (*e.g.* glass-fiber optics). Although additional strategies can be employed to improve the flexibility of a layer in a final device structure, such as placing it as near to the neutral plane as possible, clearly barrier layers should be as thin as possible while maintaining performance.

Ion diffusion barriers are present in existing thin-film PV stacks between the glass and transparent conducting oxide in superstrate technologies involving CdTe, OPVs, and metal halide perovskites. Amorphous $TiO_2$, $ZrO_2$, and Zn–Sn–O all can be effective ion diffusion barriers with thicknesses <20 nm.[63] In CIGS, this is an area of research with oxides such as $SiO_2$ and nitrides such as SiN and TiN to control alkali metal diffusion from soda-lime glass substrates, and also to mitigate Fe or Ti diffusion in the case of metal foil substrates.[64–67] As alkali metal diffusion has also been identified to cause potential-induced degradation in wafer Si PV, barrier coatings (*e.g.* silica) on the front sheet/back sheet is one avenue of investigation, as increasing the thickness of the SiN coating on the wafer to reduce diffusion deteriorates its performance as an anti-reflection coating.[68]

## 3.5 Anti-reflection Coatings

### 3.5.1 Function

In photovoltaics, it is desirable to couple the maximum amount of light into the cell as possible. Anti-reflection coatings (ARCs) are used for optical management in PV devices. Optimizing the above-band gap region of the solar spectrum that a device can efficiently utilize is important because ideally all of those photons would be coupled to the device to maximize efficiency. ARCs can also impact the stability of the PV device by filtering photons outside the useful part of the solar spectrum, such as the IR and UV regions, since they tend to degrade module performance. The high energy of UV light can result in long-term damage to polymers[69] used to package modules and even ''solarize'' glass[70] through changes to oxidation states. This leads to reduced optical transmission and a shortened module lifetime. Longer wavelengths that cannot be directly absorbed by the active layer result in heating. Solar cells generally have negative temperature coefficients, such that their performance is reduced with increase in temperature.

To achieve optimal optical coupling, anti-reflection (AR) layers are used to minimize unwanted reflections in PV modules. The most common front sheet used for modules is glass. With uncoated, clean glass, the reflection losses at the air/glass interface can range from approximately 4 to 9%, depending on the angle of incidence.[71] Once light has been transmitted through the front sheet, other optical coupling/AR layers are used to ensure the highest possible transmission to the PV device. As making extremely wide-band AR layers is challenging, generally they are designed to intentionally reject regions of the spectrum that are least useful or outright deleterious. As shown in Figure 3.9, from the different quantum efficiencies, a measure of how efficient a PV technology is at each wavelength, relative to the typical terrestrial reference spectrum (AM1.5G), the useful region of the spectrum can vary greatly based on the PV technology.

### 3.5.2 Mechanisms

Reflections occur at an interface when there is a difference in the refractive indices of the media comprising each side of the interface. This process is governed by the Fresnel equations:

$$R_s = \left(\frac{n_1 \cos\theta_i - n_2 \cos\theta_t}{n_1 \cos\theta_i + n_2 \cos\theta_t}\right)^2 \tag{3.10}$$

$$R_p = \left(\frac{n_1 \cos\theta_t - n_2 \cos\theta_i}{n_1 \cos\theta_t + n_2 \cos\theta_i}\right)^2 \tag{3.11}$$

where $R_s$ is the reflected power of s-polarized light, $R_p$ is the reflected power of p-polarized light, $n_1$ is the refractive index of the first medium, $n_2$ is the

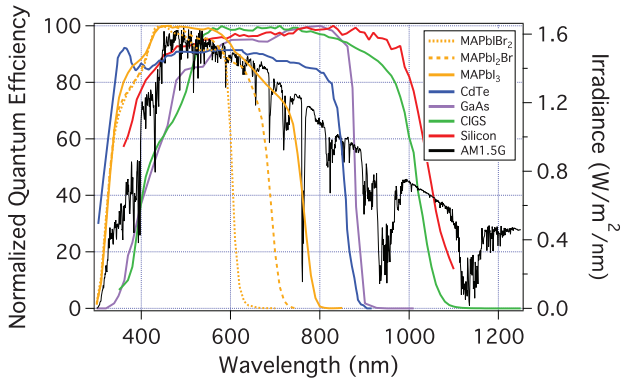


**Figure 3.9** Quantum efficiencies of various PV technologies to illustrate some of the variations in optical conversion. Three different perovskite absorber compositions with varying halide stoichiometries are included as an example of how the band gap can be changed. CIGS can also tune its band gap by varying its stoichiometry. AM1.5G is the typical reference spectrum for flat-plate terrestrial PV.

**Table 3.1** Refractive indices of common materials in a solar cell device stack.[72]

| | Air | Glass, $SiO_2$ | Si | SiN | $MgF_2$ | $TiO_2$ | ZnO | $SnO_2$ | $Al_2O_3$ |
|---|---|---|---|---|---|---|---|---|---|
| Refractive index, $n$ | 1.00 | 1.44–1.55 | 3.52–5.57 | 1.97–2.10 | 1.37–1.39 | 2.49–2.9 | 1.94–1.98 | 1.99–2.10 | 1.76–1.77 |

refractive index of the second medium, $\theta_i$ is the angle of the incident light, and $\theta_t$ is the angle of the transmitted light. For normal incidence, this reduces to

$$R_{\perp} = \left(\frac{n_1 - n_2}{n_1 + n_2}\right)^2 \tag{3.12}$$

Table 3.1 presents the refractive indices of a series of materials that are often used in PV.[72] The refractive index can vary depending on the crystal structure and axis relative to the crystal structure. Furthermore, it is rarely constant relative to wavelength. If we consider an air/glass interface at normal incidence with $n_{glass} = 1.5$, we find 4% reflection. This can easily double as it becomes off-axis. Owing to the much larger mismatch with Si, even a Si/glass interface leads to extremely high reflections. This is one of the purposes of encapsulating polymers such as ethylene vinyl acetate (EVA), which helps with optical coupling as an AR material.

AR layers mitigate reflections by providing an intermediate refractive index. This makes the transition from one medium to another less abrupt, reducing reflections. For a hypothetical ARC that seeks to minimize reflections at an air/glass interface, one might choose an ARC with a material with a refractive index $n_{ARC} = 1.25$ (the *optimal* single layer $n_{ARC}$ is the square

root of the product of the two refractive indices). In the most simplistic consideration, the transmittance, $T$, for each layer is given as follows for the case where there is zero absorption:

$$T = 1 - R \tag{3.13}$$

The transmittance across the air/ARC interface is 98.8% and the transmittance across the ARC/glass interface is 99.2%. This would make the total transmittance the product of the two transmittances, $T_{\text{total}} = T_{\text{air/ARC}} \times T_{\text{ARC/glass}} = 97.9\%$. The next level of sophistication will consider absorptive losses in the different ARCs, and then the wavelength dependence of the refractive indices. Clearly, more layers in an ARC with properly selected refractive indices can be used to reduce the reflections at each interface, with an infinite number of layers reaching zero power reflected. This is sometimes referred to as a graded refractive index (GRIN) coating.

Finally, we can take into account what happens to the reflected light within the ARC. Destructive interference effects can be leveraged by choosing the thickness of the layer carefully, such that it is one-quarter wavelength at the desired center band of transmission. This can reduce the reflections to zero or near zero in a specific wavelength range. Single-layer refractive index coatings tend to be limited in how broad this near-zero reflection can be; a window for which reflection remains <1% might be only a few hundred nanometers wide. Adding additional layers can widen this window further. The last consideration that becomes important optically is the dependence on the angle of incidence. This is especially important if an ARC is to be considered for a fixed tilt installation (*e.g.* a rooftop), as the Sun changes position over the course of a day. It is less important for modules with at least single-axis tracking, which has become a significant trend for utility-scale installations with roughly half of new installations projected to use tracking by 2021.[73]

### 3.5.3 Examples

As mentioned earlier, glass is the most common front sheet for photovoltaics. This is due to its extremely good optical transmission, low cost, electrical insulating properties, mechanical durability, and ability to protect the cells inside. In the past decade, ARCs at the air/glass interface have become common such that this is now standard for most (>90%) modules on the market.[14] These coatings are estimated to boost performance by 2–3%, increasing the overall glass transmission from ~91.5 to 94%, with 95.5% targeted by 2030 in the International Technology Roadmap for Photovoltaics (ITRPV).[73] It also reduces unwanted reflections near airports and military installations and can be used to improve the aesthetics of rooftop solar panels by making them appear a single color (black). One challenging aspect of ARCs is to ensure durability with a lifetime that is commensurate with a module's warranted performance (now 25 years in most cases). Estimates are that existing ARCs might last 15 years, with coatings under

development pushing past 20 years. Of the materials listed in Table 3.1, $MgF_2$ has the most appropriate refractive index for an air/glass interface, and is sometimes used in some less sophisticated ARCs for laboratory-scale solar cells; oxides have also proven quite popular.

Oxides can have excellent chemical durability, with $SiO_2$ and $TiO_2$ being two of the most commonly considered oxides for ARCs. Initially, this might seem surprising considering that their refractive indices are the same as that of glass or even higher. By introducing nanoscale pores in the layers, however, the refractive index can effectively be tuned by creating a composite composed of air and the base oxide.[74] Gradients in the effective refractive index can even be created, by using geometries such as those modeled after the cornea of a moth's eye.[75] Doing this can both broaden the wavelength range over which reflection is minimized and reduce the sensitivity to the angle of incidence. Numerous deposition methods have been explored to create nanoporous layers, including etching,[76] sputtering,[77] sol–gel techniques,[78] and randomly deposited particles.[79] Both multiple layers and alloys of these two (or other) materials can give further control over the refractive index.[77]

Both $TiO_2$ and $SiO_2$ are inexpensive, a requirement for PV, and hard, such that they can withstand abrasion. It has been reported that although delamination does not frequently appear to be an issue with commercial ARCs, there are concerns with mechanical abrasion due to airborne particulates/sand and also from cleaning *via* mechanical wiping or brushing of surfaces. One specific benefit of $TiO_2$ is that it absorbs in the UV region of the spectrum. As mentioned earlier, this is a tradeoff sometimes embraced by PV manufacturers since there are a relatively limited number of photons that can be directly converted by photovoltaics in the UV region of the spectrum such that the sacrificed current is very modest, but their high energies can have catastrophic long-term stability implications.

$TiO_2$ and $SiO_2$ have also found uses as (part of) the ARC in Si wafers, owing to the very high refractive index of Si. However, their use is less common in commercial PV owing to having poor passivation properties relative to the alternative AR material SiN, which is the industry standard.

In thin-film superstrate technologies such as CdTe, metal halide perovskites, and organic photovoltaics, where the solar cell is grown directly on the front sheet, the first electronically active layer of the solar cell is a TCO. TCOs must achieve a balance between electrical conductivity, which is optimized by the thickest film, and transmission, which is optimized by the thinnest film. This optimization problem can be captured in different figures of merit.[80] Typical thicknesses of TCOs for PV devices lie in the range 150–500 nm. This can easily lead to interference fringe lines. Fluorine-doped tin oxide ($SnO_2$:F) is one of the most prevalent TCOs currently used in the thin-film PV industry owing to its low cost, high temperature stability, and fairly good performance. TCO layers ~250 nm thick can cause fringe lines due to interference effects, resulting in non-uniform transmission across wavelengths in the visible region of the solar spectrum, giving the layer an apparent color. Light management has been adopted to reduce these

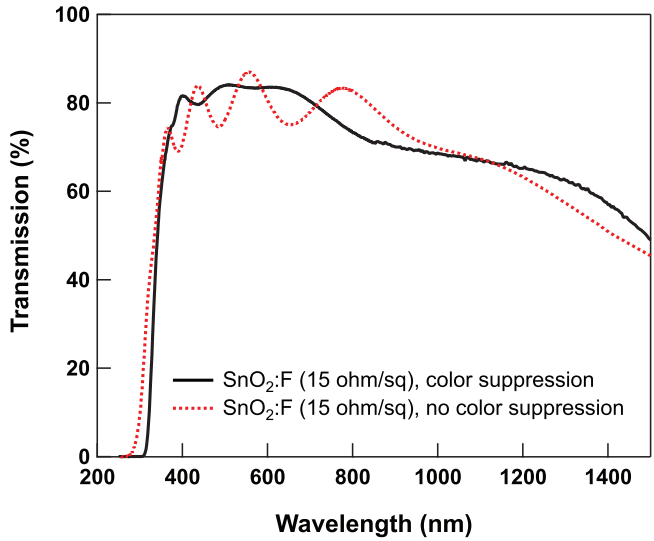


**Figure 3.10** Optical transmission of FTO films with and without a color suppression layer.

interference effects with "color suppression" layers. These layers are inserted between the TCO and the glass and may be on the order of 100 nm. Figure 3.10 shows two examples of $SnO_2$:F layers on glass with similar sheet resistances, one with and the other without a color suppression layer. This can be accomplished with multilayer approaches (*e.g.* $SnO_2/SiO_2$), a homogeneous intermediate index match which might mix alloy $SiO_2$ and $SnO_2$ and intentionally introduce carbonaceous species, or creating a graded index material where the alloy composition is varied with thickness. While these materials are typical of those used by industry, clearly other oxides could be adopted. CVD is by far the most common method used to deposit these layers, with spray pyrolysis or atmospheric pressure CVD performed on glass during the manufacturing process of the glass product while it is still hot. This is largely due to its ability to be exceedingly inexpensive while generating uniform coatings over square meter sheets.

## 3.6 Anti-soiling Coatings

### 3.6.1 Function

Things left outside tend to get dirty. The cleanliness of solar panels and mirrors for concentrating solar power influences their efficiency. Some of the earliest studies (1940s to 1970s) on flat-plate solar heat collectors in the northeastern USA suggested ~1–5% collection loss of solar radiation depending on the tilt angle due to soiling.[81] Panels with a horizontal orientation (*i.e.* parallel to the ground) had the highest losses. These early studies

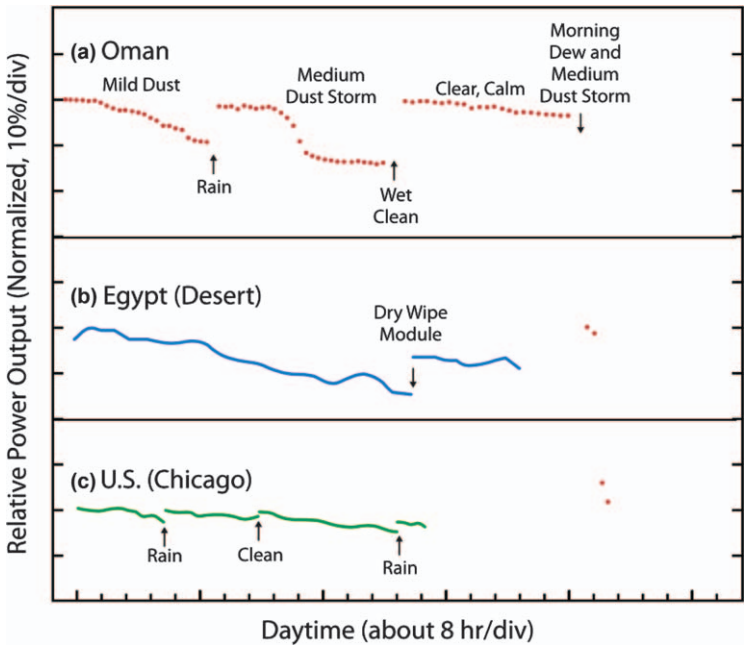


**Figure 3.11** Examples of relative output of photovoltaics deployed in different locations illustrating the effect of soiling and different cleaning events. Reproduced from ref. 82 with permission from Elsevier, Copyright 2013.

were all conducted in places with regular precipitation and low atmospheric dust. It was not until later in the 1970s and 1980s that it was widely recognized that other locations can experience significantly greater soiling. In India and the Middle East, these effects can be considerably more pronounced. Figure 3.11 presents some examples of data from three different locations (Oman, Egypt, and the USA).[82] In the Middle East, there have been numerous documented examples of massive (>30%) horizontal transmission losses in a few days. Detailed tilt angle studies have also been conducted and showed the possibility of double-digit transmission losses in the course of 1 month even with steep (60°) tilts. It is now accepted that there is a wide range of soiling losses that depend on local conditions and dust type that can range from a few percent per month to >10%, with a seasonal dependence.

The term ''dust'' is used to describe particles that are <500 μm in size.[81] These particles vary in dimensions and composition. Organic species come from numerous sources, including pollen, bacteria, fungi, spores, excrement (*e.g.* from insects and birds), and agricultural by-products such as seed dust. Inorganic dust sources include soot, silicates (*i.e.* sand) and other ceramics, and salts. The dust composition depends on location and geography influenced by factors such as industry, roadways, what might be farmed nearby,

and proximity to the coast. In the deserts of Saudi Arabia, six types of sand have been categorized. Additionally, other factors impacting the soiling of solar installations include PV tilt angle, orientation, wind conditions, ambient temperature and humidity. Sand/dust storms in regions of the world with high-quality solar insolation resources make soiling a less-studied but very critically important area of research.

Two general classes of strategies have been employed to mitigate soiling. The first strategy may be broadly classified as cleaning and includes washing with water or detergent solutions and also mechanical wiping. This has multiple drawbacks. One is that it adds cost over the lifetime of a system. Ideally, for the lowest costs, PV systems have little to no regular maintenance – most of their cost is upfront. Additionally, water is not a resource available in some locations where soiling is particularly egregious. Furthermore, cleaning processes, especially mechanically based methods, can be abrasive. Finally, cleaning is not always effective owing to the high adhesive strength that can be present.

The second strategy is broadly classified as preventive. Some of the methods can be viewed in a largely mechanical sense. These include utilizing a tracker to invert or stow the panel during night or dust storms, vibrating the surface during high dust accumulation periods (*e.g.* dust storms), and using aerodynamics to create a turbulent-flow boundary to sweep dust/reduce accumulation. Others use coatings either to actively or passively minimize dust accumulation. Active approaches rely on creating electric fields to repulse accumulation. Passive approaches use coatings to try to make dust less likely to accumulate and/or more effectively use any moisture that might come in contact with the surface.

### 3.6.2 Mechanism

There has been considerable work on the mechanisms behind soiling PV. Although the composition of airborne particulates is a critical factor, as discussed earlier, the airborne distribution can be distinct from what accumulates on a surface. The final accumulation is dependent on a number of factors. The first is gravitational settlement effects, such as weight and drag, which are based on the diameter, density, and shape of particles. The next factor involves airflow. Near a surface, flow becomes laminar and eddy current diffusion can push particles into this laminar region where there are no forces to direct them away from a surface. Furthermore, Brownian motion effects can become important for very small particles when forces are not balanced on all sides, (*e.g.* near the surface of a panel) – this also tends to bring particles towards the surface. Finally, coalescence and charging increase the likelihood of adsorption of near-surface particles. Particles suspended in air can collide and coagulate/coalesce to grow until they can no longer remain aloft. Although the above effects generally increase the probability of sticking, the incident angle and particle velocity can also decrease module soiling. Highly energetic particles in turbulent conditions

impinging at glancing angles can lead to the impinging particle rolling or bouncing along the surface until it and/or other particles that it impacts escape from the laminar portion of the air above the module surface.[82] Particles can also become electrically charged in a number of ways (*e.g.* during particle generation and particle–particle or particle–surface collisions) and even uncharged particles can have dipoles. Depending on the charge polarity, it can either increase or decrease the probability of adsorption and the strength of surface adhesion. Conductive surfaces can reduce charging effects.

All of these processes contribute towards the initial deposition and accumulation of dust on a surface. After deposition, the composition of the accumulated particles can evolve. Cuddihy[83] identified four soiling mechanisms: cementation, organic deposition, surface tension, and particle energetics. The ''cementation'' process is illustrated in Figure 3.12. This is most common in regions with high dust and humidity levels. Part of a population of deposited particulates will be water soluble (*e.g.* salts). When the salts are exposed to high-humidity events, such as dew, they can dissolve and create a suspension with water-insoluble particles. When the moisture dries, precipitates form that anchor the insoluble particles more intimately to the surface. Repeating this process can form significant buildup that firmly adheres to surfaces. Interestingly, water-soluble salts may also come from the weathering of soda-lime glass through a leaching ion-exchange process.[84] When investigating salt deposits on membranes, it was found that thin organic layers provided an initial coating under deposits, which might prime the surface for subsequent salt deposition. After salt buildup and cementation, the organic layers became less accessible and hence difficult to remove. It has been posited that a similar mechanism occurs with glass surfaces.[83]

In suspension, the surface tension of thin fluid films on small particles can exert enormous pressure. This is known to flatten bacteria on microscope slides. In the case of soiling, it can drive particles into softer surfaces. In the case of polymeric coatings, it leaves crater-shaped embedded particulates.[83]

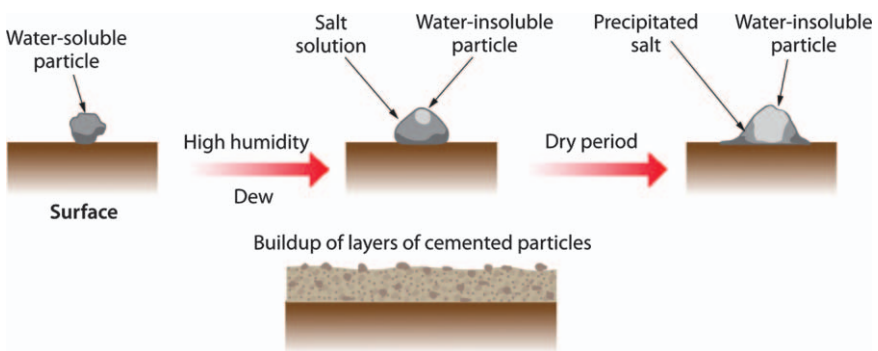


**Figure 3.12** Cementation process outlined by Sarver *et al.*[82]
Reproduced from ref. 82 with permission from Elsevier, Copyright 2013.

During the Mars rover project, there was concern that bacteria that might hitch a ride to Mars on dust particles. This led to a detailed study of how to remove particles with wind or vacuum.[83] A strong size dependence was noted, due to van der Waals interactions. It was shown that realistic, typical terrestrial wind speeds cannot remove particles as they approach 10 μm or smaller in size, with few dislodged at speeds approaching 50 $m\,s^{-1}$ or 100 mph.[83] Detailed experiments that counted and sized particle accumulation relative to tilt angle found that dust accumulation follows a cosine-type relation dependent on the incident deposition angle. This is consistent with the vertical particle flux dominating the isotropic components. Biryukov observed that particles of size from 8 to ~30 μm dominated dry dust deposition when considered in terms of both concentration (mass per unit area) and numerical distribution.[85,86]

Adhesive effects strongly impact the accumulation of surface particles. As particles fall on a surface they become held in place by electrostatic, surface energy, and capillary effects. It has been found that adhesion can increase significantly over the course of the first hour after deposition owing to capillary condensation. Bonding can further increase due to water that leaches chemicals from particles, air, and even the glass. Ultimately, this can lead to an increase in adhesion to 10 000 times the gravitational force,[87] making cleaning incredibly difficult.

To minimize soiling effects through coatings, the first requirement is to do no harm. This necessitates that a coating be optically transparent – in fact, anti-soiling coatings are typically part of a multifunctional coating with anti-reflection properties. It must be mechanically robust against abrasion (from both dust storms and cleaning) and also stable in (UV) light and throughout thermal cycling. Having elucidated the numerous mechanisms that contribute to soiling, we can begin to understand how to address these using coatings. Specifically, we will consider electrostatics, cementation, van der Waals forces, and surface energy.

Particles have an unknown charge; therefore, the safest way to passively minimize electrostatic forces is to use a conductive surface electrically connected to ground. Particularly low sheet resistance is not required to slowly dissipate any charge buildup as the total current from accumulated charged particles and/or charge transfer during particle impact is very low. A thin layer of water, for example, is sufficient to delocalize surface charge. Grounding a surface does, however, have implications associated with potential-induced degradation (PID) that need to be carefully considered, as discussed in Section 3.4.

The process of cementation requires water-soluble salts to anchor larger particles. Some of these salts can actually be leached from the glass itself. As discussed in Section 3.4 on diffusion barriers, oxide layers that block ion transport can be produced to minimize this process. However, since these salts can also originate from extrinsic sources, such as particles, only part of this problem can be resolved through diffusion barriers. There are two schools of thought on how to deal with extrinsic sources of water-soluble

salts in the presence of moisture. The more common approach at present is to make the surface more hydrophilic (typical of metal oxides), which means that water has a low contact angle and the surface is characterized by high surface energy (superhydrophilic surfaces have contact angles $<5^\circ$ and typically are very smooth). This approach allows water to spread out across a surface more easily into a very thin layer in order to improve cleaning.[88] This can reduce cementation in humid environments by preventing a large amount of water-soluble salt from drying and forming a significant anchor to insoluble particulates. The other approach is to push surface energy in the other direction to be hydrophobic (typically done with organic layers such as fluoropolymers). Hydrophobic contact angles are $90–150^\circ$ with superhydrophobic surfaces $>150^\circ$. Hydrophobic surfaces can be formed through compositional changes and texture (including submicron features for "nanotexturing").[89] The concept behind hydrophobic surfaces is to be less attractive to polar species and make water bead up so that it is more likely to form droplets that will naturally roll across a tilted PV module surface and knock particles off along the way. Disrupting dipole alignment of particulates and the surface through beading of water droplets and texturing the surface is also a strategy to reduce van der Waals interactions and overall adhesion to a module surface.

### 3.6.3 Examples and Emerging Applications

For passive anti-soiling coatings, oxides are the material of choice. Materials such as $SiO_2$, $TiO_2$, $SnO_2$, and $ZrO_2$ all are highly transparent and mechanically durable. Although fluoropolymers have been explored for flexible applications, they tend to be less robust than oxides. As discussed in Section 3.5 on anti-reflection coatings, the optical constants of these oxides are such that structures can be made with them to actually improve optical coupling to the PV device. Furthermore, $TiO_2$ and $SnO_2$ are well known for their photocatalytic properties. Photocatalysis[90] can be used to reduce soiling by breaking down organic materials. This is done with a semiconductor. Photogenerated carriers can react with water to create hydroxyl radicals, $O_2^-$, and even $H_2O_2$. These species can then react to oxidize organics. Holes in the semiconductor may also react directly with the organic in an electrochemical half-reaction. Wide band gap semiconductors such as $TiO_2$ and $SnO_2$ are of the greatest interest as anti-soiling photocatalysts since optical absorption losses should be minimized in the anti-soiling layer and high energies are needed to drive the photocatalytic degradation of organic species. Although high photon energy is required to drive photocatalysis by these wide band gap oxides, a relatively low flux of UV photons is sufficient. Assuming a quantum efficiency of 25% with 1 $\mu W\,cm^{-2}$ of UV light, as might be found in a well-lit room, a photocatalytic anti-soiling layer would be able to decompose a 1 μm thick layer of hydrocarbons every hour.[90]

Intrinsic $SnO_2$ can have moderate conductivity (1 $\Omega\,cm$), enabling it to facilitate electrostatic dissipation readily. $TiO_2$ tends to be much more

resistive, but may still be able to provide some reduction in electrostatic charging. $TiO_2$ by itself has been observed to lose transmittance and hydrophilicity over time, but pairing it with $SiO_2$ can improve its stability. Cuddihy proposed chemical substitutions to shift hydrophobicity (group I ions for more hydrophilic surfaces and group II and III ions for more hydrophobic surfaces) and potentially increase surface hardness through ionic cross-linking (*via* Al substitution).[83] Proprietary combinations of these are being increasingly implemented at scale and the wider research community has been investigating structures utilizing them and also evaluating their initial and long-term effectiveness.

Active approaches to repulse dust accumulation using electric fields date back to the early 1970s with the work of Aoyorna and Masuda.[91] Generally, patterned electrodes are used to try to generate a field or traveling wave that can sweep dust particles off a surface. Sometimes these electrodes have just been narrow wires, but they can also use transparent conducting oxides on the order of 100 nm thick. Mazumder *et al.* originally developed an electrodynamic screen approach because of dust problems in the Mars rover program. This was done with an alternating pattern of transparent indium tin oxide electrodes embedded in a polymeric low surface energy dielectric.[92] This general idea is still being refined and with demonstrations of good dust removal efficiency,[93] sometimes with wires or silver electrodes and an oxide dielectric (*e.g.* Corning® Willow® glass). However, it has yet to be implemented at large scale. High voltages (1000–3000 V) are generally required to make resuspension of particles efficient. As mentioned previously, in PV systems voltages of this magnitude have implications associated with PID. Biryukov found that AC fields were effective only for particles $>8$ μm in size and less effective at higher humidities or after dust had time to settle.[94] So far, this general approach has not been as effective to date in more humid environments and there are cost concerns, although more recently cost models have been developed to begin to capture the ''levelized cost of mirror cleaning'' (for concentrated solar power applications such as solar thermal).[95]

## 3.7 Opportunities and Challenges

Outlined in this chapter are several applications of ultrathin oxides in photovoltaics, including passivation layers, selective contact/buffer layers, recombination layers, barrier layers, anti-reflection coatings, and anti-soiling layers, with specific examples from across several PV technologies. Certain oxides, such as aluminum oxide, tin oxide, and silicon oxide, appear in examples of numerous applications. This is due, in part, to the multifunctional nature of oxide layers (*e.g.* a selective contact layer also being used as a passivant and barrier layer). However, it also leads to the question of whether oxides are truly the best materials for these applications or whether they are used because their properties and/or processing methods are better developed than those of other materials.

Solar technologies are not stand-alone, but rather build upon prior experience. As such, the first materials tested in emerging technologies will borrow from related PV fields. Silicon, CdTe, and III–V semiconductors largely paved their own way in many respects to commercial relevance as the earliest PV systems to be developed. For example, silicon strongly influences nearly all single-junction technologies and is the basis for most of our understanding of semiconductor physics, CdTe solved many challenges of thin-film PV, and III–V semiconductors influenced the fundamentals of tandems and multijunction devices. The framework from these fields trickled down to next-generation technologies, such as OPVs, quantum dots, and MHPs, and this has led to many similarities.

When searching for new opportunities, one must remember that the material need for oxides in next-generation PV is not necessarily the same as in the established technologies. Identifying these differentiators will motivate the research and development of new materials. In a different respect, emerging technologies are fabricated at smaller scale and more heavily in academic environments, leading to a higher degree of flexibility to test new, innovative materials and ideas. There is the opportunity in established fields to learn from new innovations in emerging technologies. Below we discuss high-level areas of opportunity for oxides in photovoltaics.

### 3.7.1 Multifunctionality

Multifunctionality of oxide layers in PV device stacks is a critical property, particularly in contact with the absorber layers. Universal requirements for high-efficiency solar cells are (i) selective carrier extraction, (ii) interfacial passivation, (iii) prevention of molecular or atomic diffusion into or out of the device, and (iv) optical management to ensure high external quantum efficiency. A stable, high-efficiency solar cell cannot sacrifice any of these properties and therefore oxide layer functionality cannot be looked at in isolation. It is challenging to find materials that satisfy all requirements simultaneously; however, it is important to evaluate a material's success in its entirety rather than solely its ''primary'' function. There are opportunities for advancement in the field through targeting improvements in oxide ''secondary'' functions, particularly in emerging PV fields.

### 3.7.2 Deposition Methods

Emerging applications and technologies require ''soft'' oxide deposition techniques, which were not necessarily a requirement for Si, CdTe, and III–V semiconductors. In this case, ''soft'' refers to low temperature and low kinetic energy. Thermal evaporation, solution processing, and ALD have been demonstrated as soft oxide deposition techniques for OPVs and MHPs, but the types and properties of oxides deposited by these techniques are very limited. One interesting deposition technique that has not been as heavily researched in the emerging PV fields is remote plasma sputtering.

Remote plasma sputter systems separate the plasma generation from the deposition surface and limit the substrate to only low-energy ion exposure. There are opportunities to develop highly scalable soft deposition techniques and to increase the range of material systems and improve material properties that can be deposited by such methods.

### 3.7.3 Cost, Stability, and Circularity

Utility-scale solar installations provide electrons to the grid as a commodity resource. Ultimately, the growth of solar power generation will depend on economics. Oxide processing can have strong implications on this calculation through capital equipment cost (depreciation) and throughput, materials expense, device yield, and stability. Upfront processing costs are easy to calculate, but stability effects can be more challenging and nuanced. Module reliability is often tested through rigorous multi-stressor standardized tests designed to target and accelerate specific degradation modes. A challenge with materials development is that new processing methods and new materials can result in unexpected degradation modes which may not be immediately detected in existing stress tests. One challenge with scaling new, low-cost deposition processes is uniformity over large areas. Pinholes, in particular, are of high concern for ultrathin oxides as they can lead to unintentional interfaces in the device stack. Impurities and/or new oxide systems can also lead to degradation modes that differ from previous generations of the technology and may not be readily apparent. These types of modes may not readily occur under single stress conditions (*e.g.* heat) but rather under coupled stresses observed in the field (*e.g.* heat + moisture + bias or in the presence of by-products from packaging – such as acetic acid from ethyl vinyl acetate encapsulants). When new degradation modes are not detected by established test methods before deployment, they can lead to massive costs when they appear in fielded modules.

Circularity is a critical concept when considering solar cells as a truly renewable, terawatt-scale energy technology. At the moment, Si solar cells (>90% of the global market) are mostly part of a linear economy, where fresh materials enter the supply chain to form new solar cells that enter a landfill at their end of life. Although recycling of Si modules is becoming more prevalent in Europe, it is still costly and not considered as part of the initial cost. Originally, owing to concerns over toxicity, CdTe had always been recycled, becoming an additional source of Te. In order to sustain solar technologies on a large scale, these processes will have to become circular and of low cost (in the case of Si), where used solar cells can be refurbished or recycled and brought back into service. Oxide development may contribute towards improving the circularity of photovoltaics by (i) improving the lifetime of the solar cell, (ii) developing processes to refurbish or reclaim the materials, including metals/oxides used in the device, (iii) minimizing the total material usage in each module, (iv) utilizing Earth-abundant materials, and (v) materials selection with reclamation in mind (*i.e.* select elements that would not form catastrophic impurities in recycled materials).

### 3.7.4 Challenges for Specific Oxide Applications

There are several opportunities for specific oxide applications in PV. While passivation layers are not completely technology agnostic, there is overlap between absorber systems due to the commonality of passivation mechanisms. Passivation layer development requires system-by-system optimization, specifically in the context of interfacial chemical stability. In this chapter, we have primarily discussed electronic passivation (*i.e.* reduction of the interface recombination velocity); however, the property of self-passivation can play a critical role in device stability.

One additional consideration for use of ultrathin oxides when pairing with some materials relates the lattice mismatch of a native oxide to the base material as described by the Pilling–Bedworth ratio. When this ratio deviates beyond a certain point, the oxide is no longer self-passivating and is inherently unstable, meaning that it can either spall off and reveal new underlying material or open pores, ultimately leading to the complete oxidation of the material. Silicon forms a self-passivating oxide which effectively prevents the oxidation of layers below the surface. This is one of the reasons why silicon has been so successful for CMOS and solar technologies. Although not all absorbers will form self-passivating oxides, paying attention to the propensity of a layer to self-passivate and considering ways to introduce a stable lattice-matched oxide can help improve device stability in the reality of imperfect packaging.

Selective contacts are highly system dependent because they rely on proper band alignment with the absorber. Furthermore, process order, process compatibility (*e.g.* thermal budget), and impurity sensitivity must be considered and can limit the feasibility of certain architectures. Selective contacts can be improved by considering the multifunctional nature of the layer, with properties including carrier selectivity, interfacial passivation, optical transparency, conductivity, and barrier properties. Currently, oxides for selective contacts in emerging technologies, such as MHPs, are limited by processing restrictions. The field could benefit from the development of soft deposition approaches to allow oxide-selective contacts on top of process-sensitive absorber materials.

Recombination layers are largely technology agnostic, but can be sensitive to the application (*e.g.* how many junctions and whether or not solar concentration is used). The typical tradeoffs are transparency and through-plane conductivity when tuning the optical and electronic properties of a material; however, both of these can be improved by making the layer very thin. The challenge is to maintain high device yield over large areas with ultrathin layers. Further improvements can be obtained by developing low-cost methods for easy and flexible integration of more than one type of PV technology.

Moisture and ionic barrier layers are not sensitive to the specific PV technology; however, PV technologies do exhibit varying degrees of moisture sensitivity. Some applications may also require mechanical flexibility, which

is usually achieved by decreasing the overall barrier thickness. Primary efforts being made in the area of barrier layers are decreasing the defect density (*e.g.* pinholes) over large areas and also reducing the fabrication cost, deposition temperature, required barrier thickness and/or number of layers in the barrier.

Finally, anti-reflection coatings and anti-soiling coatings are also technology agnostic, but must be tuned for the band gap and operating location of the solar cell. In the case of anti-soiling coatings, a universal approach has yet to be determined, as observed through the success of both hydrophobic and hydrophilic surfaces. Ongoing research efforts are focused on the cost, optical properties, and stability of these layers.

## References

1. W. Shockley and H. J. Queisser, *J. Appl. Phys.*, 1961, **32**, 510–519.
2. R. N. Hall, *Phys. Rev.*, 1952, **87**, 387.
3. W. Shockley and W. T. Read, *Phys. Rev.*, 1952, **87**, 835–842.
4. S. M. Sze and K. K. Ng, *Physics of Semiconductor Devices*, John Wiley & Sons, Inc., Hoboken, New Jersey, 3rd edn, 2006.
5. P. Würfel and U. Würfel, *Physics of Solar Cells : From Basic Principles to Advanced Concepts*, Wiley-VCH Verlag GmbH & Co., Weinheim, Germany, 3rd edn, 2016.
6. H. Hasegawa, T. Sato, S. Kasai, B. Adamowicz and T. Hashizume, *Sol. Energy*, 2006, **80**, 629–644.
7. A. Ramstad, G. Brocks and P. J. Kelly, *Phys. Rev. B: Condens. Matter Mater. Phys.*, 1995, **51**, 14504–14523.
8. F. J. Giessibl, *Science*, 1995, **267**, 68–71.
9. S. Philipps and W. Warmuth, *Photovoltaics Report*, Fraunhofer Institute for Solar Energy Systems, ISE, 2020.
10. A. G. Aberle, *Prog. Photovoltaics*, 2000, 473–487.
11. R. S. Bonilla, B. Hoex, P. Hamer and P. R. Wilshaw, *Phys. Status Solidi A*, 2017, **214**, 1700293.
12. Champion Module Efficiencies, https://www.nrel.gov/pv/assets/pdfs/champion-module-efficiencies.20200708.pdf, 2020.
13. M. Woodhouse, B. Smith, A. Ramdas and R. Margolis, *Crystalline Silicon Photovoltaic Module Manufacturing Costs and Sustainable Pricing: 1H 2018 Benchmark and Cost Reduction Road Map*, National Renewable Energy Laboratory, Golden CO, 2019.
14. *International Technology Roadmap for Photovoltaic (ITRPV)*, 9th edn, 2018.
15. B. Hoex, S. B. S. Heil, E. Langereis, M. C. M. van de Sanden and W. M. M. Kessels, *Appl. Phys. Lett.*, 2006, **89**, 04112.
16. R. Hezel and K. Jaeger, *J. Electrochem. Soc.*, 1989, **136**, 518–523.
17. M. J. Kerr and A. Cuevas, *Semicond. Sci. Technol.*, 2001, **17**, 35–38.
18. R. S. Johnson, G. Lucovsky and I. Baumvol, *J. Vac. Sci. Technol., A*, 2001, **19**, 1353–1360.

19. M. Cho, H. B. Park, J. Park, C. S. Hwang, J.-C. Lee, S.-J. Oh, J. Jeong, K. S. Hyun, H.-S. Kang, Y.-W. Kim and J.-H. Lee, *J. Appl. Phys.*, 2003, **94**, 2563–2571.
20. C. L. Perkins, T. Ablekim, T. M. Barnes, D. Kuciauskas, K. G. Lynn, W. Nemeth, M. O. Reese, S. K. Swain and W. K. Metzger, *IEEE J. Photovolt.*, 2018, **8**, 1858–1861.
21. J. M. Kephart, A. Kindvall, D. Williams, D. Kuciauskas, P. Dippo, A. Munshi and W. S. Sampath, *IEEE J. Photovolt.*, 2018, **8**, 587–593.
22. B. Vermang, V. Fjällström, J. Pettersson, P. Salomé and M. Edoff, *Sol. Energy Mater. Sol. Cells*, 2013, **117**, 505–511.
23. Y. Lee, S. Lee, G. Seo, S. Paek, K. T. Cho, A. J. Huckaba, M. Calizzi, D.-W. Choi, J.-S. Park, D. Lee, H. J. Lee, A. M. Asiri and M. K. Nazeeruddin, *Adv. Sci.*, 2018, **5**, 1800130.
24. K. A. Bush, A. F. Palmstrom, Z. J. Yu, M. Boccard, R. Cheacharoen, J. P. Mailoa, D. P. McMeekin, R. L. Z. Hoye, C. D. Bailie, T. Leijtens, I. M. Peters, M. C. Minichetti, N. Rolston, R. Prasanna, S. Sofia, D. Harwood, W. Ma, F. Moghadam, H. J. Snaith, T. Buonassisi, Z. C. Holman, S. F. Bent and M. D. McGehee, *Nat. Energy*, 2017, **2**, 17009.
25. J. P. Correa Baena, L. Steier, W. Tress, M. Saliba, S. Neutzner, T. Matsui, F. Giordano, T. J. Jacobsson, A. R. Srimath Kandada, S. M. Zakeeruddin, A. Petrozza, A. Abate, M. K. Nazeeruddin, M. Grätzel and A. Hagfeldt, *Energy Environ. Sci.*, 2015, **8**, 2928–2934.
26. A. F. Palmstrom, G. E. Eperon, T. Leijtens, R. Prasanna, S. N. Habisreutinger, W. Nemeth, E. A. Gaulding, S. P. Dunfield, M. Reese, S. Nanayakkara, T. Moot, J. Werner, J. Liu, B. To, S. T. Christensen, M. D. McGehee, M. F. A. M. van Hest, J. M. Luther, J. J. Berry and D. T. Moore, *Joule*, 2019, **3**, 1–12.
27. A. F. Palmstrom, J. A. Raiford, R. Prasanna, K. A. Bush, M. Sponseller, R. Cheacharoen, M. C. Minichetti, D. S. Bergsman, T. Leijtens, H.-P. Wang, V. Bulović, M. D. McGehee and S. F. Bent, *Adv. Energy Mater.*, 2018, **8**, 1800591.
28. H. L. Hartnagel, A. L. Dawar, A. K. Jain and C. Jagadish, *Semiconducting Transparent Thin Films*, Institute of Physics Publishing, Bristol, UK, 1995.
29. L. Bertoluzzi, C. C. Boyd, N. Rolston, J. Xu, R. Prasanna, B. C. O'Regan and M. D. McGehee, *Joule*, 2020, **4**, 109–127.
30. S. Lany, J. Osorio-Guillén and A. Zunger, *Phys. Rev. B*, 2007, **75**, 241203.
31. M. D. Irwin, D. B. Buchholz, A. W. Hains, R. P. H. Chang and T. J. Marks, *Proc. Natl. Acad. Sci.*, 2008, **105**, 2783–2787.
32. E. L. Ratcliff, J. Meyer, K. X. Steirer, A. Garcia, J. J. Berry, D. S. Ginley, D. C. Olson, A. Kahn and N. R. Armstrong, *Chem. Mater.*, 2011, 4988–5000.
33. C. C. Boyd, R. C. Shallcross, T. Moot, R. Kerner, L. Bertoluzzi, A. Onno, S. Kavadiya, C. Chosy, E. J. Wolf, J. Werner, J. A. Raiford, C. de Paula, A. F. Palmstrom, Z. J. Yu, J. J. Berry, S. F. Bent, Z. C. Holman, J. M. Luther, E. L. Ratcliff, N. R. Armstrong and M. D. McGehee, *Joule*, 2020, **4**, 1759–1775.

34. A. Ennaoui, S. Siebentritt, M. C. Lux-Steiner, W. Riedl and F. Karg, *Sol. Energy Mater. Sol. Cells*, 2001, **67**, 31–40.
35. C. Platzer-Björkman, T. Törndahl, D. Abou-Ras, J. Malmström, J. Kessler and L. Stolt, *J. Appl. Phys.*, 2006, **100**, 044506.
36. G. E. Eperon, T. Leijtens, K. A. Bush, R. Prasanna, T. Green, J. T.-W. Wang, D. P. McMeekin, G. Volonakis, R. L. Milot, R. May, A. F. Palmstrom, D. J. Slotcavage, R. A. Belisle, J. B. Patel, E. S. Parrott, R. J. Sutton, W. Ma, F. Moghadam, B. Conings, A. Babayigit, H.-G. Boyen, S. F. Bent, F. Giustino, L. M. Herz, M. B. Johnston, M. D. McGehee and H. J. Snaith, *Science*, 2016, **354**, 861–865.
37. J. Werner, G. Dubuis, A. Walter, P. Löper, S.-J. Moon, S. Nicolay, M. Morales-Masis, S. De Wolf, B. Niesen and C. Ballif, *Sol. Energy Mater. Sol. Cells*, 2015, **141**, 407–413.
38. J. A. Raiford, R. A. Belisle, K. A. Bush, R. Prasanna, A. F. Palmstrom, M. D. McGehee and S. F. Bent, *Sustainable Energy Fuels*, 2019, **3**, 1517–1525.
39. A. De Vos, *J. Phys. D: Appl. Phys.*, 1980, **13**, 839–846.
40. G. Conibeer, *Mater. Today*, 2007, **10**, 42–50.
41. D. Feldman, V. Ramasamy, R. Fu, A. Ramdas, J. Desai and R. Margolis, *U.S. Solar Photovoltaic System and Energy Storage Cost Benchmark: Q1 2020*, Report NREL/TP-6A20-77324, National Renewable Energy Lab, 2021.
42. M. O. Reese, S. Glynn, M. D. Kempe, D. L. McGott, M. S. Dabney, T. M. Barnes, S. Booth, D. Feldman and N. M. Haegel, *Nat. Energy*, 2018, **3**, 1002–1012.
43. M. P. Lumb, M. K. Yakes, M. González, I. Vurgaftman, C. G. Bailey, R. Hoheisel and R. J. Walters, *Appl. Phys. Lett.*, 2012, **100**, 213907.
44. S. M. Bedair, M. F. Lamorte and J. R. Hauser, *Appl. Phys. Lett.*, 1979, **34**, 38–39.
45. J. F. Geisz, R. M. France, K. L. Schulte, M. A. Steiner, A. G. Norman, H. L. Guthrey, M. R. Young, T. Song and T. Moriarty, *Nat. Energy*, 2020, **5**, 326–335.
46. Z. J. Yu, J. V. Carpenter and Z. C. Holman, *Nat. Energy*, 2018, **3**, 747–753.
47. T. R. Klein, B. G. Lee, M. Schnabel, E. L. Warren, P. Stradins, A. C. Tamboli and M. F. A. M. van Hest, *ACS Appl. Mater. Interfaces*, 2018, **10**, 8086–8091.
48. M. Schnabel, H. Schulte-Huxel, M. Rienäcker, E. L. Warren, P. F. Ndione, B. Nemeth, T. R. Klein, M. F. A. M. van Hest, J. F. Geisz, R. Peibst, P. Stradins and A. C. Tamboli, *Sustainable Energy Fuels*, 2020, **4**, 549–558.
49. E. L. Warren, M. G. Deceglie, M. Rienäcker, R. Peibst, A. C. Tamboli and P. Stradins, *Sustainable Energy Fuels*, 2018, **2**, 1141–1147.
50. G. N. Parsons, S. E. Atanasov, E. C. Dandley, C. K. Devine, B. Gong, J. S. Jur, K. Lee, C. J. Oldham, Q. Peng, J. C. Spagnola and P. S. Williams, *Coord. Chem. Rev.*, 2013, **257**, 3323–3331.
51. W. Luo, Y. S. Khoo, P. Hacke, V. Naumann, D. Lausch, S. P. Harvey, J. P. Singh, J. Chai, Y. Wang, A. G. Aberle and S. Ramakrishna, *Energy Environ. Sci.*, 2017, **10**, 43–68.

52. R. H. Doremus, *J. Appl. Phys.*, 2006, **100**, 101301.
53. D. J. Coyle, *Prog. Photovoltaics Res. Appl.*, 2013, **21**, 156–172.
54. D. J. Coyle, H. A. Blaydes, R. S. Northey, J. E. Pickett, K. R. Nagarkar, R.-A. Zhao and J. O. Gardner, *Prog. Photovoltaics Res. Appl.*, 2013, **21**, 173–186.
55. M. D. Kempe, M. O. Reese and A. A. Dameron, *Rev. Sci. Instrum.*, 2013, **84**, 025109.
56. J. Meyer, P. Görrn, F. Bertram, S. Hamwi, T. Winkler, H.-H. Johannes, T. Weimann, P. Hinze, T. Riedl and W. Kowalsky, *Adv. Mater.*, 2009, **21**, 1845–1849.
57. B. M. Henry, A. G. Erlat, A. McGuigan, C. R. M. Grovenor, G. A. D. Briggs, Y. Tsukahara, T. Miyamoto, N. Noguchi and T. Niijima, *Thin Solid Films*, 2001, **382**, 194–201.
58. S. K. Cho, T. Y. Cho, W. J. Lee, M. S. Um, W. J. Choi, J. H. Lee, J. Ryu and S. H. Choa, *Plasma Processes Polym.*, 2019, **16**, 1800170.
59. A. Morlier, S. Cros, J. P. Garandet and N. Alberola, *Sol. Energy Mater. Sol. Cells*, 2013, **115**, 93–99.
60. C. F. Struller, P. J. Kelly, N. J. Copeland and C. M. Liauw, *J. Vac. Sci. Technol., A*, 2012, **30**, 041502.
61. P. E. Burrows, G. L. Graff, M. E. Gross, P. M. Martin, M. K. Shi, M. Hall, E. Mast, C. Bonham, W. Bennett and M. B. Sullivan, *Displays*, 2001, **22**, 65–69.
62. A. A. Dameron, S. D. Davidson, B. B. Burton, P. F. Carcia, R. S. McLean and S. M. George, *J. Phys. Chem. C*, 2008, **112**, 4573–4580.
63. J. J. Finley and F. H. Gillery, US Pat., 5830252, *Alkali metal diffusion barrier layer*, 1998.
64. J. H. Scofield, S. Asher, D. Albin, J. Tuttle, M. Contreras, D. Niles, R. Reedy, A. Tennant and R. Noufi, *Proceedings of 1994 IEEE 1st World Conference on Photovoltaic Energy Conversion - WCPEC*, 1994, vol. 1, pp. 164–167.
65. P. Blösch, F. Pianezzi, A. Chirilă, P. Rossbach, S. Nishiwaki, S. Buecheler and A. N. Tiwari, *J. Appl. Phys.*, 2013, **113**, 054506.
66. A. Chirila, P. Reinhard, F. Pianezzi, P. Bloesch, A. R. Uhl, C. Fella, L. Kranz, D. Keller, C. Gretener, H. Hagendorfer, D. Jaeger, R. Erni, S. Nishiwaki, S. Buecheler and A. N. Tiwari, *Nat. Mater.*, 2013, **12**, 1107–1111.
67. J. M. Raguse, C. P. Muzzillo, J. R. Sites and L. Mansfield, *IEEE J. Photovolt.*, 2017, **7**, 303–306.
68. S. C. Pop, R. Schulze, B. Brophy, S. Maghsoodi, Y. S. Yang, Z. R. Abrams and P. Gonsalves, *2015 IEEE 42nd Photovoltaic Specialist Conference (PVSC)*, 2015, pp. 1–6.
69. M. D. Kempe, *Sol. Energy Mater. Sol. Cells*, 2010, **94**, 246–253.
70. M. D. Kempe, T. Moricone and M. Kilkenny, *Proc. SPIE 7412, Reliability of Photovoltaic Cells, Modules, Components, and Systems II*, 2009.
71. A. Gombert, K. Rose, A. Heinzel, W. Horbelt, C. Zanke, B. Bläsi and V. Wittwer, *Sol. Energy Mater. Sol. Cells*, 1998, **54**, 333–342.
72. W. M. Haynes, *CRC Handbook of Chemistry and Physics: A Ready-reference Book of Chemical and Physical Data*, 2016.

73. *International Technology Roadmap for Photovoltaics (ITRPV)*, 11th edn, 2020.
74. B. E. Yoldas, *Appl. Opt.*, 1980, **19**, 1425–1429.
75. S. J. Wilson and M. C. Hutley, *Opt. Acta*, 1982, **29**, 993–1009.
76. M. J. Minot, *J. Opt. Soc. Am.*, 1976, **66**, 515–519.
77. M. F. Schubert, F. W. Mont, S. Chhajed, D. J. Poxson, J. K. Kim and E. F. Schubert, *Opt. Express*, 2008, **16**, 5290–5298.
78. K. Cathro, D. Constable and T. Solaga, *Sol. Energy*, 1984, **32**, 573–579.
79. X. Li, X. Du and J. He, *Langmuir*, 2010, **26**, 13528–13534.
80. T. M. Barnes, M. O. Reese, J. D. Bergeson, B. A. Larsen, J. L. Blackburn, M. C. Beard, J. Bult and J. van de Lagemaat, *Adv. Energy Mater.*, 2012, **2**, 353–360.
81. M. Mani and R. Pillai, *Renewable Sustainable Energy Rev.*, 2010, **14**, 3124–3131.
82. T. Sarver, A. Al-Qaraghuli and L. L. Kazmerski, *Renewable Sustainable Energy Rev.*, 2013, **22**, 698–733.
83. E. F. Cuddihy, *Sol. Energy Mater.*, 1980, **3**, 21–33.
84. P. B. Adams, *J. Non-Cryst. Solids*, 1984, **67**, 193–205.
85. S. A. Biryukov, *J. Aerosol Sci.*, 1996, **27**, S77–S78.
86. S. Biryukov, *J. Aerosol Sci.*, 1998, **29**, 129–139.
87. R. S. Berg, *Heliostat Dust Buildup and Cleaning Studies*, Sandia National Lab, https://www.osti.gov, 1978.
88. J. Drelich, E. Chibowski, D. D. Meng and K. Terpilowski, *Soft Matter*, 2011, **7**, 9804–9828.
89. P. Roach, N. J. Shirtcliffe and M. I. Newton, *Soft Matter*, 2008, **4**, 224–240.
90. A. Fujishima, T. N. Rao and D. A. Tryk, *J. Photochem. Photobiol., C*, 2000, **1**, 1–21.
91. M. Aoyorna and S. Masuda, *Proc. Gen. Conf. Inst. Electron. Eng. Jpn*, 1971, 821.
92. M. Mazumder, M. N. Horenstein, J. W. Stark, P. Girouard, R. Sumner, B. Henderson, O. Sadder, I. Hidetaka, A. S. Biris and R. Sharma, *IEEE Trans. Ind. Appl.*, 2013, **49**, 1793–1800.
93. R. Sharma, C. A. Wyatt, J. Zhang, C. I. Calle, N. Mardesich and M. K. Mazumder, *IEEE Trans. Ind. Appl.*, 2009, **45**, 591–596.
94. S. A. Biryukov, *J. Aerosol Sci.*, 1996, **27**, S415–S416.
95. N. Joglekar, E. Guzelsu, M. Mazumder, A. Botts and C. Ho, *A Levelized Cost Metric for EDS-Based Cleaning of Mirrors in CSP Power Plants*, ASME, 2014.

CHAPTER 4

# *Blocking Layers for Controlling Directional Charge Transport in Dye-sensitized Photoelectrochemical Cells*

J. R. SWIERK

Department of Chemistry, State University of New York at Binghamton, P.O. Box 6000, Vestal, NY 13902, USA
Email: jswierk@binghamton.edu

## 4.1 Introduction

Charge transfer plays a foundational role in solar energy capture and conversion. Absorption of a photon generates an excited state that must be productively utilized within a moment of time. Regardless of whether the fate of the excited electron is to be used as power for an electrical device, stored in a battery, or used to drive a catalyst for fuel production, controlling the electron transfer dynamics is paramount. Although initial excitation occurs on a nanosecond or faster timescale, subsequent productive and unproductive pathways occur across multiple timescales ranging from nanoseconds to milliseconds or longer. Managing these multiple timescales is the key challenge that must be overcome for productive energy conversion and storage.

The strategies for controlling charge transfer vary depending on the specific system for energy conversion and the requirements for how that

Energy and Environment Series No. 30
Ultrathin Oxide Layers for Solar and Electrocatalytic Systems
Edited by Heinz Frei and Daniel V. Esposito

Published by the Royal Society of Chemistry, www.rsc.org

system will be deployed. For example, the design of a photoelectrochemical cell for solar water splitting must consider efficient light absorption and charge separation, productive catalysis, and stability in an aqueous environment, whereas the design of a standard solar cell does not need to consider the last two. This chapter is specifically focused on the use of thin oxide blocking layers that are a few nanometers thick or less and that permit desirable electron transfer steps while retarding undesirable steps. Although the basic principles are broadly applicable to any photoelectrochemical system, the discussion of these blocking layers will be presented in the context of systems that utilize molecular photosensitizers to harvest and convert solar energy into a useful electrochemical potential that can drive fuel-forming reactions. These systems offer a high degree of tunability in terms of light harvesting and reduction potentials, and also modularity to mix and match different components easily. Many of the key insights into thin blocking layers have been developed in these dye-sensitized systems and therefore present the fullest picture of their properties and application.

### 4.1.1 Photosynthesis

At some level, all examples of dye-sensitized energy conversion draw inspiration from biological photosynthesis. Although a detailed discussion of photosynthesis is beyond the scope of this chapter, it provides a useful example of efficient charge transfer in dye-sensitized energy conversion and offers insights relevant to the design of thin oxide blocking layers.

The overall process of photosynthesis is achieved by series of membrane-bound proteins and freely diffusing redox mediators. Figure 4.1 shows the spatial and energetic arrangement of key components within photosystem II. Light absorption occurs *via* a series of light-harvesting antenna pigments that funnel their excitation energy to a P680 chlorophyll dimer in photosystem II or P700 chlorophyll dimer in photosystem I. Electron transfer within either reaction center is rapid, with a series of electron transfers resulting in a physical charge separation of ~3 nm achieved in less than 1 ns (Figure 4.1). There are two key insights relevant to the design of dye-sensitized systems and blocking layers: (1) while each electron transfer step results in a small loss of potential energy, the physical separation of the charge reduces geminate recombination by multiple orders of magnitude; (2) the ''staircase'' of potential that facilitates electron transfer also introduces directionality and prevents the electron from reversing its transit back along the electron transfer chain. Both of these effects are leveraged to generate a long-lived charge-separated state. This is crucial because water oxidation catalysis at the oxygen-evolving complex in photosystem II occurs on a microsecond to millisecond timescale.[1] Turnover frequencies for abiotic catalysts are often slower,[2] making the requirement for long-lived charge-separated states even more critical.

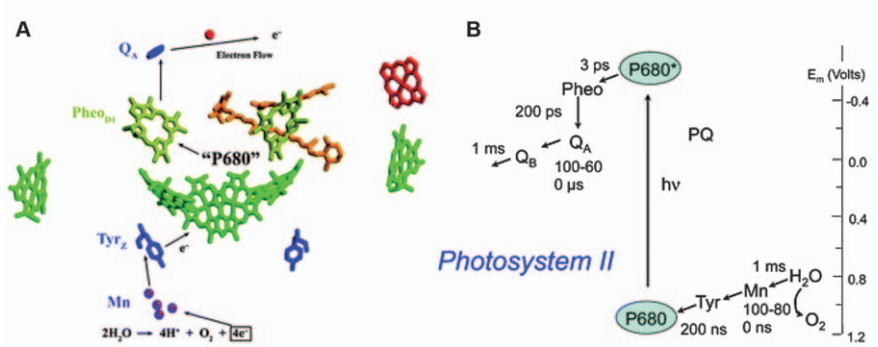


**Figure 4.1** (A) Structure of photosystem II complex near the reaction center region, with the protein background removed. Light energy is transferred from the chlorophyll antenna regions to the P680 reaction center special chlorophyll pair, which undergoes photooxidation. The released electron first proceeds to an initial pheophytin (Pheo) electron acceptor before being transferred to a quinone electron acceptor ($Q_A$). Eventually, the electron is transferred to a mobile plastoquinone carrier, $Q_B$ [not shown in (A)], which can be released from photosystem II to continue the electron transfer chain. The oxidized P680 reaction center is re-reduced by initially oxidizing a nearby tyrosine (Tyr), which stabilizes the charge-separated state against back-reaction. The oxidized Tyr then oxidizes an $Mn_4$/Ca cluster (Mn), which catalyzes water oxidation (four-electron process) and immobilizes the reactive intermediates of this reaction. (B) Redox potentials relative to the normal hydrogen electrode within the photosystem II reaction center and electron transfer times between the various components.
(A, B) Reproduced from ref. 2 and 80 with permission from the Royal Society of Chemistry.

### 4.1.2 Dye-sensitized Solar Cells

The prototype dye-sensitized energy conversion system is the dye-sensitized solar cell (DSSC). In a typical DSSC, a 3D network of oxide nanoparticles is sintered to prepare an electrically conductive, mesoporous photoanode. A molecular light-absorbing dye (also known as a photosensitizer) is anchored to the surface of the film through functional groups, most often a carboxylic acid. Under illumination, an electron on the photosensitizer is excited and undergoes rapid transfer into the conduction band of the oxide film. The oxidized photosensitizer on the surface is rapidly regenerated by a redox mediator in solution, which allows the injected electron to diffuse through the 3D film until being transported to a dark cathode, where it is used to reduce the oxidized mediator.[3] Recombination between injected electrons and the oxidized photosensitizers on the surface is a minor issue for DSSCs because the oxidized photosensitizer is rapidly regenerated by the mediator in solution. More problematic in DSSCs can be undesired electron transfer between injected electrons and the oxidized mediator.

### 4.1.3 Water-splitting Dye-sensitized Photoelectrochemical Cells

Inspired by both natural photosynthesis and the success of DSSCs, the water-splitting dye-sensitized photoelectrochemical cell (WS-DSPEC) utilizes a similar architecture to DSSCs to achieve overall water splitting. A high surface area support, typically comprised of sintered semiconductor nanoparticles, is functionalized with light-absorbing dyes and catalysts. It is the presence of the catalyst that represents the chief difference between DSSCs and WS-DSPECs. Geminate recombination of injected electrons and oxidized photosensitizers is a minor issue in DSSCs because the reversible redox mediator rapidly reduces the oxidized photosensitizer. In the case of WS-DSPECs, slow catalytic turnover means that recombination between injected electrons and the oxidized photosensitizer is a major issue. Although both dye-sensitized photoanodes and photocathodes have been demonstrated,[4] the majority of the work has focused on WS-DSPEC photoanodes and we will largely focus the present discussion on these photoelectrodes.

Figure 4.2 shows a general scheme for WS-DSPECs. Under illumination, the photosensitizer absorbs light, thereby generating an excited electron that can be transferred to the conduction band of the semiconductor support (steps 1 and 2). Injected electrons diffuse through the nanoparticulate film (step 3) until collected by a transparent conductive oxide current collector at

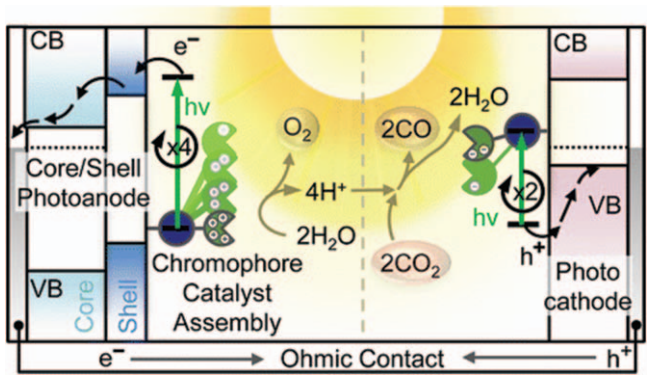


**Figure 4.2** Schematic diagram of a water-splitting dye-sensitized photoelectrochemical cell (WS-DSPEC). The photoanode is made from a mesoporous semiconductor (*e.g.* $TiO_2$) and functionalized with light-absorbing dyes and water oxidation catalysts. Under illumination (1) an excited electron is transferred into the conduction band of the semiconductor (2) and then transported through the mesoporous film (3) to a transparent conducting oxide current collector. At the same time, the oxidized dye is reduced by oxidizing the water oxidation catalyst (4), which subsequently accumulates four holes and oxidizes water to generate oxygen (5) and protons. The protons are reduced at a dark cathode using the electrons previously generated by injection from the dye.
Reproduced from ref. 5 with permission from American Chemical Society, Copyright 2016.

the back of the nanoparticle film, at which point those electrons are shuttled to a dark cathode. At the same time, hole hopping on the surface between adjacent photosensitizer molecules (step 4) brings the hole to a water oxidation catalyst, where it is used to drive the four-electron oxidation of water to molecular oxygen and four protons (step 5). These protons are eventually reduced at the cathode to generate molecular hydrogen.

Typically, the supports for WS-DPEC photoanodes are similar to those for DSSCs – mesoporous 3D networks of sintered nanoparticles. Nanoparticulate anatase $TiO_2$ is most commonly used, although nanoparticulate $SnO_2$ and rutile $TiO_2$ have also been utilized in WS-DSPEC photoanodes because of the more positive conduction band potentials.[2,5,6] A more positive conduction band potential leads to more driving force for electron injection and therefore faster injection kinetics and larger injection yields (see below). Electron mobility in nanoparticulate semiconductor films is several orders of magnitude smaller compared with single-crystal semiconductors. This results from an exponential distribution of sub-band gap trap states, which form as a consequence of surface defects and defects at the particle–particle junction.[7] Furthermore, penetration of the electrolyte into the mesoporous structure screens local electric field effects and limits diffusion. The inherently porous nature of the film also imposes geometrical restrictions on the movement of electrons and restricts charge transport.[8]

The choice of photosensitizer is an important design element in WS-DSPECs as the photosensitizer needs to have an excited-state potential that is sufficiently negative to inject into the semiconductor and the oxidized form of the photosensitizer must have a reduction potential that is sufficiently positive to drive water oxidation. Ruthenium polypyridyl dyes are the most common photosensitizers (Figure 4.3A). The metal-to-ligand charge-transfer band of these complexes lies in the blue part of the spectrum (~450 nm). Excitation places electron density onto a bipyridine ligand, thereby facilitating charge injection into the semiconductor. This excited state persists for hundreds of nanoseconds, which also facilitates efficient electron transfer into the oxide support.[9] A major attraction of ruthenium polypyridyl dyes is that the individual bipyridine ligands can be readily modified to incorporate different anchoring groups, linkers to catalysts, and substituents to tune the properties of the photosensitizer.[10] Porphyrins and other organic chromophores have also been used in WS-DSPECs.[11–15] The choice of anchor plays a significant role in dye selection. Although a carboxylic acid linker offers excellent electronic coupling between the dye and underlying oxide, in the aqueous environment of WS-DSPECs carboxylic acids are susceptible to hydrolysis and are typically avoided in WS-DSPECs. Phosphonate linkers are very common and although they offer poor electronic coupling, they still allow rapid electron injection and a robust linkage. Finally, hydroxamate linkages, although not widely used, offer an excellent balance of electronic coupling and stability.[16]

Both homogeneous, molecular catalysts and heterogeneous, solid catalysts have been demonstrated in WS-DSPECs. The best results to date have

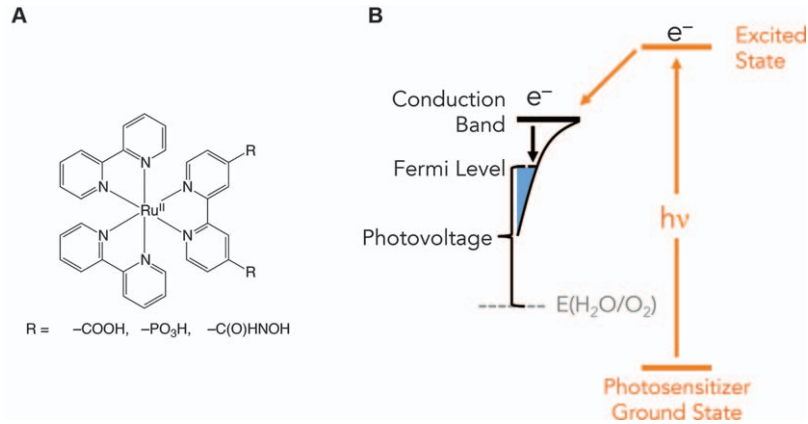


**Figure 4.3** (A) Example of a ruthenium polypyridyl complex with different possible anchoring groups. (B) Schematic showing excitation of an electron from the ground state of the photosensitizer, injection into the conduction band of the semiconductor, and trapping of the electron into sub-band gap trap states. The occupancy of these states determines the position of the Fermi level within the semiconductor, while the difference between the oxidation potential of water and the Fermi level determines the photovoltage of the electrode.

featured molecular water oxidation catalysts, most often featuring ruthenium.[17–19] Nanoparticle catalysts are also widely used. The original report on WS-DSPECs utilized an $IrO_x$ nanoparticle directly coordinated to the ruthenium dye,[20] while subsequent studies utilized molecular linkers[21] or directly sintered the $IrO_x$ to the underlying $TiO_2$ support.[22] Other oxide catalysts such as $CoO_x$ have also been demonstrated.[14] One particularly interesting strategy involves the use of atomic layer deposition to stabilize and entomb assemblies of linked chromophores and catalysts.[23]

Although DSSCs can routinely obtain (and exceed) the 10 $mA\,cm^{-2}$ current density necessary to match the solar flux, WS-DSPECs struggle to achieve even 1 $mA\,cm^{-2}$ current density. Many of the limitations on the performance of WS-DSPECs result from the interplay between the underlying semiconductor and dye. Figure 4.3B shows a schematic of the basic electron injection steps involved in WS-DSPECs. The injection yield (number of excited electrons transferred from the photosensitizer to the semiconductor) increases as the difference in energy between the photosensitizer excited state and conduction band edge increases. Injection kinetics also have some dependence on this energy difference, although the picture is more complex. For example, the negative conduction band potential of anatase $TiO_2$ (−0.2 V *vs.* NHE) decreases the driving force for injection for an excited electron and leads to decreased injection yields.[24,25] On the other hand, the substantially more positive $SnO_2$ conduction band leads to a larger difference in energy with the

photosensitizer excited state and therefore high injection yields. Unfortunately, the high electron mobility within $SnO_2$ also results in efficient electron recombination between the injection electron and dye radical cation on the surface.[26] Also, the photovoltage generated by the WS-DSPEC depends on the difference between the potential for water oxidation at the operational pH and the position of the Fermi level within the semiconductor (Figure 4.3B). As a consequence, materials with a more positive conduction band potential (*e.g.* $SnO_2$) also offer smaller photovoltages. The position of the Fermi level (and therefore photovoltage) can also be lowered by a number of unproductive pathways. Proton intercalation into the $TiO_2$ can occur as charge compensation and lead to the formation of long-lived electrostatic traps, which subsequently increase the rate of recombination.[8] Transfer of electrons from the conduction band of the semiconductor to an oxidized oxygen evolution reaction (OER) catalyst is yet another unproductive pathway that limits WS-DSPECs.[27] Finally, desorption of dye molecules leads to an irreversible decrease in performance for WS-DSPECs.[28] Desorption can be mitigated but typically at the cost of using a linker with poorer electronic coupling between the semiconductor and dye.[29]

### 4.1.4 Core–Shell Architectures to Control Charge Transfer

In one way or another, all of the unproductive processes in WS-DSPECs result from poorly controlled interfacial charge transfer. The need to manage interfacial charge transfer has led to the development of core–shell architectures for use in WS-DSPECs. To generate the core–shell structure, a thin, conformal coating is placed on top of the mesoporous, nanoparticulate network.[19] Although the first demonstration of a core–shell architecture in WS-DSPECs relied on dip coating of electrodes,[30] atomic layer deposition (ALD) is the preparation method of choice.[17,31] ALD relies on the vapor-phase deposition of a reaction precursor (*e.g.* $TiCl_4$) on a surface. Because ALD occurs under vacuum conditions, the precursor will form a monolayer and then cease further deposition. The reactive precursor is removed by vacuum and the sample is exposed to a second precursor, which is often water when the intended material is an oxide. This second precursor reacts with the first to generate a reactive surface. Sequential pulses of the first and second precursors build up the material one atomic layer at a time. For the high surface area supports used in WS-DSPECs, it is common to allow long residence times for the precursors to allow for complete coverage of the mesoporous structure. Depending on the choice of core and shell materials, the core structure can either result in a ''staircase'' of conduction band potentials or function as a wide band gap-tunneling layer. Dye and catalyst molecules are usually absorbed on top of the shell material but work by Meyer's group has demonstrated that the chromophore can be incorporated directly into the shell layer as a method of enhancing stability.[28,32]

## 4.2 Characterization

### 4.2.1 Materials Characterization

The preparation of core–shell architectures on mesoporous films presents unique characterization challenges. For shells prepared by ALD, shell thicknesses are typically determined by using the same deposition conditions to deposit material on a planar surface that can be characterized by ellipsometry. For ALD deposition on high surface area, nanoparticulate films, the deposition times are greatly increased to allow for penetration through the 3D network of the film. The overall thickness of the shell is generally assumed to be determined by the number of precursor pulses and independent of surface area or deposition time. Electron microscopy of core–shell films scraped off of the transparent conducting oxide support generally confirm the validity of this assumption.[24] Energy-dispersive X-ray spectroscopy (EDS) and transmission electron microscopy (TEM) of samples typically show localization of the shell material on the surface of the oxide support.[24] For example, Figure 4.4 shows a false-color EDS image of a $TiO_2$ nanoparticle with a conformal shell of $Al_2O_3$, demonstrating both the conformal nature and thinness of the $Al_2O_3$ shell. TEM measurements of thicker shells also showed conformal surface coatings.[30,33]

Surface area measurements of the photoelectrode are typically made using Brunauer–Emmett–Teller theory to study the adsorption and desorption of

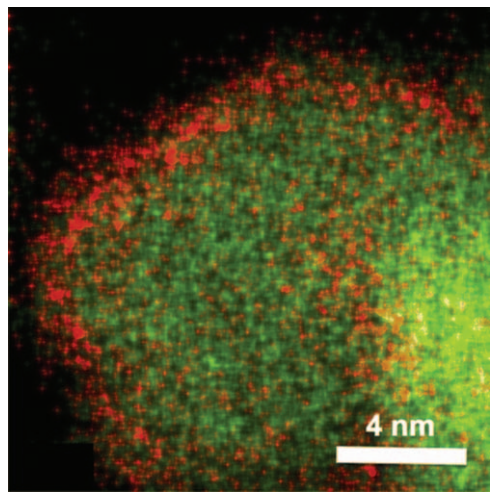


**Figure 4.4** High-resolution scanning/transmission electron microscopy and energy-dispersive X-ray spectroscopy mapping of $TiO_2$ particles with a <0.4 nm overlayer of $Al_2O_3$ prepared by atomic layer deposition showing the location of the $Al_2O_3$ on the edge of the particle. Aluminum is colored red and titanium is colored green.
Reproduced from ref. 24 with permission from American Chemical Society, Copyright 2016.

$N_2$ or Ar onto/from film samples. While the surface area can vary greatly as a function of the material and preparation method, typically the surface area is roughly 100 times greater than the geometric area of the films.[22] The use of powder X-ray diffraction is also common in the characterization of the mesoporous films and it is used to confirm the crystallographic phase of the nanoparticle support and to estimate the average particle size.

### 4.2.2 Transient Absorption Spectroscopy

Transient absorption spectroscopy (TAS) relies on photoinduced changes in absorption to follow charge-transfer dynamics on the femtosecond and longer timescale. In the context of the material presented in this chapter, TAS measurements generally observe the formation and disappearance of a dye radical cation, which forms after electron injection. All TAS measurements rely on a brief laser pulse to excite the sample and to probe the charge-transfer dynamics using a white light source.

Ultrafast TAS measurements utilize the same sub-picosecond laser source for both excitation (pump) and probe sources. In an experiment, the laser pulse is split into two beams, which use an optical delay line to arrive at the sample at different times. The probe source is passed through a white light generator that produces a broad supercontinuum. Ultrafast measurements can span from tens of femtoseconds to a few nanoseconds and most often probe the injection dynamics from the photosensitizer-excited state into the conduction band of the semiconductor. Nanosecond and longer TAS measurements still utilize a laser to excite the sample but the probe is now a separate, broadband white light source (*e.g.* a xenon arc lamp). At this timescale, the pump and probe are separated in time using an electrical delay. Injection is typically complete within 1 ns, or at the very least a minor component over a few nanoseconds remains, so that recombination of the injected electron and photosensitizer radical cation on the surface is mainly observed in these nanosecond and longer TAS measurements.

### 4.2.3 Terahertz (THz) Spectroscopy

Terahertz (THz) radiation lies in the far-infrared part of the spectrum (0.3–30 THz, 1 mm–10 μm) and is attenuated by mobile charge carriers.[29,34] The transmission of THz radiation depends directly on the conductivity of the sample. For a photoexcited sample, the conductivity ($\sigma$) is directly proportional to the product of the electron mobility, $\mu$, and the change in the carrier density, $N$ (*i.e.* the number of injected electrons):

$$\Delta\mathrm{THz} \propto \Delta\sigma \propto \Delta\mu N \tag{4.1}$$

Time-resolved THz spectroscopy (TRTS) is an optical pump, THz probe technique that can be used as a non-contact method to probe the time- and frequency-dependent photoconductivity of a sample. Figure 4.5 (left) shows a schematic of a general TRTS system. The output of an ultrafast laser is split

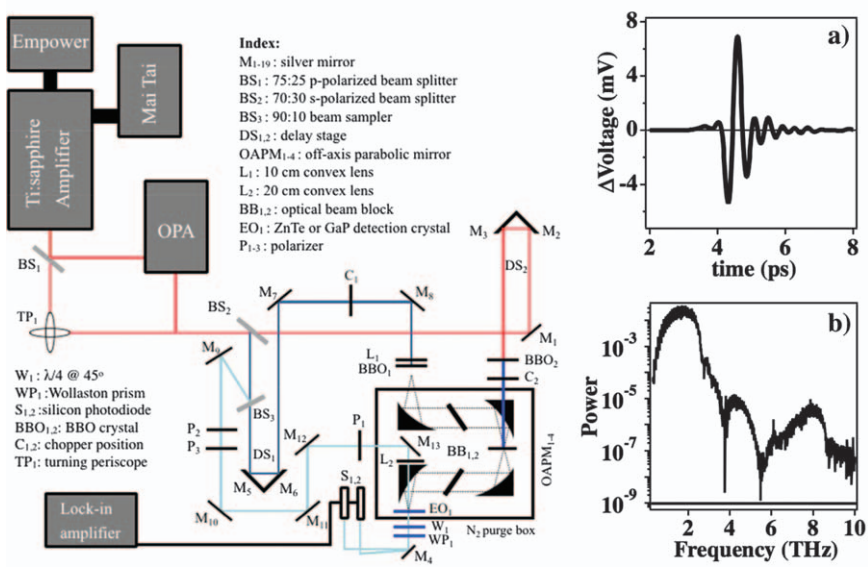


**Figure 4.5** Left: schematic diagram of the THz spectroscopy setup for both optical pump THz probe (OPTP) and time-resolved THz spectroscopy (TRTS). The pump beam (red), the generation beam (dark blue), and the detection beam (light blue) are depicted. Right: a THz time-domain (a) pulse and frequency-domain spectrum (b) are shown.
Reproduced from ref. 81 with permission from American Chemical Society, Copyright 2016.

into three beams, one used to excite the sample (dark blue line), one used to generate THz radiation (dotted gray lines), and one used as a detection pulse (light blue line). A THz pulse is obtained by focusing the probe beam into a small spot to generate a plasma. Time resolution is obtained by varying the time delay between the excitation and probe pulses ($DS_2$).

TRTS data can be collected in one of two ways. In an optical pump THz probe (OPTP) measurement, the change in the peak amplitude of a THz pulse is measured as a function of delay time after an optical pump pulse (Figure 4.5a). OPTP measurements enable charge injection, trapping, and recombination dynamics on a sub-picosecond to a few nanoseconds timescale to be monitored, although it is important to note that OPTP measurements cannot distinguish between recombination and trapping without additional information. Rate constants for the various processes can be determined by fitting an exponential function to the change in transmitted THz to delay time.

Alternatively, the full transient electric field of the THz pulse can be collected at a specific delay time. Fourier transformation of the transients produces the frequency-dependent conductivity spectrum (Figure 4.5b), which is then referenced to the non-photoexcited material. The difference spectrum can then be fitted to a conductivity model (*e.g.* Drude–Smith) to extract charge carrier density and scattering time.

### 4.2.4 Electrochemical Methods

Electrochemical methods are commonly used to understand the electronic structure of WS-DSPECs, particularly the transport behavior and trap state distribution in the oxide support.[35] Cyclic voltammetry is perhaps the simplest technique and involves the reversible cycling of an applied potential and measurement of the current response. Typically these measurements are made in three-electrode cells and referenced to a reference electrode such as the normal hydrogen electrode (NHE). Dempsey and co-workers used cyclic voltammetry to probe mesoporous $TiO_2$ and $SnO_2$ films in aqueous solutions and characterized the exponential distribution of intra-band gap trap states.[26] Open-circuit photovoltage measurements can be used to gain insight into the density of injected electrons under steady-state illumination and also the recombination time for injected electrons.[27]

Methods based on impedance spectroscopy can be particularly useful. In a typical electrochemical impedance spectroscopy (EIS) measurement, a fixed potential is applied to the cell and then a small AC perturbation potential is applied on top of the fixed potential.[36] The frequency of the AC perturbation is typically swept from kHz to MHz. Changes in the phase between the applied voltage and observed current response can be interpreted using an equivalent circuit and simultaneous information about the charge transfer and transport resistances and also capacitive effects on the electrode can be obtained. EIS is a well-known technique in the study of DSSCs[36,37] although less commonly applied to the study of WS-DSPECs. A simple transmission line model is used in DSSCs (Figure 4.6), where interfacial electron transfer is described by a capacitance ($c_\mu$) relating to the build-up of trapped electrons in addition to a resistance ($r_{ct}$). Diffusion through the solution ($Z_d$) and charge transfer at both the transparent conducting oxide (TCO) and cathode have also been described. In WS-DSPECs, impedance measurements were used to probe recombination related to a sintered $IrO_x$ catalyst, the capacitance of electrons trapped in long-lived trap states, and the charge transport resistance.[27]

Finally, intensity-modulated photocurrent spectroscopy (IMPS) and intensity-modulated photovoltage spectroscopy (IMVS) are techniques closely related to EIS. In IMPS/IMVS, the DSSC or WS-DSPEC is held at a fixed potential and the light intensity is modulated with a sinusoidal frequency. Much like in EIS, the difference in phase between the modulated light source and current or voltage response can be used to characterize charge-transfer and transport resistances. IMPS/IMVS is particularly well suited to characterizing the electron transport time, *i.e.* the timescale required for electrons generated at the front of the film to migrate to the back current collector. Xu and Mallouk used IMPS, and also numerical simulations, to characterize electron diffusion in WS-DPSECs, recombination with the photosensitizer, and regeneration of the photosensitizer using hydroquinone in lieu of a water oxidation catalyst.[25]

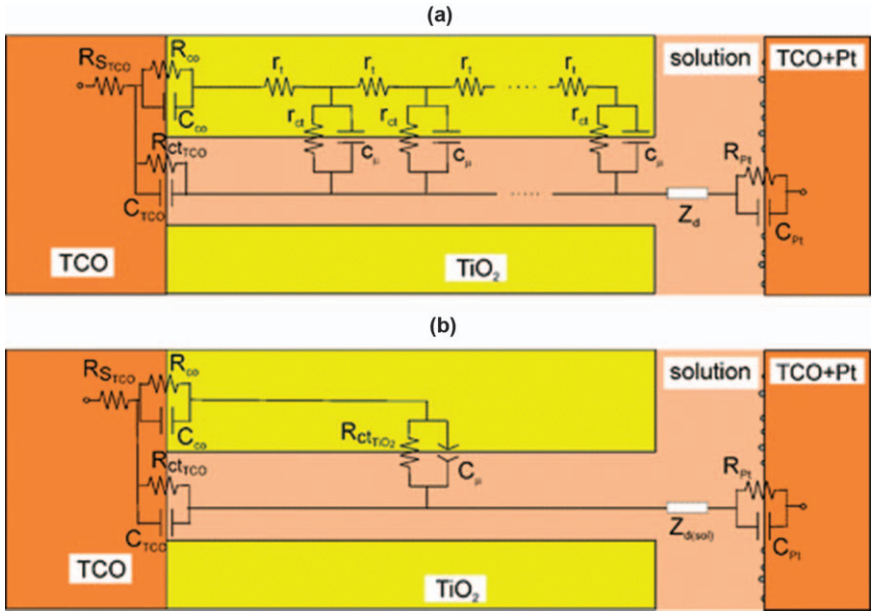


**Figure 4.6** (a) General transmission line model of DSCs. $r_{ct}$ is the charge-transfer resistance of the charge recombination process between electrons in mesoscopic $TiO_2$ film and in electrolyte; $c_\mu$ is the chemical capacitance of $TiO_2$ film; $r_t$ is the transport resistance of electrons in $TiO_2$ film; $Z_d$ is the Warburg element showing the Nernst diffusion in electrolyte; $R_{Pt}$ and $C_{Pt}$ are the charge-transfer resistance and double-layer capacitance at the counter electrode (platinized TCO glass); $R_{TCO}$ and $C_{TCO}$ are the charge-transfer resistance and the corresponding double-layer capacitance at the exposed TCO/electrolyte interface; $R_{CO}$ and $C_{CO}$ are the resistance and the capacitance at TCO/$TiO_2$ contact; $R_s$ is the series resistance, including the sheet resistance of TCO glass and contact resistance of the cell; $L$ is the thickness of the mesoscopic $TiO_2$ film. (b) Simplified model at high illumination intensities. Reproduced from ref. 37 with permission from American Chemical Society, Copyright 2017.

## 4.3 Electronic Structure

The behavior and performance of a semiconductor are determined by the position of the conduction band (CB) edge, valence band (VB) edge, density of states, and charge carrier mobility. pH plays a key role in the position of the CB and VB as both will undergo a Nernstian shift of 59.16 mV with each unit increase in pH. Density of states and carrier mobility are largely determined by the atomic orbitals that comprise the CB. For example, the CB in $TiO_2$ is primarily generated from 3d orbitals whereas the CB in $SnO_2$ is comprised of 5p orbitals. This results in a much higher effective mass of $TiO_2$ CB electrons and therefore a higher density of states for the $TiO_2$ CB compared with the CB for $SnO_2$. The increased density of states is thought to cause faster injection rates into $TiO_2$ than into $SnO_2$.[38]

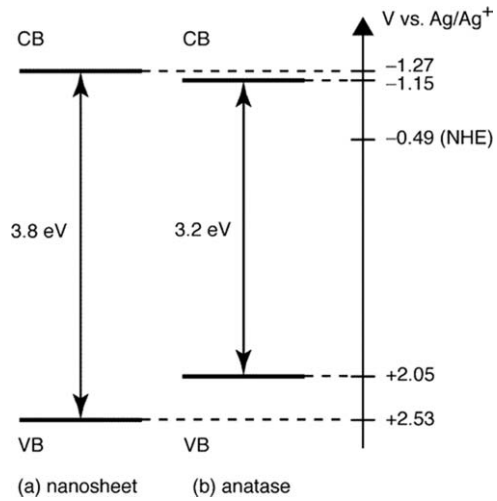


**Figure 4.7** Schematic illustration of electronic band structure: (a) titania nanosheets and (b) anatase.
Reproduced from ref. 40 with permission from American Chemical Society, Copyright 2004.

One challenge in considering ultrathin semiconductor layers is that well-understood properties for bulk semiconductors can change when nanostructured. Computational modeling suggests that quantum confinement at thicknesses less than 2 nm leads to a deviation from bulk materials.[39] Studies on $TiO_2$ nanosheets, which have a thickness of 0.7 nm, demonstrate wider band gaps than bulk anatase $TiO_2$ (Figure 4.7).[40] Electron mobility in 2D oxide materials is much more strongly dependent on the surrounding medium than in bulk materials and conductivity in 2D oxide nanosheets tends to be poor, with high resistivities.[41] Many of the core–shell structures used to control bidirectional electron transfer have shell thicknesses within this range, adding to the complexity of characterizing these systems.

Another key challenge in the study of nanostructured semiconductors is the formation of defects. In the case of $TiO_2$, under-coordinated $Ti^{3+}$, oxygen vacancies, and intercalated protons can all function as traps for electrons and lead to a decrease in electron mobility.[7] In nanostructured semiconductors, an exponential distribution of localized, sub-band gap trap states is typical, with injected electrons relaxing into these trap states.[24,26] Charge transport then occurs as a series of trapping and detrapping events.[42] Thus, surface chemistry plays a critical role in controlling the properties of sintered 3D oxide films. OPTP measurements of mesoporous, nanoparticulate films exposed to a single monolayer of an ALD coating show an increase in the number of mobile carriers and the elimination of a trapping feature on a nanosecond timescale.[24,31,43] As a monolayer is too thin to have any band structure and the introduction of a tunneling barrier is not expected to increase charge injection, this beneficial effect of a monolayer ALD coating is

ascribed to the passivation of surface trap states. The typical increase in THz attenuation with a monolayer coating is ~25% higher than for the bare material, which indicates how significant surface trapping is in affecting injected electrons.

### 4.3.1 Insulating Layers for DSSCs

Thin, conformal coatings of wide band gap insulators have been investigated in DSSCs as tunneling barriers to inhibit recombination. Typically with less than 1 nm deposited on top of a mesoporous $TiO_2$ or $SnO_2$ support, a variety of insulating materials have been explored as shells, including $Nb_2O_5$, $Al_2O_3$, $ZrO_2$, MgO, $Ga_2O_3$, $Ta_2O_5$, $SiO_2$, $CaCO_3$, $HfO_2$, $In_2O_3$, and others.[44–52] Most often these materials are deposited by ALD but in some reports a dip coat strategy was used, although that method results in a less conformal coating of the $TiO_2$ surface and may introduce pinhole defects. Typically, addition of a thin insulating shell leads to an increase in the overall power conversion efficiency without significantly impacting the properties such as dye loading or surface area.

In some reports, the short-circuit photocurrent, which reflects injected electron density, increases with the presence of an insulating shell layer; however, the more noticeable effect is usually on the open-circuit photovoltage, which in an n-type DSSC is defined as the difference between the Fermi level in the semiconductor photoanode and the reduction potential of the oxidized mediator at the cathode. The position of the Fermi level in the photoanode depends on the density of electrons in the semiconductors and thus by extension also depends on the injection yield and rates of recombination. Thicker shells can decrease the injection yield and the injection kinetics are usually slowed when injecting through an insulating shell.[53] As the rate of injection is typically at least 100 times faster than any recombination step, the kinetic redundancy in DSSCs is able to tolerate a decrease in injection kinetics. Instead, the mechanism of action for the improvement of DSSC performance with thin insulating shells is generally ascribed to a decrease in the recombination kinetics. Early reports on $TiO_2$ electrodes dip-coated with wide band gap oxides used transient absorption spectroscopy[45] and EIS[54] to demonstrate slower recombination between injected electrons with both surface-bound dye photosensitizer radical cations and oxidized mediator ions in solution. The decrease in the recombination rate was ascribed to passivation of surface trap states and to an increased barrier for recombination of injected electrons. Prasittichai and co-workers,[55,56] using ALD coating to prepare wide band gap shells, demonstrated that a single monolayer functions to passivate surface trap states that promote recombination events. As the shell becomes thicker, it becomes a tunneling barrier. The tunneling decay parameter for tunneling through the shell, $\beta$, shows a strong dependence on the tunneling barrier, *i.e.* the difference between the CB edge of the core material and that of the shell material (Figure 4.8).

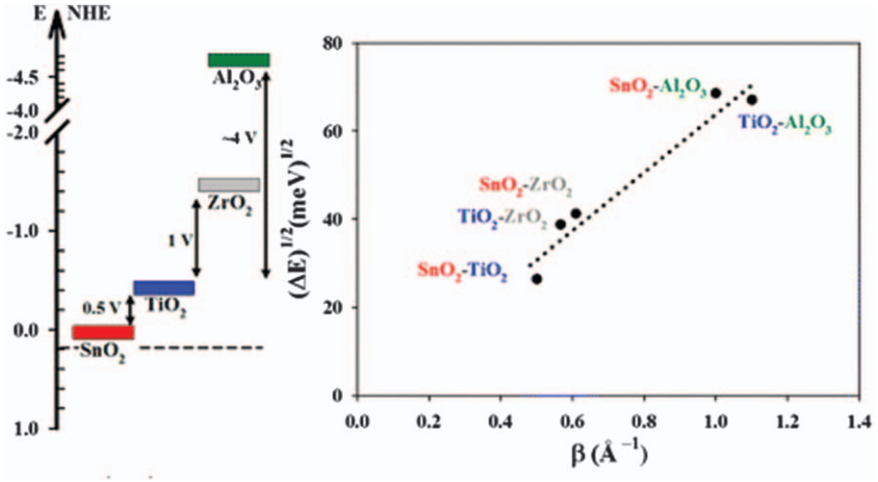


**Figure 4.8** Left: energy diagram of metal oxide conduction band edge positions. The dashed line represents the potential of the transferring electron. Right: plot of the square root of the tunneling barrier height *versus* the experimentally determined value of the tunneling decay parameter $\beta$ for various source electrode–barrier layer combinations. The slope of the plot is $65 \pm 9$ $(\text{meV})^{\frac{1}{2}}$ Å.
Reproduced from ref. 56 with permission from American Chemical Society, Copyright 2013.

A later study by Chandiran *et al.*[46] used a variety of techniques to study the effect of ALD overcoats of $Ga_2O_3$, $ZrO_2$, $Nb_2O_5$, and $Ta_2O_5$ on $TiO_2$ and revealed that the choice of shell material played a large role in tuning the recombination behavior and to a lesser extent the injection dynamics. One key insight from their work was that $Ga_2O_3$ and $ZrO_2$ could function as good tunneling barriers. Depending on the coating thickness, both oxides either had little impact on or increased the open-circuit voltage, which was ascribed to a decrease in the recombination rate; the distribution of intra-band gap trap states did not change with addition of a $ZrO_2$ or a $Ga_2O_3$ surface coating. With thin shells of both materials, the short-circuit current density improved before decreasing with thicker shells. Transient photoemission measurements demonstrated that the excited-state lifetime of the dye on the surface of the coated $TiO_2$ electrodes actually increased, which suggests a decrease in the injection kinetics, and instead the increase in the short-circuit current was ascribed to an increase in the collection efficiency of the electrode. Interestingly, when $Nb_2O_5$ or $Ta_2O_5$ was used as the shell material instead, the open-circuit potential decreased with all layer thicknesses. Characterization of the trap state distribution revealed that the use of pentavalent oxides induced shallow defect levels at the interface with $TiO_2$. This decreased the Fermi level in the $TiO_2$, leading to a decrease in photovoltage. The recombination rate also increased significantly with $Nb_2O_5$ and $Ta_2O_5$, which was explained by the fact that the surface of those oxides is

more negatively charged and may be attracting the positively charged $Co^{3+}$ redox mediator to the surface, thus facilitating the recombination pathways.

Herz and co-workers investigated dip-coat layers of MgO on $SnO_2$ using a variety of characterization methods.[57] Although not characterized in detail, the dipping method used was thought to produce a single monolayer of MgO on the surface of the $SnO_2$. The key finding in this work was that the $SnO_2$ conduction band edge shifted by at least 200 mV, which led to a marked increase in the open-circuit potential. This finding is consistent with the suggestion that overcoat materials with a high point of zero charge (*i.e.* more basic materials) will lead to higher photovoltages.[45] The proposed explanation is that the $TiO_2$ will experience a more basic environment that will then lead to a band shift towards negative potentials, exactly as would be expected if the $TiO_2$ were placed in a basic electrolyte.

### 4.3.2 SnO Core–$TiO_2$ Shell Architecture for WS-DSPECs

The best understood core–shell architecture in WS-DSPECs is based on using mesoporous, nanoparticulate $SnO_2$ supports coated with an ALD shell of $TiO_2$ (Figure 4.9). The CB for bulk crystalline anatase $TiO_2$ is ~750 mV more negative than that for $SnO_2$.[31] Assuming that a $TiO_2$ shell exhibited similar band potentials, this would result in a stepwise potential structure

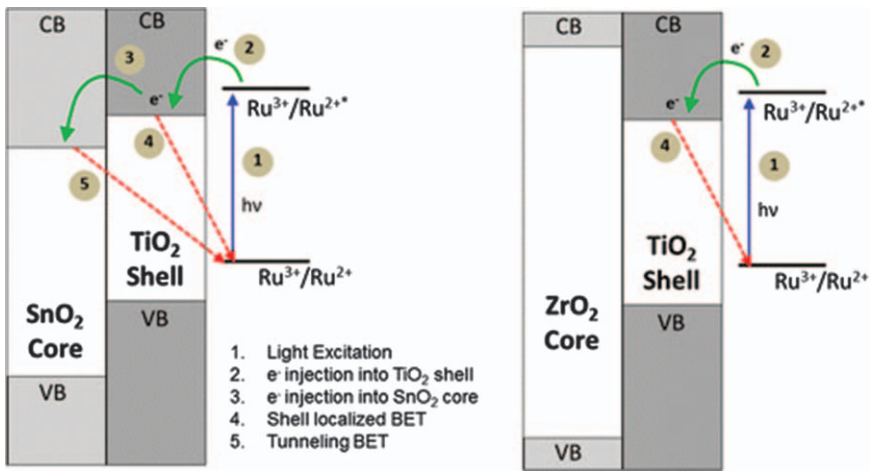


**Figure 4.9** Qualitative scheme showing CB energies in (left) $SnO_2$ core–$TiO_2$ shell and (right) $ZrO_2$ core–$TiO_2$ shell films. Various electron transfer steps are numbered and shown. Upon photoexcitation of the RuP chromophore, the electron probably initially injects into the CB of the shell material. The electron can then localize into the core of $SnO_2$ (left) but remains in the shell material for films with a $ZrO_2$ core (right). Recombination can occur between both the shell- and core-localized electrons with the oxidized chromophore.
Reproduced from ref. 58 with permission from American Chemical Society, Copyright 2015.

where an excited electron could first transfer into the CB of the $TiO_2$ and then into the CB of $SnO_2$. The attraction of using $SnO_2$ is that the less negative CB potential provides a significant driving force for electron injection and typically leads to high injection yields, which play an important role in WS-DSPECs with high efficiencies. As additionally shown in Figure 4.9, it is also common to use a $ZrO_2$ core–$TiO_2$ shell sample specifically to probe the structure of the $TiO_2$ layer. In this configuration, electron injection into the shell is still permitted but the CB edge of $ZrO_2$ sits too high in energy to facilitate further electron transfer.

McCool *et al.*[31] explored varying thicknesses (0.63–25.2 Å) of $TiO_2$ shells on $SnO_2$ cores using OPTP. Because OPTP is sensitive to electron mobility, it provides an excellent probe of the electron location in a core–shell architecture. Figure 4.10a shows the OPTP response as a function of shell thickness and Figure 4.10b focuses specifically on the short-timescale (<4 ps) OPTP response. With the thinnest shells (0.63 and 1.26 Å), electron injection proceeded directly from the excited state of a phosphonated derivative of a tris(2,2′-bipyridine)ruthenium dye into the $SnO_2$ core. The number of mobile charges increased compared with bare $SnO_2$, a phenomenon often observed with OPTP and attributed to passivation of surface trap states, but there are no features on the short-timescale traces. Beginning with shell thicknesses of 5 Å and greater, the OPTP data exhibited a new feature at short times (<4 ps) that becomes increasingly pronounced with increase in shell thickness. At 25.2 Å, this feature appears on an instrument response-limited timescale (<0.5 ps) and then over the course of 2–3 ps disappears before being followed by a much larger attenuation of the transmitted THz. The short-timescale feature was ascribed to injection into the $TiO_2$, followed by trapping at defects located at the $SnO_2$/$TiO_2$ interface, and finally thermal detrapping into the $SnO_2$ core. This study suggests that a band structure in $TiO_2$ shells begins to form at a shell thickness of 5 Å. Emission experiments with $ZrO_2$ core–$TiO_2$ shell films demonstrated significant excited-state quenching when the shell thicknesses were 3–5 Å, which supports the $TiO_2$ developing a band structure at those thicknesses and being able to function as an electron acceptor.

The kinetics of injection and recombination were also studied using ultrafast visible TAS with 13–23 Å thick $TiO_2$ shells on $SnO_2$ cores, sensitized with the same ruthenium chromophore as above.[33] The $TiO_2$ shells were prepared using the same ALD method as in the OPTP experiments and resulted in nominally identical architectures. In agreement with the OPTP results, rapid, multi-exponential charge injection into the $TiO_2$ shells was observed that was independent of shell thickness. Most of the injected charges, ~60%, underwent recombination on a timescale of hundreds of picoseconds. Injection experiments into $ZrO_2$ core–$TiO_2$ shell films revealed a similarly fast recombination component. As electrons cannot transfer into the wide band gap $ZrO_2$ core from the $TiO_2$ shell, this was taken as evidence for recombination from defects within the $TiO_2$ shell. The population of oxidized dye molecules still present at 1 ns underwent recombination over

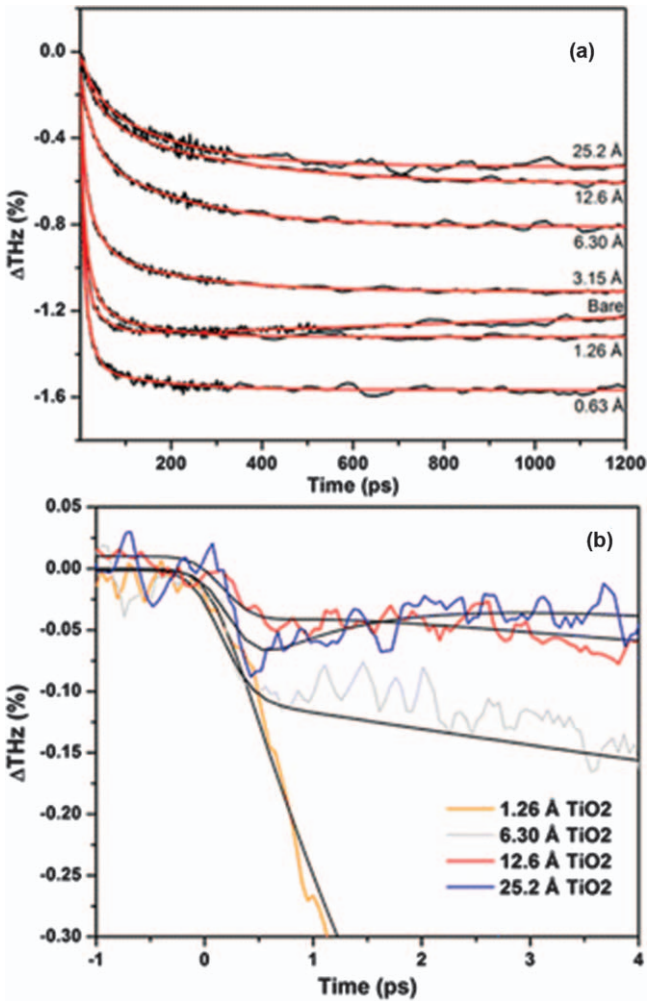


**Figure 4.10** (a) Long-timescale optical pump terahertz probe (OPTP) traces for $SnO_2$–$TiO_2$ electrodes with varying shell thicknesses. (b) Short-timescale plot of the OPTP traces of a collection of samples from (a) in order to show the evolution of the initial injection into the $TiO_2$ shell with increasing thickness. OPTP scans were collected in 0.1 M $HClO_4$ aqueous solution (pH 1).
Reproduced from ref. 31 with permission from American Chemical Society, Copyright 2016.

multiple timescales, with the longest timescale corresponding to millisecond recombination. This millisecond component is not present with bare $SnO_2$ and increases in length with increase in shell thickness. As a result, the long-timescale component was ascribed to recombination of electrons in the $SnO_2$ core that needed to tunnel through the $TiO_2$ shell to recombine with oxidized photosensitizers on the surface.

The nature of recombination through the $TiO_2$ shell has been probed experimentally and the tunneling dynamics quantified. Prasittichai *et al.* studied tunneling from a mesoporous $SnO_2$ electrode through a $TiO_2$ shell prepared by ALD to a triiodide redox mediator in solution.[56] Although the study did not deal with photoinduced electron transfer, electrochemical methods were used to study the rate of electron transfer through the shell. A similar passivation of surface trap states was observed with one monolayer of $TiO_2$ and a decay parameter, $\beta$, of 0.5 $Å^{-1}$ through the $TiO_2$ shell was obtained.

Dempsey and co-workers later explored tunneling through both amorphous and crystalline $TiO_2$ shells that ranged from 0 to 7.1 nm and observed recombination on a timescale from nanoseconds to hundreds of microseconds.[58] With increasing shell thickness they observed a decrease in injection yields measured at 10 ns, which is consistent with the rapid recombination observed in ultrafast TAS, and also observed increased recombination times with thicker shells. Typical for dye-sensitized oxides, the recombination could not be described with a simple exponential model and instead the time required for the initial bleach related to electron injection to recover by 50%, $\tau_{\frac{1}{2}}$, was used as the metric for quantifying recombination. As the shell thickness increased from 0 to 3.4 nm the $\tau_{\frac{1}{2}}$ value also increased, but beyond 3.4 nm there was no meaningful change in $\tau_{\frac{1}{2}}$ (Figure 4.11). Recombination from dye-sensitized $ZrO_2$ core–$TiO_2$ shell films was also explored, and at shell thicknesses >3.4 nm exhibited recombination dynamics identical with those for $SnO_2$ core–$TiO_2$ shell films. At shell thicknesses <3.4 nm, the recombination kinetics were markedly different compared with the $SnO_2$ core–$TiO_2$ shell films (Figure 4.11). These data were analyzed

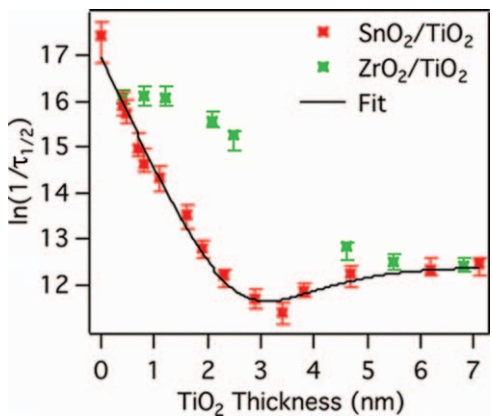


**Figure 4.11** Plot of $\ln(1/\tau_{\frac{1}{2}})$ *versus* $TiO_2$ thickness for amorphous $SnO_2$–$TiO_2$ films at equal injection yields (red) and $ZrO_2$–$TiO_2$ films at equal injection yields (green). The fit models the back electron transfer dynamics with contributions from both tunneling and localized shell recombination. Reproduced from ref. 58 with permission from American Chemical Society, Copyright 2015.

using a mixed model that incorporated both tunneling from the core through the shell and recombination from states in the $TiO_2$ shell. Tunneling occurred through $TiO_2$ shells up to 3.4 nm thick with a $\beta$ value of 0.25 $Å^{-1}$. Beyond 3.4 nm of $TiO_2$, recombination from electrons trapped in the $TiO_2$ shell dominated. Surprisingly, upon annealing the as-deposited $SnO_2$ core–$TiO_2$ shell films, the recombination data matched analogous data from $ZrO_2$ core–$TiO_2$ shell films. It was proposed that delamination of the shell from the core might occur upon crystallization of the $TiO_2$, thereby breaking the electronic contact.

Meyer and co-workers studied the structure of $SnO_2$ core–$TiO_2$ shell architectures in detail.[59,60] Rather than a sharp interface between the core and shell, their results suggested a graded interface best described as $SnO_2/Sn_xTi_{1-x}O_2/TiO_2$. Spectroelectrochemical characterization of annealed and unannealed films at reducing potentials resulted in spectroscopic signatures that were distinct from either $SnO_2$ or $TiO_2$ and could not be reproduced by adding the two spectra together. Furthermore, Tauc plot analysis showed a continual variation in band gap size with shell thickness from ~3.6 eV (consistent with $SnO_2$) to 3.0 eV (consistent with $TiO_2$). Finally, electrochemical data suggested an interfacial layer between the core and shell with a high density of trap states. Measurements of the film capacitance as a function of applied potential suggested the presence of electronic states at more positive potentials than either $SnO_2$ or $TiO_2$. Electron injection into these states would offer a larger thermodynamic driving force and may help to explain the enhanced device performance observed with $SnO_2$ core–$TiO_2$ shell electrodes (see below).

Raman characterization of the annealed films revealed that the $TiO_2$ shells crystallized into the rutile polymorph of $TiO_2$.[59] In the unannealed films, transport proceeds exclusively through the $SnO_2$ core; however, in the annealed films the transport can proceed both through the $SnO_2$ core and through a second channel assigned to transport through the rutile $TiO_2$ shell. This second transport channel has a negative effect on charge recombination because the unannealed, amorphous $TiO_2$ shell functions as a both a spatial and an energetic barrier to charge recombination. The conductive rutile $TiO_2$ layer is apparently a less effective barrier to charge recombination. Subsequent measurements of the activation barrier for charge recombination added support to the proposed picture of a rutile $TiO_2$ shell.[61] Typical activation barriers for back electron transfer from the $TiO_2$ conduction band to ruthenium polypyridyl photosensitizers or triphenylamine range from around 12 to 27 kJ $mol^{-1}$. Using a ruthenium dye linked to a triphenylamine unit, Troian-Gautier *et al.* explored activation barriers for recombination from both $TiO_2$ and $SnO_2$ core–$TiO_2$ shell architectures using temperature-dependent TAS.[61] They observed notably higher barriers for recombination with the $SnO_2$ core–$TiO_2$ shell structure. This was consistent with other studies that investigated recombination kinetics on rutile $TiO_2$ and observed slower recombination times.[6,62]

### 4.3.3 $TiO_2$ Layers on Transparent Conducting Oxides

Sitting at the intersection of DSSCs and WS-DSPECs are thin $TiO_2$ layers deposited on transparent conducting oxides (TCOs). In the context of DSSCs, these $TiO_2$ blocking layers play a critical role in facilitating efficient device performance, whereas in WS-DSPECs high surface area films of mesoporous antimony- or indium-doped tin oxides covered in thin layers of $TiO_2$ demonstrate active photocurrent generation.

In DSSCs, recombination at the fluorine-doped tin oxide (FTO)/electrolyte interface dominates at short-circuit conditions. Thin $TiO_2$ blocking layers deposited on the FTO are used to retard this recombination pathway and typically do not significantly impact the open-circuit photovoltage or fill factor of the solar cell. As the blocking layer, which is inserted between the mesoporous film and TCO substrate, cannot impact injection efficiency, the role of the blocking layer is to enhance the efficiency of charge collection at the TCO/semiconductor interface. Although there is some evidence that the blocking layer enhances charge collection by offering improved contact for the $TiO_2$ particles,[63] it is generally thought that the primary function of the blocking layer is to prevent electron recombination between the oxidized mediator in solution and the TCO.[64,65]

In WS-DSPECs, the dominant electron recombination pathway is between injected electrons and the oxidized dye radical cations on the surface of the semiconductor. As a consequence, a blocking layer at the TCO/semiconductor interface is generally viewed as unnecessary; however, one promising strategy is to use a mesoporous TCO support instead of a semiconductor support.[66] In principle, this should permit efficient electron transport through the entirety of the electrode and lead to an increase in current efficiency. Deposition of an ALD $TiO_2$ shell forms a rectifying layer, necessary for current generation, where electron injection into $TiO_2$ is followed by transfer from $TiO_2$ into the TCO core. The recombination dynamics for this system have not been studied in detail but are presumably controlled by the same factors as in the $SnO_2$ core–$TiO_2$ shell systems described above. An interesting extension to this strategy is to insert a thin (<0.5 nm) layer of $Al_2O_3$ between the $TiO_2$ shell and TCO core.[67] This layer of $Al_2O_3$ functions as a second, wide band gap tunneling barrier to slow recombination. With thin $Al_2O_3$ layers, the recombination can be slowed by as much as an order of magnitude. With thicker layers, the rate of recombination increases relative the TCO core–$TiO_2$ shell structure without $Al_2O_3$. Presumably with thin layers the $Al_2O_3$ layer acts as tunneling barrier but with thicker layers hinders the electron transfer out of the $TiO_2$ and thereby promotes recombination from the shell to the oxidized dye cation on the surface.

### 4.3.4 Electronic Structure of the $SnO_2$ Core–$ZrO_2$ Shell Architecture

$ZrO_2$ is often used as a wide band gap analogue for $SnO_2$ or $TiO_2$. Because of the large, negative CB potential, photosensitizers are unable to inject into

the $ZrO_2$ CB. For this reason, it is often used as an inert core or shell material, as seen in the above discussion of $ZrO_2$ core–$TiO_2$ shell structures. It is therefore surprising that in acid, $SnO_2$ core–$ZrO_2$ shell films permit photoinduced electron transfer through the $ZrO_2$ shell.[43] OPTP traces of $SnO_2$ core–$ZrO_2$ shell films sensitized with a phosphonated ruthenium polypyridyl sensitizer in perchloric acid show rapid electron transfer on a sub-100 ps timescale (Figure 4.12A). Varying the $ZrO_2$ shell thickness from 0 to 4.1 nm decreased the concentration of mobile carriers after excitation; however, even at 4.1 nm of $ZrO_2$ the transmission of THz radiation had increased by only 50% relative to the bare $SnO_2$, which indicates a high injection yield through 4.1 nm of nominally insulating $ZrO_2$. Injection from the dye excited state into the $ZrO_2$ CB is thermodynamically unfeasible and calculations of estimated tunneling efficiency demonstrated that even under the most optimistic set of circumstances, direct tunneling through more than 0.6 nm of $ZrO_2$ was unlikely to occur.

To understand the mechanism of transport, current–voltage measurements of $ZrO_2$ films deposited on planar $Al_2O_3$ were undertaken. Before exposure to acid, the current through the $ZrO_2$ film was on the order of picoamps. After 3 h of exposure to 0.1 M $HClO_4$, the current increased by nearly 10 orders of magnitude. In addition, the current response also increased in parts of the $ZrO_2$ film that had not been exposed to acid, indicating

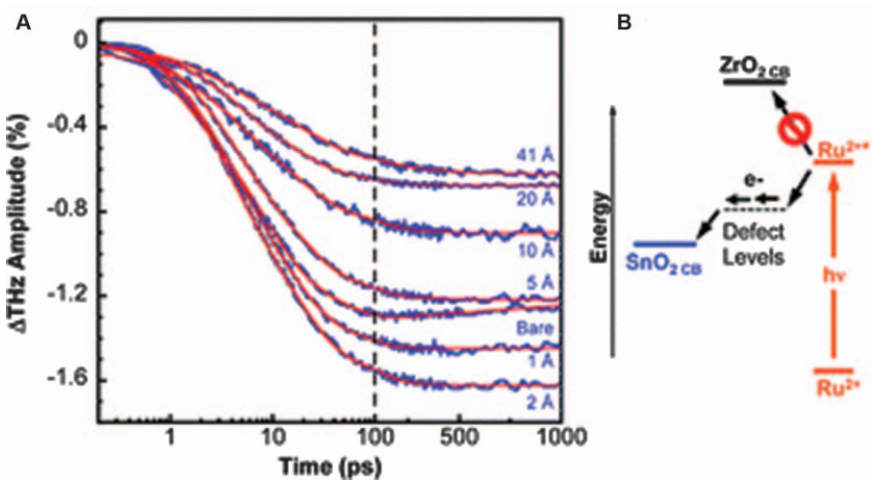


**Figure 4.12** (A) Optical pump THz probe (OPTP) electron injection profiles monitored to 1000 ps following photoexcitation at 400 nm of phosphonated Ru(II)-sensitized bare $SnO_2$ and $SnO_2$ core–$ZrO_2$ shell (1–41 Å) films in 0.1 M aqueous $HClO_4$. Red lines are fits to a multiexponential injection model. Dynamics from 0 to 100 ps are presented on a logarithmic scale on the *x*-axis whereas dynamics from 100 to 1000 ps are presented on a linear scale. (B) Schematic energy level scheme for dye-sensitized $SnO_2$ core–$ZrO_2$ shell films used in OPTP measurements.
Reproduced from ref. 43 with permission from the Royal Society of Chemistry.

diffusion of the protons through the $ZrO_2$ lattice. X-ray photoelectron spectroscopy measurements of the $SnO_2$ core–$ZrO_2$ shell films suggested that exposure to acid results in incorporation of protons into the $ZrO_2$ and that these protons induced defects in the $ZrO_2$ lattice. Unlike the $SnO_2$ core–$TiO_2$ shell films, there were no features in the OPTP traces that could be assigned to electrons in $ZrO_2$. On the basis of these data, an uncommon trap-assisted tunneling mechanism through the $ZrO_2$ was proposed (Figure 4.12B).

## 4.4 Device Level Effects

The key metrics of performance for DSSCs and WS-DSPECs differ. For DSSCs, the power conversion efficiency is the key metric and is defined by the open-circuit voltage ($V_{oc}$), the short-circuit current ($I_{sc}$), and the fill factor ($FF$), which is a measure of the squareness of the solar cell current response. The efficiency is defined as

$$\eta = \frac{V_{oc} I_{sc} FF}{P_{in}} \tag{4.2}$$

where $P_{in}$ is the input power. As such, much of the effort in DSSCs is oriented towards optimizing $V_{oc}$ and $I_{sc}$. Thin tunneling layers on the mesoporous semiconductor can impede recombination, thereby enhancing $V_{oc}$, whereas thin blocking layers between the TCO and mesoporous film can enhance the collection efficiency of the cell and therefore $I_{sc}$.

In WS-DSPECs, the key performance metrics differ. Although intended as solar water splitters, most WS-DSPECs are not actually carrying out photo-assisted water splitting. This is because the Fermi level in the semiconductor is often below the $H^+/H_2$ reduction potential and unable to drive proton reduction at the cathode. The low Fermi level is a consequence of material choice, efficient recombination, and/or low injection efficiencies. Instead, a bias is often applied or a second photoelectrode is used to provide sufficient driving force for proton reduction. As a consequence, the key performance metrics when assessing WS-DSPECs are the photocurrent under illumination and the Faradaic efficiency of the current. Stability is also a critical factor as the current in WS-DSPECs decays irreversibly under extended illumination. This is ascribed to the intercalation of protons into the material, which can then function as trap states.[8] Although significant strides have been made towards more stable currents, at present this irreversible current decay is still a general problem in WS-DSPECs.

### 4.4.1 Effects of Thin Oxide Layers on the Performance of DSSCs

Since the initial report of DSSCs by O'Regan and Grätzel in 1991,[68] rapid improvements in performance and stability have occurred. Every aspect of the DSSC has undergone considerable research, with dyes that capture a broader

fraction of the solar spectrum and higher potential redox mediators responsible for many of the most spectacular improvements. The use of compact, $TiO_2$ blocking layers between the TCO and mesoporous film has also played a role in the improvement in DSSC performance. As discussed above, recombination between the oxidized mediator in solution and the TCO is a significant loss pathway in DSSCs, which can be suppressed with a blocking layer on top of the TCO. Earlier work on blocking layers often produced unclear or contradictory results, with a notable report from Ito *et al.* showing that the sensitizer N719 could act as its own blocking layer and that inclusion of a $TiO_2$ layer offered little benefit.[69] A subsequent report using ''planar'' organic dyes demonstrated the value of a blocking layer in spectacular fashion, with a 160% increase in device efficiency.[70] This report also clearly demonstrated that electron recombination to the mediator was coming from the TCO. The use of a blocking layer is now common practice in DSSCs.

Core–shell motifs have been demonstrated with a variety of core materials and wide band gap oxide shells.[47,71,72] Despite $TiO_2$ being the most common electrode material for n-type DSSCs, the impact of an overlayer on $TiO_2$ on the overall power conversion efficiency is typically modest.[45] Instead, more significant improvements in efficiency can be observed with $SnO_2$ core photoelectrodes.[44] Large increases in both $I_{sc}$ and $V_{oc}$ are observed for $SnO_2$ core–shell electrodes. In contrast, the gains for $TiO_2$ core–shell electrodes are largely confined to an increase in $V_{oc}$ and are usually much smaller than with $SnO_2$. This difference can be largely explained by the difference in recombination dynamics. In $TiO_2$, recombination is slower and rapid regeneration of the oxidized dye inhibits back electron transfer to the oxidized photosensitizer. As a consequence, the impact of the shell material is limited and mostly influences the surface chemistry *via* passivation to increase the Fermi level within the core. Recombination from $SnO_2$ is notably faster and as a consequence better able to compete with photosensitizer regeneration. In this case, the thin shell is effective at attenuating the recombination pathway, which leads to a higher concentration of electrons able to be collected.

### 4.4.2 Performance of Core–Shell Structures in WS-DSPECs

The performance in the earliest examples of WS-DSPECs was quite poor and typically failed to achieve current densities in excess of tens of microamps under simulated solar conditions.[20,73,74] Improvements in catalyst design[21,22] led to steady improvements in photocurrents from tens to hundreds of microamps and the use of illumination greater than one sun demonstrated the ability of WS-DSPECs to sustain mA $cm^{-2}$ currents.[18] Even from the first report of WS-DSPECs, fast recombination outcompeting slow catalyst turnover was identified as the major factor driving low photocurrent densities.[20] Although improvements in catalysts, photosensitizers, and materials have led to improvements in WS-DSPEC performance, it was the introduction of core–shell architectures that led to the greatest improvements in cell performance and stability.

The first example of a core–shell photoelectrode was demonstrated by Mallouk and co-workers in 2012 and utilized a $TiO_2$ photoanode dip-coated with either $ZrO_2$ or $Nb_2O_5$ in addition to a ruthenium sensitizer covalently linked to an $IrO_x$ nanoparticle.[30] Both shell materials resulted in an increase in photocurrent over uncoated $TiO_2$ although a rapid, irreversible loss of photocurrent was apparent in all cases. The improvement in performance was driven by a lengthening of the recombination time, approaching 1 ms.

Subsequent examples of core–shell architectures have relied on ALD coatings of the mesoporous support. In 2013, Alibabaei *et al.* demonstrated a photoanode using a $TiO_2$ shell to cover a mesoporous indium-doped tin oxide (ITO) TCO support.[66] Although the photocurrent without the $TiO_2$ shell was not reported, the $TiO_2$-coated photoelectrode demonstrated a peak photocurrent of nearly 250 $\mu A\,cm^{-2}$ and decayed to slightly under 100 $\mu A\,cm^{-2}$ over the course of 30 s. That system featured a molecular water oxidation catalyst tethered to the photosensitizer. A later example using the same sensitized $TiO_2$ shell–ITO core electrode but covered with a layer of heterogeneous iridium oxide water oxidation catalyst demonstrated peak photocurrents nearing 500 $\mu A\,cm^{-2}$.[75] Insertion of a 0.55 nm $Al_2O_3$ layer between the $TiO_2$ shell and TCO core results in a roughly threefold improvement in current density and incident photon to current efficiency (IPCE),[67] although it is important to note that the current densities were still on the tens of microamps scale. A further improvement was achieved by inserting a compact $TiO_2$ blocking layer between the planar TCO and the mesoporous TCO.[76] Both the peak photocurrent and the photocurrent after 30 s of illumination were improved relative to a device without any blocking layer. No visible changes in the kinetics were observed so this enhancement was ascribed to improved physical contact between the planar TCO and mesoporous film.

In terms of performance, more success has been observed with $SnO_2$ core–$TiO_2$ shell photoanodes. The first report to feature $SnO_2$ core–$TiO_2$ shell photoanodes utilized a 3 nm thick, annealed $TiO_2$ shell and a ruthenium photosensitizer linked to a molecular ruthenium water oxidation catalyst.[19] Photocurrents in excess of 400 $\mu A\,cm^{-2}$ were observed with a Faradaic efficiency of 22%. Using the same photoelectrode design, a subsequent study[77] improved on the linkage between the chromophore and water oxidation catalyst and demonstrated a significant enhancement of photocurrent with peak photocurrents of nearly 1.6 $mA\,cm^{-2}$. A comparison with mesoporous $TiO_2$ was also made and although similar peak currents could be observed, polarization of the current to less than 0.2 $mA\,cm^{-2}$ was rapid ($\sim$1 s). Rapid polarization of current is thought to be related to a build-up of oxidized photosensitizer on the photoelectrode surface, which leads to fast recombination of injected electrons.[8] The $TiO_2$ shell can retard that recombination and permit the regeneration of the oxidized photosensitizer before recombination occurs.

The use of organic dyes on $SnO_2$ core–$TiO_2$ shell photoanodes has shown significant promise. An initial report of an organic donor–$\pi$-acceptor photosensitizer and co-deposited water oxidation catalyst demonstrated a

maximum photocurrent of 1.4 mA $cm^{-2}$.[17] Unfortunately, Faradaic efficiency measurements demonstrated that most of the current was related to oxidative decomposition of the dye. Interestingly, this study also looked at the photocurrent with hydroquinone. Hydroquinone can be used a reversible redox mediator and is sometimes used in WS-DSPECs to approximate dye regeneration kinetics with a moderate to good water oxidation catalyst. This competes with recombination to the oxidized photosensitizer on the surface of the semiconductor and offers insights into the potential performance of the photoanode in the limit of efficient photosensitizer regeneration kinetics. With hydroquinone, current densities in excess of 2.5 mA $cm^{-2}$ were observed over the course of 15 min. This experiment demonstrated that higher current densities could be sustained on $SnO_2$ core–$TiO_2$ shell photoanodes and that the slow regeneration of the oxidized photosensitizer by a water oxidation catalyst is the key issue limiting performance. In order to address the decomposition of the photosensitizer, a sensitized $SnO_2$ core–$TiO_2$ shell photoanode was coated with a layer of $Al_2O_3$ to entomb the dye and the catalyst was deposited on top of this layer (Figure 4.13A).[78] The $Al_2O_3$ overcoat functions to prevent desorption of the dye from the surface of the $TiO_2$ shell. This strategy achieved peak photocurrents of ~0.7 mA $cm^{-2}$ (Figure 4.13B), but importantly exhibited Faradaic efficiencies for oxygen generation of ~80%. Adjusting the substituents on the photosensitizer led to a variation in the observed current efficiency (Figure 4.13C).

Oxidation of HBr using a $SnO_2$ core–$TiO_2$ shell photoanode achieved high current densities (Figure 4.14a). In part, the high current density results from the use of $Br^-$ as a reductant for the oxidized photosensitizer instead of water, which is kinetically more difficult to oxidize. A larger portion of the photocurrent, however, could be assigned to the use of the core–shell electrode. Figure 4.14b shows the current response for a core–shell electrode (red line) an analogous photoanode composed of mesoporous $TiO_2$ (black line). Transient absorption experiments demonstrated that the eightfold enhancement in current was related to the slower recombination kinetics caused by the $TiO_2$ shell.

The above studies demonstrate that $SnO_2$ core–$TiO_2$ shell photoanodes can sustain high, stable current densities and that rapid regeneration of the oxidized photosensitizer is still critical to prevent decomposition. Drawing inspiration from the use of $Al_2O_3$ layers to protect the oxidized dye, Meyer and co-workers introduced NiO as an intermediate redox layer.[79] In this design, an $SnO_2$ core–$TiO_2$ shell photoanode is first sensitized with a photosensitizer and then the sensitized photoanode is coated with an ALD overcoat of NiO. The water oxidation catalyst is subsequently deposited on top of this NiO layer. An NiO thickness of 0.6 nm was established to provide optimal performance, namely a sustained (>2 h) photocurrent of ~1 mA $cm^{-2}$ and a Faradaic efficiency of 86%. In the proposed mechanism of photocurrent generation, an excited electron is first injected into the $TiO_2$ shell, whereupon the oxidized dye is regenerated by the NiO overcoat. The hole in the NiO is then transferred to the catalyst to accomplish water

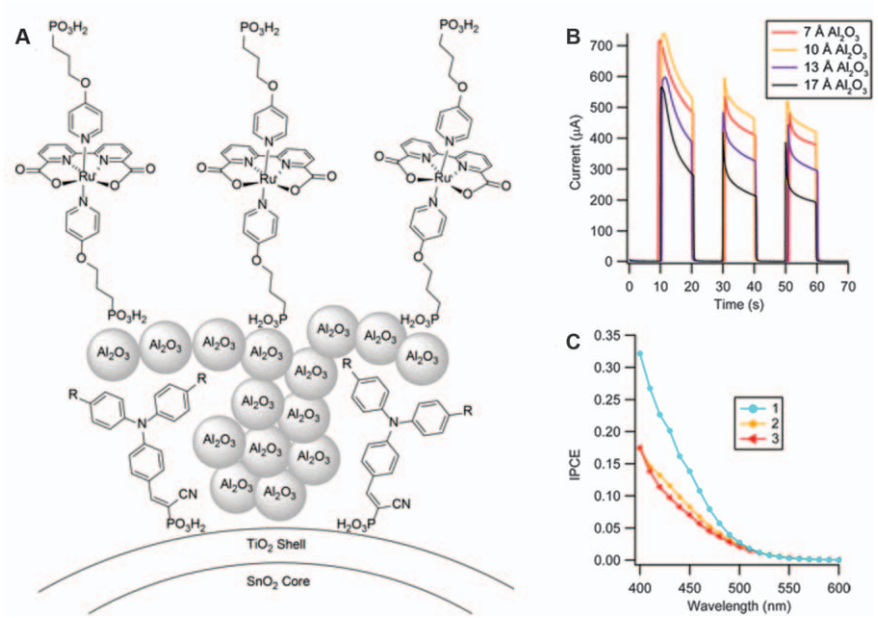


**Figure 4.13** (A) Surface structure of the $SnO_2$–$TiO_2$ core–shell electrode sensitized with a 1-cyano-2-[4-(diphenylaminophenyl)vinyl]phosphonic acid derivative and stabilized with an overcoat of $Al_2O_3$. A ruthenium water oxidation catalyst is deposited on top of the $Al_2O_3$. (B) Photocurrent *versus* time responses for the electrode structure in (A) under <1 sun illumination at the indicated $Al_2O_3$ overlayer thickness. (C) Incident photon to current efficiencies (IPCE) for the electrodes with different R substituents on the photosensitizer [R = (1) H, (2) Me, and (3) OMe]. The electrolyte consisted of 0.1 M $CH_3COOH$–$CH_3COONa$, 0.4 M $NaClO_4$, with an external bias of 0.4 V *vs.* NHE.
Reproduced from ref. 78 with permission from American Chemical Society, Copyright 2017.

oxidation. A 5 nm thick shell of $TiO_2$ was used on the $SnO_2$ core, although the authors did not comment on this. Presumably this is because 5 nm is the approximate thickness where tunneling no longer contributes to the recombination and the maximum recombination time is achieved.[58]

## 4.5 Conclusion and Outlook

Thin oxide blocking layers play an increasingly important role in the development of new technologies for energy conversion. Although broadly applicable to any technology that relies on electron transfer, the most visible and successful examples to date have involved dye-sensitized energy conversion systems. The performance of these systems is controlled by kinetics, specifically the interplay of various productive and unproductive electron transfer pathways. As discussed in the preceding sections, thin oxide blocking layers often play the role of a rectifier by allowing charge to pass in

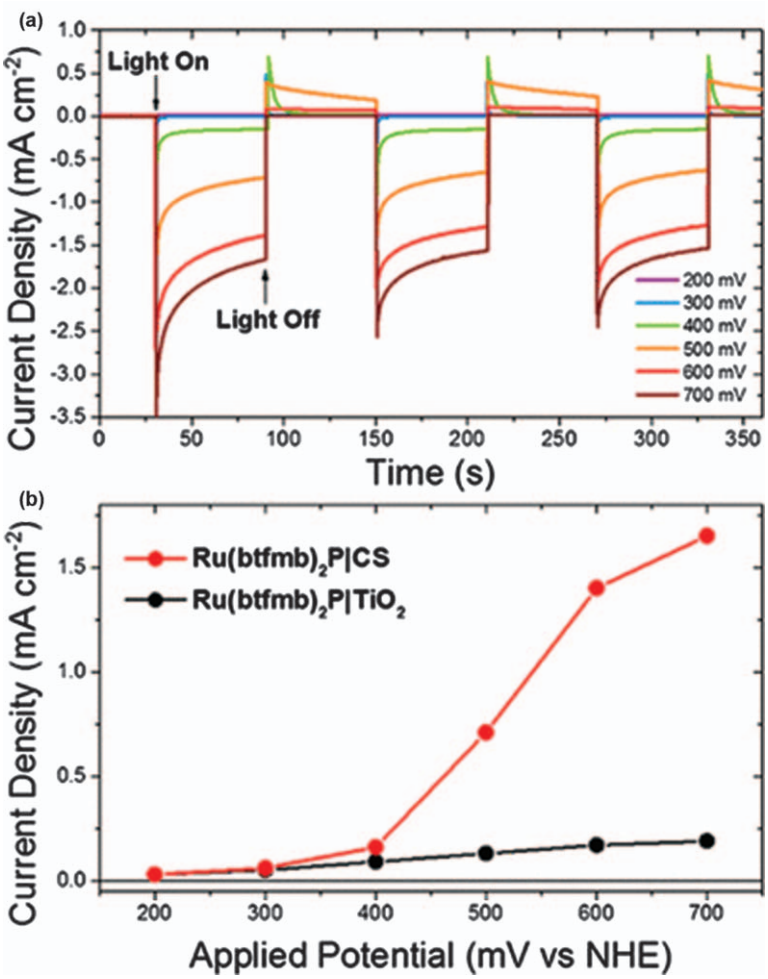


**Figure 4.14** (a) Three light-on/light-off current responses of a $Ru(btfmb)_2P|CS$ thin film at the indicated applied potentials *vs.* NHE. (b) Current density magnitudes measured after 1 min of illumination of $Ru(btfmb)_2P|CS$ (red) and $Ru(btfmb)_2P|TiO_2$ (black) as a function of the applied potential. btfmb = 4,4′-bis(trifluoromethyl)-2,2′-bipyridine; P = 2,2′-bipyridyl-4,4′-diphosphonic acid; CS = $SnO_2$ core–$TiO_2$ shell electrode. Reproduced from ref. 82 with permission from American Chemical Society, Copyright 2017.

one direction (*e.g.* electron injection) and retarding the flow of charge in the other direction (*e.g.* recombination). In both DSSCs and WS-DSPECs, this rectifying behavior has been leveraged for increased power conversion efficiencies, stability, and solar fuel production. The current record WS-DSPEC from Meyer and co-workers[79] elegantly demonstrates the potential of thin oxide layers. Not only is the photoanode based on an $SnO_2$ core–$TiO_2$ shell

support that offers slow electron recombination but also the photoelectrode utilizes an NiO overcoat as a redox mediator and dye stabilization layer. In both cases, the thin, conformal oxide layers function to control the flow of charge and permit high photocurrents.

Despite the success of different blocking layers in controlling electron transfer, there are still fundamental gaps in our understanding. The most notable is the origin of slow electron recombination from core–shell architectures, particularly in $SnO_2$ core–$TiO_2$ shell supports. Although the picture of a potential staircase that permits electron transfer into the core but prohibits back electron transfer out of the core is straightforward and appealing, recent studies suggest that a more complicated interface that probably plays a role in slow recombination kinetics. Understanding the nature and function of this interface is key to understanding electron transfer in these core–shell systems. Here computational methods may play a critical role in helping to model the interface between the core and the shell. In particular, the nature of the interface and defects is poorly understood.

Likewise, many of the thin oxide shell layers are prepared using ALD. There is an implicit assumption in most reports that these layers exhibit properties similar to or identical with those of bulk semiconductors; however, that assumption may not be a good one. In unannealed films, there is a lack of crystallinity that calls into question how similar the material can be to a crystalline solid. Even after annealing, there is no question that these ALD films are more defect rich than the typical bulk solid. Many film thicknesses are of the order of magnitude where band structure begins to develop. Although comparison with 2D nanomaterials (*e.g.* nanosheets) can be useful in understanding how quantum confinement may impact the electronic structure of thin oxide layers, there are notable differences. For example, many 2D materials are highly charged and crystalline and experience a large degree of interaction with the surrounding solvent, which can impact the overall properties of the material. Those descriptors are not readily applied to many of the thin oxide films described in this chapter, so there may be a limitation to comparison. Once again, application of computational methods to understand the electronic structure of oxide shells may provide useful insights into the transition from tunneling barrier to bulk semiconductor.

Finally, there is a significant opportunity to understand the rectifying behavior of these thin oxide layers. These layers are often not considered in these terms, particularly in the realm of dye-sensitized energy conversion, but considerations through that lens may lead to a better understanding of their use and rational design. In the context of dye-sensitized energy conversion systems, this means a better understanding of the relationships between charge-transfer pathways (*e.g.* injection, transport, recombination) and fundamental properties related to the shell or blocking layer (*e.g.* band offsets, tunneling decay parameter, trap state distributions). Thinner layers with better rectifying behavior are an important step towards achieving higher injection yields and lower recombination rates.

The wide parameter space, demonstrated utility, and opportunities for further improvement suggest that thin oxide layers will continue to have a critical role in the development of energy conversion technologies. Collaboration between chemists, materials scientists, engineers, and physicists is likely to produce new understandings of how the electronic structure develops in these thin (<5 nm) oxide films. Improvements in performance and stability will depend on how well those insights can be leveraged for the rational development of new materials and device architectures.

## References

1. G. F. Moore and G. W. Brudvig, *Annu. Rev. Condens. Matter Phys.*, 2011, **2**, 303–327.
2. J. R. Swierk and T. E. Mallouk, *Chem. Soc. Rev.*, 2013, **42**, 2357–2387.
3. M. Grätzel, *Prog. Photovoltaics Res. Appl.*, 2006, **14**, 429–442.
4. V. Nikolaou, A. Charisiadis, G. Charalambidis, A. G. Coutsolelos and F. Odobel, *J. Mater. Chem. A*, 2017, **5**, 21077–21113.
5. M. K. Brennaman, R. J. Dillon, L. Alibabaei, M. K. Gish, C. J. Dares, D. L. Ashford, R. L. House, G. J. Meyer, J. M. Papanikolas and T. J. Meyer, *J. Am. Chem. Soc.*, 2016, **138**, 13085–13102.
6. J. R. Swierk, K. P. Regan, J. Jiang, G. W. Brudvig and C. A. Schmuttenmaer, *ACS Energy Lett.*, 2016, **1**, 603–606.
7. N. S. McCool, J. R. Swierk, C. T. Nemes, T. P. Saunders, C. A. Schmuttenmaer and T. E. Mallouk, *ACS Appl. Mater. Interfaces*, 2016, **8**, 16727–16735.
8. J. R. Swierk, N. S. McCool, T. P. Saunders, G. D. Barber and T. E. Mallouk, *J. Am. Chem. Soc.*, 2014, **136**, 10974–10982.
9. P. G. Giokas, S. A. Miller, K. Hanson, M. R. Norris, C. R. K. Glasson, J. J. Concepcion, S. E. Bettis, T. J. Meyer and A. M. Moran, *J. Phys. Chem. C*, 2013, **117**, 812–824.
10. K. Hanson, M. K. Brennaman, A. Ito, H. Luo, W. Song, K. A. Parker, R. Ghosh, M. R. Norris, C. R. K. Glasson, J. J. Concepcion, R. Lopez and T. J. Meyer, *J. Phys. Chem. C*, 2012, **116**, 14837–14847.
11. J. R. Swierk, D. D. Méndez-Hernández, N. S. McCool, P. Liddell, Y. Terazono, I. Pahk, J. J. Tomlin, N. V. Oster, T. A. Moore, A. L. Moore, D. Gust and T. E. Mallouk, *Proc. Natl. Acad. Sci. U. S. A.*, 2015, **112**, 1681–1686.
12. G. Moore, S. Konezny, H. Song, R. Milot, J. D. Blakemore, M. L. Lee, V. S. Batista, C. A. Schmuttenmaer, R. H. Crabtree and G. W. Brudvig, *J. Phys. Chem. C*, 2012, **116**, 4892–4902.
13. J. Jiang, J. R. Swierk, K. L. Materna, S. Hedström, S. H. Lee, R. H. Crabtree, C. A. Schmuttenmaer, V. S. Batista and G. W. Brudvig, *J. Phys. Chem. C*, 2016, **120**, 28971–28982.
14. J. T. Kirner and R. G. Finke, *ACS Appl. Mater. Interfaces*, 2017, **9**, 27625–27637.
15. C. Decavoli, C. L. Boldrini, N. Manfredi and A. Abbotto, *Eur. J. Inorg. Chem.*, 2020, **2020**, 978–999.

16. L. A. Martini, G. F. Moore, R. L. Milot, L. Z. Cai, S. W. Sheehan, C. A. Schmuttenmaer, G. W. Brudvig and R. H. Crabtree, *J. Phys. Chem. C*, 2013, **117**, 14526–14533.
17. K.-R. Wee, B. D. Sherman, M. K. Brennaman, M. V. Sheridan, A. Nayak, L. Alibabaei and T. J. Meyer, *J. Mater. Chem. A*, 2016, **4**, 2969–2975.
18. Y. Gao, X. Ding, J. Liu, L. Wang, Z. Lu, L. Li and L. Sun, *J. Am. Chem. Soc.*, 2013, **135**, 4219–4222.
19. B. D. Sherman, D. L. Ashford, A. M. Lapides, M. V. Sheridan, K.-R. Wee and T. J. Meyer, *J. Phys. Chem. Lett.*, 2015, **11**, 3213–3217.
20. W. J. Youngblood, S.-H. A. Lee, Y. Kobayashi, E. A. Hernandez-Pagan, P. G. Hoertz, T. A. Moore, A. L. Moore, D. Gust and T. E. Mallouk, *J. Am. Chem. Soc.*, 2009, **131**, 926–927.
21. Y. Zhao, J. R. Swierk, J. D. Megiatto, B. Sherman, W. J. Youngblood, D. Qin, D. M. Lentz, A. L. Moore, T. A. Moore, D. Gust and T. E. Mallouk, *Proc. Natl. Acad. Sci. U. S. A.*, 2012, **109**, 15612–15615.
22. J. R. Swierk, N. S. McCool, T. P. Saunders, G. D. Barber, M. E. Strayer, N. M. Vargas-Barbosa and T. E. Mallouk, *J. Phys. Chem. C*, 2014, **118**, 17046–17053.
23. A. M. Lapides, B. D. Sherman, M. K. Brennaman, C. J. Dares, K. R. Skinner, J. L. Templeton and T. J. Meyer, *Chem. Sci.*, 2015, **6**, 6398–6406.
24. J. R. Swierk, N. S. McCool, C. T. Nemes, T. E. Mallouk and C. A. Schmuttenmaer, *J. Phys. Chem. C*, 2016, **120**, 5940–5948.
25. P. Xu and T. E. Mallouk, *J. Phys. Chem. C*, 2019, **123**, 299–305.
26. R. R. Knauf, M. K. Brennaman, L. Alibabaei, M. R. Norris and J. L. Dempsey, *J. Phys. Chem. C*, 2013, **117**, 25259–25268.
27. J. R. Swierk, N. S. McCool and T. E. Mallouk, *J. Phys. Chem. C*, 2015, **119**, 13858–13867.
28. K. Hanson, M. K. Brennaman, H. Luo, C. R. K. Glasson, J. J. Concepcion, W. Song and T. J. Meyer, *ACS Appl. Mater. Interfaces*, 2012, **4**, 1462–1469.
29. R. L. Milot and C. A. Schmuttenmaer, *Acc. Chem. Res.*, 2015, **48**, 1423–1431.
30. S.-H. A. Lee, Y. Zhao, E. A. Hernandez-Pagan, L. Blasdel, W. J. Youngblood and T. E. Mallouk, *Faraday Discuss.*, 2012, **155**, 165–176.
31. N. S. McCool, J. R. Swierk, C. T. Nemes, C. A. Schmuttenmaer and T. E. Mallouk, *J. Phys. Chem. Lett.*, 2016, **7**, 2930–2934.
32. K. Hanson, M. D. Losego, B. Kalanyan, G. N. Parsons and T. J. Meyer, *Nano Lett.*, 2013, **13**, 4802–4809.
33. M. K. Gish, A. M. Lapides, M. K. Brennaman, J. L. Templeton, T. J. Meyer and J. M. Papanikolas, *J. Phys. Chem. Lett.*, 2016, **7**, 5297–5301.
34. K. P. Regan, J. R. Swierk, J. Neu and C. A. Schmuttenmaer, *J. Phys. Chem. C*, 2017, **121**, 15949–15956.
35. F. Fabregat-Santiago, I. Mora-Seró, G. Garcia-Belmonte and J. Bisquert, *J. Phys. Chem. B*, 2003, **107**, 758–768.
36. F. Fabregat-Santiago, J. Bisquert, G. Garcia-Belmonte, G. Boschloo and A. Hagfeldt, *Sol. Energy Mater. Sol. Cells*, 2005, **87**, 117–131.
37. F. Fabregat-Santiago, J. Bisquert, E. Palomares, L. Otero, D. Kuang, S. M. Zakeeruddin and M. Grätzel, *J. Phys. Chem. C*, 2007, **111**, 6550–6560.

38. P. Tiwana, P. Docampo, M. B. Johnston, H. J. Snaith and L. M. Herz, *ACS Nano*, 2011, **5**, 5158–5166.
39. D. Varsano, G. Giorgi, K. Yamashita and M. Palummo, *J. Phys. Chem. Lett.*, 2017, **8**, 3867–3873.
40. N. Sakai, Y. Ebina, K. Takada and T. Sasaki, *J. Am. Chem. Soc.*, 2004, **126**, 5851–5858.
41. J. E. ten Elshof, *Curr. Opin. Solid State Mater. Sci.*, 2017, **21**, 312–322.
42. A. J Frank, N. Kopidakis and J. V. de Lagemaat, *Coord. Chem. Rev.*, 2004, **248**, 1165–1179.
43. J. R. Swierk, N. S. McCool, J. A. Röhr, S. Hedström, S. J. Konezny, C. T. Nemes, P. Xu, V. S. Batista, T. E. Mallouk and C. A. Schmuttenmaer, *Chem. Commun.*, 2018, **54**, 7971–7974.
44. A. Kay and M. Grätzel, *Chem. Mater.*, 2002, **14**, 2930–2935.
45. E. Palomares, J. N. Clifford, S. A. Haque, T. Lutz and J. R. Durrant, *J. Am. Chem. Soc.*, 2003, **125**, 475–482.
46. A. K. Chandiran, M. K. Nazeeruddin and M. Grätzel, *Adv. Funct. Mater.*, 2014, **24**, 1615–1623.
47. Y. Diamant, S. Chappel, S. G. Chen, O. Melamed and A. Zaban, *Coord. Chem. Rev.*, 2004, **248**, 1271–1276.
48. Z.-S. Wang, M. Yanagida, K. Sayama and H. Sugihara, *Chem. Mater.*, 2006, **18**, 2912–2916.
49. T. C. Li, M. S. Góes, F. Fabregat-Santiago, J. Bisquert, P. R. Bueno, C. Prasittichai, J. T. Hupp and T. J. Marks, *J. Phys. Chem. C*, 2009, **113**, 18385–18390.
50. M. Shanmugam, M. F. Baroughi and D. Galipeau, *Thin Solid Films*, 2010, **518**, 2678–2682.
51. J. Bandara and U. W. Pradeep, *Thin Solid Films*, 2008, **517**, 952–956.
52. T. P. Brennan, J. T. Tanskanen, K. E. Roelofs, J. W. F. To, W. H. Nguyen, J. R. B akke, I.-K. Ding, B. E. Hardin, A. Sellinger, M. D. McGehee and S. F. Bent, *J. Phys. Chem. C*, 2013, **117**, 24138–24149.
53. J. Guo, C. She and T. Lian, *J. Phys. Chem. C*, 2007, **111**, 8979–8987.
54. F. Fabregat-Santiago, J. García-Cañadas, E. Palomares, J. N. Clifford, S. A. Haque, J. R. Durrant, G. Garcia-Belmonte and J. Bisquert, *J. Appl. Phys.*, 2004, **96**, 6903–6907.
55. C. Prasittichai and J. T. Hupp, *J. Phys. Chem. Lett.*, 2010, **1**, 1611–1615.
56. C. Prasittichai, J. R. Avila, O. K. Farha and J. T. Hupp, *J. Am. Chem. Soc.*, 2013, **135**, 16328–16331.
57. P. Docampo, P. Tiwana, N. Sakai, H. Miura, L. Herz, T. Murakami and H. J. Snaith, *J. Phys. Chem. C*, 2012, **116**, 22840–22846.
58. R. R. Knauf, B. Kalanyan, G. N. Parsons and J. L. Dempsey, *J. Phys. Chem. C*, 2015, **119**, 28353–28360.
59. E. M. James, M. T. Bennett, R. E. Bangle and G. J. Meyer, *Langmuir*, 2019, **35**, 12694–12703.
60. E. M. James, T. J. Barr and G. J. Meyer, *ACS Appl. Energy Mater.*, 2018, **1**, 859–867.
61. L. Troian-Gautier, R. N. Sampaio, E. J. Piechota, M. D. Brady and G. J. Meyer, *J. Chem. Phys.*, 2019, **150**, 041719.

62. A. Kafizas, X. Wang, S. R. Pendlebury, P. Barnes, M. Ling, C. Sotelo-Vazquez, R. Quesada-Cabrera, C. Li, I. P. Parkin and J. R. Durrant, *J. Phys. Chem. A*, 2016, **120**, 715–723.
63. M. S. Góes, E. Joanni, E. C. Muniz, R. Savu, T. R. Habeck, P. R. Bueno and F. Fabregat-Santiago, *J. Phys. Chem. C*, 2012, **116**, 12415–12421.
64. I.-P. Liu, W.-H. Lin, C.-M. Tseng-Shan and Y.-L. Lee, *ACS Appl. Mater. Interfaces*, 2018, **10**, 38900–38905.
65. P. J. Cameron and L. M. Peter, *J. Phys. Chem. B*, 2003, **107**, 14394–14400.
66. L. Alibabaei, M. K. Brennaman, M. R. Norris, B. Kalanyan, W. Song, M. D. Losego, J. J. Concepcion, R. A. Binstead, G. N. Parsons and T. J. Meyer, *Proc. Natl. Acad. Sci.*, 2013, **110**, 20008–20013.
67. D. Wang, B. H. Farnum, M. V. Sheridan, S. L. Marquard, B. D. Sherman and T. J. Meyer, *ACS Appl. Mater. Interfaces*, 2017, **9**, 33533–33538.
68. B. O'Regan and M. Grätzel, *Nature*, 1991, **353**, 737–740.
69. S. Ito, P. Liska, P. Comte, R. Charvet, P. Péchy, U. Bach, L. Schmidt-Mende, S. M. Zakeeruddin, A. Kay, M. K. Nazeeruddin and M. Grätzel, *Chem. Commun.*, 2005, **248**, 4351–4353.
70. A. Burke, S. Ito, H. Snaith, U. Bach, J. Kwiatkowski and M. Grätzel, *Nano Lett.*, 2008, **8**, 977–981.
71. M. Law, L. E. Greene, A. Radenovic, T. Kuykendall, J. Liphardt and P. Yang, *J. Phys. Chem. B*, 2006, **110**, 22652–22663.
72. N. G. Park, M. G. Kang, K. M. Kim, K. S. Ryu, S. H. Chang, D. K. Kim, J. van de Lagemaat, K. D. Benkstein and A. J. Frank, *Langmuir*, 2004, **20**, 4246–4253.
73. R. Brimblecombe, A. Koo, G. C. Dismukes, G. F. Swiegers and L. Spiccia, *J. Am. Chem. Soc.*, 2010, **132**, 2892–2894.
74. L. Li, L. Duan, Y. Xu, M. Gorlov, A. Hagfeldt and L. Sun, *Chem. Commun.*, 2010, **46**, 7307–7309.
75. K. E. Michaux, A. A. Gambardella, L. Alibabaei, D. L. Ashford, B. D. Sherman, R. A. Binstead, T. J. Meyer and R. W. Murray, *J. Phys. Chem. C*, 2015, **119**, 17023–17027.
76. R. L. Coppo, B. H. Farnum, B. D. Sherman, N. Y. Murakami Iha and T. J. Meyer, *Sustainable Energy Fuels*, 2017, **1**, 112–118.
77. B. D. Sherman, Y. Xie, M. V. Sheridan, D. Wang, D. W. Shaffer, T. J. Meyer and J. J. Concepcion, *ACS Energy Lett.*, 2017, **2**, 124–128.
78. M. S. Eberhart, D. Wang, R. N. Sampaio, S. L. Marquard, B. Shan, M. K. Brennaman, G. J. Meyer, C. Dares and T. J. Meyer, *J. Am. Chem. Soc.*, 2017, **139**, 16248–16255.
79. D. Wang, F. Niu, M. J. Mortelliti, M. V. Sheridan, B. D. Sherman, Y. Zhu, J. R. McBride, J. L. Dempsey, S. Shen, C. J. Dares, F. Li and T. J. Meyer, *Proc. Natl. Acad. Sci. U. S. A.*, 2020, **117**, 12564–12571.
80. R. J. Pace, R. Stranger and S. Petrie, *Dalton Trans.*, 2012, **41**, 7179–7189.
81. K. P. Regan, C. Koenigsmann, S. W. Sheehan, S. J. Konezny and C. A. Schmuttenmaer, *J. Phys. Chem. C*, 2016, **120**, 14926–14933.
82. M. D. Brady, R. N. Sampaio, D. Wang, T. J. Meyer and G. J. Meyer, *J. Am. Chem. Soc.*, 2017, **139**, 15612–15615.

CHAPTER 5

# *Performance Enhancement of $TiO_2$-encapsulated Photoelectrodes Based on III–V Compound Semiconductors*

YU WANG[a] AND STEPHEN B. CRONIN*[b]

[a] Mork Family Department of Chemical Engineering and Materials Science, University of Southern California, Los Angeles, CA 90089, USA; [b] Ming Hsieh Department of Electrical Engineering, Department of Chemistry, and Department of Physics and Astronomy, University of Southern California, Los Angeles, CA 90089, USA
*Email: scronin@usc.edu

## 5.1 Introduction

The intermittence of solar energy presents a serious challenge when trying to incorporate a high percentage of solar power into the electric power grid. To solve this problem, photoelectrochemical (PEC) water splitting and $CO_2$ reduction can be used to store solar energy in the form of chemical bonds that can be released later. Although the use of $TiO_2$ alone in water splitting under UV light irradiance has been demonstrated, its band gap is too wide ($E_g = 3.2$ eV) for it to be used for efficient solar energy conversion.[1] Based on the Shockley–Queisser limit, the band gap of a semiconductor should be in the range 1.2–1.4 eV for optimum solar power utilization.[2] Various III–V compound semiconductors, such as GaAs, GaP, and InP, are promising candidates,

Energy and Environment Series No. 30
Ultrathin Oxide Layers for Solar and Electrocatalytic Systems
Edited by Heinz Frei and Daniel V. Esposito

Published by the Royal Society of Chemistry, www.rsc.org

and their theoretical photocurrent densities are much higher than that of $TiO_2$ alone under one-sun illumination.[3] However, these semiconductors are not stable and often undergo photocorrosion in the photocatalytic production of solar fuels.

Figure 5.1a,b show the optical microscopy and atomic force microscopy (AFM) images of a bare p-type GaP photocathode after 8 h of $CO_2$ reduction reaction in $CO_2$-saturated 0.5 M NaCl aqueous solution under 532 nm light illumination.[4] The surface of the bare GaP substrate changed color and became rougher. The root mean square (RMS) roughness is about $\pm 54$ nm (shown in Figure 5.1c). It is desirable to provide a thin and pinhole-free oxide layer to protect the underlying photoelectrode while not preventing charge transfer. Atomic layer deposition (ALD) is a powerful tool to facilitate these goals because it can provide a conformal oxide layer with thickness control at the ångström level. McIntyre's group first demonstrated that 2 nm $TiO_2$ surface coatings grown by ALD can prevent the corrosion of a silicon photoanode from the oxygen evolution reaction (OER) while allowing electrons to tunnel through, and they are sufficiently transparent in the visible wavelength range.[5] Later, the protection of a nanotextured p-type InP photocathode by a $TiO_2$ passivation layer in the hydrogen evolution reaction (HER) was demonstrated.[6]

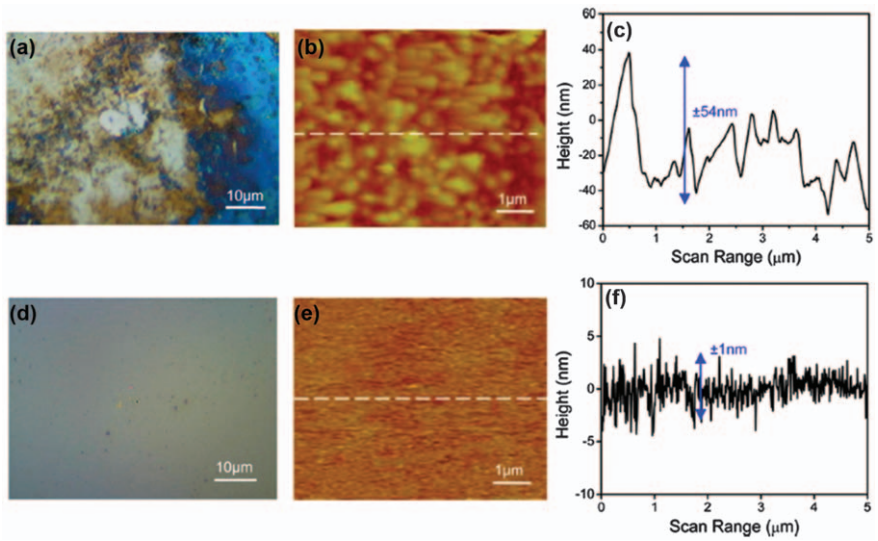


**Figure 5.1** (a) Optical microscopy image, (b) atomic force microscopy (AFM) image, and (c) surface topography of the surface of a bare p-type GaP photocathode after 8 h of $CO_2$ reduction reaction at an applied potential of $-0.5$ V *vs.* NHE in $CO_2$-purged 0.5 M NaCl solution under 532 nm laser illumination. (d) Optical microscopy, (e) AFM, and (f) surface topography of the surface of a GaP photocathode passivated with a 5 nm $TiO_2$ layer after 8 h of $CO_2$ reduction reaction.
Reproduced from ref. 4 with permission from American Chemical Society, Copyright 2014.

As Figure 5.1d,e show, upon 5 nm $TiO_2$ passivation, the GaP surface is stable with a uniform color after 8 h of $CO_2$ reduction reaction, and the RMS roughness is only $\pm 1$ nm (shown in Figure 5.1f). The change in the morphology and appearance of as-fabricated $TiO_2$–GaP photocathodes is minimal before and after the reaction. In addition, $Ti^{3+}$ surface states, which originate from oxygen vacancies, can lower the binding energy of reactant molecules and intermediates,[6–9] and the built-in electric field formed between n-type $TiO_2$ film and p-type III–V semiconductors can enhance the charge separation process for photogenerated electron–hole pairs.[10] Therefore, by passivating III–V compound semiconductors with $TiO_2$ films, strongly absorbing materials can be combined with highly catalytic materials to achieve efficient and stable solar energy conversion.

## 5.2 Fabrication, Characterization, and Surface States of $TiO_2$ Layers

### 5.2.1 Fabrication Methods

ALD provides a facile deposition technique for producing thin films of various materials, from metal oxides to noble metals.[11,12] During the deposition, the target substrate is kept in a vacuum chamber under a pressure of $<1$ Torr, and is exposed alternately to pulses of each chemical precursor. In each half-reaction, an individual source is pulsed into the reaction chamber for a certain amount of time to form one monolayer of part of the target material through a self-saturating process. Then, a carrier gas such as nitrogen or argon is purged into the chamber to eliminate unreacted precursor or by-products, followed by the pulse and purge of another chemical precursor. This process is repeated until the desired thickness of the target material is achieved.[11] For a $TiO_2$ layer, $TiCl_4$ or tetrakis(dimethylamido)titanium (TDMAT) is used as a titanium source and water is used as an oxygen source.[5,7,13,14] There are several advantages of ALD over other chemical vapor deposition (CVD) or physical vapor deposition (PVD) methods. First, the as-deposited film is conformal and pinhole free because of its self-limiting characteristics. Second, the thickness can be controlled at the ångström level because of its cycle-by-cycle deposition nature so that the as-deposited film can be made very thin and precise.[11] These two properties are critical for protecting the underlying semiconductor photoelectrodes while not inhibiting charge transfer in PEC processes. Although the deposition rate is very slow compared with other deposition methods, only a few nanometers thick $TiO_2$ layer is needed to achieve the optimal PEC performances of these photoelectrodes.[6,7,9,15]

### 5.2.2 Characterization Methods

The as-deposited $TiO_2$ films can be characterized by several experimental methods, including high-resolution transmission electron microscopy (HRTEM), electron energy-loss spectroscopy (EELS), and X-ray photoemission

spectroscopy (XPS). HRTEM is used to analyze the film morphology and crystallinity, and the spatial chemical composition profile can be extracted by EELS. Figure 5.2a–c show typical HRTEM images of ALD-deposited $TiO_2$ films with 25, 75, and 500 deposition cycles at 250 °C on p-type GaAs substrates.[8] During the deposition, $TiCl_4$ is used for the first half-cycle as the Ti source, followed by water vapor as the O source. Figure 5.2d–f show the EELS spatial profiles of Ti and O species corresponding to different numbers of deposition cycles. For 25-cycle depositions (shown in Figure 5.2a), the oxygen signal increases 0.5 nm before the Ti signal, which indicates that the native GaAs oxide still exists below the $TiO_2$ film. However, the native oxide of GaAs is removed by the $TiO_2$ film with 75 cycles of deposition (shown in Figure 5.2b). The reason for this is that $Cl^-$ ions from the $TiCl_4$ precursor partially removed GaAs native oxide after 25 cycles. This is further verified by the EELS spatial maps in Figure 5.2e, showing that both the O and Ti signals together increase in the same position for the 75-cycle deposition. With 500 cycles of ALD deposition, the $TiO_2$ film forms a crystalline structure with an interplane distance of $3.5 \pm 0.1$ Å (shown in Figure 5.2c). Thick crystalline $TiO_2$ will greatly inhibit charge transfer owing to its wide band gap and insulating nature, thus offering no improvement in photocatalytic performance for III–V compound semiconductors unless it is thin enough (<2 nm) to allow electrons to tunnel through.[14] Hu *et al.* also showed that unannealed $TiO_2$ coatings up to 143 nm thick can still maintain their amorphous, highly conductive, and transparent natures, while preventing corrosion for Si, GaAs, and GaP photoanodes during water oxidation reactions in 1 M KOH solution. In that work, they used

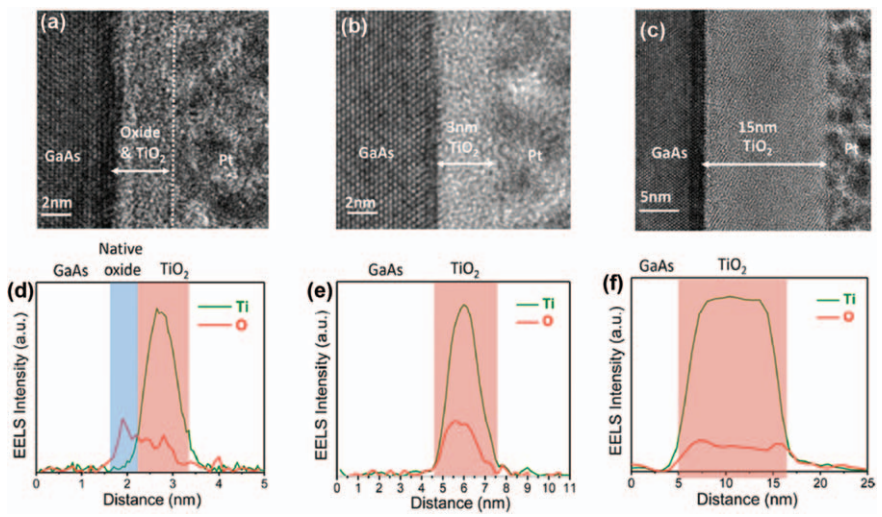


**Figure 5.2** HRTEM images of $TiO_2$ passivation films with (a) 25, (b) 75, and (c) 500 cycles of ALD deposition on p-type GaAs substrates. EELS spatial maps of Ti L edge and O K edge for (d) 25, (e) 75, and (f) 500 ALD deposition cycles. Reproduced from ref. 8 with permission from American Chemical Society, Copyright 2015.

a lower deposition temperature (150 °C) and different Ti precursor [tetrakis(dimethylamido)titanium (TDMAT)] in their ALD process.[16]

### 5.2.3 Catalytic Outer Surface States

$Ti^{3+}$ defect states on the surface of amorphous $TiO_2$ films can lower the potential barrier and promote charge transfer, thus enhancing the PEC performance of III–V compound semiconductors. In order to quantify the importance of those defect states, plane wave density function theory (PW-DFT) has been used to calculate the adsorption energy of $CO_2$ and $H_2O$ molecules adsorbed on the $TiO_2$ surface. Figure 5.3a shows the anatase $TiO_2$ structure used in the PW-DFT calculation by Alexandrova's group,[7,8] and the adsorption energy is calculated based on the following equation:

$$E_{ads} = E[\text{surf} + \text{molecule}] - E[\text{surf}] - E[\text{molecule}] \quad (5.1)$$

Both stoichiometric and defective anatase (with an oxygen vacancy) were analyzed in their study (only defective anatase is shown in Figure 5.3). Relevant to the HER, $E_{ads}$ is −1.26 and −1.50 eV for a neutral $H_2O$ molecule adsorbed on stoichiometric and defective anatase, respectively. The O atom in the $H_2O$ molecule tends to fill the oxygen vacancy, and the two H atoms

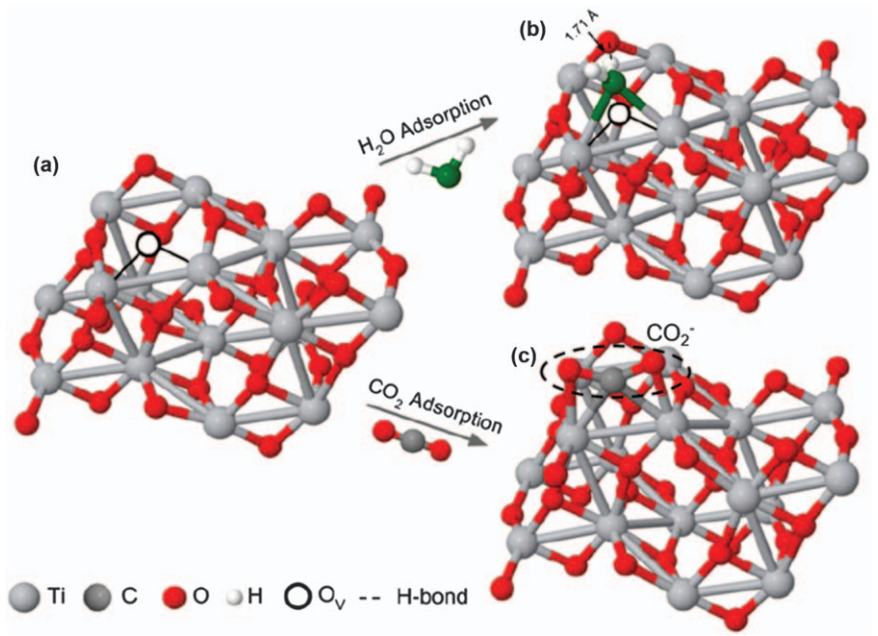


**Figure 5.3** Defective anatase structure used in PW-DFT calculation with oxygen vacancies (a) before adsorption, (b) after $H_2O$ molecule adsorption and relaxation, and (c) after $CO_2$ molecule adsorption and relaxation. Adapted from ref. 8 with permission from American Chemical Society, Copyright 2015.

form hydrogen bonds with the neighboring surface oxygens on the $TiO_2$ film.[8] For the $CO_2$ reduction reaction, the calculation shows that $E_{ads}$ is $-0.48$ eV for stoichiometric anatase and $-0.94$ eV for defective anatase. In addition, the linear $CO_2$ molecule becomes bent when it occupies the bridging oxygen vacancy, as shown in Figure 5.3c. Upon adsorption, the calculation also shows that $CO_2$ gains an electron ($-0.897e$) from the $TiO_2$ substrate spontaneously, meaning that no overpotential is required to form $CO_2^-$ intermediates that can subsequently form methanol and CO in aqueous and non-aqueous electrolytes.[7,9]

### 5.2.4 Quantifying Surface States

The density of defective states in $TiO_2$ overlayers can be characterized by XPS. Figure 5.4 shows the typical XPS spectra of different thicknesses of $TiO_2$ films deposited on GaAs surfaces.[13] Here, the core-level binding energies of Ti $2p_{1/2}$ and Ti $2p_{3/2}$ are 464.7 and 459.0 eV, respectively (Figure 5.4a). Additionally, the lower binding energy of 457.1 eV corresponds to $Ti^{3+}$ states, and the area ratios of $Ti^{3+}$ to Ti $2p_{1/2}$ are 0.15, 0.09, and 0.061 for the 1, 3, and 5 nm thick $TiO_2$ films, respectively. This indicates a higher density of defective states in thinner $TiO_2$ films. As will be shown in later sections, thinner $TiO_2$ films also have better

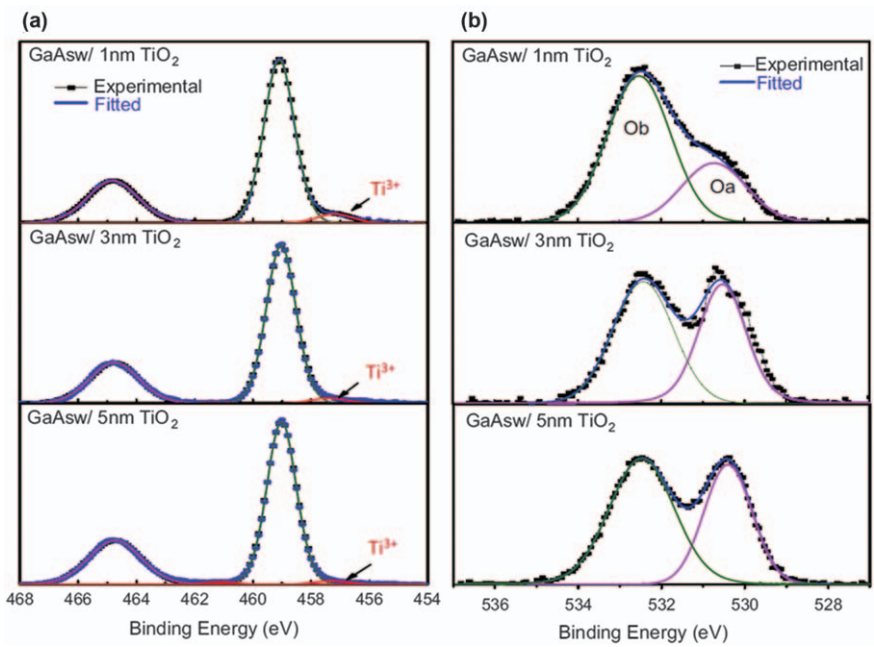


**Figure 5.4** (a) Ti 2p and (b) O 1s core-level XPS spectra of different thicknesses of $TiO_2$ films on p-type GaAs substrates.
Reproduced from ref. 13 with permission from Elsevier, Copyright 2016.

performance in photocatalytic reactions, such as water splitting and $CO_2$ reduction. Furthermore, two O peaks are shown in Figure 5.4b, originating from $TiO_2$ layers. Two symmetrical Gaussian peaks are fitted from experimental data, which are denoted Oa and Ob from the O 1s core level.[17] For a 1 nm $TiO_2$-encapsulated GaAs substrate, the native oxide may contribute to the O 1s peaks. For 3 and 5 nm thick $TiO_2$-encapsulated substrates, the native oxide is removed by the ALD process as indicated in Figure 5.2. The Oa peak results from O atoms from stoichiometric $TiO_2$ and the Ob peak is attributed to oxygen vacancies. The area ratios between the Ob and Oa peaks are 2.4, 1.6, and 1.4 for 1, 3, and 5 nm thick $TiO_2$ films, respectively; therefore, the density of oxygen vacancies also increases as the $TiO_2$ layer becomes thinner.

## 5.3 Photocatalytic Enhancement of $TiO_2$-encapsulated III–V Semiconductors

### 5.3.1 InP

InP has a direct band gap of ~1.35 eV and is suitable for the optimum utilization of the terrestrial solar spectrum according to the Shockley–Quiesser limit.[2] It has surface-recombination velocities of $10^4$ and $10^5$ cm s$^{-1}$ for n- and p-type, respectively, which are low compared with other III–V semiconductors.[18] Also, the optical absorption of InP is high and can be further enhanced by nanotexturing technique.[6,7,19] Low surface-recombination velocities combined with high optical absorption will lead to a pronounced short-circuit current density (up to 37 mA cm$^{-2}$ in a proton reduction reaction).[6] Furthermore, it has a desirable position of the conduction band edge with respect to $H^+/H_2$ and $CO_2/CO_2^-$ redox potentials, thereby making Zn-doped p-type InP a suitable photocathode in water splitting and $CO_2$ reduction reactions. The cost of InP can be further reduced by using a non-epitaxial grown thin-film substrate rather than single-crystalline wafers.[15] Aharon-Shalom and Heller demonstrated the HER using p-type InP (Rh–H alloy) and p-type InP (Re–H alloy) as photocathodes in 1982.[20] In their findings, the applied bias photon-to-current efficiencies (ABPE) were 13.3 and 11.4%, respectively. ABPE used here is calculated based on the comparison between the applied potential at photocathodes and the thermodynamic potential generated from an ideal fuel cell cathode:[21]

$$\eta = \left[\frac{\left(V_{\mathrm{App}} - V_{\mathrm{H_2}}\right) \times J}{P_0}\right] \times 100\% \tag{5.2}$$

where $V_{\mathrm{App}}$ is the applied potential at photocathodes *vs.* RHE, $V_{\mathrm{H_2}}$ is the reduction potential of $H^+/H_2$ *vs.* RHE (which is 0 V here), $J$ is the cell output current density, and $P_0$ is the incident light power density. However, InP is not stable and undergoes photocorrosion in aqueous solutions. A $TiO_2$ encapsulation layer grown by ALD can be used to address this problem because

of its chemical stability and high uniformity. In addition, n-type $TiO_2$ has a large offset in the valence band edge compared with p-type InP, which induces an energy barrier for holes in InP to reach the $TiO_2$ surface and reduces interface electron–hole recombination.[22] This decrease in recombination will enable a higher photovoltage to be generated and lead to a positive onset potential shift for the photocathode that makes the design of tandem cells for unassisted water splitting possible in the future. Also, the conduction band of InP is well aligned with respect to that of $TiO_2$, and the built-in electric field between p-type InP and n-type $TiO_2$ also assists electron extraction while repelling holes. The combination of all these effects makes the $TiO_2$-passivated p-type InP substrate a highly electron-selective photocathode for reduction reactions. Depositing co-catalysts on top of $TiO_2$ will further enhance the photoelectrochemical performance by decreasing kinetic overpotential losses. We discuss the performance of the p-type InP photocathode in the HER and $CO_2$ reduction separately in detail below.

Figure 5.5 shows a comparison of the photoelectrochemical HER performance of p-type InP with a doping level of $3–5\times10^{17}\,cm^{-3}$ with and without the $TiO_2$ encapsulation layer in 1 M $HClO_4$ solution under AM1.5 simulated solar spectra, reported by Lin *et al.*[10] Here, the $TiO_2$ film was deposited by ALD with a 10 nm thickness at 250 °C, and titanium isopropoxide and water were used as precursors. The surface of the as-deposited $TiO_2$ film was treated by 2 nm Pt sputtering as a co-catalyst. Figure 5.5a shows the measured photocurrent density as a function of applied voltage with respect to the reversible hydrogen electrode (RHE). The onset potentials of p-type InP with and without $TiO_2$ were extracted from the *J–V* plot as 0.81 and 0.63 V *vs.* RHE, respectively. Hence, the $TiO_2$ passivation increases by almost 200 mV in photocurrent onset potential. This large onset potential provides a large fraction of 1.23 V needed for water splitting in an acidic environment.[23–25] The InP/$TiO_2$ photocathode has a photocurrent density of 25.2 $mA\,cm^{-2}$, which is similar to 24 $mA\,cm^{-2}$ for bare InP. Lee *et al.* reported a photocurrent density of 37 $mA\,cm^{-2}$ with a p-type InP nanopillar photocathode passivated by 3–5 nm $TiO_2$ layers in conjunction with a 2 nm Ru co-catalyst.[6] The high photocurrent density is due to enhanced light absorption and less hydrogen gas bubble accumulation resulting from nanotexturing the surface. Figure 5.5b shows chronoamperometry measurements at high positive potentials *vs.* RHE for both samples. Here, the InP/$TiO_2$ sample shows 19.3 and 9.9 $mA\,cm^{-2}$ at 0.6 and 0.7 V *vs.* RHE, respectively. In contrast, bare InP has a much lower photocurrent density at these applied potentials. In addition, the incident photon-to-charge conversion efficiency (IPCE) was measured in a laboratory-built setup using a 150 W xenon lamp combined with a 1/8 m monochromator. The IPCE for the InP/$TiO_2$ sample was 70–80% under an applied potential of 0.2 V *vs.* RHE with an incident light wavelength of 400–800 nm, whereas for bare InP only it was less than 30% (Figure 5.5c). The IPCE measurements were conducted under a low illumination intensity in order to study the surface effects of photocathodes, and showed that $TiO_2$ encapsulation improves the minority carrier extraction capability.

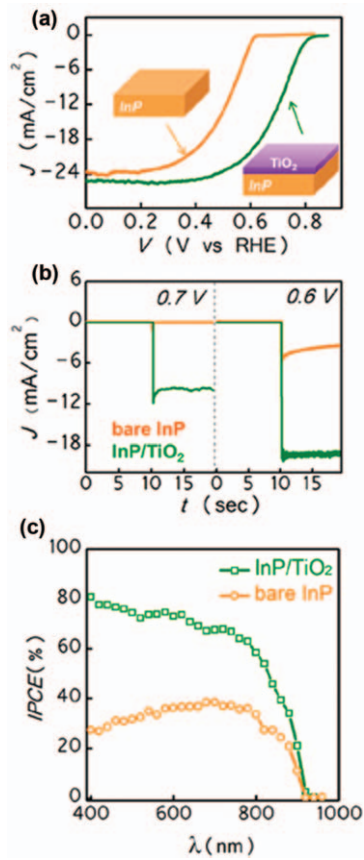


**Figure 5.5** (a) Photocurrent density measurements as a function of applied potential *vs.* RHE of $InP/TiO_2$ (green curve) and bare InP (orange curve). (b) Chronoamperometry measurement of both samples at 0.6 and 0.7 V applied potentials *vs.* RHE with chopped light irradiation. (c) Incident photon-to-charge conversion efficiency (IPCE) of $InP/TiO_2$ and bare InP with an applied potential of 0.2 V *vs.* RHE in 1 M $HClO_4$ solution. Adapted from ref. 10 with permission from American Chemical Society, Copyright 2015.

In order to obtain carrier concentrations and flat band potentials of p-type InP and n-type $TiO_2$, Mott–Schottky (MS) measurements were carried out as shown in Figure 5.6a,b. Here, the space charge region capacitance was measured as a function of applied potential *vs.* RHE. A sinusoidal small voltage with 5 mV amplitude and 10 kHz frequency was injected together with DC bias. The carrier concentrations and flat band potentials can be extracted based on the MS equation for a p-type semiconductor:[26,27]

$$\frac{1}{C^2} = \left(\frac{2}{e\varepsilon\varepsilon_0 N_d A^2}\right)\left(-V + V_{fb} - \frac{kT}{e}\right) \tag{5.3}$$

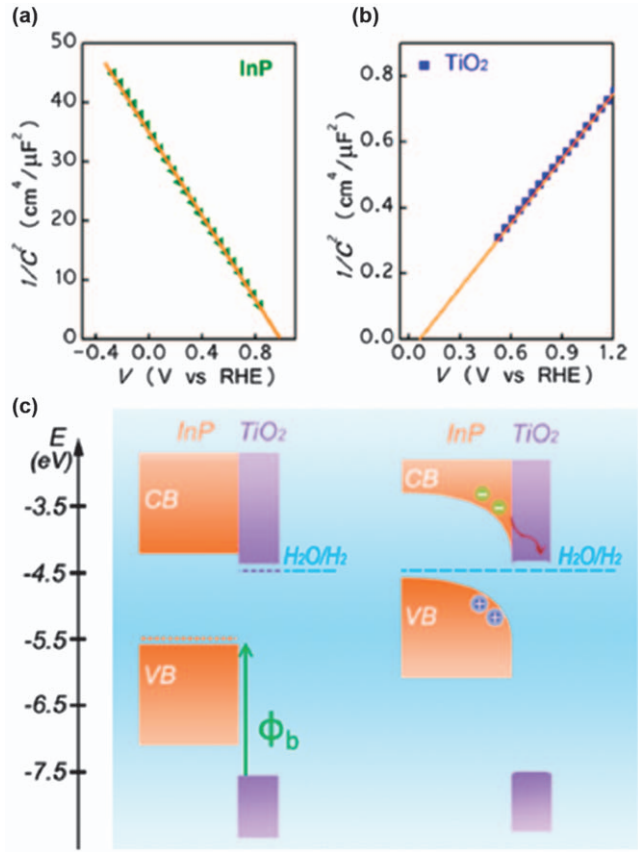


**Figure 5.6** Mott–Schottky (MS) plots of (a) p-type InP substrate and (b) 50 nm $TiO_2$ deposited on an FTO substrate. (c) Band diagram of InP/$TiO_2$ in 1 M $HClO_4$ solution based on extracted flat band potentials, carrier concentrations and band gaps.
Reprinted with permission from ref. 10 with permission from American Chemical Society, Copyright 2015.

where $C$ is the measured capacitance, $e$ is the electron charge, $\varepsilon$ is the dielectric constant, $\varepsilon_0$ is the permittivity of vacuum, $N_d$ is the carrier density, $A$ is the surface area of the photocathode, $V$ is the applied potential *vs.* the reduction potential for the half-reaction of interest (which is RHE for the HER), $V_{fb}$ is the flat band potential, $k$ is the Boltzmann constant, and $T$ is the room temperature. As Figure 5.6a shows, the negative slope of the MS plot indicated p-type doping of the InP substrate, and a carrier density of $3.2\times10^{17}\,cm^{-3}$ was extracted from the slope of linear fitting of the MS curve. A flat band potential of 0.98 V *vs.* RHE of InP was estimated from the $x$-axis intercept of the linear fitted line. The $TiO_2$ film grown by ALD and deposited on a fluorine-doped tin oxide (FTO) substrate has a positive slope in MS plot, which indicates n-type doping. A carrier density of about $3.0\times10^{18}\,cm^{-3}$ and a flat band potential of

0.04 V *vs.* RHE were extracted from the linear fitted line in Figure 5.6b. With all these estimated properties combined with the band gap of InP and $TiO_2$, the energy band diagram of InP/$TiO_2$/electrolyte can be determined (shown in Figure 5.6c). A type II heterojunction in which two materials form a staggered gap results from a p-type InP substrate and n-type $TiO_2$ passivation layer, and their conduction band edges are close to each other, thereby assisting transfer of photogenerated electrons from InP to the $TiO_2$ surface. However, the large offset of the valence band edges between these two layers acts like a blocking layer for holes, leading to lower interface recombination rates. As discussed earlier, this results in a more positive onset potential and higher IPCE for InP/$TiO_2$ photoelectrodes. For this reason, high performance of the InP/$TiO_2$ photocathode with a large onset potential and low surface recombination rates was demonstrated. However, the relatively high cost of InP wafers presents a challenge for large-scale commercial application. The approach of using thin films can address the cost problem by reducing the overall material use while keeping all the benefits of InP in photoelectrochemical performance in the HER. Hettick *et al.* demonstrated non-epitaxial growth of thin-film InP on Mo substrates by a vapor–liquid–solid (VLS) method.[15] The as-deposited InP thin film combined with ALD-grown $TiO_2$ and Pt co-catalyst showed a 29.4 mA $cm^{-2}$ saturated photocurrent density and a 0.63 V *vs.* RHE onset potential, displaying competent performance in the HER compared with single-crystalline InP wafers.

Photoelectrochemical $CO_2$ reduction in aqueous solution by p-type InP nanopillars encapsulated by an ALD-grown $TiO_2$ layer was demonstrated by Qiu *et al.*[7] Figure 5.7 shows a schematic diagram together with scanning electron microscopy (SEM) and transmission electron microscopy (TEM) images of a fabricated photocathode. Here, the nanopillars are 80 nm in diameter and 400–600 nm in length with a 250 nm period (shown in Figure 5.7b). A 3 nm thick layer of $TiO_2$ was coated on the surface of InP nanopillars using $TiCl_4$ and water as precursors. Subsequently, Cu was evaporated onto the $TiO_2$ surface with a nominal thickness of 0.5 nm. As Figure 5.7d shows, the as-deposited Cu formed nanoparticles with a diameter of ~20 nm rather than a thin continuous film. The surface of the Cu nanoparticles was oxidized to form an amorphous layer of CuO.

Figure 5.8 shows *J–V* measurements of p-type InP nanopillars with and without $TiO_2$ in 0.5 M KCl aqueous solution with continuous $CO_2$ bubbling under 532 nm light irradiation. Here, the effect of adding a Cu co-catalyst was excluded in order to study only the role played by the $TiO_2$ encapsulation layer on the PEC performance. As Figure 5.8a shows, the photocurrent density is dramatically increased with the $TiO_2$ encapsulation layer compared with bare InP at all applied potentials *vs.* NHE. The onset potential of the InP/$TiO_2$ sample is 0.1 V higher than that of bare InP nanopillars. The positive shift of the onset potential is attributed to decreased interface recombination rates and a larger built-in potential between the n-type $TiO_2$ layer and p-type InP nanopillars.[10,28] The NMR spectra in Figure 5.8c show the methanol product peaks using InP nanopillars with and without $TiO_2$

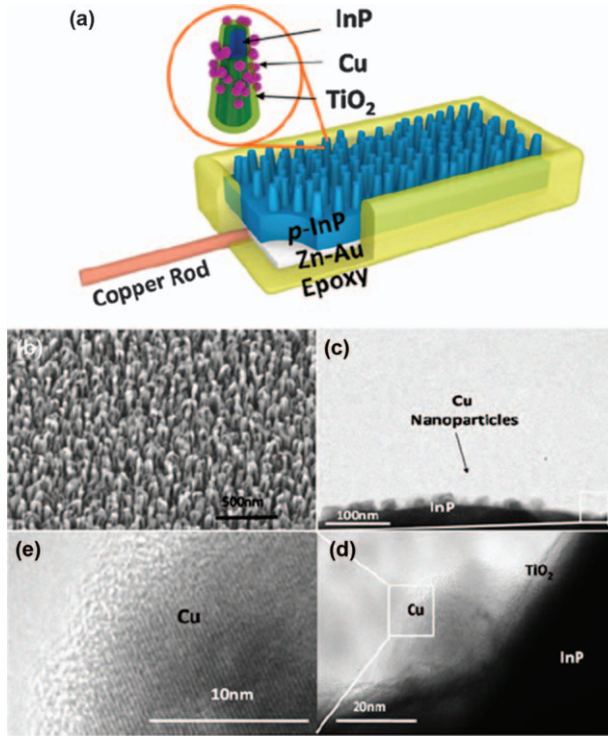


**Figure 5.7** (a) Schematic diagram of an as-fabricated InP/$TiO_2$/Cu photocathode. (b)–(e) SEM and TEM images of InP nanopillars with $TiO_2$ layers and Cu nanoparticles on the top.
Reproduced from ref. 7 with permission from American Chemical Society, Copyright 2015.

encapsulation as photocathodes at an applied potential of −0.6 V *vs.* NHE under 532 nm irradiation. For $CO_2$ reduction in aqueous solution under the assumption that $CO_2$ molecules do not interact with any other molecules in solution or heterogeneous interfaces in the system, the first step of reduction for $CO_2$ is to form the $CO_2^-$ intermediate, and the redox potential of $CO_2/CO_2^-$ is −1.9 V *vs.* NHE. In the energy diagram, $E^\circ(CO_2/CO_2^-)$ is 1.6 eV above the conduction band edge of InP.[29,30] The applied potential here is −0.6 V *vs.* NHE, which is 1.3 V more positive compared with the $CO_2/CO_2^-$ redox potential (−1.9 V *vs.* NHE). The Faradaic efficiency (FE) describes the efficiency of transferred charge facilitating the target electrochemical reaction, which can be calculated based on the following equation:

$$FE = \frac{nNF}{Q} \times 100\% \tag{5.4}$$

where $n$ is the number of electrons transferred for each product molecule, $N$ is the amount of product in moles in the reaction, $F$ is the Faraday constant,

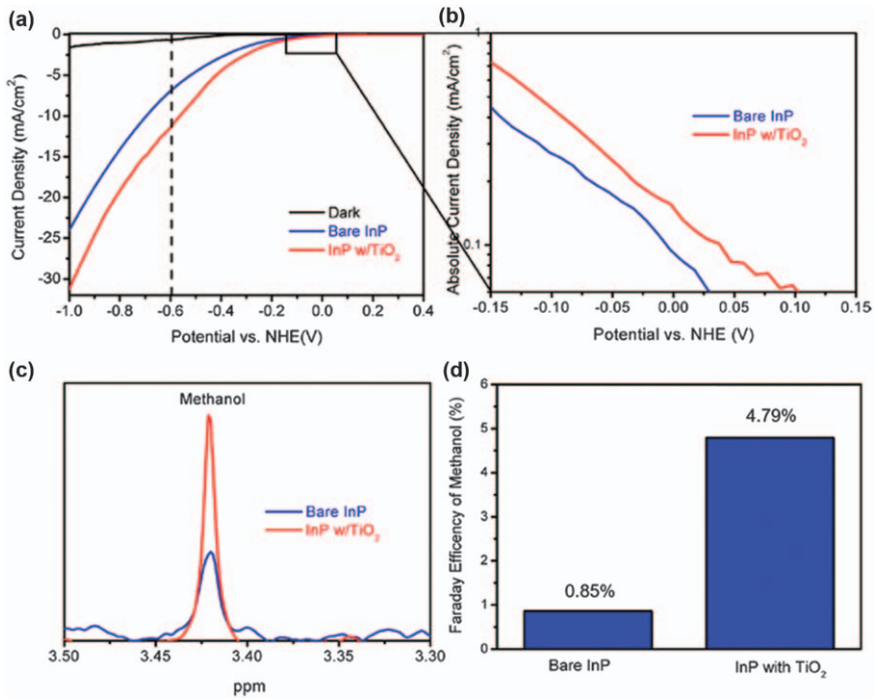


**Figure 5.8** (a) Photocurrent density measured as a function of applied potential *vs.* NHE for p-type InP nanopillars with and without $TiO_2$ passivation under 532 nm monochromatic irradiance in $CO_2$-saturated 0.5 M KCl solution. The dashed line indicates the potential applied during methanol production. (b) Logarithmic plot of *J–V* measurements near the onset potential region. (c) Methanol peaks in NMR spectra. (d) Faradaic efficiencies of the methanol produced for these two photocathodes.
Reproduced from ref. 7 with permission from American Chemical Society, Copyright 2015.

and *Q* is the total amount of charge passed through. Figure 5.8d shows the FE of methanol production for these two photocathodes, where InP nanopillars with a $TiO_2$ layer show FE = 4.79%, which is 5.7 times higher than that of bare InP nanopillars. The enhanced FE indicates higher selectivity of the InP/$TiO_2$ photocathode, which is also attributed to $Ti^{3+}$ defect states. As discussed earlier, the catalytically active $Ti^{3+}$ defect states (*i.e.* oxygen vacancies) substantially lowered the energy required for $CO_2$ molecules adsorbed on the $TiO_2$ surface to acquire electrons and form $CO_2^-$ intermediates (Figure 5.3).

In order to study further the selectivity of the Cu co-catalyst on methanol production in PEC $CO_2$ reduction, a 0.5 nm nominal thickness Cu layer was evaporated onto the surface of as-fabricated photocathodes. As shown in Figure 5.7, the as-deposited Cu formed nanoparticles 20 nm in diameter instead of a continuous thin film. The surface area of the nanoparticles is dramatically increased compared with that of a thin film, which is beneficial

to the PEC reaction. The *J–V* measurements in Figure 5.9a show that the InP/$TiO_2$/Cu photocathode has the highest photocurrent density at all applied potentials *vs.* NHE. At −0.6 V *vs.* NHE, the photocurrent density of the InP/$TiO_2$/Cu substrate is around $-15$ mA cm$^{-2}$, whereas for bare InP with and without the Cu co-catalyst it is only $-7.5$ mA cm$^{-2}$. For bare InP nanopillars, although adding Cu nanoparticles does not change the *J–V* curve profile (Figure 5.9a), the FE is improved from 0.85 to 2.8% for methanol production (Figure 5.9b). In addition, deposition of Cu nanoparticles on the $TiO_2$ surface enhanced the FE from 4.79% (Figure 5.8d) to 8.7% (Figure 5.9b). These observations clearly demonstrate the selectivity enhancement of Cu nanoparticles towards methanol production over the HER in aqueous solution. In aqueous solution, the HER is always competing with $CO_2$ reduction, for two reasons. First, the overpotential of the $H_2O/H_2$ redox reaction is lower than or similar to that of most $CO_2$ reduction reactions, such as methanol, methane, and carbon monoxide production. Second, the solubility of $CO_2$ in water is very limited, around 0.033 M at room temperature under 1 atm.[31] The accessibility of $CO_2$ molecules for these photocathodes is substantially lower than that of water molecules or hydrogen ions. In order to increase further the selectivity of $CO_2$ reduction over the HER, Zeng *et al.* demonstrated 89% FE towards CO on a 3 nm $TiO_2$-passivated p-type InP photocathode in $CO_2$-saturated non-aqueous solution, which consists of 0.02 M 1-ethyl-3-methylimidazolium tetrafluoroborate ([EMIM]$BF_4$) ionic liquid in acetonitrile.[9] The applied potential is −1.57 V *vs.* NHE and the light source is a 532 nm beam. Here, in addition to photocatalytically active $Ti^{3+}$ defect states, as discussed earlier, an EMIM–$CO_2$* complex can be formed between [EMIM] ions and $CO_2^-$ intermediates. These complexes can further lower the overpotential associated with the $CO_2$/CO redox reaction. With the Pt co-catalyst, the FE was further enhanced to 99% towards CO with an applied

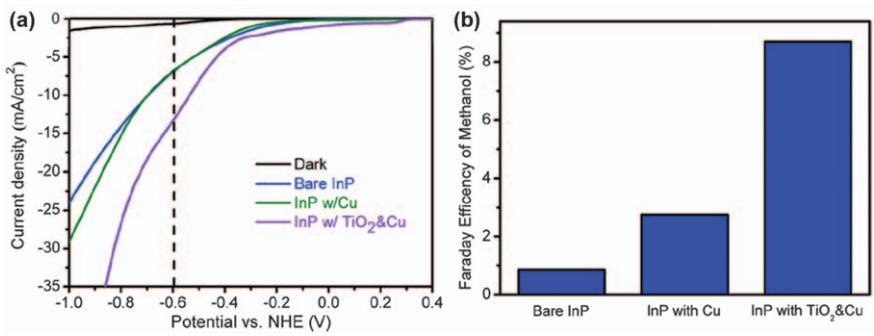


**Figure 5.9** (a) *J–V* measurements and (b) Faradaic efficiencies for methanol production with bare InP nanopillars and InP/Cu and InP/$TiO_2$/Cu photocathodes under 532 nm monochromatic irradiance in $CO_2$-saturated 0.5 M KCl solution. The dashed line indicates the potential applied during the methanol production experiment.
Reproduced from ref. 7 with permission from American Chemical Society, Copyright 2015.

potential of −0.77 V *vs.* NHE, which showed a 0.78 V underpotential *vs.* the $CO_2$/CO redox potential (−1.55 V *vs.* NHE).

### 5.3.2 GaP

GaP is another III–V semiconductor and has a direct band gap of 2.25 eV with more than 18% absorption under solar light. As with InP, it also is not stable during PEC reactions resulting from photocorrosion.[4,32] By introducing a passivating $TiO_2$ layer on top, the chemical stability of GaP is dramatically increased. In addition, the large valence band offset combined with a built-in electric field between p-type GaP and n-type $TiO_2$ assists electron extraction while blocking holes.[4] Over the past decade, a new method has emerged for improving the photocatalytic efficiency by utilizing the plasmon resonance of metal nanostructures.[33–38] Since the conduction band energy of GaP is well matched to the resonance energy of Au nanoparticles, adding plasmonic Au nanoparticles can further enhance the photocatalytic performance of the GaP/$TiO_2$ photocathode.[32] We first discuss the application of GaP as a photocathode in water splitting, followed by a discussion of $CO_2$ reduction.

Figure 5.10a shows a GaP/$TiO_2$ photocathode for HER fabricated by Qiu *et al.*[32] Here, a $TiO_2$ layer grown by ALD at 250 °C was deposited on the surface of Zn-doped p-type GaP with a doping concentration of $2\times10^{18}$ $cm^{-3}$. $TiCl_4$ and water were used as titanium and oxygen sources, respectively. The photocurrent densities of InP photocathodes with various $TiO_2$ layer thicknesses were measured as a function of applied potential *vs.* an Ag/AgCl reference electrode in 0.5 M $Na_2SO_4$ aqueous solution (pH 7) under 532 nm light illumination (shown in Figure 5.10b). RHE = 0 V is also indicated in the *J–V* plot (Figure 5.10b) as a dashed line. Here, the onset potential of the bare GaP photocathode was about −0.66 V *vs.* Ag/AgCl. For $TiO_2$-passivated GaP samples, the onset potential showed a positive shift with increase in $TiO_2$ thickness (shown in Figure 5.10c). The onset potential of the sample of GaP with a 10 nm $TiO_2$ layer shifted by 0.46 V compared with that of the bare GaP substrate. This positive shift is attributed to the increased built-in electric field from the p–n junction between GaP and $TiO_2$, since GaP is positively doped by Zn and $TiO_2$ is negatively doped resulting from oxygen vacancies. The built-in potential can be calculated using the following equation:

$$V_{bi} = \frac{W_D^2}{2\varepsilon_0\varepsilon_a\varepsilon_d}\frac{N_aN_d(N_a\varepsilon_a + N_d\varepsilon_d)}{(N_a + N_d)^2} \tag{5.5}$$

where $W_D$ is the depletion width of the p–n junction and increases with increase in $TiO_2$ thickness, $\varepsilon_0$ is the permittivity of vacuum, $\varepsilon_a$ and $\varepsilon_d$ are the dielectric constants of GaP and $TiO_2$, respectively, and $N_a$ and $N_d$ are doping concentrations for GaP and $TiO_2$, respectively. The calculated built-in potential based on this equation is shown in Figure 5.10c, indicated by dashed line, which exhibited a similar trend to the experimentally measured relative

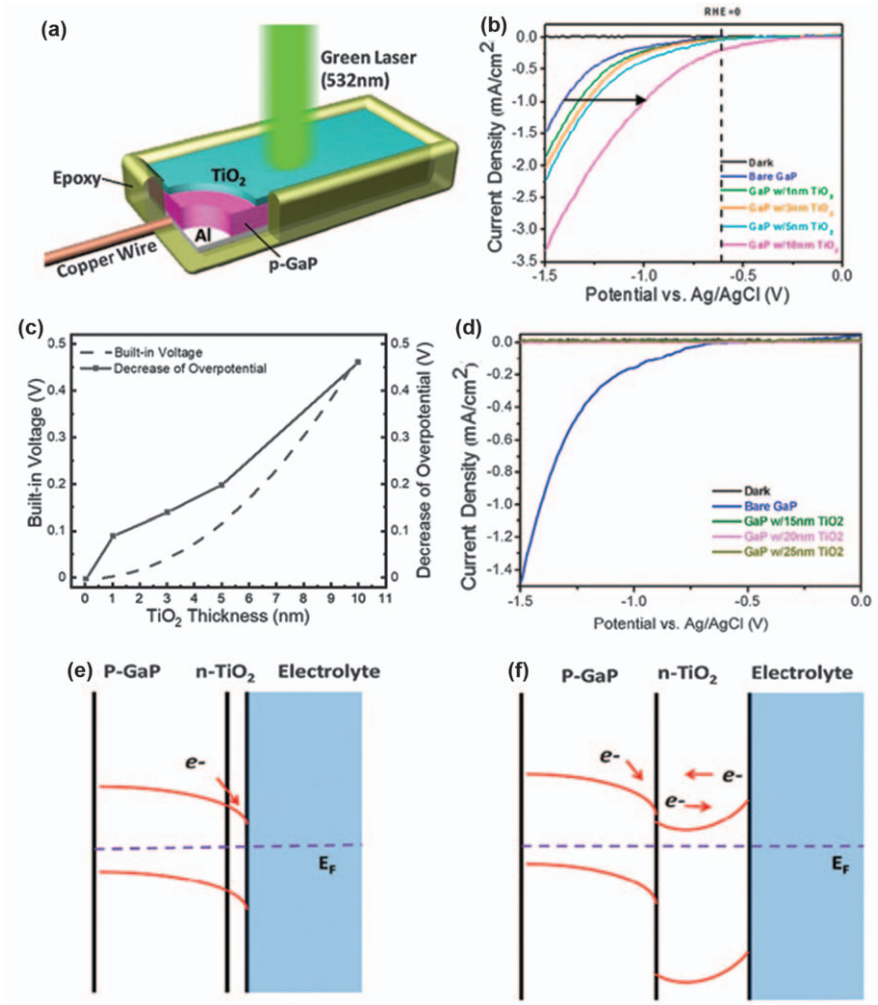


**Figure 5.10** (a) Schematic diagram of an as-fabricated GaP/$TiO_2$ photocathode. (b) Photocurrent densities measured as a function of applied potential *vs.* an Ag/AgCl reference electrode for GaP with different thicknesses of a $TiO_2$ passivation layer under illumination with 1 W $cm^{-2}$ monochromatic light of wavelength 532 nm in 0.5 M $Na_2SO_4$ solution (pH 7). The dashed line indicates RHE = 0 V. (c) Measured relative shift of onset potentials (solid line) and calculated built-in electric field (dashed line) with respect to $TiO_2$ thickness. (d) *J–V* measurement of GaP samples with thicker $TiO_2$ passivation layers. Band diagrams of GaP photocathode with (e) thin and (f) thick $TiO_2$ layers.
Adapted from ref. 32 with permission from the Royal Society of Chemistry.

positive shift of the onset potential of $TiO_2$-passivated GaP with respect to bare GaP (solid line in Figure 5.10c). The band diagrams of the GaP/$TiO_2$/electrolyte with thin and thick $TiO_2$ layers are shown in Figure 5.10e,f. The

downward band bending of p-type GaP at the GaP/$TiO_2$ interface will facilitate photogenerated electron transfer towards the electrolyte, while the upward band bending of n-type $TiO_2$ at the $TiO_2$/electrolyte interface prevents the electron transfer from $TiO_2$ to water adsorbates. Therefore, it is surprising to observe that GaP/$TiO_2$ still functions as a photocathode with a 10 nm thick $TiO_2$ passivation layer. This is due to the complete depletion of the $TiO_2$ layer when the layer is relatively thin. However, when the $TiO_2$ thickness increased to 15 nm, the photocurrent density decreased dramatically to near zero at all measured applied potentials *vs.* an Ag/AgCl electrode, as shown in Figure 5.10d.

The effect of plasmonic Au nanoparticles on the photocatalytic performance of GaP/$TiO_2$ photocathodes was also studied (Figure 5.11).[32] Here, a 5 nm nominal thickness of Au was evaporated onto the as-fabricated photocathodes. An island-like morphology was formed with this deposition and the gaps between islands were about 2–3 nm in length. The electric fields

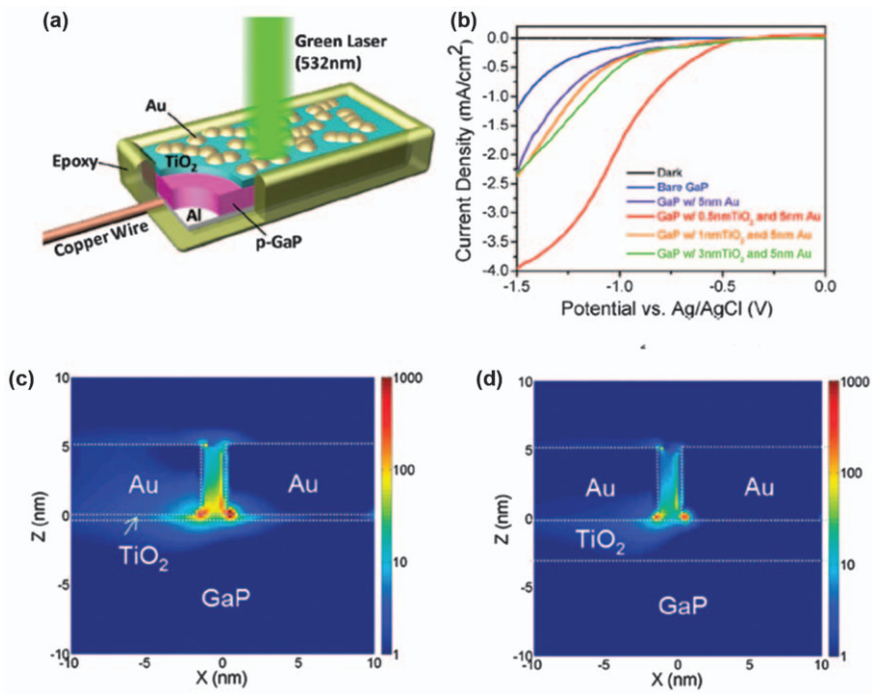


**Figure 5.11** (a) Schematic illustration of the GaP/$TiO_2$/Au photocathode geometry. (b) Photocurrent densities measured with respect to applied voltage *vs.* an Ag/AgCl reference electrode under illumination with 1 W $cm^{-2}$ monochromatic light of wavelength 532 nm in 0.5 M $Na_2SO_4$ solution. Simulated electric field distributions in the cross-section of the photocathode/electrolyte interface for (c) a 0.5 nm and (d) a 3 nm $TiO_2$ passivation layer.
Reproduced from ref. 32 with permission from the Royal Society of Chemistry.

were highly concentrated at the edges of Au islands near these nanogaps, which was also validated by surface-enhanced Raman spectroscopy and photocatalytic measurements in other materials.[39–44] Figure 5.11b shows *J–V* measurements of GaP/$TiO_2$ photocathodes decorated with 5 nm Au nanoparticles under illumination with 1 W $cm^{-2}$ monochromatic light of wavelength 532 nm in 0.5 M $Na_2SO_4$ solution for the HER. The GaP/Au with $TiO_2$ encapsulation showed better performance than bare GaP, exhibiting a 0.2 V positive shift of the HER onset potential. Furthermore, Au evaporation made GaP/$TiO_2$ photocathodes perform even better, where samples with a 0.5 nm $TiO_2$ layer showed the highest photocurrent density at all measured potentials *vs.* Ag/AgCl, with a fourfold enhancement with respect to a bare GaP substrate at −0.7 V *vs.* Ag/AgCl. This behavior results from the trade-off between the localized concentrated electric fields due to the plasmonic effect and built-in p–n junction potential. Figure 5.11c shows the calculated electric field distribution for one Au nanogap at the photocathode/electrolyte interface with a 0.5 nm $TiO_2$ passivation layer using the finite difference time domain (FDTD) method. Here, a 1000-fold enhancement factor is observed for the electric field intensity near the nanogap with respect to that of the incident light. The enhancement of photocatalytic performance by the plasmonic effect is due to three reasons. First, the highly concentrated electric field promotes the generation of more electron–hole pairs near the photocathode/electrolyte interface and charge separation region. Second, the increased intensity of light at the heterojunction produces a higher open-circuit voltage, leading to a more positive shift of the onset potential for the HER. Third, hot electrons generated from plasmon resonance decay from Au nanoparticles may participate directly in the HER.[33,34,45–47] Hence the photocatalytic performance of GaP is greatly enhanced by $TiO_2$ encapsulation combined with plasmonic Au nanoparticles.

The application of p-type GaP in photocatalytic $CO_2$ reduction was demonstrated by Zeng *et al.*[4] Figure 5.12a shows *J–V* measurements for GaP with various thicknesses of a $TiO_2$ layer (up to 10 nm) in $CO_2$-saturated aqueous solution consisting of 0.5 M NaCl and 10 mM pyridine under 532 nm light irradiation. The addition of pyridine increases the selectivity for $CO_2$ to be reduced to methanol through a series of steps involving one-electron transfer at low overpotentials.[48,49] A bare p-type GaP photocathode shows an onset potential of −0.15 V *vs.* NHE. For GaP samples passivated with a $TiO_2$ layer, a clear positive shift of the onset potential was observed that increased with increase in the $TiO_2$ layer thickness (Figure 5.12b). For GaP with a 10 nm $TiO_2$ layer, the onset potential shifted by 0.52 V compared with that of bare GaP. This positive shift is attributed, first, to the built-in potential between p-type GaP and n-type $TiO_2$. Under the assumption of complete depletion of thin $TiO_2$ layers, the built-in potential also increases as the thickness of the $TiO_2$ layer increases. We can calculate this potential based on eqn (5.5) as discussed earlier. Figure 5.12c shows the calculated built-in voltage as a function of $TiO_2$ thickness, and reveals a similar trend to the experimentally measured overpotential decrease in Figure 5.12b. In addition, the large valence band

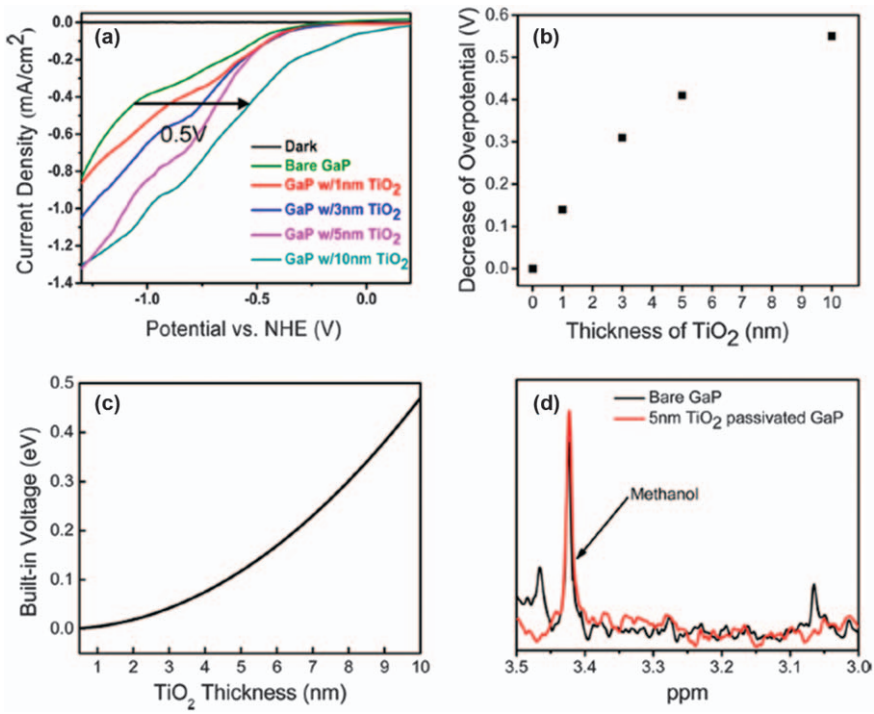


**Figure 5.12** (a) Photocurrent densities measured as a function of applied potential *vs.* NHE for GaP photocathodes with different thicknesses of a $TiO_2$ layer in $CO_2$-saturated aqueous solution consisting of 0.5 M NaCl and 10 mM pyridine under 532 nm illumination. (b) Decrease in overpotential plotted against $TiO_2$ thickness. (c) Built-in voltage of GaP/$TiO_2$ p–n junction calculated as a function of $TiO_2$ thickness. (d) NMR spectra for bare GaP and GaP with a 5 nm $TiO_2$ layer at an applied potential of −0.5 V *vs.* NHE.
Reproduced from ref. 4 with permission from American Chemical Society, Copyright 2014.

offset between $TiO_2$ and GaP makes the interface act like a hole-blocking layer, leading to decreased recombination rates. However, when the $TiO_2$ thickness is >10 nm, no enhancement in photocurrent is observed. This is due to band bending between n-type $TiO_2$ and the electrolyte that will block electrons from entering the electrolyte and participate in reduction reactions. In addition, $TiO_2$ will change from a conducting amorphous structure to an insulating crystalline structure when it is thicker than 10 nm. Furthermore, when the $TiO_2$ layer is thin and less than 10 nm, photogenerated electrons inside GaP can travel ballistically without equilibrating to the conduction band edge of $TiO_2$.[4] However, as the $TiO_2$ layer becomes thicker and reaches >10 nm, the electrons will travel diffusively and need a higher overpotential to participate in the reaction because the conduction band of GaP has a higher conduction band energy than that of $TiO_2$.

Figure 5.12d shows the NMR spectra of the electrolyte after operating GaP photocathodes with and without $TiO_2$ for 8 h under an applied potential of $-0.5$ V *vs.* NHE under illumination for 8 h with 532 nm monochromatic light. Here, the measured data clearly show the methanol peak for both samples. However, the bare GaP photocathode shows severe photocorrosion on the surface whereas the $TiO_2$-encapsulated GaP is still stable after the measurement. The FE for GaP with a 5 nm $TiO_2$ layer is about 55%. In order to eliminate the possibility of other carbon sources in the solution, isotopically labeled $^{13}CO_2$ was used in the reaction and the $^{13}CH_3OH$ peak was observed in the NMR spectra. In addition, when Ar was bubbled through the solution instead of $CO_2$, no methanol was detected in the NMR characterization. Hence $CO_2$ is indeed the carbon source for this reduction reaction. When pyridine was not added to the solution, the methanol peak could still be detected, but the yield decreased by two-thirds. This is because pyridine catalysts help lower the energy barrier of $CO_2$ reduction through inner-sphere type electron transfer.[50] In conclusion, $TiO_2$ passivation not only stabilized the GaP surface, but also enhanced its photocatalytic performance, and adding pyridine further increased the selectivity for methanol production.

### 5.3.3 GaAs

GaAs is a direct band gap semiconductor with a band gap energy of 1.42 eV, which makes it a good light absorber under solar illumination. However, the surface recombination velocity of GaAs is about $10^6$ cm s$^{-1}$, which is higher than those of most other III–V compound semiconductors by 1–2 orders of magnitude, thereby lowering its efficiency in photocatalytic applications.[51,52] The surface of GaAs also lacks stability and changes color during the photocatalysis. By depositing a thin layer of $TiO_2$ on the surface, the dangling bonds will be passivated, leading to decreased surface recombination rates. The stability issue is also minimized by $TiO_2$ passivation.[8,13]

Figure 5.13a shows a schematic illustration of a p-type GaAs photocathode encapsulated by $TiO_2$ fabricated by Qiu *et al.*[13] A Ti–Au film was evaporated onto the back side of the GaAs to form an ohmic contact. $TiO_2$ was deposited by ALD at 250 °C with $TiCl_4$ as the titanium source and water as oxygen source. Figure 13b shows a cross-sectional HRTEM image of GaAs with a 3 nm $TiO_2$ layer. Here, $TiO_2$ forms an amorphous structure instead of a crystalline anatase structure. As discussed earlier, amorphous $TiO_2$ has a better conducting ability than crystalline films, thus showing better photocatalytic ability. Pt was deposited here only for the purpose of TEM imaging and was not used in the photoelectrochemical measurement. The photocurrent densities were measured with respect to the applied potential *vs.* RHE in 0.5 M $H_2SO_4$ aqueous solution (pH 0) under AM1.5 illumination to drive the hydrogen evolution half-reaction (Figure 5.13c). Here, the onset potential of bare GaAs is about $-0.05$ V *vs.* RHE. Upon $TiO_2$ passivation, there is a clear positive shift in onset potential for GaAs photocathodes with a passivation layer up to 5 nm thick. Among them, GaAs with a 1 nm $TiO_2$

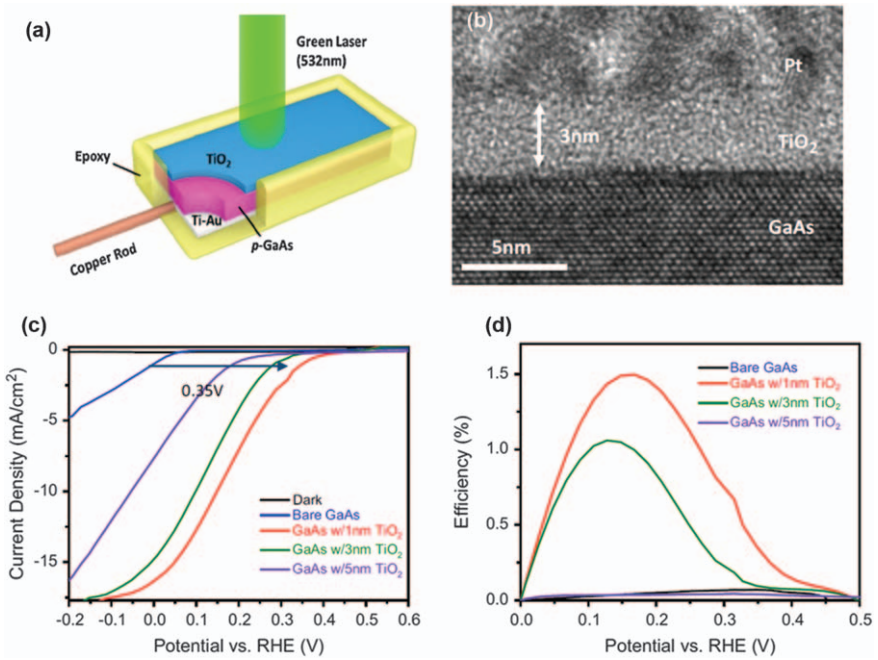


**Figure 5.13** (a) Schematic illustration of a $TiO_2$-passivated p-type GaAs photocathode. (b) HRTEM image of GaAs with a 3 nm $TiO_2$ layer. (c) *J–V* measurements and (d) calculated ABPE based on eqn (5.2) for GaAs photocathodes with different thicknesses of the $TiO_2$ layer in 0.5 M $H_2SO_4$ aqueous solution under AM1.5 illumination.
Reproduced from ref. 13 with permission from Elsevier, Copyright 2016.

layer shows the largest shift of 0.35 V at 1 mA $cm^{-2}$ compared with bare GaAs, which is indicated in the *J–V* plot. At an applied potential of 0 V *vs.* RHE, the photocurrent density of GaAs with a 1 nm $TiO_2$ layer increases by a factor of 32 with respect to that of bare GaAs.

Figure 5.13d shows the estimated ABPE for GaAs encapsulated with various thicknesses of $TiO_2$ together with a bare GaAs photocathode. GaAs with a 1 nm $TiO_2$ layer shows the highest efficiency of 1.5% when the applied potential is 0.2 V *vs.* RHE. It should be noted that no co-catalyst was added in the study. The purpose of the study was to analyze the effect of $TiO_2$ rather than to achieve the best performance. The reason why 1 nm $TiO_2$-encapsulated GaAs shows the highest onset potential and hydrogen conversion efficiency is that it has the highest concentration of defect states. As discussed earlier, the XPS spectra (Figure 5.4a) show the highest area ratio of $Ti^{3+}$ to Ti $2p_{1/2}$ for a 1 nm $TiO_2$ layer. In addition, the area ratio between Ob and Oa is also highest for a 1 nm $TiO_2$ film (Figure 5.4b), and Ob is associated with oxygen vacancies. As the $TiO_2$ thickness is increased to more than 10 nm, the photocatalytic ability of the GaAs/$TiO_2$ photocathode is dramatically

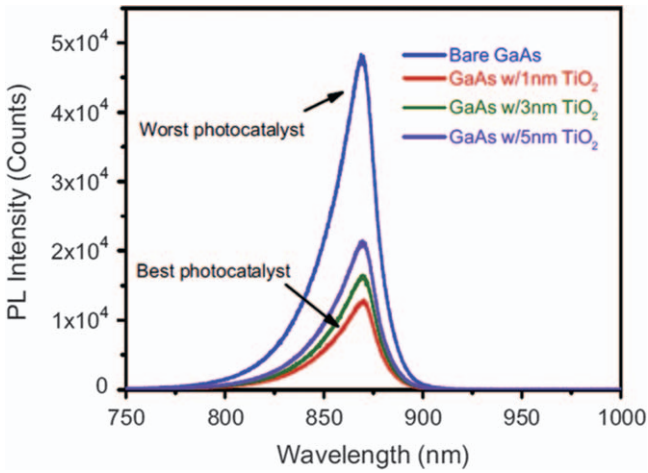


**Figure 5.14** PL spectra of p-type GaAs photocatalysts with different thicknesses of $TiO_2$ encapsulation layer under 532 nm irradiation. Reproduced from ref. 13 with permission from Elsevier, Copyright 2016.

suppressed. This is due to the transfer from a thin amorphous conducting phase to a thick crystalline insulating phase (Figure 5.2). Qiu *et al.* also studied $CO_2$ reduction using GaAs/$TiO_2$ and found a similar trend.[8]

Photoluminescence (PL) spectroscopy has been used to explore further the role of $TiO_2$ encapsulation in electron–hole recombination process within GaAs photocathodes. Figure 5.14 shows the PL spectra for different thicknesses of $TiO_2$ layers on GaAs surfaces.[13] Here, samples with the lowest PL efficiency showed the highest photocatalytic performance, and *vice versa*. GaAs with a 1 nm $TiO_2$ layer has a fivefold lower PL intensity compared with bare GaAs but demonstrates the best photocatalytic performance in the HER in 0.5 M $H_2SO_4$ solution. This finding was initially surprising because materials with strong PL intensity typically tend to show high performance in solar cells and photocatalytic applications. However, the $Ti^{3+}$ surface states described above can also cause additional electron–hole recombination, thus lowering the PL intensity and shortening photoexcited carrier lifetimes. However, the benefits of surface states in lowering the reaction potential barrier and promoting electrochemical charge transfer at the $TiO_2$/electrolyte interface outweigh their roles as non-radiative recombination centers.

## 5.4 pH and Electrode Potential Stability Range

### 5.4.1 Pourbaix Diagram of Titanium

In order to further study the stability of $TiO_2$ under various applied potentials and pH values, a Pourbaix diagram of titanium is worth considering. Marcel Pourbaix first proposed using an electrode potential–pH equilibrium diagram

to summarize the corrosion conditions of a given metal, where the *y*-axis is the applied potential, typically plotted with respect the standard hydrogen electrode (SHE), and the *x*-axis is the pH value of the aqueous environment.[53] Pourbaix diagrams are constructed using thermodynamic principles under the assumption that the metal reaches an equilibrium with its environment.[54] Figure 5.15 shows the Pourbaix diagram of the Ti–$H_2O$ system, in which each region in the diagram indicates the most thermodynamically stable titanium chemical compound. If the most stable chemical compound in the region is the metal itself, it is labeled *immunity*. If the dissolved ion is the most stable species, then it is labeled *corrosion*. If the metal oxide is the most stable in that region, the label *passivation* is used in Figure 5.15.

There are three different kinds of boundary lines between each region within the Pourbaix diagram. The horizontal lines indicate the reactions involved that depend only on the applied potential and not on the pH value. For example, the boundary line between the Ti and $Ti^{2+}$ region is horizontal, and the reaction involved is the following:

$$Ti^{2+} + 2e^- \rightarrow Ti \tag{5.6}$$

This an electrochemical reaction and does not involve protons or hydroxide ions. The reduction potential *E vs.* SHE can be calculated using the Nernst equation:

$$E = E^0 - (2.303RT/nF)\log(1/[Ti^{2+}]) \tag{5.7}$$

where $E^\circ$ is the standard reduction potential of the $Ti^{2+}$/Ti reaction, $R$ is the ideal gas constant, $T$ is the absolute temperature, $n$ is the number of electrons transferred in the reaction equation, $F$ is the Faraday constant and

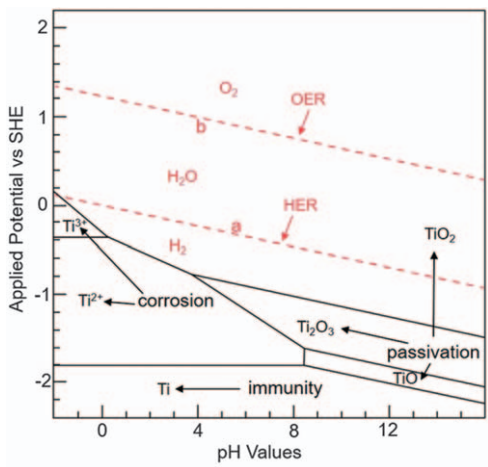


**Figure 5.15** Pourbaix diagram for titanium at 25 °C.

$[Ti^{2+}]$ is the concentration of $Ti^{2+}$. Based on $E^\circ = -1.63$ V *vs.* SHE and $n = 2$, eqn (5.7) can be rewritten as

$$E = -1.63 + 0.0296 \log [Ti^{2+}] \tag{5.8}$$

As eqn (5.8) shows, the reduction potential is a function of $Ti^{2+}$ concentration. Conventionally, a minimum concentration of $Ti^{2+}$ of $1.0\times10^{-6}$ M provides the condition for Ti to be corroded in the Pourbaix diagram construction. Putting this into eqn (5.7) gives a reduction potential of $E = -1.81$ V *vs.* SHE for the $Ti^{2+}$–Ti reaction, as shown in Figure 5.15. When the applied potential is more negative than $-1.81$ V, the concentration of $Ti^{2+}$ is lower than $1.0\times10^{-6}$ M, and the most stable species is then Ti metal. We say that Ti is *immune* under this condition, as labeled in Figure 5.15. In contrast, when the applied potential is more positive than $-1.81$ V *vs.* SHE, the $Ti^{2+}$ concentration is higher than $1.0\times10^{-6}$ M, and Ti therefore undergoes corrosion and $Ti^{2+}$ becomes the most stable species.

The second type of boundary lines in the Pourbaix diagram is vertical. These only involve changes in pH values and chemical reactions that do not require electron transfer. Consequently, the applied potential does not affect the reaction in this category. For example, the $Ti^{2+}$–TiO reaction proceeds as follows:

$$Ti^{2+} + H_2O \rightarrow TiO + 2H^+ \tag{5.9}$$

Based on the standard Gibbs free energy change:

$$\Delta G^\circ = -2.303RT \log K \tag{5.10}$$

where $\Delta G^\circ$ is the standard Gibbs free energy change and $K$ is the equilibrium constant, for eqn (5.9) $\Delta G^\circ = 14\,870$ cal mol$^{-1}$ and

$$K = \frac{[H^+]^2}{[Ti^{2+}]} \tag{5.11}$$

Combining eqn (5.10) and (5.11) yields

$$14870 \text{ cal mol}^{-1} = -2.303(1.98 \text{ cal mol}^{-1} \text{ K}^1)(298 \text{ K}) \log([H^+]^2/[Ti^{2+}]) \tag{5.12}$$

which can be reduced to

$$\log[Ti^{2+}] = 10.94 - 2\text{pH} \tag{5.13}$$

If we use a $Ti^{2+}$ concentration of $1.0\times10^{-6}$ M as the minimum value, the calculated pH value will be 8.47. Therefore, when the pH value is higher than 8.47, the $Ti^{2+}$ concentration is lower than $1.0\times10^{-6}$ M, causing TiO to be the most stable species. This region is called *passivation* since the metal oxide has the highest stability. On the other hand, when the pH value drops below

8.47, the concentration of $Ti^{2+}$ is higher than $1.0\times10^{-6}$ M, causing corrosion on the metal surface, as shown in Figure 5.15.

The third kind of reactions not only depend on the applied potential but are also affected by the pH value. The associated boundary lines are shown to be slanted in the Pourbaix diagram. For the $Ti^{2+}$–$TiO_2$ reaction:

$$Ti^{2+} + 2H_2O \rightarrow TiO_2 + 4H^+ + 2e^- \tag{5.14}$$

the Nernst equation gives

$$E = E^0 - (2.303RT/nF)\log([H^+]^4/[Ti^{2+}]) \tag{5.15}$$

For anhydrous $TiO_2$, eqn (5.15) can be reduced to

$$E = -0.502 - 0.1184\text{pH} - 0.0296\ \log[Ti^{2+}] \tag{5.16}$$

Using the concentration of $1.0\times10^{-6}$ M as the minimum value, we can draw this potential–pH line associated with the $Ti^{2+}$–$TiO_2$ reaction in the Pourbaix diagram, and the stability regions can also be labeled based on the same discussion as used previously. All the stability regions can be drawn using this method. One convenient aspect of the Pourbaix diagrams is that the two independent parameters (applied potential and pH value) are chosen such that the boundary lines between different stable regions are always linear. That is to say, a given pH value is chosen to linearize the equilibrium relations with applied potential. Therefore, in the Pourbaix diagram, the 2D potential–pH plane is divided into various regions of stability by straight lines.

The dashed line labeled ''a'' in Figure 5.15 is associated with the HER. As we know, in acidic solution, the HER is

$$2H^+ + 2e^- \rightarrow H_2 \tag{5.17}$$

The Nernst equation for this reaction at 25 °C and 1 atm of $H_2$ is

$$E = 0 - (2.303RT/nF)\log(1/[H^+]^2\| - 0.0591\text{pH} \tag{5.18}$$

In basic solution, the HER is

$$2H_2O + 2e^- \rightarrow H_2 + 2OH^- \tag{5.19}$$

and the Nernst equation is

$$E = -0.83 - \frac{2.303RT}{nF}\log[OH^-]^2 = -0.0591\text{pH} \tag{5.20}$$

Whereas the HER originates from different reactions in acidic and basic solutions, the Nernst equation has the same final expression and depends only on the pH of the solution. The dashed line ''a'' in Figure 5.15 is drawn

based on this equation. At a certain pH value, when the applied potential is below $-0.0591\text{pH}$, the HER is driven and $H_2$ is the most stable chemical compound. When the applied potential is above this value, the water molecule or proton is the most stable species.

The line labeled ''b'' in Figure 5.15 corresponds to the oxygen evolution reaction (OER):

$$2H_2O \rightarrow O_2 + 4H^+ + 4e^- \tag{5.21}$$

The associated Nernst equation at 25 °C and 1 atm of $O_2$ is

$$E = 1.23 - 0.0591\text{pH} \tag{5.22}$$

Above this potential at a given pH value, the OER is driven forwards and $O_2$ is the most stable species. Below this potential, the water molecule is stable. Therefore, when the applied potential is between the ''a'' and ''b'' lines, water is stable. In addition, the HER is driven below the ''a'' line and the OER is driven above the ''b'' line.

Based on the Pourbaix diagram of the Ti–$H_2O$ system plotted in Figure 5.15, we note that titanium is expected to be passivated by its oxides when driving the HER over a wide range of pH values and at moderate HER overpotentials. It is for this reason that $TiO_2$ passivation on III–V semiconductors is indeed a good strategy for preventing photocorrosion in the HER. For $CO_2$ reduction reactions, it is much more complicated because the $CO_2$ molecules can be reduced to many different products in the same electrochemical or photoelectrochemical experiment, such as methanol, carbon monoxide, methane, and formic acid.[55] When driving the reduction reaction associated with each product, titanium may be in the *corrosion* region based on the Pourbaix diagram and not able to protect the underlying photocathode. Even if we can draw the lines associated with different $CO_2$ reduction reactions on the Pourbaix diagram, under certain applied potentials and pH values, when titanium is in the *immunity* or *passivation* region, activation energy barriers may be too high such that the reaction rate for producing this product is low. This leads to the production of less thermodynamically stable products with low activation energy barriers. Improving the selectivity of $CO_2$ reduction catalysts is an active area of research.

### 5.4.2 Limits of Pourbaix Diagrams

Several aspects must be considered when using Pourbaix diagrams to predict the most stable chemical compounds for a metal in an aqueous environment. The chemical behavior of the metal or metal oxide in the electrolyte mostly depends on the composition of the layer that is in immediate contact with the electrolytic medium. This topmost or surface layer may be amorphous rather than crystalline and tends to be hydrated. As discussed previously, Qiu *et al.* showed that a 1 nm $TiO_2$-passivated p-type GaAs photocathode exhibits the most positive shift of onset potential, and a 1 nm $TiO_2$ layer shows an amorphous structure under TEM imaging.[8] Although both amorphous and

crystalline $TiO_2$ can provide protection, the amorphous form is more conducting, thus exhibiting a higher photocurrent density at the same applied potential. In addition, the chemical behavior also depends on the composition of the solution layer near the interfaces. When considering ion migration and diffusion at the interface between the solution and metallic phases, the composition of the solution phase near the interface may differ dramatically from the initial or mean composition of the electrolyte. For this reason, certain corrections must be made when using Pourbaix diagrams, such as for the deviation of the real solid or liquid phase from the ideal form.[54]

Since the Pourbaix diagrams are constructed based on thermodynamic principles, no information about the reaction rates is provided. For a certain metal, it may be in the *passivation* region under some applied potential and pH value through forming a surface oxide or hydroxide layer, and the rate of formation of the passivation layer may be very slow such that pure metallic phase is still exposed to the electrolyte, leading to more corrosion. On the other hand, even if the passivation layer forms rapidly, it may not be sufficient to reduce the rate of the corrosion reaction between the underlying metal and the electrolyte below the tolerable limit. Therefore, the corrosion may still proceed by ion diffusion through the passivation layer, which is also ignored in the Pourbaix diagram. To study the reaction mechanism and associated intermediates, surface Pourbaix diagrams are indispensable. Li *et al.* investigated the proton–electron interplay at the interface between rutile $TiO_2$ and electrolyte to construct surface Pourbaix diagrams for the water oxidation reaction.[56] In their study, different surface Pourbaix diagrams were simulated using different values of the Helmholtz layer capacitance and $TiO_2$ doping level.

## 5.5 Outlook

Although the chemical stability and PEC performance of III–V compound semiconductors are greatly improved by $TiO_2$ encapsulation, several other strategies are currently under exploration for further enhancement. One of these is to nanostructure the $TiO_2$ layer to provide various waveguide modes for incident light coupling.[57–59] Since efficient photoelectrodes require catalysts to decrease the overpotentials of target reactions, those catalysts make the light-facing surface more opaque, thus reducing the amount of light absorbed by underlying photoelectrodes. Yalamanchili *et al.* demonstrated high broadband light transmission on $TiO_2$ nanocones decorated on a $p^+$–n Si photoanode with Ni as the catalyst for the OER.[59] Based on their FDTD simulation, these nanocones serve both as a protection and an anti-reflection layer that allows >85% transmission of broadband light although they only cover less than 50% of the total Si surface with a 50 nm thick Ni layer covering the remainder of the surface. The fabricated photoanode shows saturation at a photocurrent density of 28 $mA\,cm^{-2}$ under 100 $mW\,cm^{-2}$ AM1.5 solar illumination in 1.0 M KOH aqueous solution for the OER.

It is difficult for a single III–V compound semiconductor to generate enough photovoltage to overcome overpotential losses and split water autonomously (*i.e.* without an externally applied voltage). However, semiconductors can be combined to form a multijunction tandem cell for unassisted water splitting.[60–63] Khaselev and Turner demonstrated unassisted water splitting based on a monolithic PEC–photovoltaic device with a solar-to-hydrogen conversion (STH) efficiency of 12.4% under 11 sun illumination in 3 M $H_2SO_4$ solution.[60] In their device, p-$GaInP_2$ serves as the top cell for the HER, which is connected to a p–n GaAs bottom cell through a tunneling diode interconnect, and a Pt counter electrode is wired to the bottom cell to drive the OER. However, this device suffered localized damage without a surface protection layer. Later, Verlage *et al.* showed stable unassisted water splitting performances for over 40 h of operation with an STH efficiency of >10% on a monolithically $TiO_2$-protected device under AM1.5 solar illumination in 1 M KOH solution. The as-fabricated device consists of GaAs/$InGaP_2$/$TiO_2$/Ni as the photoanode to drive the OER, which is connected to an Ni–Mo-coated counter electrode for the HER.[61] They also showcased a fully integrated wireless device based on an NiMo/GaAs/$InGaP_2$/$TiO_2$/Ni structure conducting the HER and OER on each side. This membrane-based prototype showed an STH efficiency of 8.6% under AM1.5 solar illumination in 1 M KOH solution with separate collection of $H_2$ and $O_2$ streams.

In addition to $TiO_2$, other metal oxide protection layers are also being studied for III–V compound semiconductors in PEC applications. Sun *et al.* showed that sputtered $NiO_x$ film can also be used to protect $p^+$–n InP photoanodes in the OER under AM1.5 illumination in 1.0 M KOH aqueous solution.[64] In addition to protection, the as-sputtered conductive $NiO_x$ film also serves as the catalyst and anti-reflective layer. Based on the Pourbaix diagram, tantalum is also very resistant to corrosion and has larger regions of passivation and immunity than titanium.[53,54] The passivation of $Ta_2O_5$ on III–V semiconductors for photoelectrochemical applications is also an active topic of research that holds much promise for future photocatalytic systems.

In conclusion, this chapter has discussed the benefits of n-type $TiO_2$ passivation on p-type III–V semiconductors for photocatalytic applications, including chemical stability, large valence band offset, built-in potential, and surface defect states. The effects of nanotexturing, co-catalysts, and plasmonic nanoparticles on the photocatalytic performance for those III–V semiconductors were also discussed. Three types of factors, thermodynamic principles, kinetics, and phase equilibria structures, must all be considered when evaluating the electrochemical stability of $TiO_2$-passivated photocathodes. When combined with kinetic and structural analysis, the Pourbaix diagrams provide a powerful tool in understanding the corrosion conditions for metals in practical experiments and energy conversion applications. Future research efforts will probably be focused on nanostructuring protective oxide layer films, combining different III–V semiconductors for unassisted water splitting, and exploring other metal oxide protection layers in PEC applications.

## Acknowledgements

This research was supported by the Air Force Office of Scientific Research (AFOSR) grant No. FA9550-19-1-0115 (Y.W.) and the Department of Energy (DOE) award No. DE-SC0019322 (S.B.C.).

## References

1. A. Fujishima and K. Honda, *Nature*, 1972, **238**, 37–38.
2. W. Shockley and H. J. Queisser, *J. Appl. Phys.*, 1961, **32**, 510–519.
3. C. Liu, N. P. Dasgupta and P. Yang, *Chem. Mater.*, 2014, **26**, 415–422.
4. G. Zeng, J. Qiu, Z. Li, P. Pavaskar and S. B. Cronin, *ACS Catal.*, 2014, **4**, 3512–3516.
5. Y. W. Chen, J. D. Prange, S. Dühnen, Y. Park, M. Gunji, C. E. D. Chidsey and P. C. McIntyre, *Nat. Mater.*, 2011, **10**, 539–544.
6. M. H. Lee, K. Takei, J. Zhang, R. Kapadia, M. Zheng, Y.-Z. Chen, J. Nah, T. S. Matthews, Y.-L. Chueh, J. W. Ager and A. Javey, *Angew. Chem., Int. Ed.*, 2012, **51**, 10760–10764.
7. J. Qiu, G. Zeng, M.-A. Ha, M. Ge, Y. Lin, M. Hettick, B. Hou, A. N. Alexandrova, A. Javey and S. B. Cronin, *Nano Lett.*, 2015, **15**, 6177–6181.
8. J. Qiu, G. Zeng, M.-A. Ha, B. Hou, M. Mecklenburg, H. Shi, A. N. Alexandrova and S. B. Cronin, *Chem. Mater.*, 2015, **27**, 7977–7981.
9. G. Zeng, J. Qiu, B. Hou, H. Shi, Y. Lin, M. Hettick, A. Javey and S. B. Cronin, *Chem. – Eur. J.*, 2015, **21**, 13502–13507.
10. Y. Lin, R. Kapadia, J. Yang, M. Zheng, K. Chen, M. Hettick, X. Yin, C. Battaglia, I. D. Sharp, J. W. Ager and A. Javey, *J. Phys. Chem. C*, 2015, **119**, 2308–2313.
11. R. W. Johnson, A. Hultqvist and S. F. Bent, *Mater. Today*, 2014, **17**, 236–246.
12. J.-P. Niemelä, G. Marin and M. Karppinen, *Semicond. Sci. Technol.*, 2017, **32**, 093005.
13. J. Qiu, G. Zeng, M. Ge, S. Arab, M. Mecklenburg, B. Hou, C. Shen, A. V. Benderskii and S. B. Cronin, *J. Catal.*, 2016, **337**, 133–137.
14. A. G. Scheuermann, J. D. Prange, M. Gunji, C. E. D. Chidsey and P. C. McIntyre, *Energy Environ. Sci.*, 2013, **6**, 2487–2496.
15. M. Hettick, M. Zheng, Y. Lin, C. M. Sutter-Fella, J. W. Ager and A. Javey, *J. Phys. Chem. Lett.*, 2015, **6**, 2177–2182.
16. S. Hu, M. R. Shaner, J. A. Beardslee, M. Lichterman, B. S. Brunschwig and N. S. Lewis, *Science*, 2014, **344**, 1005–1009.
17. C. Rath, P. Mohanty, A. C. Pandey and N. C. Mishra, *J. Phys. D: Appl. Phys.*, 2009, **42**, 205101.
18. C. A. Hoffman, K. Jarašiūnas, H. J. Gerritsen and A. V. Nurmikko, *Appl. Phys. Lett.*, 1978, **33**, 536–539.
19. K. T. Fountaine, W.-H. Cheng, C. R. Bukowsky and H. A. Atwater, *ACS Photonics*, 2016, **3**, 1826–1832.

20. E. Aharon-Salom and A. Heller, *J. Electrochem. Soc.*, 1982, **129**, 2865–2866.
21. K. Shankar, J. I. Basham, N. K. Allam, O. K. Varghese, G. K. Mor, X. Feng, M. Paulose, J. A. Seabold, K.-S. Choi and C. A. Grimes, *J. Phys. Chem. C*, 2009, **113**, 6327–6359.
22. X. Yin, C. Battaglia, Y. Lin, K. Chen, M. Hettick, M. Zheng, C.-Y. Chen, D. Kiriya and A. Javey, *ACS Photonics*, 2014, **1**, 1245–1250.
23. S. W. Boettcher, E. L. Warren, M. C. Putnam, E. A. Santori, D. Turner-Evans, M. D. Kelzenberg, M. G. Walter, J. R. McKone, B. S. Brunschwig, H. A. Atwater and N. S. Lewis, *J. Am. Chem. Soc.*, 2011, **133**, 1216–1219.
24. A. Heller and R. G. Vadimsky, *Phys. Rev. Lett.*, 1981, **46**, 1153–1156.
25. J. R. McKone, A. P. Pieterick, H. B. Gray and N. S. Lewis, *J. Am. Chem. Soc.*, 2013, **135**, 223–231.
26. K. Gelderman, L. Lee and S. W. Donne, *J. Chem. Educ.*, 2007, **84**, 685.
27. P. P. Sahoo, B. Zoellner and P. A. Maggard, *J. Mater. Chem. A*, 2015, **3**, 4501–4509.
28. B. J. Morgan and G. W. Watson, *J. Phys. Chem. C*, 2010, **114**, 2321–2328.
29. K. Chandrasekaran and L. O. M. Bockris, *Surf. Sci.*, 1987, **185**, 495–514.
30. J. O. M. Bockris and J. C. Wass, *Mater. Chem. Phys.*, 1989, **22**, 249–280.
31. L. W. Diamond and N. N. Akinfiev, *Fluid Phase Equilib.*, 2003, **208**, 265–290.
32. J. Qiu, G. Zeng, P. Pavaskar, Z. Li and S. B. Cronin, *Phys. Chem. Chem. Phys.*, 2014, **16**, 3115–3121.
33. Y. Wang, I. Aravind, Z. Cai, L. Shen, G. N. Gibson, J. Chen, B. Wang, H. Shi, B. Song, E. Guignon, N. C. Cady, W. D. Page, A. Pilar and S. B. Cronin, *ACS Appl. Mater. Interfaces*, 2020, **12**, 17459–17465.
34. Y. Wang, L. Shen, Y. Wang, B. Hou, G. N. Gibson, N. Poudel, J. Chen, H. Shi, E. Guignon, N. C. Cady, W. D. Page, A. Pilar, J. Dawlaty and S. B. Cronin, *Faraday Discuss.*, 2019, **214**, 325–339.
35. M. L. Brongersma, N. J. Halas and P. Nordlander, *Nat. Nanotechnol.*, 2015, **10**, 25–34.
36. P. Narang, R. Sundararaman and H. A. Atwater, *Nanophotonics*, 2016, **5**, 96–111.
37. S.-M. Lee, W. Li, P. Dhar, S. Malyk, Y. Wang, W. Lee, A. Benderskii and J. Yoon, *Adv. Energy Mater.*, 2015, **5**, 1500761.
38. J. Chen, C. S. Bailey, Y. Hong, L. Wang, Z. Cai, L. Shen, B. Hou, Y. Wang, H. Shi, J. Sambur, W. Ren, E. Pop and S. B. Cronin, *ACS Photonics*, 2019, **6**, 787–792.
39. H. Shi, Z. Cai, J. Patrow, B. Zhao, Y. Wang, Y. Wang, A. Benderskii, J. Dawlaty and S. B. Cronin, *ACS Appl. Mater. Interfaces*, 2018, **10**, 33678–33683.

40. H. Shi, R. T. Pekarek, R. Chen, B. Zhang, Y. Wang, I. Aravind, Z. Cai, L. Jensen, N. R. Neale and S. B. Cronin, *J. Phys. Chem. C*, 2020, **124**, 17000–17005.
41. W. Hou, Z. Liu, P. Pavaskar, W. H. Hung and S. B. Cronin, *J. Catal.*, 2011, **277**, 149–153.
42. Z. Liu, W. Hou, P. Pavaskar, M. Aykol and S. B. Cronin, *Nano Lett.*, 2011, **11**, 1111–1116.
43. Z. Liu, W. H. Hung, M. Aykol, D. Valley and S. B. Cronin, *Nanotechnology*, 2010, **21**, 105304.
44. R. P. Van Duyne, J. C. Hulteen and D. A. Treichel, *J. Chem. Phys.*, 1993, **99**, 2101–2115.
45. S. Mukherjee, F. Libisch, N. Large, O. Neumann, L. V. Brown, J. Cheng, J. B. Lassiter, E. A. Carter, P. Nordlander and N. J. Halas, *Nano Lett.*, 2013, **13**, 240–247.
46. G. Tagliabue, J. S. DuChene, M. Abdellah, A. Habib, D. J. Gosztola, Y. Hattori, W.-H. Cheng, K. Zheng, S. E. Canton, R. Sundararaman, J. Sá and H. A. Atwater, *Nat. Mater.*, 2020, **19**, 1312–1318.
47. I. Aravind, Y. Wang, Z. Cai, L. Shen, B. Zhao, S. Yang, Y. Wang, J. M. Dawlaty, G. N. Gibson, E. Guignon, N. C. Cady, W. D. Page, A. Pilar and S. B. Cronin, *Crystals*, 2021, **11**, 118.
48. D. J. Boston, C. Xu, D. W. Armstrong and F. M. MacDonnell, *J. Am. Chem. Soc.*, 2013, **135**, 16252–16255.
49. E. Barton Cole, P. S. Lakkaraju, D. M. Rampulla, A. J. Morris, E. Abelev and A. B. Bocarsly, *J. Am. Chem. Soc.*, 2010, **132**, 11539–11551.
50. Y. Yan, E. L. Zeitler, J. Gu, Y. Hu and A. B. Bocarsly, *J. Am. Chem. Soc.*, 2013, **135**, 14020–14023.
51. J. Lloyd-Hughes, S. K. E. Merchant, L. Fu, H. H. Tan, C. Jagadish, E. Castro-Camus and M. B. Johnston, *Appl. Phys. Lett.*, 2006, **89**, 232102.
52. C.-C. Chang, C.-Y. Chi, M. Yao, N. Huang, C.-C. Chen, J. Theiss, A. W. Bushmaker, S. LaLumondiere, T.-W. Yeh, M. L. Povinelli, C. Zhou, P. D. Dapkus and S. B. Cronin, *Nano Lett.*, 2012, **12**, 4484–4489.
53. M. Pourbaix, *Atlas of Electrochemical Equilibria in Aqueous Solutions*, National Association of Corrosion Engineers, Houston, Texas, 1974.
54. E. McCafferty, in *Introduction to Corrosion Science*, ed. E. McCafferty, Springer, New York, NY, 2010, pp. 95–117, DOI: 10.1007/978-1-4419-0455-3_6.
55. J.-Y. Liu, X.-Q. Gong, R. Li, H. Shi, S. B. Cronin and A. N. Alexandrova, *ACS Catal.*, 2020, **10**, 4048–4058.
56. J.-Q. Li, L. Meng, M. Sprik and J. Cheng, *J. Phys. Chem. C*, 2020, **124**, 19003–19014.
57. J. T. Choy, J. D. B. Bradley, P. B. Deotare, I. B. Burgess, C. C. Evans, E. Mazur and M. Lončar, *Opt. Lett.*, 2012, **37**, 539–541.
58. C. C. Evans, C. Liu and J. Suntivich, *Opt. Express*, 2015, **23**, 11160–11169.

59. S. Yalamanchili, E. Verlage, W.-H. Cheng, K. T. Fountaine, P. R. Jahelka, P. A. Kempler, R. Saive, N. S. Lewis and H. A. Atwater, *Nano Lett.*, 2020, **20**, 502–508.
60. O. Khaselev and J. A. Turner, *Science*, 1998, **280**, 425.
61. E. Verlage, S. Hu, R. Liu, R. J. R. Jones, K. Sun, C. Xiang, N. S. Lewis and H. A. Atwater, *Energy Environ. Sci.*, 2015, **8**, 3166–3172.
62. P. Varadhan, H.-C. Fu, Y.-C. Kao, R.-H. Horng and J.-H. He, *Nat. Commun.*, 2019, **10**, 5282.
63. J. L. Young, M. A. Steiner, H. Döscher, R. M. France, J. A. Turner and T. G. Deutsch, *Nat. Energy*, 2017, **2**, 17028.
64. K. Sun, Y. Kuang, E. Verlage, B. S. Brunschwig, C. W. Tu and N. S. Lewis, *Adv. Energy Mater.*, 2015, **5**, 1402276.

CHAPTER 6

# *Metal Oxide Co-catalyst Nanolayers on Photoelectrodes*

J. QIU,*[a] M. R. NELLIST[b] AND S. W. BOETTCHER[b]

[a] Department of Chemistry and Biochemistry, San Francisco State University, 1600 Holloway Avenue, San Francisco, CA 94132, USA; [b] Department of Chemistry and Biochemistry, University of Oregon, 1254 Franklin Boulevard, Eugene, OR 97403, USA
*Email: qiu@sfsu.edu

## 6.1 Introduction to Photoelectrochemical Water Oxidation

As abundant natural resources, water and sunlight are ideal candidates for fuel production. Water can be split into oxygen gas ($O_2$) and hydrogen gas ($H_2$), and sunlight is by far the largest readily available source of renewable energy. To store intermittent solar energy, photoelectrochemical (PEC) processes that mimic photosynthesis, the process satisfying the energy needs of many organisms on Earth, can be used to store the solar energy in chemical bonds.[1] Green plants capture sunlight and convert water ($H_2O$) and carbon dioxide ($CO_2$) into carbohydrates – a form of chemical energy stored that can be released later to fuel the organisms' activities. Hydrogen gas is an energy carrier and clean fuel. It can be burned in turbines to generate mechanical power or electricity, generating water as the only by-product, used in a fuel cell to generate electricity, combined with $CO_2$ or biomass to make liquid fuels in efficient thermochemical processes, or combined with $N_2$ to make fertilizer.[2] Currently, most hydrogen is produced by steam–methane reforming, although

Energy and Environment Series No. 30
Ultrathin Oxide Layers for Solar and Electrocatalytic Systems
Edited by Heinz Frei and Daniel V. Esposito

Published by the Royal Society of Chemistry, www.rsc.org

the use of renewable electricity to drive water electrolysis at scale is likely to be a viable cost competitor over the next decade.

An alternative approach is to produce hydrogen from water directly at a semiconductor surface using sunlight as the only energy source.[1] Semiconductor materials can absorb photons and convert them into excited electronic carriers (electrons and holes). These charge carriers with excess free energy can promote desired chemical and electrochemical reactions, provided that they are able to participate in the productive kinetic processes before recombination occurs. Honda and Fujishima first reported PEC water splitting with titanium dioxide ($TiO_2$) electrodes in 1972.[3] This work sparked studies of many different photoelectrode and photocatalyst materials for PEC water splitting, especially since the 1980s.[4]

To convert water into hydrogen at high performance driven only by sunlight, a semiconductor needs to satisfy a number of requirements. On the one hand, the ideal band gap of a semiconductor should be in the range 1–1.5 eV to permit the optical absorption of a large portion of the solar spectrum, as only photons with energy greater than the band gap can be absorbed. On the other hand, the energy separation between the valence and conduction bands in the semiconductor must be significantly larger than the water-splitting free energy of 1.23 eV, considering the significant overpotentials involved in water oxidation and reduction reactions, if a single band gap absorber is to be used.[5] Furthermore, to realize efficiently all the functions of charge separation, collection, and charge transfer across a semiconductor/electrolyte interface, excellent semiconductor properties are needed, including high mobility, low recombination rates, and good stability under PEC conditions.[6]

In a typical PEC water-splitting cell, $H_2$ is formed at the photocathode and water oxidation occurs at the photoanode, leading to the formation of oxygen gas. eqn (6.1) and (6.2) (where $h$ = hole) show the half-reactions in basic electrolyte. The relevant reactions can be found in acidic electrolyte by adding protons to each side of the balanced half-reactions.

$$\text{Cathode:} \quad 2H_2O + 2e^- \rightarrow H_2 + 2OH^- \tag{6.1}$$

$$\text{Anode:} \quad 4OH^- + 4h^+ \rightarrow O_2 + 2H_2O \tag{6.2}$$

The photocathodes are comprised of p-type semiconductors and the photoanodes n-type semiconductors. The semiconductor electrodes, as light absorbers, generate electrons and holes upon sunlight excitation. In a simple PEC water-splitting cell based on a photoanode, photogenerated holes flow towards the surface in the photoanode and oxidize water or hydroxide to form oxygen gas. Electrons flow to a metallic catalytic electrode, where they reduce protons or water to hydrogen gas. In tandem designs, the cathode can also be photoactive.[1] To increase the reaction kinetics on the semiconductor surface, ''co-catalyst'' or ''electro-catalyst'' layers are also usually added.[1,5] However, even with the co-catalysts, the oxygen evolution reaction (OER) on the anode is slow compared with the hydrogen evolution reaction (HER) on the cathode, which hinders the overall efficiency of PEC water splitting. Photoanodes are

also often influenced by undesired processes, such as corrosion of the semiconductor (due to the very positive working potential at the surface), electrical resistance in the electrode material or through surface interfacial layers, and deleterious surface states that increase recombination.[7] Each of these processes can in turn be affected by the presence of electrocatalyst layers. Despite the importance of the interfacial processes between semiconductor, electrocatalyst, and solution, these interfaces have recently been targeted for more detailed study with new methods and electroanalytical techniques. This chapter is focused specifically on the interface of photoanodes and metal oxide co-catalyst layers involved in PEC water oxidation processes.

## 6.2 Light Absorbers and Metal Oxide Co-catalyst Nanolayers

When the photoanode is coated with co-catalyst nanolayers, the relative energy band alignment of the semiconductor absorbers with the co-catalyst layers will strongly affect the resulting efficiency of the OER. Therefore, it is critical to understand the energetics of the interface between the photoanode and the solid-state co-catalyst layers under PEC conditions.

### 6.2.1 The Semiconductor Photoanode and Co-catalyst Interface

The model traditionally employed to represent an n-type semiconductor/electrolyte interface is based on Schottky barrier concepts (*i.e.* of a semiconductor–metal junction), where the Fermi level of the metal is replaced with the equilibrium potential of the solution ($E_{sol}$), multiplied by the elementary charge $q$.[6] In practice, $E_{sol}$ can be difficult to measure because of the slow electrochemical kinetics. When the semiconductor absorbs photons with energy greater than the band gap ($E_g$), electron–hole pairs are created. Since the concentration of holes in the dark is much smaller than the concentration of electrons for an n-type semiconductor, the hole is referred to as the minority charge carrier. In thebulk of the semiconductor where the electron concentration is much higher than the hole concentration, recombination is a fast pseudo-first-order process. On the surface of the n-type semiconductor, the equilibrium electron concentration at the surface is orders of magnitude lower than in the bulk of the semiconductor owing to surface band bending.[7] The majority of the holes created by illumination can oxidize water molecules or hydroxide into oxygen gas if the OER kinetics on the semiconductor surface are fast enough while the electrons move from the photoanode into the external circuit to the (photo)cathode.

When a metal oxide co-catalyst layer is deposited on the surface of a photoanode for PEC water oxidation, a common model to describe the semiconductor–catalyst–electrolyte system comprises a semiconductor that absorbs light and separates charge carriers in series with a catalyst layer that boosts the kinetics of the OER process. At the simplest level, one could assume that the addition of the catalyst does not affect the band bending or Schottky

barrier height in the semiconductor. However, this simple model fails to explain some experimental results, such as the changes in photovoltage and photocurrent, after deposition of OER catalysts on n-type semiconductor photoanodes.

Figure 6.1 shows a model of the catalyst-coated photoanode that explicitly accounts for charge transfer between the system components. The net current from the semiconductor to the catalyst ($J_{sem}$) is the sum of the positive hole current ($J_h$) from the valence band and the negative recombination current from electrons ($J_e$) in the conduction band. At low applied potentials with small band bending, the hole current is balanced by the electron current and there is no net current. At larger positive applied potentials, band bending increases and the recombination current decreases as the electron concentration at the conduction band edge is decreased. The catalyst is thus charged to a more positive potential where water oxidation becomes more favorable. The net catalytic current ($J_{cat}$) must match the net junction current ($J_{sem} = J_h + J_e$) at the steady state, assuming that no current flows directly from the semiconductor to the solution.

The addition of a co-catalyst layer, in addition to providing a lower barrier pathway for holes to flow into the solution and generate $O_2$, is also likely to affect the charge-carrier selectivity of the semiconductor surface, for example by changing the degree of band bending or introducing or passivating surface states. In fact, several studies have attributed the changes in photoelectrode characteristics after co-catalyst coating entirely to changes in surface

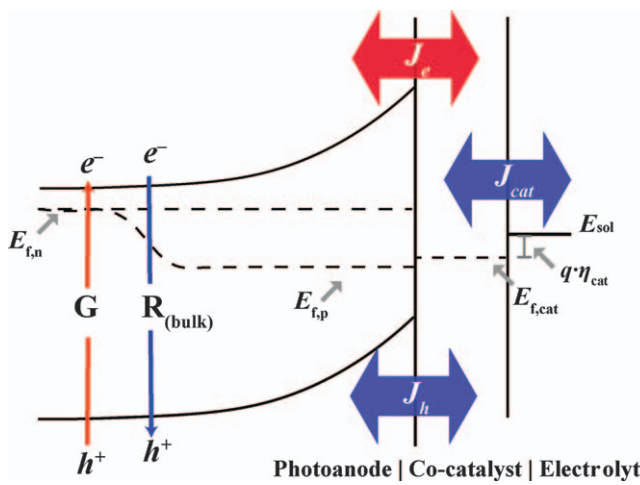


**Figure 6.1** Band diagram of a photoanode with a co-catalyst layer for PEC water oxidation. G represents the generation of electron–hole pairs and R(bulk) represents the bulk electron and hole recombination. $E_{f,n}$ is the quasi-Fermi level of the electrons, $E_{f,p}$ is the quasi-Fermi level of the holes, $E_{f,cat}$ is the Fermi level of the co-catalyst layer, $E_{sol}$ is the Fermi level of the electrolyte, $\eta_{cat}$ is the overpotential of the co-catalyst layer, and $q$ is the elementary charge.

recombination and/or band bending, interface charge trapping, and optical effects,[8,9] as opposed to catalytic effects that were first envisioned. Experimental work using a second working electrode in PEC measurements to study directly the role of these catalytic layers is discussed in Sections 6.3 and 6.4.

### 6.2.2 Common Light-absorbing Photoanodes and Their Optical and Electronic Properties

The primary function of the semiconductor in a PEC cell is to absorb light and produce mobile and long-lived electrons and holes. The band gaps of the common semiconductor photoanodes are in the range 1.5–3.2 eV to harvest solar energy. Thermodynamically, it is often stated that surface holes are at sufficient oxidizing potentials to drive the OER if the valence band (VB) edge of the semiconductor is lower than the thermodynamic potential of water oxidation, $\varepsilon_{H_2O/O_2}$, in the absence of Fermi level pinning. However, the energy levels at the photoanode surface can be affected by adsorbed ionic species, and the surface states by changing the potential of the Helmholtz layer. Surface states located in the band gap of the semiconductor can also affect the energetics of the holes on the surface of a photoanode.[11] Finally, it is worth emphasizing that the actual thermodynamic oxidizing power of the population of excited minority carriers – here holes – relates to the quasi-Fermi level, not the band edge position. For the next OER reaction to proceed in the forward direction under standard conditions, it is not sufficient only for the valence band edge to be more positive than $\varepsilon_{H_2O/O_2}$: $E_{f,p}/q$ must also be more positive than $\varepsilon_{H_2O/O_2}$.[12]

Since the demonstration of $TiO_2$ in PEC water splitting, hundreds of other oxide photoelectrodes that operate with ultraviolet (UV) and/or visible light have been studied.[10,13] The binary oxides titanium dioxide ($TiO_2$),[14,15] tungsten oxide ($WO_3$),[16,17] and iron oxide ($Fe_2O_3$)[11,18,19] have particularly been studied extensively. More recently, more complex compositions such as bismuth vanadate ($BiVO_4$),[20–22] copper tungstate ($CuWO_4$),[23,24] and tantalum oxynitride ($TaO_xN_y$)[25] have been studied. Given the large number of elements that can be combined into multicomponent semiconductors, many new and potentially high-performance compositions may remain to be discovered, for example by high-throughput experimental or computational screening,[26,27] although defects in such multicomponent oxides can be difficult to control.

Figure 6.2 shows the band-gap and nominal band-edge positions of the above-mentioned commonly studied semiconductors in PEC water splitting.[13,28] Although the valence band energies of the UV light-absorbing semiconductors $TiO_2$ and $WO_3$ are lower than those of $Fe_2O_3$ and $BiVO_4$, they face the issue of inefficient light absorption. Such low valence band energy levels of $TiO_2$ and $WO_3$ are strongly dictated by the O 2p levels with the empty metal d bands in $Ti^{4+}$ and $W^{6+}$ forming the conduction band.[29] To overcome the inefficient absorption of the $d^0$ oxides (*i.e.* $TiO_2$ and $WO_3$), binary oxides based on transition metal cations with $d^n$ electronic configurations and ternary metal oxides with combined cations can be engineered to achieve a

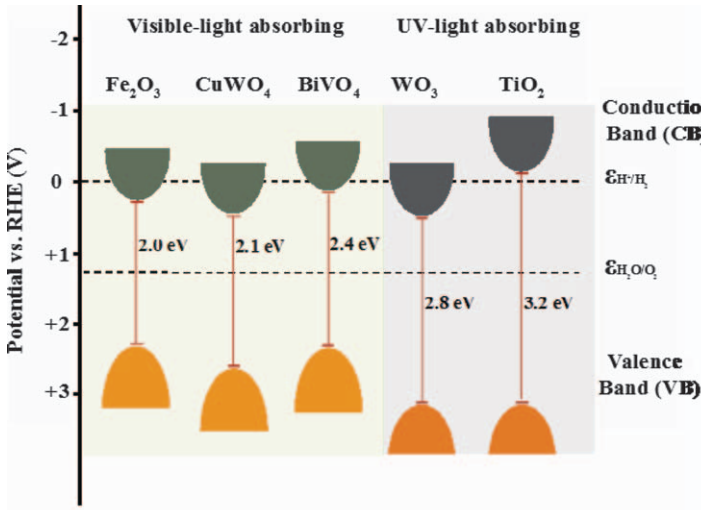


**Figure 6.2** Band gaps and valence and conduction bands for common oxide semiconductors for PEC applications. The water reduction potential ($\varepsilon_{H^+/H_2}$) and oxidation potential ($\varepsilon_{H_2O/O_2}$) are shown as dashed lines. Assuming the band-edge energies show Nernstian behaviors with respect to the electrolyte pH, the semiconductor band gap ($E_g$) is referenced to the reversible hydrogen electrode (RHE) and the water redox energy levels. Reproduced from ref. 28 with permission from American Chemical Society, Copyright 2012.

smaller band gap. For example, hematite ($\alpha$-$Fe_2O_3$) is stable and has a band gap of 2.1 eV. Monoclinic $BiVO_4$ is the highest performance ternary metal oxide photoanode studied to date and has a band gap of 2.4 eV.[20] The small band gap of $Fe_2O_3$ is strongly influenced by the d–d transitions in the metal. The smaller band gap of monoclinic $BiVO_4$ results from the coupling of bands.[30] The $d^0$ cation $V^{5+}$ mixes with the $s^2$ cation $Bi^{3+}$, leading to coupling between the Bi 6s and the O 2p electronic states, while coupling between the d band from the $V^{5+}$ cation and the p band from the $Bi^{3+}$ cation maintains a low conduction band edge.[30] The semiconductors $TiO_2$, $\alpha$-$Fe_2O_3$, and $BiVO_4$ in the form of thin-film photoanodes will be used as model systems in discussing the interfacial properties of the semiconductor and metal oxide co-catalyst layer in Sections 6.3 and 6.4.

Considerable effort has been focused on $Fe_2O_3$ given its high Earth abundance and potential low cost of manufacture, capability of absorbing visible light, and stability in basic electrolytes. However, carrier transport and photogenerated charge separation in $Fe_2O_3$ are problematic because of the low polaron mobility.[31] Solar water oxidation photocurrents up to $\sim$4 mA cm$^{-2}$ have been achieved for $Fe_2O_3$,[19,32] but this is considerably lower than the theoretical maximum photocurrent of 12 mA cm$^{-2}$ with a standard irradiation of one sun (100 mW cm$^{-2}$ at AM1.5 G).[32] The high recombination rates of charge carriers in $Fe_2O_3$ render the efficient extraction of

photogenerated charges and the generation of a high photovoltage significant, and perhaps insurmountable, posing challenges for its practical application as a photoanode.[33,34] The slow water oxidation kinetics at the hematite surface competing with surface-state recombination also contribute to the large positive photocurrent onset potential.[35]

A planar $BiVO_4$ photoanode with *in situ*-formed oxygen vacancies was recently shown to achieve a record charge separation efficiency of 98.2% at 1.23 V *vs.* RHE under AM1.5 G illumination.[22] When first reported in 1999, the quantum yield of $BiVO_4$ in photocatalytic $O_2$ evolution at 450 nm was only 9%.[20] Appreciable photocurrents and maximum incident photon-to-current (IPCE) efficiency at 420 nm of 44% were demonstrated by Sayama *et al.* in 2006.[21] Later studies revealed that the limited photocurrent and poor electron transport of $BiVO_4$ are attributable to limited overlap between V 3d–V 3d states and V 3d–Bi 6p orbitals in the conduction band.[13] Although nanostructured $BiVO_4$ has improved photocurrents compared with the planar counterpart,[36,37] the photocurrents remained limited by the slow surface reaction kinetics. Another key issue facing $BiVO_4$ is photocorrosion during the OER. The photochemical dissolution of $BiVO_4$ and oxidation due to photogenerated holes are responsible for the short-term stability of $BiVO_4$.[38,39] Similarly to $Fe_2O_3$, the photocurrent onset potential of $BiVO_4$ is more positive than that of $TiO_2$, owing in part to the slow OER kinetics of the minority holes,[36] but also to the smaller band gap and bulk recombination. Coatings with Ni- and Fe-based metal oxide and (oxy)-hydroxide co-catalyst layers on the surface of $BiVO_4$ photoanodes enhance the photocurrent and also stability against photocorrosion.[22,40]

### 6.2.3 Deposition of Metal Oxide Co-catalyst Nanolayers on Light Absorbers

While the efficiency of some photoanodes, such as $TiO_2$ and $WO_3$, is limited in large part by inefficient light absorption, the major problems faced with the smaller band gap photoanodes are surface charge recombination, poor interfacial charge-transfer efficiency, and photo- or photochemical corrosion.[33,39]

To overcome these issues, strategies have been developed to engineer the physical structures of the photoanodes or engineer the surface of the photoanodes. Nanostructuring has been applied to enhance the PEC performance by decoupling the dimensions for light absorption and for photogenerated charge-carrier collection.[18] Surface treatment of the semiconductors targets different functions, such as surface protection, passivation of surface states, modification of the band bending and band-edge positions, and enhancement of charge separation or surface reactivity.[41]

Surface co-catalyst layers have been demonstrated to lead to particularly large changes of the photoelectrode characteristics, such as onset potential, photovoltage, and photocurrent, although their precise functions and mechanisms are not always clear.[8] The expectation for the surface co-catalyst layer is that it accepts the photogenerated holes from the photoanode surfaces and provides reaction sites to catalyze the water oxidation reaction. Transition metal

oxide-based OER electrocatalysts, such as the Ni/Co/Fe-oxide/(oxy)hydroxide family, have the highest known activities in neutral to basic media.[42,43] Such OER electrocatalysts have also been shown to lower the onset potential and increase the photocurrent of photoanodes in PEC water oxidation.[22,44]

Different strategies, such as photoassisted electrodeposition,[45,46] photochemical deposition,[44,45,47] and atomic layer deposition,[48] have been explored to functionalize the photoanode surface with co-catalyst layers. The chemical composition, spatial distribution, and loading/thickness of co-catalyst layers can be controlled and adjusted by the approach. For example, cobalt phosphate (Co–Pi) was photodeposited on the surface of a hematite photoanode by oxidizing $Co^{2+}$ to $Co^{3+}$ in phosphate buffer with photogenerated holes leading to deposition. Because the redox potential of the $Co^{2+}/Co^{3+}$ couple is similar to that of $H_2O/O_2$, n-type semiconductors that evolve $O_2$ can also oxidize $Co^{2+}$ ions to deposit Co–Pi catalysts under light illumination and with the appropriate applied bias.[49] Since photoassisted electrodeposition allows deposition only where visible light generates oxidizing equivalents, it was shown to provide a more uniform distribution of Co–Pi onto $\alpha$-$Fe_2O_3$ than was obtained by electrodeposition in the dark.[45] This strategy also worked well for the photodeposition of iron oxyhydroxide (FeOOH) on $BiVO_4$.[40] The ability to tune the applied bias during the photoassisted electrodeposition allows for more flexibility to choose the composition of the co-catalyst layers. Photodeposition also works for both planar and nanostructured photoanodes.

When depositing co-catalyst thin films on the surface of planar photoanodes, photochemical metal–organic deposition (PMOD), physical vapor deposition, and atomic layer deposition (ALD) have also often been used. The co-catalyst nanolayer $NiFeO_x$ deposited on the surface of hematite thin-film photoanodes *via* the PMOD approach lowered the onset potential and increased the photocurrent of composite electrodes where the semiconductor is planar.[44,47,50] An advantage of PMOD is that the composition of the metal oxide nanolayers is tunable by adjusting the precursors.[50,51] Assuming that the major role of the co-catalyst layers is to improve the surface kinetics of the OER process, a higher loading of metal oxide co-catalyst layer is desired without affecting other processes. Different optimal loadings of the metal oxidation co-catalyst nanolayers on the photoanode surface were observed, which could be attributed to the co-catalyst deposition method and the morphology of the photoanodes.[50,52] This is discussed in more detail in Sections 6.3 and 6.4.

### 6.2.4 Chemical Transformation of Metal Oxide Layers in Electrolytes

Depending on the deposition methods, the co-catalyst layers produced can be in the form of metal, metal oxide, metal hydroxide, or metal oxyhydroxide. Chemical transformation between one another can be induced under electrochemical conditions. The co-catalyst layers produced with PMOD methods are amorphous metal oxide films[51] and can be converted into

hydroxide/oxyhydroxide by electrochemical potential cycling to create electrochemically accessible metal sites.[44,47] Photoassisted electrodeposition, on the other hand, typically directly yields the metal hydroxide/oxyhydroxide.

According to the Pourbaix diagrams of nickel, iron, and cobalt, the predominant thermodynamically stable phases are typically oxyhydroxides in neutral to basic oxidizing conditions.[43] The oxidation state of the metal cations, the electronic properties, and even the physical structure/morphology of the metal oxide nanolayers are subject to change upon PEC oxidation. The metal hydroxides $M(OH)_2$ (M = Ni, Co, Fe) are electronic insulators but become more conductive when oxidized to the metal oxyhydroxides, MOOH (M = Ni, Co, Fe).[53] The oxidation reaction of $M(OH)_2$ to MOOH is shown in eqn (6.3). Structurally, the Ni-, Co-, and Fe-based hydroxide/oxyhydroxide co-catalyst layers are considered to be electrolyte permeable and can incorporate ions during redox reactions and induce catalyst volume changes.[54] The chemical properties, electronic properties, and mechanical stabilities of these metal oxide/hydroxide/oxyhydroxide layers also depend strongly on the composition of the metal cations.[53] Although the Ni/Co/Fe oxide/oxyhydroxide family, with varying metal-to-cation ratios, have different electrocatalytic activities and electrical conductivities, the trends of these properties have not necessarily been found to reflect the performance of the composite photoelectrodes.[50]

$$M(OH)_2 + OH^- \xrightarrow{\text{oxidation potential}} MOOH + H_2O + e^- \qquad (6.3)$$

The processes involved in PEC water oxidation are more complex than those in the electrocatalytic OER reactions. Therefore, the trend of OER electrocatalyst efficiency does not always agree with the trend of the overall efficiency of the electrocatalysts on photoanodes. For example, the less active OER electrocatalyst FeOOH works better as a co-catalyst layer on $BiVO_4$ than the more-active Ni(Fe)OOH.[46] Additionally, the same Ni(Fe)OOH co-catalyst layers do not provide the same enhancement for different photoanodes.[44,46] These experimental observations highlight the importance of understanding the co-catalyst layer and photoanode interface, especially the dynamic state of the co-catalyst and its effects on interfacial charge transfer. This is discussed in more detail in the next section.

## 6.3 Dual Working Electrode Measurements on Composite Photoelectrode Thin Films

The primary need for the co-catalyst layer on the surfaces of semiconducting photoanodes is to minimize the kinetic overpotential ($\eta$) losses associated with driving the OER. The PEC performance of photoanodes usually improves with the addition of co-catalyst layers, in which the onset potential becomes more negative and the photocurrent increases. However, the mechanism is not well understood in every case.[8] Competing hypotheses have been proposed for the decrease in the onset potential of Co–Pi-decorated $\alpha$-$Fe_2O_3$ and $BiVO_4$.

One hypothesis supports the catalytic roles of the co-catalyst layer. For example, PEC measurements suggest that Co–Pi suppresses electron–hole recombination on the surface of the photoanode $BiVO_4$ by increasing the OER kinetics, but does not otherwise alter the characteristics of the electrode/electrolyte interface.[55] Similarly, Co–Pi layers on hematite were found to be catalytic based on PEC and impedance measurements.[35] Another hypothesis, supported by experimental data acquired from optical measurements, such as intensity-modulated photocurrent spectroscopy (IMPS) and photoinduced absorption, suggests that the Co–Pi co-catalyst layer reduces the surface recombination of $BiVO_4$ without significantly influencing the charge-transfer kinetics,[56] and water oxidation occurs predominantly on the surface of $BiVO_4$ instead of Co–Pi – a surprising conclusion given that $BiVO_4$ does not have the typical cations with partially filled d bands and redox activity found in known OER catalysts.[57] IMPS data also suggested that when $NiFeO_x$ was added to hematite, the apparent rate of recombination decreased more than that of hole transfer in the composite photoelectrode, compared with an uncatalyzed control sample. It was therefore proposed that $NiFeO_x$ primarily serves as a passivation layer rather than a catalytic layer – a surprising conclusion as $NiFeO_x$ is the fastest known water oxidation catalyst.[58] Transient absorption studies showed that anodic bias depletes the surface electron density of $\alpha$-$Fe_2O_3$ and hinders electron–hole pair recombination.[59] It was alternatively proposed then that the $CoO_x$ layer [*i.e.* the cobalt (oxy)hydroxide layer resulting from Co–Pi electrodeposition] plays a similar role to the anodic bias by forming a Schottky-type heterojunction that increases the band bending in the $\alpha$-$Fe_2O_3$ photoanode.[59]

These varied experimental results and interpretations indicate that a unifying understanding of the photoanode semiconductor and co-catalyst interface is needed. Specifically, understanding the dynamic state of the co-catalyst nanolayer, and the fate of the photogenerated holes on the surface of the photoanodes, provides insight into the roles of the co-catalyst layers. This information is useful for designing improved devices since the interface between the photoanode and co-catalyst is responsible for separating charge and building photovoltage.

When a bare photoanode is immersed in the electrolyte, the solid/liquid interface generally forms a Schottky junction and creates band bending.[6] The degree of band bending depends on the Fermi level of the semiconductor relative to the reduction potential of the solution; if the solution contains redox species with sufficiently fast kinetics to allow equilibrium with the electrons in the semiconductor, electronic equilibrium at the interface can be quickly established. For most water-splitting photoanodes, this is not the case. The reaction kinetics with the oxygen redox couple are not sufficiently fast to dominate the energy equilibration with the semiconductor. Therefore, the degree of band bending is set by other processes, for example equilibration with surface states.[11,31]

The addition of a co-catalyst nanolayer further modifies the interface energetics and also the charge-transfer kinetics of the photoanode surface. If the co-catalyst layer is dense and metallic, the interface between the

photoanode and the co-catalyst layer can be described by the well-developed theory of semiconductor–metal Schottky contacts.[60] As described in Section 6.2.4, the active states of the Ni/Co/Fe-based metal oxide OER catalysts in neutral or alkaline electrolytes are hydroxides and oxyhydroxides. They often exhibit broad redox waves associated with bulk oxidation/reduction processes and free movement of ions throughout the catalyst layer.[42,53,61] Upon oxidation of the metal cations in the co-catalyst layers, negative counter ions, such as $OH^-$, move between the electrolyte and the ion-permeable catalyst layer to compensate the additional positive charge. The change in the oxidation state of the catalyst layer is equivalent to the change of the Fermi level of the catalyst nanolayer.[62,63]

The potential drop and interfacial charge transfer across the photoanode and the co-catalyst layer therefore might be expected to be affected by the charge state of any ion-permeable co-catalyst layers. In conventional PEC measurements, the photoanode and co-catalyst system are used as a single working electrode through an ohmic back contact to the semiconductor, hence the potential drop across individual components is unknown. To address this measurement problem, a dual working electrode (DWE) measurement was developed, in which both the photoanode and the co-catalyst layer are used as independent working electrodes and their potentials/currents can be independently controlled or measured.[47,62,64]

### 6.3.1 Experimental Setup of Dual Working Electrode (DWE) Measurements

In a typical three-electrode PEC experiment, only one working electrode is used with the counter and reference electrodes, and it is connected to the ohmic back contact of the semiconductor. The DWE approach adds an additional electrode with independent control by a second channel on the potentiostat. This allows one to measure the interface properties directly by passing current between the two electrodes (as one would measure solid-state photoactive interfaces), or measure the photovoltage at the catalyst surface relative to the semiconductor bulk.

The geometric area of the active surface in a typical device can vary, but is often small, ~0.01–0.25 $cm^2$. A schematic of the ''macroscopic'' DWE setup is shown in Figure 6.3. This approach generally works well only for smooth

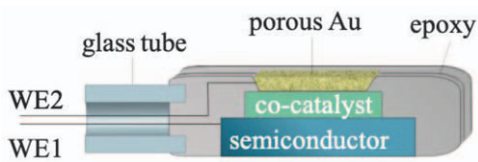


**Figure 6.3** Scheme of a dual working electrode photoelectrode setup. Reproduced from ref. 64 with permission from American Chemical Society, Copyright 2019.

electrodes based on thin films, single crystals, or other planar semiconductor surfaces. When fabricating the DWE system, an electrical contact is first attached to the photoanode semiconductor, such as a $TiO_2$ or $\alpha$-$Fe_2O_3$ thin film (WE1). The contacting metal is selected such that it forms an ohmic contact. If the material is $BiVO_4$ or $\alpha$-$Fe_2O_3$ deposited on a conductive oxide such as indium tin oxide (ITO), Ag paint and Sn–Cu wire can be used at an edge once the semiconductor has been scratched away to expose the conductive underlayer. For single crystals such as $TiO_2$, more complicated procedures must be followed to ensure good ohmic contact.[62]

The co-catalyst nanolayer deposited on the photoanode needs to cover the photoanode without pinholes, otherwise when the second working electrode contact is deposited, which is usually a thin gold film prepared by vacuum evaporation, shorting between the second working electrode and the semiconductor can occur. Deposition methods that yield uniform co-catalyst layers on photoanode surfaces include thermal evaporation,[65] PMOD,[51] and in some cases spin coating or electrodeposition.[62] The substrate on which the semiconductor and co-catalyst layer were deposited is attached to one end of a 3.5 mm diameter glass tube with the contact wire threaded inside the tube and out of the other end. Epoxy is used to insulate all the connections to WE1 such that only the uniform and pinhole-free thin film is exposed. The second electrical contact is then applied to the co-catalyst layer by evaporating a thin layer of Au film ($\sim$10 nm) onto the catalyst surface to serve as the second working electrode (WE2). Au is selected owing to its low intrinsic OER activity, high conductivity, excellent electrochemical stability, and electrolyte permeability at sufficiently thin deposition thicknesses. Experimentally, the thermal evaporation rate of the gold films was controlled at $\sim$2 $A\,s^{-1}$ and the film thickness was targeted at 10 nm by adjusting the deposition time and monitoring with a quartz crystal microbalance.[47,62,65] Both the evaporation rate and the final thickness of the film are vital for the quality of the deposited gold film as a working electrode and can be optimized with different evaporation tools. A second wire is attached to the edge of this Au contact with Ag print, making sure to avoid getting the Ag print on the region of the Au that is in direct contact with the catalyst film. This second working electrode enables the current/potential to be measured or controlled at the catalyst film independent of the semiconductor WE1.

### 6.3.2 Following Interfacial Charge Transfer Through Catalyst Thin Films with DWE Measurements

To determine the precise function of the co-catalyst layers on the semiconductor photoanodes, two key questions should be answered. First, what is the dynamic state (structure, oxidation state, *etc.*) of the co-catalysts under operating conditions? Second, where and how do electrons and photogenerated holes transfer between semiconductor, catalyst film, and solution phase?[66]

The answers to these questions will help resolve competing hypotheses regarding whether the co-catalyst layer acts as an OER catalyst or as a ''spectator''

by chemically passivating the semiconductor surface states responsible for electron–hole pair recombination – or both simultaneously.[8,35,44]

The DWE method has been applied to different photoanodes with OER co-catalyst layers to measure directly the flow of charge carriers at the semiconductor/co-catalyst interface. As described above, the experimental approach relies on electrical contact to the co-catalyst layer (WE2) to measure directly the catalyst's operating potential *in situ* during PEC water oxidation. The systems studied have included photoanodes with different band gaps, including single-crystalline $TiO_2$,[62] polycrystalline $\alpha$-$Fe_2O_3$,[47] and single-crystalline n-Si thin films.[65] Ni(Fe) hydroxide/oxyhydroxide nanolayers in basic electrolytes, one of the most efficient OER electrocatalysts, were deposited on these photoanodes to catalyze the PEC water oxidation reaction.

The DWE measurements were first applied to the $TiO_2$–Ni(Fe)OOH system, where Fe was not intentionally introduced but present in the form of electrolyte impurities that are incorporated in the catalyst layer.[66,67] The potentials of the photoanode semiconductor ($V_{sem}$) and the co-catalyst layer ($V_{cat}$) were independently measured or controlled. In the $TiO_2$–Ni(Fe)OOH system, when the co-catalyst potential (WE2) was held at different values with the system under illumination, it was found that the photoanode potential (WE1) was largely unaffected. This results in a linear dependence of the effective interfacial open-circuit voltage between semiconductor and catalyst ($V_{oc} = V_{sem} - V_{cat}$), where $V_{cat}$ is the potential of the catalyst layer measured by the thin, permeable, Au top film. This behavior is not expected from a simple Schottky model of a semiconductor/catalyst interface where the photovoltage of the buried semiconductor catalyst junction would be independent of the potential applied to the catalyst layer (relative to the solution). These observations led to the proposal of an ''adaptive'' junction at this interface. What this means is that because electrolyte can permeate the catalyst layer, any charge placed on the catalyst layer, for example by oxidation of the catalyst, is compensated by ions internal within the catalyst film. It also means that electrolyte can permeate all the way to the semiconductor surface. Hence changing the potential and therefore the average oxidation state of the catalyst has little effect on the band bending in the semiconductor (for a given applied potential to the back ohmic contact). By highly oxidizing the catalyst layer, its Fermi level is driven very positive (low on a typical band diagram), leading to, effectively, a large interface barrier.[62]

Compared with $TiO_2$, hematite suffers from significant bulk and surface electron and hole recombination and typically has a significantly higher density of surface states,[11] rendering it a more complex system when coated with a co-catalyst layer. To study a model $\alpha$-$Fe_2O_3$–Ni(Fe)$O_xH_y$ system, a co-catalyst layer of $Ni_{0.8}Fe_{0.2}O_xH_y$ (~60 nm) was deposited *via* PMOD on the surface of a hematite thin film[47] that was smooth and previously grown by ALD.[68] Unlike a single-crystalline $TiO_2$ photoanode, the various facets and grain boundaries of polycrystalline hematite could affect the interfacial properties. Additionally, the surfaces of $Fe_2O_3$ are often populated by surface states with varying densities and energies, which have been shown to trap

surface holes and mediate the water oxidation processes.[11] Hence, water oxidation can in principle occur on either the semiconductor surface *via* the surface states or within the co-catalyst layer.

To determine the fate of the photogenerated holes, two measurements were made using the DWE method with a hematite photoanode.[47] First, the catalyst potential ($V_{cat}$ *vs.* $\varepsilon_{O_2/OH^-}$) was held at a series of fixed values while the photocurrent density at hematite WE1 ($J_{sem}$) and the current density from the co-catalyst layer collected at WE2 ($J_{cat}$) were measured simultaneously (Figure 6.4). The current density measured at hematite (WE1) increases upon illumination, whereas the current density collected from the co-catalyst layer (WE2) decreases by the same amount. To maintain the potential of the co-catalyst layer at a fixed value (which is set by the potentiostat), WE2 must modulate the current flow into/out of the catalyst layer (to compensate for any collected holes) by injecting electrons into the catalyst (or, equivalently,

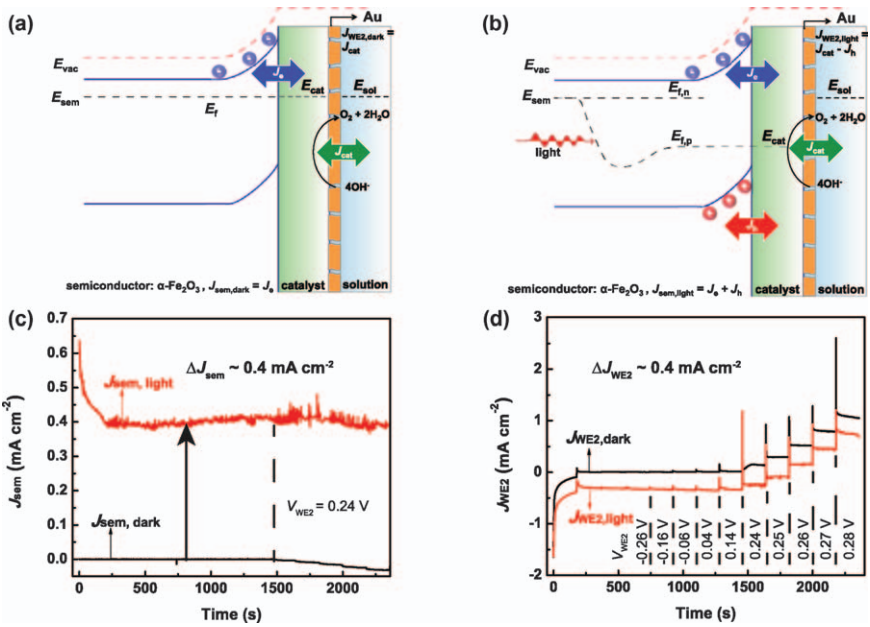


**Figure 6.4** Measurements of photogenerated hole transfer at the α-$Fe_2O_3$/$Ni_{0.8}Fe_{0.2}O_x$ interface with DWE. (a) Scheme of the band bending of the interface in the dark. (b) Scheme of the band bending of the interface under illumination. (c) Current densities of α-$Fe_2O_3$ measured from WE1 when $V_{sem}$ is held at 0 V *vs.* $\varepsilon_{O_2/OH^-}$ both in the dark (black curve) and under illumination (red curve) while controlling the potentials of the catalyst $V_{cat}$ *vs.* $\varepsilon_{O_2/OH^-}$ in a chronoamperometry experiment. (d) Current densities measured from WE2 under different potentials of the catalyst $V_{cat}$ *vs.* $\varepsilon_{O_2/OH^-}$ with $V_{sem}$ held at 0 V *vs.* $\varepsilon_{O_2/OH^-}$ in the dark (black curve) and under illumination (red curve).
Reproduced from ref. 47 with permission from American Chemical Society, Copyright 2017.

removing the injected holes). The DWE PEC measurement can therefore be used to track directly the flow of photogenerated holes. Comparing the magnitude of the light-induced current density changes at WE1 and WE2, and showing them to be equivalent, demonstrates that the majority of those holes transfer into the catalyst film over a wide range of conditions.

The catalytic role of the $Ni_{0.8}Fe_{0.2}O_xH_y$ layer was further confirmed by assessing whether the potential reached by the catalyst film on hematite was sufficient to drive water oxidation. Identical co-catalyst films ($Ni_{0.8}Fe_{0.2}O_xH_y$) were deposited on a conducting ITO and a hematite surface, followed by a thin Au layer on top of the catalyst. Both systems were fabricated into DWE devices. The oxygen evolution current of the co-catalyst film was then measured at a series of potentials applied to the ITO and plotted *versus* the potential measured on the top Au contact. The potential of the catalyst on hematite was then measured, using the top Au contact, as a function of the photocurrent measured at the semiconductor back contact under illumination. It was found that the catalyst layer is oxidized to similar potentials driving the OER for a given current density, independent of whether the holes originate from ITO or are photogenerated in hematite. This shows that $Ni_{0.8}Fe_{0.2}O_xH_y$ is oxidized by the photogenerated holes to an operating potential sufficient to drive water oxidation at rates commensurate with the measured photocurrent (on WE1). Thus, the $Ni_{0.8}Fe_{0.2}O_xH_y$ catalyst layer acts as both a *hole collector* and an *OER catalyst* on hematite thin films. Recently, hematite photoanodes covered with a nickel hydroxide electrocatalyst were studied by X-ray absorption techniques.[69] The results showed that Ni metal centers in the nickel oxide layer are oxidized to nickel oxyhydroxide with Ni reaching a higher oxidation state ($Ni^{IV}$) by photogenerated holes from hematite, and thicker catalyst films (~80 nm) tend to accumulate more holes than thin films (~2 nm).[69]

In addition to measuring the interfacial voltage and fate of charge carriers in $TiO_2$ and hematite photoanodes, the DWE method was also applied to understand the increase in efficiency of Si photoanodes coated with Ni layers of different thicknesses.[65] Photoanodes composed of n-Si are of practical interest[70–73] if they can be protected from photocorrosion and combined with efficient electrocatalysts, owing to the excellent electronic properties of Si for solar energy conversion.

A thin (~2 nm) metallic Ni layer on an n-Si photoanode along with its native $SiO_2$ layer makes it a relatively high-performance metal–insulator–semiconductor photoanode.[74] The Ni could serve as a protection layer, electrocatalyst for the OER (when oxidized), and some type of charge-separating heterojunction to the n-Si simultaneously. To understand better the fundamental interface energetics and charge-transfer kinetics aspects of the sufficiently thin Ni protection layers (≤5 nm) relative to thicker layers, DWE measurements were applied.[65] The Si photoanodes were coated with Ni layers of different thicknesses (3, 5, and 20 nm) *via* thermal evaporation. The electrode was electrochemically cycled following a standard activation protocol, in which the surface of the metallic Ni was converted into the electrochemically

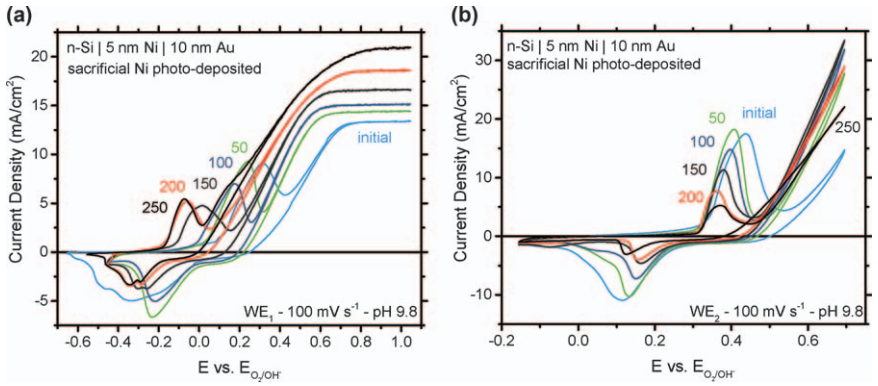


**Figure 6.5** Evolution of the PEC response over many electrochemical cycles for an Ni-coated n-Si photoanode. (a) Using WE1, the illuminated photoanode is cycled through the potential range shown. After every 50th cycle, the experiment is paused while voltammetry data are collected *via* WE2. (b) The cyclic voltammograms of the Ni layer collected *via* WE2 every 50 cycles show the catalyst's intrinsic activity and how it changes (shifts to the left indicate better activity). The results demonstrate the DWE's ability to separate catalytic effects from junction effects. Although the onset of photocurrent shifts cathodic with continued cycling as shown in (a), this shift is not accounted for by changes in the intrinsic catalytic activity shown in (b). After an initial 50-cycle activation period, the catalyst activity remains largely constant while the photoelectrode performance continues to improve with additional cycling.
Reproduced from ref. 65 with permission from the Royal Society of Chemistry.

active $Ni(OH)_2$–NiOOH.[65] The DWE technique was used to determine that thin Ni catalyst–protection layers enhance Si photoanodes *via* changes to the rectifying junction compared with thick Ni layers. With sufficiently thin layers, the solution permeates regions of the protection layer and passivates the underlying Si. The increase in activity was attributed to the development of pinched-off Si–Ni point contacts, but this hypothesis has not yet been directly proven. The DWE technique was useful, however, because it allowed the separation of effects due to catalytic enhancement of the photoelectrode from junction enhancement effects. As the photoanodes were electrochemically cycled, the onset of water oxidation became more cathodic (Figure 6.5a). By using WE2, the catalyst layer was independently cycled (Figure 6.5b) and it was shown that the catalytic activity remained constant (after an initial activation period) and therefore changes in catalytic activity could not be causing the overall enhanced photoanode performance with cycling. The electrochemical potential of the catalyst layer was measured as a function of potential applied to the semiconductor back contact and revealed an ~440 mV photovoltage for the best devices, after activation. This represents a 300 mV increase in the photovoltage compared with devices with thicker (~20 nm) Ni protection layers. Control experiments at different illumination densities proved

that this increase was not due to the change in photovoltage with light intensity. Further, DWE tests indicated that even the best devices retained their buried junction behavior (*i.e.* they do not show the adaptive junction behavior discussed above), indicative of direct contact between remaining metallic Ni nanoparticles and the Si surface. Through these measurements, the DWE technique showed that the enhanced photoelectrode efficiency originated specifically from changes to the rectifying junction and that the junction remained buried despite these changes.

By observing the range of behaviors on different photoanode–co-catalyst systems discussed above, two general types of junctions were found. The adaptive junction model was proposed to depict the interface between semiconductors and ion-permeable hydroxide/oxyhydroxide electrocatalyst layers (Figure 6.6a). The Fermi level of the ion-permeable co-catalyst layer is subject to change upon redox activities and forms charge-separating heterojunctions with the semiconductor. In the photoanode systems such as $TiO_2$ and hematite, the co-catalyst layer collects photogenerated holes from the semiconductor, charging to potentials sufficient to drive water oxidation. The co-catalyst layer studied thus serves as a *hole collector* and *water oxidation catalyst*. When a buried junction is formed (Figure 6.6b), such as in the case of n-Si–Ni, the improved photocurrent onset could be attributed to the pinched-off contact points, where a spatially heterogeneous junction with different energy barriers is developed. The contact between the Si and the metallic Ni nanoparticles results in the buried junction and the $Ni(OH)_2$–NiOOH on the surface of the Ni nanoparticles contributes to the OER catalytic activity. This hypothesis of the pinched-off Si–Ni point contacts was further directly tested and proved with the potential-sensing electrochemical AFM (PS-EC-AFM) technique as discussed in Section 6.4.

Although macroscopic DWE measurements help illuminate the interfacial properties of several photoanode systems, they are generally limited to

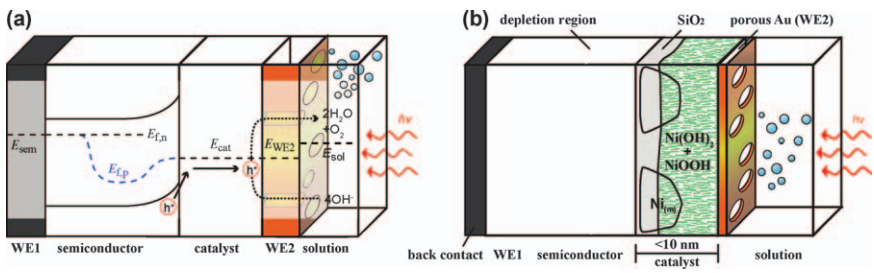


**Figure 6.6** Conceptual model showing the co-catalyst layer and the semiconductor interface. (a) The co-catalyst layer collects holes and drives the water oxidation reaction when the interface forms an adaptive junction. (b) The co-catalyst layer forms a partially buried junction with the semiconductor.
Part (a) reproduced from ref. 64 with permission from American Chemical Society, Copyright 2019. Part (b) reproduced from ref. 65 with permission from the Royal Society of Chemistry.

systems with smooth electrocatalyst layers that are compatible with vacuum deposition of the secondary electrical contact. This limits the range of systems that can be explored, most notably precluding examination of the electrodeposited cobalt phosphate (Co–Pi) catalyst on $\alpha$-$Fe_2O_3$ and also nanostructured semiconductors. To address this issue, the PS-EC-AFM technique is discussed in Section 6.4; it permits surface–catalyst potential measurements on systems that were not previously possible, including photoassisted electrodeposited catalysts on metal oxide semiconductors. Compared with macroscopic DWE measurements, which require pinhole-free catalyst films, PS-EC-AFM is not limited by the morphology of the catalysts and is also able to provide spatially resolved operating potential information on heterogeneous catalyst layers.

### 6.3.3 Impacts of Loading of Metal Oxide Catalysts

Based on the understanding achieved from the DWE studies, the major functions of the electrocatalyst nanolayers generally are to accept photogenerated holes from the photoanodes and catalyze the OER reactions.[47,64] To increase the catalytic activities, a higher co-catalyst loading (and thus more active surface area) is expected to drive the OER reaction at a lower overpotential. However, when coupled with the photoanode, other variables such as the semiconductor morphology and parasitic absorption of light also need be considered. The studies described above also do not show fully how the catalyst layers modulate the exact interface barriers, and how to optimize interfacial charge-carrier selectivity (*i.e.* to make the interface hole selective) remains a practical challenge to achieving higher photovoltages.

In the $TiO_2$ and n-Si photoanode systems described in Section 6.3.2, the electrodes are illuminated from the front side and the co-catalyst nanolayers could parasitically absorb light.[62,65] This is also referred to as front illumination in the literature.[37] Therefore, an optimal co-catalyst layer needs be determined to balance the light absorption of the photoanode and catalytic activity of the co-catalyst. A model describing the coupling of light-absorbing oxygen evolution reaction (OER) electrocatalyst thin films such as $Ni(OH)_2$–NiOOH with semiconductor photoelectrodes was proposed.[75] The optical absorption spectra and electrokinetics of metal oxide co-catalyst layers of certain thicknesses were considered under PEC conditions and it was found that ultrathin ($\sim$1 nm or less) co-catalyst films generally optimize the PEC performance of photoelectrodes under front illumination. In a different scenario, such as the hematite photoanode, the semiconductor is photoexcited from a transparent back contact, ITO glass, and therefore the optical absorption is not a primary consideration for the thickness of the co-catalyst layer. Such illumination is referred to as back illumination.[52]

The optimal loading of the co-catalyst layer on a hematite photoanode has been discussed in different reports.[35,52] One simple, but critically important, mechanism of recombination that is unique to co-catalyst-coated porous semiconductors with high surface area is catalyst-to-back contact shunting.

It was shown that a thick layer of catalytic Co–Pi layer (~25 nm) on a mesoporous hematite electrode led to a worse PEC performance compared with sparse catalyst coating.[52] For these systems, pinholes in the porous semiconductor can fill with catalyst during deposition and act as electrically conductive shunt pathways to the back contact.[50] Under illumination, photogenerated holes transfer to the catalyst but then recombine with electrons at the catalyst/conductor interface. This shunting–recombination was confirmed on hematite thin-film model systems.[50] Eliminating the shunt pathways through the co-catalyst is critical to achieving high-performance catalyst-coated photoanodes. There are several ways to do this. If one is building a three-dimensional nanostructured/porous semiconductor one could coat the conducting electrode support completely with a thin layer of the semiconductor prior to depositing the nanostructured semiconductor. Selective photoassisted electrodeposition of thin catalyst layers on the semiconductor surface or using electrically insulating catalyst layers also prevent shunting. A final option is to passivate the pinholes selectively with an insulator to block direct contact. This might be possible with electrodeposition of an insulator.

## 6.4 Electrochemical Atomic Force Microscopy Measurements on Nanostructures

Even after completion of initial DWE work by Lin and Boettcher on model $TiO_2$ photoanodes,[62] a number of competing hypotheses related to the role of Co–Pi and whether or not it served as a hole collector, catalyst, or interface modulator on systems such as $BiVO_4$ and $Fe_2O_3$ remained untested.[76] Experiments with the traditional DWE setup have been limited by the deposition technique employed. For example, benchmark water oxidation catalysts for photoanodes are typically photoelectrodeposited and result in inconsistent coverage over the photoanode surface.[35,46] This is unsuitable for study with traditional DWE approaches because (1) the surface roughness is too great to have a vacuum-deposited gold WE2 that is electrically interconnected but thin enough not to perturb the electrolyte permeability of the film, and (2) areas with no catalyst coverage will cause the WE2 to electrically short directly to the underlying semiconductor surface, changing the interface properties and possibly collecting current directly from the semiconductor. Finally, the most-commonly used metal oxide semiconductors are polycrystalline and highly structured in three dimensions, making the traditional DWE technique very difficult to implement.

To address these challenges, the DWE setup was implemented at the nanoscale using electrochemical AFM. The new technique, termed potential-sensing electrochemical atomic force microscopy (PS-EC-AFM), allowed *operando* surface-potential measurements of the catalyst layers for a host of photoanode structures previously not viable for study.[77,78] This PS-EC-AFM method was also a milestone towards spatially resolving photovoltage and catalyst activity.

### 6.4.1 Experimental Setup of Potential-sensing Electrochemical Atomic Force Microscopy Measurements

Like the DWE setup, PS-EC-AFM utilizes a semiconductor with an ohmic back contact, such that the majority-carrier Fermi level position can be modulated by a potentiostat relative to a reference electrode. This is referred to as the first working electrode, or WE1. Additionally, the use of a conventional reference electrode and counter electrode can be enabled through careful design of the PS-EC-AFM electrochemical cell. The key difference from the traditional DWE is the replacement of the thin evaporated Au second working electrode with an electrically conductive AFM probe (Figure 6.7a). This setup was facilitated by the commercial development of high-quality, batch-manufactured insulated probes with an exposed conductive (Pt) nanosized tip (Figure 6.7b).[79] The insulation of the probes prevents capacitive charging and parasitic reactions from taking place on the probe during experiments.

Using AFM, the electrode surface can be topographically mapped to identify regions that are coated with catalyst. The sensitive force control of an AFM instrument allows the probe to be planted on (or into) the surface of the catalyst with a reliable and reproducible pressure. The AFM cell and stage were designed to allow bottom illumination of the sample, permitting true *operando* measurements. The conductive AFM probe can measure the operating potential of a given catalyst layer while the semiconductor sample is biased and illuminated and water oxidation is taking place provided that the photocurrent density is maintained below 1 mA $cm^{-2}$ to prevent issues with bubbles affecting the AFM tip.

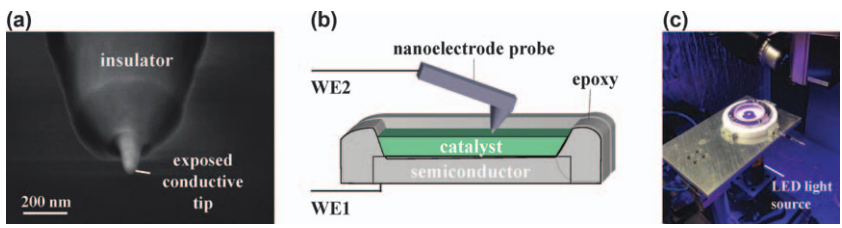


**Figure 6.7** PS-EC-AFM experimental setup. (a) Cross-section of a custom-made AFM EC cell used in potential-sensing measurements, where the substrate serves as WE1 and a nanoelectrode probe as WE2. A hole in the bottom of the cell allows bottom illumination of semiconductor samples. Additionally, the cell incorporates an Ag/AgCl reference electrode and Pt counter electrode. (b) SEM image of the insulated nanoelectrode probe with exposed conductive tip. The tip height is ~200 nm with a diameter of ~50 nm. (c) Custom-made AFM cell and stage. A light source can be placed under the AFM stage to allow bottom illumination.
Parts (a) and (c) reproduced from ref. 77 with permission from Springer Nature, Copyright 2017. Part (b) reproduced from ref. 64 with permission from American Chemical Society, Copyright 2019.

### 6.4.2 Interfacial Charge-transfer Measurements with PS-EC-AFM Measurements

In qualifying the PS-EC-AFM technique, it was critical first to demonstrate the ability of the probe to measure surface potentials of simple metallic electrodes in solution. Using the custom-made AFM cell and stage (Figure 6.7c), Ti-coated glass–Au was used as WE1. The cell was filled with potassium phosphate buffer and the AFM probe (WE2) was landed on the surface of the Ti–Au electrode. A bias was applied to WE1 using a potentiostat and the same potentiostat was used to measure the surface potential *via* WE2 attached to the AFM tip. The potential of WE1 was stepped positive in increments of 100 mV. Immediately, the potential measured *via* the tip matched the potential applied to WE1 and mirrored the potential steps applied, indicating that the contact between tip and surface, in electrochemical conditions, was sufficiently good to allow fast electronic equilibration and equalize the electrochemical potential of the electrons.

With the success of preliminary surface potential measurements, catalyst-coated conductive substrates were prepared for PS-EC-AFM testing and analysis. For a conductive substrate, ITO is a good platform for catalyst studies owing to its poor OER activity. This allows for the reasonable assumption that all OER activity originates from the catalyst-coated surface and not the ITO substrate.

Like the proof-of-principle surface potential measurements made on Ti–Au substrates, similar measurements were made for the Co–Pi-coated ITO. A bare ITO sample was loaded into the AFM cell and the cell was filled with 0.5 mM $Co(NO_3)_2$ electrolyte solution. Co–Pi was anodically deposited on the surface until a 100 nm thick film was achieved. Once the cell had been loaded onto the AFM instrument, the AFM probe could be landed on the film surface. Once a uniformly coated catalyst region had been identified *via* tapping-mode imaging, the probe was planted at that location and held with a constant 25 nN force. WE1 potentials were again stepped in 100 mV increments, while WE2 (the nanoelecrode probe) monitored surface potentials (Figure 6.8a). Unlike the Ti–Au samples, at low applied potentials ($<$0.2 V *vs.* $\varepsilon_{O_2/OH^-}$) WE2 was unable to establish an electronic equilibrium with the catalyst and sense a reliable potential that responded to the potential applied to WE1. However, at higher potentials the probe measures Co–Pi potentials that are matched to those being sourced by WE1 to the ITO sample. These observations are consistent with the fact that at $<$0.2 V *vs.* $\varepsilon_{O_2/OH^-}$, $Co(OH)_2$ is electronically insulating and is electronically conductive only when it is oxidized to CoOOH.[80] This measurement also showed the relationship between catalyst potential directly measured with the EC-AFM tip and OER current, which can be used as a reference to analogous Co–Pi on hematite.

Co–Pi was then photoelectrodeposited on a planar hematite film using similar conditions to those for the deposition on an ITO sample, until a 100 nm Co–Pi film was achieved. The Co–Pi-coated hematite was loaded onto the AFM instrument and the nanoelectrode probe was again used to measure surface

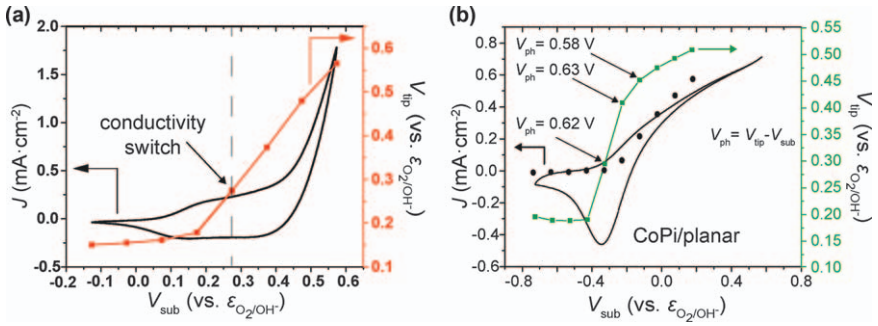


**Figure 6.8** Surface potential measurements for (a) Co–Pi-coated conductive glass and (b) planar hematite. Measurements were taken in 0.1 M potassium phosphate solution buffered to pH 6.9, with the hematite sample illuminated by a 405 nm light source calibrated to 27 mW cm$^{-2}$. The substrate was held at each potential for 1–2 min, allowing the potential measured *via* the AFM tip to stabilize. Cyclic voltammograms measured using the conducting substrate as the working electrode have been overlaid for each system. The conductivity increases for Co–Pi were observed at $V_{sub} = 0.27$ V *vs.* $\varepsilon_{O_2/OH^-}$ for conductive glass and $V_{sub} = -0.33$ V *vs.* $\varepsilon_{O_2/OH^-}$ for planar hematite.
Reproduced from ref. 77 with permission from Springer Nature, Copyright 2017.

potentials as a function of the potential applied to WE1, but in this case the holes were photogenerated *via* bottom illumination of the hematite semiconductor. As with the Co–Pi-coated ITO, the Co–Pi on hematite remained in the reduced, non-conductive form until an applied potential of −0.33 V *vs.* $\varepsilon_{O_2/OH^-}$, where the catalyst was oxidized (Figure 6.8b). The tip proceeded to equilibrate to a potential of 0.29 V *vs.* $\varepsilon_{O_2/OH^-}$, with the difference between the tip's measured potential and the applied substrate potential (∼0.6 V) being the photovoltage of the system (Figure 6.8b).

Although observations of the increased conductivity in the Co–Pi catalyst confirm that the photogenerated holes from planar hematite are transferred to the Co–Pi, it does not prove that the OER takes places within the catalyst itself. One could imagine a scenario where the oxidized Co–Pi, for example, primarily enhances performance by increasing the overall band bending. To assess whether the Co–Pi is indeed driving the OER, we examine more closely the electrical data that were collected *via* the nanoelectrode probe. Figure 6.9 shows the catalyst voltage (measured *via* the AFM tip) *versus* the overall current on the ITO–Co–Pi and photocurrent on the hematite–Co–Pi. The two curves superimpose, indicating that the Co–Pi on hematite is collecting the holes and driving the OER at a rate equal to the photocurrent. This is evident from the following. As Co–Pi is the only driver of the OER on ITO, one can deduce the total OER current being passed when the Co–Pi film is poised at a given potential. We find that for a given photocurrent for the hematite–Co–Pi sample, the potential is identical for the same current on the ITO–Co–Pi sample. The only explanation for the potential being the same

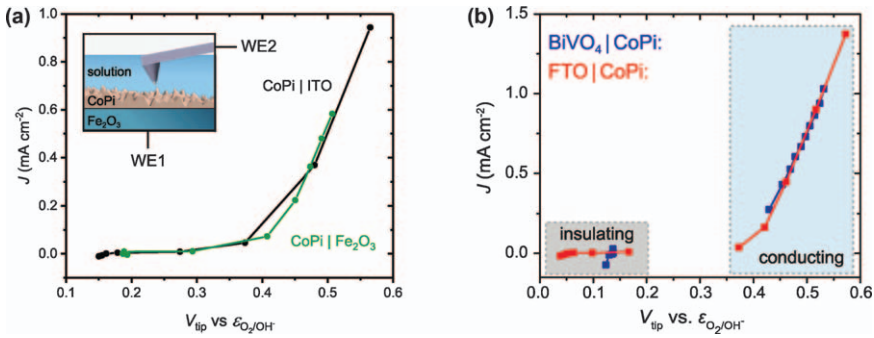


**Figure 6.9** For a given surface potential of (a) Co–Pi on ITO conductive glass (black) and Co–Pi on planar hematite (green), identical current densities are obtained. The same is true for (b) Co–Pi on FTO (red) and $BiVO_4$ (blue). Because ITO and FTO are known to be poor OER catalysts, all OER current can be assumed to pass to solution from the Co–Pi.
Part (a) reproduced from ref. 77 with permission from Springer Nature. Copyright 2017. Part (b) reproduced from ref. 82 with permission from American Chemical Society, Copyright 2018.

is that the net OER current in both cases is the same and equal to the photocurrent for hematite–Co–Pi. The OER does not appear to occur on the surface of the hematite when Co–Pi (which also will incorporate some Fe sites that further enhance OER activity) is present. These studies were repeated for Co–Pi on mesostructured hematite, with similar results.

### 6.4.3 Influence of Catalyst Loading on Metal Oxides

As with Co–Pi on hematite, the function of different electrocatalysts on $BiVO_4$ has also been the subject of many studies, with different conclusions. For example, it was proposed that the majority of the water oxidation sites are located on $BiVO_4$ and less than 5% of water oxidation proceeds on the Co–Pi layer on $BiVO_4$ based on the dynamics of photogenerated holes studied by photoinduced absorption and electrochemical techniques.[57] In this case, Co–Pi was proposed to suppress surface recombination instead of catalyzing the OER. As with the studies described in Section 6.3, the thickness of the catalyst overlayer was also suggested to impact the OER mechanism for $BiVO_4$ systems, with several instances in the literature of thicker Co–Pi layers resulting in loss of activity.[52,57,81] For a mesostructured hematite photoanode, only thin layers of Co–Pi improved the PEC performance and thicker layers (~25 nm) led to worse performance.[52] This phenomenon was termed a ''kinetic bottleneck'', in which the worse performance caused by a higher loading of the catalyst layer was attributed to the increased recombination between conduction band electrons traversing the nanostructured semiconductor from the back contact and holes accumulated in the thicker layer of Co–Pi.[52,81] However, this conclusion is at odds with the simple fundamental realization that the recombination rate

should depend on the hole density in the catalyst layer at the semiconductor surface, not the total number of holes that are accumulated in the layer. Therefore, there is no fundamental reason, from an interfacial recombination picture, to expect thicker layers to lead to more recombination. In fact, thicker layers, in this picture, would drive the OER at lower overpotentials at a lower overall hole density, if anything, reducing recombination.

To better understand the role of the Co–Pi co-catalyst on $BiVO_4$, the PS-EC-AFM technique was employed in a similar manner to the previously discussed hematite–Co–Pi systems.[82] Initial macroscopic electrochemistry measurements showed a decay of photoresponse with increased catalyst loadings. At catalyst thicknesses necessary to achieve reliable electrical contact between the probe and the catalyst (~100 nm), the device performance had nearly completely degraded and a substantial dark current was found (*i.e.* the PEC junction was not behaving as a good diode). Based on previous work studying the thickness dependence of catalyst-coated hematite, this behavior suggested that Co–Pi is shunting to the FTO. The presence of pinholes, which enabled thick catalyst overlayers to shunt to the FTO, was directly confirmed *via* electron microscopy, thus providing a clear and simple explanation for previous catalyst thickness-related trends.

To prevent shunting, thicker $BiVO_4$ films were prepared, based on a reported protocol,[83] that were free of pinhole defects by electron microscopy. Catalyst loading studies were performed and it was demonstrated that even the thickest catalyst films did not result in degradation of the photoresponse. With this milestone, thick $BiVO_4$ films coated with Co–Pi electrocatalyst could be studied using the PS-EC-AFM technique. Co–Pi-coated (thick) $BiVO_4$ and Co–Pi-coated conductive glass (FTO) samples were then prepared and inserted into the custom-made AFM EC cell.[82] The cell was filled with phosphate buffer and the AFM nanoelectrode probe was landed on the Co–Pi. Using WE1, the potential was stepped anodically while the nanoelectrode WE2 measured the corresponding surface potential. In the case of $BiVO_4$, holes were photogenerated by a light source underneath the sample. For both systems, initial surface-potential measurements did not track with changing substrate potential. However, once the potential was sufficiently anodic, a large jump in catalyst surface potential was observed. This corresponds to the conversion of cobalt hydroxide to the conductive cobalt oxyhydroxide and is consistent with the catalyst charging with holes. As in previous PS-EC-AFM studies, we compared the surface potentials of Co–Pi on $BiVO_4$ (under illumination) with those of Co–Pi on a conductive glass substrate to assess if Co–Pi on $BiVO_4$ is capable of driving water oxidation at that photocurrent density. Similar to the analogous Co–Pi-coated hematite, the surface potential of Co–Pi is the same for a range of current densities, regardless of the substrate ($BiVO_4$ or FTO) and hole source (photogenerated or injected from conducting glass), as shown in Figure 6.9b.

The impact of this work is twofold. First, it demonstrates that Co–Pi acts wholly as a catalyst when layered on $BiVO_4$. In fact, the Co–Pi behaves in a manner identical with that when it is on hematite, and this is also consistent with studies of Ni(Fe)OOH electrocatalysts on hematite. This provides a

consistent mechanism for metal (oxy)hydroxide-based catalysts on different metal oxide semiconductors with various morphologies. Second, this work demonstrates important design principles for future photoanode devices, specifically, that the catalyst is the primary hole collector and driver of water oxidation. It also demonstrates that thin, pinhole-free semiconductor films can be loaded with more catalyst material when the photoelectrode is back-illuminated, which will allow further efficiency improvements for these devices by lowering the catalytic overpotential needed to drive the OER.

### 6.4.4 Spatially Resolved Photovoltages of Si with Ni(Fe)-based Oxide Nanoparticle Catalysts

Previous systems studied using PS-EC-AFM relied upon moderate loadings (*i.e.* films typically ~100 nm thick) of catalyst on the metal oxide surface. This simplifies the measurements by creating a smoother, more robust surface, leading to better contact between the probe and the catalyst. Additionally, low catalyst loadings would conflate the heterogeneity effects of semiconductor surface morphology and grain orientation with heterogeneity of the catalyst particle behavior and interface chemistry. By studying thicker catalyst films that are electrically interconnected, these effects average and a response representative of the entire sample is obtained.

Given that catalyst nanoparticles are likely to result in heterogeneous semiconductor–catalyst nanojunctions, being able to spatially resolve the electronics of nanoscale interfaces could, however, be important for identifying which features lead to hole-selective nanojunctions. PS-EC-AFM is useful in realizing this goal because it is an *operando* technique that directly measures the electrochemical potential of the electrons at the surface using a nanoscale probe in concentrated electrolytes. These are distinct advantages for this work over techniques such as Kelvin probe force microscopy or scanning electrochemical microscopy.[78]

The ability of PS-EC-AFM to measure heterogeneity in interface properties was shown using a model system of Ni nanocontacts on n-Si.[78] This approach removes any morphological electronic variations of the underlying semiconductor and allows all spatial variations observed to be related to the Ni nanoparticles and their contact to the semiconductor. The specific model system, n-Si–Ni, has been argued to be of some practical interest also, for example as a protected Si photoanode with reasonably high PEC performance[70–72,74,84] – although pragmatically the stability and photoanode efficiencies are still too low for applications.

Ni nanocontacts can be electrodeposited on an n-Si surface using well-established procedures.[85] Using the same EC cell as used for previous PS-EC-AFM experiments, the n-Si–Ni was loaded on the AFM instrument and submerged in solution. The sample was illuminated and cycled 50 times *via* cyclic voltammetry. This ''activated'' the electrode by oxidizing the Ni nanoparticle surface, converting it to Ni(Fe)OOH, which is an active OER catalyst (Figure 6.10a). After activation, the sample was biased *via* the ohmic

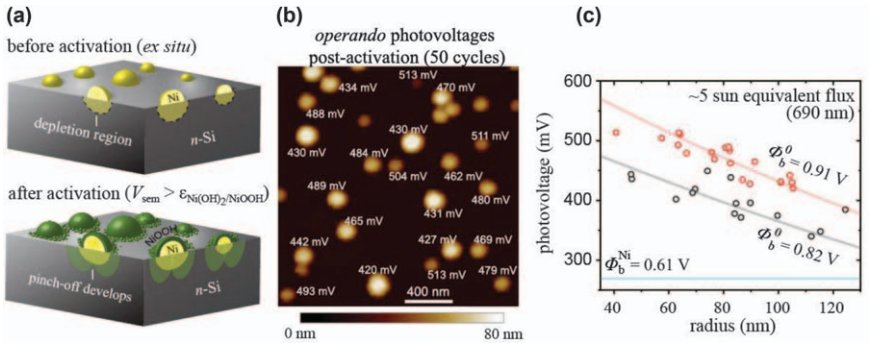


**Figure 6.10** Spatially and size-dependent photovoltages of Ni nanocontacts on n-Si. (a) Schematic of Ni nanoislands, before and after activation. As the islands are activated, the surface of the Ni is converted to the OER catalyst Ni(Fe)OOH. This process also increases the size of the depletion region, inducing the pinch-off effect. (b) Spatial mapping of Ni nanocontacts upon activation. The probe was used to measure photovoltage values individually. (c) Relationship between photovoltage and nanocontact radius. An inverse relationship between radius and photovoltage is observed, consistent with the presence of the pinch-off effect.
Reproduced from ref. 78 with permission from Springer Nature, Copyright 2019.

back contact at a potential anodic enough to keep the surface in the oxidized, conductive Ni(Fe)OOH state, while not driving significant OER current (*i.e.* <1 mA cm$^{-2}$). A topographic image of the surface was collected before the nanoelectrode probe was used to measure individually the surface potentials of the Ni islands. The corresponding photovoltage was determined by taking the difference between the potential applied *via* the substrate ohmic contact and the potentials measured using the probe (Figure 6.10b). These measurements represented the first instance of PS-EC-AFM resolving nanoscale variations of surface electrochemical potential.

One significant result of this study was the observed dependence of photovoltage on nanocontact size, with smaller islands producing larger photovoltages (Figure 6.10c). This phenomenon can largely be explained *via* the pinch-off effect. The pinch-off effect arises when the depletion region of a higher barrier (background) region overlaps with that of a lower barrier (Figure 6.10a). In the case of the Ni nanoislands, as the Ni contacts are reduced in size the surrounding Ni(Fe)OOH regions that are highly oxidized and hence have large effective work functions dominate the contact's selectivity. Physically, the higher ''effective'' barrier height associated with the smaller Ni particles results in lower electron (recombination) currents and thus higher photovoltages. The nanoscale observations thus explain the physics behind the observation that thinner Ni films lead to higher performance on macroscopic electrode structures. The selectivity of low Schottky barrier n-Si–Ni contacts for holes is enhanced *via* a nanoscale size-dependent pinch-off effect produced when surrounding high-barrier regions develop during device operation.

These demonstrations of probing the interfacial behavior of nanocontacts present a framework for studying the heterogeneity of structured polycrystalline semiconductors. Additionally, new insights into the pinch-off effect can be explored for semiconductor/catalyst interfaces, designing interfaces that leverage nanoscale effects to induce high carrier selectivity and yield higher performance photoelectrodes.

## 6.5 Conclusion

Metal oxide co-catalyst layers improve the PEC performance of photoanodes for water oxidation. To design better interfaces, it is important to measure and understand their roles and functions. Identifying the co-catalyst layer's primary influence(s) on photoelectrode performance informs researchers on what could be further optimized and to what extent. Although significant progress has been made in understanding the role of metal oxide co-catalyst nanolayers on photoelectrodes, a variety of parameters and systems need further study. The performance of the best-reported photoanodes is also still far from optimal.

Because the co-catalyst nanolayers collect photogenerated holes from the surface of photoanodes, future research could be focused on improving the semiconductor and co-catalyst junction by reducing the forward electronic current while still allowing for sufficiently facile hole collection using interfacial layers. This strategy is often used for solid-state solar cells and can be applied in PEC cells to increase the interface carrier selectivity.[86,87] Mechanisms by which such an interfacial layer could reduce the forward electron current at the semiconductor and co-catalyst junction include increasing the electrostatic barrier height (thereby reducing the density of surface majority electrons), passivating surface states (which reduces the number of acceptor states for surface electrons to transfer into), or adding a tunneling barrier (which decreases the transmission coefficient for electrons). The results also indicate that the electrical conductivity of the catalyst, its stability/transformation under electrochemical conditions, and its kinetics for the OER are all important considerations when designing photoelectrodes.

On the other hand, molecular insights into the catalytic reaction mechanism at the semiconductor and co-catalyst layer interface would be useful. PEC measurements could be coupled with spectroscopy to gain *operando* time-resolved and spatially resolved information on the semiconductor and co-catalyst layer under operation.[69,88–90] Computational approaches can also be used to understand the interfacial properties from an atomic or molecular level.[91,92] The microscopic understanding and macroscopic measurements would together contribute to building PEC devices with better performance.

## 6.6 Outlook

In future endeavors, it is very important to understand the elementary and multistep (photo)electrocatalytic electron- and ion-transfer processes at the semiconductor/co-catalyst interface. In addition to the charge-transfer

process, *operando* chemical information on the semiconductor, the co-catalyst layer, and the electrolyte need to be collected. Recently, pulsed voltammetry, *operando* X-ray absorption spectroscopy, and computational work were combined to resolve the relative contributions from chemical and electrostatic driving forces in electrochemical water oxidation with an $IrO_x$ catalyst.[93,94] The contributions critically depend on the electronic structures of the solid catalyst layers, hence understanding the electronic properties of the co-catalyst layers on the surface of a semiconductor, especially under *operando* conditions, is important. *Operando* (photo)electrochemical spectroscopic techniques such as infrared (IR) and Raman spectroscopy, X-ray absorption, and photoelectron spectroscopy (XPS) will be useful in determining the molecular bond vibrational modes, atomic bond distances, and valence states of elements in the catalyst layer. In addition to the catalyst layer, similar information could also be acquired on the semiconducting photoelectrodes. *In situ* $^1$H NMR studies have been carried out to investigate the reaction mechanism of a redox flow battery.[90] This technique could potentially be used to study the protons in the electrolytes in (photo)electrochemical water-splitting reactions. All of these *operando* measurements will add more chemical information on the interfaces among the photoelectrodes, the co-catalyst layer, and the electrolyte. Other microscopic changes such as accurate local pH changes at the semiconductor and co-catalyst interface and within the co-catalyst layer are unattainable with current techniques but are important to understand. Future developments in this direction would enrich the understanding of PEC cells.

## Acknowledgements

The work at the University of Oregon was funded by the Department of Energy, Basic Energy Sciences (award No. DE-SC0014279). J.Q. acknowledges support from start-up funds provided by San Francisco State University during the preparation of this chapter.

## References

1. M. G. Walter, E. L. Warren, J. R. McKone, S. W. Boettcher, Q. Mi, E. A. Santori and N. S. Lewis, *Chem. Rev.*, 2010, **110**, 6446.
2. P. De Luna, C. Hahn, D. Higgins, S. A. Jaffer, T. F. Jaramillo and E. H. Sargent, *Science*, 2019, **364**, 3506.
3. A. Fujishima and K. Honda, *Nature*, 1972, **238**, 37.
4. D. Kang, T. W. Kim, S. R. Kubota, A. C. Cardiel, H. G. Cha and K.-S. Choi, *Chem. Rev.*, 2015, **115**, 12839.
5. W. A. Smith, I. D. Sharp, N. C. Strandwitz and J. Bisquert, *Energy Environ. Sci.*, 2015, **8**, 2851.

6. L. M. Peter, in *Photocatalysis: Fundamentals and Perspectives*, ed. J. Schneider, D. Bahnemann, J. Ye, G. L. Puma and D. D. Dionysiou, Royal Society of Chemistry, London, 2016, ch. 1, pp. 1–28.
7. D. K. Lee, D. Lee, M. A. Lumley and K.-S. Choi, *Chem. Soc. Rev.*, 2019, **48**, 2126.
8. D. R. Gamelin, *Nat. Chem.*, 2012, **4**, 965.
9. M. Barroso, A. J. Cowan, S. R. Pendlebury, M. Grätzel, D. R. Klug and J. R. Durrant, *J. Am. Chem. Soc.*, 2011, **133**, 14868.
10. A. J. Bard, A. B. Bocarsly, F. R. F. Fan, E. G. Walton and M. S. Wrighton, *J. Am. Chem. Soc.*, 1980, **102**, 3671.
11. B. Klahr, S. Gimenez, F. Fabregat-Santiago, T. Hamann and J. Bisquert, *J. Am. Chem. Soc.*, 2012, **134**, 4294.
12. A. Kumar, P. G. Santangelo and N. S. Lewis, *J. Phys. Chem.*, 1992, **96**, 834.
13. K. Sivula and R. van de Krol, *Nat. Rev. Mater.*, 2016, **1**, 15010.
14. S. Hoang, S. Guo, N. T. Hahn, A. J. Bard and C. B. Mullins, *Nano Lett.*, 2012, **12**, 26.
15. W. H. Leng, P. R. F. Barnes, M. Juozapavicius, B. C. O'Regan and J. R. Durrant, *J. Phys. Chem. Lett.*, 2010, **1**, 967.
16. W. Li, P. Da, Y. Zhang, Y. Wang, X. Lin, X. Gong and G. Zheng, *ACS Nano*, 2014, **8**, 11770.
17. G. Wang, Y. Ling, H. Wang, X. Yang, C. Wang, J. Z. Zhang and Y. Li, *Energy Environ. Sci.*, 2012, **5**, 6180.
18. R. Franking, L. Li, M. A. Lukowski, F. Meng, Y. Tan, R. J. Hamers and S. Jin, *Energy Environ. Sci.*, 2013, **6**, 500.
19. A. Kay, I. Cesar and M. Grätzel, *J. Am. Chem. Soc.*, 2006, **128**, 15714.
20. A. Kudo, K. Omori and H. Kato, *J. Am. Chem. Soc.*, 1999, **121**, 11459.
21. K. Sayama, A. Nomura, T. Arai, T. Sugita, R. Abe, M. Yanagida, T. Oi, Y. Iwasaki, Y. Abe and H. Sugihara, *J. Phys. Chem. B*, 2006, **110**, 11352.
22. S. Wang, T. He, P. Chen, A. Du, K. Ostrikov, W. Huang and L. Wang, *Adv. Mater.*, 2020, **32**, 2001385.
23. J. E. Yourey, K. J. Pyper, J. B. Kurtz and B. M. Bartlett, *J. Phys. Chem. C*, 2013, **117**, 8708.
24. Y. Gao and T. W. Hamann, *J. Phys. Chem. Lett.*, 2017, **8**, 2700.
25. P. Zhang, J. Zhang and J. Gong, *Chem. Soc. Rev.*, 2014, **43**, 4395.
26. M. Woodhouse and B. A. Parkinson, *Chem. Soc. Rev.*, 2009, **38**, 197.
27. I. E. Castelli, T. Olsen, S. Datta, D. D. Landis, S. Dahl, K. S. Thygesen and K. W. Jacobsen, *Energy Environ. Sci.*, 2012, **5**, 5814.
28. S. Chen and L.-W. Wang, *Chem. Mater.*, 2012, **24**, 3659.
29. V. E. Henrich and P. A. Cox, *The Surface Science of Metal Oxides*, Cambridge University Press, Cambridge, 2000.
30. J. K. Cooper, S. Gul, F. M. Toma, L. Chen, P.-A. Glans, J. Guo, J. W. Ager, J. Yano and I. D. Sharp, *Chem. Mater.*, 2014, **26**, 5365.
31. C. Lohaus, A. Klein and W. Jaegermann, *Nat. Commun.*, 2018, **9**, 4309.
32. J. Y. Kim, G. Magesh, D. H. Youn, J.-W. Jang, J. Kubota, K. Domen and J. S. Lee, *Sci. Rep.*, 2013, **3**, 2681.

33. S. R. Pendlebury, X. Wang, F. Le Formal, M. Cornuz, A. Kafizas, S. D. Tilley, M. Grätzel and J. R. Durrant, *J. Am. Chem. Soc.*, 2014, **136**, 9854.
34. M. Barroso, S. R. Pendlebury, A. J. Cowan and J. R. Durrant, *Chem. Sci.*, 2013, **4**, 2724.
35. B. Klahr, S. Gimenez, F. Fabregat-Santiago, J. Bisquert and T. W. Hamann, *J. Am. Chem. Soc.*, 2012, **134**, 16693.
36. S. P. Berglund, D. W. Flaherty, N. T. Hahn, A. J. Bard and C. B. Mullins, *J. Phys. Chem. C*, 2011, **115**, 3794.
37. Y. Kuang, Q. Jia, H. Nishiyama, T. Yamada, A. Kudo and K. Domen, *Adv. Energy Mater.*, 2016, **6**, 1501645.
38. F. M. Toma, J. K. Cooper, V. Kunzelmann, M. T. McDowell, J. Yu, D. M. Larson, N. J. Borys, C. Abelyan, J. W. Beeman, K. M. Yu, J. Yang, L. Chen, M. R. Shaner, J. Spurgeon, F. A. Houle, K. A. Persson and I. D. Sharp, *Nat. Commun.*, 2016, **7**, 12012.
39. S. Zhang, M. Rohloff, O. Kasian, A. M. Mingers, K. J. J. Mayrhofer, A. Fischer, C. Scheu and S. Cherevko, *J. Phys. Chem. C*, 2019, **123**, 23410.
40. J. A. Seabold and K.-S. Choi, *J. Am. Chem. Soc.*, 2012, **134**, 2186.
41. N. Guijarro, M. S. Prévot and K. Sivula, *Phys. Chem. Chem. Phys.*, 2015, **17**, 15655.
42. M. B. Stevens, C. D. M. Trang, L. J. Enman, J. Deng and S. W. Boettcher, *J. Am. Chem. Soc.*, 2017, **139**, 11361.
43. M. B. Stevens, L. J. Enman, A. S. Batchellor, M. R. Cosby, A. E. Vise, C. D. M. Trang and S. W. Boettcher, *Chem. Mater.*, 2017, **29**, 120.
44. J.-W. Jang, C. Du, Y. Ye, Y. Lin, X. Yao, J. Thorne, E. Liu, G. McMahon, J. Zhu, A. Javey, J. Guo and D. Wang, *Nat. Commun.*, 2015, **6**, 7447.
45. D. K. Zhong, M. Cornuz, K. Sivula, M. Grätzel and D. R. Gamelin, *Energy Environ. Sci.*, 2011, **4**, 1759.
46. T. W. Kim and K.-S. Choi, *Science*, 2014, **343**, 990.
47. J. Qiu, H. Hajibabaei, M. R. Nellist, F. A. L. Laskowski, T. W. Hamann and S. W. Boettcher, *ACS Cent. Sci.*, 2017, **3**, 1015.
48. S. C. Riha, B. M. Klahr, E. C. Tyo, S. Seifert, S. Vajda, M. J. Pellin, T. W. Hamann and A. B. F. Martinson, *ACS Nano*, 2013, **7**, 2396.
49. K. J. McDonald and K.-S. Choi, *Chem. Mater.*, 2011, **23**, 1686.
50. J. Qiu, H. Hajibabaei, M. R. Nellist, F. A. L. Laskowski, S. Z. Oener, T. W. Hamann and S. W. Boettcher, *ACS Energy Lett.*, 2018, **3**, 961.
51. R. D. L. Smith, M. S. Prévot, R. D. Fagan, Z. Zhang, P. A. Sedach, M. K. J. Siu, S. Trudel and C. P. Berlinguette, *Science*, 2013, **340**, 60.
52. D. K. Zhong and D. R. Gamelin, *J. Am. Chem. Soc.*, 2010, **132**, 4202.
53. M. B. Stevens, L. J. Enman, E. H. Korkus, J. Zaffran, C. D. M. Trang, J. Asbury, M. G. Kast, M. C. Toroker and S. W. Boettcher, *Nano Res.*, 2019, **12**, 2288.
54. J. Deng, M. R. Nellist, M. B. Stevens, C. Dette, Y. Wang and S. W. Boettcher, *Nano Lett.*, 2017, **17**, 6922.
55. D. K. Zhong, S. Choi and D. R. Gamelin, *J. Am. Chem. Soc.*, 2011, **133**, 18370.

56. C. Zachäus, F. F. Abdi, L. M. Peter and R. van de Krol, *Chem. Sci.*, 2017, **8**, 3712.
57. Y. Ma, A. Kafizas, S. R. Pendlebury, F. Le Formal and J. R. Durrant, *Adv. Funct. Mater.*, 2016, **26**, 4951.
58. J. E. Thorne, J.-W. Jang, E. Y. Liu and D. Wang, *Chem. Sci.*, 2016, **7**, 3347.
59. M. Barroso, C. A. Mesa, S. R. Pendlebury, A. J. Cowan, T. Hisatomi, K. Sivula, M. Gratzel, D. R. Klug and J. R. Durrant, *Proc. Natl. Acad. Sci. U. S. A.*, 2012, **109**, 15640.
60. E. H. Rhoderick and R. H. Williams, *Metal-semiconductor Contacts*, Oxford University Press, Oxford, United Kingdom, 2nd edn, 1988.
61. S. Zou, M. S. Burke, M. G. Kast, J. Fan, N. Danilovic and S. W. Boettcher, *Chem. Mater.*, 2015, **27**, 8011.
62. F. Lin and S. W. Boettcher, *Nat. Mater.*, 2014, **13**, 81.
63. T. J. Mills, F. Lin and S. W. Boettcher, *Phys. Rev. Lett.*, 2014, **112**, 148304.
64. F. A. L. Laskowski, M. R. Nellist, J. Qiu and S. W. Boettcher, *J. Am. Chem. Soc.*, 2019, **141**, 1394.
65. F. A. L. Laskowski, M. R. Nellist, R. Venkatkarthick and S. W. Boettcher, *Energy Environ. Sci.*, 2017, **10**, 570.
66. T. J. Mills, F. A. L. Laskowski, C. Dette, M. R. Nellist, F. Lin and S. W. Boettcher, 2017, *arXiv*:1707.03112.
67. L. Trotochaud, S. L. Young, J. K. Ranney and S. W. Boettcher, *J. Am. Chem. Soc.*, 2014, **136**, 6744.
68. B. Klahr, S. Gimenez, F. Fabregat-Santiago, J. Bisquert and T. W. Hamann, *Energy Environ. Sci.*, 2012, **5**, 7626.
69. F. Malara, M. Fracchia, H. Kmentová, R. Psaro, A. Vertova, D. Oliveira de Souza, G. Aquilanti, L. Olivi, P. Ghigna, A. Minguzzi and A. Naldoni, *ACS Catal.*, 2020, **10**, 10476.
70. Y. W. Chen, J. D. Prange, S. Dühnen, Y. Park, M. Gunji, C. E. D. Chidsey and P. C. McIntyre, *Nat. Mater.*, 2011, **10**, 539.
71. A. G. Scheuermann, J. P. Lawrence, K. W. Kemp, T. Ito, A. Walsh, C. E. D. Chidsey, P. K. Hurley and P. C. McIntyre, *Nat. Mater.*, 2016, **15**, 99.
72. A. G. Scheuermann, J. D. Prange, M. Gunji, C. E. D. Chidsey and P. C. McIntyre, *Energy Environ. Sci.*, 2013, **6**, 2487.
73. I. A. Digdaya, G. W. P. Adhyaksa, B. J. Trześniewski, E. C. Garnett and W. A. Smith, *Nat. Commun.*, 2017, **8**, 15968.
74. M. J. Kenney, M. Gong, Y. Li, J. Z. Wu, J. Feng, M. Lanza and H. Dai, *Science*, 2013, **342**, 836.
75. L. Trotochaud, T. J. Mills and S. W. Boettcher, *J. Phys. Chem. Lett.*, 2013, **4**, 931.
76. T. W. Hamann, *Nat. Mater.*, 2014, **13**, 3.
77. M. R. Nellist, F. A. L. Laskowski, J. Qiu, H. Hajibabaei, K. Sivula, T. W. Hamann and S. W. Boettcher, *Nat. Energy*, 2018, **3**, 46.
78. F. A. L. Laskowski, S. Z. Oener, M. R. Nellist, A. M. Gordon, D. C. Bain, J. L. Fehrs and S. W. Boettcher, *Nat. Mater.*, 2020, **19**, 69.

79. M. R. Nellist, Y. Chen, A. Mark, S. Gödrich, C. Stelling, J. Jiang, R. Poddar, C. Li, R. Kumar, G. Papastavrou, M. Retsch, B. S. Brunschwig, Z. Huang, C. Xiang and S. W. Boettcher, *Nanotechnology*, 2017, **28**, 095711.
80. C. Costentin, T. R. Porter and J.-M. Savéant, *J. Am. Chem. Soc.*, 2016, **138**, 5615.
81. G. M. Carroll, D. K. Zhong and D. R. Gamelin, *Energy Environ. Sci.*, 2015, **8**, 577.
82. M. R. Nellist, J. Qiu, F. A. L. Laskowski, F. M. Toma and S. W. Boettcher, *ACS Energy Lett.*, 2018, **3**, 2286.
83. Y. Ma, S. R. Pendlebury, A. Reynal, F. Le Formal and J. R. Durrant, *Chem. Sci.*, 2014, **5**, 2964.
84. K. Oh, V. Dorcet, B. Fabre and G. Loget, *Adv. Energy Mater.*, 2020, **10**, 1902963.
85. G. Loget, B. Fabre, S. Fryars, C. Mériadec and S. Ababou-Girard, *ACS Energy Lett.*, 2017, **2**, 569.
86. C. D. Weber, D. P. Stay and M. C. Lonergan, *J. Phys. Chem. C*, 2016, **120**, 19951.
87. J. Geissbühler, J. Werner, S. Martin de Nicolas, L. Barraud, A. Hessler-Wyser, M. Despeisse, S. Nicolay, A. Tomasi, B. Niesen, S. De Wolf and C. Ballif, *Appl. Phys. Lett.*, 2015, **107**, 081601.
88. M. F. Lichterman, S. Hu, M. H. Richter, E. J. Crumlin, S. Axnanda, M. Favaro, W. Drisdell, Z. Hussain, T. Mayer, B. S. Brunschwig, N. S. Lewis, Z. Liu and H.-J. Lewerenz, *Energy Environ. Sci.*, 2015, **8**, 2409.
89. C. Pasquini, L. D'Amario, I. Zaharieva and H. Dau, *J. Chem. Phys.*, 2020, **152**, 194202.
90. E. W. Zhao, T. Liu, E. Jónsson, J. Lee, I. Temprano, R. B. Jethwa, A. Wang, H. Smith, J. Carretero-González, Q. Song and C. P. Grey, *Nature*, 2020, **579**, 224.
91. J. Zhang, J. Liu, L. Xi, Y. Yu, N. Chen, S. Sun, W. Wang, K. M. Lange and B. Zhang, *J. Am. Chem. Soc.*, 2018, **140**, 3876.
92. R. Rousseau, V.-A. Glezakou and A. Selloni, *Nat. Rev. Mater.*, 2020, **5**, 460.
93. H. N. Nong, L. J. Falling, A. Bergmann, M. Klingenhof, H. P. Tran, C. Spöri, R. Mom, J. Timoshenko, G. Zichittella, A. Knop-Gericke, S. Piccinin, J. Pérez-Ramírez, B. R. Cuenya, R. Schlögl, P. Strasser, D. Teschner and T. E. Jones, *Nature*, 2020, **587**, 408.
94. S. W. Boettcher and Y. Surendranath, *Nat. Catal.*, 2021, **4**, 4.

CHAPTER 7

# *Design Principles for Oxide-encapsulated Electrocatalysts*

D. V. ESPOSITO,*[a] V. GUILIMONDI,[a] J. G. VOS[b,c] AND M. T. M. KOPER[c]

[a] Chemical Engineering Department, Columbia University in the City of New York, 500 West 120th Street, New York, NY 10025, USA; [b] Magneto Special Anodes BV (an Evoqua Brand), Calandstraat 109, 3125 BA Schiedam, The Netherlands; [c] Leiden Institute of Chemistry, Leiden University, PO Box 9502, 2300 RA Leiden, The Netherlands
*Email: de2300@columbia.edu

## 7.1 Introduction

Electrocatalysts are central to the operation of electrolysis and fuel cell technologies owing to their ability to lower energy barriers and guide product selectivity for electrochemical reactions. As depicted in Figure 7.1a for a conventional heterogeneous electrocatalyst, electrochemical reactions necessarily involve transfer of one or more electrons across the interface between the electrocatalyst and an ion-conducting electrolyte phase. By controlling the electric potential applied to the electrocatalyst, and therefore the electrochemical potential of electrons therein, the rates of electrochemical reactions can be modulated by many orders of magnitude at room temperature. Ideally, an electrocatalyst is comprised of Earth-abundant elements and is capable of catalyzing the reaction of interest at high current density with minimized kinetic overpotential losses, 100% selectivity towards the desired product species, and minimal loss of activity for thousands of hours of operation. Unfortunately, there are very few examples of

Energy and Environment Series No. 30
Ultrathin Oxide Layers for Solar and Electrocatalytic Systems
Edited by Heinz Frei and Daniel V. Esposito

Published by the Royal Society of Chemistry, www.rsc.org

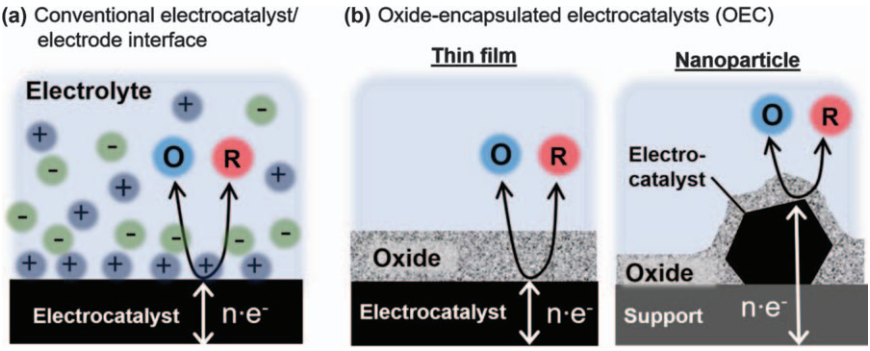


**Figure 7.1** Schematic side views of (a) the interface between a conventional electrocatalyst and liquid electrolyte, and (b) thin-film and nanoparticle-based electrocatalysts that have been encapsulated by ultrathin permeable oxide overlayers. All schematics show a generic electrochemical reaction involving oxidant (O) and reductant (*R*) species; supporting electrolyte ions are illustrated only in (a).

electrocatalysts that meet all of these criteria for industrially relevant applications.

Traditionally, electrocatalysts have often been viewed as having abrupt interfaces with liquid-phase electrolytes, and research efforts have been focused on exploring how new compositional and structural characteristics of electrocatalyst materials alter the energetics associated with their interactions with reactive intermediates at the electrocatalyst/electrolyte interface. This emphasis on understanding the energetics of reactant–electrocatalyst interactions has been central to many commonly employed electrocatalyst design strategies aided by density functional theory (DFT),[1,2] but many of these studies have ignored the fact that there are two tunable sides of the electrocatalyst/electrolyte interface. In recent years, researchers have become increasingly aware of opportunities to improve catalytic activity and selectivity through careful design of ''the other side'' of the interface, with numerous studies demonstrating that factors such as choice of supporting electrolyte ions,[3] the use of ionic liquids,[4] and surface modification with semipermeable overlayers[5,6] can drastically affect electrocatalyst performance. By expanding the electrocatalyst design space to include the electrolyte, additional control knobs are made possible in 3D space that can allow advanced electrocatalytic functionalities and overcome so-called scaling relations that limit the achievable activities and selectivities of traditional electrocatalysts.[7,8]

This chapter explores electrocatalyst architectures for which the electrolyte side of the electrocatalyst/electrolyte interface has been modified by the presence of an ultrathin, semipermeable oxide overlayer. Figure 7.1b illustrates such oxide-encapsulated electrocatalysts (OECs) in both thin-film and nanoparticle geometries of the electrocatalyst. By leveraging the diverse synthetic tools and rich materials chemistry of oxides discussed in more

detail in other chapters, OECs offer a highly tunable platform for designing electrocatalysts that can achieve simultaneously high activity, selectivity, and durability. However, the additional control knobs offered by oxide overlayers are both a blessing and a curse, as their presence can significantly complicate the task of rationally designing an electrocatalyst. Some of the additional complexity originates from the fact that encapsulated electrocatalysts require at least four extra elementary steps to occur as a part of the overall electrochemical reaction scheme shown in Figure 7.2. In addition to the transport and kinetic steps associated with a conventional electrocatalyst, encapsulated electrocatalysts also require mass transfer of reactants and products across the liquid electrolyte/overlayer interface and across the overlayer itself. It follows that a thorough understanding of transport phenomena is essential to the rational design of encapsulated electrocatalysts. In contrast, the design of conventional electrocatalysts is often carried out entirely on the basis of thermodynamics and reaction kinetics. These additional transport steps can permit advanced functionalities in encapsulated electrocatalysts, but can also lead to undesirable concentration gradients and associated overpotential losses. A primary objective of this chapter is to present guidelines based on fundamental transport and electrocatalysis principles to guide the design of oxide overlayers that maximize the desirable properties of an encapsulated electrocatalyst at target operating conditions while minimizing undesirable side-effects.

In principle, the overlayer used in an encapsulated electrocatalyst does not need to be an oxide, as evidenced by numerous studies that have used

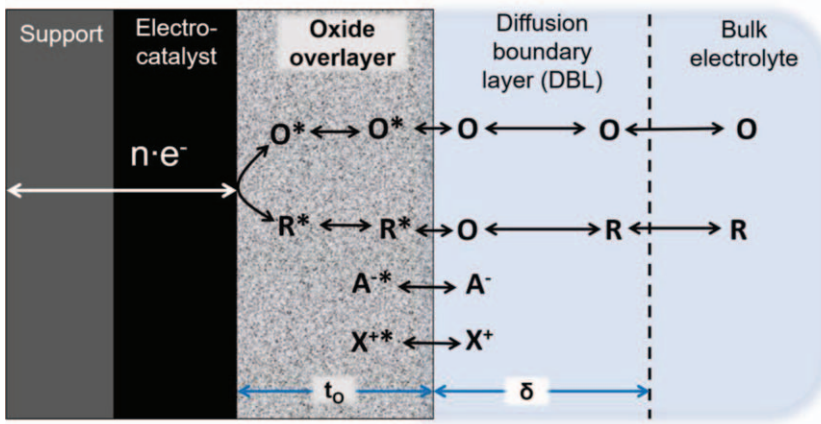


**Figure 7.2** Side view of an oxide-encapsulated electrocatalyst showing key transport phenomena associated with an electrochemical reaction between O and R occurring at the electrocatalytically active buried interface between the electrocatalyst and oxide overlayer. The thicknesses of the overlayer ($t_o$) and diffusion boundary layer ($\delta$) are not drawn to scale. $A^-$ and $X^+$ represent anions and cations, respectively, and an asterisk (*) is used to identify a species located within the oxide overlayer.

polymers[9,10] or low-dimensional van der Waals materials.[11–13] Although these other materials classes also warrant further exploration as permeable overlayers, this chapter is focused on electrocatalysts that have been encapsulated by ultrathin oxides for many of the reasons enumerated in Chapter 1. Namely, many oxides possess (i) excellent electrochemical and chemical stability, (ii) tunable porosity, (iii) diverse materials chemistry, and (iv) desirable electronic properties. The tunable porosity and unique materials chemistry of many oxide materials can be valuable for achieving selective transport properties in OECs, while also allowing electronic and steric manipulation of catalytic active sites at the buried interface. In terms of electronic properties, many oxide materials are classified as semiconductors or insulators. Although poor electronic conductivity is typically undesirable for electrocatalytic applications, such materials are desirable for OECs because an electronically insulating but ionically conductive overlayer can be conducive for electrochemical reactions to occur at the electrocatalytic buried interface of an OEC rather than the outer surface of the overlayer. In some reaction schemes, a limited amount of electronic conductivity may be desirable; in these instances, insulating oxides can be doped with impurity metals or non-metals such as nitrogen, carbon, or sulfur in order to tune their electronic properties and/or those of active sites at the buried interface.

To date, at least 10 different types of oxide materials have been used as permeable overlayers in electrocatalysis and photocatalysis, including oxides based on Ce,[14] Cr,[15,16] La,[17] Mn,[18] Mg,[19] Mo,[20] Ni,[21] Si,[22] Ti,[23] and V.[24] Almost all known examples are binary oxides, although there is no reason why ternary or quaternary oxides could not also be used as overlayers for (photo)electrocatalysts. One of the most successfully employed oxide overlayer materials is chromium(III) oxide ($Cr^{III}O_x$),[15] which has been extensively used to suppress the parasitic reduction of hypochlorous acid in the chlorate industry and has proven to be effective at blocking back-reactions during photocatalytic water splitting.[16] However, the formation of $Cr^{III}O_x$ films involves the highly toxic Cr(VI) precursor, motivating the chlorate industry to phase out its use. Fortunately, there are many other non-toxic oxide materials that have shown promise as overlayer materials. For example, molybdenum oxide ($MoO_x$)-[20] and silicon oxide ($SiO_x$)-encapsulated[25] Pt electrocatalysts have been shown to be effective as hydrogen-selective cathodes capable of suppressing the oxygen reduction reaction (ORR), making them of interest for water splitting in undivided cells. $SiO_x$ has also proven to be an effective OEC overlayer material for blocking catalyst poisons,[22] stabilizing ORR electrocatalysts,[26–28] and improving the activity of alcohol oxidation electrocatalysts.[29] $SiO_x$ and manganese oxide ($MnO_x$) overlayers have also been found to increase the selectivity of the oxygen evolution reaction in chloride-containing electrolytes, where the evolution of chlorine is facile.[18,30] More detailed accounts of the use of many of the above-mentioned oxide coatings for oxide-encapsulated photocatalysts can be found in Chapter 10. As the concept of tunable OECs has only very recently arisen, it can be anticipated that many new overlayer materials will be

identified in the coming years owing to the potentially vast number of oxide materials that could form effective overlayers.

The remainder of this chapter is structured as follows. In Section 7.2, the fundamentals of species transport through oxide overlayers are presented, including a description of commonly observed transport mechanisms and models used to describe species fluxes. Using a continuum model for planar encapsulated electrocatalysts, the relationships between species permeabilities, overlayer thickness, bulk electrolyte conditions, and concentration overpotentials are derived. These governing transport equations are then used in Section 7.3 to describe current density–potential relationships for OECs that account for both concentration and kinetic overpotential losses. In addition to a discussion of the mechanisms by which overlayers can impact reaction kinetics in OECs, two case studies analyzing transport-mediated selectivity effects are presented. Next, Section 7.4 describes the benefits of oxide overlayers for enhancing the stability of OECs, followed by an overview of experimental methods and best practices for characterizing the transport and kinetic properties of OECs in Section 7.5. Collectively, it is the aim of Sections 7.2–7.5 to present researchers with a modeling framework and experimental toolkit that can be used to assess the performance of OECs and establish design rules for overlayers that can be used to guide the discovery and optimization of this emerging electrocatalyst architecture. Finally, opportunities and challenges associated with the development of OECs for real-world electrochemical energy applications are discussed.

## 7.2 Species Transport Through Oxide Overlayers

### 7.2.1 Transport Fundamentals

One of the governing equations for describing transport phenomena in electrochemical systems is the Nernst–Planck equation, which describes the flux of a species $j$, $\boldsymbol{N_j}$, as follows:

$$\boldsymbol{N_j} = -D_j \nabla C_j - \frac{z_j F}{RT} D_j C_j \nabla \phi + C_j \mathbf{v} \tag{7.1}$$

where $D_j$ is the diffusivity of species $j$, $C_j$ is its concentration, $z_j$ is its charge, $F$ is the Faraday constant, $R$ is the gas constant, $T$ is absolute temperature, $\boldsymbol{v}$ is bulk fluid velocity, and $\phi$ is the potential. This equation follows from dilute solution theory, which assumes there are only interactions between the dissolved species and the solvent.[31] In eqn (7.1), the first term describes the flux associated with diffusion and the second and third terms give the species flux caused by migration and convention, respectively. Convection is relevant to OEC operation because the bulk fluid velocity impacts the thickness of the diffusion boundary layer ($\delta_{\mathrm{DBL}}$) and can influence bubble dynamics for multiphase flows such as gas-evolving reactions. However, convection should be negligible within the DBL and overlayer,

where the diffusion and migration terms can be expected to be dominant. These two processes are driven by concentration ($\nabla C_j$) and potential gradients ($\nabla \phi$), respectively. The flux through the DBL due to migration tends to be insignificant for high supporting electrolyte concentrations, which is often the case for electrochemical and photoelectrochemical applications. Nonetheless, migration should not be blindly ignored for OEC-based electrodes, for which migration can be expected to be important if the solubilities of supporting electrolyte ions within the overlayer are very low compared with those of the electroactive species. Although this chapter largely ignores migration, it is easy to envision scenarios where it could be important in oxide overlayers.

For both migration and diffusion, a species diffusion coefficient serves as a proportionality constant that has a large impact on its flux across the overlayer of an OEC. $D_j$ is a measure of how easily molecule $j$ is able to travel along a concentration or potential gradient, and is strongly impacted by the characteristics of both the species of interest and the medium through which it is transported. In aqueous electrolytes, solute molecules typically have diffusion coefficients in the range $1\times10^{-6}$–$1\times10^{-5}$ $cm^2\ s^{-1}$.[32] However, diffusion coefficients for species within solids are often reduced by many orders of magnitude compared with those measured in a liquid electrolyte. Within solid materials, diffusion coefficients are often referred to as effective diffusion coefficients, $D_{e,j}$, which are highly dependent on (i) the structure and composition of the solid-state material, (ii) the characteristics of the species being transported inside it, and (iii) the mechanism by which transport is occurring. Depending on the specific material and permeant species of interest, different transport models may be suitable for describing species diffusivities. Figure 7.3 illustrates four commonly considered microscopic transport models for describing species transport in solid materials, including oxides. These models are not mutually exclusive, nor do they represent every known transport model and mechanism. While more extensive descriptions of these and other models can be found elsewhere,[33–35] brief qualitative descriptions are provided here to introduce basic transport concepts that can be used to model species transport in OEC overlayers.

### *7.2.1.1 Solution Diffusion Model*

As illustrated in Figure 7.3a, this model views the solid-state material of interest as a single homogeneous phase or solution within which the permeant is absorbed. This model is frequently used to describe transport in solids that do not have well-defined pores. Rather, permeant species must exist in the interstitial spaces or ''free volume elements'' that exist between host material atoms. Given the inherently atomic scale of such spaces, size-exclusion effects are commonly observed in materials that obey this model. Furthermore, permeant molecules entering the solid from the liquid phase often need to shed or partially shed their solvation shell.[34,36]

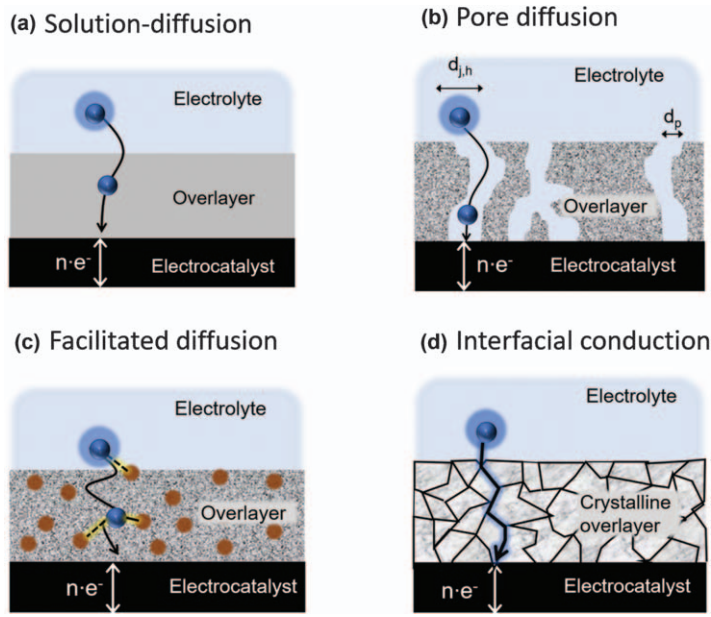


**Figure 7.3** Four commonly considered microscopic models for the transport of molecules through oxide materials, depicted for a generic electroactive molecule (blue spheres) passing through the ultrathin overlayer of an oxide-encapsulated electrocatalyst. The orange spheres in (c) represent carrier centers that form bonds with the permeant species.

### *7.2.1.2 Pore Diffusion*

Unlike the solution diffusion model, pore-diffusion models (Figure 7.3b) treat the solid material as a two-phase system, allowing them to account for heterogeneous properties at the single-pore level. Subject to the hydrophobic character of the pore interiors, such pores can support water channels, as is well known to be the case in many polymeric membranes such as Nafion.[37] Materials possessing pore diameters ($d_p$) that are larger than a molecule's hydrated diameter ($d_{j,h}$) may allow fully hydrated permeant species to enter the pores, but instances where $d_p < d_{j,h}$ are likely to require desolvation and permit selective transport *via* molecular sieving for species with different hydrated radii and solvation energies. Whether solvated or not, a permeant species within a pore can interact with pore walls in ways that support or suppress transport rates.

### *7.2.1.3 Facilitated Diffusion*

Here, chemical interactions between the permeant and solid-state material strongly impact the rate at which the former diffuses through the latter. As shown in Figure 7.3c, facilitated diffusion occurs when the permeant species forms chemical bonds with carrier centers (orange spheres) located within the overlayer matrix. One of the best known examples of facilitated diffusion in

oxides is for proton transport *via* a Grotthuss-like mechanism in which protons hop along the H-bonding network associated with bridging oxygen sites on the interior surfaces of an oxide.[38,39] Such hopping is generally favored by short hopping distances, although the orientation of adjacent carrier centers can also be important.[39] The frequency of hopping events in facilitated diffusion often coincides with the vibrational frequency associated with the bond between the permeant and host site atom(s), leading to isotope effects.[35]

#### 7.2.1.4 *Interfacial Diffusion*

This type of diffusion is most common in crystalline oxides that possess grain boundaries where interfacial chemistry/physics can allow preferential interfacial transport of ions along grain boundary interfaces that is more facile than bulk transport through the crystallites themselves (Figure 7.3d).[35] In materials for which interfacial conduction is preferred, such as perovskite oxide membranes for high-temperature cells, it is desirable to make the grain sizes as small as possible to maximize interfacial transport.[35]

#### 7.2.1.5 *Solubility Parameters and Permeabilities*

In cases where the solution diffusion and facilitated transport models are applicable, the solute or permeant species usually experiences substantial interaction with the solid-state material and can be thought of as being dissolved within it. As such, a permeant might exhibit very different properties within the overlayer than it does within the bulk liquid electrolyte. In particular, there could be significant differences in the bond coordination of the hydration shells, species polarity, and/or electronic structure once a species enters an overlayer. Collectively, the interactions between permeants and an overlayer, combined with electrode operating conditions and overlayer thickness, can greatly alter the concentration of permeant species within the overlayer compared with the bulk electrolyte. For an overlayer that is in equilibrium with a bulk electrolyte, the ratio of the concentration of species $j$ within the overlayer ($C_{j,\mathrm{o}}$) to that in the bulk electrolyte ($C_{j,\mathrm{b}}$) is given by the solubility parameter for that species ($S_j$):

$$S_j = \frac{C_{j,o}}{C_{j,\mathrm{b}}} \tag{7.2}$$

Both $S_j$ (unitless) and $D_{\mathrm{e},j}$ ($\mathrm{cm^2\,s^{-1}}$) have a large impact on the flux of species $j$ through an overlayer, but are frequently difficult to determine individually in experiments. For this reason, these two parameters are often multiplied together to give a single parameter called the species permeability, $P_j$ ($\mathrm{cm^2\,s^{-1}}$):

$$P_j = D_{\mathrm{e},j} S_j \tag{7.3}$$

Having reviewed the key principles that underlie species transport through ultrathin overlayers, we next present a simple continuum-level

model for describing mass transfer limiting current densities for OECs based on a simple planar geometry (Figure 7.1b).

### 7.2.2 Mass Transfer-limited Current Densities

At very large overpotentials, concentration gradients across the DBL and overlayer can become so significant that the reactant concentration approaches zero at the electrode surface. Under these conditions, the rate of reaction is entirely limited by transport of the limiting species to the electrode active sites, and the associated current density is referred to as the limiting current density ($i_{\text{lim}}$). In this section, expressions for $i_{\text{lim}}$ are derived for the three different cases of planar electrodes illustrated in Figure 7.4: (i) a bare electrocatalyst (BEC), (ii) an OEC with negligible concentration drop across the DBL, and (iii) an OEC with concentration drops across both the DBL and overlayer. In all three cases, it is assumed that transport of the limiting species within these layers occurs only by diffusion, for which eqn (7.1) becomes

$$\boldsymbol{N}_j = -D_j \nabla C_j \tag{7.4}$$

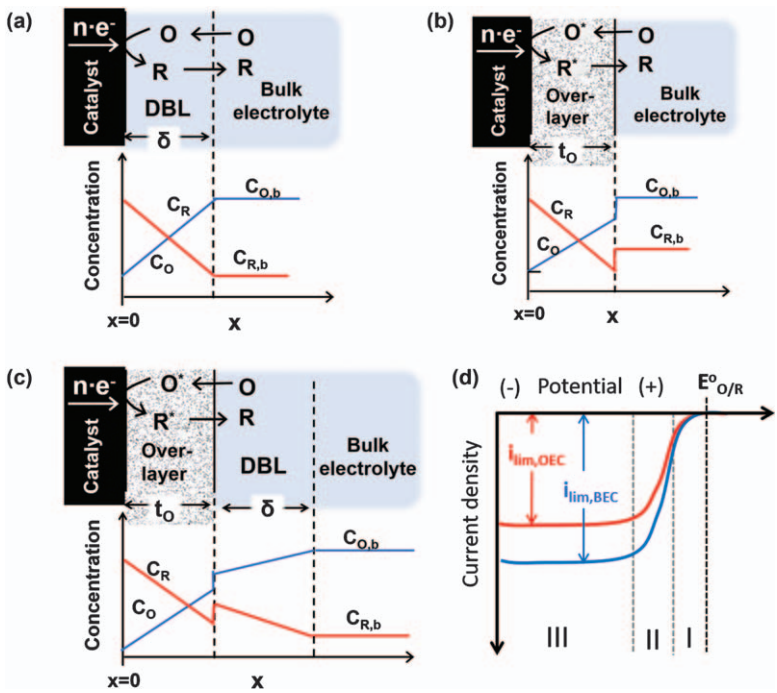


**Figure 7.4** Schematic side views of steady-state concentration overpotentials for planar electrodes consisting of (a) case 1, a bare electrocatalyst (BEC), (b) case 2, an OEC in the absence of a DBL, and (c) case 3, an OEC in the presence of a DBL. (d) Hypothetical current density–potential ($i$–$E$) curves for BEC and OEC electrodes, with potential regions corresponding to (I) kinetic, (II) mixed, and (III) mass transfer controlled current densities.

Using Faraday's law, species flux can then be expressed in terms of current density ($i$):

$$i = \frac{nF}{s_j} D_j \nabla C_j \tag{7.5}$$

where $s_j$ is the stoichiometric coefficient of species $j$, $n$ is the electron transfer number and $F$ is the Faraday constant. Throughout this chapter, $s_j$ is negative for oxidants and positive for reductants, such that oxidation and reduction currents are positive and negative, respectively. As illustrated in Figure 7.4, concentration gradients are linear for planar electrodes operating at steady state and without migration or edge effects. Thus, $\nabla C_j = \mathrm{d}C_j/\mathrm{d}x$ and is a constant for all cases considered here. The following subsections consider the limiting reactant to be the oxidant species, O, such that $j = \mathrm{O}$ and $s_j = -1$ in eqn (7.5).

### 7.2.2.1 Case 1: Bare Electrocatalyst (BEC)

For the bare electrode (Figure 7.4a), the only mass transfer resistance is that associated with diffusion of species $j$ across the DBL of thickness $\delta$. It follows that a concentration gradient only exists within the DBL such that eqn (7.5) becomes

$$i = -nFD_{\mathrm{O}} \frac{C_{\mathrm{O,b}} - C_{\mathrm{O}}(x=0)}{\delta} \tag{7.6}$$

where $D_{\mathrm{O}}$ is the diffusion coefficient of O in the liquid electrolyte and $\mathrm{d}C_{\mathrm{O}}/\mathrm{d}x$ has been expressed as a finite difference between the concentration of the oxidant in the bulk electrolyte, $C_{\mathrm{O,b}}$, and its concentration at the electrode/electrolyte interface, $C_{\mathrm{O}}(x=0)$, divided by $\delta$. Under mass transfer limiting conditions, $C_{\mathrm{O}}(x=0)$ approaches zero, and $i_{\mathrm{lim}}$ associated with the DBL, $i_{\mathrm{lim,DBL}}$, is given by

$$i_{\mathrm{lim,DBL}} = -nFk_{\mathrm{c,DBL}} C_{\mathrm{O,b}} \tag{7.7}$$

where $k_{\mathrm{c,DBL}} = D_j/\delta$ is defined here as the mass transfer coefficient for diffusion of species $j$ across the DBL.

### 7.2.2.2 Case 2: OEC Without Diffusion Boundary Layer

If the resistance to mass transfer across the DBL is negligible compared to that associated with the OEC overlayer of thickness $t_{\mathrm{o}}$, then $C_{\mathrm{O}}(x) \approx C_{\mathrm{O,b}}$ for $x > t_{\mathrm{o}}$, and eqn (7.5) can be applied to the overlayer to give

$$i = -nFD_{\mathrm{e,O,o}} \frac{S_{\mathrm{O}} C_{\mathrm{O,b}} - C_{\mathrm{O,o}}(x=0)}{t_{\mathrm{o}}} \tag{7.8}$$

where $D_{\mathrm{e,O,o}}$ is the effective diffusion coefficient of species O within the overlayer, $C_{\mathrm{O,o}}$ is the concentration of species O inside the overlayer, and

$dC_O/dx$ has been expressed as a finite difference for a linear concentration gradient. The solubility parameter for the oxidant, $S_O$, defined in eqn (7.2), is introduced to account for the difference in $C_O$ within the overlayer and bulk electrolyte at $x = t_o$. At mass transfer limiting conditions, $C_{O,o}(x = 0) \approx 0$ M such that the limiting current density associated with diffusion across the overlayer, $i_{lim,o}$, is given by

$$i_{lim,o} = -nFP_O\frac{C_{O,b}}{t_o} \tag{7.9}$$

where the product of $D_{e,O,o}$ and $S_O$ has been replaced with $P_O$ according to eqn (7.3). Eqn (7.9) can also be written in terms of $k_{c,o} = P_j/t_o$, the mass transfer coefficient for diffusion of $j$ across the overlayer.

### *7.2.2.3 Case 3: OEC With Diffusion Boundary Layer*

Often, mass transfer resistances associated with both the overlayer and DBL are important. Under steady-state conditions, the flux of species $j$ in the DBL must be equal to that in the overlayer:

$$\boldsymbol{N_j = N_{j,DBL} = N_{j,o}} \tag{7.10}$$

Considering the oxidant species, O, as the limiting species, this equation can be rewritten in terms of $i$ and using finite difference expressions to describe the $\nabla C_j$ terms within the DBL and overlayer:

$$i = -nFD_O\frac{C_{O,b} - C_O(x = t_o)}{\delta} = -nFD_{e,O,o}\frac{S_OC_O(x = t_o) - C_{O,o}(x = 0)}{t_o} \tag{7.11}$$

Evaluating the right-hand side of eqn (7.11) for $C_{O,o}(x = 0) \approx 0$ and written in terms of $P_j$, $i_{lim}$ is given by

$$i_{lim} = -nFP_O\frac{C_O(x = t_o)}{t_o} \tag{7.12}$$

Solving eqn (7.12) for the concentration at the overlayer/electrolyte interface, $C_O(x = t_o)$, and inserting the expression into the left-hand side of eqn (7.11) gives

$$i_{lim} = -\frac{nFD_O}{\delta}\left(C_{O,b} + \frac{t_oi_{lim}}{nFP_O}\right) \tag{7.13}$$

Rearranging eqn (7.13) and solving for $i_{lim}$:

$$i_{lim} = -nFC_{O,b}\left(\frac{\delta}{D_O} + \frac{t_o}{P_O}\right)^{-1} \tag{7.14}$$

By taking the reciprocal of both sides of eqn (7.14), and substituting eqn (7.7) and (7.9), $i_{lim}$ for the OEC in the presence of the DBL can be expressed in

terms of the limiting current densities associated with the DBL ($i_{\mathrm{lim,DBL}}$) and overlayers ($i_{\mathrm{lim,o}}$) in isolation, as noted previously:[40]

$$\frac{1}{i_{\mathrm{lim}}} = \frac{1}{i_{\mathrm{lim,DBL}}} + \frac{1}{i_{\mathrm{lim,o}}} \tag{7.15}$$

Eqn (7.14) or (7.15) can be used to predict $i_{\mathrm{lim}}$ for a range of different operating conditions and overlayer properties. In Figure 7.5a, the effects of $t_{\mathrm{o}}$ and $P_j$ on $i_{\mathrm{lim}}$ are shown for $P_j$ values spanning orders of magnitude for constant $C_{\mathrm{O,b}} = 0.1$ M and $k_{\mathrm{c,DBL}} = 1\times10^{-2}$ cm s$^{-1}$, the latter of which is consistent with common laboratory experimental setups in the presence of stirring. For continuous overlayers that exhibit $P_j < 5\times10^{-9}$ cm$^2$ s$^{-1}$ for the species of interest, these curves highlight the requirement that $t_{\mathrm{o}}$ must be less than ~15 nm in order to sustain meaningful current densities that would be required for applications. Figure 7.5b shows the effects of $k_{\mathrm{c,DBL}}$ on $i_{\mathrm{lim}}$ under the same conditions as in Figure 7.5a, but with constant overlayer permeability. The high sensitivity of $i_{\mathrm{lim}}$ to $k_{\mathrm{c,DBL}}$ highlights that the hydrodynamics of the bulk electrolyte, and therefore the design of the electrochemical reactor, can also have a large impact on mass transfer in OECs. Lastly, Figure 7.5c plots $i_{\mathrm{lim,o}}/i_{\mathrm{lim,DBL}}$ across a wide range of $k_{\mathrm{c,o}}$ and $k_{\mathrm{c,DBL}}$ values. This ratio is proportional to the transport resistance of the DBL to that of the overlayer. Consistent with intuition, $i_{\mathrm{lim,o}}/i_{\mathrm{lim,DBL}}$ is very small (<0.01) for high $k_{\mathrm{c,DBL}}$ and low $k_{\mathrm{c,o}}$, meaning that $i_{\mathrm{lim}} \approx i_{\mathrm{lim,o}}$ and most of the concentration drop occurs across the overlayer. Conversely, the yellow region of Figure 7.5c corresponds to situations characterized by high $k_{\mathrm{c,o}}$ and low $k_{\mathrm{c,DBL}}$, where $i_{\mathrm{lim}} \approx i_{\mathrm{lim,DBL}}$ and most of the concentration drop occurs across the DBL.

### 7.2.3 Concentration Overpotentials

Even when $|i| < |i_{\mathrm{lim}}|$, there can still be significant concentration gradients within the DBL and overlayer of an OEC that can greatly alter its polarization ($i$–$E$) curve relative to that for a BEC electrode. These concentration drops create what are often referred to as concentration overpotential losses, $\eta_{\mathrm{conc}}$. As shown in eqn (7.16), $\eta_{\mathrm{conc}}$ is defined as the difference between the potential, $E$, of a hypothetical reference electrode when it is positioned at the active electrocatalyst interface, $E(x = 0)$, and the potential measured when it is located just beyond the outer edge of the DBL, $E(x = t_{\mathrm{o}} + \delta + \Delta\delta)$:

$$\eta_{\mathrm{conc}} = E(x = 0) - E(x = t_{\mathrm{o}} + \delta + \Delta\delta) \tag{7.16}$$

Both potentials can be calculated from the Nernst equation, shown here for the reaction $\mathrm{O} + n\mathrm{e}^- \rightleftharpoons \mathrm{R}$:

$$E = E^{\circ\prime} + \frac{RT}{nF}\ln\left(\frac{C_{\mathrm{O}}}{C_{\mathrm{R}}}\right) \tag{7.17}$$

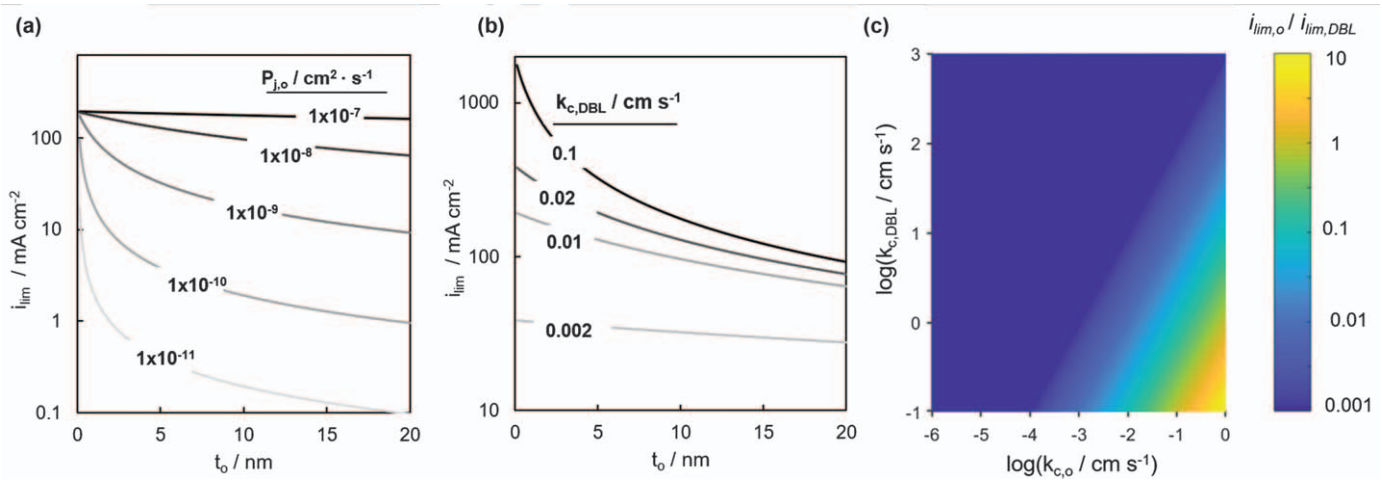


**Figure 7.5** (a) Mass transfer limiting current density ($i_{\text{lim}}$) *versus* overlayer thickness ($t_{\text{o}}$) for several different values of $P_j$ at constant $k_{\text{c,DBL}} = 1\times10^{-2}$ cm s$^{-1}$. (b) $i_{\text{lim}}$ *versus* $t_{\text{o}}$ for several values of the mass transfer coefficient associated with the diffusion boundary layer ($k_{\text{c,DBL}}$) and constant $P_j = 1\times10^{-8}$ cm s$^{-1}$. In all cases, $C_{\text{O,b}} = 0.1$ M. (c) $i_{\text{lim,o}}/i_{\text{lim,DBL}}$ for different values of $k_{\text{c,DBL}}$ and $k_{\text{c,o}}$.

where $R$ is the gas constant, $T$ is absolute temperature and $E^{\circ\prime}$ is the formal potential, which combines the standard potential $E^{\circ}$ for a redox couple with activity coefficients for both species, O and R, hence allowing the use of species concentrations in the second term instead of activities. Consequently,

$$E(x = t_o + \delta + \Delta\delta) = E^{\circ\prime} + \frac{RT}{nF}\ln\left(\frac{C_{O,b}}{C_{R,b}}\right) \tag{7.18}$$

$$E(x = 0) = E^{\circ\prime} + \frac{RT}{nF}\ln\left[\frac{C_{O,o}(x = 0)}{C_{R,o}(x = 0)}\right] \tag{7.19}$$

which can be inserted into eqn (7.16) to give eqn (7.20) after canceling out the common $E^{\circ\prime}$ terms:

$$\eta_{conc} = \frac{RT}{nF}\ln\left[\frac{C_{O,o}(x = 0)}{C_{R,o}(x = 0)}\right] - \frac{RT}{nF}\ln\left(\frac{C_{O,b}}{C_{R,b}}\right) \tag{7.20}$$

The concentrations at the buried interface, $C_{j,o}(x = 0)$ ($j$ = O, R), can be written as a function of $i$ and $i_{lim}$ based on flux balances such as eqn (7.10) and (7.11):

$$C_{O,o}(x = 0) = S_O C_{O,b}\left(1 - \frac{i}{i_{lim,O}}\right) \tag{7.21}$$

$$C_{R,o}(x = 0) = S_R C_{R,b}\left(1 - \frac{i}{i_{lim,R}}\right) \tag{7.22}$$

The limiting current density for the oxidant species ($i_{lim,O}$) is given by eqn (7.14), while eqn (7.14) must be negated for the limiting current density of the reductant species ($i_{lim,R}$) to account for the sign convention for oxidation current. Eqn (7.21) and (7.22) can then be substituted into eqn (7.20) to express $\eta_{conc}$ as

$$\eta_{conc} = \frac{RT}{nF}\ln\left(\frac{S_O}{S_R}\right) - \frac{RT}{nF}\ln\left(\frac{1 - \frac{i}{i_{lim,O}}}{1 - \frac{i}{i_{lim,R}}}\right) \tag{7.23}$$

Eqn (7.23) can be simplified to estimate $\eta_{conc}$ for $i \ll i_{lim}$ by applying a first-order Taylor series expansion about $\eta_{conc} = 0$ V, resulting in

$$\eta_{conc} = \frac{RT}{nF}\ln\left(\frac{S_O}{S_R}\right) + \frac{RT}{nF}\ln\left(\frac{1}{i_{lim,R}} - \frac{1}{i_{lim,O}}\right)i \tag{7.24}$$

according to which $\eta_{conc}$ varies linearly with $i$. Eqn (7.23) and (7.24) can be used to predict how $\eta_{conc}$ depends on overlayer characteristics ($t_o$, $P_j$) and operating conditions ($k_{c,DBL}$ and $C_{j,b}$). A simple parametric analysis of $\eta_{conc}$ in the absence of concentration drops across the DBL has been reported previously for encapsulated electrocatalysts.[5]

### 7.2.4 Transport Through Non-ideal Overlayers

The analyses in the previous two sections were based on solution-diffusion transport models applied to ideal insulating overlayers having uniform thickness, homogeneous properties, and planar geometry. In reality, overlayers can be highly non-uniform in structure and/or composition, resulting in species fluxes and concentration overpotentials that deviate greatly from those predicted by the equations in the previous sections. Brief descriptions of several common non-idealities in ultrathin oxide overlayers are provided here.

#### *7.2.4.1 Non-uniform Thicknesses*

Many deposition techniques can result in overlayers that possess a high degree of variability in their thickness. For example, line-of-site deposition techniques such as physical deposition are susceptible to shadowing effects, and sol–gel methods often lead to non-uniform overlayer thicknesses resulting from deposition of a precursor layer that tends to adjust its thickness to minimize surface tension on rough surfaces. Regardless of the cause, non-uniform overlayer thicknesses can be expected to decrease and increase transport resistances in locations where the overlayer is thinner and thicker, respectively. As a result, regions of the overlayer that are thinner than average can experience species fluxes and local current densities that are much greater than those in regions where the overlayer is thicker than average.

#### *7.2.4.2 Holes and Cracks*

Owing to thermally or chemically induced stresses associated with the synthesis and processing of ultrathin overlayers, nanoscopic defects such as pinholes or cracks can occur. The size of such holes and cracks can vary by orders of magnitude, with sizes ranging from slightly larger than the diameter of nanoscopic pores in the overlayer to hundreds or thousands of nanometers. Such defects can serve as low-resistance pathways for species transport between the bulk electrolyte and active electrocatalyst. As a result, high local reaction rates can occur at overlayer defects such that these ‘‘hot spots’’ can account for a significant fraction of an electrode’s total current even if the defects represent a small fraction of the total electrochemically active surface area. If reaction rates in the regions surrounding a nano- or microscopic defect are significantly lower, such defects can also benefit from fast 3D diffusion in the DBL in the same way that nano- or -microelectrodes do.

#### *7.2.4.3 Non-uniform Composition or Structure*

The structure and composition of an oxide overlayer can strongly influence the solubility and/or diffusivity of a permeant species, and thus its permeability. It follows that an overlayer possessing lateral variations in composition and/or structure can lead to uneven species fluxes to and from the

buried interface in a similar manner to overlayers with non-uniform thickness. Compositional changes in the transverse direction with respect to the buried interface can also alter the analysis in the previous sections by creating non-linear concentration profiles.

#### 7.2.4.4 *Electrical Conductivities*

This chapter has only considered OEC overlayers that are electronically insulating such that electrochemical reactions occur only at the electrocatalyst/overlayer buried interface. However, the ability of an overlayer to conduct electrons and/or holes could impact (i) ion transport through the overlayer, (ii) solvent coordination within overlayer pores or free volume elements, and/or (iii) the ability of electrochemical reactions to occur *inside* or at the *outer surface* of the overlayer itself. Coupled electron–ion transport has often been reported in various oxide materials,[41,42] which are sometimes referred to as mixed ionic electronic conductors.[43] The ability to conduct both ions and electrons/holes could have implications for species permeabilities, local electric field strengths, and confinement effects within an OEC overlayer. Furthermore, electron transport to or from the overlayer/electrolyte interface could greatly affect the reaction selectivity for complex reaction networks by allowing one or more electrochemical reaction to occur at that interface provided that the overlayer possesses sufficient catalytic activity for the reaction(s) of interest. The occurrence of reactions within or at the outer surface of the overlayer could have a negative or positive influence on the desired OEC performance, depending on the specific reaction system under consideration. It must be noted that oxides that are normally classified as insulators can still possess sufficient conductivity to support meaningful current densities at the outer surface of an ultrathin overlayer, since the electron/hole transport distance across the overlayer is so short.

## 7.3 Influence of Overlayers on Reaction Kinetics

This section describes mechanisms by which overlayers can alter the activity and/or selectivity of OECs compared with BECs operating in otherwise identical conditions. A particular focus is placed on mechanisms that leverage the transport properties of the overlayer to alter the selectivity in complex reaction systems containing parallel and/or branching reaction networks. These transport-mediated mechanisms rely on the ability of semipermeable overlayers to alter the relative concentrations of reactants at the buried interface. After first describing a Butler–Volmer framework for modeling polarization curves that span kinetic, mixed, and transport-controlled regions (Figure 7.4d), this section explores two model reaction systems that exemplify transport-mediated selectivity for electrodes operating in the transport- and mixed-controlled potential regions. Lastly, the effects of confinement on the reaction kinetics at the buried interface are discussed.

### 7.3.1 Combining Transport and Kinetic Losses in OECs

In the absence of concentration or ohmic overpotential losses, the current density–potential (*i–E*) curves of an electrode, also known as ''polarization curves'', are commonly modeled using the Butler–Volmer equation:[31]

$$i = i_0[\exp(\alpha_a f\eta_s) - \exp(-\alpha_c f\eta_s)] \tag{7.25}$$

where $i_0$ is the exchange current density, $f = F/RT$, and $\eta_s$ is the activation or surface overpotential; $\eta_s$ is the electronic driving force required to overcome the kinetic barrier(s) for the electrochemical reaction. Eqn (7.25) also contains the anodic and cathodic transfer coefficients, $\alpha_a = (1-\beta)n$ and $\alpha_c = \beta n$, respectively. The transfer coefficient $\beta$ is defined as the fraction of the applied potential across an electrode/electrolyte interface that leads to a decrease in the reaction barrier for the cathodic reaction. As seen in its full derivation,[31] the Butler–Volmer equation is a power law rate expression for a reversible electrochemical reaction, where the rate constants and concentration terms have been incorporated into $i_0$.

For electrodes operating under conditions where $C_j(x=0) \approx C_{j,b}$, eqn (7.25) may be suitable for describing polarization curves. However, any significant changes of reactant and/or product concentrations at the electrode/electrolyte interface from their bulk values can lead to substantial deviations of the experimental *i–E* curve from that predicted by the Butler–Volmer equation due to concentration overpotentials. Owing to the extra transport resistance associated with species transport through the overlayer in OECs, the polarization curves for these electrodes are even more likely to deviate from Butler–Volmer behavior. To account for transport effects, eqn (7.25) can be modified such that $\eta_{conc}$ and $\eta_s$ are simultaneously taken into account:[44]

$$\frac{i}{i_0} = \left(1 - \frac{i}{i_{lim,R}}\right)\exp(\alpha_a f\eta) - \left(1 - \frac{i}{i_{lim,O}}\right)\exp(-\alpha_c f\eta) \tag{7.26}$$

In this modified Butler–Volmer equation, $i_0$ is a constant based on the rate constants and bulk concentrations of redox species the electrolyte, while $i_{lim,j}$ ($j$ = O or R) is given by eqn (7.7) for a BEC or eqn (7.14) for an OEC. In Figure 7.6a, the influence of transport on the *i–η* curve of BEC and OEC electrodes characterized by identical kinetic parameters and $k_{c,DBL}$ is displayed. The solid blue line was generated using eqn (7.25), meaning that $\eta$ is entirely kinetic for this curve and characteristic of a BEC in the absence of any significant concentration gradient across the DBL. Using eqn (7.26), $\eta_{conc}$ associated with a DBL characterized by $k_{c,DBL} = 2\times10^{-2}$ cm s$^{-1}$ gives a slight shift in the polarization curve of the BEC to more negative potentials (dashed blue curve). When OEC electrodes are considered based on overlayers characterized by $P_O = P_R = 1\times10^{-9}$ cm$^2$ s$^{-1}$, the additional transport resistance associated with diffusion through the overlayer gives rise to clearly observable limiting current densities at sufficiently negative potentials. The polarization curves from Figure 7.6a were also used to generate

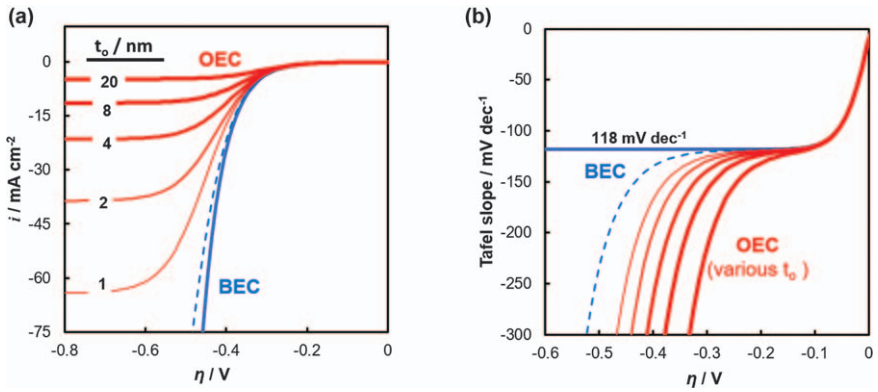


**Figure 7.6** (a) Cathodic branch of modeled polarization curves for the reaction $O + e^- \rightleftharpoons R$ for BEC (blue curves) and OEC (red curves) electrodes characterized by the same kinetic parameters ($i_0 = 1\times10^{-5}$ A cm$^{-2}$, $\beta = 0.5$) and bulk electrolyte conditions ($C_O = C_R = 0.1$ M, $T = 298$ K, $k_{c,DBL} = 2\times10^{-2}$ cm s$^{-1}$). For the OEC, $P_O = P_R = 1\times10^{-9}$ cm$^2$ s$^{-1}$ and curves are shown for different $t_o$. For the BEC electrode, the solid line is based on the Butler–Volmer equation, and the dashed blue curve was generated using eqn (7.26). (b) Potential-dependent Tafel slopes for the same polarization curves from (a) plotted as a function of $\eta$.

Tafel plots (not shown) and to calculate the Tafel slope (mV per decade) as a function of $\eta$ as shown in Figure 7.6b. While the blue curve based on the Butler–Volmer equation for a BEC shows the expected Tafel slope of 118 mV per decade for all potentials where the oxidation contribution is negligible, this figure shows how the presence of $\eta_{conc}$ significantly reduces the range of potentials where the true kinetically limited Tafel slope is observed. As discussed in Section 7.5, great care must be taken to deconvolute kinetic from transport effects in OECs.

### 7.3.2 Transport-mediated Reaction Selectivity

This section presents two case studies that illustrate how the transport properties of OEC overlayers can alter the reaction selectivity relative to a BEC. Both cases consider model reactions occurring at planar electrodes operating at the steady state and possessing overlayers with uniform thickness.

#### *7.3.2.1 Case Study 1*

This example considers two unimolecular, one-electron reactions occurring in parallel:

$$\text{Reaction 1:} \quad A + e^- \rightarrow B$$

$$\text{Reaction 2:} \quad C + e^- \rightarrow D$$

It is assumed that the electrode is operated at a potential for which both reactions take place under mass transfer limiting conditions, meaning that $C_A(x=0)=C_C(x=0)\approx 0$ M. Under these conditions, the partial current densities associated with each reaction are equal to their respective $i_{lim}$ values according to eqn (7.14). These limiting partial current densities for reactions 1 ($i_{lim,1}$) and 2 ($i_{lim,2}$) can then be used to determine the selectivity or branching ratio towards product B, $S_{B/D}$, according to

$$S_{B/D}=\frac{r_B}{r_D}=\frac{i_{lim,1}/n_1}{i_{lim,2}/n_2} \tag{7.27}$$

By using eqn (7.14) to describe $i_{lim,1}$ and $i_{lim,2}$ in eqn (7.27), one can map out the impacts of reactant permeabilities and bulk concentrations on $S_{B/D}$. In Figure 7.7a, $S_{B/D}$ was calculated for different combinations of reactant permeabilities while keeping bulk concentrations, $k_{c,DBL}$, and $t_o$ constant. As expected, $P_A>P_C$ favors the formation of B ($S_{B/D}>1$) whereas $P_A<P_C$ favors product D ($S_{B/D}<1$) for these conditions. However, Figure 7.7b shows that the relative concentrations of the reactants in the bulk electrolyte can also alter the selectivity by orders of magnitude, emphasizing the importance of considering not only the relative permeabilites of competing reactants but also their bulk concentrations.

### *7.3.2.2 Case Study 2*

Next, we explore the influence of OEC overlayers on the selectivity towards products generated by two coupled reactions while operating at potentials where both kinetics and transport affect reaction rates. The elementary reaction steps for this reaction network are as follows:

$$\begin{aligned}
&\text{Step 1: Adsorption of A:} && A+e^-+S\rightleftharpoons A_{ad}\\
&\text{Step 2: Formation of B:} && A_{ad}+A_{ad}\rightarrow B+2S\\
&\text{Step 3: Adsorption of C:} && C+e^-+S\rightleftharpoons C_{ad}\\
&\text{Step 4: Formation of D:} && A+C_{ad}+e^-\rightarrow D+S
\end{aligned}$$

where A and C are reactants, B and D are products, and S is an open surface site. The subscript ''ad'' indicates that a species is adsorbed on a surface site, and the absence of a subscript indicates that a species is in the electrolyte phase. In this mechanism, reactants A and C first adsorb on the electrocatalyst surface through a Volmer step involving an electron transfer. Next, two competing surface reactions can occur to produce products B and D. B is produced through a Volmer–Tafel mechanism (Steps $1+2$) that involves the reaction of two $A_{ad}$ species through a non-electrochemical Tafel step. Simultaneously, $C_{ad}$ can react with solution-phase A through an Volmer–Heyrovský mechanism (Steps $3+4$) to generate product D. Both surface reaction steps are assumed to be irreversible under the operating potentials and involve rapid desorption of the products such that B and D do not occupy

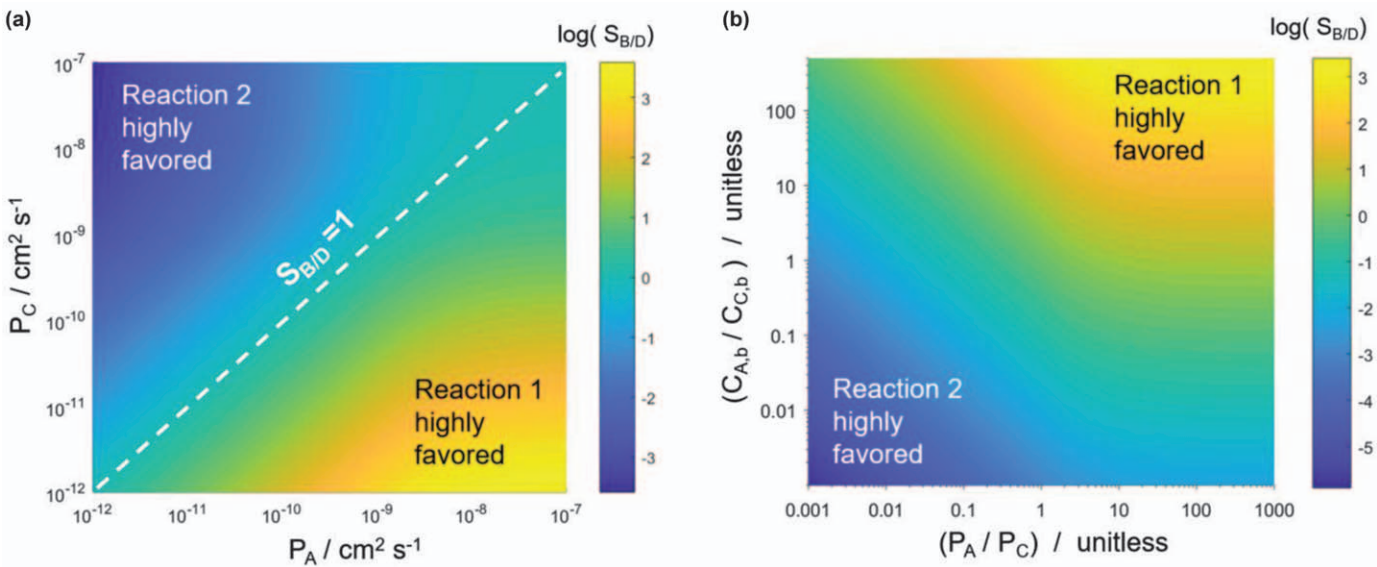


**Figure 7.7** Modeling the effects of encapsulation on the selectivity of an OEC for two competing parallel reactions under mass transfer limiting conditions. The color maps showing how $S_{B/D}$ depends on (a) $P_A$ and $P_C$ for constant bulk concentrations ($C_{A,b} = C_{C,b} = 0.1$ M), and (b) the ratio of permeabilities ($P_A/P_C$) and concentrations ($C_{A,b}/C_{C,b}$) for $C_{C,b} = 0.01$ M and $P_C = 1\times10^{-9}$ cm$^2$ s$^{-1}$. For both figures, $t_o = 2$ nm and $k_{c,DBL} = 2\times10^{-2}$ cm s$^{-1}$.

surface sites. Because both Steps 2 and 4 consume molecule A, the two reactions are coupled. However, Step 2 has a second-order dependence on $A_{ad}$, whereas Step 4 only has a first-order dependence on A. As shown below, this difference in reaction order for a common reactant can lead to strong mass transfer-dependent selectivity ratios $S_{D/B}$ and $S_{B/D}$.

Since competing Steps 2 and 4 are coupled and involve more than one distinct surface adsorbate, the Butler–Volmer rate expressions given by eqn (7.25) and (7.26) do not apply. Therefore, it is necessary to derive the rate expressions for the rate-limiting steps of each reaction. Here, the surface reaction steps are assumed to be rate limiting and irreversible, with rate expressions for the areal rate of production of B ($r_B$, mol cm$^{-2}$ s$^{-1}$) and D ($r_D$, mol cm$^{-2}$ s$^{-1}$) given by eqn (7.28) and (7.29), respectively:

$$r_B = k_2 {C_{A,s}}^2 \tag{7.28}$$

$$r_D = k_4 C_A(x=0) C_{C,s} e^{-\beta_4 f \eta_4} \tag{7.29}$$

where $k_n$ is the rate constant for step $n$, $C_A(x=0)$ (mol cm$^{-3}$) is the concentration of species A at the electrocatalyst interface ($x=0$), $C_{j,s}$ (mol cm$^{-2}$) is the surface concentration of adsorbate species $j$, $\beta_4$ is the transfer coefficient for Step 4, and $\eta_4$ is the difference between the electrode potential and standard reduction potential for Step 4. Using Faraday's law, we note that $r_B$ and $r_D$ in eqn (7.28) and (7.29) can also be written as partial current densities $i_B$ and $i_D$, respectively. Assuming that (i) all adsorption sites are equivalent, (ii) the heats of adsorption for A and C are independent of coverage, (iii) there is no multilayer adsorption, and (iv) the electrode operates isothermally, Langmuir adsorption isotherms can be used to describe the surface coverages and associated $C_{j,s}$ for each adsorbed species. For a surface containing $N$ adsorbates, all of which adsorb through one-electron reduction processes, the coverage of species $j$, $\theta_j$, is derived from adsorption rate expressions and a site balance to give

$$\theta_j = \frac{C_{j,s}}{C_{S,t}} = \frac{K_j^{ad} C_j(x=0) e^{-\beta_j f \eta_j}}{1 + \sum_{k=1}^{N} K_k^{ad} C_k(x=0) e^{-\beta_k f \eta_k}} \tag{7.30}$$

where $C_{S,t}$ is the total site density on the surface (sites cm$^{-2}$), $K_j^{ad}$ is the adsorption equilibrium constant for species $j$, and the exponential terms account for the potential-dependent activation energy for electrochemical adsorption steps. Within those terms, $\beta_y$ ($y=j$ or $k$) is the transfer coefficient associated with the electrochemical adsorption process for species $j$ or $k$, and $\eta_y$ ($y=j$ or $k$) is the activation overpotential for adsorption of $j$ or $k$.

Inserting expressions for $C_{A,s}$ and $C_{C,s}$ obtained from eqn (7.30) into eqn (7.28) and (7.29) gives the following rate expressions for $r_B$ and $r_D$:

$$r_B = k_2 \left(C_{S,t} K_A^{ad}\right)^2 \left( \frac{C_A(x=0) e^{-\beta_A f \eta_A}}{1 + K_A^{ad} C_A(x=0) e^{-\beta_A f \eta_A} + K_C^{ad} C_C(x=0) e^{-\beta_C f \eta_C}} \right)^2 \tag{7.31}$$

$$r_D = k_4 C_{S,t} K_C^{ad} C_A(x=0)\left(\frac{C_C(x=0)e^{-\beta_C f\eta_C}e^{-\beta_4 f\eta_4}}{1 + K_A^{ad}C_A(x=0)e^{-\beta_A f\eta_A} + K_C^{ad}C_C(x=0)e^{-\beta_C f\eta_C}}\right) \tag{7.32}$$

To solve for $r_B$ and $r_D$ (or $i_B$ and $i_D$) as a function of electrode potential, additional equations are needed to solve for the unknown interfacial concentrations $C_A(x=0)$ and $C_C(x=0)$. These are obtained from the steady-state continuity equations for species A and C within the DBL (BEC and OEC) and overlayer (OEC only), subject to the following boundary conditions: (i) the concentrations of A and C at the DBL/bulk electrolyte interface are set to the bulk electrolyte concentrations, (ii) the diffusive fluxes of A and C at the electrocatalyst interface are set equal to their rate of consumption ($r_A = -2r_B - r_D$, $r_C = -r_D$), and for the OEC only, (iii) the species fluxes within the overlayer and electrolyte phases are set equal at the overlayer/DBL interface. This analysis is almost identical with that already carried out Sections 7.2.2 and 7.2.3, giving expressions for $C_A(x=0)$ and $C_C(x=0)$ consistent with eqn (7.21):

$$C_{A,o}(x=0) = S_A C_{A,b}\left(1 - \frac{i_B + i_D}{i_{lim,A}}\right) \tag{7.33}$$

$$C_{C,o}(x=0) = S_C C_{C,b}\left(1 - \frac{i_D}{i_{lim,C}}\right) \tag{7.34}$$

Inserting eqn (7.33) and (7.34) for $C_A(x=0)$ and $C_C(x=0)$ into eqn (7.31) and (7.32) gives a non-linear system of equations that can be used to solve for the concentration profiles, surface coverages, partial current densities, and $S_{D/B}$ as a function of potential. The same system of equations applies for both BEC and OEC electrodes. To distinguish between them, the $i_{lim}$ terms in eqn (7.33) and (7.34) are described by eqn (7.7) and (7.14) for the BEC and OEC, respectively.

Figure 7.8 shows representative results for this coupled reaction system based on the operating conditions and kinetic parameters given in the caption. For this case study, it is assumed that the bulk concentrations of the reactants are equal to each other, but their permeabilities in the OEC overlayer vary by over one order of magnitude. Modeling was carried out for both OEC and BEC electrodes. As shown in Figure 7.8a, the BEC electrode exhibits a higher coverage of A than C based on the chosen kinetic parameters. The higher $\theta_A$ favors the formation of B through the second-order reaction based on two adsorbed A molecules (Step 2), while the low $\theta_C$ decreases $i_D$ associated with Step 3, which is first order in $C_{C,s}$. As a result, the BEC electrode shows relatively low $S_{D/B}$ at more negative potentials associated with significant current densities (Figure 7.8c). Figure 7.8c also shows

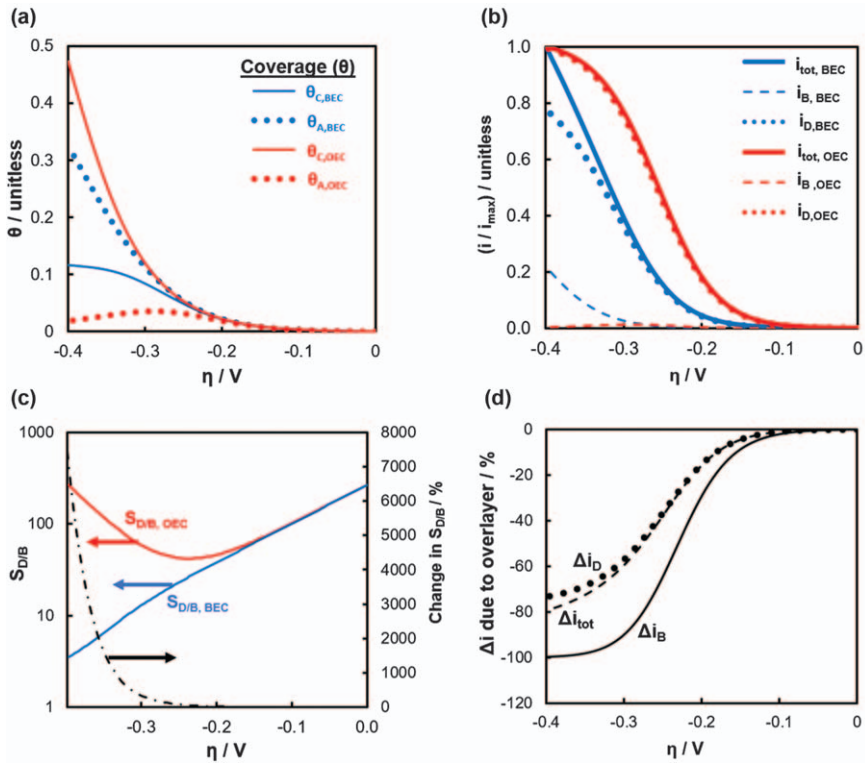


**Figure 7.8** Modeling the effects of encapsulation on adsorbate coverage and reaction selectivity for parallel coupled reactions. (a) Coverages of adsorbates A and C for BEC and OEC electrodes as a function of overpotential. (b) Partial and total current densities as a function of overpotential for the same electrodes. (c) Potential-dependent selectivities towards products D and B for BEC and OEC electrodes. (d) Change in partial and total current densities resulting from the presence of the overlayer in the OEC relative to the baseline current densities predicted for the BEC. Simulations were carried out for the following conditions: $C_A = C_C = 0.05$ M, $C_{S,t} = 1\times10^{15}$ sites cm$^{-2}$ ($1.7\times10^{9}$ mol cm$^{-2}$), $k_{c,DBL,A} = 5\times10^{-2}$ cm s$^{-1}$, $k_{c,DBL,C} = 2\times10^{-2}$ cm s$^{-1}$, $P_A = 1\times10^{-9}$ cm$^2$ s$^{-1}$, $P_C = 1\times10^{-7}$ cm$^2$ s$^{-1}$, $t_o = 2$ nm (for OEC only), $K_A^{ad} = 10$ M$^{-1}$, $K_C^{ad} = 10$ M$^{-1}$, $k_2 = 8.2\times10^{11}$ cm$^2$ mol$^{-1}$ s$^{-1}$, $k_4 = 3.6\times10^{6}$ cm$^3$ mol$^{-1}$ s$^{-1}$, $\beta_A = 0.5$, $\beta_C = 0.5$, $\beta_4 = 0.25$, and $E^{\circ}_1 = E^{\circ}_2$.

that the OEC electrode is predicted to achieve $S_{D/B}$ values that are >1000% larger than those achieved with the BEC electrode despite operating under identical conditions and assuming that the kinetic constants in the model are identical for the two electrodes. The root cause of the enhanced selectivity of the OEC towards product D is that the permeabilities of the two reactants within the overlayer were assumed to be very different ($P_A = 1\times10^{-9}$ cm$^2$ s$^{-1}$ $\ll$ $P_C = 1\times10^{-7}$ cm$^2$ s$^{-1}$). As seen in Figure 7.8a, these

selective transport properties of the overlayer lead to significant increases in $\theta_C$ and decreases in $\theta_A$ relative to those modeled for the BEC. These changes in surface coverage caused by the presence of the overlayer promote $i_D$ relative to $i_B$ (Figure 7.8b), leading to the large increases in $S_{D/B}$ noted in Figure 7.8c. Conversely, solving this system of equations for overlayers characterized by $P_A \gg P_C$ would cause the opposite effect: the overlayer would promote $\theta_A$ and $i_B$ relative to $\theta_C$ and $i_D$, leading to decreases in $S_{D/B}$ (*i.e.* increases in $S_{B/D}$) relative to the BEC. This example highlights the ability of using OECs to adjust reaction selectivities through modification of permeabilities, and therefore fluxes, of reactants to the buried interface. However, this added control knob can also come at a cost. As seen in Figure 7.8d, the larger concentration gradients incurred by the OEC suppress not only the undesired reaction, but also the desired reaction. Thus, case study 2 exhibits a trade-off between current density and selectivity, which is important to consider when deciding the optimal overlayer thickness, operating conditions, and electrocatalyst loading.

### 7.3.3 Confinement Effects on Electrocatalysis at Buried Interfaces

Case study 2 assumed that the kinetic rate constants and adsorption equilibrium constants were identical for the side-by-side comparison of OEC and BEC electrodes. In reality, there is plenty of evidence suggesting that the intrinsic kinetics of processes occurring at electrochemically active buried interfaces can be greatly altered due to so-called "confinement effects".[45–48] These effects are relevant to active sites confined within a medium or microenvironment that changes the local chemical, physical, or electronic properties of that site and/or the electroactive species located there relative to the properties measured under otherwise identical operating conditions at a conventional electrolyte/electrode interface. The electrocatalytic buried interface of an OEC, where reactions may occur at interstitial spaces or nanoscopic voids at a solid/solid interface, is an example of a microenvironment. A reactant species at the buried interface of an OEC, such as that illustrated in Figure 7.9a, is likely to experience physical, chemical, and electronic interactions with not only the active electrocatalyst, but also the atoms in the oxide overlayer. These interactions can result in changes to the physical orientation and positioning of a species (*i.e.* steric effects), and also changes to its electronic structure. All of these effects can be expected to alter the potential energy surface for reactions at the buried interface, resulting in changes in energy barriers, turnover frequencies, and/or product distributions.

An example of confined electrocatalysis in OECs was reported by Labrador and co-workers, who studied carbon monoxide (CO) stripping voltammetry on $SiO_x$-encapsulated Pt thin films.[29] CO stripping voltammetry is often used to quantify the electrochemical surface area (ECSA) and probe the CO binding strength of an electrocatalyst surface. As can be seen in Figure 7.9b

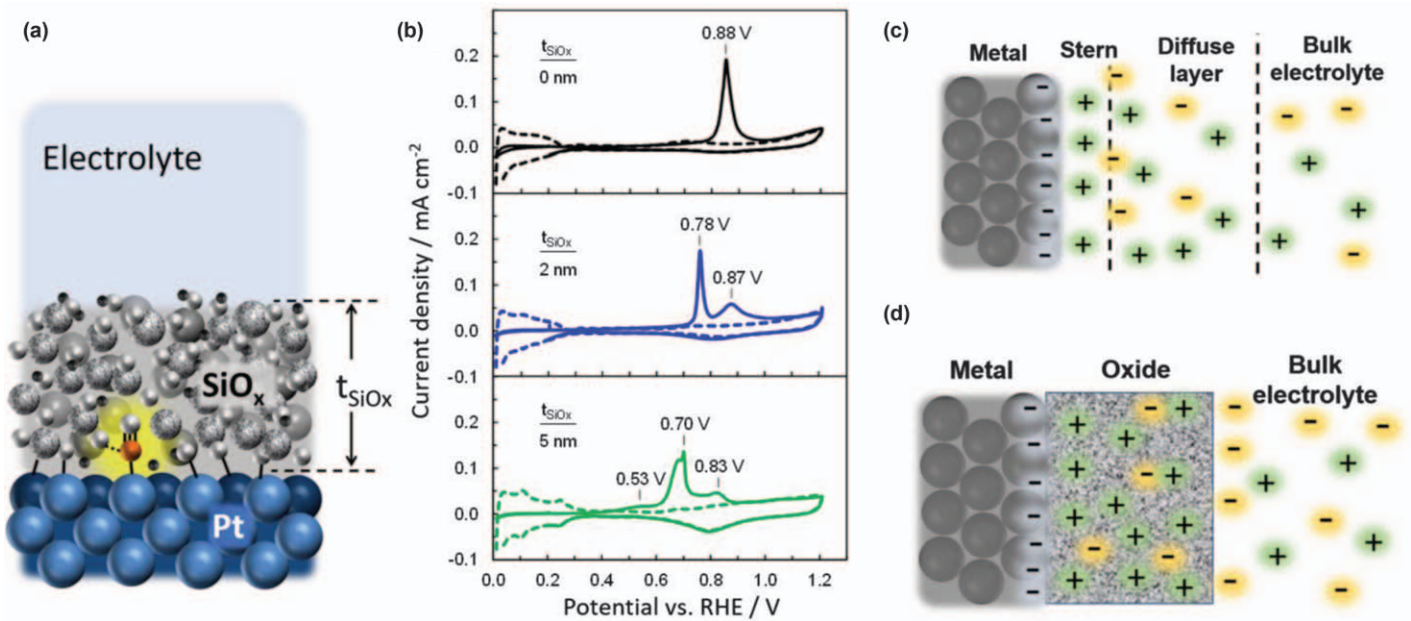


**Figure 7.9** (a) Schematic side view of an $SiO_x$-encapsulated Pt electrode with a CO molecule adsorbed at the buried interface. (b) CO stripping voltammetry curves measured in 0.5 M $H_2SO_4$ at a scan rate of 20 mV $s^{-1}$ for Pt (black), 2 nm $SiO_x$|Pt (blue), and 5 nm $SiO_x$|Pt (green). Solid curves represent the first cyclic voltammetric (CV) cycle that was carried out with CO adsorbed on the electrode surface, and dashed curves represent the second CV cycle that was performed after CO was stripped from the electrode surface during the first cycle. (c) Side-view of a BEC/electrolyte interface illustrating the stern and diffuse double layer regions within the liquid electrolyte for a negatively charged electrode. (d) Side-view of OEC/electrolyte interface illustrating hypothetical distribution of ions within a semi-permeable oxide overlayer having a higher solubility for cations than anions.
Part (b) reproduced from ref. 29 with permission from American Chemical Society, Copyright 2018.

(black curve), a bare Pt electrocatalyst in 0.5 M $H_2SO_4$ supporting electrolyte gives a CO stripping peak centered around +0.9 V *vs.* RHE. This value is very positive relative to the reversible potential for the CO–$CO_2$ reaction, reflecting the fact that CO binds strongly to Pt surfaces and requires a large driving force to oxidize it to $CO_2$. However, the CO stripping curves for Pt thin-film electrodes encapsulated by ultrathin $SiO_x$ overlayers are substantially altered from the BEC control (Figure 7.9b, blue and green curves). The integrated area of the CO stripping curve remains similar to that of bare Pt, verifying that the ECSA of the $SiO_x$|Pt electrode has not changed substantially, but the onset and peak potentials for the CO oxidation peaks are shifted negative by 200–300 mV. These shifts cannot be explained by transport phenomena, but rather must be associated with changes in the energetics of CO oxidation. It was hypothesized that silanol groups from the $SiO_x$ overlayer that are proximal to Pt sites at the buried interface are responsible for the negative shifts thanks to their ability to facilitate CO oxidation through the so-called bifunctional effect[49] that has often been reported for CO and alcohol oxidation on oxide-supported Pt electrocatalysts.[50] However, other confinement effects could not be ruled out.

Confinement effects can also impact the properties of spectator ions and/or solvent molecules such as water.[51] Since the choice of supporting electrolyte ions and solvent can have large impacts on electrocatalysis,[3,4,52] it stands to reason that tailoring the properties of spectator ions and solvent molecules through confinement effects presents another opportunity to tune reaction activity and/or selectivity in microenvironments. In OECs, one potentially important implication of confinement effects on spectator ions and the solvent is to alter the electric field strength at the buried interface by changing the structure of the electrochemical double layer (EDL). In conventional electrocatalysts, large potential drops associated with the EDL occur within the first several ångströms of the electrode/electrolyte interface for concentrated electrolytes,[53] and can be accompanied by very large electric field strengths ($E$) that directly or indirectly impact electrocatalytic reactions.[52] For example, a 1 V potential drop across a 3 Å thick EDL equates to an average $E$ within the double layer on the order of $10^9$ V m$^{-1}$. Such fields can strongly affect the orientation and/or structure of solvent molecules, spectator ions, and/or electroactive reactants.[52–56] As illustrated in Figure 7.9c, the EDL is comprised of an inner (Stern) layer of specifically adsorbed ions with opposite polarity of the surface charges on the electrode, in addition to a diffuse outer layer comprised of both anions and cations. The Gouy–Chapman–Stern (GCS) model is often used to describe how the potential profile across the EDL and total potential difference between the metal ($\varphi^M$) and bulk solution ($\varphi^S$) are affected by ionic charge, ion concentrations, temperature, and the permittivity ($\varepsilon$) of the electrolyte.[53] It is conceivable that permeable oxide overlayers can dramatically affect the distribution of charges and associated electric fields at the electrified buried interface. One hypothetical scenario for an OEC is illustrated in Figure 7.9d, which considers the case where the electrocatalyst has a negative surface

charge and the overlayer exhibits high solubility for cationic species. Many more possible charge distributions are possible, depending on the operating conditions, solute species, and overlayer structure and composition. In the case of a uniform charge distribution throughout the oxide and ignoring interfacial edge effects, it follows from integration of Poisson's equation that $\boldsymbol{E}$ within the overlayer is given by

$$\boldsymbol{E} = \nabla\phi = \frac{1}{\varepsilon_o}\int_{x=0}^{x=t_O} \rho(x)\mathrm{d}x \approx \frac{\rho t_o}{\varepsilon_o} \tag{7.35}$$

where $\rho$ is the charge density within the overlayer and $\varepsilon_o$ is the permittivity of the overlayer within the operating environment. Although eqn (7.35) is overly simplistic for complex OEC systems and unlikely to give accurate values of $\boldsymbol{E}$ for real OEC systems, it highlights the possibility of tuning $\boldsymbol{E}$, and therefore kinetic parameters, by altering the properties of the oxide overlayer (*e.g.* $t_o$, $\rho$, $\varepsilon_o$).

## 7.4 Influence of Oxide Overlayers on Electrocatalyst Stability

### 7.4.1 Mechanisms for Stability Enhancement by Encapsulation

One of the most significant and commonly observed benefits of oxide encapsulation is improved stability of the underlying active electrocatalyst. As illustrated in Figure 7.10, electrocatalysts can be susceptible to many

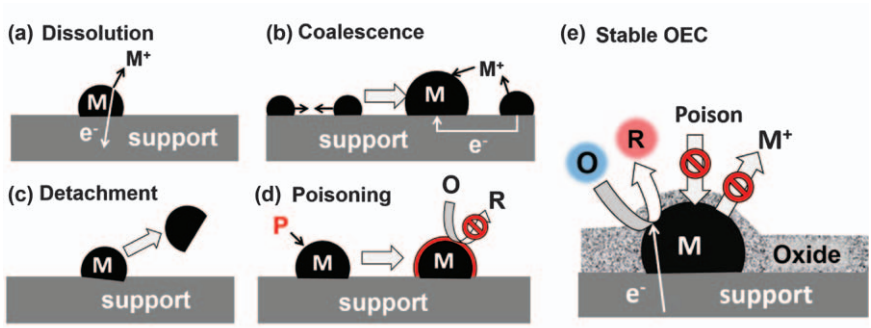


**Figure 7.10** Stability benefits of the OEC design. Depicted are common mechanisms of nanoparticle electrocatalyst degradation, namely (a) electrochemical dissolution due to oxidation, (b) coalescence or agglomeration of smaller into larger particles, (c) physical detachment from the support due to poor adhesion, and (d) poisoning whereby an impurity or poison species is adsorbed on the active electrocatalyst and significantly reduces its activity towards the desired reaction ($O + e^- \rightarrow R$). (e) Side view of a nanoparticle MCEC that is resistant to all four modes of degradation illustrated in (a)–(d).
Adapted from ref. 5 with permission from American Chemical Society, Copyright 2018.

different degradation mechanisms, including, but not limited to, (i) dissolution or corrosion of the electrocatalyst, (ii) physical detachment of electrocatalytic nanoparticles from the electrode support, (iii) coalescence or ripening of smaller nanoparticles into larger particles, and (iv) poisoning of active sites on the electrocatalyst by exposure to impurities. Determination of which mechanism(s) are most important will depend strongly on the properties of the active electrocatalyst, the support material, and operating conditions such as electrolyte composition and electrode potential. Fortunately, the OEC architecture offers a strategy to mitigate all of the aforementioned degradation mechanisms, provided that the overlayer itself is stable. By serving as a protective nanoscale glue that adheres to both the electrocatalyst and the surrounding support material, an overlayer can prevent detachment of a nanoparticle from its support and/or migration along its surface. Similar stability benefits have been observed for oxide-encapsulated catalysts employed for high-temperature thermal catalysis applications, as discussed in Chapter 8.

Consistent with the description above, researchers have shown that $SiO_x$ overlayers deposited on carbon-supported Pt and Pd electrocatalysts can greatly suppress or even eliminate nanoparticle coalescence and loss of ECSA during cyclic voltammetric (CV) cycling as oxygen reduction reaction (ORR) electrocatalysts.[26–28] As seen in the ORR linear sweep voltammograms for Pt|C and $SiO_x$|Pt|C electrodes in Figure 7.11a and b, respectively, negligible degradation in the performance of the $SiO_x$|Pt|C electrode was observed over 1500 cycles, whereas the unencapsulated Pt|C electrode showed a gradual loss in activity. Concurrently, transmission electron microscopy (TEM) characterization of fresh and used electrocatalysts revealed that the average particle size of the conventional electrocatalysts increased by ~82% whereas the average size of the encapsulated Pt nanoparticles increased by only 25% (Figure 7.11c,d).[28]

### 7.4.2 Adhesion and Geometric Considerations for OEC Stability

Key to the ability of oxide overlayers to impart stability benefits to OECs is the interfacial adhesion between (i) the oxide overlayer and the active electrocatalyst and (ii) the overlayer and support material. If the adhesive forces anchoring the overlayer to the electrocatalyst and/or support are too weak, delamination of the overlayer and loss of OEC functionality can be expected.

The adhesion between an ultrathin overlayer and an electrocatalyst or support material can depend on several factors, including (i) the strength of adhesive interactions between atoms in the overlayer and catalyst, (ii) the density and type of interfacial bonds, and (iii) the morphology and shape of the electrocatalyst and support materials. The first two factors can be expected to depend heavily on the materials chemistry associated with solid/solid interfaces, but may also be impacted by the presence of solvent molecules and/or local pH and potential.[57] Depending on the specific metal–

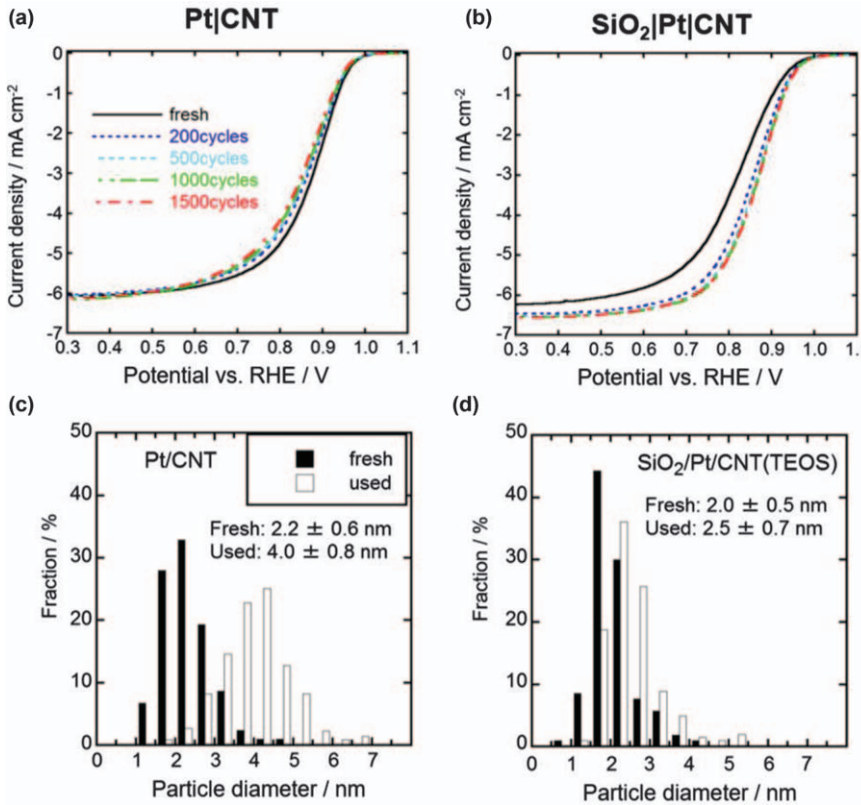


**Figure 7.11** Polarization curves associated with the oxygen reduction reaction in $O_2$-saturated 0.1 M $HClO_4$ for (a) carbon nanotube (CNT)-supported Pt nanoparticles (Pt|CNT) and (b) $SiO_2$-encapsulated Pt|CNT ($SiO_2$|Pt|CNT). Curves were obtained at a scan rate of 10 mV $s^{-1}$ and a rotation rate of the working electrode of 1600 rpm. Histograms of Pt nanoparticles measured by TEM for fresh and used (c) Pt|CNT and (d) $SiO_2$|Pt|CNT samples that were subjected to 1500 CV cycles between 0.05 and 1.20 V *vs.* RHE at 100 mV $s^{-1}$ in $N_2$-purged 0.1 M $HClO_4$. Reproduced from ref. 28 with permission from the Royal Society of Chemistry.

oxide combination, the adhesion energy associated with the solid/solid interface can vary from less than 1 J $m^{-2}$ up to ~6 J $m^{-2}$.[58,59] Adhesion is a rich topic spanning a multitude of applications and described by several different theories, depending on the mechanism of bonding.[60,61] Although adhesion strength is generally expected to be maximized at high bond strength and bond density, the optimized configuration for the buried interface of an OEC may not necessarily coincide with that which maximizes the adhesion strength. High bond strength and bond density can be expected to promote overlayer adhesion, but might also limit the number of accessible active sites at the buried interface.[57] In contrast to the overlayer/

electrocatalyst interface, a high density of strong interfacial bonds between the overlayer and an inert support material may be desirable since no reactions should occur at this inert buried interface. Furthermore, overlayer/support interfaces characterized by high adhesion energies may conceivably serve as ''anchor points'' that help reduce delamination even if the adhesion energy at the overlayer/electrocatalyst nanoparticle interface is lower.

Another challenge for interfacial stability in OECs is reconstruction of the catalyst and/or overlayer phases, either of which can lead to breaking and/or making of interfacial bonds. It is well known that conventional electrocatalysts can reconstruct in the electrochemical operating environment to form structural configurations that are very different from that of the ''as-made'' electrocatalyst,[62–64] and structural changes at the OEC buried interface can similarly be expected.[57] Reconstruction at the buried interface is especially likely for OEC ''precatalysts'' that initially contain nanoscopic interlayers at the overlayer/electrocatalyst interface that result from partial oxidation of the underlying metallic electrocatalyst. For example, Beatty *et al.* used a combination of linear sweep voltammetry and X-ray photoelectron spectroscopy (XPS) to identify and characterize the presence of a platinum oxide ($PtO_x$) interlayer at the buried interface of $SiO_x$-encapsulated Pt thin films.[65] Analysis revealed that as-made samples possessed $PtO_x$ interlayers with equivalent thicknesses of 0.7–2.1 atomic layers, and that the interlayers were reduced back to metallic Pt when sufficiently negative potentials were applied during electrochemical measurements. It was also found that the stability of the $SiO_x|Pt$ electrodes subjected to CV cycling decreased when the upper scan vertex was increased to values that resulted in repeated formation and reduction of the $PtO_x$ interlayer, demonstrating the importance of accounting for the interlayer in the design and operation of these particular OECs.

Operating conditions and electrocatalyst loadings can also be expected to affect significantly the adhesion of the overlayer to the electrocatalyst and support materials. Repeated cycling of potential between oxidizing and reducing conditions, and also frequent cycling over large ranges of humidity and/or temperature, could create large interfacial stresses that promote delamination. Another consideration is the local current density at electrochemically active buried interfaces. In general, one can expect that interfacial stability will become more challenging at higher reaction rates, which can be accompanied by greater pH extremes for reactions involving the consumption or production of $H^+$ or $OH^-$. High concentrations of either species may promote dissolution of the underlying electrocatalyst or the oxide overlayer, and/or attack of the interfacial bonds between the overlayer and electrocatalyst. Additionally, high reaction rates involving product species that have both low permeability and solubility in the overlayer could result in high local pressures that lead to the formation of bubbles. The growth and/or cavitation of bubbles can be accompanied by large mechanical forces that can damage electrodes;[66,67] it stands to reason that these forces could promote overlayer delamination in OECs if they are formed at

voids at the buried interface. Fortunately, the Young–Laplace equation indicates that extremely high pressures are required to form nanoscopic bubbles,[68] making bubble formation at buried interfaces less likely for dense conformal coatings. However, further investigation is needed.

## 7.5 Experimental Methods for Assessing the Performance of OECs

The addition of an overlayer to an electrocatalyst introduces more complexity to the already non-trivial tasks of gaining a mechanistic understanding of electrocatalyst operation and accurately evaluating key performance metrics. In particular, it can be challenging to deconvolute the multiple influences of an overlayer on OEC properties and performance. In this section, best practices for experimental investigations of OECs are described that can be used to help overcome these challenges.

### 7.5.1 Preparation of OECs

Many synthesis methods exist for the preparation of oxide overlayers and OECs, and detailed accounts of atomic layer deposition (ALD) and wet chemical approaches are described in Chapters 2/8 and 9, respectively. Regardless of the synthesis method chosen, it is crucial that researchers studying OECs also prepare uncoated BEC electrodes made of identical electrocatalyst and/or support materials to quantify and deconvolute overlayer effects on electrode performance more easily. To reduce the system complexity further and establish clear structure–property relationships for oxide overlayers, it is often desirable to start an investigation using well-defined planar OEC electrodes for which uniform oxide overlayers are deposited on single crystals or electrocatalytic thin films with minimal surface roughness.[22,40,69] Smooth electrocatalytic thin films can be deposited by a variety of synthesis techniques on low surface area conductive substrates such as degeneratively doped Si or glassy carbon. Such low surface area model OEC electrodes generally have the primary benefits of (i) making it easier to deposit continuous overlayers with uniform thickness by a range of techniques, (ii) eliminating the role of nanoparticle size effects on catalysis, and (iii) providing a simple 1D geometry that is more conducive to modeling and using various *in situ* and *ex situ* characterization tools. Once a basic understanding of a planar OEC system has been achieved, the design rules obtained from those studies can be applied to more complex OEC architectures such as encapsulated nanoparticles on high surface area supports.

### 7.5.2 Characterizing the ECSA of OEC Electrodes

To compare electrocatalyst performance metrics accurately, it is essential that catalyst reaction rates be compared based on the ECSA, which can vary

greatly depending on the sample roughness and electrocatalyst loading.[70–72] The ECSA links the apparent kinetics to the intrinsic or ''true'' kinetics of the catalyst, and is a measure of the number of active sites for catalysis. As mentioned in Section 7.4.2, oxide overlayers may change the ECSA through local strong interactions and confinement effects on the catalyst surface. It is therefore highly advisable to study the ECSA before and after encapsulation.

The ECSA is most often measured by CV, which can provide a quick insight into the transient charging behavior of the surface. Charging currents, which are linearly related to the scan rate in the absence of mass transfer limitations, are surface confined, and hence proportional to the ECSA. A readily accessible method for estimating the ECSA is to determine the double-layer capacity $C_{dl}$ from a potential region where only charging of the double layer is known to occur, which is possible for many electrochemical interfaces. From the value of $C_{dl}$, a correlation with the ECSA may be drawn, where for two samples with identical surface chemistry, a doubling of $C_{dl}$ implies a doubling of the ECSA. Furthermore, a value of the specific capacitance, $C_{dl}^*$, may be available, which describes the double-layer capacity per unit surface area of an identical catalyst surface that has perfectly flat geometry such that its real surface area and geometric surface area are identical. If $C_{dl}^*$ is known for the system, the ECSA can be determined and subsequently used to calculate the specific surface area, which is the ratio of the real surface area to the geometric surface area. However, it must be noted that $C_{dl}$ is not wholly specific to the ''catalytic'' surface area, as it is easily affected by unknown pseudo (*i.e.* non-double-layer charging related) capacitive processes, the electrolyte composition, bulk conductivity changes, and choice of the catalyst support material.[73,74] $C_{dl}$ can furthermore be strongly dependent on the scanning conditions, such as the range of the potential window and its position relative to the potential of zero charge for the electrode.[73] Even though in the literature the ECSA and $C_{dl}$ are often assumed to be directly related, caution must be exercised when comparing $C_{dl}$ values between differing surfaces, such as before and after catalyst encapsulation. For a little-studied system, the exact relationship between $C_{dl}$ and the ECSA can be uncertain, and $C_{dl}$ usually serves as an order of magnitude estimation of the ECSA at best.

It is occasionally possible to characterize the ECSA of an electrocatalyst by studying surface-confined faradaic reactions that show charging behavior similar to the double layer, and thus have a pseudo-capacitance $C_{dl}'$ associated with them. Common examples are the adsorption/desorption of H and O on Pt, adsorption/desorption of O on Au, and transitions in the formal metal oxidation state of conductive metal oxides, such as in $RuO_2$ and $IrO_2$. Such reactions often have known potential ranges, allowing their contribution to the recorded signal to be precisely determined. Because they are highly specific to the catalyst sites, values of $C_{dl}'$ are more strongly related to the ECSA, and accurate values for their specific pseudo-capacitances, $C_{dl}^{*\prime}$, are often available.[75,76] Faradaic charging reactions can furthermore be

exploited to characterize the active sites by introducing known adsorbates or catalyst poisons into the bulk solution that alter the adsorption/desorption properties of the active sites.[77] However, the influence of a poisoning agent may be significantly altered, or even entirely absent, after encapsulation. Such data can provide insights into the selective transport properties of the overlayer, and also the energetics associated with adsorption/desorption of these species at the buried interface.[22] Another potential complication of encapsulation when determining the ECSA of an OEC is that overlayers can introduce transport limitations that lead to ECSA values that decrease with increasing scan rate.[22] This can occur if the time constant for diffusion of the adsorbate in the overlayer is similar to or greater than the time constant characteristic of a given CV scan rate. When this happens, the potential scan across the adsorption/desorption region will appear ''smeared out'', and the ECSA is underestimated. Therefore, it is important that ECSAs are reported based on measurements using scan rates that do not artificially decrease ECSA due to transport limitations.

### 7.5.3 Deconvoluting Transport Effects from Kinetic Effects

Tafel plots are commonly used to evaluate electrochemical kinetics. Such plots should be corrected for any *iR* drops arising from the bulk solution, and can be recorded either at the steady state based on successive potential holding steps or at the pseudo-steady state using a sufficiently slow continuous scan rate. For BEC electrodes operating in the absence of transport limitations, the slope of a Tafel plot is intrinsic to the reaction mechanism and independent of the surface area, meaning that it is less susceptible to complications in ECSA determination.[78] According to the Butler–Volmer equation, a single-step, outer-sphere electron transfer is predicted to show a linear Tafel plot, with a single value governing its slope at all potentials (see Figure 7.6b), provided that the overpotential exceeds 118 mV such that curvature due to the backward reaction may be neglected.[44] For most electrochemical reactions characterized by complex multistep mechanisms involving at least one adsorbed intermediate, the Tafel plot may show multiple regions with a linear slope. Importantly, the value(s) of the Tafel slope in the linear region(s) can provide valuable information about the rate-limiting step.[79]

As described in Section 7.3.1, mass transport limitations often result in lower than expected currents and greater curvature in Tafel plots, which is seen in ''derivative curves'' for which the local Tafel slope is plotted as a function of potential or overpotential. Figure 7.6b illustrates these concepts for a ''simple'' one-electron transfer reaction that shows a single Tafel slope of ~118 mVper decade at suitably irreversible potentials when only kinetic losses are present. In practice, mass transfer limitations result in very narrow potential windows of constant Tafel slopes. For OECs with thick enough overlayers, Figure 7.6b shows that the kinetically limited Tafel slope can become almost completely masked. Consistent with this picture, the

disappearance of a previously visible linear region in a Tafel plot after encapsulation might suggest that kinetic control has been replaced by diffusion control in the overlayer.

As described in Section 7.2, mass transport across the DBL can also strongly affect the limiting current densities and *i–E* characteristics of an OEC electrode. To help deconvolute transport losses across the DBL and overlayer, and also from kinetic losses, it is recommended to characterize OECs using flow cell or rotating electrode setups that allow hydrodynamic control over the DBL thickness. When using a rotating disk electrode (RDE) setup, the DBL thickness can be systematically adjusted by varying the rotation rate while transport characteristics of the overlayer should remain unaffected. Hence choosing a suitably high rotation rate will make the mass transfer coefficient associated with the DBL much higher than that associated with the overlayer ($k_{c,DBL} \gg k_{c,O}$) such that $i_{lim,o} \ll i_{lim,DBL}$ (see Figure 7.5) and the concentration drop across the DBL is negligible compared with that across the overlayer. By comparing $i_{lim}$ under different rotation rates, it is possible to determine diffusion coefficients and permeabilities in the DBL and overlayer, respectively. As described elsewhere,[80] it is also possible to characterize $k_{c,DBL}$ and $P_j$ in a conventional three-electrode setup by comparing $i_{lim}$ for OEC and BEC electrodes under otherwise identical hydrodynamic conditions. However, an RDE or flow cell setup is generally preferred thanks to the ability to access higher $k_{c,DBL}$, which is especially useful for reactions involving limiting reactants that are present at low concentrations in the bulk electrolyte.

Another advantage of an RDE setup is that it can be equipped with a secondary ring electrode that can be independently controlled with a potentiostat and used as a sensor to measure the extent of multiple reactions simultaneously. Such rotating ring-disk electrodes (RRDEs) have commonly been utilized to measure peroxide formation in model oxygen reduction catalysts in fuel cells, but the method has been extended to study the parallel evolution of oxygen and chlorine,[81] and also selectivity in the $CO_2$ reduction reaction.[82,83] Figure 7.12 shows an example of how an RRDE setup can be used to monitor the effect of an overlayer on reaction selectivity when two parallel reactions are occurring under the conditions of interest. In this study, manganese oxide ($MnO_x$) overlayers with variable thicknesses, as expressed in terms of the charge of their reductive dissolution, $Q_{MnO_x}$, were grown on iridium oxide ($IrO_x$) electrocatalysts and evaluated for their ability to facilitate selectively the oxygen evolution reaction (OER) in a chloride environment. The partial current densities for the competing chlorine evolution reaction (CER) were derived using a Pt ring electrode held at a potential where it can selectively reduce the $Cl_2$ generated by the CER while being inactive to reduction of $O_2$ formed by the OER. In the absence of a coating, $IrO_x$ shows a very high selectivity for $Cl_2$ over $O_2$. The top panel in Figure 7.12a shows that the CER partial current ($i_{CER}$) decreases to less than 1% of its original value as the thickness of the $MnO_x$ overlayer increases. However, it is important to note that the overlayer also negatively affects the

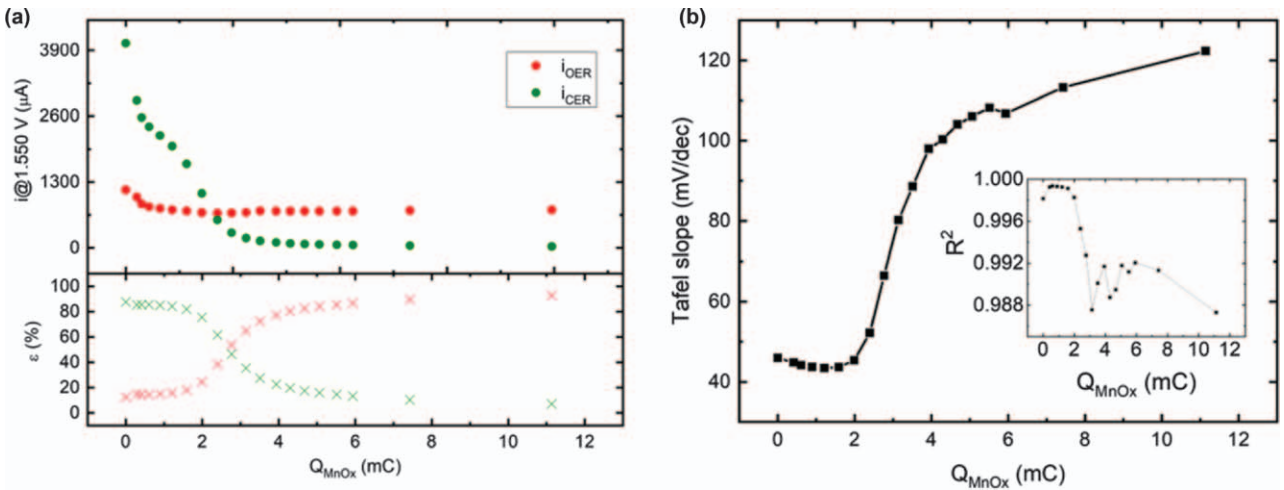


**Figure 7.12** (a) Top panel: measured partial currents of the evolution of oxygen ($i_{OER}$) and chlorine ($i_{CER}$) on an $MnO_x$-encapsulated iridium oxide ($IrO_x$) electrocatalyst in an acidic aqueous electrolyte containing 0.5 M $KHSO_4$ and 30 mM KCl. Bottom panel: corresponding molar selectivities ($\varepsilon$). (b) Tafel slopes derived from the chlorine evolution current, measured on the ring electrode, as a function of the $MnO_x$ overlayer thickness.
Reproduced from ref. 18 with permission from American Chemical Society, Copyright 2018.

partial current associated with the OER, $i_{OER}$, which decreases by 34% compared with that measured in the absence of an overlayer. Overall, the $MnO_x$ overlayers cause a dramatic shift in selectivity (Figure 7.12a, bottom panel). Figure 7.12b shows Tafel slopes measured for the CER as a function of overlayer thickness; the Tafel slope increases from a typical value of 40 mV per decade to values higher than 100 mV per decade, while the Tafel curves become notably more curved (Figure 7.12b, inset). These observations indicate that mass transport of chloride to the $MnO_x/IrO_x$ buried interface becomes controlling for chlorine evolution for thick $MnO_x$ overlayers. With an RRDE, it is therefore possible to simultaneously study the selectivity between competing reactions on an OEC, and also the corresponding kinetic and transport properties.

### 7.5.4 Stability Tests

Industrial electrochemical devices are commonly operated on thousand-hour timescales, and the electrocatalyst must have an accordingly long lifetime. To approximate the catalyst performance over extended times, accelerated stability test (AST) protocols are used. Care must be taken to ensure that the AST protocol is representative for the process conditions.[84–86] In addition to testing stability under steady-state conditions at constant current density or potential, potentiodynamic techniques such as CV or multistep chronoamperometry can be useful to emulate potential jumps associated with switching a device on and off.

Unique to OECs, it is important to assess the durability of both the underlying electrocatalyst and overlayer. Therefore, in addition to monitoring the stability of electrochemical performance, it is advisable to characterize overlayer integrity and catalyst morphology before and after electrochemical measurements. For smooth thin-film OECs, ellipsometry can prove useful for monitoring nanometer-level changes in thickness,[65] and XPS can be used to monitor changes in oxidation states and the atomic ratios of elements in the overlayer and catalyst. TEM and SEM can also provide valuable insights into electrocatalyst degradation,[28] but care should be taken that images are representative of the entire sample. When possible, measurements carried out at the identical location(s) of the same sample before and after electrochemistry are ideal. Lastly, inductively coupled plasma mass spectrometry (ICP-MS) can be valuable for detecting trace amounts of dissolved elements from the catalyst, substrate, and/or the overlayer.

## 7.6 Outlook: Challenges and Opportunities for OECs

Oxide overlayers present significant challenges and opportunities for advancing electrochemical technologies. On the one hand, tunable overlayers create a very different design space for electrocatalysts, introducing new control knobs that can allow advanced functionality and overcome performance limits that hinder conventional electrocatalysts. However, many of

these control knobs are coupled to each other, creating new trade-offs and limitations that must be taken into account during the design of OECs. Many trade-offs involve species transport, which is key to enabling some of the advanced functionalities of OECs, but can lead to undesirable side-effects such as concentration overpotentials while creating challenges for quantifying kinetic parameters. Stated otherwise, the very features that make OECs so interesting and promising often make them exceptionally challenging to study.

Further refinement of the design principles that govern these trade-offs will be essential for accelerating the development of OECs, but several key challenges must be overcome. First, studying electrified, reactive buried interfaces is not easy owing to the high-dimensional nature of the potential energy surfaces describing electrochemical reactions in 3D, heterogeneous confined environments. This task is made all the more challenging considering that the presence of the OEC overlayer reduces the number of techniques capable of characterizing the reactive buried interface. For example, electrochemical scanning tunneling microscopy and atomic force microscopy techniques, which have provided invaluable fundamental insights for conventional BECs, are physically incapable of directly probing a buried interface. Such limitations create a strong need for the further development of techniques and methods – both experimental and computational – that are better suited to characterizing electrochemical buried interfaces and deconvoluting the various kinetic and transport influences of overlayers on the performance of OECs. *In situ* and *operando* tools, including but not limited to spectroscopy and scattering techniques based on electromagnetic radiation that can penetrate through ultrathin overlayers, are expected to be especially valuable for characterizing the buried interface and viewing reactive intermediates in the reactive environment.

Advances in atomistic simulation tools such as DFT and molecular dynamics are also needed to understand confinement effects in OECs better and help deconvolute kinetic and transport effects. Most electrocatalysis DFT studies conducted to date have neglected details related to the roles that electrode potential/electric fields, solvent effects, and/or supporting electrolyte ions play in altering the energy landscape. Although such simplifications may be permissible for predicting trends in reactivity for BECs for some electrochemical reactions, it is becoming increasingly apparent that these ''secondary'' details can be very important for accurately describing the catalytic properties of active sites located in confined environments. Advances in *ab initio* methods have allowed the aforementioned influences to be successfully accounted for with varying degrees of success,[51,52,55,87] but doing so in a confined environment comprised of (at least) two distinct materials can be expected to introduce additional complexities and increase computational costs even further. The task of carrying out atomistic simulations of transport and/or catalysis in OECs becomes even more challenging and costly if the oxide material is amorphous. In general, amorphous or

highly disordered materials require larger cell sizes and statistical sampling of properties, and it can be difficult to confirm that the atomic-scale structure and composition of the simulated oxide is an accurate representation of the experimental material. The use of machine learning techniques[88] to help bridge the gap between expensive and accurate computational methods such as wavefunction theory and DFT with less expensive and less accurate methods such as classical molecular dynamics is one promising approach to increase the throughput of computational efforts to study OECs. Further developments in these computational methodologies, combined with carefully coordinated experimental efforts, are urgently needed to uncover atomic-level design principles for OEC operation.

Ultimately, atomistic simulation tools should be coupled with continuum-level models to allow for multiscale models that are capable of predicting OEC performance and could be invaluable for accelerating the discovery of new OEC materials. In comparison with the number of known oxide materials and metallic electrocatalysts that have been studied as conventional BECs, the research community has barely scratched the surface in its exploration of combinations of overlayer/electrocatalyst/support materials. By varying overlayer conductivity, the number of overlayers, and/or multiple co-catalysts, the number of permutations increases even further. Towards this end, advances in high-throughput synthesis and characterization techniques[89] for making and evaluating OECs are needed to explore more quickly these new materials combinations and variant OEC architectures. When new OEC materials are discovered that have promising performance, researchers must also work to bridge the ''materials gap'' between well-defined model OEC electrodes and high surface area OEC particle-based electrodes that may be integrated into commercial electrolyzer and fuel cell designs. Even for conventional electrocatalysts, optimization of catalyst ink formulations and porous transport layers (PTLs) can be a slow, Edisonian process. The presence of an oxide coating has important implications not only for the operation of the electrocatalyst itself, but also for the selection of ionomers and efficient transport of reactants, products, and electrons at larger length scales. The importance of understanding such PTL-level design rules for OEC-based electrodes should not be underestimated. Additionally, accelerated durability testing of OEC-containing devices for thousands of hours under industrially relevant operating conditions will be essential to proving the viability of the OEC approach. Together with fundamental R&D efforts, such device-level experimentation is anticipated to be crucial for advancing OEC-based electrodes towards commercialization for a wide range of current and emerging electrochemical energy applications.

## Acknowledgements

D.V.E. acknowledges funding from the US National Science Foundation (NSF, Award No. CBET-1752340), the US Department of Energy, Office of Energy Efficiency and Renewable Energy (Award No. DE-EE0008838), and the

Qatar National Research Foundation (QNRF, Award #NPRP12S-0131-190024), with co-funding from Qatar Shell Research and Technology Center. Any opinions, findings, and conclusions or recommendations expressed in this chapter are those of the author(s) and do not necessarily reflect the views of the US NSF or of the QNRF. D.V.E and V.G. also acknowledge support from Shell International Exploration & Production New Energies Research & Technology Dense Energy Carriers Program. J.G.V. and M.T.M.K. acknowledge funding support from the Netherlands Organization for Scientific Research (NWO) in the framework of the fund New Chemical Innovations, project 731.015.204 ELECTROGAS, with financial support of Akzo Nobel Chemicals/Nouryon, Shell Global Solutions, Magneto Special Anodes (an Evoqua Brand), and Elson Technologies. D.V.E. acknowledges insightful discussions with and feedback from Alexander Urban and Nongnuch Artrith on several sections of this chapter.

## References

1. J. K. Norskov, T. Bligaard, J. Rossmeisl and C. H. Christensen, *Nat. Chem.*, 2009, **1**, 37–46.
2. F. Calle-Vallejo and M. T. M. Koper, *Electrochim. Acta*, 2012, **84**, 3–11.
3. J. Suntivich, E. E. Perry, H. A. Gasteiger and Y. Shao-Horn, *Electrocatalysis*, 2013, **4**, 49–55.
4. M. Alvarez-Guerra, J. Albo, E. Alvarez-Guerra and A. Irabien, *Energy Environ. Sci.*, 2015, **8**, 2574–2599.
5. D. V. Esposito, *ACS Catal.*, 2018, **8**, 457–465.
6. Y. S. Liu, K. Y. Leung, S. E. Michaud, T. L. Soucy and C. C. L. McCrory, *Comments Inorg. Chem.*, 2019, **39**, 242–269.
7. Z. W. Seh, J. Kibsgaard, C. F. Dickens, I. B. Chorkendorff, J. K. Norskov and T. F. Jaramillo, *Science*, 2017, **355**, 1–12.
8. A. Vojvodic and J. K. Norskov, *Natl. Sci. Rev.*, 2015, **2**, 140–143.
9. Z. J. Han, R. Kortlever, H. Y. Chen, J. C. Peters and T. Agapie, *ACS Cent. Sci.*, 2017, **3**, 853–859.
10. A. K. Buckley, M. Lee, T. Cheng, R. V. Kazantsev, D. M. Larson, W. A. Goddard, F. D. Toste and F. M. Toma, *J. Am. Chem. Soc.*, 2019, **141**, 7355–7364.
11. Y. N. Zhou, W. Chen, P. Cui, J. Zeng, Z. N. Lin, E. Kaxiras and Z. Y. Zhang, *Nano Lett.*, 2016, **16**, 6058–6063.
12. H. B. Li, J. P. Xiao, Q. Fu and X. H. Bao, *Proc. Natl. Acad. Sci. U. S. A.*, 2017, **114**, 5930–5934.
13. Y. C. Fu, A. V. Rudnev, G. K. H. Wiberg and M. Arenz, *Angew. Chem., Int. Ed.*, 2017, **56**, 12883–12887.
14. K. Obata and K. Takanabe, *Angew. Chem., Int. Ed.*, 2018, **57**, 1616–1620.
15. V. Smulders, N. Simic, A. S. O. Gomes, B. Mei and G. Mul, *Electrochim. Acta*, 2019, **296**, 1115–1121.
16. K. Maeda, K. Teramura, D. L. Lu, N. Saito, Y. Inoue and K. Domen, *Angew. Chem., Int. Ed.*, 2006, **45**, 7806–7809.

17. M. Yoshida, K. Maeda, D. L. Lu, J. Kubota and K. Domen, *J. Phys. Chem. C*, 2013, **117**, 14000–14006.
18. J. G. Vos, T. A. Wezendonk, A. W. Jeremiasse and M. T. M. Koper, *J. Am. Chem. Soc.*, 2018, **140**, 10270–10281.
19. S. Chen, S. Shen, G. Liu, Y. Qi, F. Zhang and C. Li, *Angew. Chem., Int. Ed.*, 2015, **54**, 3047–3051.
20. A. T. Garcia-Esparza, T. Shinagawa, S. Ould-Chikh, M. Qureshi, X. Y. Peng, N. N. Wei, D. H. Anjum, A. Clo, T. C. Weng, D. Nordlund, D. Sokaras, J. Kubota, K. Domen and K. Takanabe, *Angew. Chem., Int. Ed.*, 2017, **56**, 5780–5784.
21. K. Domen, A. Kudo, T. Onishi, N. Kosugi and H. Kuroda, *J. Phys. Chem.*, 1986, **90**, 292–295.
22. N. Y. Labrador, E. L. Songcuan, C. De Silva, H. Chen, S. J. Kurdziel, R. K. Ramachandran, C. Detavernier and D. V. Esposito, *ACS Catal.*, 2018, **8**, 1767–1778.
23. C. S. Pan, T. Takata, M. Nakabayashi, T. Matsumoto, N. Shibata, Y. Ikuhara and K. Domen, *Angew. Chem., Int. Ed.*, 2015, **54**, 2955–2959.
24. B. Endrodi, V. Smulders, N. Simic, M. Wildlock, G. Mul, B. Mei and A. Cornell, *Appl. Catal., B*, 2019, **244**, 233–239.
25. W. J. Jo, G. Katsoukis and H. Frei, *Adv. Funct. Mater.*, 2020, **30**, 1–11.
26. K. Park, T. Ohnishi, M. Goto, M. So, S. Takenaka, Y. Tsuge and G. Inoue, *Int. J. Hydrogen Energy*, 2020, **45**, 1867–1877.
27. S. Takenaka, H. Miyamoto, Y. Utsunomiya, H. Matsune and M. Kishida, *J. Phys. Chem. C*, 2014, **118**, 774–783.
28. S. Takenaka, T. Miyazaki, H. Matsune and M. Kishida, *Catal. Sci. Technol.*, 2015, **5**, 1133–1142.
29. J. E. Robinson, N. Y. Labrador, H. Chen, B. E. Sartor and D. V. Esposito, *ACS Catal.*, 2018, **8**, 11423–11434.
30. A. A. Bhardwaj, J. G. Vos, M. E. S. Beatty, A. F. Baxter, M. T. M. Koper, N. Y. Yip and D. V. Esposito, *ACS Catal.*, 2021, **11**, 1316–1330.
31. J. S. Newman and K. E. Thomas-Alyea, *Electrochemical* Systems, J. Wiley and Hoboken, N. J., 3rd edn, 2004.
32. Physical Constants of Organic Compounds'' in *CRC Handbook of Chemistry and Physics*, ed. J. R. Rumble, CRC Press/Taylor & Francis, Boca Raton, FL, vol. 101st edn, 2020, Internet Version.
33. K. D. Kreuer, S. J. Paddison, E. Spohr and M. Schuster, *Chem. Rev.*, 2004, **104**, 4637–4678.
34. L. Wang, M. S. H. Boutilier, P. R. Kidambi, D. Jang, N. G. Hadjiconstantinou and R. Karnik, *Nat. Nanotechnol.*, 2017, **12**, 509–522.
35. Y. Meng, J. Gao, Z. Zhao, J. Amoroso, J. Tong and K. S. Brinkman, *J. Mater. Sci.*, 2019, **54**, 9291–9312.
36. R. Epsztein, E. Shaulsky, N. Dizge, D. M. Warsinger and M. Elimelech, *Environ. Sci. Technol.*, 2018, **52**, 4108–4116.
37. A. Z. Weber and J. Newman, *Chem. Rev.*, 2004, **104**, 4679–4726.

38. J. C. Fogarty, H. M. Aktulga, A. Y. Grama, A. C. T. van Duin and S. A. Pandit, *J. Chem. Phys.*, 2010, **132**, 174704.
39. J. Godet and A. Pasquarello, *Phys. Rev. Lett.*, 2006, **97**, 1–4.
40. J. A. Bau and K. Takanabe, *ACS Catal.*, 2017, **7**, 7931–7940.
41. C. N. Brodsky, D. K. Bediako, C. Y. Shi, T. P. Keane, C. Costentin, S. J. L. Billinge and D. G. Nocera, *ACS Appl. Energy Mater.*, 2019, **2**, 3–12.
42. C. Costentin and D. G. Nocera, *J. Phys. Chem. C*, 2019, **123**, 1966–1973.
43. M. Acosta, F. Baiutti, A. Tarancón and J. L. MacManus-Driscoll, *Adv. Mater. Interfaces*, 2019, **6**, 1900462.
44. A. J. Bard and L. R. Faulkner, in *Electrochemical Methods: Fundamentals and Applications*, John Wiley & Sons, Inc., 2nd edn, 2000, ch. 3, p. 864.
45. A. D. Doyle, J. H. Montoya and A. Vojvodic, *ChemCatChem*, 2015, **7**, 738–742.
46. Y. Zhou, W. Chen, P. Cui, J. Zeng, Z. Lin, E. Kaxiras and Z. Zhang, *Nano Lett.*, 2016, **16**, 6058–6063.
47. Y. Fu, A. V. Rudnev, G. K. H. Wiberg and M. Arenz, *Angew. Chem.,, Int. Ed.*, 2017, **56**, 12883–12887.
48. H. Li, J. Xiao, Q. Fu and X. Bao, *Proc. Natl. Acad. Sci. U. S. A.*, 2017, **114**, 5930–5934.
49. G. A. Tritsaris and J. Rossmeisl, *J. Phys. Chem. C*, 2012, **116**, 11980–11986.
50. C. C. Ting, C. H. Liu, C. Y. Tai, S. C. Hsu, C. S. Chao and F. M. Pan, *J. Power Sources*, 2015, **280**, 166–172.
51. L. Bellarosa, R. García-Muelas, G. Revilla-López and N. López, *ACS Cent. Sci.*, 2016, **2**, 109–116.
52. M. M. Waegele, C. M. Gunathunge, J. Li and X. Li, *J. Chem. Phys.*, 2019, **151**, 160902.
53. A. J. Bard and L. R. Faulkner, in *Electrochemical Methods: Fundamentals and Applications*, John Wiley & Sons, Inc., 2nd edn, 2000, ch. 3, p. 864.
54. S. Srinivasan, in *Fuel Cells: From Fundamentals to Applications*, Springer US, Boston, MA, 2006, https://doi.org/10.1007/0-387-35402-6_2, pp. 27–92.
55. K.-Y. Yeh and M. J. Janik, *J. Comput. Chem.*, 2011, **32**, 3399–3408.
56. M. Liu, Y. Pang, B. Zhang, P. De Luna, O. Voznyy, J. Xu, X. Zheng, C. T. Dinh, F. Fan, C. Cao, F. P. G. de Arquer, T. S. Safaei, A. Mepham, A. Klinkova, E. Kumacheva, T. Filleter, D. Sinton, S. O. Kelley and E. H. Sargent, *Nature*, 2016, **537**, 382–386.
57. J. Qu and A. Urban, *ACS Appl. Mater. Interfaces*, 2020, **12**, 52125–52135.
58. A. A. Volinsky, N. R. Moody and W. W. Gerberich, *Acta Mater.*, 2002, **50**, 441–466.
59. R. Tang-Kong, R. Winter, R. Brock, J. Tracy, M. Eizenberg, R. H. Dauskardt and P. C. McIntyre, *ACS Appl. Mater. Interfaces*, 2018, **10**, 37103–37109.

60. J. E. E. Baglin, in *Materials and Processes for Surface and Interface Engineering*, ed. Y. Pauleau, Kluwer, Dordrecht, 1995, vol. 290.
61. M. Ohring, in *Materials Science of Thin Films- Deposition and Structure*, Elsevier, 2nd edn., 2002, ch. 12, pp. 764–775.
62. H. L. Jiang, Q. He, Y. K. Zhang and L. Song, *Acc. Chem. Res.*, 2018, **51**, 2968–2977.
63. A. G. Rajan, J. M. P. Martirez and E. A. Carter, *ACS Catal.*, 2020, **10**, 11177–11234.
64. X. Deng, F. Galli and M. T. M. Koper, *J. Am. Chem. Soc.*, 2018, **140**, 13285–13291.
65. M. E. S. Beatty, H. Chen, N. Y. Labrador, B. J. Lee and D. V. Esposito, *J. Mater. Chem. A*, 2018, **6**, 22287–22300.
66. J. Sun, X. Fan, W. L. Guo, L. H. Liu, X. Liu, J. Deng and C. Xu, *Sensors*, 2015, **15**, 31811–31820.
67. B. H. Han, K. A. Stoerzinger, V. Tileli, A. D. Gamalski, E. A. Stach and Y. Shao-Horn, *Nat. Mater.*, 2017, **16**, 121–126.
68. Q. J. Chen, L. Luo, H. Faraji, S. W. Feldberg and H. S. White, *J. Phys. Chem. Lett.*, 2014, **5**, 3539–3544.
69. M. Yoshida, K. Takanabe, K. Maeda, A. Ishikawa, J. Kubota, Y. Sakata, Y. Ikezawa and K. Domen, *J. Phys. Chem. C*, 2009, **113**, 10151–10157.
70. S. Trasatti and O. A. Petrii, *Pure Appl. Chem.*, 1991, **63**, 711–734.
71. M. S. Burke, L. J. Enman, A. S. Batchellor, S. H. Zou and S. W. Boettcher, *Chem. Mater.*, 2015, **27**, 7549–7558.
72. C. C. L. McCrory, S. H. Jung, J. C. Peters and T. F. Jaramillo, *J. Am. Chem. Soc.*, 2013, **135**, 16977–16987.
73. T. Pajkossy and D. M. Kolb, *Electrochim. Acta*, 2001, **46**, 3063–3071.
74. J. G. Vos, Z. C. Liu, F. D. Speck, N. Perini, W. T. Fu, S. Cherevko and M. T. M. Koper, *ACS Catal.*, 2019, **9**, 8561–8574.
75. T. Biegler, D. A. J. Rand and R. Woods, *J. Electroanal. Chem.*, 1971, **29**, 269–277.
76. B. Piela and P. K. Wrona, *J. Electroanal. Chem.*, 1995, **388**, 69–79.
77. V. Climent and J. M. Feliu, *J. Solid State Electrochem.*, 2011, **15**, 1297–1315.
78. M. Huynh, C. Y. Shi, S. J. L. Billinge and D. G. Nocera, *J. Am. Chem. Soc.*, 2015, **137**, 14887–14904.
79. B. V. Tilak and B. E. Conway, *Electrochim. Acta*, 1992, **37**, 51–61.
80. M. E. S. Beatty, E. I. Gillette, A. T. Haley and D. V. Esposito, *ACS Appl. Energy Mater.*, 2020, **3**, 12338–12350.
81. J. G. Vos and M. T. M. Koper, *J. Electroanal. Chem.*, 2018, **819**, 260–268.
82. A. Goyal, G. Marcandalli, V. A. Mints and M. T. M. Koper, *J. Am. Chem. Soc.*, 2020, **142**, 4154–4161.
83. F. Zhang and A. C. Co, *J. Electrochem. Soc.*, 2020, **167**, 1–8.
84. J. Zhao and X. G. Li, *Energy Convers. Manage.*, 2019, **199**, 1–22.
85. A. Maljusch, O. Conradi, S. Hoch, M. Blug and W. Schuhmann, *Anal. Chem.*, 2016, **88**, 7597–7602.

86. S. S. Zhang, X. Z. Yuan, H. J. Wang, W. Merida, H. Zhu, J. Shen, S. H. Wu and J. J. Zhang, *Int. J. Hydrogen Energy*, 2009, **34**, 388–404.
87. Y. Li and M. J. Janik, *Curr. Opin. Electrochem.*, 2019, **14**, 124–132.
88. N. Artrith, *J. Phys.: Energy*, 2019, **1**, 1–14.
89. M. L. Green, C. L. Choi, J. R. Hattrick-Simpers, A. M. Joshi, I. Takeuchi, S. C. Barron, E. Campo, T. Chiang, S. Empedocles, J. M. Gregoire, A. G. Kusne, J. Martin, A. Mehta, K. Persson, Z. Trautt, J. Van Duren and A. Zakutayev, *Appl. Phys. Rev.*, 2017, **4**, 1–18.

CHAPTER 8

# *Synthesis Techniques for Ultrathin Oxide Layers of Heterogeneous Catalysts*

ZHENG LU AND JEFFREY W. ELAM*

Applied Materials Division, Argonne National Laboratory, Argonne, IL 60439, USA
*Email: jelam@anl.gov

## 8.1 Introduction

### 8.1.1 Heterogeneous Catalysis

A catalyst is a substance that increases the rate of a chemical reaction without being consumed. Catalysts can reduce the overall activation energy to transform reactants into products by opening a new reaction pathway involving a different transition state. Moreover, catalysts can direct the chemistry towards a particular desirable set of products, resulting in selective chemistry. The word ''catalysis'' originates from the Greek words ''*kata*'' and ''*luein*'', meaning breaking down. In 1836, J. J. Berzelius first defined a catalyst as a compound that can increase the rate of a chemical reaction without being consumed by the reaction.[1] Fermentation is one of the earliest examples of catalytic chemical processing in which yeast enzymes catalyze the conversion of sugar in grain or grapes to produce ethyl alcohol.

Energy and Environment Series No. 30
Ultrathin Oxide Layers for Solar and Electrocatalytic Systems
Edited by Heinz Frei and Daniel V. Esposito

Published by the Royal Society of Chemistry, www.rsc.org

Catalysis can be divided into two main types, heterogeneous catalysis and homogeneous catalysis. In heterogeneous catalysis, the catalyst is in a different phase to the reactants. Typically, the reactants are liquids or gases whereas the catalysts are solids. In homogeneous catalysis, the catalyst is in the same phase as the reactants, and the presence of a solvent that can dissolve the catalyst is essential. Owing to the easy separation of the catalyst from the final products, heterogeneous catalysis is widely deployed in industrial chemical processing, and continuous operation has allowed the development of large-scale chemical processes. It was reported that 90% of the current chemical processes used in the chemical and petrochemical industries utilize heterogeneous catalysts.[2] Increasing demand in the chemical, pharmaceutical, petrochemical, organic synthesis, and oil refining industries is the major driving force for catalyst market growth.

Heterogeneous catalysis technology has been widely used for many years. In 1800, the first formal scientific reports of heterogeneous catalysis were published independently by Joseph Priestley and Martinus van Marum. Both worked on the dehydrogenation of ethyl alcohol over metals and viewed the metals as a source of reaction heat but did not recognize their role as catalysts.[3] In 1875, the industrial catalyst technology had its real beginning with the use of platinum catalysts in large-scale sulfuric acid production.[4] In 1903, ammonia oxidation for making nitric acid as the ingredient for fertilizers was developed by Ostwald on platinum catalysts.[1] In the period 1908–1914, German chemists Fritz Haber and Carl Bosch developed the Haber–Bosch process to synthesize ammonia from hydrogen and atmospheric nitrogen based on osmium catalysts, which can accelerate the scission of the triple bond in nitrogen. Later, a much less expensive iron-based catalyst was developed by BASF researcher Alwin Mittasch. This single discovery made a huge impact on agriculture by allowing food production at rates needed to support today's global population.[5] In 1955, Karl Ziegler in Germany discovered that by using a $TiCl_3$ catalyst, ethylene and propylene could be polymerized to form long-chain molecules. Giulio Natta in Italy discovered that when propylene is used in this process, it can be ordered in a regular way to yield polymers with unique properties. The Ziegler–Natta catalysts have been used in commercial manufacture since 1956 and had a striking impact on the academic and scientific roles of macromolecular chemistry as a discipline, and led to a significant growth of the polymer industry. For this breakthrough, Ziegler and Natta received the Nobel Prize in Chemistry in 1963.[6] In the following years, heterogeneous catalysis grew steadily, with an impressive stream of discoveries. An example is the use of noble metal catalysts for the emission control of waste gases from automobiles. Catalytic converters, which possess a honeycomb shape and are coated with finely dispersed platinum, rhodium, and/or palladium, are inserted between the engine and the outlet of the exhaust pipe. The exhaust gases contain carbon monoxide, nitric oxide, and unburnt hydrocarbons, which

are converted to carbon dioxide, nitrogen, and water vapor.[7] Another example is the microporous solid acidic zeolite catalyst used in the fluid catalytic cracking process, which is one of the most important petroleum refinery processes to convert the heavy fractions of crude oils into lighter hydrocarbon products.[8]

### 8.1.2 Catalyst Deactivation

For most heterogeneous catalysts, only certain active sites such as unsaturated sites or deposited metal or metal oxide sites participate in the reaction of interest. These active sites interact with the adsorbed reactant molecules to initiate the reaction.[9] Catalyst deactivation, *i.e.* the loss of catalytic activity and/or selectivity over time, is a ubiquitous problem in industrial processes. The costs of catalyst regeneration, replacement, and process shutdown total billions of dollars per year. Several mechanisms may explain heterogeneous catalyst deactivation: (1) poisoning, which relates to the irreversible chemisorption of species, including reactants, products, or impurities, on catalytic sites; (2) fouling, which is the deposition of species such as carbon produced by hydrocarbon decomposition (*i.e.* coke) on supported metal catalysts that block catalytic sites and pores; (3) thermal degradation and sintering, which reduce the catalytic surface area due to particle growth at high reaction temperatures; (4) active supported metal loss through vaporization or volatile compound formation, which can be significant over a wide range of reaction conditions; and (5) the loss of catalytic material due to mechanical forces such as abrasion.[10]

Various methods have been developed to counter catalyst deactivation. For example, to prevent fouling, carbon gasification agents such as $H_2O$ and $O_2$ can be added.[11] Catalyst poisoning is largely caused by impurities in the feed stream and can therefore be reduced by minimizing these impurities. For instance, decreasing the concentration of sulfur compounds below 0.1 ppm in conventional methanation and Fischer–Tropsch process feeds prolonged the catalyst lifetime to $\sim$2 years.[12] Sintering of metal particle catalysts can be minimized by decreasing the reaction temperature below 0.3 times the melting point of the metal or by blending higher melting point metals with the base metal.[13] Due to the enhanced anchoring effect of the strong metal–support interaction between ceria and metals, the addition of ceria is essential in the washcoat to prepare catalysts for the three-way catalytic converter to stabilize the precious metals.[14] Another strategy to reduce metal nanoparticle sintering is to encapsulate the metal nanoparticles in a metal oxide layer and create pores to expose the metal surface.[15] In the next section, we elaborate on the encapsulation strategy for inhibiting heterogeneous catalyst deactivation, describe synthesis methods for preparing ultrathin metal oxide encapsulation layers, and review several applications that utilize these methods.

## 8.2 Synthesis Techniques for Encapsulating Metal Nanoparticle Catalysts

Metal nanoparticles play an important role in both fundamental scientific and industrial applications of heterogeneous catalysts. Based on the assumption that surface atoms are the catalytically active sites in metal nanoparticles, smaller nanoparticles should have a higher proportion of catalytically active sites compared with larger nanoparticles owing to their greater surface-to-volume ratio. However, because surface atoms are more weakly bound than their subsurface counterparts, thermodynamics drives the aggregation or sintering of smaller nanoparticles by secondary nucleation or Ostwald ripening.[16] Encapsulating the metal nanoparticles in an ultrathin metal oxide layer can reduce sintering, but any synthetic method for encapsulation must preserve access to the catalytically active sites or the catalyst will no longer function.

### 8.2.1 Encapsulation of Metal Nanoparticles Using Zeolites

Zeolites are crystalline, microporous aluminosilicates composed of $TO_4$ tetrahedra (T denotes Si, Al, P, *etc.*) forming three-dimensional frameworks with well-defined meso- and microchannels. Zeolites are formed naturally such as in volcanic activity and are also synthesized both in academic laboratories and in industry.[17] Zeolites are used in industry for three major areas: catalysis, gas separation, and ion exchange. The advantages of zeolites as solid acidic or basic catalysts have been extensively exploited in the refining and production of petrochemicals. Owing to the well-defined pore structure, zeolites can also be used as shape-selective catalysts that allow a greater degree of product control. In gas separation, the porous structure of zeolites can be used to ''sieve'' the gas molecules by allowing molecules with certain dimensions to enter while blocking others. The materials are used, for example, for removing $H_2O$, $CO_2$, and $SO_2$ from natural gas. Inside the zeolite framework, some cations are loosely bonded and readily exchange with other cations in aqueous media. Applications include the removal of metal cations from wastewater during water purification.[18,19]

Zeolite catalysts have been widely used because of the well-controlled acidity and shape selectivity. However, metal nanoparticles supported on the open surface of zeolites are often prone to sintering and poor dispersion, which reduces the stability and selectivity of the catalysts at high operating temperatures. Encapsulating metal nanoparticles into zeolite cavities can help to improve the overall catalytic performance. With the high stability of the zeolite framework, the size of the nanoparticles can be preserved. Moreover, the shape-selective effect of zeolite micropores can help to increase the product selectivity.

Metal precursors can be introduced into the cavities of zeolites using ion exchange and subsequently be converted to metal clusters. The amount of

metal that can be introduced is restricted by the exchange capacity of the zeolite, for example, by the number of Al atoms per unit cell for Al-containing zeolites. Using this method, Cai *et al.* encapsulated Au nanoclusters with an average size of 1 nm into HY zeolite, as shown in Figure 8.1, which exhibited superior catalytic performance for the selective oxidation of 5-hydroxymethyl-2-furfural (HMF) to 2,5-furandicarboxylic acid (FDCA).[20] The yield of FDCA was >99%, which was much higher than with Au supported on $TiO_2$, $Mg(OH)_2$, and channel-type zeolite ZSM-5. From the detailed characterization, the Au nanoclusters were restricted inside the HY zeolite cages, which prevented further growth in size. Moreover, the hydroxyl groups in the zeolite cages led to electronic modification of the Au nanoparticles, which is assumed to contribute to the high efficiency in the catalytic oxidation of HMF to FDCA. Here, it should be pointed out that for zeolites featuring a neutral framework, such as zeolites made exclusively of $SiO_4$ tetrahedra, ion exchange cannot be used. However, the metal can be introduced by wet impregnation, with the amount of incorporated metal being limited by the pore volume of the zeolite.

Sulikowski *et al.* introduced the ''ship-in-a-bottle'' synthesis technique. Using this method, 12-tungstophosphoric acid was encapsulated in faujasite supercages.[21] To encapsulate the heteropolyacid, the metal was first introduced into the zeolite cavities through wet impregnation or ion exchange, which was followed by adding phosphoric acid to form the heteropolyacid $H_3PW_{12}O_{40}$. Owing to its large size, the metal complex was restricted inside

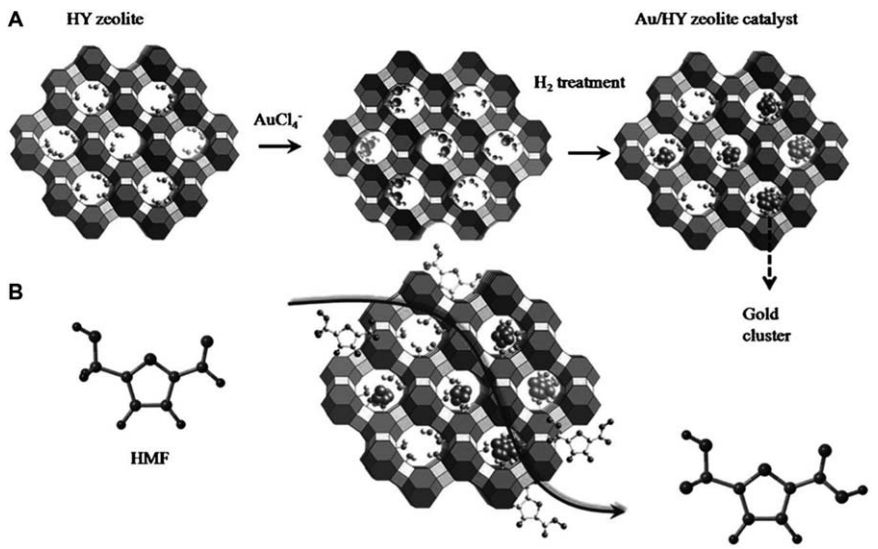


**Figure 8.1** (A) Schematic representation of Au nanoclusters synthesized in the supercages of HY zeolite induced by –OH groups. (B) Catalytic oxidation process.
Reproduced from ref. 20 with permission from John Wiley & Sons, Copyright © 2013 WILEY-VCH Verlag GmbH & Co. KGaA, Weinheim.

the zeolite supercage. This process is similar to the process of constructing a model ship inside a bottle, giving rise to the name of the synthesis technique. Yamaguchi *et al.* encapsulated Fe–bipyridine complexes into Na ion-exchanged Y-type zeolite (Na-Y) for oxidation of cyclohexene with hydrogen peroxide using this method. To synthesize this material, the Na-Y zeolite was ion exchanged using $FeSO_4 \cdot H_2O$ to yield Fe-exchanged Y-type zeolite (Fe-Y).[22] The Fe-Y was refluxed in bipyridine, followed by filtration, washing with water and methanol, and drying under vacuum at room temperature to yield a reddish pink powder. The catalyst can be recycled at least three times without significant loss of activity and selectivity to 2-cyclohexen-1-ol.[22] More recently, this technique has been used to encapsulate other metal complexes, such as Ni,[23] Cu,[24] Mn,[25] and Zn[26] complexes, into cavities or supercages of zeolites.

Metal nanoparticles can also be introduced into the zeolite cavities *via* one-pot hydrothermal synthesis. In this process, the metal nanoparticle precursor is mixed with the synthetic zeolite gel followed by crystallization of the zeolite at high temperature. As shown in Figure 8.2, Egeblad and

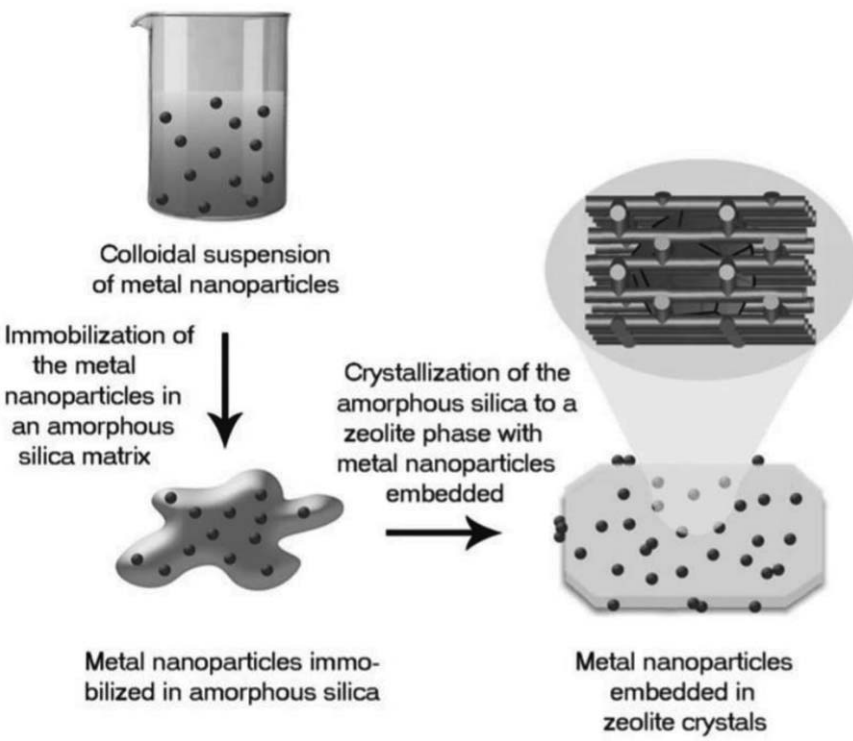


**Figure 8.2** Schematic illustration of the encapsulation of gold nanoparticles in zeolite crystals.
Reproduced from ref. 27 with permission from John Wiley & Sons, Copyright © 2010 WILEY-VCH Verlag GmbH & Co. KGaA, Weinheim.

co-workers synthesized silicalite-1 with highly dispersed encapsulated gold nanoparticles in the presence of gold colloid.[27] Using this approach, the prepared gold colloid was immobilized in an amorphous silica matrix and then encapsulated in silicalite-1 through subsequent crystallization. Apart from a few large particles that formed, most of the gold nanoparticles were maintained in the size range 1–2 nm. By heating to 500 °C, only the larger particles sintered whereas the small particles were less prone to sintering because they were fixed within the zeolite. Iglesia and co-workers encapsulated noble metal clusters of Pt, Pd, Rh, Ir, Re, and Ag within LTA zeolite using the same process.[28] To prevent premature precipitation of the metal precursor as colloidal oxyhydroxide during the hydrothermal synthesis, appropriate ligands ($NH_3$ for Pt and Ir; ethylenediamine for Pd, Rh, Re, and Ag) were used to preserve the metal cationic forms while allowing the assembly of zeolite building units around them. The mean metal cluster diameter was measured to be 1–2 nm.

Hollow zeolite capsules can be synthesized by assembling the zeolite on polymer spheres to form a polymer core–zeolite shell structure, and then removing the polymer spheres by calcination. If metal particles were contained inside the polymer spheres, after the removal of the polymer those metal particles remain encapsulated.[29] Using this strategy, various metals, such as Ag, Pd, and Pt, were confined in S-1 zeolite capsules.[30,31] Corma and co-workers reported a similar strategy to encapsulate Pt particles in two-dimensional layers of MCM-22-type zeolite.[32] The layers of MCM-22 were expanded with the insertion of a surfactant. Once the platinum particles had been introduced into the expanded layers, the surfactant was removed, leaving the stable platinum particles confined within the internal framework cavities. These subnanometer Pt species were very stable even after treatment in air at up to 540 °C and showed size-selective catalysis for the hydrogenation of alkenes.

### 8.2.2 Encapsulation of Metal Nanoparticles Using Oxide Shells

Encapsulation of metal nanoparticles in thermally stable oxide shells has been used to improve the stability of nanoparticles. The oxide shells must be thermally, mechanically, and chemically stable to sustain the working conditions. Unlike the use of intrinsically porous materials such as zeolites, pores must be formed in the oxide shells to facilitate the transfer of reactants and products to and from the catalyst. In some cases, the strong metal–support interaction effect, whereby the metal oxide support may form a shell or capping layer over the metal catalyst, may improve the overall catalytic performance. Because the oxide shell will inevitably block some of the metal surface sites, a balance between activity, selectivity, and stability must be considered when designing the nanostructure.

In the core–shell structure, the catalytically active metal nanoparticles are isolated from each other by a porous shell that stabilizes the nanoparticles against sintering. The use of amorphous, chemically and thermally stable silica has been intensively studied for encapsulating metal nanoparticles. Somorjai and co-workers reported the preparation of Pt–mesoporous silica core–shell (Pt@m$SiO_2$) nanoparticles that were thermally stable at high temperatures, as shown in Figure 8.3.[33] The mesopores provide direct access to the Pt core, rendering the Pt@m$SiO_2$ nanoparticles as catalytically active as bare Pt metal for ethylene hydrogenation and CO oxidation. The core–shell structured Pt@m$SiO_2$ nanoparticles were prepared in three steps. First, tetradecyltrimethylammonium bromide (TTAB) was applied as a capping agent on the outside of the Pt nanoparticles. Second, the as-synthesized Pt@$SiO_2$ particles were prepared by polymerization around the TTAB-capped Pt cores. Finally, the TTAB molecules were removed by calcination to produce the Pt@m$SiO_2$ core–shell nanoparticles. The Pt@m$SiO_2$ consisted of 14 nm Pt cores and mesoporous silica shells with 17 nm thickness. The silica shell mesopore size was measured to be 2–3 nm from transmission electron microscopy (TEM) images. Zhang and co-workers reported the use of a facile and scalable wet chemical process to prepare graphene nanosheet-supported metal nanoparticles covered with mesoporous silica layers.[34] In this process, the metal nanoparticles were first loaded with metal (M) using precursor metal hydroxide (MOH) onto graphene oxide (GO) nanosheets by deposition–precipitation. Subsequently, residual ammonium hydroxide from the urea used for deposition–precipitation catalyzed the hydrolysis of tetraethyl orthosilicate to form amorphous $SiO_2$ shells covering the MOH–GO composite. Finally, the as-prepared MOH–GO@m$SiO_2$ was annealed under $H_2$ to convert GO into reduced graphene oxide (rGO) and MOH into metal nanoparticles, thus producing M–rGO@m$SiO_2$ composite nanostructures. TEM images indicated an average Pt nanoparticle size of 1.65 nm encapsulated by 3 nm mesoporous silica shells. The Pt nanoparticle size remained almost unchanged up to temperatures as high as 700 °C.

Yolk–shell structures are considered as a subclass of core–shell structures in which the central portion (the yolk) is free to move within the void space of the larger core. Yolk–shell nanoparticles have attracted significant

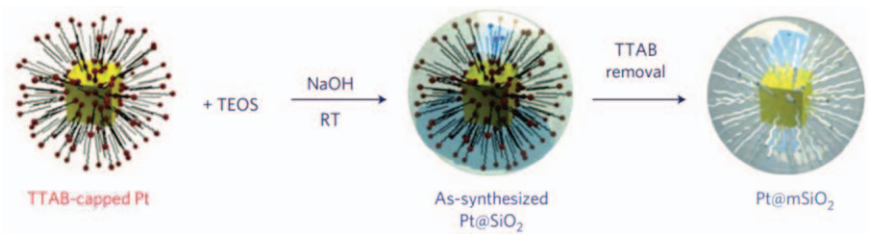


**Figure 8.3** Schematic representation of the synthesis of Pt@m$SiO_2$ nanoparticles. Reproduced from ref. 33 with permission from Springer Nature, Copyright 2009.

attention owing to their unique properties such as void space, large surface area, porous hollow shell, and low density. The importance of yolk–shell nanoparticles and their applications have been summarized in review articles.[35–41] Stucky and co-workers reported an assembly route to prepare yolk–shell catalytic nanoreactors with a 6.3 nm Au nanoparticle yolk and a mesoporous $ZrO_2$ shell, as shown in Figure 8.4A.[42] Dodecanethiol-capped 6.3 nm Au nanoparticles were synthesized as the starting material and ligand exchanged with mercaptoundecanoic acid to make them water soluble in the presence of $NH_3$. Next, the capped Au particles were coated with a silica layer to obtain the core–shell Au@$SiO_2$ composite with a spherical shell

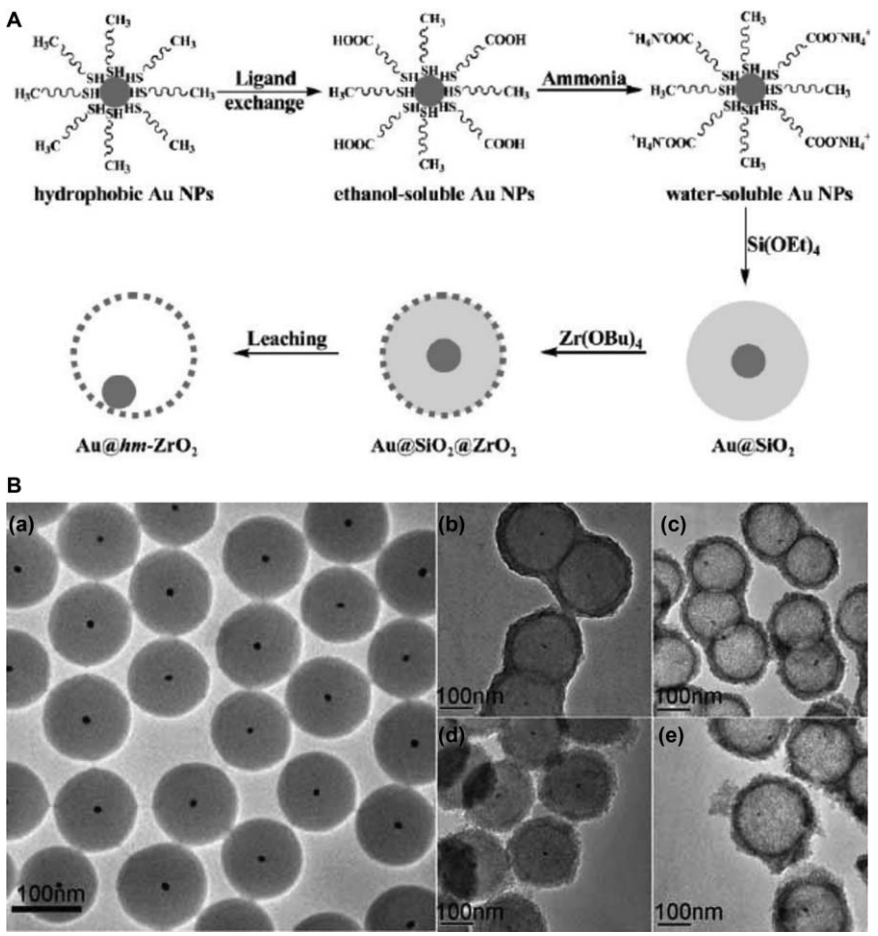


**Figure 8.4** (A) Synthetic procedure for Au@hm-$ZrO_2$ nanoreactors. (B) TEM images of (a) Au@$SiO_2$, (b) Au@$SiO_2$@$ZrO_2$, (c) Au@hm-$ZrO_2$, (d) Au@$SiO_2$@$TiO_2$, and (e) Au@hm-$TiO_2$.
Reproduced from ref. 42 with permission from John Wiley & Sons, Copyright © 2009 WILEY-VCH Verlag GmbH & Co. KGaA, Weinheim.

characterized by a diameter of about 120 nm and which contained only one Au nanoparticle, as shown by TEM in Figure 8.4Ba. The uniform Au@$SiO_2$ spheres were then coated with a layer of zirconia through the hydrolysis of $Zr(OBu)_4$ (Figure 8.4Bb). Finally, an NaOH solution was applied to remove the silica layer to create Au@hm-$ZrO_2$ nanoreactors (hm = hollow mesoporous) (Figure 8.4Bc). The as-prepared Au@hm-$ZrO_2$ nanoreactors were calcined in air at 300, 550, and 750 °C and showed very similar activity compared with the original untreated sample for the reduction of 4-nitrophenol, which indicated that the Au nanoparticles were highly stable against thermal sintering. Using a similar procedure, Au@hm-$TiO_2$ nanoreactors were also synthesized (Figure 8.4Bd and Be).

Another synthetic approach to create yolk–shell structures is *via* the Kirkendall effect, in which two solids with different interdiffusion rates are placed in contact, and the difference in rates causes the interface between them to move with time. This phenomenon has been successfully applied for synthesizing various hollow metal oxide yolk–shell structures. Alivisatos and co-workers synthesized gold–iron oxide core–hollow shell nanoparticles through the Kirkendall effect *via* the thermal decomposition of $Fe(CO)_5$ at the surface of gold nanoparticles.[43] The same group also synthesized platinum–cobalt oxide yolk–shell based on the same method.[44]

## 8.3 Encapsulation of Heterogeneous Catalysts Using Atomic Layer Deposition (ALD)

### 8.3.1 Introduction to ALD

Atomic layer deposition (ALD) is a vapor-phase deposition technique that uses sequential, self-limiting surface reactions to deposit thin films with atomic-level control over thickness and composition. Most ALD processes are based on binary reaction sequences in which two chemical precursor vapors react with the surface one at a time in a sequential manner. Since the number of surface active sites is finite, the surface reactions terminate once all of these sites have been consumed, even in the presence of excess precursor vapor. We consider $Al_2O_3$ ALD as an example, which is usually performed using alternating exposures to trimethylaluminum (TMA) and $H_2O$. In the first step, TMA is pulsed into the reaction chamber and reacts with the hydroxylated substrate until all of the hydroxyl groups have been consumed. Next, the excess TMA is purged from the chamber along with the by-product methane. Third, water vapor is pulsed into the chamber and reacts with the TMA-terminated surface until all of the methyl (Al–$CH_3$) sites have been consumed. Finally, the excess $H_2O$ and by-product methane are purged from the chamber. Note that following the $H_2O$ exposure, the $Al_2O_3$ surface is again hydroxyl terminated so that the ALD cycle may be repeated. One $Al_2O_3$ ALD cycle comprised of these four steps deposits ~1.2 Å of $Al_2O_3$ per cycle at 200 °C. A simplified depiction of the $Al_2O_3$ ALD surface chemistry is shown

in eqn (8.1) and (8.2), where the asterisks indicate the surface species and (g) signifies species in the gas phase.[45]

$$-OH^* + Al(CH_3)_3\,(g) \rightarrow -OAl(CH_3)_2{}^* + CH_4\,(g) \quad (8.1)$$

$$-OAl(CH_3)_2{}^* + 2H_2O\,(g) \rightarrow -OAl(OH)_2{}^* + 2CH_4\,(g) \quad (8.2)$$

Compared with other thin-film deposition techniques, such as chemical vapor deposition (CVD) and physical vapor deposition (PVD), ALD provides extremely uniform and conformal coatings even on complex 3D nanostructures such as porous catalyst supports. Owing to its ability to deposit thin films for a wide range of materials, including pure elements, oxides, nitrides, sulfides, and fluorides, ALD has been widely used in semiconductor engineering, microelectronics, catalysis, batteries, fuel cells, solar energy, and drug delivery. Many earlier reviews discussed ALD in detail,[46–49] and Chapters 2, 3, and 5 of this book describe the application of ultrathin ALD oxides in the fields of photoelectrochemistry and photovoltaics. In this section, we focus on the use of ALD for encapsulating heterogeneous catalysts.

### 8.3.2 ALD Tools and Methods for Coating Particles

Catalytic metal nanoparticles are typically dispersed on high surface area substrates, called catalyst supports, in the form of highly porous powders. ALD is capable of coating highly porous catalyst support powders with high precision, but in many cases the equipment and process are different from those used for coating planar substrates. The diffusion of the precursors and products into and away from reaction sites within the porous structures, and between the support particles themselves, can often be rate limiting, necessitating longer precursor exposures and some means of agitating the powder during ALD. Thus, the ALD process and reactor design are important for effective powder coating.

It is feasible to coat small quantities of porous powder (*e.g.* 1–10 g) using a conventional ALD system by uniformly spreading the powder inside a stainless-steel tray with a mesh cover on top of it. The mesh is intended to prevent spilling of the powder during handling but still provides efficient diffusion of the ALD precursors and product gases in and out of the tray. Long dose and purge times are required to allow for adequate penetration of the precursors into the pores of the powder substrate. To provide a sufficient ''soak'' time for precursor diffusion into the particle bed and within the particle pores and to maximize precursor usage, it is sometimes necessary to isolate the ALD chamber from the vacuum pump during precursor dosing (*i.e.* static dosing). However, with larger amounts of powder, it is often seen that only the top layer of the powder bed receives saturation exposures, while powder below the surface is unsaturated, resulting in a non-uniform ALD layer.[50] This problem can be avoided by using specialized ALD systems that agitate the powder, such as fluidized bed, rotary drum, or spatial ALD reactors.

Fluidized bed (FB) ALD reactors provide more efficient powder–precursor mixing and can reduce the need for long precursor ''soak'' times. In an FB ALD reactor, the powder is contained in a vertically oriented tube and the precursors are entrained in a flow of inert carrier gas injected from the bottom of the tube. The basic principle is that the upward drag force exerted by the carrier gas on the particles equals the downward gravitational force, resulting in the particles levitating and behaving as a fluid. An important parameter in fluidized beds is $U_{mf}$, the minimum velocity needed to fluidize the powder particles. $U_{mf}$ varies with the particle size, particle density, and carrier gas properties. Theoretically, the Ergun equation is used to describe the drag exerted on the particles by the fluid flow. The minimum fluidization velocity is calculated by equating this expression to the gravitation force on the particles and solving for $U_{mf}$.[51] Experimentally, the gas velocity is increased while monitoring the pressure drop across the particle bed. Initially, this pressure drop increases with increase in velocity, but when the gas velocity is raised beyond $U_{mf}$, the pressure drop becomes constant with increasing gas velocity and the particles become fluidized.[52] Mechanical vibration can be used to enhance the fluidization further.

In order to achieve the necessary temperature and pressure conditions for ALD, the FB vessel is housed inside a furnace and connected to a rotary vane pump. A typical FB ALD reactor is shown in Figure 8.5. This system includes mechanical vibration, mechanical rotation inside the reactor, and a residual

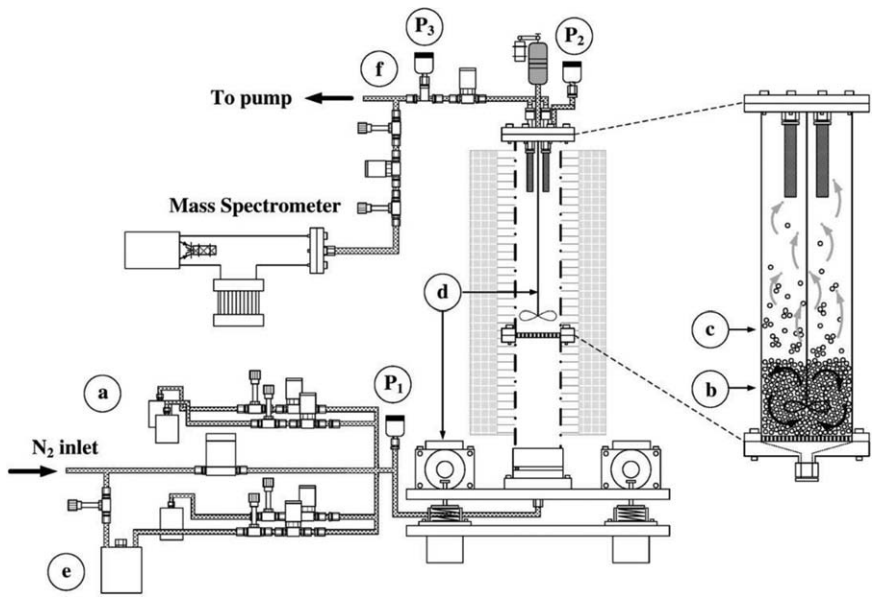


**Figure 8.5** Schematic of the fluidized bed reactor configuration with *in situ* mass spectrometry for particle ALD.
Reproduced from ref. 53 with permission from Elsevier, Copyright 2009.

gas analyzer at the outlet.[53] The pressure difference between $P_2$ and $P_1$ defines the pressure drop across the bed to determine $U_{mf}$.

One disadvantage of FB ALD is that the carrier gas velocity must be kept above $U_{mf}$ at all times during the ALD process to maintain fluidization, so that the precursor residence time in the reactor may be insufficient to achieve saturation. In this case, unreacted precursors exit the FB and are wasted. Rotary reactors were developed in order to decouple particle agitation from precursor residence time. George and co-workers developed the rotary reactor shown in Figure 8.6.[54] In this system, the ALD precursors are fed through a multiple-input manifold (a), which prevents the reactants from mixing until they have been introduced into the reactor. Static precursor exposures were achieved by closing a valve between the pump and the rotary reactor. The rotating drum (b) is connected to a motor *via* a rotary feedthrough (d), allowing the particles to be tumbled during the precursor exposures. Note the much larger volume of the ALD reactor compared with the rotating drum (b). This large reactor volume is advantageous to contain sufficient precursor to coat large substrate areas in a single static dose.

Both the FB and rotary drum reactors use conventional, or temporal, ALD in which the precursors are separated in time. Particles have also been coated by spatial ALD, in which the precursors are supplied continuously but in different physical locations separated by an inert gas purge zone. The ALD growth is achieved by moving the particles through the separated precursor zones and inert gas purge zones, allowing multiple precursor dose and purge steps to occur simultaneously. This method allows for

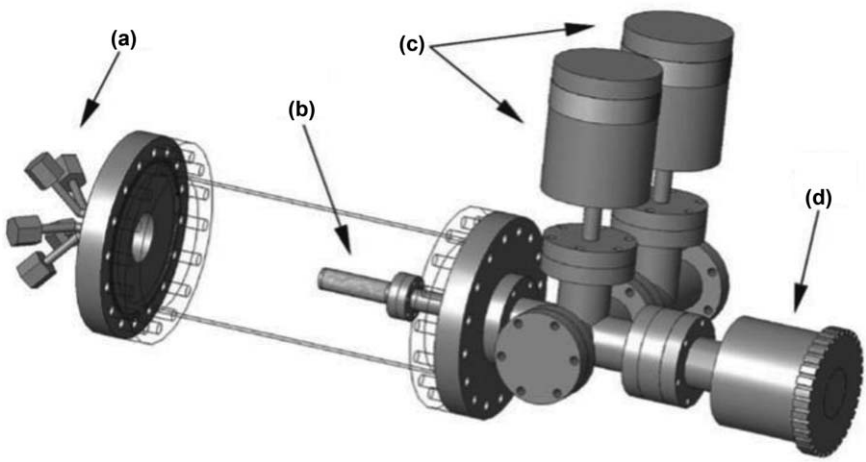


**Figure 8.6** Schematic diagram of a rotary reactor showing (a) multiple-input dosing flange, (b) rotating drum, (c) 10 and 1000 Torr capacitance manometers, and (d) magnetically coupled rotary manipulator.
Reproduced from ref. 54 with permission from AIP Publishing, Copyright 2007.

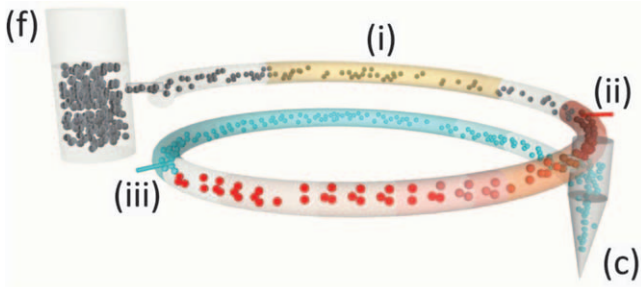


**Figure 8.7** Schematic of the spatial ALD reactor consisting of a fluidized feeding vessel (f), a pneumatic transport line made of three segments: preheating (i), precursor reaction zone (ii), and co-reactant reaction zone (iii), and a collection vessel (c).
Reproduced from ref. 57 with permission from AIP Publishing, Copyright 2015.

continuous operation, unlike the FB and rotary systems that use batch coating, with the potential for higher throughput.[55,56] As shown in Figure 8.7, van Ommen *et al.* designed a spatial ALD powder system in which the powder is transported pneumatically through a winding tube and the precursors are injected at different locations along the tube. Conditions must be established such that each precursor is completely consumed by the powder before reaching the next precursor zone to avoid CVD.[57]

### 8.3.3 ALD Coating to Enhance Catalytic Performance

Heterogeneous catalyst deactivation reduces the product yield and necessitates costly replacement or regeneration of spent catalyst, amounting to billions of dollars in lost revenue to the chemical industry. Although it is not possible to eliminate catalyst deactivation, the rate of deactivation can be minimized through control of the process conditions and catalyst formulation. In this section, we discuss methods to inhibit heterogeneous catalyst deactivation using ALD overcoating. Compared with other overcoating methods, such as sol–gel, precipitation, and CVD, ALD provides precise control over thickness and composition with superb conformality.

Two basic ALD strategies have been used to overcoat supported catalyst nanoparticles: thin films and thick films. The thin films are deposited using a small number of ALD cycles such that the nanoparticles are not completely covered, whereas the thick films use several nanometers of ALD coating that completely cover both the metal and support, followed by calcining to introduce nanopores that expose the metal surface. In both cases, the ALD coatings on the substrate can prevent sintering, while coatings on the metal can inhibit coking and improve catalyst selectivity.

### 8.3.3.1 ALD Thin-film Overcoating

It has been demonstrated theoretically and experimentally that thin ALD overcoats selectively decorate high-energy, low-coordination surface sites of metal nanoparticles. These sites are responsible for irreversible catalyst deactivation due to sintering and coke formation. Density functional theory (DFT) calculations revealed that the preferential decoration of $Al_2O_3$ ALD on Pt and Pd step edges stems from the greater free energy change on high-energy (211) surfaces compared with low-energy (111) surfaces.[58] A recent study combined first-principles calculations with microkinetic methods to show that the favorability of metal oxide ALD from 3d transition metal cyclopentadienyl precursors ($MCp_2$, M = Fe, Co, and Ni) follows the order edge > (100) > (111), which indicated that edges are covered first while the (111) facets can remain empty.[59] Diffuse reflectance infrared Fourier transform spectroscopy measurements using CO as a probe molecule (CO-DRIFTS) has been used to study the selective growth. Elam and co-workers found that $Al_2O_3$ overcoats preferentially nucleate at corners, steps, and edges of Pd nanoparticles while leaving the catalytically active Pd (111) facets accessible.[60] Lu and co-workers applied $TiO_2$ ALD overcoats on Au nanoparticles and also confirmed the preferential decoration of low-coordinated sites.[61] Qin and co-workers reported that $FeO_x$ ALD using ferrocene and $O_3$ preferentially deposited on the low-coordinated sites of Pt.[62] The decoration of the catalysts by $FeO_x$ ALD improved the selectivity of cinnamyl alcohol from 45% for bare Pt catalyst to 84% in the hydrogenation of cinnamaldehyde.

### 8.3.3.2 ALD Thick-film Overcoating

Although sub-monolayer ALD coatings can reduce sintering and coking, even greater inhibition of deactivation can be achieved by completely burying the catalytic metal nanoparticles under a thick ALD coating followed by heat treatment to create porous channels in the ALD film that allow reactants to access the catalyst and products to diffuse back in the opposite direction. Elam and co-workers studied the development of nanoscale porosity in ALD layers of $TiO_2$ and $Al_2O_3$ as a function of annealing temperature.[63] Using small-angle X-ray scattering (SAXS) and X-ray diffraction (XRD), they monitored the ALD overcoat structure during thermal annealing and discovered that nanopore formation coincided with the amorphous to crystalline phase transition for both of the ALD layers. With increase in annealing temperature, the nanopore size increased irreversibly. Stair and co-workers discovered a tunable relationship between overall water content and pore volume of the ALD layers.[64] The ALD films deposited at higher temperatures contained less water and produced smaller pores after annealing. Both studies reported that nanoscale pores form at temperatures between 500 and 650 °C.

Pore formation upon annealing thick ALD overcoat layers uncovers the catalytically active sites of the buried metal nanoparticles. As illustrated in

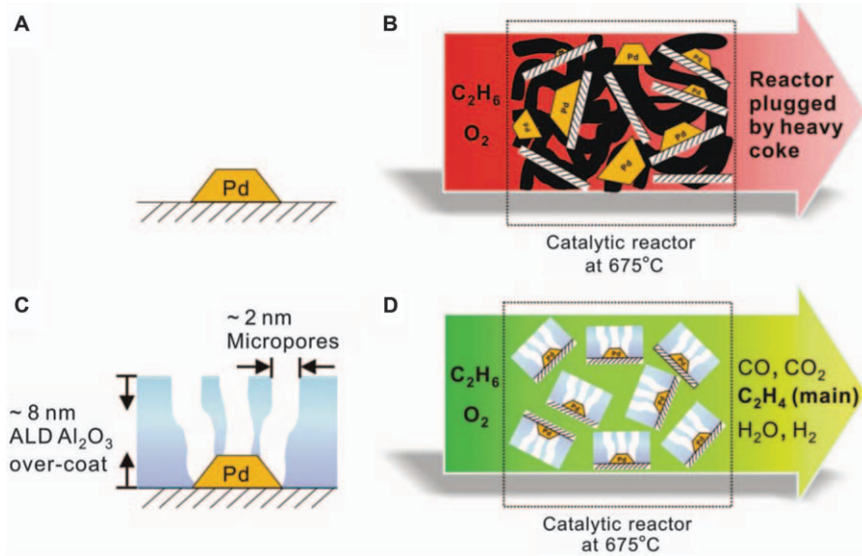


**Figure 8.8** Schematic model of $Pd/Al_2O_3$ catalysts with and without ALD $Al_2O_3$ overcoat during the oxidative dehydrogenation of ethane (ODHE) reaction at 675 °C. (A) The uncoated $Pd/Al_2O_3$ catalyst; (B) the uncoated $Pd/Al_2O_3$ catalyst during ODHE reaction; (C) the Pd catalyst with ALD $Al_2O_3$ overcoat; (D) the ALD $Al_2O_3$ overcoated $Pd/Al_2O_3$ catalyst during ODHE reaction.
Reproduced from ref. 65 with permission from The American Association for the Advancement of Science, Copyright 2012.

Figure 8.8, overcoating-supported palladium nanoparticles with 45 cycles of alumina significantly reduced deactivation by coking and sintering in the oxidative dehydrogenation of ethane (ODHE) at 675 °C, as reported by Stair *et al.*[65] High-resolution TEM measurements yielded an $Al_2O_3$ overcoat thickness of $7.7 \pm 0.4$ nm. Prior to calcination, the Pd nanoparticles were completely covered since all the CO chemisorption peaks disappeared. The CO chemisorption peaks returned after calcining the material at 500 °C in oxygen, and became larger after calcination at 700 °C. The effect of overcoating on the thermal stability of Pd nanoparticles was determined by using scanning transmission electron microscopy (STEM). The as-prepared $Pd/Al_2O_3$ had a particle size of $2.8 \pm 0.5$ nm. After 30 min of reaction, the uncoated Pd particles grew substantially larger ($4.6 \pm 1.9$ nm) and the size distribution became broader due to sintering. Moreover, the rate of product formation decreased to zero in less than 30 min and the reactor was completely plugged owing to coke formation. However, the 45 ALD $Al_2O_3$ cycle overcoated Pd particles were essentially unchanged in size ($2.8 \pm 0.5$ nm) even after 1700 min of reaction and showed dramatic improvements in ethylene yield and stable activity for ~1700 min. The CO-DRIFTS spectra showed that the ALD $Al_2O_3$ overcoat preferentially blocked the low-coordinated Pd surface sites that favor C–C bond scission and hydrogen

stripping to produce $C_1$ fragments that lead to coke, $CH_4$, CO, and $CO_2$. The selective blockage of the low-coordinated sites also explained the stability improvement because Ostwald ripening proceeds *via* the release of low-coordinated surface metal atoms to form larger particles.

Copper chromite is an effective catalyst for the selective hydrogenation of 2-furfuraldehyde. However, this catalyst suffers from deactivation due to coke formation and the migration of chromium over the copper. Marshall and co-workers found that a thin ALD $Al_2O_3$ layer could increase the catalyst stability for gas-phase 2-furfuraldehyde hydrogenation.[66] The catalyst stability improved and there was almost no deactivation within 5 h after 45 ALD $Al_2O_3$ cycles. To introduce porosity in the ALD $Al_2O_3$ layers, the catalysts were treated in flowing $N_2$ at 700 °C. XRD and X-ray absorption fine structure (XAFS) analysis suggested the formation of copper aluminate. They also applied ALD $Al_2O_3$ overcoats on $Al_2O_3$-supported Pd catalysts for the same reaction and found that the 2-furfuraldehyde hydrogenation selectivity was improved due to preferential covering of the Pd step edges, leaving the terrace sites active for furan formation.[67] Dumesic and co-workers stabilized supported copper catalysts for the liquid-phase hydrogenation of 2-furfuraldehyde using ALD $Al_2O_3$ overcoats.[68–70] In addition to stabilizing the nanoparticles, they proposed that the acidic ALD $Al_2O_3$ formed metal–acid bifunctional catalyst sites. The acidity of the $Al_2O_3$ overcoat layer catalyzed the etherification of furfuryl alcohol with 1-butanol to form furfuryl butyl ether. To support this assertion, they performed ALD overcoating of the more acidic $NbO_x$, and measured the etherification rate to be an order of magnitude higher. A later study by Marshall and co-workers examined ALD $TiO_2$ overcoating of copper chromite catalysts.[71] They found that 75% activity was preserved following 20 ALD $TiO_2$ cycles (Figure 8.9) and attributed this behavior to the weaker interaction between $TiO_2$ and copper chromite compared with $Al_2O_3$. Huber and co-workers reported similar results when they compared ALD $Al_2O_3$ and $TiO_2$ overcoats to enhance the stability of cobalt catalysts for aqueous-phase reactions.[72] Their study showed that a thin, 1.2 nm ALD $TiO_2$ overcoating could prevent both leaching and sintering of cobalt particles, whereas $Al_2O_3$ overcoating caused the formation of an irreducible cobalt aluminate phase that had no catalytic activity. In addition to the examples presented above, previous studies have examined ALD overcoating to improve the catalytic performance of other metals, including Au,[61] Pt,[73] and Ni.[74]

### *8.3.3.3 Overcoating by Area-selective ALD*

In the examples presented above, the ALD occurs simultaneously on both the metal nanoparticles and on the substrate. It is sometimes advantageous for the overcoat to grow only on the substrate without coating the metal nanoparticle, or *vice versa*. Area-selective ALD is a method that can control the growth to occur only at certain, chemically distinct locations. For example, if the metal nanoparticles are first protected with a blocking layer

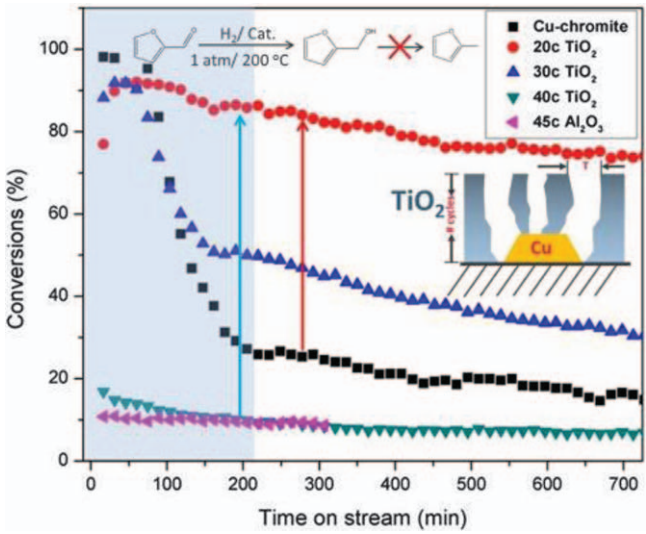


**Figure 8.9** Conversion *versus* time on-stream for the selective hydrogenation of furfural.
Reproduced from ref. 71 with permission from Elsevier, Copyright 2015.

prior to the ALD, then the ALD overcoating will occur only on the substrate and not on the protected nanoparticles. The blocking agent can then be removed. Stair and co-workers studied four types of blocking agent, nitriles, amines, thiols, and hfac ligand (hfac = hexafluoroacetylacetonate), and found that the amines and thiols showed the highest binding affinity and protection for palladium nanoparticles.[75] Chen and co-workers reported using area-selective ALD to construct oxide nanotraps to anchor platinum nanoparticles, with the synthetic procedure shown in Figure 8.10a.[76] In this study, 1-octadecanethiol (ODT) was used as the blocking agent owing to the strong binding between the thiol group and the platinum nanoparticles (Figure 8.10b,c). $Co_3O_4$ was then deposited on the $Al_2O_3$ support by ALD. The $Co_3O_4$ did not grow on the Pt nanoparticles because the ODT is unreactive towards the $Co_3O_4$ ALD precursors. Finally, after removing the blocking agent ODT *via* calcination in air, the $Co_3O_4$ nanotraps were formed surrounding the bare platinum nanoparticles as shown in Figure 8.10d,e. As a control, 50 cycles of $Co_3O_4$ were directly deposited on $Pt/Al_2O_3$ without ODT treatment (sample denoted $Co_3O_4$@$Pt/Al_2O_3$), confirming uniform $Co_3O_4$ coverage of both Pt nanoparticles and the substrate (Figure 8.10f,g). Owing to the formation of the $Pt/Co_3O_4$ interface, the CO oxidation temperature and activation energy decreased. The thermal stability of the platinum nanoparticles was evaluated after calcination treatments at 600 °C in air. After calcination, the Pt nanoparticles in the $Co_3O_4$ nanotraps had an average size of 2.9 nm whereas the Pt nanoparticles without the $Co_3O_4$ nanotraps increased to an average size of 9.7 nm.

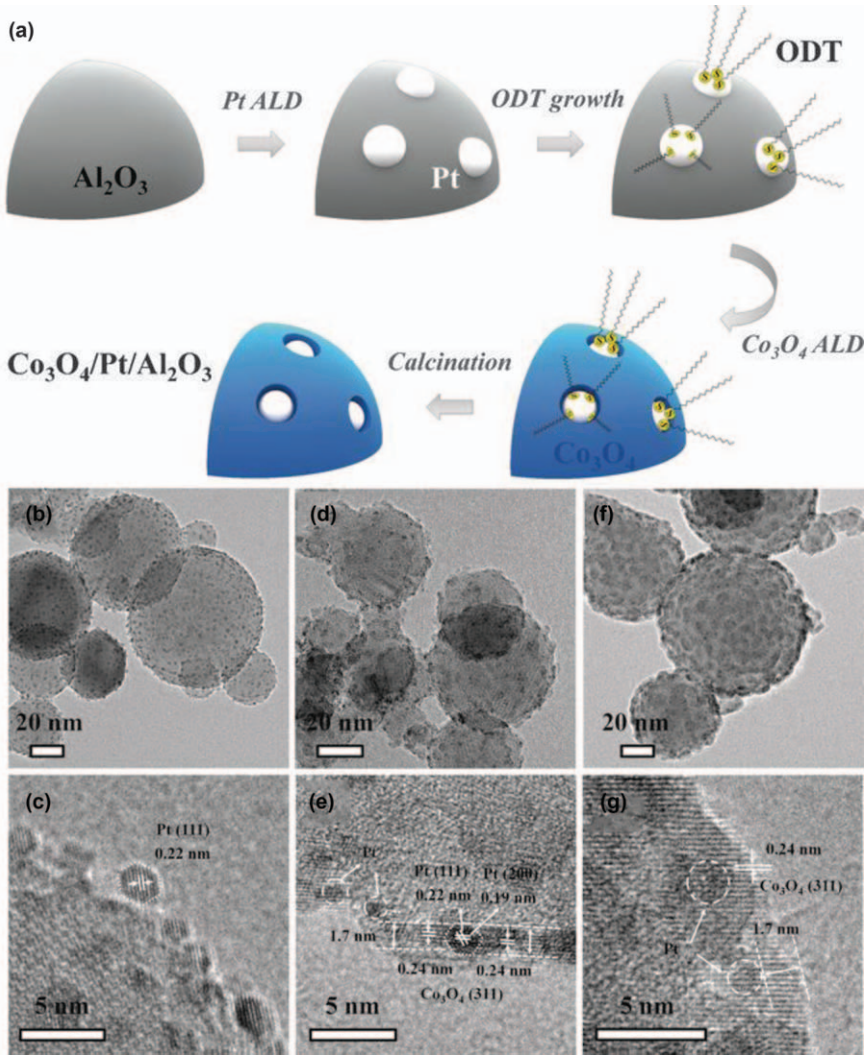


**Figure 8.10** Preparation of $Co_3O_4$ nanotrap-anchored Pt nanoparticles on $Al_2O_3$ supports based on area-selective ALD. TEM results for (b,c) $Pt/Al_2O_3$, (d,e) $Co_3O_4/Pt/Al_2O_3$, and (f,g) $Co_3O_4@Pt/Al_2O_3$.
Reproduced from ref. 76 with permission from John Wiley & Sons, Copyright © 2017 WILEY-VCH Verlag GmbH & Co. KGaA, Weinheim.

In some cases, the blocking agents can be the ligands from the ALD precursors. For instance, Figure 8.11 shows a schematic model for the ABC-type ALD method reported by Lu and Stair for the synthesis of highly dispersed palladium nanoparticles.[77] In the first step, the initial support was exposed to $Pd(hfac)_2$ and the hfac ligands remained on the palladium. Next, TMA was introduced to react with the surface hydroxyl groups on the support surface at 80 °C followed by $H_2O$ to form $Al_2O_3$. The protection afforded by

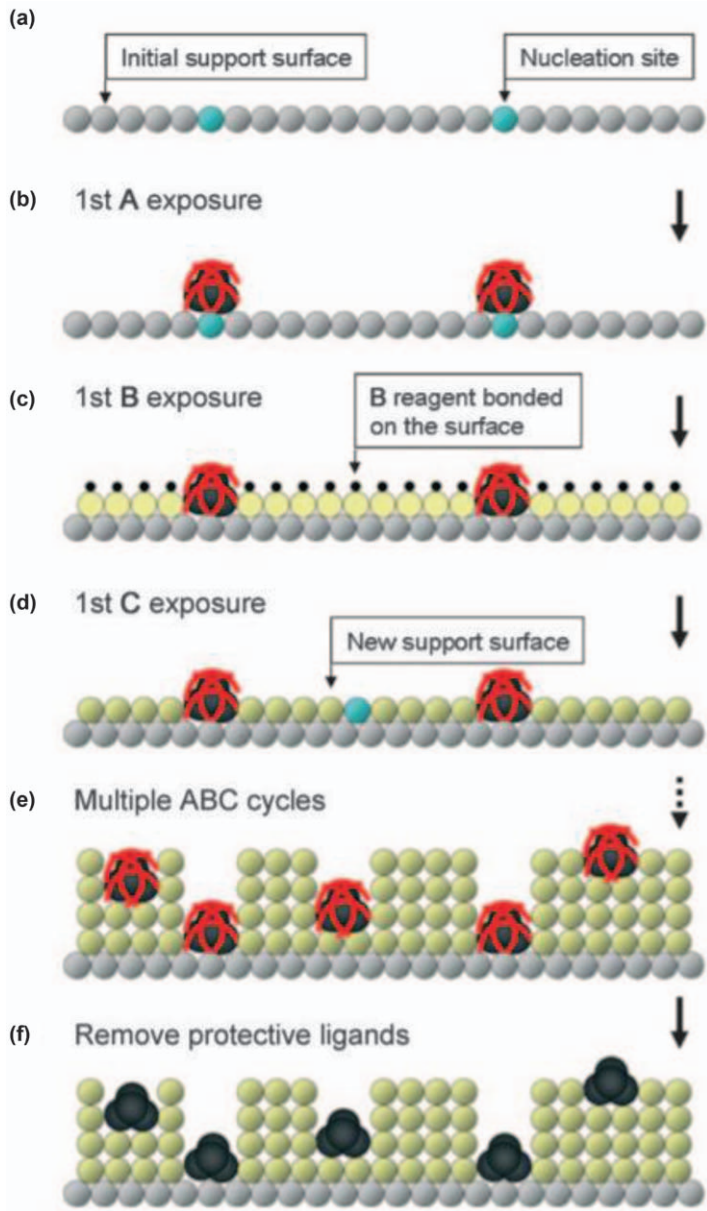


**Figure 8.11** Schematic model of ABC-type ALD.
Reproduced from ref. 77 with permission from John Wiley & Sons, Copyright © 2010 WILEY-VCH Verlag GmbH & Co. KGaA, Weinheim.

the hfac ligands prevented the ALD of $Al_2O_3$ on the palladium. The ABC sequence [$Pd(hfac)_2$, TMA, $H_2O$] could be repeated a number of times to increase the surface density of protected palladium nanoparticles, after

which the hfac ligands were removed by calcination to re-expose the palladium nanoparticles.

In some cases, it is desirable to coat only the metal nanoparticles while avoiding growth on the surrounding substrate. An example is the ALD of bimetallic nanoparticles where the ALD of the individual metal components should occur only on the bimetallic nanoparticle to adjust the composition and structure. Owing to synergetic effects between different metals, bimetallic nanoparticle catalysts have been widely studied for their enhanced activity and selectivity compared with their monometallic counterparts. In some cases, core–shell nanoparticles can be synthesized using area-selective ALD. Chen and co-workers proposed a synthesis strategy for Pd core–Pt shell nanoparticles utilizing octadecyltrichlorosilane (ODTS) self-assembled monolayers (SAMs) to modify the surface, as shown in Figure 8.12.[78] The ODTS SAMs formed exclusively on the native oxide substrate and were controlled purposely to be less than a full monolayer to incorporate pinholes. The pinholes in the ODTS layer still have reactive hydroxyl (–OH) groups exposed to initiate the nucleation of palladium ALD to form the metal cores. In the next step, Pt ALD is performed, resulting in a Pt shell because the Pt precursors react only with the palladium cores. During both the Pd and Pt ALD, the surface covered with closely packed ODTS molecules was inactive because the methyl ($-CH_3$) end-groups were inert in the ALD process. Elam and co-workers reported a method to synthesize bimetallic nanoparticles using ALD by adjusting the deposition temperatures and

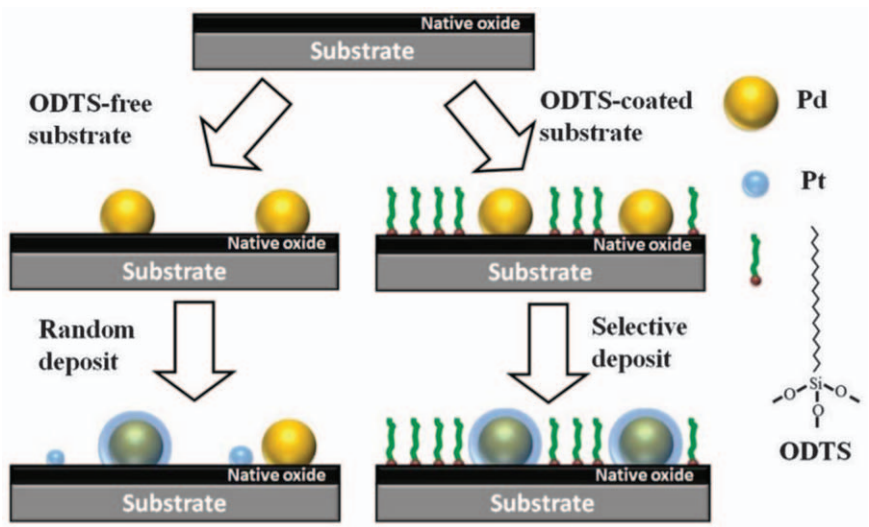


**Figure 8.12** Schematic illustration of the fabrication of core–shell nanoparticles through area-selective ALD on an ODTS-modified substrate. Reproduced from ref. 78, https://doi.org/10.1038/srep08470, under the terms of the CC BY 4.0 license http://creativecommons.org/licenses/by/4.0/.

co-reactants.[79] Palladium ALD using $Pd(hfac)_2$ and $H_2$ at 150 °C exhibited linear growth without any nucleation delay on Pt and Ru metal surfaces. In contrast, no Pd growth was observed on $Al_2O_3$, $TiO_2$, and $ZrO_2$ surfaces under the same conditions. Similarly, platinum ALD showed linear growth on Pd and Ru surfaces using trimethyl(methylcyclopentadienyl)platinum(IV) ($MeCpPtMe_3$) and $O_2$ at 150 °C. Again, the Pt growth on $Al_2O_3$, $TiO_2$, and $ZrO_2$ surfaces was negligible. This selective ALD of the secondary metal on the primary metal surface but not on the support provides another strategy for synthesizing supported bimetallic nanoparticles. This method can generate core–shell or mixed alloy bimetallic nanoparticles depending on the interdiffusion rates of the two metals.

### *8.3.3.4 Overcoating by Molecular Layer Deposition (MLD)*

Analogous to ALD, molecular layer deposition (MLD) is based on sequential and self-limiting surface reactions between precursor vapors and a surface. However, whereas ALD generates inorganic thin films, MLD uses organic precursors to produce polymers or organic–inorganic hybrid films.[80,81] An example is the MLD of alucone using TMA and ethylene glycol [EG, HO–$(CH_2)_2$–OH]. The alucone MLD film retains the ethylene groups from the EG precursor and exhibits materials properties between those of $Al_2O_3$ and organic polymers. Many other metalcone films have been prepared by MLD, including zircone, magnesicone, titanicone, vanadicone, and hafnicone.[82–86] For applications in catalysis, it is crucial for the overcoat film to be porous. The organic components inside the MLD layers can be removed by thermal treatment or water etching, leaving the residual porous layers to inhibit sintering of the metal nanoparticles.[87,88] Supported nickel catalysts are used for dry reforming of methane (DRM) in industry but suffer from deactivation due to coking and sintering. Medlin and co-workers used porous alucone layers to inhibit the sintering of Ni nanoparticles.[89] The catalysts were evaluated at 700 °C to gauge the effectiveness of the MLD layers. Compared with the uncoated catalyst, the DRM rates increased over time and remained stable for 108 h when the catalysts were modified with 10 MLD alucone cycles. The average thickness of the MLD layer measured by TEM was 2.4 nm. Rosowski and co-workers applied both ALD of $Al_2O_3$ and MLD of alucone on nickel catalysts for DRM.[90] They discovered that the ALD-modified Ni catalysts were inactive owing to the formation of inactive $NiAl_2O_4$, whereas the MLD-modified Ni catalysts showed impressive activity and stability.

## 8.4 Conclusions and Perspective

Encapsulation of nanoparticles is an effective method to improve catalyst selectivity, activity, and stability. The ability to achieve thin-film deposition with atomic-scale precision makes ALD a promising tool for the encapsulation of metal nanoparticles in heterogeneous catalysis. In this chapter, we have presented a series of ALD overcoating strategies for this purpose.

By precisely tailoring the interface properties of the overcoat film and nanoparticles, such as film thickness, composition, porosity, and blocking agent bonding, excellent catalytic performance can be obtained. However, there are still challenges that remain to be addressed. The preferential decoration at low-coordinated sites has been demonstrated by ALD; if those sites were active in some cases, the ALD overcoating would inhibit the catalyst performance. In addition, there are cases where the overcoat film and metal nanoparticles have strong interactions that could form irreducible phases, which would be detrimental to performance. For ALD overcoating to become commercially viable, scalable coating strategies must be developed that maximize throughput and precursor utilization.

## References

1. G. A. Somorjai and Y. Li, *Introduction to Surface Chemistry and Catalysis*, John Wiley & Sons, New York, 2010.
2. R. A. Van Santen, *Modern Heterogeneous Catalysis: An Introduction*, John Wiley & Sons, New York, 2017.
3. G. Rothenberg, *Catalysis: Concepts and Green Applications*, John Wiley & Sons, New York, 2017.
4. C. H. Bartholomew and R. J. Farrauto, *Fundamentals of Industrial Catalytic Processes*, John Wiley & Sons, New York, 2011.
5. B. E. Smith, R. L. Richards and W. E. Newton, *Catalysts for Nitrogen Fixation: Nitrogenases, Relevant Chemical Models and Commercial Processes*, Springer Science & Business Media, Berlin, 2013.
6. G. Fink, R. Mülhaupt and H. H. Brintzinger, *Ziegler Catalysts: Recent Scientific Innovations and Technological Improvements*, Springer Science & Business Media, Berlin, 2012.
7. K. C. Taylor, *Catalysis*, Springer, Berlin, 1984.
8. R. Sadeghbeigi, *Fluid Catalytic Cracking Handbook*, Elsevier, Amsterdam, 1995.
9. U. Hanefeld and L. Lefferts, *Catalysis: An Integrated Textbook for Students*, John Wiley & Sons, New York, 2018.
10. M. D. Argyle and C. H. Bartholomew, *Catalysts*, 2015, **5**, 145.
11. C. H. Bartholomew, *Catal. Rev. Sci. Eng.*, 1982, **24**, 67.
12. B. C. Enger and A. Holmen, *Catal. Rev.*, 2012, **54**, 437.
13. C. H. Bartholomew, *Stud. Surf. Sci. Catal.*, 1994, **88**, 1.
14. J. Kašpar, P. Fornasiero and M. Graziani, *Catal. Today*, 1999, **50**, 285.
15. B. J. O'Neill, D. H. Jackson, J. Lee, C. Canlas, P. C. Stair, C. L. Marshall, J. W. Elam, T. F. Kuech, J. A. Dumesic and G. W. Huber, *ACS Catal.*, 2015, **5**, 1804.
16. C. H. Bartholomew, *Appl. Catal., A*, 2001, **212**, 17.
17. B. M. Weckhuysen and J. Yu, *Chem. Soc. Rev.*, 2015, **44**, 7022.
18. M. W. Ackley, S. U. Rege and H. Saxena, *Microporous Mesoporous Mater.*, 2003, **61**, 25.
19. S. K. Ouki and M. Kavannagh, *Water Sci. Technol.*, 1999, **39**, 115.

20. J. Cai, H. Ma, J. Zhang, Q. Song, Z. Du, Y. Huang and J. Xu, *Chem. – Eur. J.*, 2013, **19**, 14215.
21. B. Sulikowski, J. Haber, A. Kubacka, K. Pamin, Z. Olejniczak and J. Ptaszyński, *Catal. Lett.*, 1996, **39**, 27.
22. S. Yamaguchi, T. Fukura, K. Takiguchi, C. Fujita, M. Nishibori, Y. Teraoka and H. Yahiro, *Catal. Today*, 2015, **242**, 261.
23. A. Choudhary, B. Das and S. Ray, *Inorg. Chim. Acta*, 2017, **462**, 256.
24. K. K. Bania and R. C. Deka, *J. Phys. Chem. C*, 2013, **117**, 11663.
25. S. Rayati, S. Shokoohi and E. Bohloulbandi, *J. Iran. Chem. Soc.*, 2016, **13**, 1983.
26. M. Maurya, S. Titinchi, S. Chand and I. M. Mishra, *J. Mol. Catal. A: Chem.*, 2002, **180**, 201.
27. A. B. Laursen, K. T. Højholt, L. F. Lundegaard, S. B. Simonsen, S. Helveg, F. Schüth, M. Paul, J. D. Grunwaldt, S. Kegnæs, C. H. Christensen and K. Egeblad, *Angew. Chem. Int. Ed.*, 2010, **49**, 3504.
28. Z. Wu, S. Goel, M. Choi and E. Iglesia, *J. Catal.*, 2014, **311**, 458.
29. A. Dong, Y. Wang, Y. Tang, N. Ren, Y. Zhang and Z. Gao, *Chem. Mater.*, 2002, **14**, 3217.
30. A. Dong, N. Ren, W. Yang, Y. Wang, Y. Zhang, D. Wang, J. Hu, Z. Gao and Y. Tang, *Adv. Funct. Mater.*, 2003, **13**, 943.
31. J. Shi, X. Li, Q. Wang, Y. Zhang and Y. Tang, *J. Catal.*, 2012, **291**, 87.
32. L. Liu, U. Diaz, R. Arenal, G. Agostini, P. Concepción and A. Corma, *Nat. Mater.*, 2017, **16**, 132.
33. S. H. Joo, J. Y. Park, C.-K. Tsung, Y. Yamada, P. Yang and G. A. Somorjai, *Nat. Mater.*, 2009, **8**, 126.
34. L. Shang, T. Bian, B. Zhang, D. Zhang, L. Z. Wu, C. H. Tung, Y. Yin and T. Zhang, *Angew. Chem. Int. Ed.*, 2014, **53**, 250.
35. G. Li and Z. Tang, *Nanoscale*, 2014, **6**, 3995.
36. M. Pérez-Lorenzo, B. Vaz, V. Salgueiriño and M. A. Correa-Duarte, *Chem. – Eur. J.*, 2013, **19**, 12196.
37. J. Liu, S. Z. Qiao, J. S. Chen, X. W. D. Lou, X. Xing and G. Q. Lu, *Chem. Commun.*, 2011, **47**, 12578.
38. C. Fan, L. Zhang, S. Wang, D. Wang, L. Lu and A. Xu, *Nanoscale*, 2012, **4**, 6835.
39. H. Li, Z. Bian, J. Zhu, D. Zhang, G. Li, Y. Huo, H. Li and Y. Lu, *J. Am. Chem. Soc.*, 2007, **129**, 8406.
40. J. Liu, H. Xia, D. Xue and L. Lu, *J. Am. Chem. Soc.*, 2009, **131**, 12086.
41. I. S. Lee, N. Lee, J. Park, B. H. Kim, Y.-W. Yi, T. Kim, T. K. Kim, I. H. Lee, S. R. Paik and T. Hyeon, *J. Am. Chem. Soc.*, 2006, **128**, 10658.
42. X. Huang, C. Guo, J. Zuo, N. Zheng and G. D. Stucky, *Small*, 2009, **5**, 361.
43. E. V. Shevchenko, M. I. Bodnarchuk, M. V. Kovalenko, D. V. Talapin, R. K. Smith, S. Aloni, W. Heiss and A. P. Alivisatos, *Adv. Mater.*, 2008, **20**, 4323.
44. Y. Yin, R. M. Rioux, C. K. Erdonmez, S. Hughes, G. A. Somorjai and A. P. Alivisatos, *Science*, 2004, **304**, 711.
45. R. L. Puurunen, *J. Appl. Phys.*, 2005, **97**, 9.

46. R. W. Johnson, A. Hultqvist and S. F. Bent, *Mater. Today*, 2014, **17**, 236.
47. J. R. Bakke, K. L. Pickrahn, T. P. Brennan and S. F. Bent, *Nanoscale*, 2011, **3**, 3482.
48. J. Van Delft, D. Garcia-Alonso and W. Kessels, *Semicond. Sci. Technol.*, 2012, **27**, 074002.
49. M. Knez, K. Nielsch and L. Niinistö, *Adv. Mater.*, 2007, **19**, 3425.
50. D. Longrie, D. Deduytsche and C. Detavernier, *J. Vac. Sci. Technol., A*, 2014, **32**, 010802.
51. Y. Mawatari, Y. Tatemoto and K. Noda, *Powder Technol.*, 2003, **131**, 66.
52. D. M. King, X. Liang, Y. Zhou, C. S. Carney, L. F. Hakim, P. Li and A. W. Weimer, *Powder Technol.*, 2008, **183**, 356.
53. D. M. King, J. A. Spencer II, X. Liang, L. F. Hakim and A. W. Weimer, *Surf. Coat. Technol.*, 2007, **201**, 9163.
54. J. A. McCormick, B. L. Cloutier, A. W. Weimer and S. M. George, *J. Vac. Sci. Technol., A*, 2007, **25**, 67.
55. P. Poodt, D. C. Cameron, E. Dickey, S. M. George, V. Kuznetsov, G. N. Parsons, F. Roozeboom, G. Sundaram and A. Vermeer, *J. Vac. Sci. Technol., A*, 2012, **30**, 010802.
56. P. Poodt, A. Lankhorst, F. Roozeboom, K. Spee, D. Maas and A. Vermeer, *Adv. Mater.*, 2010, **22**, 3564.
57. J. R. van Ommen, D. Kooijman, M. D. Niet, M. Talebi and A. Goulas, *J. Vac. Sci. Technol., A*, 2015, **33**, 021513.
58. J. Lu, B. Liu, N. P. Guisinger, P. C. Stair, J. P. Greeley and J. W. Elam, *Chem. Mater.*, 2014, **26**, 6752.
59. Y. Wen, J. Cai, J. Zhang, J. Yang, L. Shi, K. Cao, R. Chen and B. Shan, *Chem. Mater.*, 2018, **31**, 101.
60. H. Feng, J. Lu, P. C. Stair and J. W. Elam, *Catal. Lett.*, 2011, **141**, 512.
61. C. Wang, H. Wang, Q. Yao, H. Yan, J. Li and J. Lu, *J. Phys. Chem. C*, 2016, **120**, 478.
62. Q. Hu, S. Wang, Z. Gao, Y. Li, Q. Zhang, Q. Xiang and Y. Qin, *Appl. Catal., B*, 2017, **218**, 591.
63. S. Karwal, T. Li, A. Yanguas-Gil, C. P. Canlas, Y. Lei, A. U. Mane, J. A. Libera, S. Seifert, R. E. Winans and J. W. Elam, *J. Vac. Sci. Technol., A*, 2018, **36**, 01A103-1.
64. C. George, P. Littlewood and P. C. Stair, *ACS Appl. Mater. Interfaces*, 2020, **12**, 20331.
65. J. L. Lu, B. S. Fu, M. C. Kung, G. M. Xiao, J. W. Elam, H. H. Kung and P. C. Stair, *Science*, 2012, **335**, 1205.
66. H. B. Zhang, C. Canlas, A. J. Kropf, J. W. Elam, J. A. Dumesic and C. L. Marshall, *J. Catal.*, 2015, **326**, 172.
67. H. B. Zhang, X. K. Gu, C. Canlas, A. J. Kropf, P. Aich, J. P. Greeley, J. W. Elam, R. J. Meyers, J. A. Dumesic, P. C. Stair and C. L. Marshall, *Angew. Chem. Int. Ed.*, 2014, **53**, 12132.
68. A. C. Alba-Rubio, B. J. O'Neill, F. Shi, C. Akatay, C. Canlas, T. Li, R. Winans, J. W. Elam, E. A. Stach, P. M. Voyles and J. A. Dumesic, *ACS Catal.*, 2014, **4**, 1554.

69. B. J. O'Neill, D. H. K. Jackson, A. J. Crisci, C. A. Farberow, F. Y. Shi, A. C. Alba-Rubio, J. L. Lu, P. J. Dietrich, X. K. Gu, C. L. Marshall, P. C. Stair, J. W. Elam, J. T. Miller, F. H. Ribeiro, P. M. Voyles, J. Greeley, M. Mavrikakis, S. L. Scott, T. F. Kuech and J. A. Dumesic, *Angew. Chem. Int. Ed.*, 2013, **52**, 13808.
70. B. J. O'Neill, J. T. Miller, P. J. Dietrich, F. G. Sollberger, F. H. Ribeiro and J. A. Dumesic, *ChemCatChem*, 2014, **6**, 2493.
71. H. Zhang, C. Canlas, A. J. Kropf, J. W. Elam, J. A. Dumesic and C. L. Marshall, *J. Catal.*, 2015, **326**, 172.
72. J. Lee, D. H. Jackson, T. Li, R. E. Winans, J. A. Dumesic, T. F. Kuech and G. W. Huber, *Energy Environ. Sci.*, 2014, **7**, 1657.
73. M. Wang, Z. Gao, B. Zhang, H. Yang, Y. Qiao, S. Chen, H. Ge, J. Zhang and Y. Qin, *Chem. – Eur. J.*, 2016, **22**, 8438.
74. D. W. Kim, K.-D. Kim, H. O. Seo, N. K. Dey, M. J. Kim, Y. D. Kim, D. C. Lim and K. H. Lee, *Catal. Lett.*, 2011, **141**, 854.
75. N. A. Ray, R. P. Van, Duyne and P. C. Stair, *J. Phys. Chem. C*, 2012, **116**, 7748.
76. X. Liu, Q. Zhu, Y. Lang, K. Cao, S. Chu, B. Shan and R. Chen, *Angew. Chem. Int. Ed.*, 2017, **56**, 1648.
77. J. Lu and P. C. Stair, *Angew. Chem. Int. Ed.*, 2010, **49**, 2547.
78. K. Cao, Q. Zhu, B. Shan and R. Chen, *Sci. Rep.*, 2015, **5**, 8470.
79. J. Lu, K.-B. Low, Y. Lei, J. A. Libera, A. Nicholls, P. C. Stair and J. W. Elam, *Nat. Commun.*, 2014, **5**, 1.
80. S. M. George, B. Yoon and A. A. Dameron, *Acc. Chem. Res.*, 2009, **42**, 498.
81. B. H. Lee, B. Yoon, V. R. Anderson and S. M. George, *J. Phys. Chem. C*, 2012, **116**, 3250.
82. B. H. Lee, V. R. Anderson and S. M. George, *Chem. Vap. Deposition*, 2013, **19**, 204.
83. A. I. Abdulagatov, K. E. Terauds, J. J. Travis, A. S. Cavanagh, R. Raj and S. M. George, *J. Phys. Chem. C*, 2013, **117**, 17442.
84. J. Kint, F. Mattelaer, S. S. T. Vandenbroucke, A. Muriqi, M. M. Minjauw, M. Nisula, P. M. Vereecken, M. Nolan, J. Dendooven and C. Detavernier, *Chem. Mater.*, 2020, **32**, 4451.
85. K. Van de Kerckhove, F. Mattelaer, J. Dendooven and C. Detavernier, *Dalton Trans.*, 2017, **46**, 4542.
86. B. H. Lee, V. R. Anderson and S. M. George, *ACS Appl. Mater. Interfaces*, 2014, **6**, 16880.
87. X. Liang, M. Yu, J. Li, Y.-B. Jiang and A. W. Weimer, *Chem. Commun.*, 2009, **46**, 7140.
88. C. Chen, P. Li, G. Wang, Y. Yu, F. Duan, C. Chen, W. Song, Y. Qin and M. Knez, *Angew. Chem. Int. Ed.*, 2013, **52**, 9366.
89. T. D. Gould, A. Izar, A. W. Weimer, J. L. Falconer and J. W. Medlin, *ACS Catal.*, 2014, **4**, 2714.
90. P. Ingale, C. Guan, R. Kraehnert, R. N. D. Alnoncourt, A. Thomas and F. Rosowski, *Catal. Today*, 2021, **362**, 47.

CHAPTER 9

# *Ultrathin Oxide Coatings Synthesized* Via *Wet Chemical Processes for Electrocatalytic Systems*

Y. XING

Department of Biomedical, Biological and Chemical Engineering, University of Missouri, Columbia, MO 65211, USA
Email: xingy@missouri.edu

## 9.1 Introduction

In electrocatalytic systems, such as fuel cells and water electrolyzers, electrocatalysts with high dispersion are needed to increase catalyst utilization and reduce costs. They are often supported on a substrate with high specific surface area for improving durability and reducing mass transfer limitations. Any substrates used for this purpose have to be electrically conductive so that electrons generated or consumed by electrochemical reactions can be transported between electrocatalyst active sites and the external circuit that connects the anode and cathode. Carbon has long been used as an electrode material in electrochemical processes because it is electrically conductive, readily made with high surface area, and easily available at low cost. However, carbon does not have a wide window of thermodynamic stability in aqueous solutions owing to the

Energy and Environment Series No. 30
Ultrathin Oxide Layers for Solar and Electrocatalytic Systems
Edited by Heinz Frei and Daniel V. Esposito

Published by the Royal Society of Chemistry, www.rsc.org

relatively low standard reduction potential ($E_0$) associated with its oxidation to $CO_2$:[1]

$$C + 2H_2O \rightarrow CO_2 + 4H^+ + 4e^-,\ E_0 = 0.207\ \text{V}\ \textit{vs.}\ \text{NHE} \qquad (9.1)$$

Electrochemical corrosion of carbon has been found to be a serious problem in many kinetically accelerated processes,[2–5] including but not limited to reactions that occur within proton exchange membrane (PEM) fuel cells, rechargeable metal–air batteries, and PEM electrolyzers for water splitting. Electrocatalyst degradation can be severe owing to corrosion of the carbon support, especially in acidic electrolytes.[6–8] New support materials are needed that are both electrically conductive and chemically resistant to acid corrosion.

The need for alternative support materials to replace carbon has led to extensive research on metal oxides. Previous studies have demonstrated that not many candidate materials are suitable for use in harsh acidic environments. Research in recent decades has been mostly focused on two promising metal oxides, titanium and niobium oxides.[9–18] Despite the fact that both are amphoteric oxides, they are relatively stable in acidic solutions over a range of potentials. Figure 9.1 shows the Pourbaix diagrams for Ti and Nb and their thermodynamically favorable chemical states over wide ranges of potential and pH.[19,20] The red hatched boxes mark the region of $E_0 = 0.0$–$2.0$ V and pH = 0.0–2.0, which are approximately the electrochemical window and acidity of interest for PEM fuel cells and electrolyzers. It can be seen that the $TiO_2$ is stable, but $Nb_2O_5$ is unstable at pH values below ~0.6, which favor its conversion to become a soluble niobium

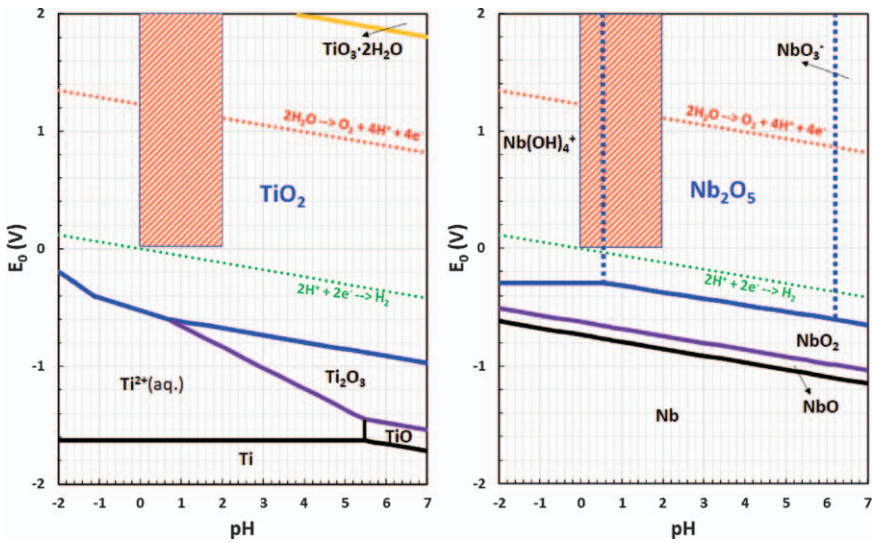


**Figure 9.1** Pourbaix equilibrium diagrams showing ranges of stabilities of titanium oxides and niobium oxides at 25 °C.
Data adapted from ref. 19 and 20.

hydroxide species. Based on this consideration, titanium oxide is generally preferred over niobium oxide.

One problem with these oxides is that they are wide band gap semiconductors (>3.0 eV for $TiO_2$ and >3.2 eV for $Nb_2O_5$ depending on the crystalline structure) in their pure form and do not conduct electrons well. Therefore, much research has been carried out to increase their conductivity. To increase the electrical conductivity of $TiO_2$, several methods have been proposed. For example, reducing $TiO_2$ to a Magneli phase ($Ti_nO_{2n-1}$) is one method.[13,15,21,22] The Magneli phase is an oxygen-deficient metal oxide, which has a much higher electrical conductivity ($\sim 10^{-3}$ S cm$^{-1}$).[23] It was shown that Pt supported on the Magneli phase $Ti_4O_7$ (or Pt/$Ti_4O_7$) has an oxygen reduction reaction (ORR) activity comparable to or better than that of commercial Pt supported on carbon black (Pt/C).[13] To obtain the Magneli phase, very high temperatures (>1000 °C) have to be used to chemically reduce $TiO_2$ (*e.g.* in hydrogen). However, such high-temperature processes can significantly reduce the metal oxide surface area owing to sintering.[24] Similarly, semiconductor $NbO_2$, which can be obtained by reducing $Nb_2O_5$ between 900 and 1300 °C, was singled out as a candidate.[22] It was reported that Pt on nano- to submicron-sized niobium oxide powders ($NbO_2$ or $Nb_2O_5$) can be an efficient electrocatalyst for ORRs.[12,25] Pt/$NbO_2$ mixed with carbon black has almost a three times larger mass activity for ORRs at 0.9 V *vs.* RHE (reversible hydrogen electrode) compared with that for Pt/C while simultaneously displaying enhanced stability.[12]

Another method to make metal oxides electrically conductive is to dope them with different elements. For example, $TiO_2$ has been studied with various dopants, such as Nb, C, Ta, V, and N.[9,26–38] Semiconducting oxides with elemental doping can have an increased electrical conductivity with increased extrinsic charge carriers at relatively low dopant concentrations. They can also become degenerate semiconductors with a significantly increased conductivity when the dopant concentration is very high (*e.g.* >1%). For example, $TiO_2$ heavily doped with Nb was found to become a degenerate semiconductor.[39–41] The Fermi level is moving close to the conduction band edge, making it behave more like a metal.[42] A conductivity of 440 S cm$^{-1}$ was obtained in a Nb-doped $TiO_2$ coating catalyst support for PEM electrolyzers.[43] This is advantageous in electrochemical applications such as in fuel cells and electrolyzers that need to have a metal oxide support with good electrical conductivity.

In addition to the requirement for high electrical conductivity, a good catalyst support should have a high surface area, or small particle size, to allow high catalyst dispersion on it without aggregation. A high catalyst dispersion, and thus implied high utilization, is very important for noble metal catalysts, a low loading of which is required to reduce the cost associated with the electrocatalyst material. To avoid high-temperature sintering and achieve high specific surface areas, metal oxides can be deposited on another substrate, in the form of nanoparticles or nanocoatings. In particular, efforts have been made recently to develop techniques to deposit titania and niobia nanocoatings on different forms of carbon.

Carbon black and carbon nanotubes (CNTs) have been used as electrode supports because they have very high specific surface areas and much higher electrical conductivities than metal oxides.[44] One approach to take advantage of these desirable properties of carbon supports and the high chemical stability of oxides is to encapsulate the carbon support with ultrathin metal oxide supports. If the metal oxide coatings can completely encapsulate the carbon, protecting it from corrosion, then carbon corrosion can be avoided. Therefore, in addition to being a template in making high surface area metal oxides, they can be part of the composite catalyst support to provide much higher electrical conductivity and mechanical strength. They are also much lighter than metal oxides, hence reducing the weight of electrodes.

Nanocoatings can be made by many different techniques.[45] The established chemical vapor deposition (CVD) method has been used to deposit atomic- and nanoscale coatings on surfaces.[46,47] In this method, a reactive vapor-phase chemical reacts on a solid surface to form a coating at the nanoscale. As described in detail in Chapters 2, 3, and 8, another widely used method for fabricating ultrathin metal oxide coatings is atomic layer deposition (ALD).[48–50] ALD processes also use vapor-phase chemical precursors and need various oxygen sources such as water vapor, molecular $O_2$, and ozone ($O_3$) to react with chemical precursors.[51] A nanocoating can be deposited on a substrate surface in a layer-by-layer fashion at the atomic scale. Because CVD and ALD are gas-phase processes, they work well on macroscopic (planar) surfaces, but conventional CVD and ALD reactors are limited in making coatings on nanoscale substrates such as nanoparticles. Nanoparticles are difficult, if not impossible, to disperse in a gas phase without agglomeration.[49] Although significant progress has been made in particle ALD processes, as described in Chapter 8, nanoparticle coating processes in a gas (*e.g.* aerosols) are generally more difficult to control than in a liquid (*e.g.* colloidal sols). Consequently, liquid-phase processes are usually preferred when making nanocoatings on nanoscale substrates.

The commonly used sol–gel deposition (SGD) processes are liquid-phase processes and have been studied extensively in depositing coatings on both macroscopic and nanoscale substrates.[52] They have been used to coat nanoparticles of different shapes, and also nanofibers. Because SGD processes are often carried out in a bulk solution, it is difficult to control the coating thickness, especially for nanocoatings less than 10 nm thick. Extra steps need to be taken to make ultrathin metal oxide coatings on nanoparticles. Although the recently developed condensed layer deposition (CLD) process also takes place in a bulk solution, typically a liquid hydrocarbon, it utilizes a condensed nanoscale water film that introduces an additional control knob for making nanocoatings with excellent control of the thickness.[53] It is especially applicable to making nanocoatings on nanoscale substrates that can be dispersed in the hydrocarbon oil phase. It provides a much easier way to control coating thicknesses down to ~1 nm. The remainder of this chapter describes SGD and CLD techniques for making

metal oxide nanocoatings, in particular titania and niobia nanocoatings, on nanoscale substrates. Select applications of the nanocoatings in electrocatalysis are also discussed.

## 9.2 Ultrathin Metal Oxide Coatings from Sol–Gel Deposition Processes

### 9.2.1 Sol–Gel Process

The sol–gel deposition (SGD) process is a mature technology for making metal oxide thin films and particles.[52,54] It is a liquid-phase hydrolysis or polymerization process, conducted in aqueous or alcoholic solutions, with thermodynamically driven and acid- or base-promoted processes. The process starts by dissolving metal salts, most commonly metal alkoxides, in a solvent. Next, hydrolysis reactions occur within the solution to form sols, which are colloidal particles. Following sol formation, deposition and gelation of the sols on substrates can produce thin films or particles, as shown in Figure 9.2.

A typical SGD coating process involves three steps. First, hydrolysis and condensation reactions lead to the formation of colloidal particles, which can aggregate into sols or gels, depending on the solution pH, species acidities, water content, metal coordination number, *etc.* A typical sol–gel formation process from a metal alkoxide, $M(OR)_x$, would include the following reactions:[45,52]

Hydrolysis reactions:

$$M(OR)_x + H_2O \rightarrow (HO)_1\text{–}M(OR)_{x-1} + ROH \tag{9.2}$$

...

$$(HO)_{x-1}\text{–}M(OR)_1 + H_2O \rightarrow M(OH)_x + ROH \tag{9.3}$$

Condensation/polymerization reactions:

$$(OR)_{x-1}M\text{–}(OH)_1 + (HO)_1\text{–}M(OR)_{x-1} \rightarrow (RO)_{x-1}M\text{–}O\text{–}M(OR)_{x-1} + H_2O \tag{9.4}$$

...

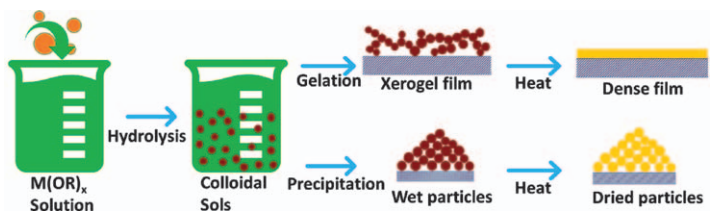


**Figure 9.2** Schematic diagram of the sol–gel process in the formation of a thin film or particles from hydrolysis of a metal alkoxide.

$$y[(HO)_1\text{–}M(OR)_{x-2}(OH)_1] \rightarrow (HO)_1\text{–}[M(OR)_{x-3}\text{–}O]_{y-1}\text{–}M(OR)_1\text{–}(OH)_1 + (y-1)H_2O \quad (9.5)$$

$$(OR)_{x-1}M\text{–}(OH)_1 + (RO)_1\text{–}M(OR)_{x-1} \rightarrow (OR)_{x-1}M\text{–}O\text{–}M(OR)_{x-1} + ROH \quad (9.6)$$

...

$$(OR)_{x-y}M\text{–}(OH)_y + y[(RO)_1\text{–}M(OR)_{x-1}] \rightarrow (OR)_{x-y}M\text{–}O_y\text{–}[M(OR)_{x-1}]_y + yROH \quad (9.7)$$

For complete hydrolysis, the metal alkoxide would be converted to metal hydroxide. For example, complete hydrolysis of titanium tetraisopropoxide (TTiP), $Ti(OC_3H_7)_4$, proceeds as follows:

$$Ti(OC_3H_7)_4 + 2H_2O \rightarrow Ti(OH)_4 + 4C_3H_7OH \quad (9.8)$$

which releases propanol into the solution. In incomplete hydrolysis reactions, organic ligands left in the sols can go through polymerization reactions. Such reaction pathways will depend on several factors, such as water content, solution pH, temperature, *etc.*[45,55]

Second, the sols thus formed are deposited on a substrate by spraying, dipping, spin coating, or attachment. The colloidal particles can be further polymerized or gelled during the deposition process to form a networked coating or film. Depending on the coating process, the sols can form xerogels with branched structures.

Third, heat treatment can result in a dense thin film, removing water and organic ligands from the coating, eventually converting the metal hydroxide to metal oxide. Depending on the heat treatment conditions and metal oxide of interest, the thin film can be amorphous or crystalline; it can also be very porous with high specific surface area.[55] A sol is generally a dispersion of colloidal particles in the size range 10–1000 nm. As a result, a coating of less than 10 nm is difficult to obtain by depositing a single layer of sol particulates on a surface.[45,55] Ultrathin films could be produced in the early stages of the hydrolysis and condensation process when individual sol particles have not yet fully taken shape.

In making coatings on nanoscale substrates, some coating processes are not feasible. For example, it would not be possible to spray a sol onto a nanoparticle, like spraying a surface with macroscopic dimensions. Nanoscale substrates have to be dispersed in the sol solution and scavenge the colloidal particles on their surfaces through attachment, which may rely on interactions such as van der Waals or ionic binding forces. Consequently, the surface of the nanoparticles plays a critical role in the coating process. Often, substrate nanoparticles have to be surface functionalized to facilitate attachment, and certain functional groups may be needed to obtain uniform nanocoatings on the nanoscale substrate.[9,10]

### 9.2.2 Ultrathin Metal Oxide Coatings from Sol–Gel Processes

One of the best known examples of making nanocoatings on nanoparticles through an SGD process is to make silica or titania coatings on gold nanoparticles using the Stöber method.[56–58] The Stöber method is a sol–gel process developed by Werner Stöber's group to prepare size-controlled silica particles with a high degree of uniformity.[59] However, often the Stöber method does not produce a uniform coating on nanoparticles without surface functionalization.[58] For example, 3-aminopropyltrimethoxysilane was used to functionalize gold nanoparticles as an activation step, followed by $SiO_2$ growth on the gold surface through hydrolysis and condensation using tetraethyl orthosilicate (TEOS) in an ethanol–water solvent with ammonia.[60] By controlling the TEOS concentration, the coating thickness can be controlled from a few nanometers to a few tens of nanometers (see Figure 9.3). The solvent has a 6 : 1 ratio of ethanol to water with water at 7.873 M and ammonia at 0.212 M. The 5 nm thick silica coating was made using 0.0479 M TEOS and the 20 nm thick coating using 0.479 M TEOS.[60]

Similarly, mesoporous silica nanocoatings were prepared on Au nanoparticles using aminopropyltriethoxysilane for activation together with the surfactant cetyltrimethylammonium bromide (CTAB).[61] In an improved method, CTAB was used to make silica sols in the form of micelles, which were further assembled on gold nanoparticles to produce mesoporous but thick nanocoatings, as shown in Figure 9.4.[62]

In comparison with silica coatings, titania coatings are more difficult to prepare.[63,64] The main reason may be that there is not a good activation step with a suitable surfactant, as there is when making silica coatings. Additionally, silicon is a group IVA semiconductor, whereas Ti is a group IVB

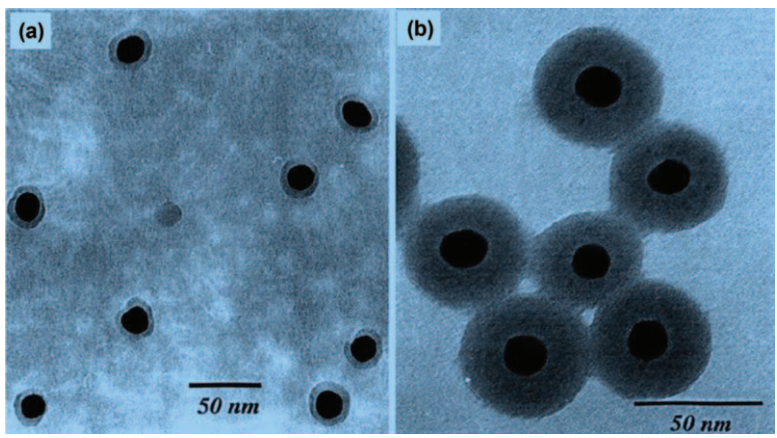


**Figure 9.3** Silica nanocoating made on 20 nm gold nanoparticles using the modified Stöber method with (a) a 5 nm thick coating and (b) a 20 nm thick coating.
Adapted from ref. 60.

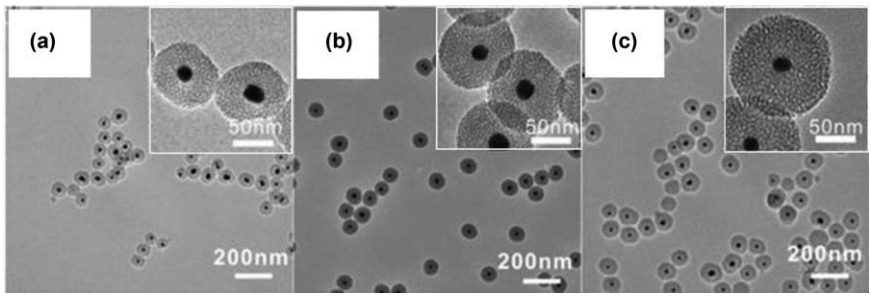


**Figure 9.4** Mesoporous silica nanocoatings made on Au nanoparticles by using CTAB to prepare silica micelles first and then attaching them on Au nanoparticles with different thicknesses: (a) $75 \pm 5$, (b) $84 \pm 3$, and (c) $100 \pm 4$ nm.
Reproduced from ref. 62 with permission from the Royal Society of Chemistry.

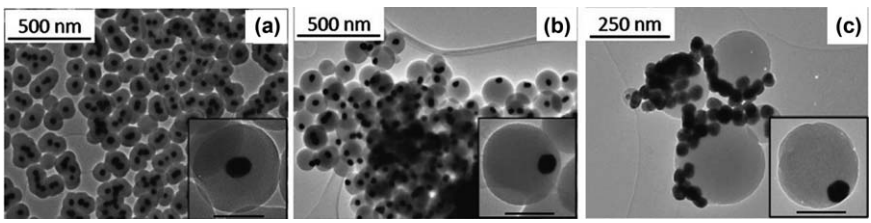


**Figure 9.5** Silica, titania, and their composite coatings made on gold nanoparticles. (a) Pure silica on Au; (b) silica–titania on Au; (c) pure titania on Au.
Reproduced from ref. 63 with permission from the Royal Society of Chemistry.

transition metal. The former lacks d orbitals whereas the latter has unfilled $d^2$ orbitals. This difference could have a large effect on their alkoxide hydrolysis and condensation reactions, which can depend on the partial charges on their alkoxide compounds. For example, the partial charge on $Si(OEt)_4$ is $+0.32$ and that on $Ti(OEt)_4$ is $+0.63$, making the former less likely to be attacked by a nucleophilic agent and thus resulting in a much slower reaction process.[54,65] Consequently, a titania coating made from a titanium alkoxide precursor is not uniform on Au nanoparticles owing to the faster reaction (see Figure 9.5).[63]

In comparison with coating Au nanoparticles, making continuous coatings on carbons has been more difficult to achieve using SGD processes. Several studies have been performed on coating CNTs for use in electrochemical processes.[9,66–70] Surface functionalization of the CNTs is crucial for achieving uniform and conformal coatings by SGD methods. The formation of smaller sols is another determining factor. Since the sol particle size is often on the order of 10 nm or more, a coating of the sol on CNTs can easily reach up to 100 nm in thickness.[9,66–70] As shown in Figure 9.6, $TiO_2$ coatings were made on CNTs using an SGD process that yields coating thicknesses of

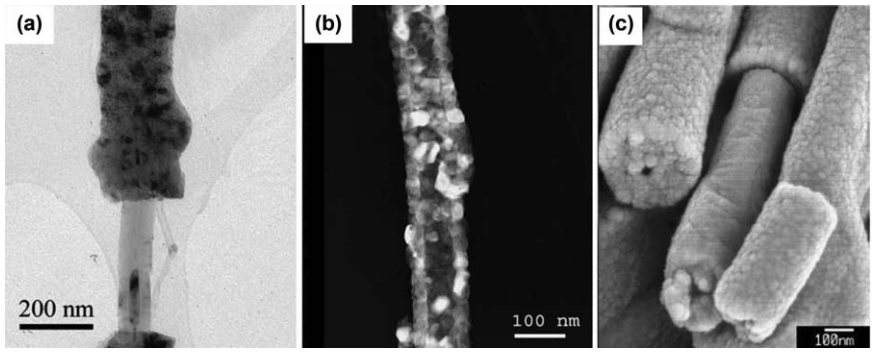


**Figure 9.6** Transmission electron microscopy (TEM) images of $TiO_2$-coated CNTs. (a) Anatase $TiO_2$ coating (broken) on a CNT. (b) $TiO_2$ nanotubes after CNT removal (heated at 550 °C). (c) Scanning electron microscopy (SEM) image of the $TiO_2$ nanotubes, showing a coating thickness of ~100 nm. Reproduced from ref. 66 with permission from the Royal Society of Chemistry.

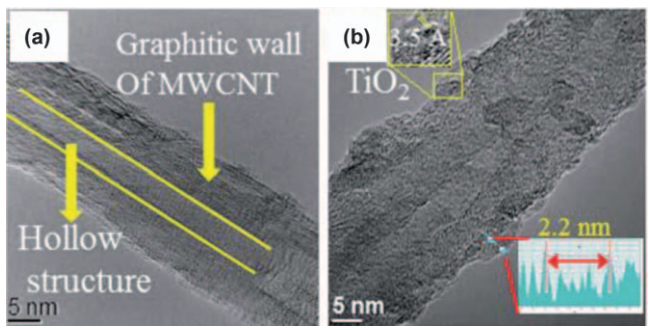


**Figure 9.7** (a) TEM image of a multiwalled CNT (MWCNT). (b) $TiO_2$ nanocoating made on a CNT that has a thickness of ~3 nm, with a rough morphology. Reproduced from ref. 69 with permission from the Royal Society of Chemistry.

about 100 nm.[66] The sol particles can still be seen in the coatings after heat treatment at 550 °C during transition from hydroxide to oxide.

Ultrathin $TiO_2$ coatings have been made on CNTs using a process in which extra control steps were applied. A very dilute solution of titanium butoxide in propanol was used to which a very dilute solution of water in propanol ($6.1\times10^{-5}$ M) was added dropwise to reduce aggregation and growth of the sols.[69] It took 4 days to make a nanocoating of thickness ~3 nm, as shown in Figure 9.7. Another approach was focused on surface functionalization of the CNTs, including sonochemical treatment for uniform functionalization of the CNT surface and using benzyl alcohol as a surfactant for surface attachment/activation.[9] It was observed that benzyl alcohol can lead to smaller colloidal sol particles and result in smooth surface coatings.[66,71] TTiP

was used as the precursor and the coating process was conducted in an ethanol–water solution. A smooth coating with a thickness of <10 nm was obtained in this process, as shown in Figure 9.8.[9] The coating process took 2 h.

Following the same technique, $Nb_2O_5$ nanocoatings were made on CNTs.[10] In this case, niobium ethoxide was used as the metal oxide precursor. The CNTs were again sonochemically functionalized and benzyl alcohol was used as a surfactant. The niobia coatings were smooth and covered the whole of the CNTs, as shown in Figure 9.9. The coatings were amorphous as synthesized, but became crystalline $Nb_2O_5$ under heat treatment. When the CNTs were removed through carbon oxidation, $Nb_2O_5$ nanotubes were formed (Figure 9.9B).

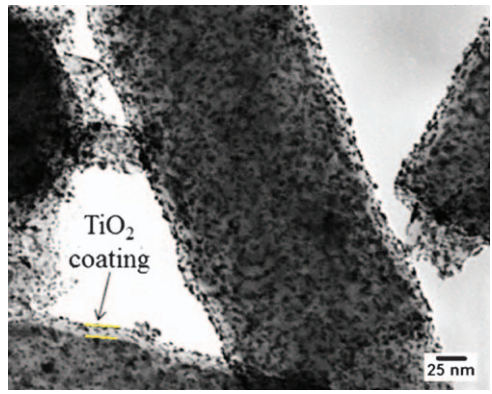


**Figure 9.8** Ultrathin $TiO_2$ coating on a CNT. Black dots are catalytic Pt nanoparticles. Reproduced from ref. 9 with permission from the Royal Society of Chemistry.

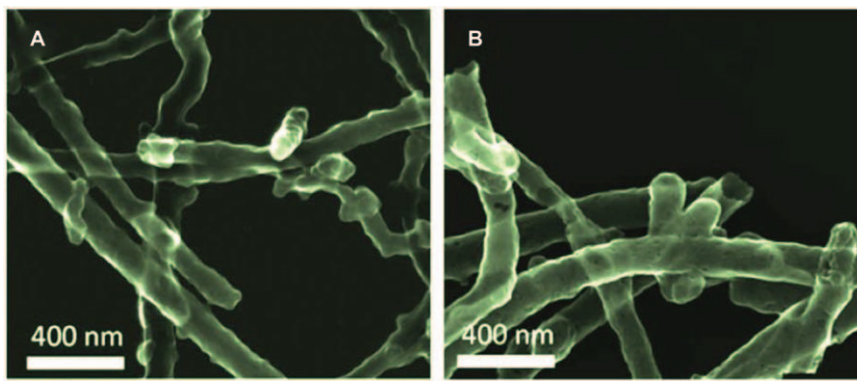


**Figure 9.9** SEM images of (A) CNTs coated with amorphous niobia and (B) thin $Nb_2O_5$ nanotubes after removing the CNTs, showing the coatings. Reproduced from ref. 10 with permission from the Royal Society of Chemistry.

### 9.2.3 Sol–Gel Metal Oxide Nanocoatings as Electrocatalyst Supports

Metal oxide nanocoatings on CNTs have been used as catalyst supports. These coatings on a nanoscale substrate basically are of nanoscale size. They therefore have a high specific surface area and are suitable to act as a catalyst support. Platinum is an effective electrocatalyst that is often deposited on metal oxides. Pt catalysts have stronger interactions with metal oxides than with carbon, allowing the stabilization of very small Pt nanoparticles that would normally be susceptible to coalescence and/or detachment when deposited on a pure carbon support. They also have electronic interactions with the metal oxide support to enhance catalytic activity, for example, in ORRs, as discussed later.

It has been shown that carbon-doped $TiO_2$ nanocoatings are a good support for Pt nanoparticles with good activity towards ORRs in $H_2SO_4$ electrolyte.[9] As shown in Figure 9.10, the durability of the Pt electrocatalyst was greatly enhanced by supporting it on metal oxide nanocoatings on CNTs than on carbon black (Pt/C, E-TEK). The best catalyst was Pt supported on carbon-doped $TiO_2$ on CNTs, which produced a half-wave potential of 0.75 V *vs.* RHE, which is only slightly less than the 0.77 V *vs.* RHE half-wave potential for the Pt/C control electrode in 0.5 M $H_2SO_4$ electrolyte. However, electrochemical tests showed that its mass activity loss at 0.8 V *vs.* RHE is only 1.7% after 5000 cycles, much better than that for Pt/C, which showed a 56% loss after 5000 cycles. This enhanced catalyst durability is indicative of both the support stability and the catalyst stability. It has been demonstrated that carbon corrosion can be severe in carbon black owing to electrochemical oxidation.[2] Corrosion of the support leads to severe catalyst degradation and loss of electrochemically active surface area, therefore resulting in a significant decrease in activity. On the other hand, the metal oxide nanocoating support is stable in sulfuric acid electrolyte and its interactions with the metal catalyst also make the catalyst stable. Consequently, Pt supported on metal oxide nanocoatings has a much improved performance compared with Pt supported on carbon.

As discussed in the Introduction, one of the drawbacks of metal oxides is that they do not conduct electrons well. As a result, doping is used to make them conductive. $TiO_2$ nanocoatings have been doped with carbon to make them electrically conductive.[9] It was shown that a $TiO_2$ nanocoating without carbon doping is not electrochemically active and is not a good catalyst support, as shown in Figure 9.11. In contrast to the black curve in Figure 9.11, there are other studies that did not make particular efforts to make the metal oxides conductive, but still showed that the oxide could serve as an effective support with sufficient electrical conductivity.[69] A couple of reasons might explain the findings in those studies. One is that the nanocoatings are very thin, thin enough to permit electron transfer across the nanocoating by quantum mechanical tunneling. As mentioned above, it was shown that a *ca.* 3 nm $TiO_2$ nanocoating without any doping has an

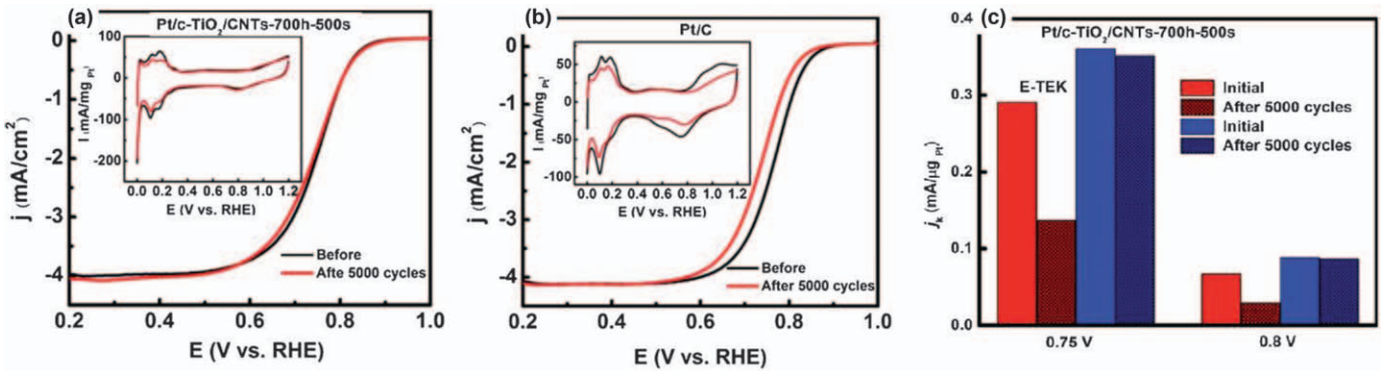


**Figure 9.10** Electrocatalyst durability during ORR testing. (a) Pt supported on carbon-doped $TiO_2$ nanocoatings on CNTs. (b) Pt supported on carbon black (Pt/C from E-TEK). (c) Comparison between the durability of the two electrocatalysts, showing that Pt supported on $TiO_2$ nanocoatings is much more durable than Pt/C.
Reproduced from ref. 9 with permission from the Royal Society of Chemistry.

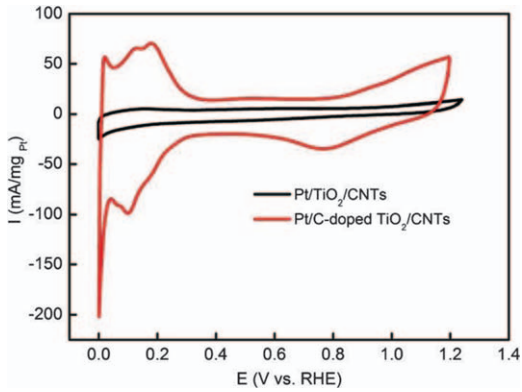


**Figure 9.11** Cyclic voltammograms of two supported Pt electrocatalysts, one supported on undoped $TiO_2$ nanocoatings and the other supported on carbon-doped $TiO_2$. The difference in the curves is attributed to the higher electrical conductivity of the doped $TiO_2$ coatings.
Reproduced from ref. 9 with permission from the Royal Society of Chemistry.

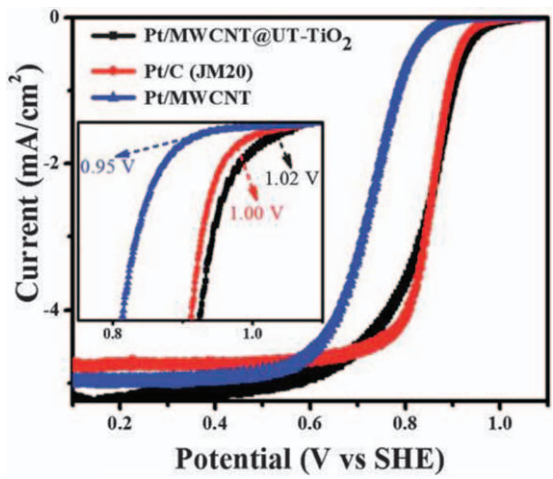


**Figure 9.12** ORR activity for a Pt catalyst supported on an ultrathin (UT) $TiO_2$ nanocoating on a multiwalled CNT (MWCNT) and Pt/C, and also Pt on an MWCNT. The inset shows the onset potentials of the ORRs of the three catalysts.
Reproduced from ref. 69 with permission from the Royal Society of Chemistry.

activity comparable to or better than that of Pt/C (see Figure 9.12), although its durability is not improved much (~45% decrease in electrochemical surface area *versus* ~56% decrease for Pt/C after 1000 cycles).[69] The second reason is that the metal oxides did not form a continuous coating on the carbon, but had holes in the coatings or even formed discrete metal oxide

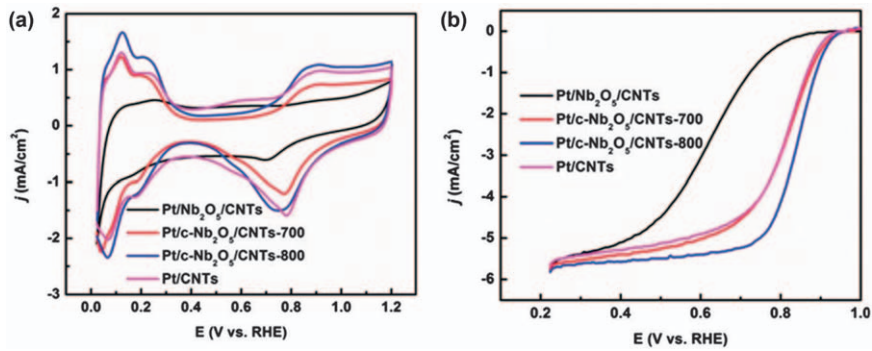


**Figure 9.13** Performances of Pt electrocatalysts supported on niobia nanocoatings. (a) Cyclic voltammetry curves and (b) ORR polarization curves. Reproduced from ref. 10 with permission from the Royal Society of Chemistry.

particles on the support. In this case, Pt catalysts could have direct contact with and direct electron transfer through the carbon substrates. However, an undesirable implication of a discontinuous oxide coating is that the carbon support has some direct contact with the electrolyte, meaning that the carbon corrosion problem is not completely prevented. To identify the causes further, more studies are needed.

Similarly, niobia nanocoatings were used as a Pt catalyst support for ORRs.[10] To make the niobia nanocoatings electrically conductive, the metal oxide nanocoatings were also doped with carbon. Upon doping, it was found that the $Nb_2O_5$ was converted to $NbO_2$, which is a suboxide with much better electrical conductivity. When Pt catalysts were deposited on the niobia nanocoatings, they showed a good ORR activity with a half-wave potential at 0.83 V *vs.* RHE in a 0.1 M $HClO_4$ electrolyte (see Figure 9.13). The mass activity in ORRs was twice that of the Pt supported on bare CNTs. Furthermore, the durability tests showed only a 5% decrease in electrochemical surface area after 5000 cycles.

## 9.3 Metal Oxide Nanocoatings from Condensed Layer Deposition

### 9.3.1 The Condensed Layer Deposition Process

The condensed layer deposition (CLD) technique is a recently developed wet process to make nanoscale metal oxide coatings.[53] It is especially suitable for making nanocoatings on nanoscale substrates, such as nanoparticles, nanofibers, and nanoaggregates of particles. The CLD process uses a liquid hydrocarbon (*i.e.* oil phase) to disperse nanoscale substrates on which a metal oxide nanocoating is to be made through hydrolysis. In contrast to the hydrolysis in the SGD processes, the hydrolysis in the CLD process occurs in a thin layer of water condensed on the substrate surface, not in the bulk

aqueous or alcoholic solution, thus providing a fundamentally different alternative for making nanocoatings. An illustration of the CLD process is shown in Figure 9.14. In CLD, the nanoscale substrates are dispersed in a water-containing liquid hydrocarbon (*e.g.* heptane) solution, within which oversaturated water condenses on the substrates to form a nanoscale film of water. Subsequent injection of a chemical precursor into the dispersion leads to reaction of the precursor with the water film to form a metal oxide nanocoating on the substrate.

It is well known that water is immiscible with hydrocarbon oil. Mixing water with oil can result in water-in-oil or oil-in-water emulsions, depending on which is the continuous phase and which is the dispersing phase.[72] When oil is the continuous phase and water is the dispersing phase, a water-in-oil emulsion is formed. In such emulsions, water is in the form of droplets. On the other hand, water does dissolve in an oil, albeit in trace amounts. For example, the solubility of water in heptane is 61 ppm (by volume) at 20 °C.[73] This makes it easily possible to have water oversaturated in an oil due to this ultralow solubility. When oversaturation occurs, water will nucleate heterogeneously and form a water layer on the substrates dispersed in the oil phase. The substrates serve as nucleation sites for water condensation, and eventually a thin film of water forms on the substrates.[53] It was observed that this condensed water film is at the sub-nanometer scale. When a chemical precursor that can undergo hydrolysis (*e.g.* metal–organic precursor) is introduced into the oil phase, it diffuses to the surface of the solid substrate and reacts with the water layer *via* hydrolysis. Thus, a metal oxide nanocoating is deposited right on the substrate surface.

In addition to being compatible with dispersing nanoscale substrates using mechanical (*e.g.* sonication) or physicochemical (surfactants) means, the liquid hydrocarbon oil phase must also be able to dissolve the organic precursor of interest. Hydrocarbons can generally dissolve chemical precursors such as metal–organic compounds or organometallic compounds. Provided that the precursor is hygroscopic or moisture sensitive, it can react with water in a hydrolysis reaction to produce the desired oxide coating. Examples of such precursors include metal alkoxides, metal alkyls, and

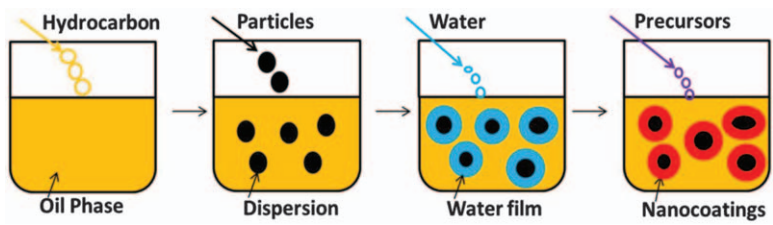


**Figure 9.14** Schematic illustration of the condensed layer deposition (CLD) process for making nanocoatings on nanoparticles.
Reproduced from ref. 53, https://doi.org/10.1038/s43246-020-0010-9, under the terms of the CC BY 4.0 license, http://creativecommons.org/licenses/by/4.0/.

many of their derivatives, *e.g.* titanium tetraisopropoxide, niobium ethoxide, trimethylaluminum, and diethylzinc.

It has been demonstrated that the CLD process is not limited by the substrate morphology (*e.g.* round or elongated shapes), as shown in Figure 9.15.[53] The coating made through the CLD process is basically conformal to the shape of the substrate surface, even at corners and convex points. The conformal deposition is attributed to the formation of a uniform nanoscale film of water on the nanoparticles, facilitated by the interfacial tension between the polar water and non-polar hydrocarbons. The Young–Laplace equation describes the relationship between the interfacial pressure and the surface tension:[74]

$$\nabla p = n\frac{\gamma(T)}{R} \tag{9.9}$$

at temperature $T$, where $\gamma$ is the interfacial tension between water and the hydrocarbon, $R$ is the radius of curvature of the interface, and $n = 2$ for

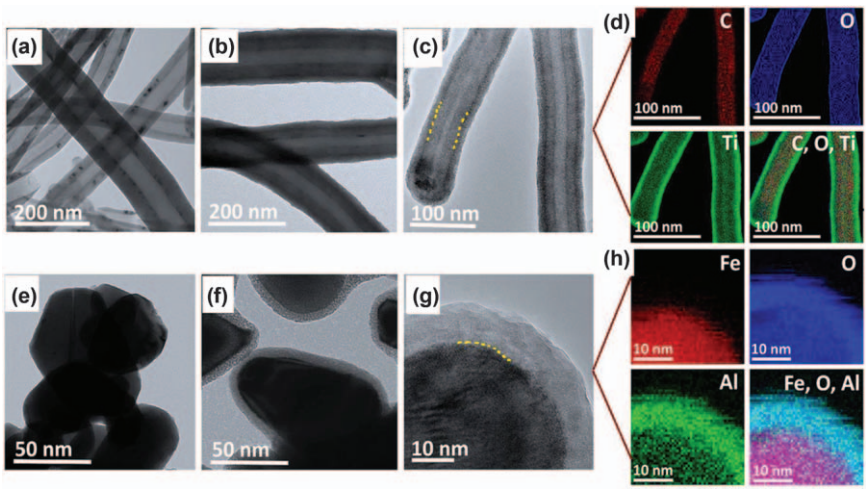


**Figure 9.15** Synthesis of nanocoatings *via* CLD. (a) TEM image of uncoated CNTs. (b), (c) Bright-field TEM images of titania nanocoatings on CNTs, showing conformability to the fiber shape, with the yellow dash-dotted lines as a guide for the eye. (d) Energy-filtered TEM elemental mapping of the titania nanocoating, showing elements C, O, and Ti individually and collectively. (e) TEM image of uncoated iron oxide particles (IOPs). (f), (g) Bright-field TEM images of alumina nanocoatings on IOPs, which show conformal coatings even at sharp edges. (h) Scanning transmission electron microscopy–electron energy loss spectroscopy (STEM–EELS) elemental mapping of the alumina nanocoating, showing Fe, O, and Al individually and collectively.

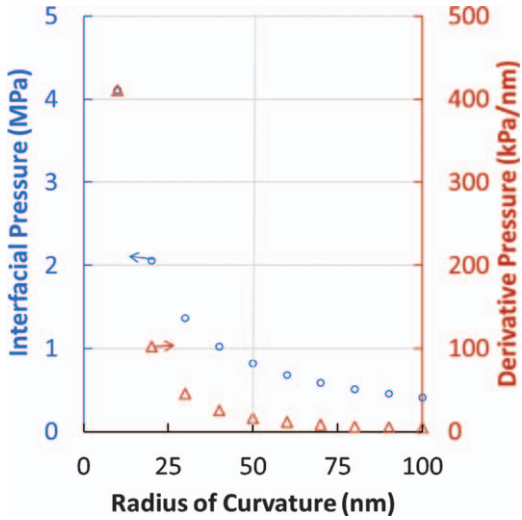


**Figure 9.16** Interfacial pressure between polar water and non-polar heptane *versus* the radius of curvature. The partial derivative of the pressure relative to change in radius of curvature is also shown. The interfacial tension used is 20.53 mN m$^{-1}$ for water–heptane at 20 °C.
Reproduced from ref. 53, https://doi.org/10.1038/s43246-020-0010-9, under the terms of the CC BY 4.0 license, http://creativecommons.org/licenses/by/4.0/.

spherical and $n = 1$ for cylindrical shapes. Since the dimension of $R$ is at the nanoscale, the interface pressure can be extremely high.[75] For example, for $R = 50$ nm the interfacial pressure is ~0.8 MPa (or ~8 atm), as shown in Figure 9.16, which is extremely high. Any change in the radius of curvature would be suppressed, since any protrusion in the water film would result in an even larger change in pressure, as can be seen from the derivative:

$$\left|\left(\frac{\partial \nabla p}{\partial R}\right)_T\right| = n\frac{\gamma(T)}{R^2} \tag{9.10}$$

Consequently, the water film would be always conformal to the substrate surface, producing a smooth film of water on the substrate.

Examination of the water film on substrates with fibrous and spherical shapes showed that they are indeed conformal to the substrate surfaces, as shown in Figure 9.17.[53] The procedure involved first condensing water on CNTs and iron oxide particles, then the substrates were plunged into ethane, a high heat capacity liquid, for instantaneous freezing of the water. The ice layers were then imaged in a cryogenic transmission electron microscope. It can be seen that the ice layers exhibit uniform thickness on both substrates.

The fact that the condensed water layer can spread out on the surface of the substrates makes the CLD process a unique process for depositing

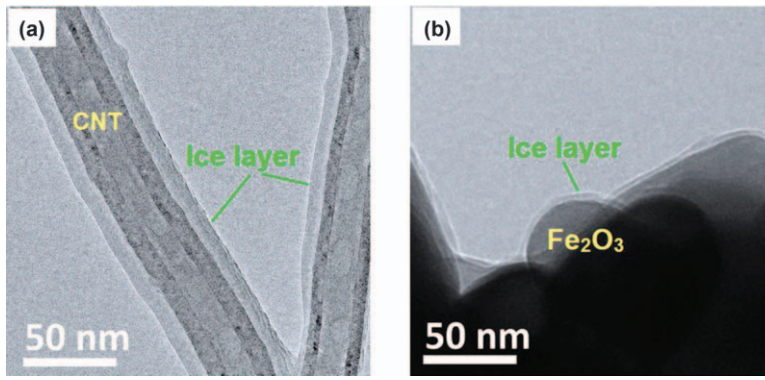


**Figure 9.17** Ice layers observed on (a) CNTs and (b) iron oxide particles after instantly freezing a water film that had condensed on the substrates during the CLD process.
Reproduced from ref. 53, https://doi.org/10.1038/s43246-020-0010-9, under the terms of the CC BY 4.0 license, http://creativecommons.org/licenses/by/4.0/.

conformal nanocoatings on nanoscale substrates, with a range of thicknesses. In addition, there are a few other advantages of the CLD technique:

1. Many metal–organic or organometallic precursors can be dissolved in liquid hydrocarbons, which makes it possible to deposit a variety of metal oxide coatings.
2. The single-pass process without cycling can save significant processing time (mostly completed in 30 min).
3. The low-temperature (approximately room temperature) deposition process makes it easy to operate.
4. There is no need for extra safety measures, such as vacuum equipment or gas traps. If there is an unreacted precursor, it can be neutralized by adding extra water to the liquid hydrocarbon.
5. The liquid hydrocarbon is not a consumable and can be easily purified by distillation and reused.

### 9.3.2 Metal Oxide Nanocoatings from Condensed Layer Deposition

One of the most commonly studied coating materials that can be made by a wide range of coating processes is alumina made from trimethylaluminum (TMA). Alumina nanocoatings can be easily deposited with the CLD technique[53] (see Figure 9.18).

Reaction of TMA, a metal alkyl compound, with water in a complete reaction would proceed according to

$$Al(CH_3)_3\ (l) + 1.5H_2O\ (l) \rightarrow 0.5Al_2O_3\ (s) + 3CH_4\ (g) \qquad (9.11)$$

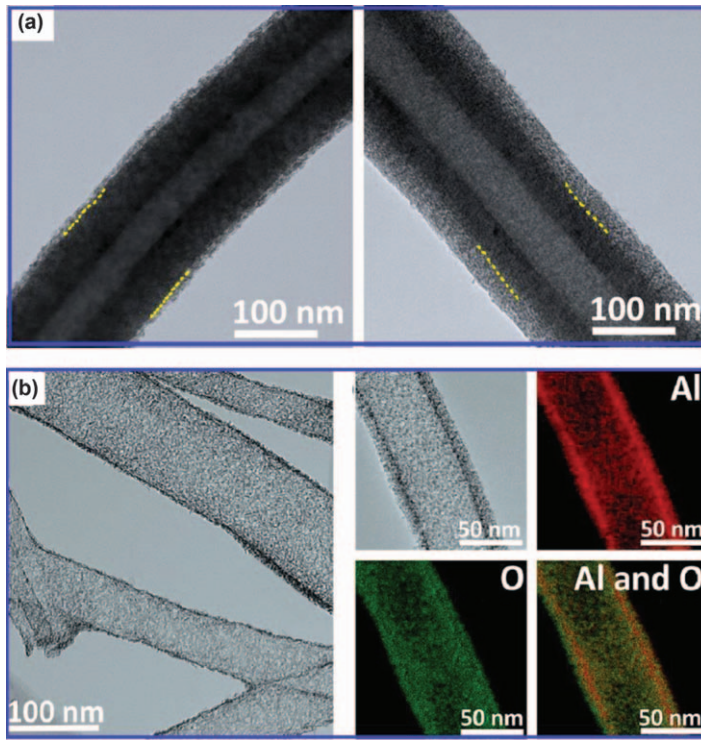


**Figure 9.18** (a) TEM images of alumina nanocoatings on CNTs with two thicknesses. (b) TEM images and elemental mapping of the $Al_2O_3$ nanotubes after removal of the CNTs, resulting in a porous structure. Reproduced from ref. 53, https://doi.org/10.1038/s43246-020-0010-9, under the terms of the CC BY 4.0 license, http://creativecommons.org/licenses/by/4.0/.

In this process, TMA dissolved in heptane was added to heptane dispersed with functionalized CNTs to react with the water film condensed on them. The TMA reaction is an exothermic reaction with an energy release of 482.3 kJ $mol^{-1}$ under standard conditions. The huge energy release can result in local heating and favors crystallization of the alumina instead of producing an amorphous material. It was demonstrated that the CLD-produced alumina nanocoatings have a γ-AlOOH crystalline phase in the as-synthesized coatings.[53] When the alumina nanocoatings were heat treated at 600 °C in air, they became crystalline $Al_2O_3$. When the CNTs were burned off in the oxidation process, the nanocoatings became $Al_2O_3$ nanotubes with a highly porous structure (see Figure 9.18b). This is an indication that reaction (9.11) did not go to completion owing to a local shortage of water, rather than a shortage of the total amount of water. The extremely fast reaction of TMA and water renders the reaction diffusion limited. As a result, the diffusion of water to the reaction site cannot catch up with the reaction rate, thus leading to the formation of intermediate species, such as

$(OH)–Al(CH_3)_2$, in the nanocoating. When the nanocoating was undergoing heat treatment, gas release produced the porous structure.

The CLD technique was also used to make titania nanocoatings on CNTs using metal alkoxides, as shown in Figure 9.19a.[53] In this case, titanium ethoxide dissolved in heptane was used to react with the condensed water film on CNTs dispersed in heptane. The complete reaction to form the metal oxide, $TiO_2$, is

$$Ti(OC_2H_5)_4\ (l) + 2H_2O\ (l) \rightarrow TiO_2\ (s) + 4C_2H_5OH\ (l) \qquad (9.12)$$

This reaction is slightly exothermic with an energy release of 10.7 kJ $mol^{-1}$, assuming that $TiO_2$ is in the anatase form. The as-deposited titania nanocoatings showed an amorphous phase. The amorphous titania nanocoatings can be converted to crystalline $TiO_2$ after heat treatment at 600 °C. When the

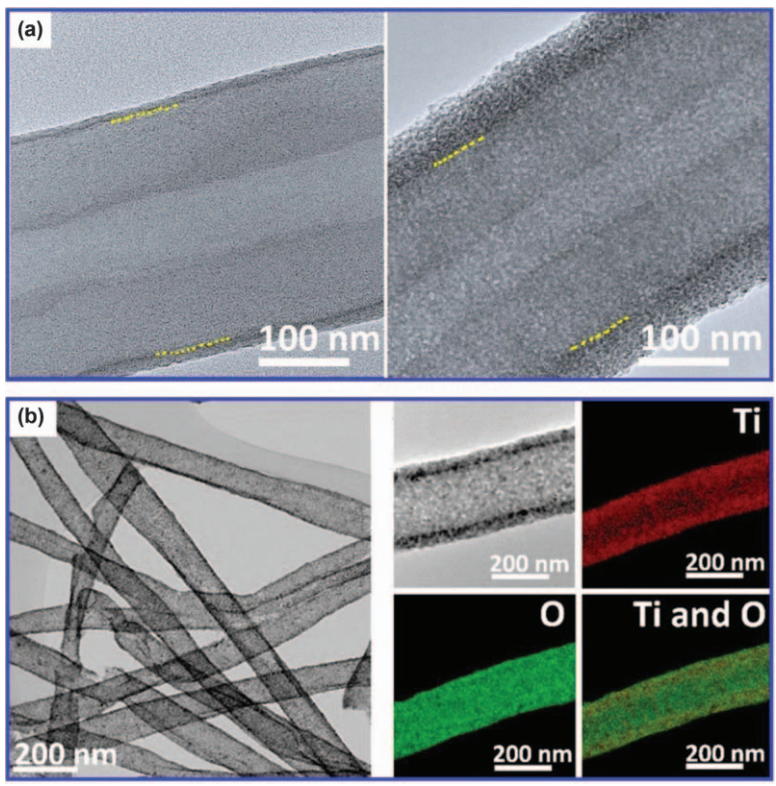


**Figure 9.19** (a) TEM images of titania nanocoatings on CNTs with two thicknesses. (b) TEM images and elemental mapping of the $TiO_2$ nanotubes after removal of the CNTs, resulting in a porous structure.
Reproduced from ref. 53, https://doi.org/10.1038/s43246-020-0010-9, under the terms of the CC BY 4.0 license, http://creativecommons.org/licenses/by/4.0/.

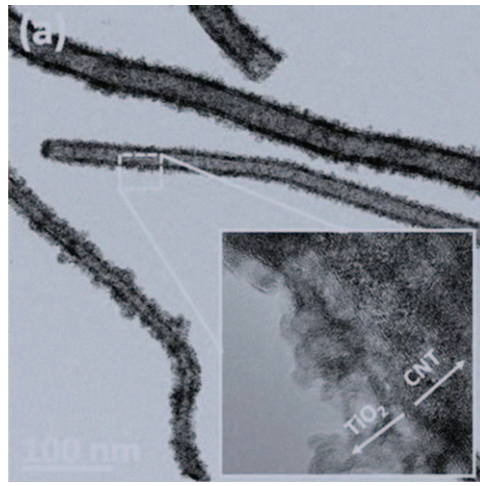


**Figure 9.20** A fluffy $TiO_2$ nanocoating on CNTs with extremely high surface areas. Reproduced from ref. 76, https://doi.org/10.1149/1945-7111/aba96c, under the terms of the CC BY 4.0 license, http://creativecommons.org/licenses/by/4.0/.

CNTs have been oxidized off, the coatings become $TiO_2$ nanotubes, similar to the $Al_2O_3$ nanotubes but less porous (see Figure 9.19b).

In another case, the CLD technique was used to deposit fluffy $TiO_2$ nanocoatings as supports for fuel cell catalysts, as shown in Figure 9.20.[76] The fluffy $TiO_2$ nanocoatings were made by using TTiP through reaction (9.9). Whereas titanium ethoxide generally produces dense $TiO_2$ coatings, TTiP with longer chain organic ligands produces fluffy nanocoatings. These large ligands are not removed easily from the nanocoatings during hydrolysis and condensation processes. They would partly remain in the coatings, especially for incomplete reactions, which in turn generate a fluffy structure once the organic residues have been removed during heat treatment. The fluffy nanocoatings have an extremely high specific surface area of more than 300 $m^2\,g^{-1}$, which makes them a good catalyst support to achieve high metal catalyst dispersion.

Similarly to the $TiO_2$ nanocoatings, $Nb_2O_5$ nanocoatings were made using niobium ethoxide as chemical precursor on carbon black (see Figure 9.21).[53] The niobium ethoxide would react with water in a complete hydrolysis reaction according to

$$Nb_2(OC_2H_5)_5\ (l) + 5H_2O\ (l) \rightarrow Nb_2O_5\ (s) + 10C_2H_5OH\ (l) \qquad (9.13)$$

This reaction is also an exothermic reaction with an energy release of 1648.5 $kJ\,mol^{-1}$ based on the thermochemical properties of the compounds involved.[77] With this large energy release, the reaction observably goes much faster than that with titanium ethoxide. However, the niobia coating

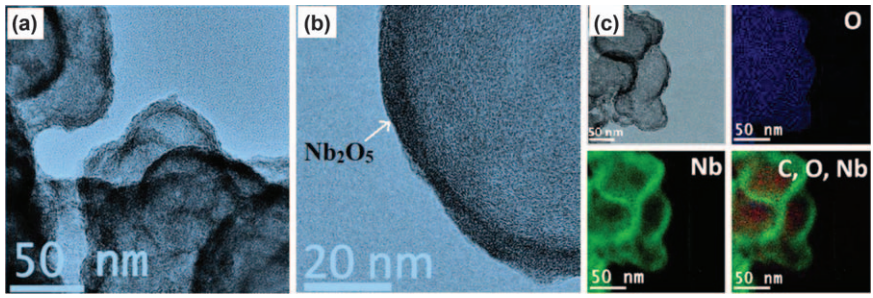


**Figure 9.21** (a) TEM image of niobia nanocoating on carbon black. (b) High-magnification TEM image of the $Nb_2O_5$ nanocoating. (c) Elemental mapping of the niobia nanocoatings.
Reproduced from ref. 53, https://doi.org/10.1038/s43246-020-0010-9, under the terms of the CC BY 4.0 license, http://creativecommons.org/licenses/by/4.0/.

produced is also amorphous, as confirmed by X-ray diffraction analysis. The nanocoating is converted to $Nb_2O_5$ after heat treatment.

### 9.3.3 Nanocoatings from CLD for Electrocatalytic Systems

As shown above, the CLD technique is well suited for making conformal nanocoatings of metal oxides on nanoscale substrates, especially on CNTs or carbon black. These nanocoatings can have high surface areas and can serve as good electrocatalyst supports. In a recent study, niobia nanocoatings deposited on carbon black were used to support Pt nanoparticles for ORRs.[78] It was shown that a 5 nm thick niobia nanocoating can completely coat carbon black with a uniform thickness (see Figure 9.22). The Pt nanoparticles deposited on the metal oxide nanocoatings showed a narrow size distribution with a size of 3.8 nm, which is a good size for ORRs.[79]

The electrocatalyst was further studied for its electrocatalytic performance. It was shown that it is more active than Pt/C with a 25 mV shift in half-wave potential in ORRs in 0.5 M sulfuric acid electrolyte, as shown Figure 9.23. In addition, the electrocatalyst showed a high durability with only a 1.7% decrease in half-wave potential after 5000 cycles. There is basically no decrease in ORR mass activity after 5000 cycles at 0.9 V *vs.* RHE.

The excellent ORR activity was attributed to metal–support interactions. The Pt donates electrons back to the metal oxides due to electron-deficient oxygen vacancies in the oxides.[80] As a result, it is more difficult for Pt to be oxidized by water to form Pt–OH, which blocks the active sites. Furthermore, it was suggested that the mismatch between the lattice of Pt and that of the metal oxide could result in a contraction of Pt–Pt bonds, inducing a strain effect in the Pt catalyst.[81] The high durability was again attributed to the metal oxide nanocoating support being stable in the sulfuric acid electrolyte and the stabilization effect of the metal oxides being due to the metal–support interactions.[9]

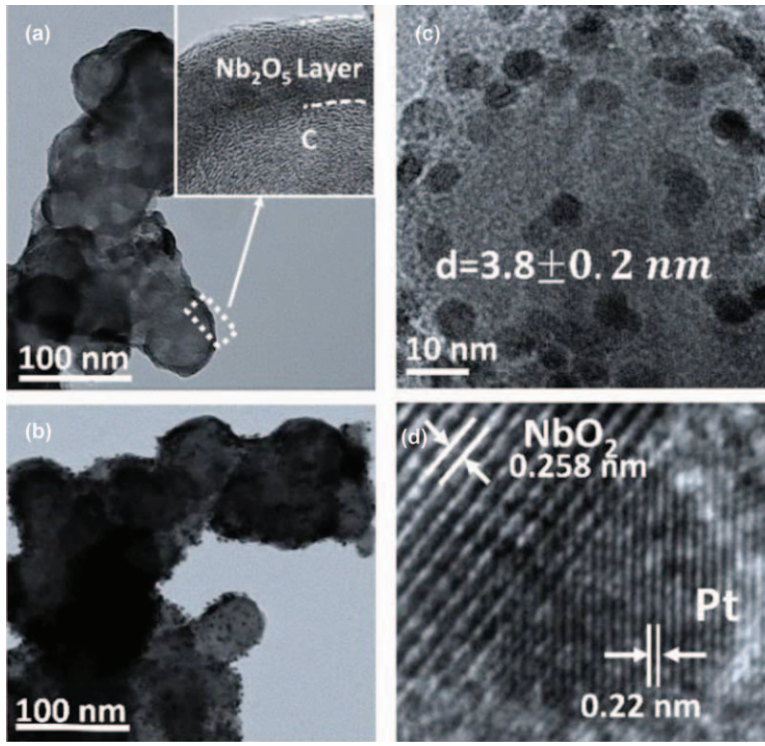


**Figure 9.22** (a) TEM image showing carbon-doped $Nb_2O_5$ nanocoatings on carbon black. (b) TEM image showing Pt supported on the niobia nanocoatings in (a). (c) High-resolution TEM image showing Pt nanoparticles with a uniform dispersion. (d) Lattice fringes of the Pt and the metal oxide showing a suboxide of $NbO_2$, the conductive form of niobia.
Reproduced from ref. 78 with permission from John Wiley & Sons, Copyright © 2020 WILEY-VCH Verlag GmbH & Co. KGaA, Weinheim.

In another study, fluffy $TiO_2$ nanocoatings (see Figure 9.20) were used to support Pt as an ORR catalyst.[76] $SnO_2$ was deposited on the $TiO_2$ support first as a co-catalyst to Pt, as shown in Figure 9.24. It can be seen that the Pt nanoparticles can be uniformly dispersed in the fluffy nanocoatings. The co-catalyst $SnO_2$ is also seen to be uniformly dispersed. One of the advantages of the fluffy nanocoatings is that they have an extremely high specific surface area of 310 $m^2 g^{-1}$ [determined *via* nitrogen adsorption in Brunauer–Emmett–Teller (BET) measurements], leading to better dispersion and utilization of the supported Pt electrocatalyst. $SnO_2$ was used as a co-catalyst, or bifunctional catalyst, to shift the Pt oxidation to higher overpotentials. Further, $SnO_2$ can contribute protons from its reaction with water locally to facilitate ORRs on Pt. The fluffy $TiO_2$ structure also contributed to the stabilization of the $SnO_2$, which is normally not very stable in acidic electrolytes.[82] Consequently, the Pt–$SnO_2$/$TiO_2$ catalyst was shown to have doubled the mass activity with respect to that of Pt/C to 0.9 V *vs.* RHE.

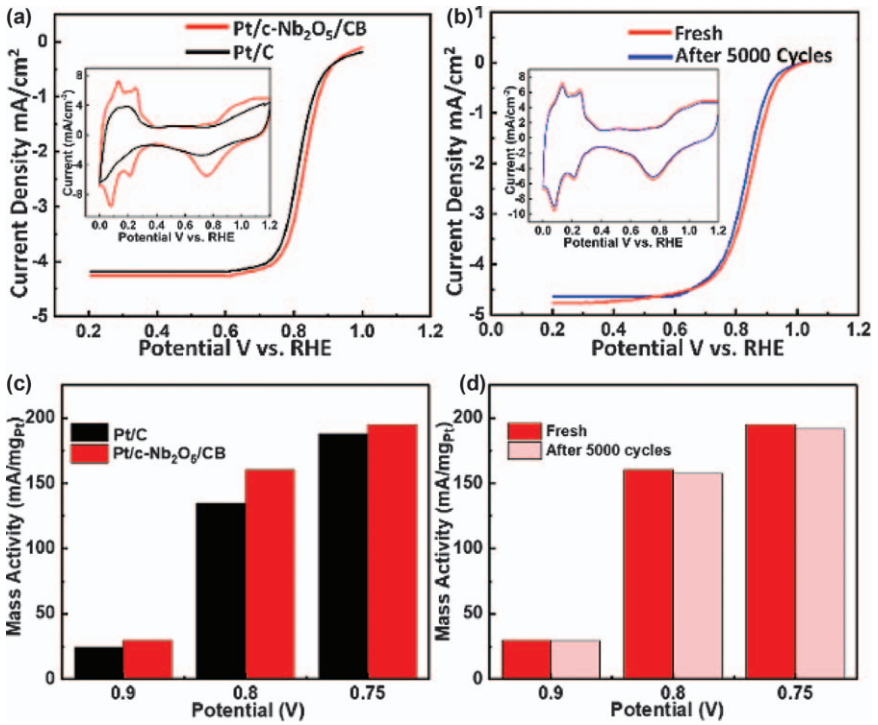


**Figure 9.23** (a) ORR in $O_2$-saturated 0.5 M $H_2SO_4$ at a scan rate 10 mV $s^{-1}$ (the inset shows the cyclic voltammograms). (b) Durability tests before and after 5000 cycles for Pt supported on carbon-doped $Nb_2O_5$ on carbon black (CB). (c) ORR mass activity comparison between the two catalysts. (d) ORR mass activities at different overpotentials in the fresh and cycled catalysts.
Reproduced from ref. 78 with permission from John Wiley & Sons, Copyright © 2020 WILEY-VCH Verlag GmbH & Co. KGaA, Weinheim.

## 9.4 Conclusions and Outlook

This chapter has discussed ultrathin metal oxide coatings and their applications in electrocatalytic reactions. The sol–gel deposition (SGD) and condensed layer deposition (CLD) techniques were discussed as wet chemical processes to prepare ultrathin coatings, or nanocoatings. Of particular relevance to electrochemical reactions occurring in acidic electrolytes, titania and niobia nanocoatings were presented.

The SGD technique has been demonstrated to be a useful technique for depositing thin films in aqueous and alcoholic solutions with a variety of chemical precursors, including metal alkoxides. It is a technique with reactions in bulk solutions in which a nanoscale substrate can be dispersed. However, it is difficult to control the film thickness down to less than 10 nm. The substrate surface has to be functionalized to achieve a uniform coating. Additionally, surface priming may be needed to ensure a complete coat on

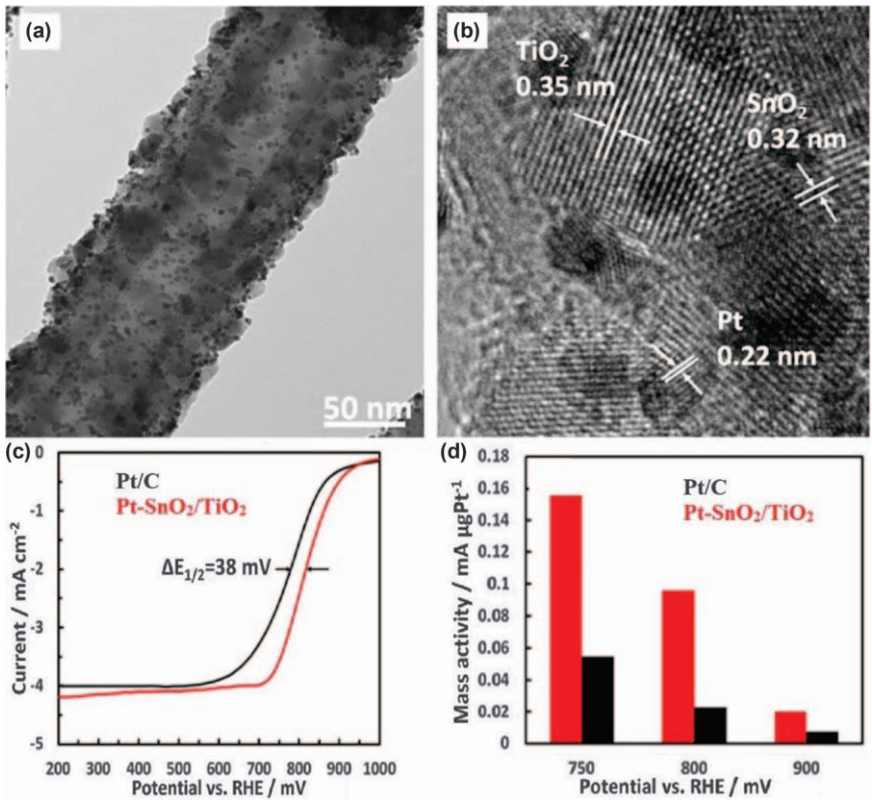


**Figure 9.24** (a) A Pt–$SnO_2$ catalyst supported on fluffy $TiO_2$ nanocoatings. (b) The lattice fringes of the three components in the catalyst. (c) ORR activity showing a 38 mV improvement of Pt–$SnO_2$/$TiO_2$ over that of Pt/C. (d) Mass activities of the Pt–$SnO_2$/$TiO_2$ catalyst, showing improved activities at different overpotentials.
Reproduced from ref. 76, https://doi.org/10.1149/1945-7111/aba96c, under the terms of the CC BY 4.0 license, http://creativecommons.org/licenses/by/4.0/.

the substrate surface. The CLD technique also uses a bulk solution to disperse nanoscale substrates but consists of liquid hydrocarbon. In this process, however, the hydrolysis reactions occur only on the substrate surface, not in the bulk solution. This advantage makes it easier to control the coating thickness and ultrathin coatings of less than 10 nm can easily be deposited. Additionally, the CLD technique can utilize a wider variety of metal–organic or organometallic precursors since they are often soluble in hydrocarbons. The CLD technique is also much less time consuming and can deposit nanocoatings in one pass at room temperatures.

For application in electrocatalytic reactions in acidic electrolytes, the ultrathin metal oxide coatings are intended to protect the underlying carbon as a high surface area template. However, the metal oxide nanocoatings can

often have larger surface areas when a porous or fluffy structure can be made. When the carbons are completely encapsulated in the metal oxides, they do not need to be removed since they are protected from corrosion. The carbons can actually contribute to the electrical conductivity and provide mechanical strength to the electrode material.

CLD is a recent coating deposition technique that has been shown to be capable of depositing various metal oxides on different substrates, especially titania and niobia nanocoatings on carbons for electrocatalysts. Further development of the technique could lead to the preparation of nanocoatings for other applications where metal oxides are needed. A deeper fundamental understanding of hydrolysis and condensation in a nanoscale water layer on a substrate is expected to make the CLD technique even more versatile for various electrocatalytic applications where metal oxide nanocoatings are desired.

## References

1. K. Kinoshita, *Carbon: Electrochemical and Physicochemical Properties*, John Wiley & Sons, New York, 1988.
2. L. Li and Y. Xing, *J. Electrochem. Soc.*, 2006, **153**, A1823.
3. S. Maass, F. Finsterwalder, G. Frank, R. Hartmann and C. Merten, *J. Power Sources*, 2008, **176**, 444–451.
4. P. Trogadas, T. F. Fuller and P. Strasser, *Carbon*, 2014, **75**, 5–42.
5. L. Castanheira, W. O. Silva, F. H. Lima, A. Crisci, L. Dubau and F. D. R. Maillard, *ACS Catal.*, 2015, **5**, 2184–2194.
6. S. Chen, H. A. Gasteiger, K. Hayakawa, T. Tada and Y. Shao-Horn, *J. Electrochem. Soc.*, 2009, **157**, A82.
7. S. Zhang, X.-Z. Yuan, J. N. C. Hin, H. Wang, K. A. Friedrich and M. Schulze, *J. Power Sources*, 2009, **194**, 588–600.
8. B. Merzougui and S. Swathirajan, *J. Electrochem. Soc.*, 2006, **153**, A2220.
9. K. Huang, K. Sasaki, R. R. Adzic and Y. Xing, *J. Mater. Chem.*, 2012, **22**, 16824–16832.
10. K. Huang, Y. Li, L. Yan and Y. Xing, *RSC Adv.*, 2014, **4**, 9701–9708.
11. L. Yan, K. Huang, Y. Chen and Y. Xing, *ECS Electrochem. Lett.*, 2014, **3**, F27.
12. K. Sasaki, L. Zhang and R. R. Adzic, *Phys. Chem. Chem. Phys.*, 2008, **10**, 159–167.
13. T. Ioroi, H. Senoh, S.-I. Yamazaki, Z. Siroma, N. Fujiwara and K. Yasuda, *J. Electrochem. Soc.*, 2008, **155**, B321.
14. S.-Y. Huang, P. Ganesan and B. N. Popov, *Appl. Catal., B*, 2010, **96**, 224–231.
15. F. Walsh and R. Wills, *Electrochim. Acta*, 2010, **55**, 6342–6351.
16. A. Bauer, K. Lee, C. Song, Y. Xie, J. Zhang and R. Hui, *J. Power Sources*, 2010, **195**, 3105–3110.
17. L. Zhang, L. Wang, C. M. Holt, B. Zahiri, Z. Li, K. Malek, T. Navessin, M. H. Eikerling and D. Mitlin, *Energy Environ. Sci.*, 2012, **5**, 6156–6172.

18. S.-Y. Huang, P. Ganesan, S. Park and B. N. Popov, *J. Am. Chem. Soc.*, 2009, **131**, 13898–13899.
19. M. Pourbaix, *Atlas of Electrochemical Equilibria in Aqueous Solution*, NACE Foundation, 1974.
20. E. Asselin, T. M. Ahmed and A. Alfantazi, *Corros. Sci.*, 2007, **49**, 694–710.
21. W.-Q. Han and Y. Zhang, *Appl. Phys. Lett.*, 2008, **92**, 203117.
22. J. I. Martinez, H. A. Hansen, J. Rossmeisl and J. K. Nørskov, *Phys. Rev. B*, 2009, **79**, 045120.
23. J. Smith, F. Walsh and R. Clarke, *J. Appl. Electrochem.*, 1998, **28**, 1021–1033.
24. K. Huang, Y. Li and Y. Xing, *J. Mater. Res.*, 2013, **28**, 454.
25. F.-D. Kong, G.-P. Yin, C.-Y. Du, S. Zhang, Y.-T. Qu, L. Du, Z.-Q. Xu and A.-X. Ling, *Catal. Commun.*, 2015, **68**, 67–72.
26. C. Hao, H. Lv, Q. Zhao, B. Li, C. Zhang, C. Mi, Y. Song and J. Ma, *Int. J. Hydrogen Energy*, 2017, **42**, 9384–9395.
27. D. Hassen, M. Shenashen, S. El-Safty, M. M. Selim, H. Isago, A. Elmarakbi, A. El-Safty and H. Yamaguchi, *J. Power Sources*, 2016, **330**, 292–303.
28. C. Hao, H. Lv, C. Mi, Y. Song and J. Ma, *ACS Sustainable Chem. Eng.*, 2016, **4**, 746–756.
29. H. Lv, G. Zhang, C. Hao, C. Mi, W. Zhou, D. Yang, B. Li and C. Zhang, *RSC Adv.*, 2017, **7**, 40427–40436.
30. A. Kumar and V. Ramani, *ACS Catal.*, 2014, **4**, 1516–1525.
31. M. T. Anwar, X. Yan, S. Shen, N. Husnain, F. Zhu, L. Luo and J. Zhang, *Int. J. Hydrogen Energy*, 2017, **42**, 30750–30759.
32. Y.-J. Wang, D. P. Wilkinson, V. Neburchilov, C. Song, A. Guest and J. Zhang, *J. Mater. Chem. A*, 2014, **2**, 12681–12685.
33. C. D'Urso, G. Bonura and A. Aricò, *Int. J. Hydrogen Energy*, 2017, **42**, 28011–28021.
34. H. Cheng, X. Feng, D. Wang, M. Xu, K. Pandiselvi, J. Wang, Z. Zou and T. Li, *Electrochim. Acta*, 2015, **180**, 564–573.
35. C. He, S. Sankarasubramanian, I. Matanovic, P. Atanassov and V. Ramani, *ChemSusChem*, 2019, **12**, 3468–3480.
36. I. Jiménez-Morales, F. Haidar, S. Cavaliere, D. J. Jones and J. Rozière, *ACS Catal.*, 2020, **10**, 10399–10411.
37. C. He, X. Wang, S. Sankarasubramanian, A. K. Yadav, K. Bhattacharyya, X. Liang and V. K. Ramani, *ACS Appl. Energy Mater.*, 2020, **3**, 5774–5783.
38. Y.-H. Qin, Y. Li, T. Lam and Y. Xing, *J. Power Sources*, 2015, **284**, 186–193.
39. Y. Furubayashi, T. Hitosugi, Y. Yamamoto, K. Inaba, G. Kinoda, Y. Hirose, T. Shimada and T. Hasegawa, *Appl. Phys. Lett.*, 2005, **86**, 252101.
40. A. V. Emeline, Y. Furubayashi, X. Zhang, M. Jin, T. Murakami and A. Fujishima, *J. Phys. Chem. B*, 2005, **109**, 24441–24444.
41. G. Sahasrabudhe, J. Krizan, S. L. Bergman, R. J. Cava and J. Schwartz, *Chem. Mater.*, 2016, **28**, 3630–3633.

42. B. Van Zeghbroeck, *Principles of Semiconductor Devices*, Colarado University, 2004.
43. A. G. Hufnagel, S. Häringer, M. Beetz, B. Böller, D. Fattakhova-Rohlfing and T. Bein, *Nanoscale*, 2019, **11**, 14285–14293.
44. R. A. Caruso, J. H. Schattka and A. Greiner, *Adv. Mater.*, 2001, **13**, 1577–1579.
45. R. A. Caruso and M. Antonietti, *Chem. Mater.*, 2001, **13**, 3272–3282.
46. J.-H. Park and T. Sudarshan, *Chemical Vapor Deposition*, ASM international, 2001.
47. H. O. Pierson, *Handbook of Chemical Vapor Deposition: Principles, Technology and Applications*, William Andrew, 1999.
48. S. M. George, *Chem. Rev.*, 2010, **110**, 111–131.
49. A. W. Weimer, *J. Nanopart. Res.*, 2019, **21**, 9.
50. H. Van Bui, F. Grillo and J. R. van Ommen, *Chem. Commun.*, 2017, **53**, 45–71.
51. R. L. Puurunen, *J. Appl. Phys.*, 2005, **97**, 9.
52. C. J. Brinker, A. J. Hurd, P. R. Schunk, G. C. Frye and C. S. Ashley, *J. Non-Cryst. Solids*, 1992, **147–148**, 424–436.
53. A. M. Jasim, X. He, T. A. White and Y. Xing, *Commun. Mater.*, 2020, **1**, 9.
54. C. J. Brinker and G. W. Scherer, *Sol-gel Science: The Physics and Chemistry of Sol–gel Processing*, Academic press, 2013.
55. C. J. Brinker, R. Sehgal, S. Hietala, R. Deshpande, D. Smith, D. Loy and C. Ashley, *J. Membr. Sci.*, 1994, **94**, 85–102.
56. I. A. Rahman and V. Padavettan, *J. Nanomater.*, 2012, **2012**, 8.
57. W. Li and D. Zhao, *Adv. Mater.*, 2013, **25**, 142–149.
58. Y. J. Wong, L. Zhu, W. S. Teo, Y. W. Tan, Y. Yang, C. Wang and H. Chen, *J. Am. Chem. Soc.*, 2011, **133**, 11422–11425.
59. W. Stöber, A. Fink and E. Bohn, *J. Colloid Interface Sci.*, 1968, **26**, 62–69.
60. M. L. Surve, Master's thesis, University of Missouri–Rolla, 2003.
61. P. Botella, A. Corma and M. T. Navarro, *Chem. Mater.*, 2007, **19**, 1979–1983.
62. J.-T. Song, X.-S. Zhang, M.-Y. Qin and Y.-D. Zhao, *Dalton Trans.*, 2015, **44**, 7752–7756.
63. D. D. Lekeufack, A. Brioude, A. Mouti, J. Alauzun, P. Stadelmann, A. W. Coleman and P. Miele, *Chem. Commun.*, 2010, **46**, 4544–4546.
64. X. Wang and R. A. Caruso, *J. Mater. Chem.*, 2011, **21**, 20–28.
65. J. Livage, M. Henry and C. Sanchez, *Prog. Solid State Chem.*, 1988, **18**, 259–341.
66. D. Eder and A. H. Windle, *J. Mater. Chem.*, 2008, **18**, 2036–2043.
67. S. H. Sharif Zein and A. R. Boccaccini, *Ind. Eng. Chem. Res.*, 2008, **47**, 6598–6606.
68. K. Hemalatha, A. Prakash, K. Guruprakash and M. Jayakumar, *J. Mater. Chem. A*, 2014, **2**, 1757–1766.
69. N. G. Akalework, C.-J. Pan, W.-N. Su, J. Rick, M.-C. Tsai, J.-F. Lee, J.-M. Lin, L.-D. Tsai and B.-J. Hwang, *J. Mater. Chem.*, 2012, **22**, 20977–20985.

70. Z. Li, B. Gao, G. Z. Chen, R. Mokaya, S. Sotiropoulos and G. Li Puma, *Appl. Catal., B*, 2011, **110**, 50–57.
71. D. Eder and A. H. Windle, *Adv. Mater.*, 2008, **20**, 1787–1793.
72. M. Fanun, *Microemulsions: Properties and Applications*, CRC press, 2008.
73. C. Tsonopoulos, *Fluid Phase Equilib.*, 1999, **156**, 21–33.
74. H. Liu and G. Cao, *Sci. Rep.*, 2016, **6**, 23936.
75. S. M. A. Malek, F. Sciortino, P. H. Poole and I. Saika-Voivod, *J. Phys.: Condens. Matter*, 2018, **30**, 144005.
76. A. M. Jasim, S. Al-Salihi and Y. Xing, *J. Electrochem. Soc.*, 2020, **167**, 116526.
77. M. W. Chase Jr, *J. Phys. Chem. Ref. Data, Monogr.*, 1998, **9**, 1.
78. A. M. Jasim, G. Xu, S. Al-Salihi and Y. Xing, *ChemistrySelect*, 2020, **5**, 11431–11437.
79. K. Kinoshita, *Electrochemical oxygen technology*, John Wiley & Sons, 1992.
80. Y. Liu and W. E. Mustain, *J. Am. Chem. Soc.*, 2013, **135**, 530–533.
81. L. Zhang, L. Wang, C. M. Holt, T. Navessin, K. Malek, M. H. Eikerling and D. Mitlin, *J. Phys. Chem. C*, 2010, **114**, 16463–16474.
82. S. Geiger, O. Kasian, A. M. Mingers, K. J. J. Mayrhofer and S. Cherevko, *Sci. Rep.*, 2017, **7**, 4595.

CHAPTER 10

# *Applications of Metal Oxide Layers on Particulate Photocatalysts for Water Splitting*

Z. PAN,[a,†] T. HISATOMI[a] AND K. DOMEN*[a,b]

[a] Research Initiative for Supra-Materials, Shinshu University, 4–17–1 Wakasato, Nagano-shi, Nagano 380-8553, Japan; [b] Office of University Professors, The University of Tokyo, 2–11–16 Yayoi, Bunkyo-ku, Tokyo 113-8656, Japan
*Emails: domen@chemsys.t.u-tokyo.ac.jp; domen@shinshu-u.ac.jp

## 10.1 Introduction

Global consumption of fossil fuels has surged over the past several decades, leading to increasing concerns related to possible energy shortages and also environmental pollution and climate change. Solar energy is an attractive alternative to fossil fuels, especially if this energy can be stored in the form of chemical fuels that are energetically dense, storable and environmentally friendly. One promising approach towards this goal is water splitting driven by sunlight over particulate photocatalysts to generate $H_2$.[1] This process can

[†]Present address: Department of Applied Chemistry, Faculty of Science and Technology, Chuo University, 1–13 Kasuga, Bunkyo-ku, Tokyo 112-8551, Japan.

Energy and Environment Series No. 30
Ultrathin Oxide Layers for Solar and Electrocatalytic Systems
Edited by Heinz Frei and Daniel V. Esposito

Published by the Royal Society of Chemistry, www.rsc.org

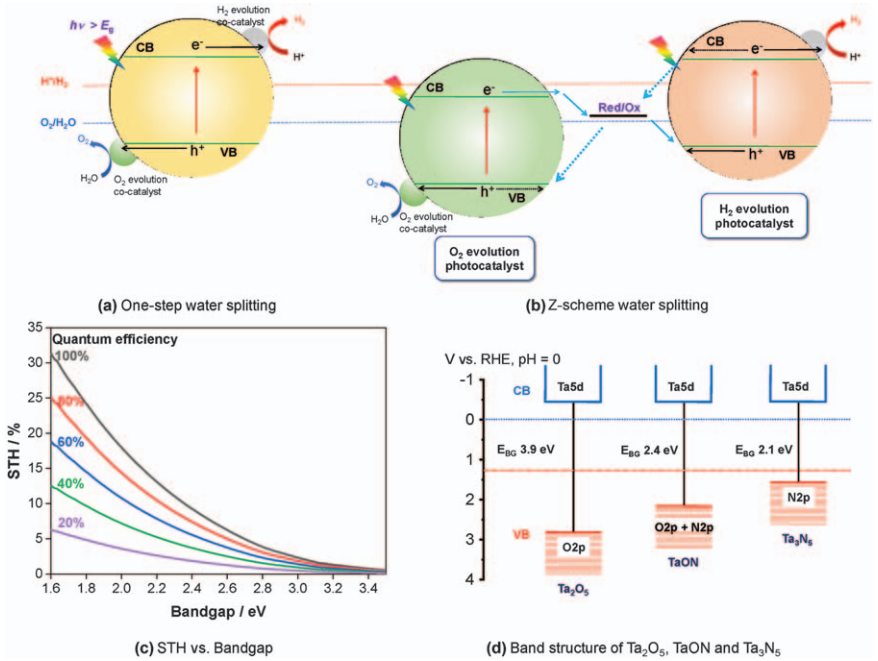


**Figure 10.1** (a) Reaction processes involved in one-step excitation water splitting. (b) Reaction processes involved in Z-scheme water splitting. (c) Calculated STH values for photocatalytic water splitting as functions of band gap for various quantum efficiencies. (d) Valence band engineering of $Ta_2O_5$ to form TaON and $Ta_3N_5$.
(d) Reproduced from ref. 14 with permission from American Chemical Society, Copyright 2003.

potentially be achieved using either one-step excitation (Figure 10.1a) or Z-scheme (two-step excitation) systems (Figure 10.1b). In the former case, both $H_2$ and $O_2$ are evolved on individual particles of a single photocatalyst. In the latter case, $H_2$ and $O_2$ are evolved on two different types of photocatalyst particles, and the remaining charge carriers are recombined with the aid of a mediator. Photocatalytic one-step excitation water splitting involves four necessary basic processes: light absorption by a photocatalyst to generate electron–hole pairs, charge separation in the bulk of the photocatalyst, charge transfer to the reaction sites, and surface reactions for the evolution of both $H_2$ and $O_2$.[2]

Photocatalytic reactions are initiated by light absorption. In such a process, electrons in the valence band (VB) of the photocatalyst are excited to the conduction band (CB) while positive holes are generated in the VB, producing electron–hole pairs. The band structure of a photocatalyst establishes its light absorption characteristics, and the light absorption of the material in turn determines the maximum solar-to-hydrogen energy conversion efficiency (STH) that can be achieved. Obtaining an STH value

of 5% from a one-step-excitation system requires that the band gap of the photocatalyst is less than 2.8 eV. This is true only in the best-case scenario in which the apparent quantum efficiency (the ratio of the number of photons used for photocatalytic water splitting to the number of incident photons) is 100% up to the light absorption edge (Figure 10.1c). However, the band gap of an oxide photocatalyst having a band structure suitable for water splitting is typically in excess of 3.0 eV, which is too large to achieve an STH high enough for practical applications. The band gaps of such materials are large because the potential of the VB edge composed of O 2p orbitals is too positive with respect to the $O_2$ evolution potential. One approach to solving this problem is the development of (oxy)nitride or (oxy)sulfide semiconductors based on so-called VB engineering. As shown in Figure 10.1d, in such materials the VB is composed of O 2p orbitals mixed with more negative N 2p orbitals, such that the VB is shifted negatively whereas the CB is essentially unchanged. Unfortunately, although several (oxy)nitrides and (oxy)sulfides have been developed, including $LaMg_{1/3}Ta_{2/3}O_2N$ and $Sm_2Ti_2O_5S_2$, these materials tend to be unstable during use.[3] It is therefore important to stabilize these photocatalysts. This can be accomplished by extracting holes from the VBs of these materials using $O_2$ evolution co-catalysts such as $CoO_x$,[4] or by coating the catalysts with a protective layer made of a compound such as $TiO_2$.[5]

Once electron–hole pairs have been generated in these systems, they may separate and migrate to the active sites at which surface reactions occur. During this process, the Fermi level of the photocatalyst will split into quasi-Fermi levels associated with the concentrations of electrons and holes, and the difference between these levels reflects the charge separation efficiency. Specifically, a difference of at least 1.23 V is required to achieve photocatalytic water splitting. Many photocatalysts have band structures that permit photocatalytic water splitting, meaning that the CB edge is more negative than the $H_2$ evolution potential and the VB edge is more positive than the $O_2$ evolution potential. However, the charge separation efficiency in these materials is often inadequate to promote water splitting, especially when the band gap is narrow. Both charge separation and charge transfer are governed by the drift and diffusion of charge carriers, which are correlated with optoelectronic factors such as the mobilities of charge carriers in the photocatalyst. In addition, these processes compete with charge recombination both in the bulk material and at the surface. Various strategies to improve charge separation, facilitate charge transfer, and suppress charge recombination have been reported, including passivating the surface by applying a metal oxide such as $ZrO_2$.[6]

The surface reactions on a photocatalyst can be regarded as microelectrochemical reactions, the overpotential of which (comprising primarily the activation and concentration overpotentials) is determined by the kinetics of the reaction sites and the mass transfer of reagents and products. The addition of an $H_2$ evolution co-catalyst such as metallic Rh is vital to reducing the

activation overpotential of the photocatalytic material. The standard potential for $H_2$ evolution is more negative than that for $O_2$ reduction, meaning that the latter reaction is thermodynamically favored. Moreover, the distance between $H_2$ and $O_2$ evolution sites on a photocatalyst is usually in the region of several tens of nanometers.[7] Consequently, the $H_2$ evolution reaction on a co-catalyst competes with backward reactions such as $O_2$ reduction and the recombination of $H_2$ and $O_2$. Therefore, to achieve efficient photocatalytic water splitting, the co-catalyst must have sufficient activity to reduce the overpotential and sufficient selectivity to suppress the backward reactions. For this purpose, the co-catalyst is typically coated with a permselective layer such as a $Cr_2O_3$ shell.[8] In addition to loading a co-catalyst for $H_2$ evolution, the photocatalyst surface must be hydrophilic to facilitate mass transfer and thereby minimize the concentration overpotential. A hydrophilic surface can be obtained by applying a layer of an oxide such as MgO.[9]

A Z-scheme system (Figure 10.1b) involves similar reaction processes to those that occur in a one-step excitation system. However, the associated surface reactions are more complicated, involving $H_2$ evolution, oxidation of the mediator on the $H_2$ evolution photocatalyst, reduction of the mediator on the $O_2$ evolution photocatalyst, and $O_2$ evolution as the forward reactions. These processes also compete with backward reactions, including $O_2$ reduction, $H_2$ and $O_2$ recombination, oxidation of the mediator on the $O_2$ evolution photocatalyst, and reduction of the mediator on the $H_2$ evolution photocatalyst. Because of these complex surface reactions, it is crucial to provide highly selective reaction sites when constructing a Z-scheme system.[10]

As noted above, surface engineering of the photocatalyst and/or co-catalyst by applying metal oxides has been a common means of optimizing photocatalytic devices. This chapter reviews five aspects of this strategy: (i) suppressing backward reactions on co-catalysts or photocatalysts, (ii) increasing the surface hydrophilicity of photocatalysts, (iii) passivating the surfaces of photocatalysts, (iv) modifying the redox selectivity of photocatalysts in photocatalytic Z-scheme systems, and (v) protecting the surfaces of photocatalysts during use. It should be noted that metal oxides such as $RuO_2$ and $IrO_2$ are also widely used as co-catalysts for photocatalytic water splitting, but these applications are not discussed here because they have been thoroughly summarized in previous review articles.[11–13]

## 10.2 Suppression of Back Reactions on Co-catalysts and Photocatalysts

A photocatalytic system typically has two components: a particulate semiconductor for light absorption and a nano-sized co-catalyst to reduce the overpotential for $H_2$ or $O_2$ evolution. In particular, $H_2$ evolution co-catalysts are required for the majority of photocatalytic systems. However, although

these co-catalysts facilitate $H_2$ evolution as a forward reaction, they also promote the thermodynamically favored $O_2$ reduction reaction and the formation of water from $H_2$ and $O_2$. This occurs because the $H_2$ and $O_2$ evolution sites are located in close proximity to one another in photocatalytic systems.[15] Moreover, the surfaces of some photocatalysts can also facilitate these backward reactions,[5] which remain a significant challenge to the development of efficient photocatalytic systems for water splitting. One strategy for suppressing these backward reactions is to apply an oxide layer to the co-catalyst and/or photocatalyst, and this section provides a detailed discussion of the application of NiO and $Cr_2O_3$ coatings to co-catalysts and the use of amorphous $TiO_2$ coatings on photocatalysts. Other oxide layers having similar functions, including lanthanoid oxides, $MoO_x$ and $SiO_2$, are also introduced and briefly examined.

### 10.2.1 NiO on Ni to Suppress Back Reactions

Domen and co-workers developed a photocatalytic water splitting system based on $SrTiO_3$ in 1980.[16–18] They intended to prepare an intimate p–n junction between NiO and $SrTiO_3$ by reducing $Ni^{2+}$ to metallic Ni and then reoxidizing the metal to NiO, as shown in Figure 10.2a. This approach required a high-temperature reoxidation process to convert the metallic Ni completely to high-quality p-type NiO. Interestingly, the data showed that the resulting catalyst was more active when a reoxidation temperature below 200 °C was employed (Figure 10.2b). Further studies based on spectroscopy revealed that an Ni–NiO core–shell structure instead of pure p-type NiO was formed as a result of the reduction and mild reoxidation treatments.[19,20] During photocatalytic water splitting, the metallic Ni core received electrons from the CB of the $SrTiO_3$ and provided $H_2$ evolution sites, while the NiO shell that had been generated *in situ* functioned as a permselective layer. This layer prevented $O_2$ from reaching the Ni core and causing backward reactions such as $H_2O$ formation and $O_2$ reduction (Figure 10.2a). Consequently, photocatalytic water splitting was achieved (Figure 10.2c). Increasing the reoxidation temperature completely converted the Ni to NiO and the photocatalytic water splitting activity decreased. However, in subsequent studies, NiO was also found to be an effective $H_2$ evolution co-catalyst for a number of oxide photocatalysts, such as $NaTaO_3$.[21–27] It is evident that the optimal conditions for loading the co-catalyst vary with the type of photocatalyst.

### 10.2.2 $Cr_2O_3$ on Metal/Metal Oxide Co-catalysts

The formation of permselective thin oxide layers by reduction and oxidation treatments is not applicable to all metal species. As an example, Rh is more electrochemically active with regard to $H_2$ evolution than Ni,[27] but $Rh_2O_3$ is not permselective and can actually promote backward reactions. Therefore, it would be desirable to develop permselective oxide layers that are

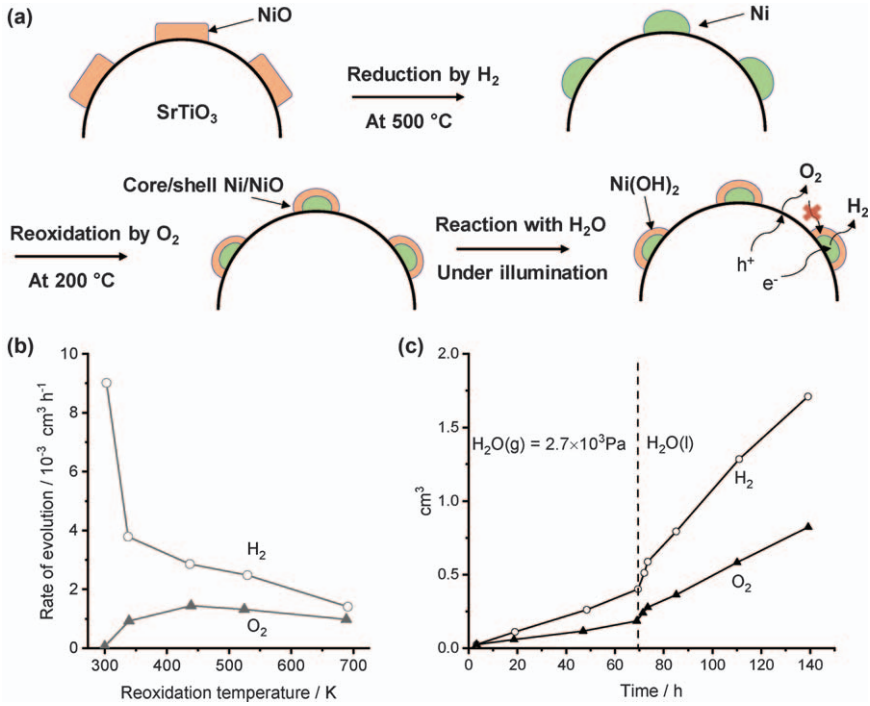


**Figure 10.2** (a) Schematic diagram showing the structure of an $NiO_x/SrTiO_3$ photocatalyst after various treatments. (b) Effect of the reoxidation temperature on photocatalytic water splitting. (c) Time course of gas evolution during photocatalytic water (gas or liquid) splitting over $NiO_x/SrTiO_3$. (a) Adapted from ref. 20 with permission from American Chemical Society, Copyright 1986. (b, c) Reproduced from ref. 18 with permission from American Chemical Society, Copyright 1982.

universally applicable. During the electrolysis of an aqueous salt solution to produce $NaClO_3$ in industry, Cr(VI) is an important additive that increases the Faradaic efficiency of $H_2$ evolution.[28,29] During the electrolysis, Cr(VI) is reduced to Cr(III) to generate a $Cr(OH)_3{\cdot}nH_2O$ film. The deposition of $Cr(OH)_3{\cdot}nH_2O$ is a self-limiting process because the film has low electrical conductivity and, therefore, impedes the reduction of additional Cr(VI) species. This thin film also blocks the migration of relatively large $O_2$ molecules while being permeable to $H^+$ and $H_2O$ as reactants and $H_2$ as a product. This property suppresses unwanted side reactions such as $O_2$ reduction and permits highly selective $H_2$ evolution at the cathode. Inspired by the application of $Cr_2O_3$ films in electrolysis systems, $Cr_2O_3$ layers have been widely used as permselective coatings on metal/metal oxide co-catalysts to suppress backward reactions during photocatalytic water splitting.[8,30–37] Maeda *et al.* reported the first application of this technique.[8] As shown in Figure 10.3a, although metal-loaded $(Ga_{1-x}Zn_x)(N_{1-x}O_x)$ was almost inactive for the photocatalytic water splitting reaction because of significant backward

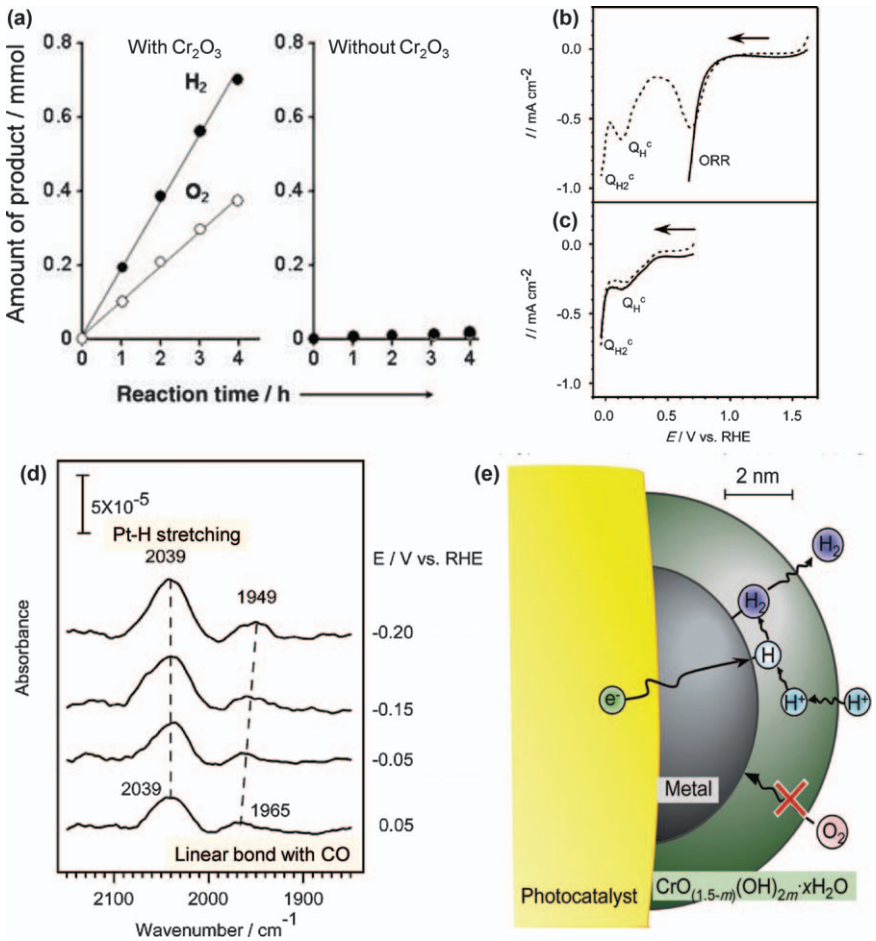


**Figure 10.3** (a) Time course of photocatalytic water splitting using Rh-loaded $(Ga_{1-x}Zn_x)(N_{1-x}O_x)$ with/without $Cr_2O_3$ under visible light irradiation ($\lambda > 400$ nm). Cyclic voltammograms obtained from (b) bare and (c) $Cr_2O_3$-coated Pt electrodes in aqueous 0.5 M $Na_2SO_4$ adjusted to pH 3.6 with Ar bubbling (dotted line) and $O_2$ bubbling (solid line). (d) Potential-dependent SNIFTIR spectra of adsorbed hydrogen atoms on a $Cr_2O_3$-coated Pt electrode in aqueous 0.5 M $Na_2SO_4$ adjusted to pH 3.6 with $H_2SO_4$ and $N_2$ bubbling (reference potential: +0.65 V *vs.* RHE). (e) Schematic diagram of the $H_2$ evolution reaction on core–shell co-catalyst/$Cr_2O_3$ loaded on a photocatalyst.
(a) Reproduced from ref. 8 with permission from John Wiley & Sons, Copyright © 2006 WILEY-VCH Verlag GmbH & Co. KGaA, Weinheim. (b–e) Reproduced from ref. 38 with permission from American Chemical Society, Copyright 2009.

reactions, applying a $Cr_2O_3$ layer to the metallic co-catalysts allowed successful water splitting. In this work, $K_2CrO_4$ was used as a precursor to generate a $Cr_2O_3$ layer *in situ* so as to coat the metallic co-catalysts

**Table 10.1** Photocatalytic water splitting activities of $(Ga_{1-x}Zn_x)(N_{1-x}O_x)$ specimens loaded with various co-catalysts. Reproduced from ref. 30 with permission from John Wiley & Sons, Copyright © 2010 WILEY-VCH Verlag GmbH & Co. KGaA, Weinheim.

| | | Gas evolution rate ($\mu mol\ h^{-1}$) | |
|---|---|---|---|
| Co-catalyst | $Cr_2O_3$ deposition | $H_2$ | $O_2$ |
| Rh | No | <1 | <1 |
| | Yes | 179 | 88 |
| Pt | No | <1 | <1 |
| | Yes | 32 | 16 |
| Pd | No | <1 | <1 |
| | Yes | 15 | 5.2 |
| $NiO_x$ | No | 7.4 | 3.6 |
| | Yes | 15 | 7.4 |
| $RuO_2$ | No | 36 | 18 |
| | Yes | 47 | 24 |
| $Rh_2O_3$ | No | 1.4 | Trace |
| | Yes | 70 | 36 |

functioning as $H_2$ evolution sites, based on photodeposition following reaction (10.1).

$$2CrO_4^{2-} + 6e^- + (n+5)H_2O \rightarrow Cr_2O_3 \cdot nH_2O + 10OH^- \quad (10.1)$$

Additional research indicated that $Cr_2O_3$ layers were applicable to both metallic and metal oxide co-catalysts.[30] The photocatalytic water splitting activities of $(Ga_{1-x}Zn_x)(N_{1-x}O_x)$ loaded with metallic or metal oxide co-catalysts before and after depositing a $Cr_2O_3$ layer are summarized in Table 10.1.

The role and function of $Cr_2O_3$ layers during photocatalytic water splitting were examined by Yoshida *et al.* in trials using model electrodes.[38] In their work, a $Cr_2O_3$ layer was found to block molecular $O_2$ so as to effectively suppress cathodic $O_2$ reduction on a Pt electrode (Figure 10.3b,c). In contrast, this layer did not impede the transportation of H species, as confirmed by the appearance of a peak at 2039 $cm^{-1}$ (attributed to Pt–H stretching involving terminal H atoms) in subtractively normalized interfacial Fourier transform infrared reflection (SNIFTIR) spectra (Figure 10.3d). The absence of a peak due to terminal H adsorbed on the $Cr_2O_3$ at 1581 $cm^{-1}$ also demonstrated that this layer did not absorb H species. Based on these results, a model for $H_2$ evolution on a core–shell metal (oxide)/$Cr_2O_3$ co-catalyst was established, as illustrated in Figure 10.3e. In this model, the $Cr_2O_3$ functions as a permselective layer that allows the diffusion of $H^+$ and $H_2$ but inhibits the movement of $O_2$. A subsequent study by Qureshi *et al.* showed that the $Cr_2O_3$ layer was also impermeable to ferricyanide, $IO_3^-$, $S_2O_8^{2-}$, $H_2O_2$, and gaseous CO.[39]

$Cr_2O_3$ also forms composites with certain metal oxides that can work as co-catalysts.[5,40–47] Thaminimulla *et al.* investigated the effect of adding metals to $NiO_x$ loaded on $K_2La_2Ti_3O_{10}$ to promote photocatalytic water splitting.[40] Various metal additives were tested, but only Cr showed a

**Table 10.2** Photocatalytic activities of $(Ga_{1-x}Zn_x)(N_{1-x}O_x)$ specimens loaded with Cr and a transition metal during overall water splitting under UV irradiation ($\lambda > 300$ nm). Reproduced from ref. 44 with permission from Elsevier, Copyright 2006.[a]

| Co-catalyst | | | Activity ($\mu mol\,h^{-1}$) | |
|---|---|---|---|---|
| Metal element in metal oxide | Loading amount (wt%) | Cr co-loading amount (wt%) | $H_2$ | $O_2$ |
| Fe | 1 | 1 | 73 | 36 |
| Co | 1 | 1 | 48 | 24 |
| Ni | 1.25 | 0.125 | 685 | 336 |
| Cu | 1 | 1 | 585 | 292 |
| Ru | 1 | 0.1 | 181 | 84 |
| Rh | 1 | 1.5 | 3835 | 1988 |
| Pd | 1 | 0.1 | 205 | 96 |
| Ag | 1 | 1 | 11 | 2.3 |
| Ir | 1 | 0.1 | 41 | 17 |
| Pt | 1 | 1 | 775 | 357 |

[a]Reaction conditions: catalyst, 0.3 g; distilled water, 370–400 mL; light source, high-pressure mercury lamp (450 W); inner irradiation-type reaction vessel made of Pyrex.

positive effect, increasing the photocatalytic activity by ~10% and improving the durability of the material. The effects of adding Cr to various metal oxide co-catalysts loaded on $(Ga_{1-x}Zn_x)(N_{1-x}O_x)$ were examined in detail in a subsequent study.[44] The data in Table 10.2 demonstrate that the photocatalytic water splitting activities of metal oxide/$(Ga_{1-x}Zn_x)(N_{1-x}O_x)$ specimens were significantly increased upon incorporating Cr, and the combination of Rh and Cr was the most effective approach in terms of improving the photocatalytic water splitting. Interestingly, both $Rh_2O_3$ and $Cr_2O_3$ have corundum structures and are considered to form mixed oxides having the general formula $Rh_{2-y}Cr_yO_3$. These oxides promote the $H_2$ evolution reaction while being inactive with respect to $O_2$ reduction and the recombination of $H_2$ and $O_2$.[43] Therefore, $Rh_{2-y}Cr_yO_3$-loaded photocatalysts exhibited high photocatalytic water splitting activity, although the working mechanism for $Cr_2O_3$ in $Rh_{2-y}Cr_yO_3$ is still unclear because this material appears not to form a $Cr_2O_3$ shell. It would be helpful to elucidate the fine structure of the $Rh_{2-y}Cr_yO_3$ co-catalyst because the activity of $Rh_{2-y}Cr_yO_3$/$(Ga_{1-x}Zn_x)(N_{1-x}O_x)$ is even higher than that of $Cr_2O_3$/Rh/$(Ga_{1-x}Zn_x)(N_{1-x}O_x)$. In a recent study, the Cr component in $Rh_{2-y}Cr_yO_3$-loaded $SrTiO_3$ was shown to form a Cr-enriched shell on the surface of the catalyst.[48] On this basis, it is believed that a permselective $Cr(OH)_3{\cdot}nH_2O$ film is present in such materials, as is also the case for $Cr_2O_3$/noble metal co-catalysts.

### 10.2.3 Amorphous $TiO_2$ (a-$TiO_2$) Layers on Photocatalysts

Pan *et al.* developed a 600 nm class photocatalyst, $LaMg_{1/3}Ta_{2/3}O_2N$, for one-step excitation water splitting,[5] and Figure 10.4a shows the evolution of

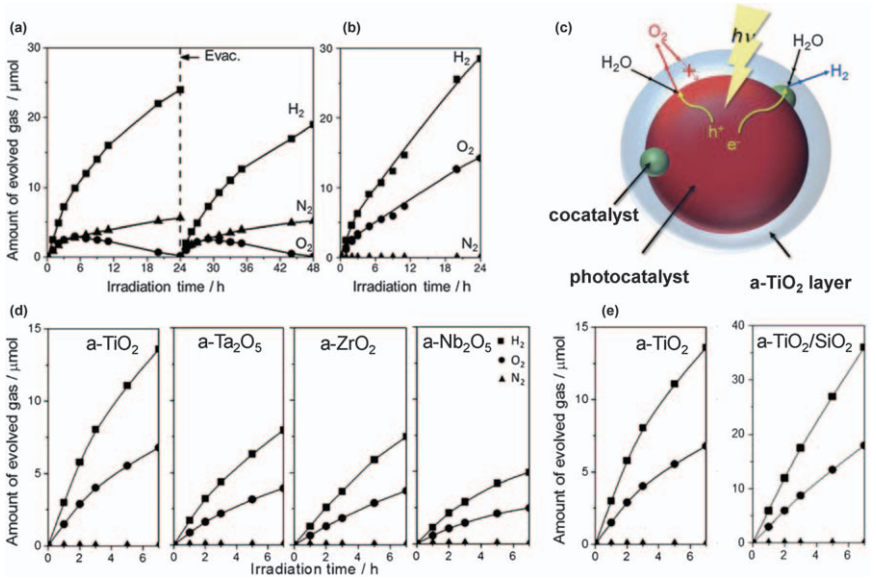


**Figure 10.4** Gas evolution during water splitting over (a) $Rh_{2-x}Cr_xO_3/LaMg_{1/3}Ta_{2/3}O_2N$ and (b) a-$TiO_2$/$Rh_{2-x}Cr_xO_3/LaMg_{1/3}Ta_{2/3}O_2N$. (c) Reaction mechanism for water splitting on an a-$TiO_2$-coated photocatalyst. (d) Gas evolution during water splitting on $Rh_{2-x}Cr_xO_3/LaMg_{1/3}Ta_{2/3}O_2N$ coated with various amorphous oxide layers. (e) Gas evolution during water splitting on $Rh_{2-x}Cr_xO_3/LaMg_{1/3}Ta_{2/3}O_2N$ coated with a-$TiO_2$ or a-$TiO_2$/$SiO_2$. Reaction conditions: catalyst, 0.2 g; reaction solution, pure water (250 mL); Xe lamp (300 W); side irradiation-type reaction vessel made of Pyrex.
(a–c) Reproduced from ref. 5 with permission from John Wiley & Sons, Copyright © 2015 WILEY-VCH Verlag GmbH & Co. KGaA, Weinheim.
(d, e) Reproduced from ref. 49 with permission from John Wiley & Sons, Copyright © 2016 WILEY-VCH Verlag GmbH & Co. KGaA, Weinheim.

various gases obtained from $Rh_{2-x}Cr_xO_3/LaMg_{1/3}Ta_{2/3}O_2N$ during water splitting. The continuous evolution of $N_2$ suggests that the $LaMg_{1/3}Ta_{2/3}O_2N$ was prone to self-oxidation by photogenerated holes. In addition, the amount of $O_2$ evolved increased over the first 5 h and then gradually decreased, suggesting that $O_2$ was consumed by back reactions. As discussed in the previous section, $Rh_{2-x}Cr_xO_3$ acts as a co-catalyst only for $H^+$ reduction to evolve $H_2$, and will not promote $O_2$ reduction or $H_2O$ formation. Hence the consumption of $O_2$ during photocatalytic water splitting as seen in Figure 10.4a indicates that $O_2$ reduction proceeded on the surface of the $LaMg_{1/3}Ta_{2/3}O_2N$. The surfaces of other photocatalysts may also induce $O_2$ reduction, considering that these materials are used to degrade hazardous compounds by photocatalysis.[50] One study showed that applying a $Cr_2O_3$ layer to $Rh_{2-x}Cr_xO_3/LaMg_{1/3}Ta_{2/3}O_2N$ was not effective because this layer was selectively deposited solely on the $Rh_{2-x}Cr_xO_3$ to provide reduction sites, rather than on the surface of the $LaMg_{1/3}Ta_{2/3}O_2N$. To address this issue,

a conformal coating of amorphous $TiO_2$ (a-$TiO_2$) was applied to the $Rh_{2-x}Cr_xO_3/LaMg_{1/3}Ta_{2/3}O_2N$ by photodeposition using a water-soluble Ti peroxide complex as the precursor. The oxygen in this complex had an oxidation number of −1, so could be either reduced to $H_2O$ or oxidized to $O_2$, while the $Ti^{4+}$ was hydrolyzed to amorphous $TiO_2$ *via* reactions (10.2) and (10.3) (where $h$ = hole).

$$Ti(O_2)_2 + 4e^- + (2+n)H_2O \rightarrow TiO_2 \cdot nH_2O + 4OH^- \quad (10.2)$$

$$Ti(O_2)_2 + 4h^+ + (2+n)H_2O \rightarrow TiO_2 \cdot nH_2O + 4H^+ + 2O_2\uparrow \quad (10.3)$$

Because of these special reaction characteristics, the irradiation of a photocatalyst in an aqueous solution containing the Ti peroxide complex generated an amorphous oxyhydroxide coating over the entire photocatalyst surface. After coating with this a-$TiO_2$ layer, $Rh_{2-x}Cr_xO_3/LaMg_{1/3}Ta_{2/3}O_2N$ steadily evolved stoichiometric amounts of $H_2$ and $O_2$ and overall water splitting was achieved, as shown in Figure 10.4b.

Takata *et al.* investigated the working mechanism of the a-$TiO_2$ layer.[51] Their research demonstrated that the layer itself did not function as an electron–hole transport layer as in a photoelectrode[52–55] or a photocatalyst.[56,57] Instead, the oxide served as a molecular sieve that was permeable to specific ions and molecules, similarly to a $Cr_2O_3$ layer. The working mechanism for a-$TiO_2$/(co-catalyst/photocatalyst) having a core–shell structure is illustrated in Figure 10.4c. In this process, the a-$TiO_2$ layer is generated by hydrolysis, such that the layer is hydrated in water and has a flexible structure, and the $H_2O$ molecules and $H^+$ ions in the hydrated a-$TiO_2$ layer can serve as reactants during water splitting. $H_2$ and $O_2$ molecules generated on the co-catalyst/photocatalyst are transported across the flexible a-$TiO_2$ layer driven by a pressure gradient. In contrast, the transport of $H_2$ and $O_2$ in the reverse direction is not possible because of the higher pressure beneath the oxide layer. In this manner, the a-$TiO_2$ layer prevents both $O_2$ reduction and water formation from $H_2$ and $O_2$. Although an accumulation of $H_2$ at the co-catalyst/photocatalyst interface will increase the overpotential for $H_2$ evolution and thus decrease the water splitting activity to some extent, this will not lead to $H_2$ oxidation on the co-catalyst because the co-catalyst serves as a reduction site. The high polarity and hydrophilicity of a-$TiO_2$ also improves the reaction selectivity because the transfer of less polar (that is, less hydrophilic) molecules such as $O_2$ from the reaction solution to the co-catalyst/photocatalyst surface is suppressed.[51] Oxyhydroxides of other group IV and V transition metals, such as Zr, Ta, and Nb,[51] can also serve as permselective amorphous layers similarly to a-$TiO_2$, although the resultant photocatalytic activities vary (as can be seen from Figure 10.4d).

### 10.2.4 Other Oxide Layers

$Cr_2O_3$ layers have been widely applied in various photocatalytic systems, but continue to have challenges related to durability.[39] Specifically, $Cr_2O_3$ is

gradually oxidized by photoexcited holes to $Cr^{6+}$ ions that subsequently dissolve. This problem can be mitigated by co-loading oxygen evolution co-catalysts to facilitate the extraction of photoexcited holes.[58,59] Moreover, $Cr_2O_3$ can be oxidized by $O_2$ and dissolve in strongly acidic or mildly basic solutions under dark conditions.[39] These effects lead to concerns regarding the durability of photocatalytic systems and also long-term effects on human health, due to the toxicity of $Cr^{6+}$ species. For these reasons, permselective layers made of other oxides, including $La_2O_3$, $MoO_x$, and $SiO_2$, have been developed, all of which function in a similar manner to $Cr_2O_3$, that is, by suppressing the back reactions while not impeding the $H_2$ evolution reaction.

### 10.2.4.1 Lanthanoid Oxides

Yoshida *et al.* applied an $La_2O_3$ modifier layer to $Rh/(Ga_{1-x}Zn_x)(N_{1-x}O_x)$ for overall water splitting under visible light irradiation.[60] This $La_2O_3$ layer was prepared using a wet chemical method based on reaction (10.4). In this process, $La^{3+}$ ions are hydrolyzed in an alkaline solution containing $NaBH_4$ to generate non-rigid structures in the aqueous medium, including hydrates, hydroxides and various oxides.

$$2La^{3+} + 6OH^- + (n-3)H_2O \xrightarrow{NaBH_4} La_2O_3 \cdot nH_2O \tag{10.4}$$

As a result of these structures, the layer exhibits selectivity permeability of various ions and molecules, similarly to a $Cr_2O_3$ layer. This preparation method is applicable to most photocatalysts regardless of their reactivity because it does not involve a photodeposition process. However, these $La_2O_3$ layers are unstable in acidic aqueous solutions because this compound is a weakly alkaline oxide. Some other lanthanoid oxide layers (based on Pr, Sm, Gd, or Dy) also function similarly, but Ce and Eu oxide layers are not applicable, probably because they are unstable under the reaction conditions.

### 10.2.4.2 Molybdenum Oxide

Although $H_2$ evolution is more favored in acidic media than in nearly neutral or basic media, $Cr_2O_3$ and $La_2O_3$ layers are not stable in acidic environments. Therefore, with the aim of improving $H_2$ evolution kinetics, $MoO_x$ was developed as a permselective layer that tolerates acidic media.[61] An $MoO_x$ layer can be deposited from an acidic solution containing $H_2MoO_4$ and $KClO_4$ with pH values from 1.1 to 4.9, on the basis of reaction (10.5):

$$H_2MoO_4 + (2x-6)e^- + (6-2x)H^+ + (n-4+x)H_2O \xrightarrow{ClO_4^-} MoO_x \cdot nH_2O \tag{10.5}$$

$MoO_x/Pt/SrTiO_3$ has been shown to split water in a stable manner under illumination whereas $Pt/SrTiO_3$ does not, because of the progression of

back reactions in the case of the latter. Furthermore, $MoO_x$/Pt/$SrTiO_3$ has been found to remain active in acidic media for at least several hours. *Operando* X-ray absorption spectroscopy data have confirmed that the $MoO_x$ layers in such previous work were composed of polyanionic trimetric molybdenum(IV) units in an amorphous Mo-based hydrated oxyhydroxide having a microporous network structure filled with water. During water splitting, $H_2$ evolution occurs on the metal/photocatalyst surface, such that a substantial amount of $H_2$ accumulates at the $MoO_x$/metal interface, representing a supersaturated condition. As a result, a large chemical potential gradient is generated and $H_2$ permeates through the amorphous microporous $MoO_x$ layer. Conversely, the concentrations of gaseous $H_2$ and $O_2$ are low in the bulk of the solution, so these species tend not to reach the surface of the metal, such that back reactions are suppressed.

### *10.2.4.3 Silicon Dioxide*

$SiO_2$ was developed as an environmentally friendly, low-cost and chemically stable permselective layer for photocatalytic water splitting.[62] An $SiO_2$ layer can be photodeposited on Pt serving as a $H_2$ evolution co-catalyst on $SrTiO_3$, using tetraethyl orthosilicate (TEOS) dissolved in an aqueous ethanol solution containing tetramethylammonium (TMA) and $NaNO_3$. During this photodeposition process, photoexcited electrons reduce $NO_3^-$ and generate $NO_2^-$ and $OH^-$ on the Pt co-catalyst, after which the $OH^-$ ions hydrolyze the TEOS to produce $SiO_2$ as in reaction (10.6):

$$Si(OCH_3)_4 + 2NO_3^- + 4e^- + nH_2O \xrightarrow{TMA^+} SiO_2 \cdot nH_2O + 2NO_2^- + 4(OCH_3)^- \quad (10.6)$$

The positively charged TMA ions serve as structure-directing agents to coordinate the $SiO_2$ to the negatively charged Pt, and also help to form porous structures in the $SiO_2$ layer. The resulting $SiO_2$ layer is ~7 nm thick, and is therefore thicker than a photodeposited $Cr_2O_3$ layer (which is on the order of 2 nm). This layer has been found to lower ferricyanide oxidation by 95%, oxygen reduction by 86%, and hydrogen oxidation by 43%. These reactions are also suppressed more effectively as the size of the reactant is increased, suggesting that the $SiO_2$ layer is permselective because it acts as a molecular sieve.

## 10.3 Improved Photocatalyst Hydrophilicity

$H_2$ evolution on a co-catalyst is initiated with a Volmer reaction followed by either a Heyrovsky or Tafel reaction. In the Volmer and Heyrovsky steps, hydronium ions (in an acidic medium) or water molecules (in a basic medium) must be adsorbed on the active sites so that the subsequent elementary reactions can occur.[63] $O_2$ evolution on a co-catalyst or at native

reaction sites on a photocatalyst is initiated by the transformation of water molecules in an acidic solution or hydroxide ions in a basic solution to surface-bound hydroxyl groups with the accumulation of holes.[64,65] Therefore, a hydrophilic surface capable of readily adsorbing hydronium ions, hydroxide ions, and water molecules is preferable for photocatalytic water splitting. The degree of surface hydrophilicity or hydrophobicity also affects the deposition of co-catalysts. As an example, it has been reported that

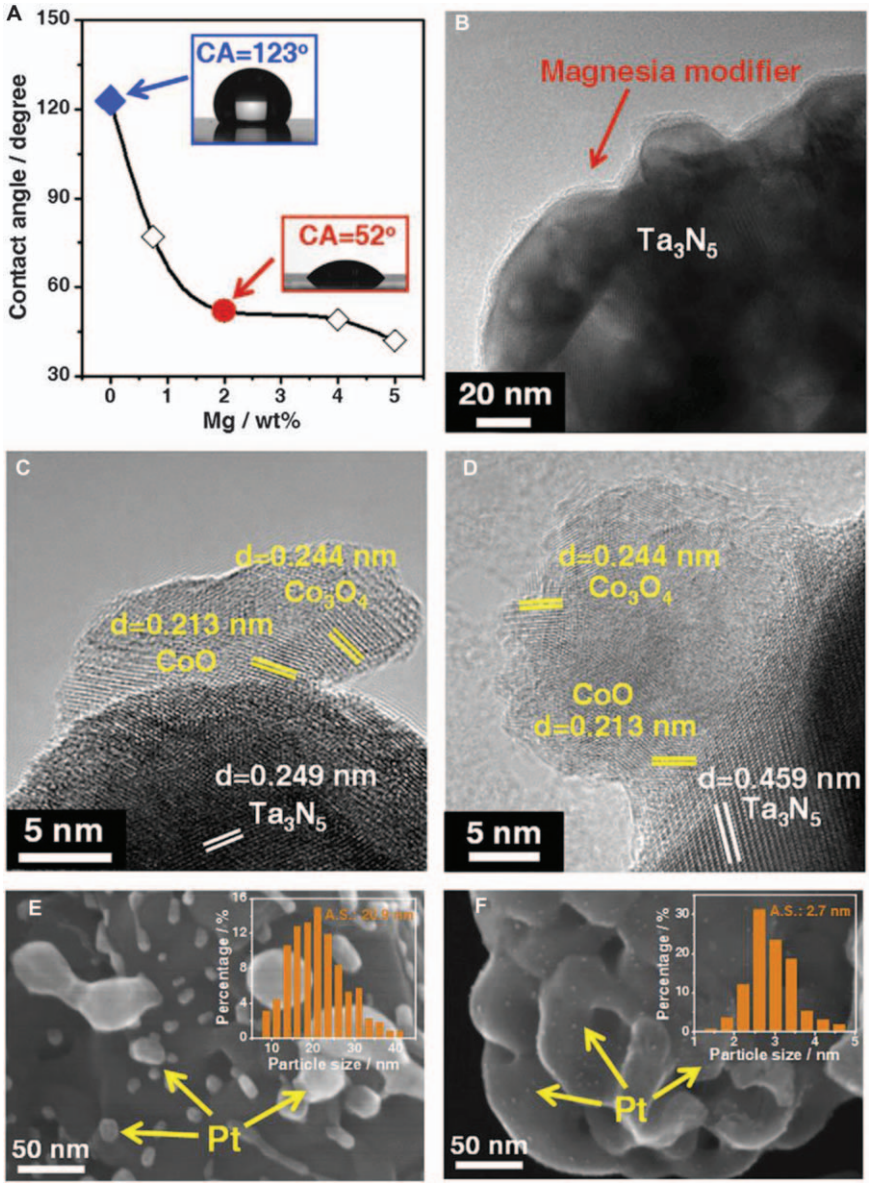

hydrophobic surfaces tend to lead to aggregated and poorly adhered co-catalysts.[66] Most oxides inherently have hydrophilic surfaces because these surfaces are easily hydrogenated in aqueous solution and thus are covered with hydroxyl groups. In contrast, (oxy)nitrides (which exhibit strong visible light absorption) are generally less hydrophilic and, therefore, improving the surface hydrophilicity of such materials could be vital to improving photocatalytic water splitting activity. One viable approach to enhancing surface hydrophilicity is to coat the photocatalyst with a layer of a hydrophilic oxide such as MgO or $SiO_2$.

### 10.3.1 Hydrophilic MgO Nanolayers on $Ta_3N_5$ to Improve $H_2$ and $O_2$ Evolution

As shown in Figure 10.5A, $Ta_3N_5$ gives a water contact angle of 123°, indicating a hydrophobic surface. Chen *et al.* obtained hydrophilic $Ta_3N_5$ by applying an MgO nanolayer to $Ta_3N_5$ particles based on a process in which $Ta_2O_5$ particles impregnated with $Mg^{2+}$ ions were subjected to thermal nitridation.[9,67] Figure 10.5A demonstrates that the resulting MgO-coated $Ta_3N_5$ showed a contact angle of 52°, indicating a more hydrophilic surface. The MgO layer in this case was 2–5 nm thick (Figure 10.5B) and was applied as a conformal coating on the $Ta_3N_5$. It was subsequently hydrolyzed to $Mg(OH)_2$ having numerous surface hydroxyl groups in water. Consequently, this layer was unable to block the transport of $H^+$ and $OH^-$ ions during the water splitting reaction. This hydrophilic layer also produced an intimate interface between the co-catalysts and photocatalyst such that the co-catalyst particles were dispersed more evenly. The morphologies of co-catalysts (Pt as an $H_2$ evolution co-catalyst and $CoO_x$ as an $O_2$ evolution co-catalyst) deposited on pristine $Ta_3N_5$ and MgO-modified $Ta_3N_5$ are presented in Figure 10.5C–10.5F. The $CoO_x$ particles deposited on the MgO-modified $Ta_3N_5$ evidently had a more regular morphology and greater contact area with the $Ta_3N_5$ than those loaded on the pristine $Ta_3N_5$ (Figure 10.5C and 10.5D). In addition, the average Pt particle size decreased from 20.9 to

**Figure 10.5** Effects of MgO nanolayer modification on the hydrophilicity–hydrophobicity of $Ta_3N_5$ and the dispersion of loaded co-catalysts. (A) Contact angle values of MgO-modified $Ta_3N_5$ samples as a function of magnesium content. (B) Transmission electron microscopy (TEM) image of an MgO-modified $Ta_3N_5$ sample. High-resolution TEM images of $CoO_x$ on (C) pristine $Ta_3N_5$ and (D) MgO-modified $Ta_3N_5$. Field-emission scanning electron microscopy (SEM) images and histograms of particle size distributions (insets) for typical samples of (E) Pt/$Ta_3N_5$ and (F) Pt/MgO-modified $Ta_3N_5$.
(A–D) Reproduced from ref. 9 with permission from John Wiley & Sons, Copyright © 2015 WILEY-VCH Verlag GmbH & Co. KGaA, Weinheim. (E, F) Reproduced from ref. 67 with permission from Elsevier, Copyright 2016.

2.7 nm when the $Ta_3N_5$ was coated with an MgO layer. Field-emission scanning electron microscopy images showed small, well-dispersed Pt nanoparticles on the MgO-modified $Ta_3N_5$, whereas larger Pt particles were found on the pristine $Ta_3N_5$ (Figure 10.5E and 10.5F). The MgO layer at the interface between the co-catalyst and photocatalyst was only ~2 nm thick, and photogenerated charge carriers were able to migrate between the co-catalyst and the photocatalyst by tunneling through the MgO layer. The MgO layer also functioned as a passivation layer to suppress the formation of surface defects on the $Ta_3N_5$ and so restrict surface charge recombination. This effect was determined based on analyses using time-resolved infrared spectroscopy, which showed that the lifetimes of photogenerated charge carriers were longer in the MgO-modified $Ta_3N_5$ than in the pristine $Ta_3N_5$.

Because of the advantages provided by the MgO coating, $CoO_x$/MgO-modified $Ta_3N_5$ showed 23 times higher photocatalytic $O_2$ evolution activity than $CoO_x/Ta_3N_5$ and exhibited an apparent quantum efficiency of 11.3% in response to irradiation at 500–600 nm. In addition, Pt/MgO-modified $Ta_3N_5$ was found to have 17 times higher photocatalytic $H_2$ evolution activity than $Pt/Ta_3N_5$. To date, MgO layers have only been applied to $Ta_3N_5$, but this technique could potentially be extended to (oxy)nitrides and (oxy)sulfides.

### 10.3.2 Porous Hydrophilic $SiO_2$ Layers on $LaMg_{1/3}Ta_{2/3}O_2N$ for Improving Water Splitting Activity

As discussed in Section 10.2.3, an a-$TiO_2$ layer can suppress backward reactions on $LaMg_{1/3}Ta_{2/3}O_2N$. However, in previous work, as the water splitting reaction progressed, the photocatalytic water splitting activity of this material was observed to decline gradually (Figure 10.4e). This result suggested that the effects of the a-$TiO_2$ layer slowly decreased as $O_2$ accumulated in the reactor, presumably because the $TiO_2$ layer was imperfect. Pan *et al.* attempted to create a more effective coating by applying a layer of $SiO_2$ based on the hydrolysis of TEOS prior to coating $Rh_{2-x}Cr_xO_3/LaMg_{1/3}Ta_{2/3}O_2N$ with a-$TiO_2$.[5,49] The resulting a-$TiO_2$/$SiO_2$/$Rh_{2-x}Cr_xO_3/LaMg_{1/3}Ta_{2/3}O_2N$ showed almost the same photocatalytic water splitting activity as a-$TiO_2$/$Rh_{2-x}Cr_xO_3/LaMg_{1/3}Ta_{2/3}O_2N$ during the first hour of use (Figure 10.4e), but also exhibited improved retention of activity over a prolonged reaction period. These data imply that the $SiO_2$ enhanced the uniformity and hydrophilicity of the a-$TiO_2$ layer to prevent less polar $O_2$ molecules from approaching the photocatalyst surface from the reaction solution.

## 10.4 Passivation of the Oxynitride Surface by $ZrO_2$

Similarly to other (oxy)nitrides, TaON is synthesized *via* the thermal nitridation of its oxide precursor, $Ta_2O_5$.[14] During the nitridation process, reducing species such as $NH_2$·will not only replace oxygen atoms in the oxide with nitrogen but also reduce $Ta^{5+}$ ions to $Ta^{4+/3+}$. This effect is especially

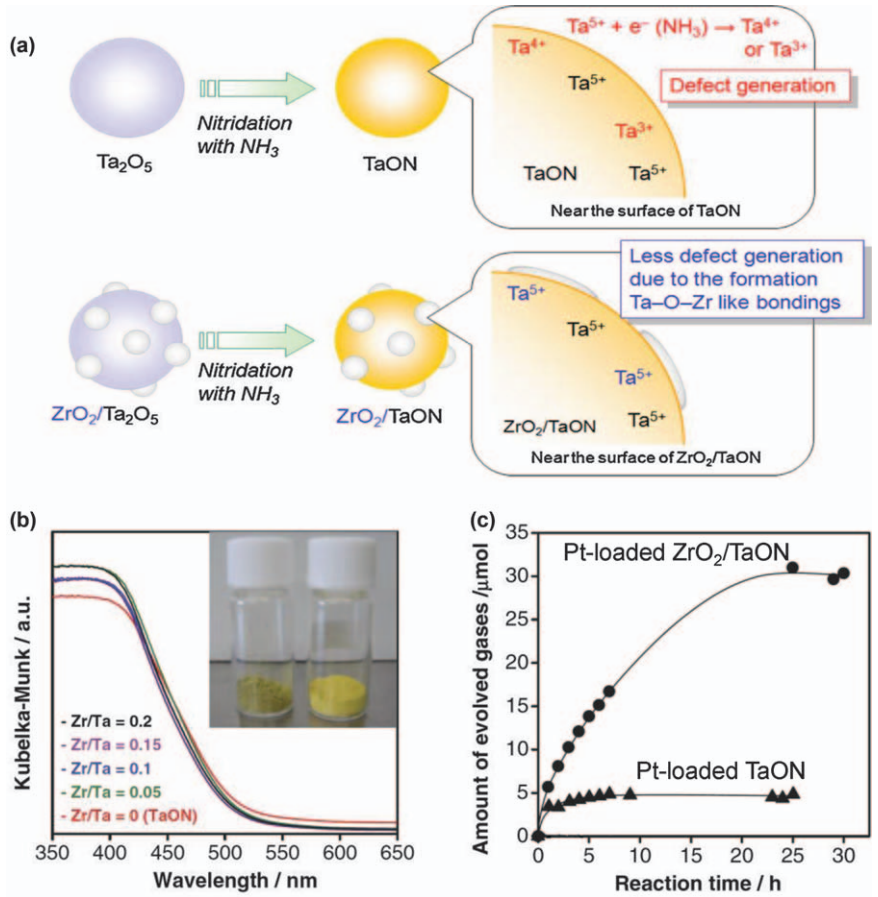


**Figure 10.6** (a) Suppression of the formation of reduced tantalum species (representing defect sites) near the TaON surface. (b) UV–visible diffuse reflectance spectra obtained from TaON with and without $ZrO_2$ modification. (c) Time courses of $H_2$ evolution from aqueous NaI solutions using Pt-loaded TaON and Pt-loaded $ZrO_2$/TaON.
Reproduced from ref. 6 with permission from The Chemical Society of Japan, Copyright 2008.

prominent on the TaON surface, as shown in Figure 10.6a. The UV–visible diffuse reflectance spectrum of TaON provided in Figure 10.6b shows a light absorption background level at wavelengths longer than 500 nm. This result indicates that the reduced tantalum species induced the formation of surface defects that functioned as recombination centers for photogenerated charge carriers. The reduction of metal ions during nitridation and the generation of defects have also been observed in Ti-based oxynitrides such as $LaTiO_2N$.[4] In an attempt to reduce the defect density in TaON, $ZrO_2$ was loaded on a $Ta_2O_5$ precursor by an impregnation method.[6] $ZrO_2$ is resistive to nitridation or reduction by $NH_2$ species, and $Ta^{5+}$ ions at the interface

were expected to bond strongly with the $ZrO_2$. In this way, the $ZrO_2$ protected surface $Ta^{5+}$ ions from being reduced and thus decreased the defect density induced in the TaON during nitridation (Figure 10.6a). This effect is reflected in the weaker background absorption of the $ZrO_2$/TaON relative to that of TaON in the spectra presented in Figure 10.6b. Moreover, the pristine TaON powder was yellowish green in color, whereas the $ZrO_2$/TaON was brilliant yellow (Figure 10.6b, inset). Under optimal conditions, the photocatalytic $H_2$ evolution activity of Pt-loaded $ZrO_2$/TaON using $I^-$ ions as electron donors was only 1.6 times higher than that of Pt-loaded TaON (Figure 10.6c). However, a Z-scheme system composed of Pt-loaded $ZrO_2$/TaON for $H_2$ evolution, $PtO_x$-loaded $WO_3$ for $O_2$ evolution, and $IO_3^-/I^-$ as a shuttle redox mediator exhibited six times higher photocatalytic water splitting activity than a TaON analog.[68] Similar positive effects of $ZrO_2$ were also confirmed when this oxide was applied to $LaMg_{1/3}Ta_{2/3}O_2N$ intended to promote $H_2$ evolution in combination with Mo-doped $BiVO_4$ in a photocatalyst sheet.[69] The ability of $ZrO_2$ to reduce surface defects is evidently similar to that of MgO, as discussed in Section 10.3.1. Considering that both $ZrO_2$ and MgO are oxide ceramics, other oxide ceramics, including $Al_2O_3$ and $CeO_2$, could also possibly have similar effects.[70]

## 10.5 Control Over the Redox Selectivity of Photocatalysts in Z-scheme Water Splitting

### 10.5.1 Rutile-type $TiO_2$ and MgO in Z-scheme Systems Containing $IO_3^-/I^-$

Inspired by natural photosynthesis in plants, Bard first proposed the Z-scheme photocatalytic water splitting system.[71] In this system, two different photocatalysts are used for $H_2$ and $O_2$ evolution, and are connected by a shuttle redox mediator (Figure 10.1b). Since Bard's initial work, various photocatalysts have been developed for the $H_2$ or $O_2$ evolution half reactions.[72–76] Even with such progress, it remains challenging to construct a Z-scheme system using the majority of these photocatalysts to promote simultaneous and stoichiometric $H_2$ and $O_2$ evolution, because the back reactions (indicated by dotted lines in Figure 10.1b) overwhelm the desired forward reactions (indicated by the solid lines). Based on careful tuning of the selectivity for the forward reaction, in 2001 Abe *et al.* developed a Z-scheme system for simultaneous and stoichiometric $H_2$ and $O_2$ evolution using Pt-loaded anatase $TiO_2$ for $H_2$ evolution, bare rutile $TiO_2$ for $O_2$ evolution and $IO_3^-/I^-$ as a shuttle redox mediator.[77] In this system, only $I^-$ was added at the beginning of the reaction, rather than a mixture of $I^-$ and $IO_3^-$, so that the steady-state concentration of $IO_3^-$ during water splitting was low. This modification minimized the back reaction (*i.e.* the reduction of $IO_3^-$) at the $H_2$ evolution side of the system. At the same time, the back reaction at the $O_2$ evolution side (*i.e.* the oxidation of $I^-$) was suppressed by adding

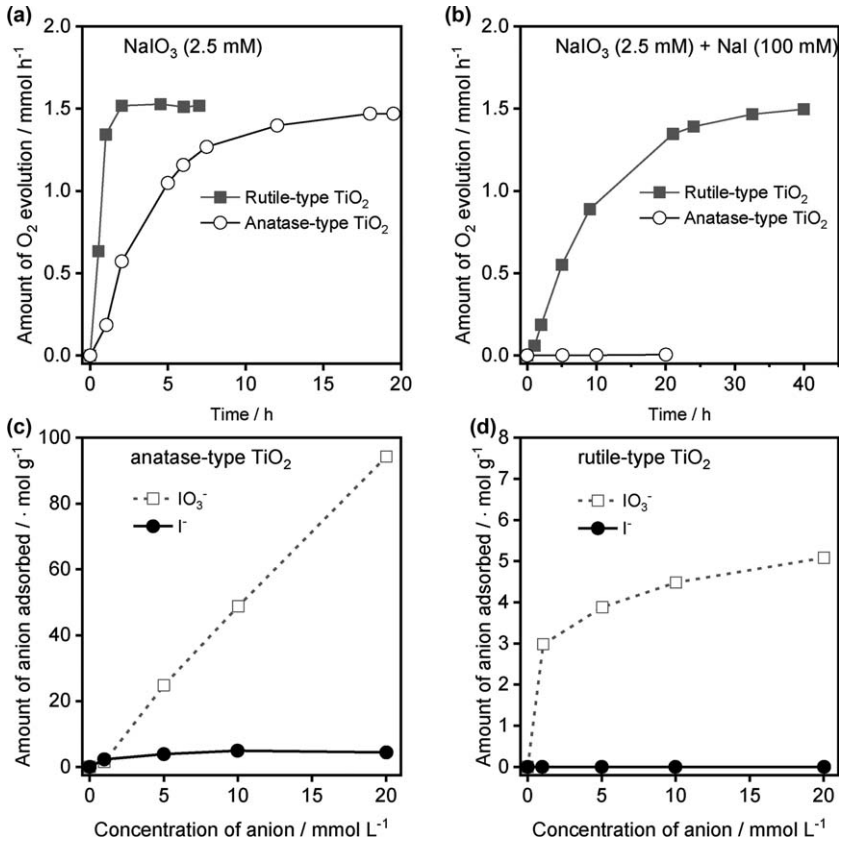


**Figure 10.7** Time course of photocatalytic $O_2$ evolution over anatase- and rutile-type $TiO_2$ photocatalysts suspended in aqueous solutions (400 mL, pH adjusted to 11 with NaOH) containing (a) 1 mmol of $NaIO_3$ and (b) 1 mmol of $NaIO_3$ with 40 mmol of NaI. The reactions were carried out using an internal irradiation-type reactor, in which a light source (400 W high-pressure Hg lamp, Riko Kagaku) was covered with a Pyrex glass cooling water jacket (cutoff $\lambda < 300$ nm) to keep the reactor temperature constant at 293 K. Adsorption properties of iodate ($IO_3^-$) and iodide ($I^-$) anions on (c) anatase-type and (d) rutile-type $TiO_2$ determined at 293 K.
(a, b) Reproduced from ref. 77 with permission from Elsevier, Copyright 2001. (c, d) Reproduced from ref. 88 with permission from Elsevier, Copyright 2010.

rutile-type $TiO_2$ that selectively promoted $O_2$ evolution even in the presence of $I^-$, which is more readily oxidized than water. As shown in Figure 10.7a,b, both anatase- and rutile-type $TiO_2$ were active for $O_2$ evolution when using $IO_3^-$ as an electron acceptor, but only the latter maintained its activity when $I^-$ was intentionally added. The subsequent experiments summarized in Figure 10.7c,d revealed that rutile-type $TiO_2$ adsorbed $IO_3^-$ ions but not $I^-$ ions, whereas anatase-type $TiO_2$ adsorbed both $IO_3^-$ and $I^-$. This unique adsorption selectivity contributed to the reaction selectivity during Z-scheme

water splitting. Similar adsorption selectivity was also exhibited by $WO_3$.[78] As a result, rutile-type $TiO_2$ and $WO_3$ have both been widely used as $O_2$ evolution photocatalysts to construct Z-scheme systems.[68,79–83]

It would be beneficial to develop a Z-scheme system incorporating (oxy)-nitrides, which have advantages over metal oxides in terms of light absorption. To avoid back reactions on $Ta_3N_5$ caused by redox mediators, Ma *et al.* developed a redox mediator-free Z-scheme system using $Ta_3N_5$ for $O_2$ evolution, in which charge transfer between particles was based on physical contact.[84] This type of interparticle electron transfer was originally discovered by Sasaki *et al.* during work with a Z-scheme system based on oxide photocatalysts.[85] However, the applicability of Z-scheme systems based on interparticle electron transfer is limited because the two photocatalysts must carry opposite charges so as to form composites based on electrostatic interactions and the significant contact resistance between photocatalyst particles. For these reasons, it would be helpful to devise means of improving the redox selectivity of photocatalysts.

Tabata *et al.* applied rutile $TiO_2$ particles as a modifier to tune the redox selectivity of $Ta_3N_5$ and used the resulting material to catalyze $O_2$ evolution in a Z-scheme system with an $IO_3^-/I^-$ shuttle redox mediator.[86] Figure 10.8a compares the photocatalytic $O_2$ evolution activities of $Ta_3N_5$ with various modifications in aqueous $NaIO_3$ solutions with or without the addition of NaI. The activity of Ir-loaded $Ta_3N_5$ modified with rutile $TiO_2$ was found to be 10 times higher than that of Ir-loaded $Ta_3N_5$. This enhancement was attributed primarily to the reduced adsorption of $I^-$ anions by the rutile-type $TiO_2$ nanoparticles deposited on the $Ta_3N_5$, as shown in Figure 10.8b. In Section 10.3.1, we introduced the concept of a hydrophilic MgO layer that improves the deposition of co-catalysts on photocatalysts. Recently, it has been confirmed that such layers can also suppress the adsorption of $I^-$ ions and therefore the oxidation of these ions, similarly to the effect of rutile-type $TiO_2$ (Figure 10.8c).[87] Therefore, Ir-loaded MgO-modified $Ta_3N_5$ was combined with $Cr_2O_3$/Pt-loaded $ZrO_2$-modified TaON to construct a Z-scheme water splitting system with an $IO_3^-/I^-$ shuttle redox mediator (Figure 10.8d).

## 10.5.2 $CeO_x$ on $O_2$ Evolution Co-catalysts

In Section 10.5.1, we introduced the concept of surface modification by rutile-type $TiO_2$ and MgO, as a means of suppressing $I^-$ oxidation and enhancing $O_2$ evolution on $Ta_3N_5$. Although this surface modification is effective, the loaded oxide nanoparticles will also tend to block reaction sites on the photocatalyst. Moreover, the modification process itself (*i.e.* the preparation of the oxide nanoparticles by a wet chemical method) may damage the photocatalyst. Consequently, these surface modifications may not necessarily upgrade the overall performance of a Z-scheme system. Therefore, it would be highly desirable to have a layer material that is universally applicable to all photocatalysts without damage and can be

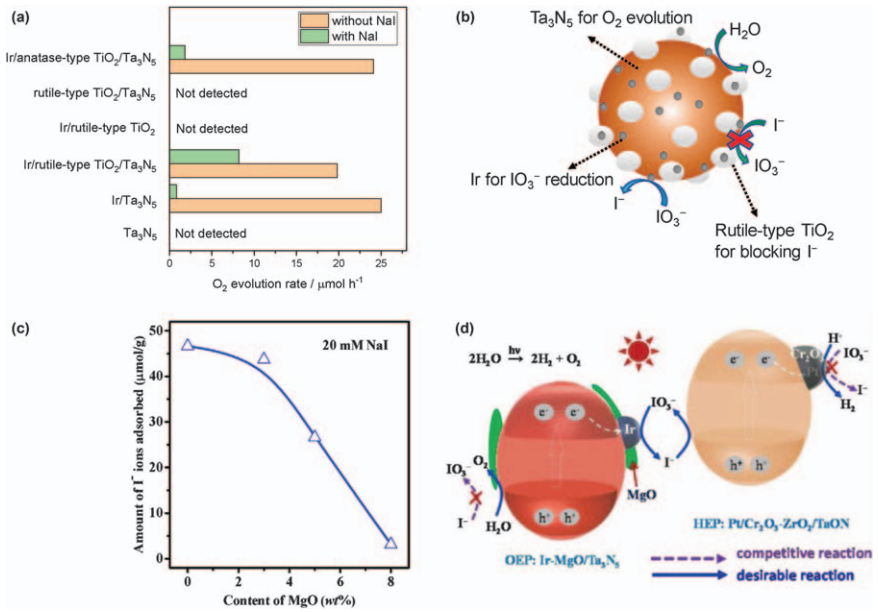


**Figure 10.8** (a) Initial $O_2$ evolution rates on $Ta_3N_5$ with various modifications in aqueous 4 mM $NaIO_3$ solution with and without 1 mM NaI under illumination. (b) Schematic illustration of $O_2$ evolution on Ir-loaded rutile-type $TiO_2$-modified $Ta_3N_5$. (c) Adsorption properties of $I^-$ ions on MgO-modified $Ta_3N_5$. (d) Schematic illustration of Z-scheme water splitting using Ir-loaded MgO-modified $Ta_3N_5$ and $Cr_2O_3$/Pt-loaded $ZrO_2$-modified TaON with an $IO_3^-/I^-$ shuttle redox mediator.
(a, b) Reproduced from ref. 86 with permission from American Chemical Society, Copyright 2010. (c, d) Reproduced from ref. 87 with permission from Elsevier, Copyright 2018.

selectively deposited solely on $O_2$ evolution sites, similarly to the deposition of $Cr_2O_3$ on $H_2$ evolution sites as discussed in Section 10.2.2.

Recently, Obata and Takanabe reported a permselective $CeO_x$ layer having these specific properties.[89] As a demonstration, a $CeO_x$ layer was anodically deposited on $NiFeO_x$ electrodes in an electrolyte solution containing $Ce(NO_3)_3$ and $CH_3COONH_4$, based on reaction (10.7):

$$Ce^{3+} + (x+n)H_2O \xrightarrow{CH_3COONH_4} CeO_x \cdot nH_2O + 2xH^+ + (2x-3)e^- \qquad (10.7)$$

As shown in Figure 10.9a, the $CeO_x$ layer had a thickness of $100-200$ nm, and was much thicker than a typical $Cr_2O_3$ coating. Nevertheless, this thick layer did not affect the electrochemical $O_2$ evolution activity of the $NiFeO_x$ in alkaline media, as shown Figure 10.9b. The permselectivity of the $CeO_x$ layer was investigated by comparing the Faradaic efficiencies obtained during $O_2$ evolution in the presence of various reducing agents, including iodide, ferricyanide, methanol, ethanol, 2-propanol, lactate and malate (Figure 10.9c). The $CeO_x$ layer clearly improved the selectivity of the $NiFeO_x$

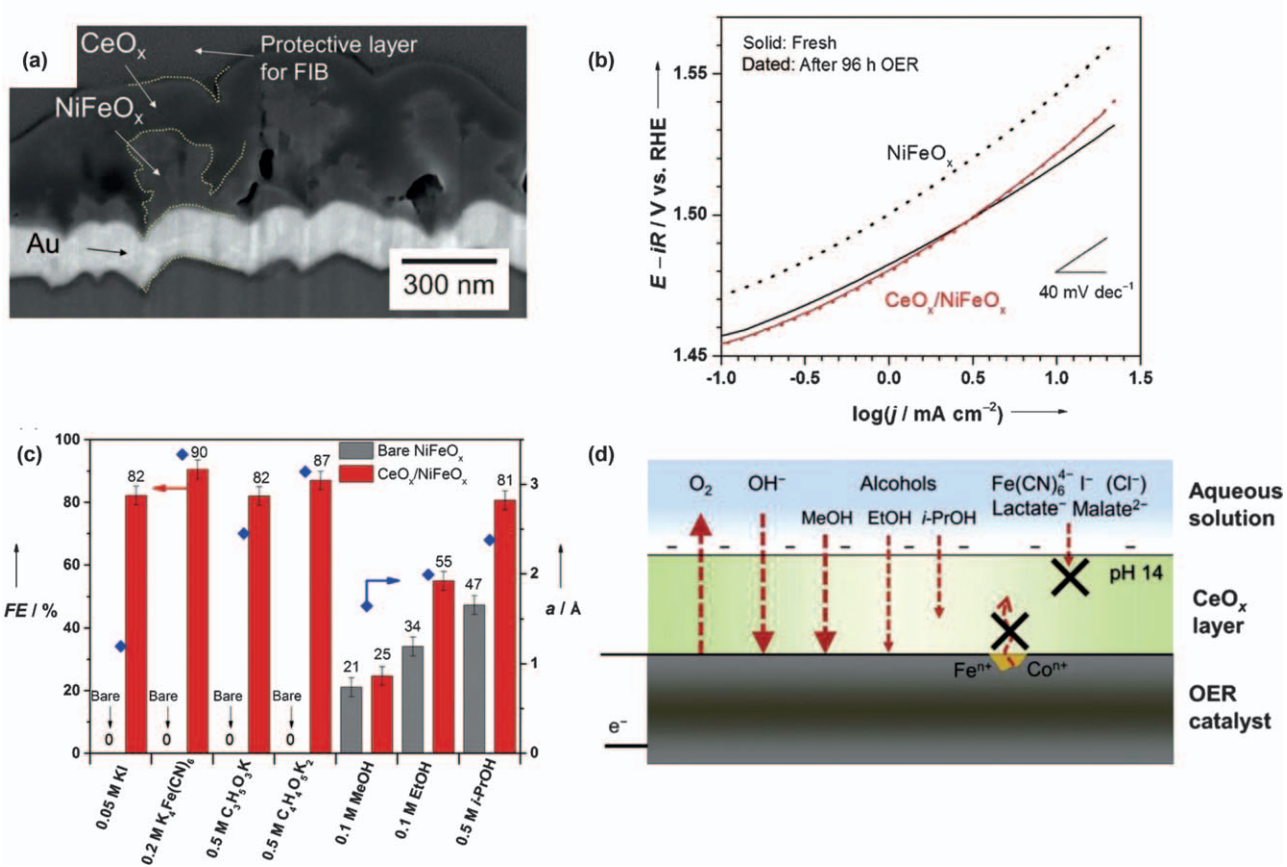


**Figure 10.9** (a) Cross-sectional SEM image of $CeO_x$-coated $NiFeO_x$. (b) Tafel plots for $NiFeO_x$ and $CeO_x$-coated $NiFeO_x$ electrodes. (c) Faradaic efficiencies of $O_2$ evolution during controlled-current electrolysis at 10 mA cm$^{-2}$ for $NiFeO_x$ and $CeO_x$-coated $NiFeO_x$ electrodes. (d) Schematic diagram of $CeO_x$ applied to an $O_2$ evolution co-catalyst to improve selectivity.
Reproduced from ref. 89 with permission from John Wiley & Sons, Copyright © 2018 WILEY-VCH Verlag GmbH & Co. KGaA, Weinheim.

by reducing reactions with redox anions as compared with neutral molecules. It is likely that the transport of anions through the $CeO_x$ layer was suppressed because this layer was negatively charged in the alkaline solution.[90] The $CeO_x$ layer as prepared by anodic deposition also had a hydrous disordered structure,[91] so the transport of $OH^-$ ions was still possible even though these ions are also negatively charged. In the case of neutral molecules, the effect of the $CeO_x$ layer was dependent on their Stokes radii. These effects suggest that the transport of the reducing agents was determined by both their size and their charge, as illustrated in Figure 10.9d.

## 10.6 Protection of Photocatalysts and Photoelectrodes by a $TiO_2$ Layer

The US Department of Energy has suggested that the levelized cost of $H_2$ production from water splitting should be between \$2 and \$4 $kg^{-1}$ $H_2$ to permit the large-scale application of $H_2$ that can compete with fossil fuel- and methane-derived $H_2$.[92,93] To reach this target, a solar-driven photocatalytic suspension reactor operating on the basis of water splitting would have to exhibit an STH efficiency in the range 5–10% and a lifetime of 7–10 years.[93] This technoeconomic analysis highlights the importance of the stability of these devices, which contrasts with observations that the activity of most photoelectrochemical and photocatalytic systems is only on the scale of hours or at most days. This rapid degradation occurs because semiconductors applied as photocatalysts or photoelectrodes can be corroded chemically and/or (photo)electrochemically. Coating with a protective layer is a common approach to avoiding corrosion, and metal oxides can act as protective layers because of their stability. Among the potential candidates, $TiO_2$ is the most widely used because of its excellent optical transmittance (band gap $> 3.0$ eV) and stability over a wide pH range. However, a photocatalyst will have both $H_2$ and $O_2$ evolution sites on the same surface. Therefore, if a protective layer applied to the photocatalyst blocks the approach of chemical species in the reaction solution, it must permit the transport of both electrons and holes in order to drive water splitting while also sustaining a state in which electrons and holes are separated to avoid recombination. Clearly, no intrinsic metal oxide can satisfy these requirements. Therefore, protective layers for photocatalysts must be permeable to both reagents and products while also stabilizing the photocatalyst. Moreover, the layer needs to be insulating to avoid forming a short-circuit between the electron and hole accumulation sites. Currently, only amorphous group IV and V transition metal oxide layers such as those made of a-$TiO_2$ (see Section 10.2.3) have been applied as protective layers for photocatalysts.[5,51] Metal oxide protective layers are also more applicable to photoelectrodes because they must conduct minority charge carriers to drive $H_2$ evolution (on a p-type semiconductor photocathode) or $O_2$ evolution

(on an n-type semiconductor photoanode). Note that the working principle of such photoelectrodes has been described in detail elsewhere.[94] The operating mechanism for $TiO_2$ as a protective layer is not identical for photocatalysts, photocathodes, and photoanodes, so each scenario is discussed separately below.

### 10.6.1 Photocatalysts

Previous work has shown that (oxy)nitrides and (oxy)sulfides are thermodynamically unstable during water oxidation.[95] As an example, $LaMg_{1/3}Ta_{2/3}O_2N$ undergoes self-oxidation by photogenerated holes, as evidenced by the evolution of $N_2$ during photocatalytic water splitting (Figure 10.4a).[5] However, this self-oxidation leading to the evolution of $N_2$ was effectively suppressed by applying an a-$TiO_2$ layer to the material (Figure 10.4b). Interestingly, a-$TiO_2$ is not conductive and, therefore, does not extract holes from $LaMg_{1/3}Ta_{2/3}O_2N$ to act as a hole storage material like $CoO_x$ or ferrihydrite.[4,51,96] It has been suggested that an a-$TiO_2$ layer on $LaMg_{1/3}Ta_{2/3}O_2N$ changes dangling nitrogen species on the surface to lattice nitrogen and thus stabilizes the catalyst,[49] although further investigation is required to elucidate the details of this mechanism. It is also believed that the a-$TiO_2$ layer maintains the photocatalytic activity by suppressing the detachment of co-catalysts.[59]

Since an a-$TiO_2$ layer is impermeable to shuttle redox mediators such as $I^-/IO_3^-$ (see Section 10.2.3) and does not conduct charge carriers, it is not helpful in Z-scheme systems in suspension form.[83] However, Z-schematic photocatalyst sheets, in which particulate photocatalysts are immobilized in a conductive layer, can benefit from the application of an a-$TiO_2$ layer because the charge transfer between the photocatalysts occurs *via* the underlying conductive layer.[97] As shown in Figure 10.10a, an $(Rh_{2-y}Cr_yO_3/LaMg_{1/3}Ta_{2/3}O_2N)$/Au/$BiVO_4$:Mo photocatalyst sheet was found to split water in conjunction with the evolution of $N_2$ because the $LaMg_{1/3}Ta_{2/3}O_2N$ was not stable during the reaction. Coating this material with an a-$TiO_2$ layer effectively protected the $LaMg_{1/3}Ta_{2/3}O_2N$ from decomposition while maintaining most of the photocatalytic water splitting activity.

### 10.6.2 Photocathodes

The bottom of the $TiO_2$ CB is located at approximately −0.1 V *vs.* RHE, which is more positive than that for most photocathodes. Moreover, $TiO_2$ is an n-type semiconductor and so may form a p–n junction with the photocathode. These two factors facilitate the transfer of electrons from the photocathode to the $TiO_2$. The top of the $TiO_2$ VB is located at ~3.0 V *vs.* RHE, so this oxide can also effectively block the migration of holes from the photocathode to the electrolyte. For these reasons, a $TiO_2$ layer is useful as a protective coating for a photocathode. Paracchino *et al.* used an atomically deposited $TiO_2$ layer having a thickness of only ~10 nm to protect a p-$Cu_2O$/n-Al:ZnO photocathode.[53] The deposition of this $TiO_2$ layer did not degrade

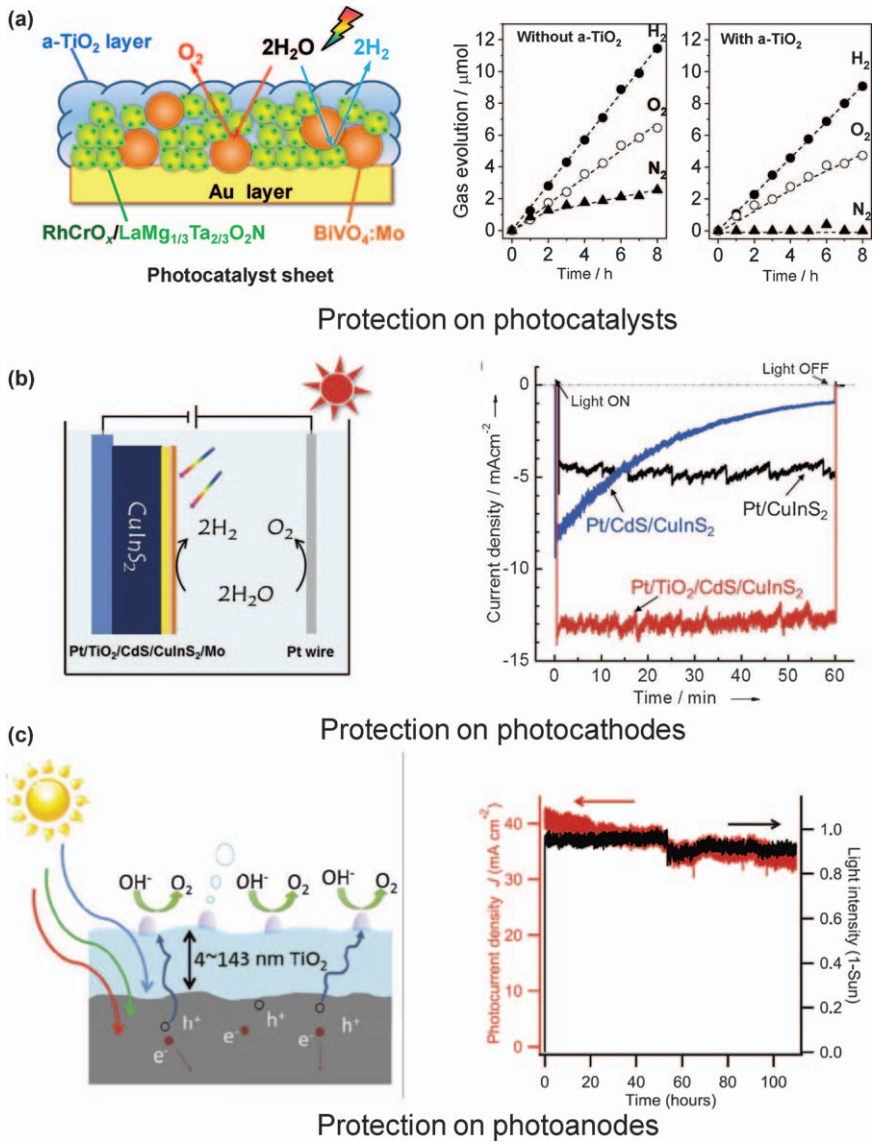


**Figure 10.10** Protective $TiO_2$ layers on (a) photocatalysts, (b) photocathodes, and (c) photoanodes. Left, working schematics; right, stability of photocatalytic water splitting, photocathodic $H_2$ evolution, and photoanodic $O_2$ evolution.

(a) Reproduced from ref. 69 with permission from American Chemical Society, Copyright 2016. (b) Reproduced from ref. 98 with permission from John Wiley & Sons, Copyright © 2014 WILEY-VCH Verlag GmbH & Co. KGaA, Weinheim. (c) Reproduced from ref. 55 with permission from The American Association for the Advancement of Science, Copyright 2014.

the photocathodic current or the photocurrent onset potential, and the photocathode was stable during $H_2$ evolution for ~1 h at pH 5, with an estimated Faradaic efficiency of close to 100%. Zhao *et al.* deposited a $TiO_2$ layer on a $CuInS_2$/CdS photocathode by reactive sputtering followed by annealing (Figure 10.10b).[98] This $TiO_2$ layer increased the photocurrent density from 8.4 to 13.0 mA cm$^{-2}$ at 0 V *vs.* RHE and the $TiO_2$-protected $CuInS_2$/CdS photocathode showed no measurable photocurrent decay over the span of 1 h. Similarly, $TiO_2$ protective layers have been applied to p-Si, a-Si, $n^+$p-Si and p-InP photocathodes.[99–102]

### 10.6.3 Photoanodes

The top of the $TiO_2$ VB (and also those of the majority of other metal oxide semiconductors) is deeper than those for most non-oxide photoanodes. Hence the holes from a photoanode cannot migrate to the electrolyte through the VB of $TiO_2$ and it is generally considered that the $TiO_2$ layer must therefore be thin enough to allow tunneling. Chen *et al.* reported an n-Si photoanode protected by an atomically deposited $TiO_2$ layer (~2 nm thick) that showed low electron tunneling resistance (<0.006 Ω cm$^2$).[52] As a result, the photocathode exhibited a suitable level of efficiency together with improved stability. However, the protection offered by such a thin layer was not perfect and the photocurrent was found to decrease gradually over a span of several hours. Hu *et al.* employed a much thicker atomically deposited $TiO_2$ layer (~100 nm) to protect Si, GaAs, GaP, and CdTe photoanodes for more than 100 h (Figure 10.10c).[55] The layer was too thick for hole tunneling but still allowed effective hole transport, and this unique ''leaky'' electronic behavior was attributed to the $Ti^{3+}$ defect band, which is centered 1.47 eV below the CB minimum.[103] In a subsequent study, the $TiO_2$ layer was confirmed to stabilize high aspect ratio Si microwires during photoanodic water oxidation for longer than 2200 h.[104]

## 10.7 Outlook

After decades of research effort focusing on photocatalytic water splitting, a photocatalyst providing a quantum efficiency of close to unity or with an absorption edge wavelength at ~640 nm has been developed.[33,36] The next stage of such research should concentrate on merging these two achievements by designing a photocatalyst having a wide absorption spectrum and high quantum efficiency that is suitable for large-scale applications. This will require the following improvements in metal oxide layers.

### 10.7.1 Suppression of Back Reactions on the Surface Under Ambient Pressure

Section 10.2.3 introduced the concept of an a-$TiO_2$ coating as a permselective layer suppressing back reactions on the surface of a photocatalyst such as

$LaMg_{1/3}Ta_{2/3}O_2N$. This type of layer is effective when a gas pressure gradient is generated that drives the one-way transport of $H_2$ and $O_2$ from the photocatalyst surface to the reaction solution across the oxide layer. Therefore, the permselectivity decreases significantly as the gas pressure is increased. Because a photocatalytic water splitting system has to operate at around ambient pressure to be practical, the use of a-$TiO_2$ layers will be insufficient and new permselective layers must be developed.

### 10.7.2 Facilitation of the Mass Transport of $H_2$ and $O_2$ as Products

Many efforts have been made to facilitate the mass transfer of reagents during photocatalytic water splitting, including applying hydrophilic metal oxide layers to photocatalysts, as discussed in Section 10.3. In contrast, the mass transfer of products (*i.e.* $H_2$ and $O_2$) has received less attention. If the migration of these gases is slow, bubbles will be formed that will cling to the photocatalyst. These bubbles can scatter light away from the photocatalyst, separate the photocatalyst from the electrolyte, and induce a concentration overpotential.[105] The formation of bubbles on photocatalyst surfaces is especially a concern in systems based on photocatalyst panels.[106] A hydrophilic surface tends to facilitate the desorption of bubbles, and a hydrophilic layer may improve the mass transfer of both reagents and products during water splitting. However, further studies are still required to elucidate the nucleation, growth, and adsorption processes for bubbles so that layers for the coating of photocatalysts can be properly tailored.

The metal oxide layers reviewed in this chapter were primarily developed based on the simplified photocatalytic water splitting models provided in Figure 10.1a,b. However, these models do not incorporate the energetics and kinetics at photocatalyst/co-catalyst/$H_2O$ interfaces, which are known to greatly modify charge separation and transfer, thus strongly affecting the overall efficiency.[2,107,108] Recently, a kinetic model has been developed to assist in elucidating such aspects of these systems.[107–109] Using this model, metal oxide layers having a significant impact on performance will be included in the design of future photocatalytic water splitting systems. These layers will have the following applications.

### 10.7.3 Suppression of Interfacial Charge Recombination Between a Photocatalyst and a Co-catalyst

The activity of a photocatalytic system varies significantly after co-catalysts have been incorporated, even when these materials have similar electrocatalytic properties during water splitting.[30,68,110] One important reason for this variation is that the co-catalyst may react with the photocatalyst, creating a chemically inhomogeneous photocatalyst/co-catalyst interface.[111] This local inhomogeneity in composition may introduce defects and in

turn accelerate Shockley–Read–Hall recombination. In addition, microscopic regions with varying energetics at the photocatalyst/co-catalyst interface can be created that facilitate charge recombination. Such problems can be mitigated by adding an interfacial layer between the photocatalyst and co-catalyst. This layer should have a chemical composition and structure similar to those of the photocatalyst to minimize the lattice mismatch while forming an ohmic contact with the co-catalyst. A degenerated photocatalyst, such as $n^+$-Si for n-Si, may be a promising choice for such interfaces.

### 10.7.4 Enhancement of Charge Separation

It is known that charge separation in a photocatalyst can be enhanced by asymmetric band bending.[108,112] This band bending can be induced by controlling the exposed facets and surface dipoles or by modulating the surface polarization. In most cases, asymmetric band bending is unintentionally induced after loading co-catalysts, even though co-catalysts are typically employed to improve surface kinetics rather than for the purpose of band bending. Therefore, a layer specially designed for the latter purpose would be highly desirable. The window layer and back surface field concepts currently used in solar cells may also be applicable to the development of such layers for photocatalysts.[113]

### 10.7.5 Alteration of the Band Edge Position

The band edge position for a photocatalyst in a solution is affected by the presence of surface dipoles and, in aqueous solutions, these dipoles are mostly related to the presence of $H^+$ and $OH^-$. As a result, the band edge position for an oxide or (oxy)nitride photocatalyst is usually fixed with respect to the $H^+/H_2$ and $O_2/H_2O$ potentials, on the basis of the Nernst equation.[114] This phenomenon limits the performance of numerous photocatalysts (such as $BiVO_4$, for which the CB minimum is more positive than the $H^+/H_2$ potential) during one-step excitation water splitting. The use of surface-adsorbed molecular species to form new surface dipoles has been assessed as an approach to tuning the band edge position,[115] although the stability of these species during photocatalytic water splitting can be an issue. One promising approach is the construction of a buried junction between the photocatalyst and the metal oxide layer. As an example, an n-Si/amorphous $TiO_2$ buried junction has been demonstrated during trials of photoelectrochemical $O_2$ evolution, even though the original VB maximum for n-Si in an aqueous solution is too negative for $O_2$ evolution.[55,116]

## References

1. T. Hisatomi, J. Kubota and K. Domen, *Chem. Soc. Rev.*, 2014, **43**, 7520–7535.
2. K. Takanabe, *ACS Catal.*, 2017, **7**, 8006–8022.

3. K. Maeda and K. Domen, *J. Phys. Chem. C*, 2007, **111**, 7851–7861.
4. F. Zhang, A. Yamakata, K. Maeda, Y. Moriya, T. Takata, J. Kubota, K. Teshima, S. Oishi and K. Domen, *J. Am. Chem. Soc.*, 2012, **134**, 8348–8351.
5. C. Pan, T. Takata, M. Nakabayashi, T. Matsumoto, N. Shibata, Y. Ikuhara and K. Domen, *Angew. Chem., Int. Ed.*, 2015, **54**, 2955–2959.
6. K. Maeda, H. Terashima, K. Kase, M. Higashi, M. Tabata and K. Domen, *Bull. Chem. Soc. Jpn.*, 2008, **81**, 927–937.
7. M. Qureshi, A. T. Garcia-Esparza, T. Shinagawa, P. Sautet, T. Le Bahers and K. Takanabe, *Sustainable Energy Fuels*, 2018, **2**, 2044–2052.
8. K. Maeda, K. Teramura, D. Lu, N. Saito, Y. Inoue and K. Domen, *Angew. Chem., Int. Ed.*, 2006, **45**, 7806–7809.
9. S. Chen, S. Shen, G. Liu, Y. Qi, F. Zhang and C. Li, *Angew. Chem., Int. Ed.*, 2015, **54**, 3047–3051.
10. K. Maeda, *ACS Catal.*, 2013, **3**, 1486–1503.
11. J. Yang, D. Wang, H. Han and C. Li, *Acc. Chem. Res.*, 2013, **46**, 1900–1909.
12. C. Ding, J. Shi, Z. Wang and C. Li, *ACS Catal.*, 2016, **7**, 675–688.
13. J. Ran, J. Zhang, J. Yu, M. Jaroniec and S. Z. Qiao, *Chem. Soc. Rev.*, 2014, **43**, 7787–7812.
14. W.-J. Chun, A. Ishikawa, H. Fujisawa, T. Takata, J. N. Kondo, M. Hara, M. Kawai, Y. Matsumoto and K. Domen, *J. Phys. Chem. B*, 2003, **107**, 1798–1803.
15. S. Bai, W. Yin, L. Wang, Z. Li and Y. Xiong, *RSC Adv.*, 2016, **6**, 57446–57463.
16. K. Domen, S. Naito, M. Soma, T. Onishi and K. Tamaru, *J. Chem. Soc., Chem. Commun.*, 1980, 543–544.
17. K. Domen, S. Naito, T. Onishi and K. Tamaru, *Chem. Phys. Lett.*, 1982, **92**, 433–434.
18. K. Domen, S. Naito, T. Onishi, K. Tamaru and M. Soma, *J. Phys. Chem.*, 1982, **86**, 3657–3661.
19. K. Domen, A. Kudo and T. Onishi, *J. Catal.*, 1986, **102**, 92–98.
20. K. Domen, A. Kudo, T. Onishi, N. Kosugi and H. Kuroda, *J. Phys. Chem.*, 1986, **90**, 292–295.
21. H. Kato and A. Kudo, *Catal. Lett.*, 1999, **58**, 153–155.
22. A. Kudo, H. Kato and S. Nakagawa, *J. Phys. Chem. B*, 1999, **104**, 571–575.
23. H. Kato and A. Kudo, *J. Phys. Chem. B*, 2001, **105**, 4285–4292.
24. H. Kato, K. Asakura and A. Kudo, *J. Am. Chem. Soc.*, 2003, **125**, 3082–3089.
25. T. Takata, K. Shinohara, A. Tanaka, M. Hara, J. N. Kondo and K. Domen, *J. Photochem. Photobiol., A*, 1997, **106**, 45–49.
26. Y.-G. Ko and W. Y. Lee, *Catal. Lett.*, 2002, **83**, 157–160.
27. D. W. Hwang, H. G. Kim, J. Kim, K. Y. Cha, Y. G. Kim and J. S. Lee, *J. Catal.*, 2000, **193**, 40–48.
28. E. Müller, *Z. Elektrochem.*, 1899, **5**, 469–473.

29. B. Endrődi, N. Simic, M. Wildlock and A. Cornell, *Electrochim. Acta*, 2017, **234**, 108–122.
30. K. Maeda, N. Sakamoto, T. Ikeda, H. Ohtsuka, A. Xiong, D. Lu, M. Kanehara, T. Teranishi and K. Domen, *Chem. – Eur. J.*, 2010, **16**, 7750–7759.
31. Q. Wang, T. Hisatomi, Q. Jia, H. Tokudome, M. Zhong, C. Wang, Z. Pan, T. Takata, M. Nakabayashi, N. Shibata, Y. Li, I. D. Sharp, A. Kudo, T. Yamada and K. Domen, *Nat. Mater.*, 2016, **15**, 611–615.
32. Z. Wang, Y. Inoue, T. Hisatomi, R. Ishikawa, Q. Wang, T. Takata, S. Chen, N. Shibata, Y. Ikuhara and K. Domen, *Nat. Catal.*, 2018, **1**, 756–763.
33. T. Takata, J. Jiang, Y. Sakata, M. Nakabayashi, N. Shibata, V. Nandal, K. Seki, T. Hisatomi and K. Domen, *Nature*, 2020, **581**, 411–414.
34. M. Kibria, S. Zhao, F. Chowdhury, Q. Wang, H. Nguyen, M. Trudeau, H. Guo and Z. Mi, *Nat. Commun.*, 2014, **5**, 3825.
35. M. G. Kibria, F. A. Chowdhury, S. Zhao, B. AlOtaibi, M. L. Trudeau, H. Guo and Z. Mi, *Nat. Commun.*, 2015, **6**, 6797.
36. Q. Wang, M. Nakabayashi, T. Hisatomi, S. Sun, S. Akiyama, Z. Wang, Z. Pan, X. Xiao, T. Watanabe, T. Yamada, N. Shibata, T. Takata and K. Domen, *Nat. Mater.*, 2019, **18**, 827–832.
37. B. Tian, W. Gao, X. Zhang, Y. Wu and G. Lu, *Appl. Catal., B*, 2018, **221**, 618–625.
38. M. Yoshida, K. Takanabe, K. Maeda, A. Ishikawa, J. Kubota, Y. Sakata, Y. Ikezawa and K. Domen, *J. Phys. Chem. C*, 2009, **113**, 10151–10157.
39. M. Qureshi, T. Shinagawa, N. Tsiapis and K. Takanabe, *ACS Sustainable Chem. Eng.*, 2017, **5**, 8079–8088.
40. C. T. K. Thaminimulla, T. Takata, M. Hara, J. N. Kondo and K. Domen, *J. Catal.*, 2000, **196**, 362–365.
41. K. Maeda, K. Teramura, D. Lu, T. Takata, N. Saito, Y. Inoue and K. Domen, *Nature*, 2006, **440**, 295.
42. K. Maeda, K. Teramura, D. Lu, T. Takata, N. Saito, Y. Inoue and K. Domen, *J. Phys. Chem. B*, 2006, **110**, 13753–13758.
43. K. Maeda, K. Teramura, H. Masuda, T. Takata, N. Saito, Y. Inoue and K. Domen, *J. Phys. Chem. B*, 2006, **110**, 13107–13112.
44. K. Maeda, K. Teramura, N. Saito, Y. Inoue and K. Domen, *J. Catal.*, 2006, **243**, 303–308.
45. K. Maeda, K. Teramura and K. Domen, *J. Catal.*, 2008, **254**, 198–204.
46. Y. Lee, K. Teramura, M. Hara and K. Domen, *Chem. Mater.*, 2007, **19**, 2120–2127.
47. Z. Pan, T. Hisatomi, Q. Wang, S. Chen, A. Iwase, M. Nakabayashi, N. Shibata, T. Takata, M. Katayama, T. Minegishi, A. Kudo and K. Domen, *Adv. Funct. Mater.*, 2016, **26**, 7011–7019.
48. C. J. Shearer, T. Hisatomi, K. Domen and G. F. Metha, *J. Photochem. Photobiol., A*, 2020, **401**, 112757.
49. C. Pan, T. Takata and K. Domen, *Chem. – Eur. J.*, 2016, **22**, 1854–1862.
50. M. R. Hoffmann, S. T. Martin, W. Choi and D. W. Bahnemann, *Chem. Rev.*, 1995, **95**, 69–96.

51. T. Takata, C. Pan, M. Nakabayashi, N. Shibata and K. Domen, *J. Am. Chem. Soc.*, 2015, **137**, 9627–9634.
52. Y. W. Chen, J. D. Prange, S. Dühnen, Y. Park, M. Gunji, C. E. Chidsey and P. C. McIntyre, *Nat. Mater.*, 2011, **10**, 539–544.
53. A. Paracchino, V. Laporte, K. Sivula, M. Grätzel and E. Thimsen, *Nat. Mater.*, 2011, **10**, 456–461.
54. J. Gu, Y. Yan, J. L. Young, K. X. Steirer, N. R. Neale and J. A. Turner, *Nat. Mater.*, 2016, **15**, 456–460.
55. S. Hu, M. R. Shaner, J. A. Beardslee, M. Lichterman, B. S. Brunschwig and N. S. Lewis, *Science*, 2014, **344**, 1005–1009.
56. R. Li, Y. Weng, X. Zhou, X. Wang, Y. Mi, R. Chong, H. Han and C. Li, *Energy Environ. Sci.*, 2015, **8**, 2377–2382.
57. K. Maeda, *Chem. Commun.*, 2013, **49**, 8404–8406.
58. T. Ohno, L. Bai, T. Hisatomi, K. Maeda and K. Domen, *J. Am. Chem. Soc.*, 2012, **134**, 8254–8259.
59. H. Lyu, T. Hisatomi, Y. Goto, M. Yoshida, T. Higashi, M. Katayama, T. Takata, T. Minegishi, H. Nishiyama, T. Yamada, Y. Sakata, K. Asakura and K. Domen, *Chem. Sci.*, 2019, **10**, 3196–3201.
60. M. Yoshida, K. Maeda, D. Lu, J. Kubota and K. Domen, *J. Phys. Chem. C*, 2013, **117**, 14000–14006.
61. A. T. Garcia-Esparza, T. Shinagawa, S. Ould-Chikh, M. Qureshi, X. Peng, N. Wei, D. H. Anjum, A. Clo, T.-C. Weng, D. Nordlund, D. Sokaras, J. Kubota, K. Domen and K. Takanabe, *Angew. Chem., Int. Ed.*, 2017, **56**, 5780–5784.
62. J. A. Bau and K. Takanabe, *ACS Catal.*, 2017, **7**, 7931–7940.
63. N. Mahmood, Y. Yao, J.-W. Zhang, L. Pan, X. Zhang and J.-J. Zou, *Adv. Sci.*, 2018, **5**, 1700464.
64. M. M. Waegele, X. Chen, D. M. Herlihy and T. Cuk, *J. Am. Chem. Soc.*, 2014, **136**, 10632–10639.
65. X. Chen, S. N. Choing, D. J. Aschaffenburg, C. D. Pemmaraju, D. Prendergast and T. Cuk, *J. Am. Chem. Soc.*, 2017, **139**, 1830–1841.
66. S. Chen, J. Yang, C. Ding, R. Li, S. Jin, D. Wang, H. Han, F. Zhang and C. Li, *J. Mater. Chem. A*, 2013, **1**, 5651–5659.
67. S. Chen, Y. Qi, Q. Ding, Z. Li, J. Cui, F. Zhang and C. Li, *J. Catal.*, 2016, **339**, 77–83.
68. K. Maeda, M. Higashi, D. Lu, R. Abe and K. Domen, *J. Am. Chem. Soc.*, 2010, **132**, 5858–5868.
69. Z. Pan, T. Hisatomi, Q. Wang, S. Chen, M. Nakabayashi, N. Shibata, C. Pan, T. Takata, M. Katayama, T. Minegishi, A. Kudo and K. Domen, *ACS Catal.*, 2016, **6**, 7188–7196.
70. X. Q. Cao, R. Vassen and D. Stoever, *J. Eur. Ceram. Soc.*, 2004, **24**, 1–10.
71. A. J. Bard, *J. Photochem.*, 1979, **10**, 59–75.
72. K. Tennakone and S. Pushpa, *J. Chem. Soc., Chem. Commun.*, 1985, 1435–1437.
73. T. Ohno, S. Saito, K. Fujihara and M. Matsumura, *Bull. Chem. Soc. Jpn.*, 1996, **69**, 3059–3064.

74. J. R. Darwent and A. Mills, *J. Chem. Soc., Faraday Trans. 2*, 1982, **78**, 359–367.
75. A. Kudo, K. Omori and H. Kato, *J. Am. Chem. Soc.*, 1999, **121**, 11459–11467.
76. S. Kohtani, A. Kudo and T. Sakata, *Chem. Phys. Lett.*, 1993, **206**, 166–170.
77. R. Abe, K. Sayama, K. Domen and H. Arakawa, *Chem. Phys. Lett.*, 2001, **344**, 339–344.
78. K. Sayama, K. Mukasa, R. Abe, Y. Abe and H. Arakawa, *Chem. Commun.*, 2001, 2416–2417.
79. K. Sayama, K. Mukasa, R. Abe, Y. Abe and H. Arakawa, *J. Photochem. Photobiol., A*, 2002, **148**, 71–77.
80. R. Abe, K. Sayama and H. Sugihara, *J. Phys. Chem. B*, 2005, **109**, 16052–16061.
81. R. Abe, T. Takata, H. Sugihara and K. Domen, *Chem. Commun.*, 2005, 3829–3831.
82. G. Ma, S. Chen, Y. Kuang, S. Akiyama, T. Hisatomi, M. Nakabayashi, N. Shibata, M. Katayama, T. Minegishi and K. Domen, *J. Phys. Chem. Lett.*, 2016, **7**, 3892–3896.
83. Z. Pan, T. Hisatomi, Q. Wang, M. Nakabayashi, N. Shibata, C. Pan, T. Takata and K. Domen, *Appl. Catal., A*, 2016, **521**, 26–33.
84. S. S. K. Ma, K. Maeda, T. Hisatomi, M. Tabata, A. Kudo and K. Domen, *Chem. – Eur. J.*, 2013, **19**, 7480–7486.
85. Y. Sasaki, H. Nemoto, K. Saito and A. Kudo, *J. Phys. Chem. C*, 2009, **113**, 17536–17542.
86. M. Tabata, K. Maeda, M. Higashi, D. Lu, T. Takata, R. Abe and K. Domen, *Langmuir*, 2010, **26**, 9161–9165.
87. Y. Qi, S. Chen, J. Cui, Z. Wang, F. Zhang and C. Li, *Appl. Catal., B*, 2018, **224**, 579–585.
88. R. Abe, *J. Photochem. Photobiol., C*, 2010, **11**, 179–209.
89. K. Obata and K. Takanabe, *Angew. Chem., Int. Ed.*, 2018, **57**, 1616–1620.
90. A. A. Keller, H. Wang, D. Zhou, H. S. Lenihan, G. Cherr, B. J. Cardinale, R. Miller and Z. Ji, *Environ. Sci. Technol.*, 2010, **44**, 1962–1967.
91. M. Balasubramanian, C. A. Melendres and A. N. Mansour, *Thin Solid Films*, 1999, **347**, 178–183.
92. DOE Technical Targets for Hyrogen Production from Photoelectrocatalytic Water Splitting, U.S. Dept. of Energy, Office of Energy Efficiency & Renewable Energy, https://www.energy.gov/eere/fuelcells/doe-technical-targets-hydrogen-production-photoelectrochemical-water-splitting. Accessed March 29, 2021.
93. B. A. Pinaud, J. D. Benck, L. C. Seitz, A. J. Forman, Z. Chen, T. G. Deutsch, B. D. James, K. N. Baum, G. N. Baum, S. Ardo, H. Wang, E. Miller and T. F. Jaramillo, *Energy Environ. Sci.*, 2013, **6**, 1983–2002.
94. S. Hu, N. S. Lewis, J. W. Ager, J. Yang, J. R. McKone and N. C. Strandwitz, *J. Phys. Chem. C*, 2015, **119**, 24201–24228.
95. S. Chen and L.-W. Wang, *Chem. Mater.*, 2012, **24**, 3659–3666.

96. G. Liu, J. Shi, F. Zhang, Z. Chen, J. Han, C. Ding, S. Chen, Z. Wang, H. Han and C. Li, *Angew. Chem., Int. Ed.*, 2014, **53**, 7295–7299.
97. Q. Wang, Y. Li, T. Hisatomi, M. Nakabayashi, N. Shibata, J. Kubota and K. Domen, *J. Catal.*, 2015, **328**, 308–315.
98. J. Zhao, T. Minegishi, L. Zhang, M. Zhong, Gunawan, M. Nakabayashi, G. Ma, T. Hisatomi, M. Katayama, S. Ikeda, N. Shibata, T. Yamada and K. Domen, *Angew. Chem., Int. Ed.*, 2014, **53**, 11808–11812.
99. P. A. Kohl, *J. Electrochem. Soc.*, 1977, **124**, 225.
100. Y. Lin, C. Battaglia, M. Boccard, M. Hettick, Z. Yu, C. Ballif, J. W. Ager and A. Javey, *Nano Lett.*, 2013, **13**, 5615–5618.
101. B. Seger, T. Pedersen, A. B. Laursen, P. C. K. Vesborg, O. Hansen and I. Chorkendorff, *J. Am. Chem. Soc.*, 2013, **135**, 1057–1064.
102. Y. Lin, R. Kapadia, J. Yang, M. Zheng, K. Chen, M. Hettick, X. Yin, C. Battaglia, I. D. Sharp, J. W. Ager and A. Javey, *J. Phys. Chem. C*, 2015, **119**, 2308–2313.
103. P. Nunez, M. H. Richter, B. D. Piercy, C. W. Roske, M. Cabán-Acevedo, M. D. Losego, S. J. Konezny, D. J. Fermin, S. Hu, B. S. Brunschwig and N. S. Lewis, *J. Phys. Chem. C*, 2019, **123**, 20116–20129.
104. M. R. Shaner, S. Hu, K. Sun and N. S. Lewis, *Energy Environ. Sci.*, 2015, **8**, 203–207.
105. P. A. Kempler, R. H. Coridan and N. S. Lewis, *Energy Environ. Sci.*, 2020, **13**, 1808–1817.
106. A. Xiong, G. Ma, K. Maeda, T. Takata, T. Hisatomi, T. Setoyama, J. Kubota and K. Domen, *Catal. Sci. Technol.*, 2014, **4**, 325–328.
107. Z. Pan, R. Yanagi, Q. Wang, X. Shen, Q. Zhu, Y. Xue, J. A. Röhr, T. Hisatomi, K. Domen and S. Hu, *Energy Environ. Sci.*, 2020, **13**, 162–173.
108. Z. Pan, J. Rohr, Z. Ye, Z. Fishman, Q. Zhu, X. Shen and S. Hu, *Sustainable Energy Fuels*, 2019, **3**, 850–864.
109. A. Kumar, P. G. Santangelo and N. S. Lewis, *J. Phys. Chem.*, 1992, **96**, 834–842.
110. X. Zhou, R. Liu, K. Sun, D. Friedrich, M. T. McDowell, F. Yang, S. T. Omelchenko, F. H. Saadi, A. C. Nielander, S. Yalamanchili, K. M. Papadantonakis, B. S. Brunschwig and N. S. Lewis, *Energy Environ. Sci.*, 2015, **8**, 2644–2649.
111. A. Heller, *Metallic Catalysts on Semiconductors: Transparency and Electrical Contact Properties*, Springer Science & Business Media, 1986.
112. D. E. Aspnes and A. Heller, *J. Phys. Chem.*, 1983, **87**, 4919–4929.
113. A. Polman, M. Knight, E. C. Garnett, B. Ehrler and W. C. Sinke, *Science*, 2016, **352**, aad4424-1–aad4424-10.
114. A. J. Nozik, *Annu. Rev. Phys. Chem.*, 1978, **29**, 189–222.
115. L. E. Garner, K. X. Steirer, J. L. Young, N. C. Anderson, E. M. Miller, J. S. Tinkham, T. G. Deutsch, A. Sellinger, J. A. Turner and N. R. Neale, *ChemSusChem*, 2017, **10**, 767–773.
116. S. Hu, M. H. Richter, M. F. Lichterman, J. Beardslee, T. Mayer, B. S. Brunschwig and N. S. Lewis, *J. Phys. Chem. C*, 2016, **120**, 3117–3129.

CHAPTER 11

# *Ultrathin Silica Layers as Separation Membranes for Artificial Photosynthesis*

WON JUN JO, HONGNA ZHANG, GEORGIOS KATSOUKIS AND HEINZ FREI*

Molecular Biophysics and Integrated Bioimaging Division, Lawrence Berkeley National Laboratory, University of California, Berkeley, CA 94720, USA
*Email: hmfrei@lbl.gov

## 11.1 Introduction

The past several years have witnessed astounding progress in the development of complete, bias-free integrated artificial photosystems for overall water splitting, and for the reduction of $CO_2$ by $H_2O$ to CO or formate. System designs rest on semiconductor-based two-photon tandem or multijunction approaches that attain power efficiencies of sunlight to fuel conversion of up to 15%, all featuring Earth-abundant materials.[1–11] Two such systems, one for water splitting and the other for CO generation, feature a membrane that is integrated into the system.[2,3,12] One of the water splitting systems reaches a power efficiency of 19%.[13]

With high power efficiency of solar water splitting and of $CO_2$ conversion to CO or formate in single integrated systems having been demonstrated and major leaps made in the use of Earth-abundant materials, a formidable challenge yet to be overcome towards an artificial photosynthesis

Energy and Environment Series No. 30
Ultrathin Oxide Layers for Solar and Electrocatalytic Systems
Edited by Heinz Frei and Daniel V. Esposito

Published by the Royal Society of Chemistry, www.rsc.org

technology is the scalability of systems at an adequate level for impact on global fuel consumption (terawatts). Furthermore, the direct conversion of sunlight to an energy-dense liquid hydrocarbon fuel is essential, but existing approaches do not adequately address these challenges. Natural photosynthesis, the only known system for making chemical compounds on the terawatt scale (120 TW),[14] features as the key design principle the closing of the photosynthetic cycle on the nanoscale with separation of the catalysis environment of $H_2O$ oxidation on the inside of the thylakoid membrane from the incompatible environment of primary reduction product generation on the outside. Accomplishing visible light-driven $CO_2$ reduction by $H_2O$ on the shortest possible length scale – nanometers – under membrane separation addresses key obstacles for scalability, namely the need for photocatalytically inactive components, which may pose a serious impediment at the enormous scale of terawatts, and the need for an aqueous electrolyte medium by enabling photocatalysis at the gas/ultrathin membrane interface. The goal is an artificial photosynthesis technology in which the sole balance of systems components are those needed for reactant delivery and product collection, and mechanical support for large-scale deployment.

To this end, robust, inorganic oxide-based nanoscale units, each featuring a built-in ultrathin separation membrane, could serve as complete independent photosynthetic units. Configuring these in the form of assemblies that extend the product separation from the nanoscale to square inch- or square decimeter-sized tiles without introducing any non-active components is envisioned. Deploying enormous numbers of such interconnected tiles over large areas of non-arable land would require the delivery of vapor-phase $CO_2$ and $H_2O$ reactants and the collection of the fuel product (assumed pure) as the sole balance of systems infrastructure. Beyond this critical scalability advantage, accomplishing the most demanding charge transport and catalytic transformations on the nanoscale under membrane separation allows inefficient processes that are intrinsic to existing approaches to be bypassed. Specifically, it enables the substantial resistance losses associated with ion transport across macroscale distances to be avoided, and back and side reactions to be minimized.[15–17]

This chapter focuses on the development and characterization of ultrathin silica membranes with embedded molecular wires for chemically separating the incompatible catalysis environments inside and outside nanoscale units in the form of nanotubes, which at the same time provide precise electronic and ample protonic communication between them. After describing the core–shell nanotube concept, the focus is on the synthesis, structure, and energetics of organic molecular wires for controlled charge transport across the silica nanolayer. This is followed by a discussion of the fabrication of fully functionalized core–shell nanotube arrays and analogous planar constructs. The latter are utilized for the quantitative evaluation and optimization of charge transfer *via* embedded wires, and

proton transport across stacked oxide nanolayers that constitute the core–shell nanotube wall, using photocurrent, electrochemical impedance spectroscopic (EIS), and cyclic voltammetric (CV) measurements. Detailed mechanistic understanding is advanced by ultrafast optical spectroscopic studies. The chapter concludes with the presentation of initial photocatalysis studies and an outlook on the further development and applications of ultrathin silica membranes.

## 11.2 Design Concept

To address the requirements of robustness of the component materials and the ability to extend the membrane separation of the incompatible $CO_2$ reduction and $H_2O$ oxidation catalysis environments of nanoscale photosynthetic units to macroscale ensembles, we use Earth-abundant inorganic oxide-based components and core–shell nanotube geometry.[16,17] The topology of arrays of such core–shell nanotubes allows us to maintain separation of the $O_2$- and fuel-evolving spaces on all length scales from the nano- to the macroscale. As shown in Figure 11.1a, the core of the photosynthetic unit is a $Co_3O_4$ nanotube, the inner surface of which provides catalytic sites for vapor-phase water oxidation to $O_2$:

$$2H_2O \rightarrow 4e^- + O_2 + 4H^+ \qquad (11.1)$$

Spinel $Co_3O_4$ was demonstrated to be an efficient $O_2$-evolving catalyst for liquid- or vapor-phase $H_2O$,[18,19] with the mechanism now fairly well understood.[20–22] The Co oxide nanotube is surrounded by an amorphous silica shell of ~3 nm thickness that acts as a membrane that is impermeable to $O_2$ and small fuel molecules while readily transmitting protons[23] and, thus, affords the separation of the $H_2O$ oxidation space from the light absorber and reduction catalysis environment. The proton conductivity assures the availability of $H^+$, generated by $H_2O$ oxidation on the inner

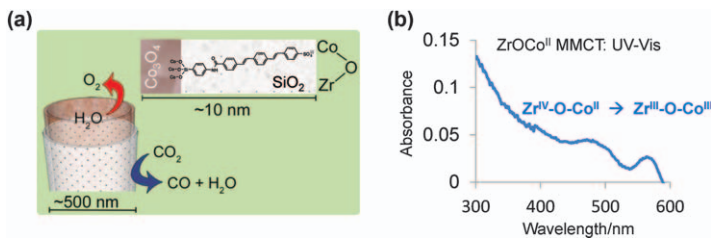


**Figure 11.1** (a) Cobalt oxide–silica core–shell nanotube featuring a silica nanomembrane as a complete photosynthetic unit for $CO_2$ photoreduction by $H_2O$. Reproduced from ref. 16 with permission from American Chemical Society, Copyright 2018. (b) UV–visible spectrum of ZrOCo metal-to-metal charge-transfer (MMCT) absorption. Reproduced from ref. 25 with permission from American Chemical Society, Copyright 2018.

$Co_3O_4$ surface, for the formation of C–H or O–H bonds of the fuel molecule upon $CO_2$ reduction on the outer side of the membrane. The light absorbers are robust, all-inorganic, heterobinuclear units such as ZrOCo covalently anchored on the outer silica surface. Absorption of visible light with concurrent separation of positive and negative charges occurs by metal-to-metal charge-transfer (MMCT) excitation, here $Zr^{IV}OCo^{II} \rightarrow Zr^{III}OCo^{III}$. The MMCT chromophores exhibit continuous absorption across the visible region with a long-wavelength onset at around 600 nm (Figure 11.1b).[17,24,25] For ZrOCo light absorbers, photoexcitation of the MMCT transition directly reduces gas-phase $CO_2$ to CO at the transient $Zr^{III}$ acceptor center:[25,26]

$$CO_2 + 2H^+ + 2e^- \rightarrow CO + H_2O \qquad (11.2)$$

or, alternatively, transfers an electron *via* the conduction band of an ultrathin $TiO_2$ shell to the Cu nanocatalyst. At the same time, the hole charge on the transient $Co^{III}$ center is energetically positioned for transfer across the silica separation membrane to the $Co_3O_4$ catalyst.[27] The ability of $ZrOCo^{II}$ units coupled to a metal oxide nanocatalyst (in this case Ir oxide) to close the photosynthetic cycle of $H_2O$ oxidation and $CO_2$ reduction to CO by an all-inorganic nanoscale unit at a remarkably high quantum efficiency of 17% has been demonstrated.[26] However, the nanoscale unit lacks a membrane, a critical component for developing scalable and safe photosynthetic systems.

Controlled charge transfer through the silica membrane is accomplished by embedded molecular wires that span the ultrathin $SiO_2$ layer separating the light absorber from the $Co_3O_4$ surface (Figure 11.1a). These are oligo(*p*-phenylenevinylene) molecules with three aryl units (PV3), tripodally anchored on Co oxide, with the length of the backbone commensurate with the thickness of the $SiO_2$ layer.[27–32] HOMO and LUMO energies of the wire molecules are selected so as to impose rectifying charge-transfer properties on the light absorber–wire assembly, as illustrated in Figure 11.2. The HOMO of PV3 is properly aligned for spontaneous hole charge transfer from excited ZrOCo to the $Co_3O_4$ catalyst for driving $H_2O$ oxidation. Efficiency-degrading back reaction of transferred holes with the excited light-absorber electron is prevented by the highly negative potential of the LUMO of PV3, thereby guiding transfer of the charges generated by ZrOCo photoexcitation in the desired directions.

The core–shell nanotube is designed to complete the light-driven conversion of $CO_2$ and $H_2O$ to fuel and $O_2$ under membrane separation. Arranging the independently operating nanotubes in the form of arrays featuring top and bottom covers, with the tube openings piercing through them, allows extension of the membrane separation of the evolving $O_2$ and fuel products on all length scales from the nano- to the macroscale.[16] The large surface area of the nanotube array allows adequate densities of light absorbers and catalytic sites per unit footprint area for the photocatalysis to keep up with the photon flux at maximum solar intensity.[17] Figure 11.3 shows a

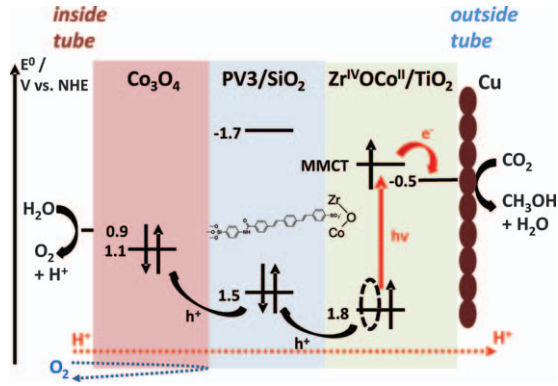


**Figure 11.2** Energy-level alignment of light absorber, PV3 wire, and catalysts for light-induced directional charge transfer for driving $H_2O$ oxidation and $CO_2$ reduction. Oxidation and reduction catalysis occurs at the gas/solid interface, with an $H^+$ gradient developing across the nanowall during photocatalytic $H_2O$ oxidation. The blue curved arrow signifies diffusion of $O_2$ through the $Co_3O_4$ atomic layer deposition (ALD) layer while being blocked by the $SiO_2$ membrane.
Adapted from ref. 24 with permission from the Royal Society of Chemistry.

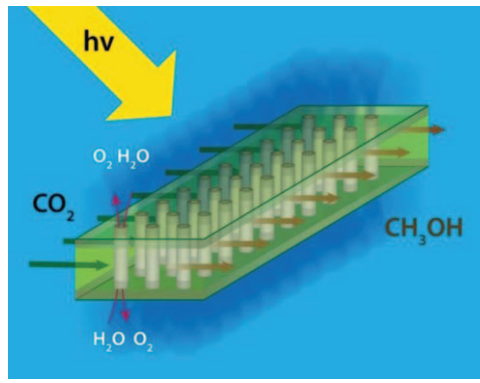


**Figure 11.3** Complete nanotube array.
Reproduced from ref. 24 with permission from the Royal Society of Chemistry.

cut-out section of such a ''tile'' in which gas-phase $CO_2$ is converted to fuel (currently CO, with $CH_3OH$ as the next target) while $H_2O$, in the form of moist air, is oxidized to $O_2$ on the inside of each nanotube. By virtue of the top and bottom tube openings, the $O_2$–$H_2O$ gas mixture inside the tubes diffuses into the surrounding atmosphere. Engineering considerations for reactant gas behavior and fuel collection will define the specific dimensions of the nanotube array tiles, of which enormous numbers will be joined together across large areas to provide fuel from $CO_2$ and $H_2O$ vapor on scale.

## 11.3 Charge-conducting Molecular Wires with Tunable Energetics

Charge transfer across the insulating silica layer is tightly controlled by embedded molecular wires, exploiting the precision with which the structure and electronic properties of molecular systems can be manipulated.

### 11.3.1 Wire Assembly and Tuning of Energetics

In order to permit optimization of the charge-transfer efficiency across the silica membrane, our approach of molecular wire assemblies is focused on the tunability of the wire energetics and loading density. To this end, a two-step assembly method was pursued, consisting of the attachment of a tripodal anchor on the $Co_3O_4$ surface followed by covalent linkage of the wire molecule by amide formation or click chemistry (Figure 11.4).[27,31,32] Trimethoxysilylaryl moieties featuring an amine (trimethoxysilylaniline, TMSA) or azide functionality (trimethoxysilylbenzyl azide, TMSBA) are established tripodal anchors with a vertical orientation on oxide surfaces.[33] Oligo(*p*-phenylenevinylene) molecules are a familiar class of molecular wires

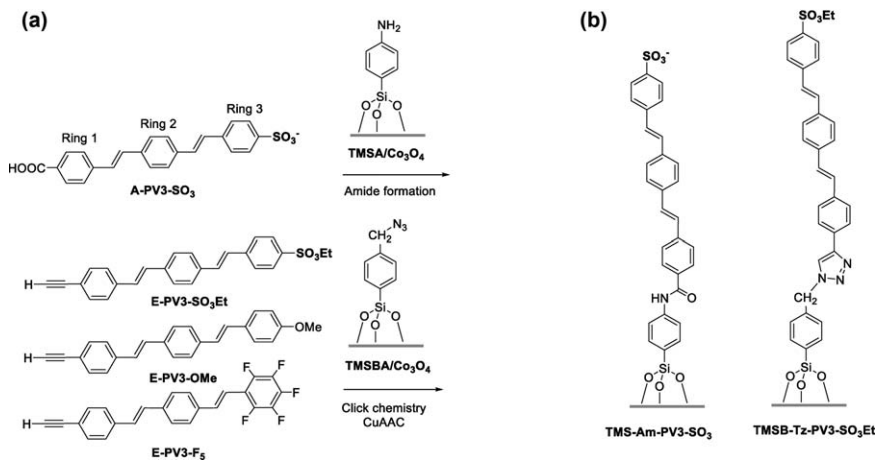


**Figure 11.4** (a) Functionalized wire molecules with electron-donating and -withdrawing groups. A-PV3-$SO_3$, −6.43 eV (1.93 V), 1.48 V; E-PV3-$SO_3$Et, −6.11 eV (1.61 V), 1.16 V; E-PV3-$F_5$, −6.18 eV (1.68 V), 1.23 V; E-PV3-OMe, −5.59 eV (1.09 V), 0.64 V. The first value is the HOMO potential of the free wire calculated by DFT (*vs.* vacuum), followed in parentheses in V *vs.* NHE. The last value is the potential of the wire linked to the anchor (*vs.* NHE). A-PV3 and E-PV3 designate wire functionalized on ring 1 by an acid or ethyne group for amide (Am) or triazole (Tz) attachment to anchor, respectively. (b) Wires attached to anchor molecules: TMS-Am-PV3-$SO_3$, −5.98 eV (1.48 V *vs.* NHE); TMSB-Tz-PV3-$SO_3$Et, −5.66 eV (1.16 V *vs.* NHE).
Reproduced from ref. 32 with permission from American Chemical Society, Copyright 2021.

for hole or electron transport[34] suitable for adjusting HOMO and LUMO energetics by synthetically modifying aryl or ethenyl moieties with electron-donating or -withdrawing groups. Moreover, the free choice of the number of aryl rings allows precise matching of the wire length and the silica membrane thickness. As discussed later in Section 11.6, $SiO_2$ atomic layer deposition (ALD) layers as thin as 2 nm completely separate small molecules, including $O_2$, with the thickness well matched with the length of wire molecules featuring three aryl units.

The HOMO potential of unmodified PV3 was reported to be around +1.4 V *vs.* NHE (normal hydrogen electrode),[28] hence reasonably well aligned with the estimated HOMO potential of the $Zr^{IV}OCo^{II}$ light absorber of +1.8 V *vs.* NHE[27] and the potential of the $Co_3O_4$ catalyst of +1.1 V *vs.* NHE[35] (the potential for $H_2O$ oxidation at pH 7 is +0.8 V) for ensuring facile hole charge transfer upon photoexcitation of the light absorber (Figure 11.2). Also, the reported potential of the PV3 LUMO of −1.7 V *vs.* NHE is properly positioned relative to the reducing potential of the excited ZrOCo light absorber of −1.4 V *vs.* NHE[27] for preventing back reaction with the hole on $Co_3O_4$ by electron crossover *via* the LUMO of the wire molecule.

In addition to wire molecules with a sulfonate (A-PV3-$SO_3$) (A = acid group) or sulfonic ethyl ester group in the *para* position of ring 3 (E-PV3-$SO_3$Et) (E = ethyne group) shown in Figure 11.4, the HOMO potential of which closely approximates that of unsubstituted PV3, wires featuring an electron-donating $OCH_3$ group in the *para* position of ring 3 (E-PV3-OMe) or an electron-withdrawing $C_6F_5$ moiety as ring 3 (E-PV3-$F_5$) were prepared. The selection of the wire modification was guided by density functional theory (DFT) calculations (B3LYP exchange correlation functional and 6–31+G** basis set) using Kohn–Sham orbital energetics as an approximation to HOMO and LUMO energies.[32] According to the calculations, the wire HOMO potentials vary within a few hundred millivolts of the $Co_3O_4$ and light-absorber potentials, which is the desired range for optimizing the energy-level alignment to reach the maximum charge-transfer efficiency (Figure 11.5).

Wires with a *p*-carboxylic acid group (for amide linkage) on aryl ring 1 and a *p*-sulfonate group on ring 3 (A-PV3-$SO_3$, where A indicates an acid group) were synthesized based on *trans*-selective Wittig–Horner reaction.[28] PV3 molecules with a *p*-ethyne group (for click chemistry) on aryl ring 1 and a *p*-sulfonic ethyl ester (E-PV3-$SO_3$Et, where E indicates an ethyne group), a *p*-methoxy on ring 3, or a pentafluorophenyl as ring 3 were synthesized *via* a combination of Pd-catalyzed cross-coupling and Wittig reactions, followed by deprotection with tetrabutylammonium fluoride of the trialkylsilylacetylene moiety.[32]

### 11.3.2 Structure and Orientation of Anchored Molecular Wires by Polarized FT-IRRAS

For the structural characterization of molecular wires anchored on the $Co_3O_4$ catalyst surface, the determination of the spatial orientation, and

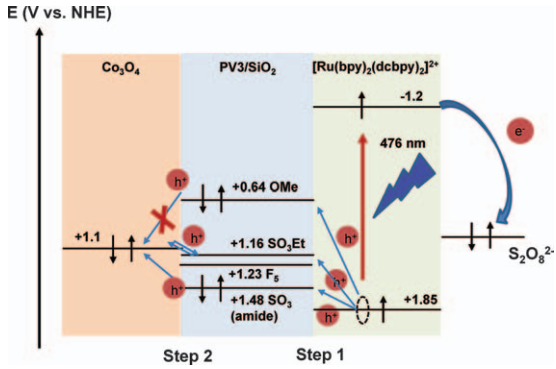


**Figure 11.5** Energy-level alignment of the HOMO of molecular wires with the HOMO of $[Ru(bpy)_2(dcbpy)]^{2+}$ light absorber and $Co_3O_4$ catalyst valence band. In this scheme, anchored wires are abbreviated OMe for E-PV3-OMe, $SO_3Et$ for E-PV3-$SO_3Et$, $F_5$ for E-PV3-$F_5$, and $SO_3$ for A-PV3-$SO_3$. Reproduced from ref. 32 with permission from American Chemical Society, Copyright 2021.

evaluation of their density, surface-sensitive polarized Fourier transform infrared reflection absorption spectroscopy (FT-IRRAS) provides the most detailed information. In this method, the IR probe beam at grazing incidence is reflected off a flat metal surface, in our case the Pt electrode, on which the sample is deposited. The key distinction from other types of IR spectroscopic methods such as transmission or attenuated total reflection (ATR) IR spectroscopy is that the perpendicularly (p) polarized electric field of the incident beam is enhanced approximately fourfold upon reflection off the metal surface while the horizontal (s) field component cancels out (is zero) (Figure 11.6a). Because only the p-component of vibrational modes of species at the surface absorbs probe light while the p- and s-absorption for molecules in the bulk phase is the same, dividing the p- by the s-polarized Fourier transform infrared (FT-IR) spectrum selectively reveals the enhanced absorption bands of species at the surface.[36,37] Therefore, we made planar samples of composition identical with that used for the $Co_3O_4$–$SiO_2$ core–shell nanotube walls with embedded wires on a Pt(100 nm)-covered Si wafer.[31] $Co_3O_4$ layers of 10 nm thickness were deposited by plasma-enhanced ALD on the Pt layer. Figure 11.6b shows the FT-IRRAS trace of TMSA after attachment to the $Co_3O_4$ surface. Tripodal anchoring $[Si(–O–Co)_3]$ is manifested by the broad intense Si–O–Co IR modes with a maximum at 1139 $cm^{-1}$ and shoulders at 1107 and 1050 $cm^{-1}$. Furthermore, comparison of the intensities of the p-polarized IRRAS trace with the non-polarized GATR (grazing angle attenuated total reflection) FT-IR spectrum of the same sample reveals a perpendicular orientation of the aryl ring and thus corroborates tripodal anchoring. As illustrated by the graphics in Figure 11.6a, if the aryl ring is oriented perpendicular to the $Co_3O_4$ plane, out-of-plane modes of the aryl moiety oscillate parallel to the Co oxide

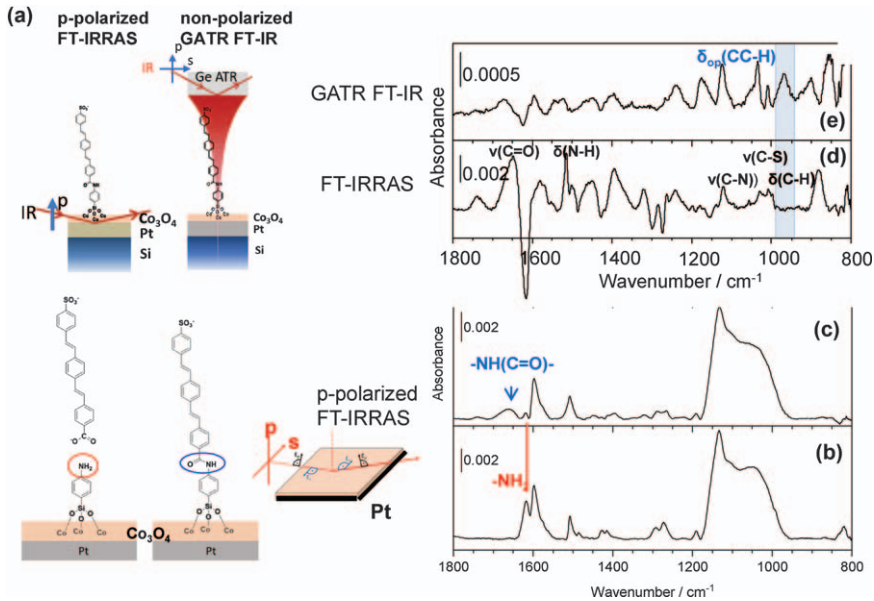


**Figure 11.6** Infrared spectra of the attachment of A-PV3-$SO_3$ wire molecules on a $Co_3O_4$ catalyst surface. (a) Schematics show the principle of FT-IRRAS and GATR FT-IR spectroscopy (top) and the attachment reaction of the wire (bottom). (b) FT-IRRAS trace of TMSA anchored on $Co_3O_4$. (c) After attachment of the wire molecule by an amide bond. (d) FT-IRRAS trace in (c) after subtraction of TMSA bands. (e) GATR FT-IR spectrum of the same sample as used for (d).
Reproduced from ref. 31 with permission from American Chemical Society, Copyright 2019.

(and Pt) surface (s-modes) whereas aryl in-plane modes are p-polarized (see the surface selection rule discussion below). In fact, an out-of-plane aryl CCH mode at 885 $cm^{-1}$ strongly absorbs in the GATR FT-IR spectrum but is completely absent in FT-IRRAS, indicating s-polarization.[31] Furthermore, all in-plane (aryl) TMSA vibrations in the region 1700–1200 $cm^{-1}$ are intense in FT-IRRAS, in agreement with p-polarization and, hence, a perpendicular orientation of the aromatic ring with respect to the Co oxide surface.[31]

As shown by the FT-IRRAS trace in Figure 11.6c, attachment of A-PV3-$SO_3$ wire by an amide linkage resulted in nearly complete loss of the intensity of the $NH_2$ group of TMSA at 1621 $cm^{-1}$ and growth of the amide I [$\nu$(C=O)] mode at 1666 $cm^{-1}$. Additional spectral changes upon wire attachment are more clearly visualized by computationally subtracting TMSA anchor bands, with the resulting difference spectrum shown in Figure 11.6d. Beyond the new amide I band at 1666 $cm^{-1}$, absorbance growth of A-PV3-$SO_3$ is observed at >1581 [$\nu$ (CC) aryl], 1521 (amide II), 1392 [$\nu$ (CC) aryl], 1321 [$\nu_{as}(SO_3H)$], 1284 [$\nu$ (C–N)], 1261 [$\nu$ (C–N)], 1122 [$\nu$ (C–S), $\nu_{sym}(SO_3^-)$], 1033 $cm^{-1}$ [in-plane alkenyl $\delta$(C=C–H), $\nu$ (CC), $\nu$ (C–S), $\nu_{sym}(SO_3^-)$]. Comparison of this p-polarized spectrum of attached wire with the non-polarized GATR

FT-IR trace of the same sample pressed against a Ge element, shown in Figure 11.6e, reveals the orientation of the molecular wire axis. Most pronounced are the intensity differences in the out-of-plane vinyl C=C–H bending region between 1000 and 900 $cm^{-1}$. There is a prominent band in the GATR FT-IR spectrum at 963 $cm^{-1}$, but no absorption in the FT-IRRAS trace in this region, which means that the mode is vibrating parallel to the surface. Because this out-of-plane vinyl C=C–H bending mode is vibrating perpendicular to the plane of the aryl–vinyl backbone, its s-polarization implies that the axis of the backbone of the anchored wire is oriented perpendicular to the $Co_3O_4$ surface. This conclusion is supported by the intensity behavior of modes in other spectral regions. An estimate of the uncertainty of the wire orientation indicates $90 \pm 12^{\circ}$.[31]

In addition to providing insight into the orientation of the anchored molecular wires, FT-IRRAS measurements provide quantitative information about the structural integrity under various experimental conditions. An important finding is that no structural changes or loss of wire molecules occur on heating a sample with anchored wires at 200 °C for several hours.

FT-IRRAS monitoring was equally important for the understanding of the structure and orientation of the various derivatized wires attached to the TMSBA anchor by click reaction. Although a comparison of the FT-IRRAS trace of TMSBA anchored on $Co_3O_4$ with the FT-IR spectrum of TMSBA crystallites indicates only minor spectral frequency differences, there is a large intensity effect of the asymmetric $N_3$ stretch at 2100 $cm^{-1}$, namely the relative intensity of the band is 13-fold lower in the p-polarized FT-IRRAS trace of anchored TMSBA than in the non-polarized transmission FT-IR spectrum of the crystalline phase.[32] The low intensity of the p-polarized anchor on $Co_3O_4$ indicates that the $N_3$ stretch is mainly s-polarized, which implies that the $N_3$ axis is oriented approximately parallel to the surface. This orientation, which is facilitated by the presence of the $CH_2$ group linking aryl and $N_3$, permits a vertical orientation of the PV3 axis upon formation of the triazole ring.

Click attachment of ethyne-derivatized wires with sulfonic ester, methoxy, or perfluorophenyl groups is readily monitored and quantified by the decrease in the $\nu_{as}(N_3)$ band, as shown in the insets of the spectra of the three PV3 molecules presented in Figure 11.7. In addition to the PV3 backbone IR bands common to these wires, including ring modes of the triazole linkage around 1170, 968, and the 840–660 $cm^{-1}$ region,[32,38,39] the spectra exhibit distinct modes characteristic of the respective substituent. For attached E-PV3-$SO_3$Et, it is an ethyl CH stretch at 2915 and 1343 [$\nu_{as}(SO_2)$], 1188 [$\nu_{sym}(SO_2)$], 930 [$\nu_{as}$(S–O–C)], 696 [$\nu_{sym}$(S–O–C)], and 569 $cm^{-1}$ [$\delta(SO_2)$] in the fingerprint region (Figure 11.7, trace 1). In the case of E-PV3-$F_5$, the perfluorophenyl group is manifested by peaks at 1520 and 1491 $cm^{-1}$ (mixed CF and aryl CC stretch modes) and bands at 1002 and 962 $cm^{-1}$ (CF stretched admixed with triazole in-plane bend) (Figure 11.7, trace 2). As can be seen in Figure 11.7, trace 3, the spectrum of attached E-PV3-OMe is significantly less intense despite the fact that the wire density is similar to that

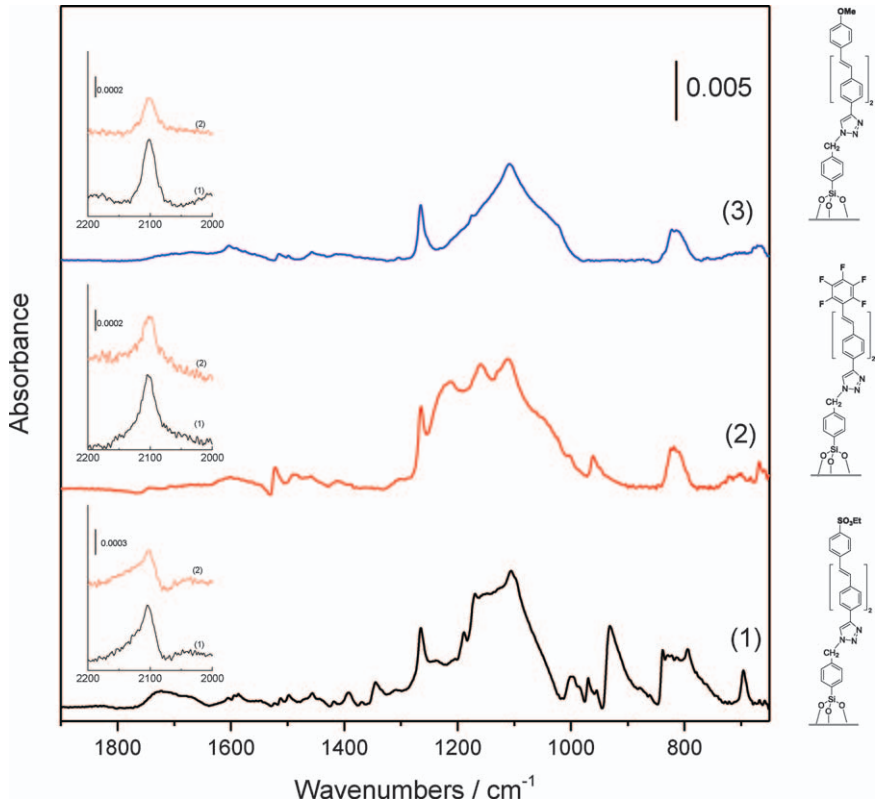


**Figure 11.7** FT-IRRAS traces of triazole-linked molecular wires with different substituents anchored by TMSBA on a $Co_3O_4$ surface are displayed as traces 1–3. The insets show the decrease of the azide stretch mode at 2100 $cm^{-1}$ (black trace, before attachment; red trace, after attachment) upon click reaction, based on which the wire density was calculated. Reproduced from ref. 32 with permission from American Chemical Society, Copyright 2021.

in the other two samples, yet the distinct signature of the methoxy substituent can nevertheless be discerned by the $CH_3$ stretch modes at 2922 and 2850 $cm^{-1}$, $\delta_{as}(CH_3)$ at 1456 $cm^{-1}$, and $\nu_{as}(C_{aryl}–O–C)$ at 1253 $cm^{-1}$.[32]

## 11.4 Fabrication of Membranes in Planar and Nanotube Assemblies

As was the case for developing assembly methods for surface-attached molecular wires and characterizing their structure and orientation, samples prepared on planar Pt surfaces are equally useful for structural characterization by FT-IRRAS of $Co_3O_4$ catalyst nanolayers, and of wire molecules after embedding in an ultrathin $SiO_2$ membrane. The spectroscopic method plays

an essential role in the quantitative assessment of the wire density during the stepwise improvement of light-driven charge transfer across the membrane by short-circuit photocurrent measurements. Planar samples are also very useful for evaluating and optimizing the proton flux across the ultrathin oxide layers, which can be easily characterized by electrochemical impedance spectroscopy (EIS) and cyclic voltammetry (CV) within this configuration. Core–shell wall compositions optimized for these transport properties using a planar configuration are subsequently implemented in the fabrication of $Co_3O_4$–$SiO_2$ core–shell nanotube arrays.

### 11.4.1 Planar Samples for Photoelectrochemical Characterization

Planar Pt electrodes were produced by e-beam evaporation, where a 2 nm Ti adhesive layer and 100 nm of Pt were deposited consecutively under high vacuum on precleaned Si wafers.[23] The reflective surface of the Pt substrate serves both as a suitable platform for FT-IRRAS probing and as an electrical contact for (photo)electrochemical experiments. Pt surfaces were coated with ultrathin $Co_3O_4$, $SiO_2$, and $TiO_2$ layers by plasma-enhanced ALD (Oxford FlexAL system situated in a Class 1000 cleanroom, or Cambridge Nanotech/Ultratech Savannah 100 system with a Meaglow hollow-cathode plasma source) in a bid to deposit the coatings at near room temperature (~40 °C) using bis(cyclopentadienyl)cobalt(II) (cobaltocene), tris(dimethylamino)silane, and tetrakis(dimethylamido)titanium(IV), respectively, as precursor.[23,40]

Analysis by FT-IRRAS allowed the determination of the structure of each oxide nanolayer. This spectroscopic technique is not only suitable for identifying ultrathin crystalline and amorphous layers, but also is sufficiently sensitive to reveal interfacial chemical bonds between them. Figure 11.8a presents FT-IRRAS measurements for a multistack $Pt/TiO_2/SiO_2/Co_3O_4$ sample illustrated schematically in Figure 11.8b, which corresponds to the composition of the core–shell nanotube wall. The bands of the Co oxide layer at 675 and 592 $cm^{-1}$ indicate a crystalline $Co_3O_4$ spinel structure[41] that is readily distinguished from other Co oxide structures, such as CoO, Co(O)OH, and $Co_2O_3$.[41–43] ALD-grown $Co_3O_4$ possesses a uniform but nanogranular morphology composed of 3–5 nm diameter crystals as visualized by scanning transmission electron microscopy–energy-dispersive X-ray spectroscopy (STEM–EDX) (Co) and atomic force microscopy analyses.[40] The granular structure of the deposit is reflected in an increased surface roughness from RMS = 0.184 nm for bare Si(100) to RMS = 0.284 nm after Co oxide coating, in agreement with previous reports of ALD-deposited Co oxide layers on silicon or glass.[44] The 2 nm $SiO_2$ layer exhibits the prominent LO (longitudinal optic) asymmetric SiOSi stretch mode characteristic of amorphous nanolayers of silica at 1236 $cm^{-1}$.[45,46] The intense band is accompanied by a shoulder at 1150 $cm^{-1}$ (in- and out-of-phase motion of two adjacent O atoms with respect to the center Si atom) (Figure 11.8a). The corresponding transverse optic (TO) asymmetric $\nu$(SiOSi) mode of amorphous silica with a sharp peak at

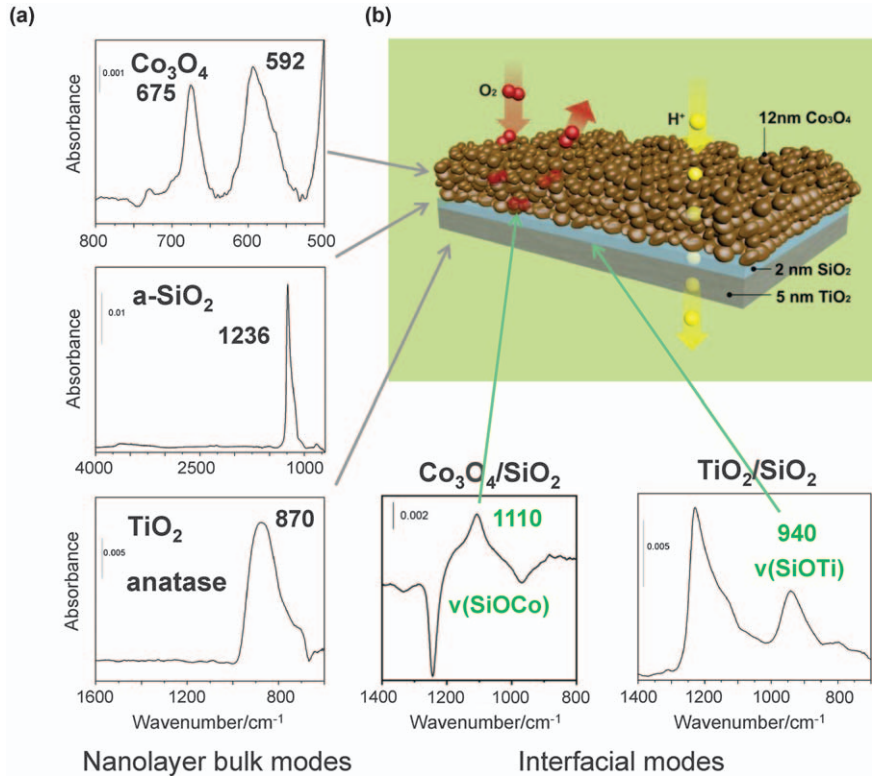


**Figure 11.8** (a) FT-IRRAS of ALD oxide layers on a Pt surface. Left: bulk vibrational modes of $Co_3O_4$ (3.5 nm), a-$SiO_2$ (2 nm), and $TiO_2$ (10 nm). Bottom: the interfacial SiOCo stretch mode of a $Co_3O_4$ (3.5 nm)/$SiO_2$ (2 nm) sample ($SiO_2$ spectrum subtracted for clarity) and of the interfacial SiOTi stretch mode of a $TiO_2$ (10 nm)/$SiO_2$ (2 nm)/$Co_3O_4$ (3.5 nm) sample ($TiO_2$ spectrum subtracted for clarity). (b) Schematic of oxide nanolayer stack indicating proton transmission through the stack and blocking of oxygen by the $SiO_2$ layer.
Reproduced from ref. 23 with permission from John Wiley & Sons, 

1080 $cm^{-1}$ is not observed because this mode cannot absorb p-polarized light.[47] Apart from the symmetric SiOSi mode at 820 $cm^{-1}$ and an extremely weak band of the OH stretch mode of isolated SiOH groups at 3747 $cm^{-1}$, no other IR bands are detected in the region 4000–600 $cm^{-1}$, confirming that the $SiO_2$ layers are free from organic impurities. The broad absorption of the $TiO_2$ layer with a maximum at 870 $cm^{-1}$ is characteristic of the LO TiOTi stretch mode of the anatase structure.[48]

Important is the discovery of interfacial covalent SiOCo (1110 $cm^{-1}$) and SiOTi linkages (940 $cm^{-1}$) between the silica and $Co_3O_4$ or $TiO_2$ layers that appear in the FT-IRRAS traces of $Co_3O_4/SiO_2$ and $TiO_2/SiO_2/Co_3O_4$ samples shown in Figure 11.8a. Spectral mode assignments are based on the close

agreement of the 1110 $cm^{-1}$ band with the Si–O–Co stretch of silane molecules anchored on $Co_3O_4$,[31] and literature reports of the Si–O–Ti mode at 940 $cm^{-1}$.[48,49] These interfacial bridges provided key insights into the efficiency and mechanism of proton transport through stacked oxide nanolayers, as discussed later in Section 11.6.

FT-IRRAS monitoring of the encasement of molecular wires by silica ALD allowed us to verify the integrity of the structure and orientation of the molecules, and to optimize the ALD protocol for minimum interference of the deposition process with the organic. Silica ALD requires an oxygen plasma for removal of residual organic ligands of the tris(dimethylamino)silane precursor, for which the standard method of heating at temperatures in excess of 550 °C[45] is not suitable in the presence of embedded organics. By monitoring FT-IRRAS under various different plasma operating conditions, a protocol featuring a 5 sccm $O_2$ purge of 45 s duration at 40 °C sample temperature followed by 5 s of plasma at 150 W (200 mTorr residual pressure) proved to be optimal. Figure 11.9a compares the spectrum before (trace 1) and after 20 cycles of $SiO_2$ ALD (trace 2) for A-PV3-$SO_3$ wires attached to a TMSA anchor on $Co_3O_4$. According to ellipsometry, the thickness of the silica layer is $3.78 \pm 0.04$ nm.[31] Whereas there is a 20% absorbance decrease of all wire bands, no IR bands of organic decomposition products are detected. This implies that the intensity decrease might be due either to attack of active oxygen species produced by the plasma pulse on wire molecules, with the breakdown products removed by the Ar purge pulse that follows the $O_2$ plasma pulse, or to the refractive index change upon ultrathin silica deposition that affects spectral intensities. Despite the relatively mild plasma conditions, no trace of residual ligands of the precursor are observed; specifically, none of the characteristic CH bands of tris(dimethylamino)silane breakdown residues in the 3000–2800 $cm^{-1}$ region are detected.[47] Deposition of an additional 20 cycles of silica ALD (Figure 11.9a, trace 3) does not result in any changes of wire band intensity, consistent with complete encapsulation of the wire molecules by the first 20 ALD cycles. The absorbance increase of the 1236 $cm^{-1}$ $SiO_2$ LO stretch mode is exactly the same as for the first 20 ALD cycles, which confirms that the silica layer grows linearly with number of ALD cycles and establishes monitoring of this $SiO_2$ mode as a convenient method for the precise comparison of the thickness of silica ALD layers of different samples.

A more detailed inspection of the effect of silica encasement on the molecular wires is obtained by the computational removal of the spectral trace that corresponds to 20 silica ALD cycles from the Pt/$Co_3O_4$/TMS-Am-PV3-$SO_3$/$SiO_2$ (20 cycle) spectrum in Figure 11.9a, trace 2. The result is presented in Figure 11.9b, trace 2, with trace 1 below showing the spectrum of the anchored wires before silica ALD. The relative intensity of the p-polarized E-PV3-$SO_3$ modes before and after deposition of 20 silica ALD cycles remains unchanged within uncertainty, indicating that the orientation of the axis of the wire molecules does not change significantly upon

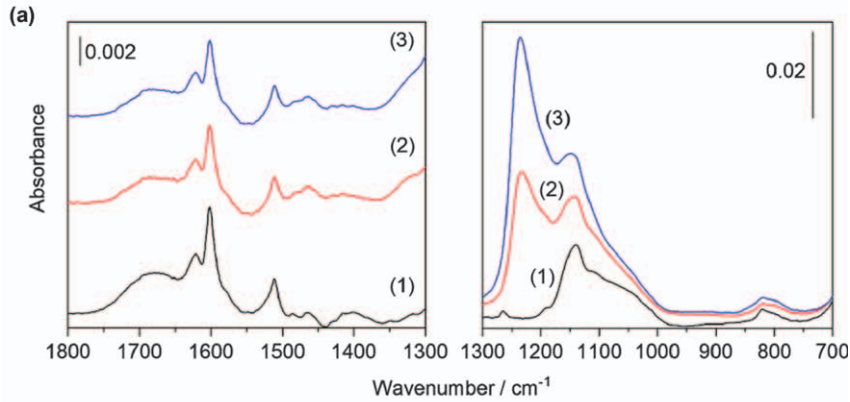
(a)
0.002
(3)
(2)
(1)
Absorbance
1800 1700 1600 1500 1400 1300
0.02
(3)
(2)
(1)
1300 1200 1100 1000 900 800 700
Wavenumber / cm-1

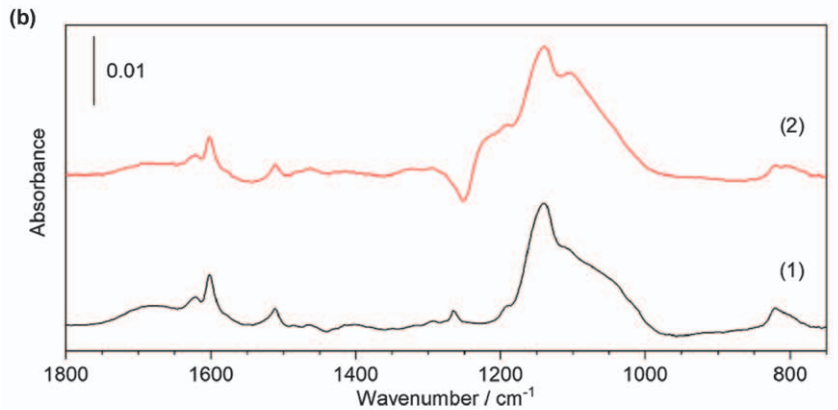
(b)
0.01
(2)
(1)
Absorbance
1800 1600 1400 1200 1000 800
Wavenumber / cm-1

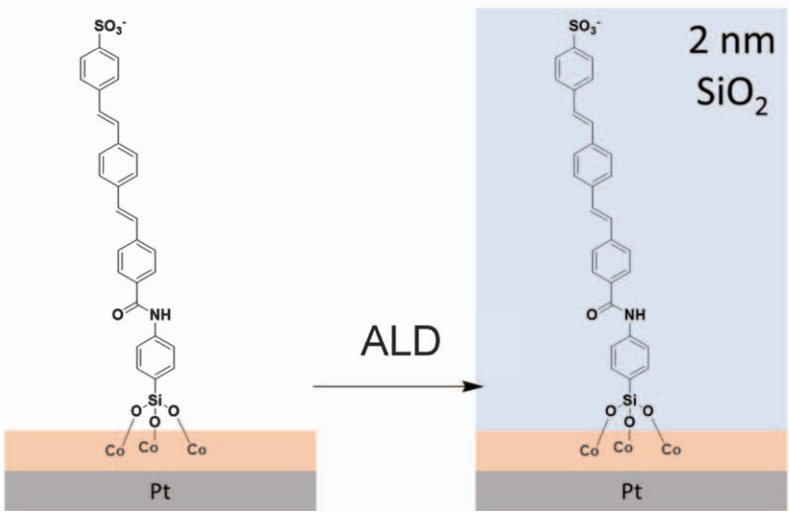
SO3-
O
NH
Si
O
O
O
Co Co Co
Pt
ALD
2 nm
SiO2

silica casting. Specifically, amide I, amide II, and aryl C–C stretch absorption bands in the 1700–1300 $cm^{-1}$ region are completely unchanged upon silica deposition. A marked change upon silica deposition is the growth of a peak at 1110 $cm^{-1}$ due to the formation of interfacial Si–O–Co bonds upon silica deposition (*cf.* Figure 11.9a). The IRRAS analysis therefore shows that the structure and orientation of the organic wire molecules are preserved with high fidelity upon casting into the ultrathin $SiO_2$ layer.

### 11.4.2 Core–Shell Nanotube Arrays for Photocatalytic Evaluation

Methods for making nanotube arrays based on sacrificial silicon nanorod templates or anodized alumina templates by coating them with chosen materials by ALD and subsequent etching for template removal provide tubes several micrometers in length with walls as thin as 8 nm and diameters of tens to hundreds of nanometers.[50–52] We have found that Si nanorod array templates prepared by microsphere lithography[53] offer a route for fabricating arrays of precisely aligned Si rods with high aspect ratio, based on which arrays of high-quality $Co_3O_4$–$SiO_2$ core–shell nanotubes with embedded molecular wires can be obtained by a combination of ALD, cryogenic dry etching, and room temperature etching. The power of ALD to achieve conformal coating of high aspect ratio structures has been convincingly demonstrated.[54] Dry etching using gases of tailored composition allows a substantial decrease in surface roughness and precise control of the morphology.[55]

Critical assembly steps were conducted according to our synthesis protocol first optimized for planar samples, as described above. Scanning electron microscopy (SEM) images shown in Figure 11.10a illustrate some of the key steps in the fabrication of square inch-sized nanotube arrays. In brief, polystyrene spheres 1 μm in diameter are spin coated on plasma-cleaned Si wafers from ethanol solution to generate a uniform single layer of the spheres. They are densely packed and form tens of microns-sized hexagonal arrays.[16] After shrinking to about 0.5 μm in diameter by $O_2$ plasma etching, the sphere-coated Si wafer is cooled to $-125$ °C and a

**Figure 11.9** FT-IRRAS of A-PV3-$SO_3$ molecular wire attached to a TMSA anchor on a $Co_3O_4$ surface after embedding in silica by ALD. (a) Pt/$Co_3O_4$/TMS-Am-PV3-$SO_3$ before silica ALD (trace 1), after 20 cycles of $SiO_2$ ALD (trace 2), and after an additional 20 cycles of $SiO_2$ ALD (trace 3). Note that different absorbance scales are used for spectral regions above and below 1300 $cm^{-1}$, and the Pt/$Co_3O_4$ background was subtracted for clarity. (b) Comparison of TMS-Am-PV3-$SO_3$ spectra before (trace 1) and after casting into silica (20 ALD cycles) (trace 2). For spectral trace 2, the silica band at 1236 $cm^{-1}$ shown in panel (a) was subtracted.
Reproduced from ref. 32 with permission from American Chemical Society, Copyright 2021.

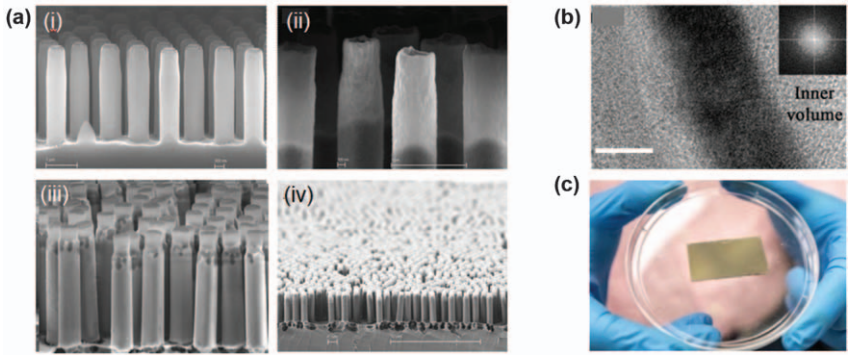


**Figure 11.10** (a) SEM images of the core–shell nanotube array fabrication process. (i) An array of $Co_3O_4/SiO_2/TiO_2$-coated Si rods after opening the top ends. (ii) Enlarged image of partly etched core–shell nanotubes. (iii, iv) Fully etched core–shell nanotube array with Si support. (b) HR-TEM image showing a longitudinal cross-section of a single $Co_3O_4$–$SiO_2$ core–shell nanotube. Scale bar: 5 nm. Inset: fast Fourier transform (FFT) image of the crystalline $Co_3O_4$ layer. Reproduced from ref. 16 with permission from American Chemical Society, Copyright 2018. (c) Photograph of a large sample of a core–shell nanotube array.

plasma mixture of $SF_6$ and $O_2$ is used to dry etch the Si wafer into an Si nanorod array 3–5 μm in length (the length is controlled by the etching time). The polymer spheres are cleanly removed from the top of the rods by $O_2$ plasma, and the rods are coated with 10 nm $Co_3O_4$, 2 nm $SiO_2$, and 5 nm $TiO_2$ by ALD using the deposition protocols described for planar constructs in the preceding section. The tops of the $Co_3O_4/SiO_2/TiO_2$-coated Si rods are selectively etched by a high-pressure $SF_6$–$CHF_3$ plasma to form open-ended rods. The resulting array is shown in Figure 11.10a(i). This particular step requires extensive fine tuning of the etching duration in order to confine removal of oxide to the tops of the nanotubes without eroding oxide coverage at the bottom (tube–silicon support junction). This allows subsequent etching of the inner Si core of the nanotubes with a plasma mixture of $SF_6$ and $O_2$ at –120 °C. Partially etched rod-tubes are shown in Figure 11.10a(ii), and fully etched tube arrays are presented for two different magnifications in Figure 11.10a(iii, iv). To obtain mechanically stable nanotube arrays upon complete removal of the Si template inside the tubes that possess the desired proton transport and chemical separation properties, layer thicknesses $Co_3O_4$ (10 nm)/$SiO_2$ (2 nm)/$TiO_2$ (5 nm) proved optimal.

For the structural characterization of ultrathin walls of individual nanotubes by high-resolution microscopy, nanotube arrays were encapsulated in a uniform flexible organic layer by vapor deposition of parylene C at room temperature. The 5 μm thick polymer allowed peel-off of the nanotube array from the Si wafer and slicing with a microtome to prepare 25–100 nm thick layers of nanotubes.[16] A high-resolution transmission electron microscopy (HR-TEM) image of a longitudinal slice with respect to the tube axis of a

single nanotube wall is shown in Figure 11.10b, which reveals the 10 nm crystalline $Co_3O_4$ layer (black) on the inner side of the tube coated with 2 nm $SiO_2$ (bright gray; in this particular preparation, a 10 nm thick $Al_2O_3$ ALD layer was used for mechanical stability, which was subsequently replaced with 5 nm $TiO_2$). The crystallinity of the $Co_3O_4$ layer is manifested by the circular diffraction pattern shown in the inset in Figure 11.10b. Together with the $Co_3O_4$ layer, the three layers constitute a nanowall less than 20 nm thick. Figure 11.10c shows a photograph of a $1.5 \times 3$ cm-sized core–shell nanotube array.

For core–shell nanotube arrays functionalized by molecular wires cast into the $SiO_2$ shell, GATR FT-IR spectroscopy proved to be an extremely useful method for monitoring the integrity of the wire molecules during the various nanofabrication steps. Figure 11.11a, trace 1, shows the GATR FT-IR spectrum of TMSA anchored on the $Co_3O_4$ nanotube surface of a $cm^2$-sized array consisting of 10 nm Co oxide deposited on the Si nanorod array. The close similarity to the FT-IRRAS trace of the corresponding planar construct deposited on Pt is apparent (Figure 11.6b), although the intensities of the bands differ because GATR FT-IR spectroscopy probes the sample with non-polarized IR light, in contrast to p-polarized FT-IRRAS. Attachment of A-PV3-$SO_3$ to the TSMA anchors by an amide linkage can readily be discerned from growth of amide I (1671 $cm^{-1}$), amide II (1520 $cm^{-1}$), and A-PV3-$SO_3$ bands at 1601, 1392, and four sharp characteristic peaks at 1037, 1009, 972, and 962 $cm^{-1}$ (Figure 11.11a, trace 2, marked by black

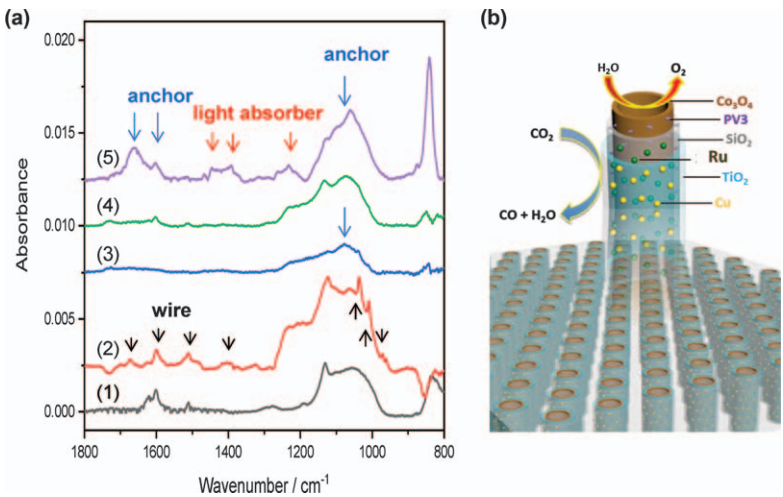


**Figure 11.11** (a) GATR FT-IR spectra of stepwise functionalization of a $Co_3O_4$–$SiO_2$ core–shell nanotube array. (1) TMSA anchor on $Co_3O_4$ nanotube; (2) after attachment of A-PV3-$SO_3$ wire by an amide bond (wire modes marked with black arrows); (3) $SiO_2$ (2 nm) by ALD; (4) TMSA anchor on the $SiO_2$ surface; (5) attachment of $[Ru(bpy)_2(dcbpy)]^{2+}$ by an amide bond. Light-absorber bands are marked with red arrows. (b) Cartoon of the functionalized nanotube.

arrows). The bands persist after 2 nm $SiO_2$ ALD (Figure 11.11a, trace 3), and thereby confirm the integrity of the attached wire molecules during the ALD process of the array. As expected, the intense p-polarized LO SiOSi band in FT-IRRAS at 1236 $cm^{-1}$ (Figure 11.9a) is replaced by the typical asymmetric $SiO_2$ stretch of amorphous silica recorded with non-polarized IR radiation at 1064 $cm^{-1}$ (Figure 11.11a, trace 3, blue arrow).

## 11.5 Charge Transport Through an $SiO_2$ Membrane

With methods for the assembly and structural characterization of an ultrathin silica membrane with embedded molecular wires established, the next task is to evaluate and improve the efficiency of hole charge transfer from the light absorber through the ultrathin silica membrane to the $Co_3O_4$ catalyst on the other side, and to elucidate the mechanism. Short-circuit photocurrent measurements offer the most sensitive method for quantifying charge transport, whereas gaining a detailed mechanistic understanding relies on observations by ultrafast optical spectroscopy. Results of these studies are presented below in turn.

### 11.5.1 Short-circuit Photocurrent Measurements

Pt-supported planar layers of $Co_3O_4$ covered with an $SiO_2$ membrane with embedded molecular wires served as working electrodes for short-circuit photocurrent measurements. Whereas robust heterobinuclear MMCT units will be utilized as light absorbers in the nanotube arrays for which the moderate visible extinction coefficient of these units is properly matched with the high surface area nanostructure for efficient solar light absorption, stronger light absorbers are required for photocurrent measurements of planar substrates with sub-monolayer coverage. To this end, familiar carboxyl-derivatized $[Ru(bpy)_2(dcbpy)]^{2+}$ complexes[56] were attached to the silica surface *via* an amide bond to randomly anchored TMSA, as shown in schematically Figure 11.12a, and monitored by FT-IRRAS.[32] These anchored light absorbers were also used in initial experiments with the nanotube arrays (Figure 11.11a, traces 4 and 5).

Charge transfer across the ultrathin silica membrane was induced by metal-to-ligand charge-transfer (MLCT) excitation of the anchored Ru complex at 476 nm in the presence of an $S_2O_8^{2-}$ sacrificial electron acceptor (1 M), generating oxidized $[Ru^{III}(bpy)(dcbpy)]^{3+}$ poised to inject hole charge into embedded TMS-Am-PV3-$SO_3$ wire molecules that resulted in a short-circuit cathodic photocurrent upon transfer to $Co_3O_4$ and Pt (Figure 11.12a). Figure 11.12b, red trace 1, shows a Faradaic photocurrent of 15.5 nA $cm^{-2}$ (476 nm, 121 mW $cm^{-2}$), whereas no Faradaic current was observed under identical conditions for a working electrode with the same composition but no wires embedded in the silica (Figure 11.12b, black curve 2). For the latter, only a capacitive cathodic photocurrent caused by the buildup of oxidized $[Ru^{III}(bpy)_2(dcbpy)]^{3+}$ complex on the silica surface

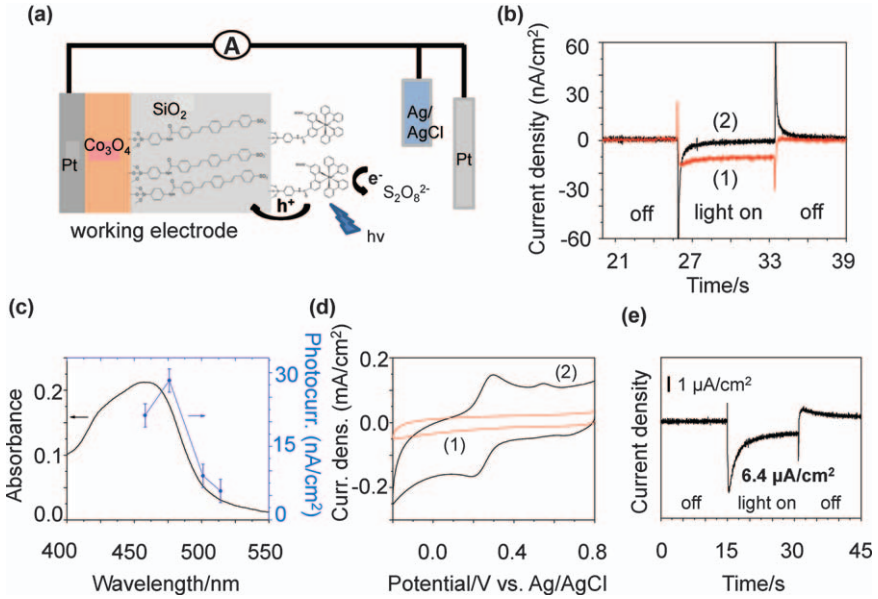


**Figure 11.12** (a) Three-electrode short-circuit photocurrent measurement. Pt wires and Ag/AgCl were used as counter and reference electrodes, respectively. Schematic diagram of the Pt working electrode featuring deposited $Co_3O_4$ with an ultrathin silica membrane with embedded TMS-Am-PV3-$SO_3$ wires and covalently attached light absorbers. (b) Trace 1: Pt/$Co_3O_4$/TMS-Am-PV3-$SO_3$/$SiO_2$/TMS-Am-Ru. Trace 2: Pt/$Co_3O_4$/$SiO_2$/TMS-Am-Ru (no wires in membrane). The circuit is held at an applied potential equal to the measured open-circuit potential. (c) Wavelength dependence of photocurrent (92 mW $cm^{-2}$). (d) Trace 1: CV with Pt/$Co_3O_4$/TMS-Am-PV3-$SO_3$/$SiO_2$ working electrode: $Fe(CN)_6^{3-}$, $1.0\times10^{-3}$ M; KCl electrolyte, 0.1 M; scan rate, 20 mV $s^{-1}$. Trace 2: CV of the same sample after deliberately introducing pinholes. (e) Short-circuit photocurrent of Pt/$Co_3O_4$/TMS-Am-PV3-$SO_3$/$SiO_2$/TMS-Am-Ru/$TiO_2$ sample upon 476 nm illumination (2580 mW $cm^{-2}$), 2.2 A-PV3-$SO_3$ $nm^{-2}$, 2.7 Ru $nm^{-2}$.
Reproduced from ref. 32 with permission from American Chemical Society, Copyright 2021.

was noted. This shows that photocurrent flows only through embedded molecular wires. The exclusive role of the embedded wires for charge transfer was demonstrated with much higher sensitivity when using an orders of magnitude higher concentration of $[Ru(bpy)_3]^{2+}$ dissolved in the electrolyte.[32] The wavelength dependence of the photocurrent confirmed that the Ru complex is the sole light absorber responsible for the observed photocurrent (Figure 11.12c), which rules out any contribution of photons absorbed by $Co_3O_4$. Furthermore, samples with or without silica-embedded wires were found to be free from pinholes, which we routinely verify by the absence of waves in CV sweeps using standard redox couples (Figure 11.12d).

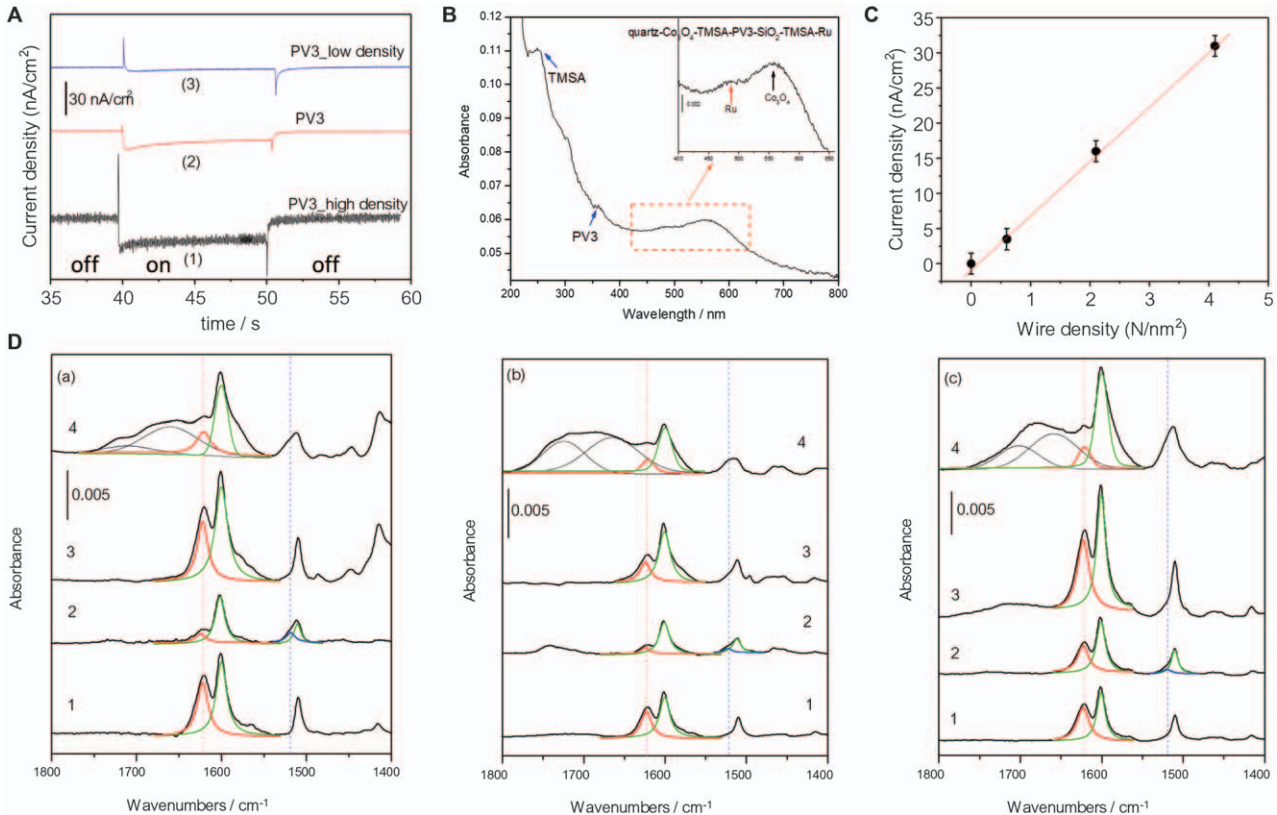
A
Current density (nA/cm²)
PV3_low density
(3)
30 nA/cm²
PV3
(2)
PV3_high density
off
on
(1)
off
time / s
B
Absorbance
quartz-Co3O4-TMSA-PV3-SiO2-TMSA-Ru
TMSA
PV3
Ru
Co3O4
Wavelength / nm
C
Current density (nA/cm²)
Wire density (N/nm²)
D
(a)
(b)
(c)
0.005
Absorbance
Wavenumbers / cm⁻¹

The quantitative assessment of molecular wire and light-absorber loading by FT-IRRAS and UV–visible spectroscopy allows a stepwise improvement of charge flux through the silica membrane by exploring various parameters, including mainly the density of embedded wire molecules. Figure 11.13A shows the increase in hole charge photocurrents with increase in wire density, from 3.3 nA $cm^{-2}$ for 0.6 A-PV3-$SO_3$ $nm^{-2}$ (trace 3) to 16.2 nA for 2.1 $nm^{-2}$ (trace 2), to 27.4 nA for 4.1 $nm^{-2}$ (trace 1). Wire densities were determined by recording the UV–visible spectrum of a $Co_3O_4$/TMS-Am-PV3-$SO_3$/$SiO_2$/TMS-Am-Ru sample deposited on a quartz slide, shown in Figure 11.13B, and FT-IRRAS of a sample with an identical composition deposited on Pt [Figure 11.13D(b)]. Using the known extinction coefficient of the TMSA anchor band at 246 nm ($\varepsilon = 13\,400$ L $mol^{-1}$ $cm^{-1}$,),[27] a surface density of 3.0 TMSA $nm^{-2}$ was calculated, which corresponds to an absorbance of $1.84\times10^{-3}$ for the 1510 $cm^{-1}$ band of the anchor. Based on this result, an A-PV3-$SO_3$ wire density of 2.1 $nm^{-2}$ was determined by measuring the decrease in absorbance of the $NH_2$ mode of the TMSA anchor at 1621 $cm^{-1}$ upon amide bond formation with the wire molecule [trace 2 in Figure 11.13D(b)]. Similarly, a light-absorber density of 1.0 $[Ru(bpy)_2(dcbpy)]^{2+}$ $nm^{-2}$ was calculated by measuring the decrease in the $NH_2$ band of TMSA anchored on the silica surface upon amide bond formation with the carboxyl group of $[Ru(bpy)_2(dcbpy)]^{2+}$ [traces 3 and 4 in Figure 11.13D(b)]. This method afforded an accurate comparison of the wire and light-absorber densities of all samples used in photocurrent experiments.

As shown in Figure 11.13C, the short-circuit photocurrent increases linearly with increase in wire density, consistent with the stronger electronic coupling and lower reorganization energy that result from a shortened average spatial separation of anchored light absorber and ring 3 of the embedded wire molecule.[57] Because the integrity of the silica separation membrane for blocking $O_2$ and other small molecules would degrade at higher embedded wire densities, the optimum wire density was determined as 4–5 $nm^{-2}$.

An equally influential factor that determines the efficiency of charge transfer across the ultrathin silica membrane is the energy-level alignment

**Figure 11.13** (A) Short-circuit photocurrent of $Co_3O_4$/TMS-Am-PV3-$SO_3$/$SiO_2$/TMS-Am-Ru samples with a wire density of (1) 4.1, (2) 2.1, and (3) 0.6 $nm^{-2}$; $S_2O_8^{2-}$, 1 M; 476 nm, 121 mW $cm^{-2}$. (B) Wire density dependence of photocurrent. (C) UV–visible spectra measured in transmission mode using an integrated sphere module (collection of scattered probe light and light in the direction of the incident beam). Inset: expanded region of $[Ru(bpy)_2(dcbpy)]^{2+}$ MLCT absorption. (D) FT-IRRAS for determining the wire and light-absorber density of each sample. (a) 4.1 A-PV3-$SO_3$ $nm^{-2}$, 2.8 Ru $nm^{-2}$; (b) 2.1 A-PV3-$SO_3$ $nm^{-2}$, 1.0 Ru $nm^{-2}$; (c) 0.6 A-PV3-$SO_3$ $nm^{-2}$, 3.7 Ru $nm^{-2}$. (1) $Co_3O_4$/TMSA; (2) $Co_3O_4$/TMS-Am-PV3-$SO_3$; (3) $Co_3O_4$/TMS-Am-PV3-$SO_3$/$SiO_2$/TMSA; (4) $Co_3O_4$/TMS-Am-PV3-$SO_3$/$SiO_2$/TMS-Am-Ru.
Reproduced from ref. 32 with permission from American Chemical Society, Copyright 2021.

of light absorber, embedded wire, and $Co_3O_4$ catalyst, as illustrated in the energy-level diagram in Figure 11.5. Fine tuning of the HOMO potential of the molecular wire permits optimization of the energy pathway for hole hopping from the excited light absorber *via* embedded wire to Co oxide. According to the HOMO potentials calculated by DFT, photocurrent measurements with the three chosen wires for click attachment featuring electron-withdrawing or -donating substituents, together with the amide-linked PV3 result, should allow us to identify the wire with optimum energy-level alignment. For samples with triazole-linked E-PV3-$SO_3$Et with a wire density of 0.7 $nm^{-2}$ (Figure 11.7, trace 1), a short-circuit photocurrent of 39.0 $nA\,cm^{-2}$ is observed (Figure 11.14a, trace 1). An $[Ru(bpy)_2(dcbpy)]^{2+}$ density of 3.6 $nm^{-2}$ was determined from the fractional absorbance decrease of the 1621 $cm^{-1}$ $NH_2$ mode of TMSA upon surface attachment recorded by FT-IRRAS, shown in Figure 11.14b. Normalized for the same wire density of 0.6 $nm^{-2}$ of the A-PV3-$SO_3$ sample, the initial photocurrent for E-PV3-$SO_3$Et is 10 times higher than the 3.3 $nA\,cm^{-2}$ measured for amide-attached A-PV3-$SO_3$ (Figure 11.14c). This large difference is attributed to the 0.32 V stronger driving force for charge transfer from Ru light absorber to triazole-attached wire HOMO (Figure 11.5, step 1).

A distinct aspect of the photocurrent behavior of samples with E-PV3-$SO_3$Et wires is that the current decreases appreciably within a few seconds (Figure 11.14a, trace 1). This phenomenon is related to the observation of an anodic capacitive photocurrent spike at onset of illumination for samples with A-PV3-$SO_3$, as can be seen in Figure 11.13A, which is due to the accumulation of reduced $[Ru^{I}(bpy)_2(dcbpy)]^{+}$. The surge of reduced light absorber indicates slow replacement of $SO_4^{2-}$, generated upon electron transfer from excited $[Ru^{II}(bpy)_2(dcbpy)]^{2+}$ to $S_2O_8^{2-}$, compared with the rate of photoexcitation of a given Ru complex. As a result, a repeatedly excited Ru complex transfers hole charge to embedded wires but is prevented from electron transfer, $S_2O_8^{2-}$ thereby remaining in the reduced state until fresh persulfate diffuses into electron transfer distance (~1 nm) near the surface. For membranes with wires whose HOMO potential is significantly more positive than the $Co_3O_4$ valence band maximum, such as is the case for A-PV3-$SO_3$ (Figure 11.5), the consequence is a diminished but otherwise stable Faradaic photocurrent. For samples featuring embedded wires whose HOMO is close to the $Co_3O_4$ valence band maximum, the hole charge density accumulating on the $Co_3O_4$ catalyst during illumination is delocalized into the embedded PV3 wire pool. This results in recombination with the electron on excited $[Ru(bpy)_2(dcbpy)]^{2+}$, thereby reducing the collection of photogenerated hole charges at the working electrode. Because the $S_2O_8^{2-}$ concentration in the vicinity of the silica surface decreases after onset of illumination, there is a concurrent increase in reduced $[Ru^{I}(bpy)_2(dcbpy)]^{+}$ density, which explains the decay of the Faradaic current seen in Figure 11.14a. As expected, application of a modest negative potential of 100 mV diminishes the delocalization of hole charge into the wires and therefore slows the photocurrent decay, and no decay is observed for an

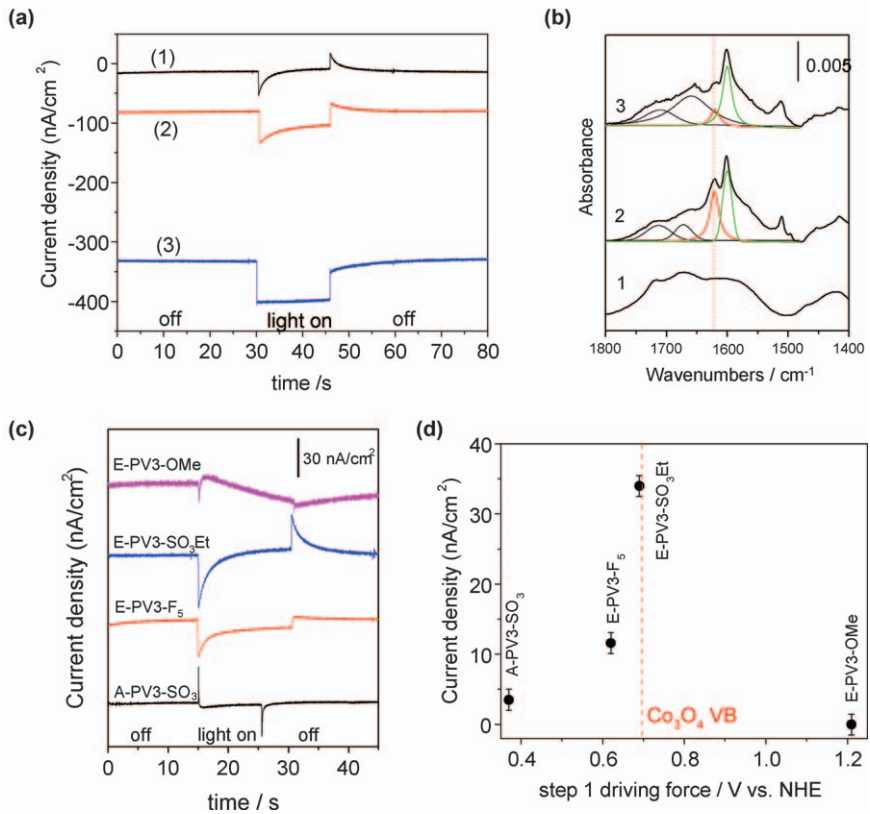


**Figure 11.14** (a) Short-circuit photocurrent of $Co_3O_4$/TMSB-Tz-PV3-$SO_3$Et/$SiO_2$/TMS-Am-Ru samples with a wire density 0.7 $nm^{-2}$ and an $[Ru(bpy)_2(dcbpy)]^{2+}$ density of 3.6 $nm^{-2}$. Trace 1: the circuit is held at an applied potential equal to the measured open-circuit potential (OCP). Trace 2: −0.1 V *vs.* OCP. Trace 3: −0.2 V *vs.* OCP. $S_2O_8^{2-}$, 1 M; 476 nm, 80 mW. (b) FT-IRRAS of the TMSA anchor on $SiO_2$ and $[Ru(bpy)_2(dcbpy)]^{2+}$ attachment: 5.4 TMSA $nm^{-2}$, 3.6 $[Ru(bpy)_2(dcbpy)]^{2+}$ $nm^{-2}$. Trace 1: Pt/$Co_3O_4$/TMSB-Tz-PV3-$SO_3$Et/$SiO_2$. Trace 2: after anchoring of TMSA. Trace 3: after attachment of $[Ru(bpy)_2(dcbpy)]^{2+}$. (c) Photocurrent of $Co_3O_4$/wire/$SiO_2$/TMS-Am-Ru. Top to bottom: E-PV3-OMe (0.5 $nm^{-2}$), 1.2 Ru $nm^{-2}$; E-PV3-$SO_3$Et (0.7 $nm^{-2}$), 3.6 Ru $nm^{-2}$ (from Figure 11.7a, trace 1); E-PV3-$F_5$ (1.46 $nm^{-2}$), 6.5 Ru $nm^{-2}$; A-PV3-$SO_3$ (0.6 $nm^{-2}$), 3.7 Ru $nm^{-2}$ (from Figure 11.13A, trace 3). (d) Photocurrent dependence on the HOMO potential of the embedded wire molecule, normalized for a wire density of 0.6 $nm^{-2}$.
Reproduced from ref. 32 with permission from American Chemical Society, Copyright 2021.

applied potential of –200 mV, as shown by traces 2 and 3 in Figure 11.14a. The same process explains the observed small dependence of light-absorber density of the photocurrent;[32] the buildup of reduced $[Ru^I(bpy)_2(dcbpy)]^+$

density upon illumination of samples with increased light-absorber density amplifies the recombination of hole charges injected into embedded wires with reduced $[Ru^{I}(bpy)_2(dcbpy)]^+$. The net effect is only a minor influence on the photocurrent despite the increased density of excited Ru complexes for higher light-absorber density.

Corresponding short-circuit photocurrent measurements for click-attached wires with electron-withdrawing substituents, E-PV3-$F_5$, and donating group, E-PV3-OMe, are also presented in Figure 11.14c. The comparison of the short-circuit photocurrent of 28.8 nA cm$^{-2}$ for the E-PV3-$F_5$ sample (1.46 nm$^{-2}$) and 39.0 nA cm$^{-2}$ for the E-PV3-$SO_3$Et sample, when normalized for wire density, gives a 2.9-fold higher charge flux for the E-PV3-$SO_3$Et sample for a 70 mV more negative HOMO potential. As can be seen in Figure 11.14c, the Faradaic photocurrent for the E-PV3-$F_5$ sample decreases significantly within a few seconds after onset of illumination. As in the case of E-PV3-$SO_3$Et, applying a negative potential of ~200 mV suppressed the photocurrent decay. In contrast, no short-circuit photocurrent was measured for a sample with embedded E-PV3-OMe wire. With a density of 0.5 E-PV3-OMe nm$^{-2}$, which is close to the density of E-PV3-$SO_3$Et, and taking into account the uncertainty of 1.5 nA for the photocurrent measurement, we calculate that the charge flux decreases from the E-PV3-$SO_3$Et sample to the E-PV3-OMe sample by a factor of 20 or larger (lower limit). Because the driving force for hole charge transfer from the Ru complex to the wire HOMO increases by 0.52 V from sulfonic ester- to methoxy-substituted wire, and therefore would be expected to result in strongly enhanced rather than suppressed photocurrent, the observed opposite trend is attributed to a strongly endoergic (uphill) process that essentially blocks hole transfer from the wire HOMO to $Co_3O_4$ (Figure 11.5). It is concluded from the observed photocurrent trends that for PV3-type wire molecules, those with a HOMO potential of around +1.3 V *vs.* NHE are optimal for efficient hole charge transfer from light absorbers with a potential of +1.8 V *vs.* NHE to a $Co_3O_4$ catalyst.

The observed short-circuit photocurrent behavior as a function of the HOMO potential of the embedded molecular wire, summarized in Figure 11.14d, reveals the critical importance of the energy-level alignment of light absorber and catalyst with the wires for achieving maximum charge flux. Given the structural characteristics of the various wires, which for the case of click-attached wires includes identical tripodal anchors on $Co_3O_4$, an identical triazole linkage, and the same PV3 molecular backbone, it is reasonable to assume that differences in the electronic coupling and the reorganization energy for hole transfer from the excited Ru complex to the embedded wire (Figure 11.5, step 1) are small compared with the driving force for this process.[57] Therefore, the large increase in the photocurrent from A-PV3-$SO_3$ to E-PV3-$F_5$ and to E-PV3-$SO_3$Et is principally attributed to the driving force increase (free-energy change) of hole transfer step 1, which is estimated as the difference between the HOMO potential of the wire and the redox potential of the light absorber. In contrast, the sharp decrease in

the charge flux for E-PV3-OMe stems from the substantial energy cost of close to 0.5 V for hole transfer from the embedded wire to $Co_3O_4$ (Figure 11.5, hole transfer step 2).

As mentioned above, a repeatedly excited Ru complex can transfer hole charge to embedded wires but remains in the reduced $[Ru^{I}(bpy)_2(dcbpy)]^{+}$ state until fresh $S_2O_8^{2-}$ diffuses sufficiently close for electron transfer to proceed. Strong support for attributing the observed small short-circuit photocurrent of tens of nA $cm^{-2}$ to slow replacement of consumed $S_2O_8^{2-}$ acceptor at the silica/electrolyte interface was obtained by photocurrent measurements of samples for which the anchored $[Ru(bpy)_2(dcbpy)]^{2+}$ was encapsulated in a 5 nm thick $TiO_2$ layer deposited by ALD. It is well established that anchored Ru bipyridyl complexes transfer electrons very efficiently to the $TiO_2$ conduction band on an ultrafast timescale.[58] Therefore, by inserting a $TiO_2$ nanolayer between the Ru light absorber and the persulfate electrolyte, efficient electron transfer from MLCT-excited $[Ru(bpy)_2(dcbpy)]^{2+}$ to the $TiO_2$ conduction band is achieved, which is followed by electron capture by $S_2O_8^{2-}$ that competes with the comparatively slow back transfer of $TiO_2$ conduction band electrons to the oxidized $Ru^{3+}$ center (multiphasic decay of tens to hundreds of microseconds).[59,60] For the $Co_3O_4$/TMS-Am-PV3-$SO_3$/$SiO_2$/TMS-Am-Ru/$TiO_2$ sample, the photocurrent after the start of 476 nm illumination at 216 mW $cm^{-2}$ was 615 nA $cm^{-2}$, exceeding the initial photocurrent of a $Co_3O_4$/TMS-Am-PV3-$SO_3$/$SiO_2$/TMS-Am-Ru sample (no $TiO_2$ layer) of similar wire density by a factor of 21 (normalized for the 476 nm laser intensity). Hence, the visible light-driven charge flux through the silica membrane *via* embedded wires by illumination of anchored light absorbers is limited by the efficiency of electron transfer from the excited Ru complex to the oxidizing agent, which is much higher for the case of the $TiO_2$ conduction band. On increasing the laser intensity from 216 to 2580 mW $cm^{-2}$ (a factor of 11.9), the current density increased by a factor of 10.4 to 6.370 μA $cm^{-2}$, as shown in Figure 11.12e (the decrease to a steady-state photocurrent of 1.2 μA $cm^{-2}$ within a few seconds is again due to the depletion of $S_2O_8^{2-}$ acceptor ions at the $TiO_2$/electrolyte interface upon continued photolysis). Taking into account the 20-fold larger photocurrent for silica membranes featuring wires with optimized energy-level alignment and wire density (E-PV3-$SO_3$Et, 5 $nm^{-2}$), a photocurrent of 0.1 mA $cm^{-2}$ is achievable (planar sample geometry). This implies a photocurrent density of 10 mA $cm^{-2}$ for a core–shell nanotube array because the effective surface area of this nanostructured material exceeds the projected area by a factor of 100, which is sufficient for the charge flux to keep up with the photon flux at maximum solar intensity.[15]

## 11.5.2 Ultrafast Optical Spectroscopy

For time-resolved optical monitoring of hole transfer from a visible light absorber *via* a wire embedded in the silica membrane to the $Co_3O_4$ catalyst core, ultrafast time resolution capable of resolving events on the

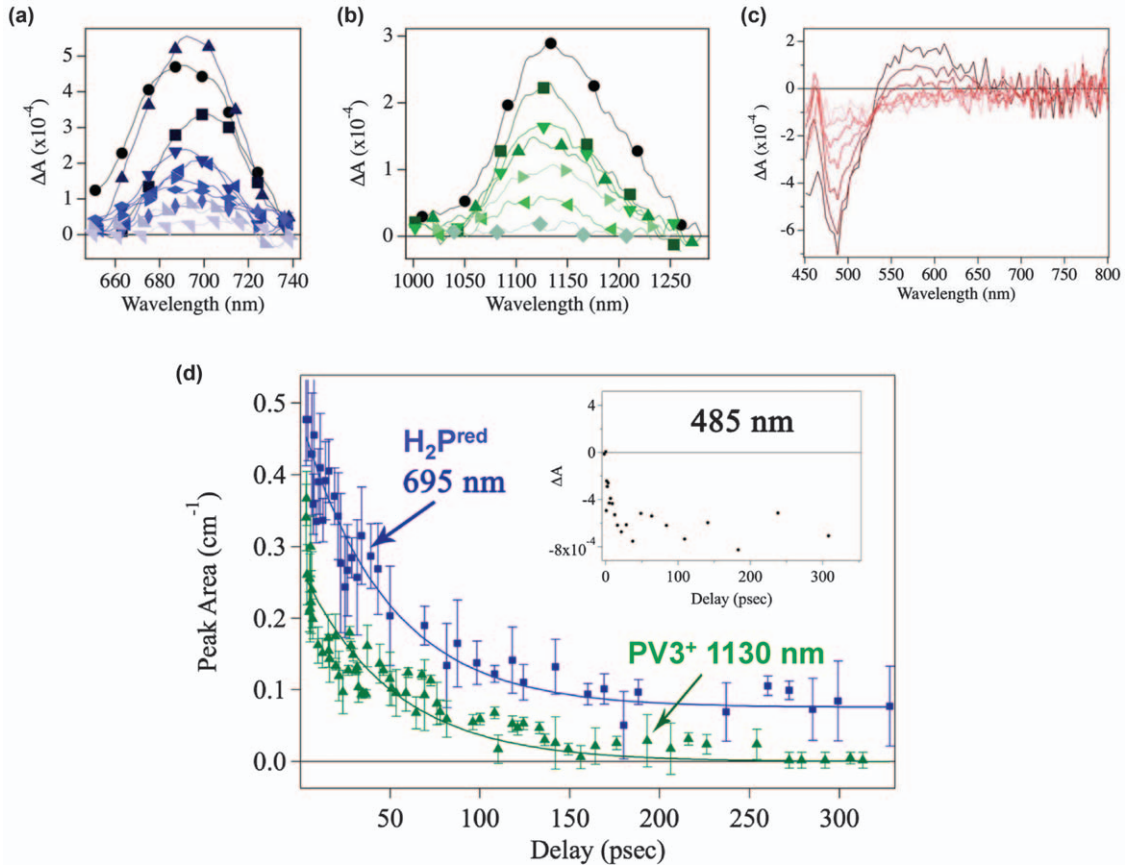
(a)
ΔA (x10$^{-4}$)
Wavelength (nm)
(b)
ΔA (x10$^{-4}$)
Wavelength (nm)
(c)
ΔA (x10$^{-4}$)
Wavelength (nm)
(d)
Peak Area (cm$^{-1}$)
Delay (psec)
$H_2P^{red}$
695 nm
PV3$^+$ 1130 nm
485 nm
ΔA
Delay (psec)

sub-picosecond timescale is needed because nanosecond absorption spectroscopy used in initial studies proved too slow for the detection of transient holes on PV3 molecules.[28,29] Interpretation and analysis of ultrafast spectroscopic data require a chromophore with an established spectroscopic signature on femto- and picosecond timescales. A metal-free porphyrin with positively charged ligands for strong adsorption on the (negatively polarized) silica shell surface possesses these properties, including an appropriate redox potential for hole transfer to PV3 molecules.[61] Furthermore, the high surface area of aqueous colloids of spherical core–shell nanoparticles is most suitable for obtaining the required spectral sensitivity for transient absorption spectroscopy on the femto- and picosecond timescales. Excitation of porphyrins anchored on a $Co_3O_4$–$SiO_2$ core–shell nanoparticle with embedded wire molecules into its strong band at 430 nm with laser pulses of 150 fs duration resulted in hole transfer to A-PV3-$SO_3$ within a few hundred femtoseconds. This is manifested by the characteristic transient absorption of reduced porphyrin radical anion with a peak at 695 nm ($H_2P^{red}$, Figure 11.15a) and PV3 radical cation ($PV3^+$, Figure 11.15b) at 1130 nm. The sub-picosecond arrival of the charge on the embedded wire is followed by decay on the tens of picoseconds timescale due to hole transfer to the $Co_3O_4$ catalyst, which competes with charge recombination with reduced light absorber (no electron acceptor is present in this experiment). The kinetics of $PV3^+$ and $H_2P^{red}$ decay are presented in Figure 11.15d. The hole charge arriving on $Co_3O_4$ is manifested by a bleach with a maximum at 485 nm. The dark red trace in Figure 11.15c shows the corresponding spectral trace at 1.04 ns, and the inset in Figure 11.15d indicates the growth kinetics of the bleach on the hundreds of picoseconds timescale. Kinetic analysis of the charge-transfer system reveals a hole charge-transfer time of 255 ps from the embedded wire to $Co_3O_4$,[61] whereas recombination with the electron on the reduced light absorber proceeds on an orders of magnitude slower timescale, as shown by the decay of the 485 nm bleach in Figure 11.15c. Importantly, the 255 ps hole transfer across the silica membrane is fast enough to outcompete ever-present diversionary charge-transfer processes that

**Figure 11.15** Transient optical absorption spectroscopy of visible light-induced hole transfer from a surface-anchored porphyrin light absorber to a $Co_3O_4$ catalyst *via* $SiO_2$-embedded PV3 wires (excitation at 430 nm with a 150 fs pulse). (a) Transient absorption of reduced porphyrin ($H_2P^{red}$, 695 nm). Selected spectral traces of the decay are shown, the detailed kinetics of which are presented in panel (d). (b) Transient absorption and decay of hole charge on wire ($PV3^+$, 1130 nm). (c) Hole charge on $Co_3O_4$ (bleach at 485 nm). The spectral traces depict the decay of the charge on the hundreds of nanoseconds timescale: From dark to light red: 1.04, 2.55, 4.95, 10.6, 24.6, 113, 2060 ns. (d) Decay of $PV3^+$ and $H_2P^{red}$ species. The inset shows the growth kinetics of the 485 nm bleach upon hole transfer from embedded $PV3^+$ to $Co_3O_4$.
Reproduced from ref. 61 with permission from American Chemical Society, Copyright 2017.

otherwise would degrade the productive use of the separated charges.[61] Given the long lifetime (1 μs) of excited TiOCo and ZrOCo units, similarly favorable hole charge-transfer kinetics are expected for systems featuring these target light absorbers.[27,62]

## 11.6 Proton Transport Through Membranes

Light-driven $H_2O$ oxidation to generate the electrons needed for $CO_2$ reduction is accompanied by the production of four $H^+$ ions per $O_2$ molecule, which react at catalytic sites for $CO_2$ reduction to form the C–H bonds of hydrocarbon products, or O–H bonds when generating CO. Therefore, the protons need to diffuse through the core–shell nanowall at a sufficiently high rate so as not to pose a kinetic bottleneck for the photocatalytic efficiency at maximum solar intensity. Using planar ultrathin oxide layers on a Pt electrode as described in Section 11.4.1 (characterized as shown in Figure 11.8), $H^+$ transport through silica layers was monitored by FT-IRRAS of Pt–H formed upon $H^+$ arrival at the silica/Pt interface ($H^+ + Pt \rightarrow Pt\text{–}H$, denoted H underpotential deposition).[63,64] Quantitative evaluation of the $H^+$ flux through single $SiO_2$, $Co_3O_4$, and $TiO_2$ layers and stacked multilayers was conducted by electrochemical impedance spectroscopy (EIS).

### 11.6.1 Monitoring the Proton Flux Across $SiO_2$ Nanolayers *Via* FT-IRRAS Isotope Tracing

FT-IRRAS affords tracing of $H^+$ and $D^+$ upon cyclic voltammetric (CV) sweeps in the range 1.2–0.02 V (*vs.* RHE), which allowed us to substantiate proton transfer through the amorphous $SiO_2$ nanolayer. Following the electrochemical measurement, the Pt/$SiO_2$ sample was dried with an Ar flow and transferred air-tight to the $N_2$-purged FT-IR spectrometer for IRRAS measurements. Figure 11.16a shows the growth of the Pt–H stretch mode at 2090 $cm^{-1}$ using a Pt/$SiO_2$ (6 nm) sample as the working electrode in the standard three-electrode cell configuration containing $N_2$-purged pH 4 electrolyte. The spectral identification was confirmed by switching to $D_2O$ electrolyte, with the 1470 $cm^{-1}$ Pt–D mode replacing Pt–H (Figure 11.16b).[23] The characteristic $H_2O$ bands at 1635 and 3500 $cm^{-1}$ are completely absent, indicating that no water molecules are trapped at the Pt/$SiO_2$ interface, and no hydration of the amorphous $SiO_2$ film occurs during the $H^+$ transfer. While the IRRAS measurements were conducted *ex situ* after drying of the Pt/$SiO_2$ sample, even the application of very short drying periods that are just sufficient to remove $H_2O$ at the outer $SiO_2$ surface did not show any residual $H_2O$ IR bands. Therefore, these findings are consistent with the conclusion that the growth of the Pt–H (Pt–D) band by H (D) underpotential deposition originates from the reduction of protons transferred from the pH 4 (pD 4) aqueous electrolyte through the conformal amorphous $SiO_2$ nanolayer to the Pt surface, rather than from the reduction of trapped $H_2O$ ($D_2O$) molecules.

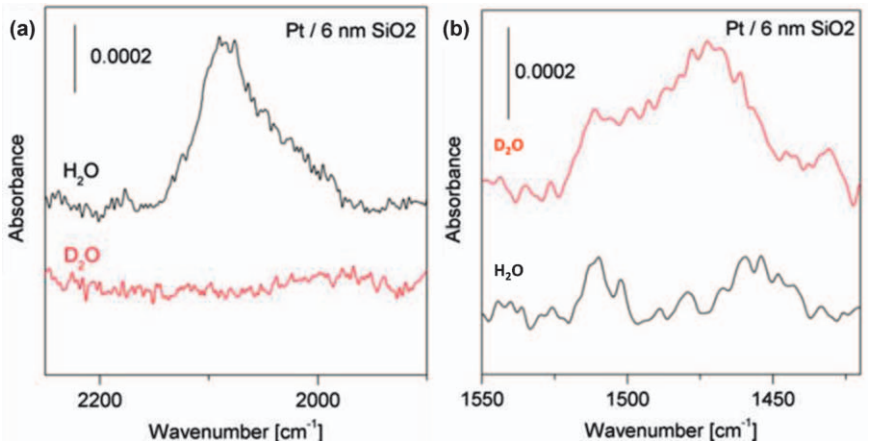


**Figure 11.16** FT-IRRAS of Pt–H and Pt–D growth observed following CV sweeps in pH 4 (pD 4) aqueous electrolyte. (a) Top trace: growth of Pt–H mode recorded after CV sweeps of a $Pt/SiO_2$ (6 nm) electrode in $H_2O$ in the range 1.2–0.02 V *vs.* RHE. Bottom trace: the same experiment in $D_2O$. (b) Spectra in the 1550–1425 $cm^{-1}$ range of the samples shown in (a). Top trace: growth of Pt–D mode after CV sweeps of a $Pt/SiO_2$ (6 nm) electrode in $D_2O$. Bottom trace: the same experiment in $H_2O$. Reproduced from ref. 23 with permission from John Wiley & Sons, Copyright © 2020 WILEY-VCH Verlag GmbH & Co. KGaA, Weinheim.

This observation is important for the understanding of $H^+$ transport through $SiO_2$ ALD layers because, for identical H underpotential deposition experiments with bare Pt at pH between 3 and 11, simulations reported in the literature indicate that $H_2O$ molecules are reduced at the Pt/aqueous interface.[65]

### 11.6.2 Electrochemical Characterization of Proton Flux and $O_2$ Impermeability of Single $SiO_2$ Nanolayers

We electrochemically characterized the $H^+$ transfer and $O_2$ impermeability of single $SiO_2$ nanolayers by using 2, 4, and 6 nm thick amorphous $SiO_2$ coatings deposited on Pt samples as working electrodes under the same experimental conditions as described above. The red CV wave for the 2 nm $SiO_2$ sample in Figure 11.17a displays a cathodic current in the range 0.4–0 V *vs.* RHE due to $H_{upd}$ at the $Pt/SiO_2$ interface. The curve closely resembles that of bare Pt (black trace), but exhibits somewhat larger $H_{upd}$ and Pt oxide features, the origins of which have been evaluated and explained in detail by Beatty *et al.*[66] CV sweeps with the identical $Pt/SiO_2$ samples in $O_2$-bubbled electrolyte solution showed only the $H_{upd}$ signal without an $O_2$ reduction wave compared with bare Pt (Figure 11.17b). These measurements reveal that an ALD-grown, pinhole-free $SiO_2$ layer of 2 nm thickness or larger completely blocks $O_2$ diffusion.

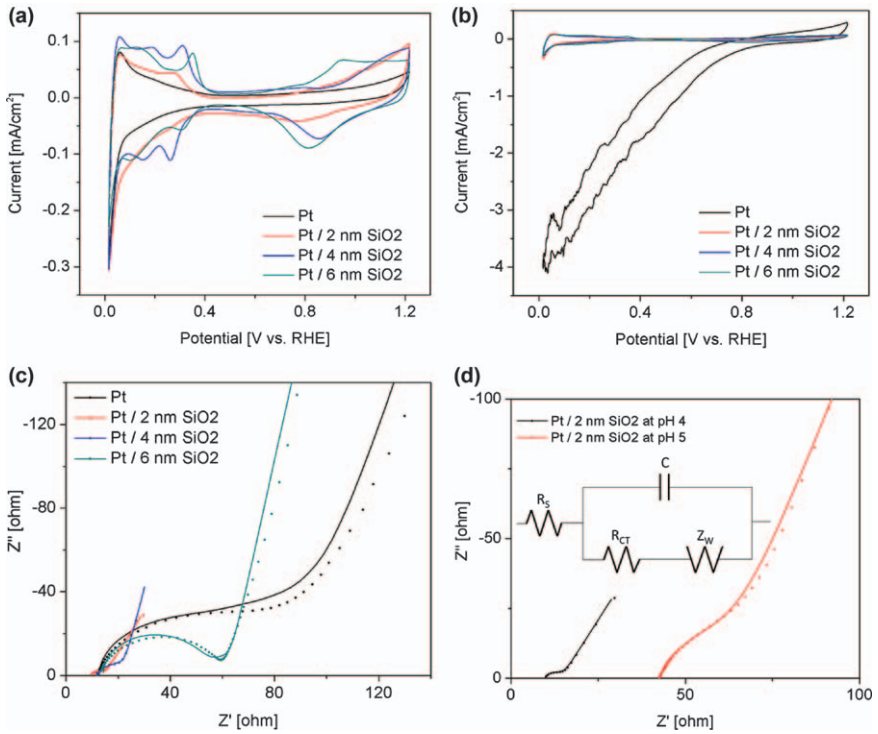


**Figure 11.17** (a) CV of a bare Pt electrode (black trace) and Pt covered with 2, 4, and 6 nm $SiO_2$ (red, blue, and green traces) at 298 K in $N_2$-saturated aqueous 0.5 M $Na_2SO_4$ solution at pH 4, adjusted with $H_2SO_4$. Scan rate, 50 mV $s^{-1}$. (b) CV in $O_2$-bubbled electrolyte solution under the same conditions. (c) EIS in $N_2$-saturated pH 4 electrolyte solution used for (a). Applied potential, 0.096 *vs.* RHE. The dots in the plot are the experimental data and the solid lines represent the results of fitting the data to the equivalent circuit (Randles circuit) shown in the inset of (d). (d) EIS of a Pt/$SiO_2$ (2 nm) electrode in $N_2$-saturated aqueous solution at pH 5 and pH 4. Applied potential, 0.096 *vs.* RHE.
Reproduced from ref. 23 with permission from John Wiley & Sons, Copyright © 2020 WILEY-VCH Verlag GmbH & Co. KGaA, Weinheim.

For accurate proton flux measurements, we utilized EIS, the preferred AC electrochemical method for monitoring the transfer and reaction rates of ion species.[67] Experiments were carried out at a potential of 0.096 V *vs.* RHE, which falls within the range where underpotential H adsorption occurs. Figure 11.17c presents Nyquist plots for 2, 4, and 6 nm $SiO_2$ ALD layers. Within this figure, the semicircle region of the Nyquist plot represents charge-transfer resistance, and the linear region at low frequencies signifies mass-transfer impedance across the $SiO_2$-coated Pt electrode.[67] According to the FT-IRRAS results, the IR growth of Pt–H upon $H_{upd}$ originates from the reduction of protons transferred from the pH 4 electrolyte through the conformal amorphous $SiO_2$ nanolayer to the Pt surface. An appropriate

equivalent circuit to quantify the $H^+$ flux from the electrolyte to the Pt surface *via* the ultrathin $SiO_2$ layer is the generalized Randles circuit shown in Figure 11.17d.[67–70] This circuit is described by the solution resistance $R_S$, the double-layer capacitance $C$ at the Pt/$SiO_2$ interface, the charge-transfer resistance $R_{CT}$ across the interface, and the mass-transfer impedance $Z_W$ (Warburg impedance) at the electrolyte/$SiO_2$ interface.[67,70,71] EIS data fitting gave $Z_W = 6.8\ \Omega$ for the 2 nm $SiO_2$ sample. Given the working electrode (WE) potential of $V = -0.36$ V (Ag/AgCl reference electrode) and neglecting the small charge-transfer resistance $R_{CT} = 2.5\ \Omega$, a cathodic current $I = V/Z_W = 0.053$ A was calculated.[72] With a WE surface area of 0.68 $cm^2$, this corresponds to a current density ($J$) of 0.078 A $cm^{-2}$. Therefore, the $H^+$ flux through the 2 nm $SiO_2$ layer under these conditions is 4900 $s^{-1}\,nm^{-2}$. The decrease in the $H^+$ flux to 1900 $s^{-1}\,nm^{-2}$ for an $SiO_2$ layer thickness of 4 nm and to 1240 $s^{-1}\,nm^{-2}$ for 6 nm agrees well with Fick's law,[67] as does the pH dependence of the $H^+$ flux (*e.g.* a factor of $10.7 \pm 4.0$ decrease from pH 4 to pH 5).[23] The agreements with Fick's law strongly support the choice of the Randles equivalent circuit and the Warburg impedance for determining the $H^+$ flux.

Analysis of the $H^+$ flux through $SiO_2$ revealed a proton mobility $\mu$ of $6.4\times10^9$ $nm^2\,s^{-1}\,V^{-1}$, corresponding to effective diffusivity $D$ of $1.6\times10^8$ $nm^2\,s^{-1}$ within the silica nanolayer. Details of the analysis are presented in ref. 23, based on equations given in ref. 73. For a comprehensive description of the fundamentals of species transport through oxide layers, the reader is referred to Chapter 7, Section 7.2, in this volume. This $D$ value is in good agreement with the theoretical value of $D = 1.7\times10^8$ $nm^2\,s^{-1}$ from molecular dynamics (MD) simulation reported for amorphous silica.[74] The activation energy $E_a$ associated with proton movement through the $SiO_2$ nanolayer for our experiments at pH 4 was determined as 5 kcal $mol^{-1}$. The mechanism of proton diffusion through amorphous silica is understood as proton hopping whereby $H^+$ ions transiently bind and dissociate from O atoms throughout the interior of the solid (Grotthuss mechanism). These oxygen sites are Si–O–Si (siloxane) bridges, SiOH (silanol) and SiO– (siloxy), all of which have been considered as part of the hopping pathway.[68,74] Hopping along strained Si–O–Si bridges (125–135°, unstrained angle 150°), which are abundant in amorphous silica, most likely plays a dominant role because *ab initio* calculations indicate a low activation barrier of around 5 kcal $mol^{-1}$,[69] in agreement with our experimental result.

### 11.6.3 Electrochemical Characterization of Proton Flux of Single $Co_3O_4$ and $TiO_2$ Nanolayers and Multi-oxide Stacked Nanolayers

Applying the EIS method for the evaluation of $H^+$ transport across $Co_3O_4$ catalyst layers using the same experimental conditions as for $SiO_2$ layers, a similarly high flux was observed for thicknesses in the range 3.5–12 nm, with

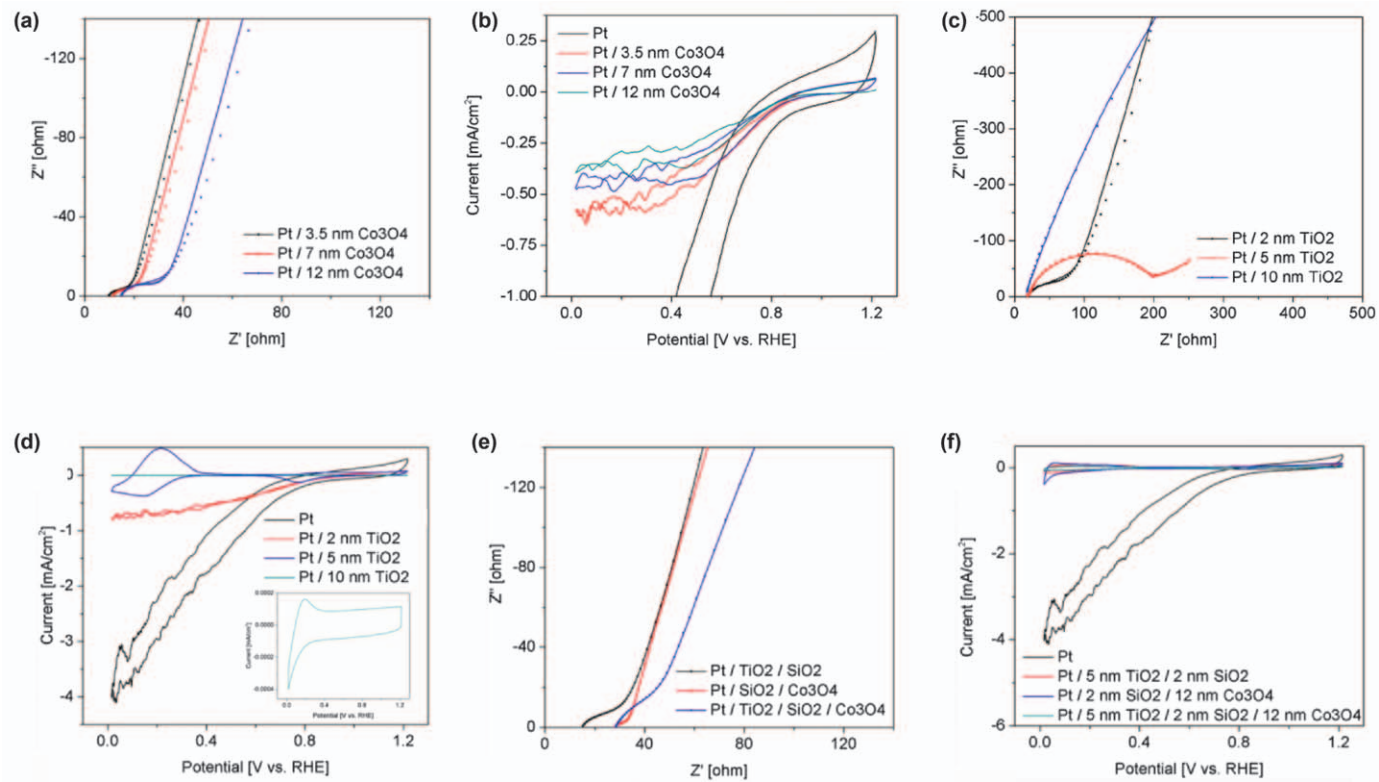
(a)
Z'' [ohm]
Z' [ohm]
Pt / 3.5 nm Co3O4
Pt / 7 nm Co3O4
Pt / 12 nm Co3O4
(b)
Current [mA/cm²]
Potential [V vs. RHE]
Pt
Pt / 3.5 nm Co3O4
Pt / 7 nm Co3O4
Pt / 12 nm Co3O4
(c)
Z'' [ohm]
Z' [ohm]
Pt / 2 nm TiO2
Pt / 5 nm TiO2
Pt / 10 nm TiO2
(d)
Current [mA/cm²]
Potential [V vs. RHE]
Pt
Pt / 2 nm TiO2
Pt / 5 nm TiO2
Pt / 10 nm TiO2
(e)
Z'' [ohm]
Z' [ohm]
Pt / TiO2 / SiO2
Pt / SiO2 / Co3O4
Pt / TiO2 / SiO2 / Co3O4
(f)
Current [mA/cm²]
Potential [V vs. RHE]
Pt
Pt / 5 nm TiO2 / 2 nm SiO2
Pt / 2 nm SiO2 / 12 nm Co3O4
Pt / 5 nm TiO2 / 2 nm SiO2 / 12 nm Co3O4

3240 $s^{-1}nm^{-2}$ for 3.5 nm and 950 $s^{-1}nm^{-2}$ for 12 nm, as shown in Figure 11.18a. In contrast to ultrathin silica layers, CV sweeps of $O_2$-bubbled solutions showed a substantial $O_2$ reduction current even for the $Co_3O_4$ (12 nm) layers (Figure 11.18b).

The proton conductivity of single $TiO_2$ nanolayers was found to be appreciable for the 5 nm sample (270 $s^{-1}nm^{-2}$) but to decrease sharply for thicker layers (Figure 11.18c). As will be shown next, the lower flux compared with $SiO_2$ and $Co_3O_4$ layers of similar thickness is due to inefficient $H^+$ transfer across the $TiO_2$ electrolyte interface, which is alleviated by replacing the aqueous interface with a $TiO_2/SiO_2$ interface. The $O_2$ permeability is also very limited for $TiO_2$ layers with thicknesses of 5 nm or greater (Figure 11.18d).

Most important for efficient photocatalytic performance of the core–shell nanotube is the $H^+$ flux through the stacked triple oxide layers that constitute the tube wall. Surprisingly, stacked $Co_3O_4/SiO_2/TiO_2$ layers of thickness 12/2/5 nm, which were found to provide stable core–shell nanotube arrays (Section 11.4.2), exhibit a high $H^+$ flux of 780 $s^{-1}nm^{-2}$. This is close to three times higher than that for single $TiO_2$ (5 nm) layers. Similarly, stacked $TiO_2/SiO_2$ layers show a similar flux increase to 880 $s^{-1}nm^{-2}$. Double-stacked $Co_3O_4$ (12 nm)/$SiO_2$ (2 nm) layers give 2520 $s^{-1}nm^{-2}$ (Figure 11.18e), which is a 2.6-fold enhancement compared with single $Co_3O_4$ (12 nm) layers. As expected, all stacked multi-oxide layers featuring an $SiO_2$ layer completely block $O_2$ (Figure 11.18f). Proton hopping along oxygens of interfacial SiOTi and SiOCo bridges uncovered by FT-IRRAS is the most likely origin of the enhancement upon incorporation of an $SiO_2$ nanolayer. The enhancement in the case of $Pt/TiO_2$ is due to the replacement of the $TiO_2$/electrolyte interface exhibiting inefficient $H^+$ transfer with the efficient $SiO_2$/electrolyte proton transfer interface and SiOTi bridges for low barrier hopping from $SiO_2$ to $TiO_2$. An analogous effect of interfacial SiOCo linkages explains the enhancement in the case of the $Pt/Co_3O_4/SiO_2$ stack. The findings reveal that an amorphous silica layer a few nanometers thick substantially boosts $H^+$ transfer across stacked multi-oxide layers.

**Figure 11.18** (a) EIS in $N_2$-saturated pH 4 electrolyte solution of Pt covered with 3.5, 7.0, and 12 nm $Co_3O_4$ (black, red, and green traces, respectively). (b) CV of the same solutions after $O_2$ bubbling. (c) EIS of $N_2$-saturated pH 4 electrolyte solution of Pt covered with 2, 5, and 10 nm $TiO_2$ (black, red, and blue traces, respectively). (d) CV of the same solutions after $O_2$ bubbling. (e) EIS of $N_2$-saturated pH 4 electrolyte solution of Pt covered with $TiO_2/SiO_2$ (black trace), $SiO_2/Co_3O_4$ (red trace), and $TiO_2/SiO_2/Co_3O_4$ (blue trace). (f) CV of the same solutions after $O_2$ bubbling. The small dots in the plots are the experimental data and the solid lines represent the results of fitting the data to the Randles circuit.

The observed proton conductivity and oxygen blocking capabilities of individual and stacked ultrathin oxide layers perfectly fit the requirements for complete nanoscale artificial photosystems with built-in membrane separation. Whereas the $SiO_2$ nanolayer completely blocks crossover of $O_2$, the oxygen permeability of ALD-grown $Co_3O_4$, which is consistent with its nanogranular nature offering grain boundary networks for both $O_2$ and $H^+$ diffusion (Section 11.4.2),[23] provides access to $H_2O$ and $O_2$ throughout the polycrystalline $Co_3O_4$ layer (a description of interfacial diffusion in crystalline oxide nanolayers is presented in Chapter 7). This results in a substantial enhancement of the water oxidation rate per unit geometric nanotube wall area. The high $H^+$ flux of 780 $s^{-1}\,nm^{-2}$ through the stacked $Co_3O_4/SiO_2/TiO_2$ nanowall goes a long way towards the required $H^+$ flux for keeping up with the photon flux at maximum solar intensity (1500 photons $s^{-1}\,nm^{-2}$, corresponding to full solar irradiance AM1.5 at ground level)[75] even for the case of planar (*i.e.* non-nanostructured) systems. For our $Co_3O_4/SiO_2/TiO_2$ nanotube geometry (Figure 11.10), the required $H^+$ flux from the inside ($Co_3O_4$) to the outside ($TiO_2$) of each tube is 40 $s^{-1}\,nm^{-2}$, which is 20 times lower than the measured flux.[23] Hence, the capacity for proton flux through the nanotube wall does not pose a kinetic bottleneck for the photocatalytic performance by a large margin.

## 11.7 Photocatalysis Under Ultrathin Membrane Separation

Ultrathin silica membranes with optimized electron and proton transport rates and desired separation properties are ready for exploring and optimizing the photocatalytic efficiency of integrated systems. In this section, our approach and ongoing experiments for evaluating visible light-driven $H_2O$ oxidation and $CO_2$ reduction at planar and core–shell nanotube array systems are discussed.

For efficient $H_2O$ oxidation at $Co_3O_4$ driven by visible light absorbers anchored on the opposite side of the silica membrane, two important questions to address are: to what extent does the silica membrane with embedded wires influence the photoinduced charge flow to the $Co_3O_4$ catalyst compared with the flow achievable in the absence of a membrane, and what is the Faradaic yield of $O_2$ evolution? To address the first question, we compared short-circuit photocurrents of planar samples with and without the silica membrane. A sample with $[Ru(bpy)_2(dcbpy)]^{2+}$ light absorbers directly anchored on the $Co_3O_4$ catalyst shows a photocurrent of 47.4 nA $cm^{-2}$ compared with 28.8 nA $cm^{-2}$ for a sample with embedded A-PV3-$SO_3$ wires under otherwise identical experimental conditions (Figure 11.19a). Hence, the charge flux in the presence of the silica membrane is 60% of the flux observed without the membrane. According to the HOMO potential dependence of the charge flux across the membrane discussed in Section 11.5, replacing A-PV3-$SO_3$ wire (HOMO +1.48 V) with E-PV3-$SO_3$Et wire

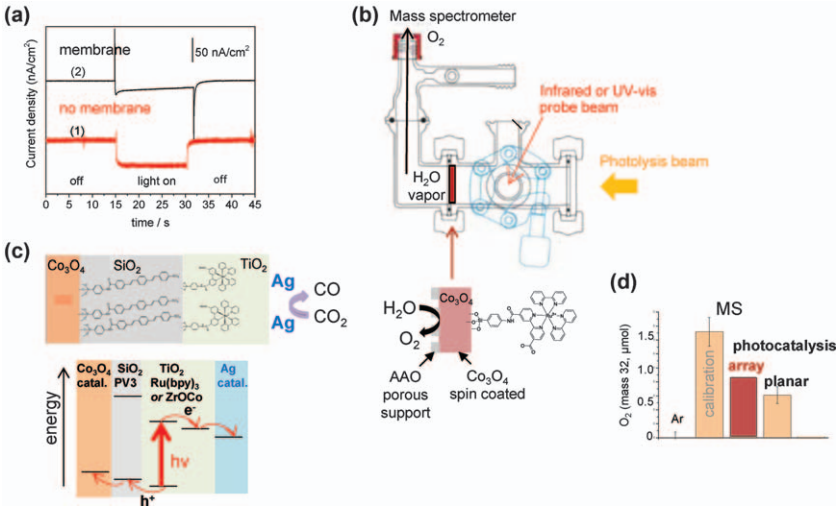


**Figure 11.19** (a) Comparison of photocurrents for samples with and without a silica membrane with embedded wires. Trace 1: sample without a silica membrane, Ru density 5.8 $nm^{-2}$. Trace 2: sample with silica membrane, A-PV3-$SO_3$ density 6.0 $nm^{-2}$, Ru density 8.8 $nm^{-2}$. Reproduced from ref. 32 with permission from American Chemical Society, Copyright 2021. (b) Free-standing $Co_3O_4$ sample with anchored light absorber supported on a thin AAO (anodized aluminum oxide) grid and photocatalysis cell for spectroscopic measurements of product evolution in compartments separated by a membrane. (c) Schematic and energy diagram of a fully functionalized nanowall. (d) Mass spectrometric monitoring of $O_2$ evolution upon visible light-driven oxidation of $H_2O$ vapor under separation of catalysis environments. Details are described in the text.

(HOMO +1.16 V) increases the photocurrent by a factor of 10.1. Therefore, wires with a HOMO potential around +1.2 V are expected to approach a charge flux across the ultrathin silica membrane equal to that observed without the membrane. This indicates that there is no substantial decrease in the charge flow rate for silica membranes with energetically optimized wire molecules while enabling tight energy control of transferred charge under chemical separation of the incompatible catalysis environments. Nevertheless, the photocurrents shown in Figure 11.19a are still in the tens of nA $cm^{-2}$ range, far too low for charge transfer from the light absorber to the $Co_3O_4$ catalyst to keep up with the photon flux at maximum solar intensity. As shown in Section 11.5, the low charge flux is due to inefficient electron transfer from the excited light absorber to the persulfate acceptor. However, when replaced with a $TiO_2$ conduction band acceptor, a photocurrent of 6.4 µA $cm^{-2}$ was observed for unoptimized A-PV3-$SO_3$ wire (Figure 11.12e); for an optimized E-PV3-$SO_3$Et wire, a photocurrent density of 0.1 mA $cm^{-2}$ is achievable (planar geometry). This means that for the core–shell nanotube array with its 100 times larger effective surface area, a

photocurrent of 10 mA $cm^{-2}$ is feasible, which is sufficient for keeping up with the photon flux at maximum solar intensity. Therefore, the charge flux through the ultrathin silica membrane of nanotubes with optimized wires will not pose a limitation for the photocatalytic efficiency of the nanotube array. Combined with the far more than adequate capacity for $H^+$ flux and complete blocking of $O_2$ and other small molecules, the ultrathin silica membrane possesses all the desired properties for an efficient separation membrane for nanoscale integration of artificial photosystems.

Photocatalytic experiments are pursued concurrently on planar and nanotube array samples. Free-standing planar samples mounted in a specialized photocatalysis cell shown schematically in Figure 11.19b afford the monitoring of photocatalytic $O_2$ evolution at the $Co_3O_4$ catalyst driven by light absorbers on the opposite side of the silica membrane. This was achieved by fabricating a square centimeter-sized planar, free-standing $Co_3O_4$ substrate supported on a thin anodized aluminum oxide (AAO) grid. Steps included spin coating of a water-soluble polymer on a silicon wafer followed by spin coating of water-insoluble polyvinylformal (PVF). This technique allows lift-off in water and capture of PVF by the thin AAO grid.[76] Spin coating of a $Co_3O_4$ nanoparticle layer a few hundred nanometers thick on PVF and subsequent removal of the sacrificial polymer by calcination results in an AAO-supported $Co_3O_4$ layer (Figure 11.19b). This was followed by the assembly of a silica nanomembrane with embedded molecular wires and attachment of light absorbers using the methods described in preceding sections for Pt-supported samples. Mounting of the planar sample in the photocatalysis cell allows spectroscopic monitoring of the photocatalytic products in the compartments separated by the membrane. The result of mass spectrometric measurement of $O_2$ evolution from $H_2O$ vapor ($H_2O$ saturated in 1 atm of Ar gas at room temperature) upon 476 nm illumination of the Ru complex directly covalently anchored on $Co_3O_4$ (persulfate electron acceptor) is shown in the bar chart in Figure 11.19d (labeled ''planar''). The bar height indicates the amount of $O_2$ (in nanomoles) generated upon 30 min of photocatalysis. For the concurrent monitoring of $CO_2$ reduction intermediates and products, the photocatalytic cell is configured with infrared windows on the light-absorber side of the membrane. Fully functionalized samples feature 5 nm $TiO_2$ layers with photodeposited Cu or Ag nanoparticle catalysts for $CO_2$ reduction (Figure 11.19c).

Oxygen evolution by visible light-driven $H_2O$ vapor oxidation of $Co_3O_4/SiO_2/TiO_2$ nanotube arrays (Figure 11.10) was demonstrated (Figure 11.19d), which confirmed that the inside surface of $Co_3O_4$ nanotubes exhibits full catalytic activity after etching of the Si nanorod template. With the nanowall composition already optimized by the study of planar samples, improvement of the photocatalytic efficiency of the nanotube array can be focused on varying the geometric array parameters, in particular the pitch (by varying the polymer bead size for fabrication of the Si nanorod array), nanotube diameter, and nanotube length (by adjusting the polymer and Si etching protocol).

## 11.8 Outlook

Ultrathin amorphous silica layers with embedded molecular wires achieve the separation of incompatible catalytic environments on the scale of a few nanometers while offering tightly controlled electronic and efficient protonic communication between them. A unique aspect of this type of membrane is the ability to optimize independently charge-transfer rates, proton flux, and chemical separation properties. This new capability allows the integration of $H_2O$ oxidation and $CO_2$ reduction photocatalysis into complete nanoscale artificial photosynthetic systems. Such nanosystems, here with nanotube morphology, form the basis for developing macroscale square inch- or square decimeter-sized units free from photocatalytically inactive components, which is an essential requirement for scale-up to enormous numbers of such interconnected tiles for deployment over large areas of nonarable land. To complete the nanotube array by installing a top and bottom cover plate with the nanotube opening piercing through them, as shown in Figure 11.3, the sacrificial Si nanorod template approach can be replaced with the anodized aluminum oxide (AAO) method.[77,78] The use of AAO as sacrificial template for growing core–shell nanotube arrays by ALD is well established.[79–81] For installing top and bottom $SiO_2$ covers of the nanotube array, sequences consisting of selective partial AAO etching, temporary protection by organic fillers, silica ALD, and mechanical polishing as practiced for the fabrication of various nanotube and nanorod arrays are envisioned.[80,82,83] Given the flexibility of the AAO method for tuning the tube diameter, length, and pitch, the $CO_2$ and $H_2O$ gas flows and photocatalysis product desorption and also photonic properties can be optimized for maximum sunlight to product conversion efficiency. The optimum size of the nanotube arrays (''tiles'') and the geometric arrangement for joining them together to form large blankets of solar fuel-generating systems will be guided by engineering considerations for efficient (gaseous) reactant delivery and product collection. Nanoscience permits the exploration of a wide variety of morphologies for nanoscale units that may be most suitable for extending their functional properties to the macroscale. Arrays of nanotubes are just one idea of how to maintain the chemical separation of $H_2O$ oxidation and $CO_2$ reduction catalysis across many orders of scale. The research field is wide open for exploring other ways of building macroscale photosystems, taking advantage of the unique properties of ultrathin oxide layers and tuning of charge and species transport functionalities.

Nanoscience techniques offer modularity, which allows the modification of structural features to progressively enhance photocatalytic performance by replacing catalysts, light absorbers, or embedded organic molecules as new, more efficient materials become available. Powerful tools such as ALD are particularly well suited for refining hierarchical structures. For example, the photocatalytic efficiency can be improved by replacing a single-photon light absorber by a two-photon tandem system, an essential step for maximizing the use of the photons of the solar spectrum. This can be achieved by

adding a second $SiO_2$ nanolayer adjoining the first layer with embedded molecular wires, the HOMO and LUMO energies of which are selected for efficient coupling of the tandem light absorbers. Another direction that requires substantial advances is the incorporation of catalysts for $CO_2$ reduction to energy-dense liquid hydrocarbon fuels. The approach of integrating catalysts with new capabilities such as multi-carbon products into nanoscale photosynthetic units while retaining already optimized properties of the overall systems design offers a rational way forward for the continued improvement of the performance of solar fuels systems.

The ability to separate incompatible environments while maintaining efficient electronic and protonic communication between them opens up the nanoscale integration of other types of components previously not deemed feasible, and the creation of new function for other fields and applications. For example, ultrathin membranes introduce opportunities to interface biological and inorganic catalysis on the nanoscale, an area of particular promise for the development of renewable energy technologies. Successful coupling of biotic and abiotic catalytic transformations allows the complementary strengths of living systems, with their unparalleled mastery of chemical synthesis, to be united with the robustness of inorganic (photo)catalysts to drive reactions that require materials that can tolerate harsh conditions. One such application is the direct conversion of sunlight to energy-dense hydrocarbon fuel by using inorganic components to generate electrons by solar water oxidation in a two-photon Z-scheme. Upon transfer to a microbe, the reducing electrons drive $CO_2$ reduction to energy-dense multi-carbon products (microbial photoelectrosynthesis). This approach has been demonstrated in a bioelectrochemcial system featuring a $TiO_2$ nanowire array serving as the photoanode for water oxidation to $O_2$, with the electrons transferred *via* an external circuit to an Si photocathode nanowire array that is separated from the photoanode by a macroscale ion-conducting polymer membrane to avoid efficiency-degrading processes.[84] Absorption of photons by the Si nanowires (second photon of the Z-scheme) results in the transfer of excited electrons to surface-adsorbed bacteria (*Sporomusa ovata*) that convert $CO_2$ from the atmosphere to acetate. While remaining to be demonstrated in a separate follow-up step, direct coupling of *Sporomusa ovata* to microbes able to convert acetate to an energy-dense liquid hydrocarbon fuel such as butanol can be envisioned. In a related biohybrid system, an Si multijunction-based solar water splitting component generating $O_2$ and $H_2$ was coupled in the same reactor container to *Ralstonia eutropha* microbes that convert $CO_2$ and the evolving $H_2$ to short-chain ($C_3$–$C_5$) alcohol molecules.[85,86]

Ultrathin silica membranes will permit the nanoscale integration of these incompatible biotic and abiotic catalysis environments, thereby breaking down long-standing barriers towards substantially reducing efficiency-degrading processes. Chief among them are large ohmic losses associated with the transport of ions over macroscale distances, attack by reactive oxygen species produced by inorganic photocatalysts on microbial matter, poisoning of electrocatalysts by impurities or leached metal ions, and

corrosion of the inorganic component by microbial activity. The efficiency of microbial fuel cells and electrosynthesis cells has long been limited by resistance losses.[87] Moreover, complete photosynthetic cycles on the nanoscale carry for biohybrids the same advantages for scale-up to the enormous levels needed for impact on global fuel consumption as the nanoscale design delivers for natural photosynthesis to reach its 120 TW power output. Current designs of bioelectrochemical systems are incongruent with the large-scale manufacturing effort needed for a practical impact.[87] The proof of concept for nanoscale integration of a microbial catalyst with an inorganic metal oxide catalyst separated by an ultrathin silica membrane has recently been demonstrated.[30]

The same approach for nanoscale integration of incompatible biotic and abiotic catalysis environments can be explored for renewable energy technologies that harness the energy of waste organics for generating electricity or powering chemical synthesis (microbial electrolysis). For example, waste-digesting bacteria such as *Shewanella oneidensis* convert the energy stored in organic compounds to the energy of reducing electrons. Whether made available as renewable electricity or directly transferred to inorganic catalysts for powering the synthesis of industrial intermediates, *e.g.* converting the waste product nitrophenol to aniline, an important industrial intermediate, adsorption of the bacteria on a silica nanomembrane with energetically tuned embedded wire molecules would allow the realization of biohybrid systems on the nanoscale. This concept has recently been demonstrated by coupling electron-generating bacteria *Shewanella oneidensis* adsorbed on a silica nanomembrane to the conduction band of an $SnO_2$ catalyst support. The electron transport across the ultrathin silica separation membrane was accomplished by CN- and $NO_2$-functionalized PV3 wire molecules the LUMO of which is energetically aligned with the potential of bacterial electrons and the $SnO_2$ conduction band.[30]

Yet another area in which biohybrid approaches provide opportunities for breaking down major barriers towards environmentally friendly and energy-efficient solutions is the fixation of atmospheric $N_2$ for the generation of fertilizers in the field. The present manufacture of fertilizers by the Haber–Bosch process is very energy intensive and is responsible for 3% of the global $CO_2$ emissions from fossil sources.[88] Equally importantly, the method of its distribution results in enormous amounts of excess fertilizer ending up in rivers and lakes, and causes substantial harm to the environment. By integrating an inorganic photocatalyst for water oxidation by solar irradiation and injecting the electrons so generated into $N_2$-reducing microbes separated by a silica nanomembrane, sunlight-powered nanobiohybrids for fertilizer production in the field can be envisioned. Such deployment of ''fertilizer on demand'' systems would provide a solution that is both energy efficient and environmentally friendly.

These are a few areas for the future exploration of ultrathin silica separation membranes where the precise energy-level alignment of the electron-transfer conduits, made possible by the embedded organic wire approach,

along with proton transmission and specific chemical separation characteristics is critical. It is similarly worth exploring the extent to which, through the choice of wide band gap oxide layer materials other than silica, the proton (or other ion) conductivity and permselectivity for various species of interest can be manipulated and fine tuned for other applications such as cascade catalysis.[89]

## Acknowledgements

Funding to support this work was provided by the Energy and Biosciences Institute through the EBI–Shell program. Portions of this work (plasma-enhanced atomic layer deposition, ellipsometry, e-beam evaporation) were performed as a User Project at The Molecular Foundry, Lawrence Berkeley National Laboratory, which is supported by the Office of Science, Office of Basic Energy Sciences, of the US Department of Energy under Contract No. DE-AC02-05CH11231.

## References

1. S. Y. Reece, J. A. Hamel, K. Sung, T. D. Jarvi, A. J. Esswein, J. J. H. Pijpers and D. G. Nocera, *Science*, 2011, **334**, 645–648.
2. E. Verlage, S. Hu, R. Liu, J. R. Jones, K. Sun, C. Xiang, N. S. Lewis and H. A. Atwater, *Energy Environ. Sci.*, 2015, **8**, 3166–3172.
3. K. Sun, R. Liu, Y. Chen, E. Verlage, N. S. Lewis and C. Xiang, *Adv. Energy Mater.*, 2016, **6**, 1600379.
4. O. Khaselev and J. A. Turner, *Science*, 1998, **280**, 425–427.
5. J. L. Young, M. A. Steiner, H. Doescher, R. M. France, J. A. Turner and T. G. Deutsch, *Nat. Energy*, 2017, **2**, 17028.
6. F. F. Abdi, L. Han, A. H. M. Smets, M. Zeman, B. Dam and R. van de Krol, *Nat. Commun.*, 2013, **4**, 2195.
7. J. W. Jang, C. Du, Y. Ye, Y. Lin, X. Yao, J. Thorne, E. Liu, G. McMahon, J. Zhu, A. Javey, J. Guo and D. Wang, *Nat. Commun.*, 2015, **6**, 7447.
8. C. Liu, J. Tang, H. M. Chen, B. Liu and P. Yang, *Nano Lett.*, 2013, **13**, 2989–2992.
9. B. Liu, C. H. Wu, J. Miao and P. Yang, *ACS Nano*, 2014, **8**, 11739–11744.
10. M. R. Shaner, K. T. Fountaine, S. Ardo, R. H. Coridan, H. A. Atwater and N. S. Lewis, *Energy Environ. Sci.*, 2014, **7**, 779–790.
11. J. Luo, J. M. Im, M. T. Mayer, M. Schreier, M. K. Nazeeruddin, N. G. Park, S. D. Tilley, H. J. Fan and M. Graetzel, *Science*, 2014, **345**, 1593–1596.
12. X. Zhou, R. Liu, K. Sun, Y. Chen, E. Verlage, S. A. Francis, N. S. Lewis and C. Xiang, *ACS Energy Lett.*, 2016, **1**, 764–770.
13. W. H. Cheng, M. H. Richter, M. M. May, J. Ohlmann, D. Lackner, F. Dimroth, T. Hannappel, H. A. Atwater and H. J. Lewerenz, *ACS Energy*, 2018, **3**, 1795–1800.
14. N. A. Campbell, J. B. Reece, M. R. Taylor and E. J. Simon, *Biology: Concepts & Connections*, Educational Pearson, New York, 5th edn, 2006.

15. S. Chabi, K. M. Papadantonakis, N. S. Lewis and M. S. Freund, *Energy Environ. Sci.*, 2017, **10**, 1320–1338.
16. E. Edri, S. Aloni and H. Frei, *ACS Nano*, 2018, **12**, 533–541.
17. W. Kim, E. Edri and H. Frei, *Acc. Chem. Res.*, 2016, **49**, 1634–1645.
18. F. Jiao and H. Frei, *Angew. Chem., Int. Ed.*, 2009, **48**, 1841–1844.
19. G. Yuan, A. Agiral, N. Pellet, W. Kim and H. Frei, *Faraday Discuss.*, 2014, **176**, 233–249.
20. M. Zhang, M. de Respinis and H. Frei, *Nat. Chem.*, 2014, **6**, 363–367.
21. H. H. Pham, M. J Cheng, H. Frei and L. W. Wang, *ACS Catal.*, 2016, **6**, 5610–5617.
22. M. Zhang and H. Frei, *Annu. Rev. Phys. Chem.*, 2017, **68**, 209–231.
23. W. J. Jo, G. Katsoukis and H. Frei, *Adv. Funct. Mater.*, 2020, **30**, 1909262.
24. W. Kim, B. A. McClure, E. Edri and H. Frei, *Chem. Soc. Rev.*, 2016, **45**, 3221–3243.
25. M. L. Macnaughtan, H. S. Soo and H. Frei, *J. Phys. Chem. C*, 2014, **118**, 7874–7885.
26. W. Kim, G. Yuan, B. A. McClure and H. Frei, *J. Am. Chem. Soc.*, 2014, **136**, 11034–11042.
27. G. Katsoukis and H. Frei, *ACS Appl. Mater. Interfaces*, 2018, **10**, 31422–31432.
28. H. S. Soo, A. Agiral, A. Bachmeier and H. Frei, *J. Am. Chem. Soc.*, 2012, **134**, 17104–17116.
29. A. Agiral, H. S. Soo and H. Frei, *Chem. Mater.*, 2013, **25**, 2264–2273.
30. J. A. Cornejo, H. Sheng, E. Edri, C. A. Ajo-Franklin and H. Frei, *Nat. Commun.*, 2018, **9**, 2263.
31. G. Katsoukis, W. J. Jo and H. Frei, *J. Phys. Chem. C*, 2019, **123**, 18905–18913.
32. H. Zhang, I. Weiss, I. Rudra, W. J. Jo, S. Kellner, G. Katsoukis, E. Galoppini and H. Frei, *ACS Appl. Mater. Interfaces*, 2021, **13**, 23532–23546.
33. P. Banet, N. Marcotte, D. A. Lerner and D. Brunel, *Langmuir*, 2008, **24**, 9030–9037.
34. W. B. Davis, W. A. Svec, M. A. Ratner and M. R. Wasielewski, *Nature*, 1998, **396**, 60–64.
35. H. Tuysuz, Y. J. Hwang, S. B. Khan, A. M. Asin and P. Yang, *Nano Res.*, 2013, **6**, 47–54.
36. P. Hollins, in *Encyclopedia of Analytic Chemistry*, ed. R. A. Meyers, Wiley, New York, 2006, p. 1.
37. Y. J. Chabal, *Surf. Sci. Rep.*, 1988, **8**, 211–357.
38. F. Billes, H. Endredi and G. Keresztury, *J. Mol. Struct.*, 2000, **530**, 183–200.
39. E. Borello and A. Zecchina, *Spectrochim. Acta*, 1963, **19**, 1703–1715.
40. E. Edri and H. Frei, *J. Phys. Chem. C*, 2015, **119**, 28326–28334.
41. Y. Li, W. Qui, F. Qin, H. Fang, V. G. Hadjiev, D. Litvinov and J. Bao, *J. Phys. Chem. C*, 2016, **120**, 4511–4516.
42. Q. Guo, X. Guo and Q. Tian, *Adv. Powder Technol.*, 2010, **21**, 529–533.
43. J. F. Huang, A. Hung, C. B. Wang and C. T. Yeh, *J. Chin. Chem. Soc.*, 2002, **49**, 819–824.

44. K. B. Klepper, O. Nilsen and H. Fjellvag, *Thin Solid Films*, 2007, **515**, 7772–7781.
45. L. F. Pena, C. E. Nanayakkara, A. Mallikarjunan, H. Chandra, M. Xiao, X. Lei, R. M. Pearlstein, A. Derecskei-Kovacs and Y. J. Chabal, *J. Phys. Chem. C*, 2016, **120**, 10927–10935.
46. B. B. Burton, S. W. Kang, S. W. Rhee and S. M. George, *J. Phys. Chem. C*, 2009, **113**, 8249–8257.
47. J. Wang, B. Zou and M. A. El-Sayed, *J. Mol. Struct.*, 1999, **508**, 87–96.
48. S. Portal and R. M. Almeida, *Phys. Stat. Sol. (a)*, 2004, **201**, 2941–2947.
49. R. M. Almeida, A. C. Marques, S. Pelli, G. C. Righini, A. Chiasera, M. Mattarelli, M. Montagna, C. Tosello, R. R. Goncalves, H. Portales, S. Chaussedent, M. Ferrari and L. Zampedri, *Philos. Mag.*, 2004, **84**, 1659–1666.
50. R. K. Joshi and J. J. Schneider, *Chem. Soc. Rev.*, 2012, **41**, 5285–5312.
51. B. B. Lakshmi, C. J. Patrissi and C. R. Martin, *Chem. Mater.*, 1997, **9**, 2544–2550.
52. H. A. Park, S. Liu, Y. Oh, P. A. Salvador, G. S. Rohrer and M. F. Islam, *ACS Nano*, 2017, **11**, 2150–2159.
53. L. Li, T. Zhai, H. Zeng, X. Fang, Y. Bando and D. Goldberg, *J. Mater. Chem.*, 2011, **21**, 40–56.
54. J. W. Elam, D. Routkevitch, P. P. Mardilovich and S. M. George, *Chem. Mater.*, 2003, **15**, 3507–3517.
55. Z. Liu, Y. Wu, B. Harteneck and D. Olynick, *Nanotechnology*, 2013, **24**, 15305–15312.
56. T. Shimidzu, T. Iyoda and K. Izaki, *J. Phys. Chem.*, 1985, **89**, 641–645.
57. R. A. Marcus and N. Sutin, *Biochim. Biophys. Acta*, 1985, **811**, 265–322.
58. J. R. Swierk, N. S. McCool, C. T. Nemes, T. E. Mallouk and C. A. Schmuttenmaer, *J. Phys. Chem. C*, 2016, **120**, 5940–5948.
59. W. Song, M. K. Brennaman, J. J. Concepcion, J. W. Jurss, P. G. Hoertz, H. Luo, C. Chen, K. Hanson and T. J. Meyer, *J. Phys. Chem. C*, 2011, **115**, 7081–7091.
60. S. H. A. Lee, Y. Zhao, E. A. Hernandez-Pagan, L. Blasdel, J. Youngblood and T. E. Mallouk, *Faraday Discuss.*, 2012, **155**, 165–176.
61. E. Edri, J. K. Cooper, I. D. Sharp, D. M. Guldi and H. Frei, *J. Am. Chem. Soc.*, 2017, **139**, 5458–5466.
62. T. Cuk, W. W. Weare and H. Frei, *J. Phys. Chem. C*, 2010, **114**, 9167–9172.
63. N. Y. Labrador, E. L. Songcuan, C. De Silva, H. Chen, S. J. Kurdziel, R. K. Ramachandran, C. Detavernier and D. V. Esposito, *ACS Catal.*, 2018, **8**, 1767–1778.
64. D. V. Esposito, *ACS Catal.*, 2018, **8**, 457–465.
65. T. Shinagawa and K. Takanabe, *Phys. Chem. Chem. Phys.*, 2015, **17**, 15111–15114.
66. M. E. S. Beatty, H. Chen, N. Y. Labrador, B. J. Lee and D. V. Esposito, *J. Mater. Chem. A*, 2018, **6**, 22287–22300.
67. A. J. Bard and L. R. Faulkner, *Electrochemical Methods*, Wiley, New York, 2nd edn, 2001, ch. 4 and ch. 10.

68. G. Lockwood and S. H. Carofalini, *J. Chem. Phys.*, 2009, **131**, 074703.
69. H. A. Kurtz and S. P. Karna, *IEEE Trans. Nucl. Sci.*, 1999, **46**, 1574–1579.
70. A. T. Heijne, O. Schaezle, S. Gimenez, F. Fabregat-Santiago, J. Bisquert, D. P. B. Strik, F. Barrière, C. J. N. Buisman and H. V. M. Hamelers, *Energy Environ. Sci.*, 2011, **4**, 5035–5043.
71. V. Freger and S. Bason, *J. Membr. Sci.*, 2007, **302**, 1–9.
72. A. J. Bard and L. R. Faulkner, *Electrochemical Methods*, Wiley, New York, 2nd edn, 2001, p. 27.
73. P. W. Atkins, *Physical Chemistry*, ed. W. H. Freeman, New York, 3rd edn, 1986, pp. 668–675.
74. J. C. Fogarty, H. M. Aktulga, A. Y. Grama, A. C. T. van Duin and S. A. Pandit, *J. Chem. Phys.*, 2010, **132**, 174704.
75. Solar Spectra, National Renewable Energy Laboratory, Golden, CO, USA, https://rredc.nrel.gov/solar/spectra/am1.5 (accessed October 2020).
76. M. Stadermann, S. H. Baxamusa, C. Aracne-Ruddle, M. Chea, S. Li, K. Youngblood and T. Suratwala, *J. Visualized Exp.*, 2015, **100**, e52832.
77. D. Perego, S. Franz, M. Bestetti, L. Cattaneo, S. Brivio, G. Tallarida and S. Spiga, *Nanotechnology*, 2013, **24**, 045302.
78. L. Wen, R. Xu, Y. Mi and Y. Lei, *Nat. Nanotechnol.*, 2017, **12**, 244–250.
79. H. A. Park, S. Liu, Y. Oh, P. A. Salvador, G. S. Rohrer and M. F. Islam, *ACS Nano*, 2017, **11**, 2150–2159.
80. M. S. Sander, M. J. Cote, W. Gu, B. M. Kile and C. P. Tripp, *Adv. Mater.*, 2004, **16**, 2052–2057.
81. A. Ruiz-Clavijo, O. Caballero-Calero and M. Martin-Gonzalez, *Nanoscale*, 2021, **13**, 2227–2265.
82. D. Perego, S. Franz, M. Bestetti, L. Cattaneo, S. Brivio, G. Tallarida and S. Spiga, *Nanotechnology*, 2013, **24**, 045302.
83. S. J. Ku, G. C. Jo, C. H. Bak, S. M. Kim, Y. R. Shin, K. H. Kim, S. H. Kwon and J. B. Kim, *Nanotechnology*, 2013, **24**, 085301.
84. C. Liu, J. J. Gallagher, K. K. Sakimoto, E. M. Nichols, C. J. Chang, M. C. Y. Chang and P. Yang, *Nano Lett.*, 2015, **15**, 3634–3639.
85. C. Liu, B. C. Colon, M. Ziesack, P. A. Silver and D. G. Nocera, *Science*, 2016, **352**, 1210–1213.
86. J. P. Torella, C. J. Gagliardi, J. S. Chen, D. K. Bediako, B. Colon, J. C. Way, P. A. Silver and D. G. Nocera, *Proc. Natl. Acad. Sci. U. S. A.*, 2015, **112**, 2337–2342.
87. B. E Logan, *Microbial Fuel Cells*, Wiley, Hoboken, 1st edn, 2008, pp. 85–110.
88. R. D. Milton, R. Cai, S. Abdellaoui, D. Leech, A. L. De Lacey, M. Pita and S. D. Minteer, *Angew. Chem. Int. Ed.*, 2017, **56**, 2680–2683.
89. I. Wheeldon, S. D. Minteer, S. Banta, S. Calabrese Barton, P. Atanassov and M. Sigman, *Nat. Chem.*, 2016, **8**, 299–309.

CHAPTER 12

# *Outlook*

D. V. ESPOSITO*[a] AND H. FREI*[b]

[a] Department of Chemical Engineering, Columbia University, New York, NY 10032, USA; [b] Molecular Biophysics and Integrated Bioimaging Division, Lawrence Berkeley National Laboratory, University of California, Berkeley, CA 94720, USA
*Emails: de2300@columbia.edu; hmfrei@lbl.gov

## 12.1 Introduction

A need for future research on ultrathin oxide layers that transcends many topics brought up in the outlook sections at the end of the individual chapters is a deeper understanding of the fundamental physical and chemical processes that occur within and at the interfaces of oxide layers. Improved knowledge of these processes is expected to be essential for guiding the design and selection of ultrathin oxides for both existing commercial technologies and novel applications. In this final chapter, major challenges for achieving these goals are outlined within the framework of modeling and experimental advances that are anticipated to be necessary to overcome them. First, challenges and opportunities related to modeling ultrathin oxides are discussed, followed by descriptions of emerging new spectroscopic techniques that are particularly well suited to probing buried oxide/semiconductor or oxide/metal interfaces. Lastly, this chapter highlights the importance of advancing experimental techniques capable of uncovering the dynamics of interfacial phenomena at ultrathin oxide layers that occur at timescales spanning many orders of magnitude.

Energy and Environment Series No. 30
Ultrathin Oxide Layers for Solar and Electrocatalytic Systems
Edited by Heinz Frei and Daniel V. Esposito

Published by the Royal Society of Chemistry, www.rsc.org

## 12.2 Challenges and Opportunities for Modeling Ultrathin Oxides

A holy grail of materials science is the ''materials by design'' paradigm, *i.e.* the ability to input desired performance metrics or properties into a computational materials design framework or simulator that returns combinations of materials, geometric variables, and operating conditions that are capable of delivering the target properties and performance.[1,2] This sort of approach has also been referred to as the ''inverse design'' approach,[3] as opposed to a more traditional approach that tends to rely on more Edisonian, trial-and-error methodologies that may eventually converge on desirable solutions but take a long time to do so. Unfortunately, ''materials by design'' is far from reality for all but the simplest applications, let alone complex composite energy conversion devices containing ultrathin oxide layers and involving multiphysics phenomena spanning many length and timescales. Recent advances in modeling and experimental capabilities have demonstrated that some of the key components required for this aspirational paradigm are nearing the level of accuracy and throughput needed to make this vision reality, but several major gaps remain. This section highlights some of the remaining computational challenges that must be overcome to enable the inverse design of ultrathin oxide layers and accelerate their adoption into existing and new solar, electrocatalytic, and thermal catalytic energy conversion technologies.

A key word in the previous paragraph is *throughput*, alluding to the fact that our hypothetical simulator tool will probably need to process at least $10^3$–$10^6$ different permutations of materials compositions, structures, operating conditions, and device architectures to be able to map out reliably the large solution space for complex devices involving ultrathin oxides. Additionally, each individual solution (*i.e.* a specific ultrathin oxide incorporated within a specific device design and operating condition) can involve a multitude of time-consuming simulations. Advances in computer and software engineering have allowed impressive leaps in the abilities of modern computing clusters to support atomistic (*i.e.* atomic-scale) simulations of oxide materials and their interfaces, but can still be a major bottleneck within the overall design framework. One particularly acute challenge relevant to ultrathin oxides is the computational cost associated with the use of atomistic simulation tools such as density functional theory (DFT) to model accurately the properties and behavior of amorphous and highly defective oxides. Owing to their lack of periodic structure and associated atomic-scale heterogeneity, amorphous materials tend to be more difficult to define *in silico* and require larger simulation volumes and/or times to permit reliable statistical sampling of their properties. Although significant progress in the application of *ab initio* computational methods to amorphous oxides has been made in recent years,[4–6] the computational throughput of atomistic simulations of amorphous oxides still severely lags

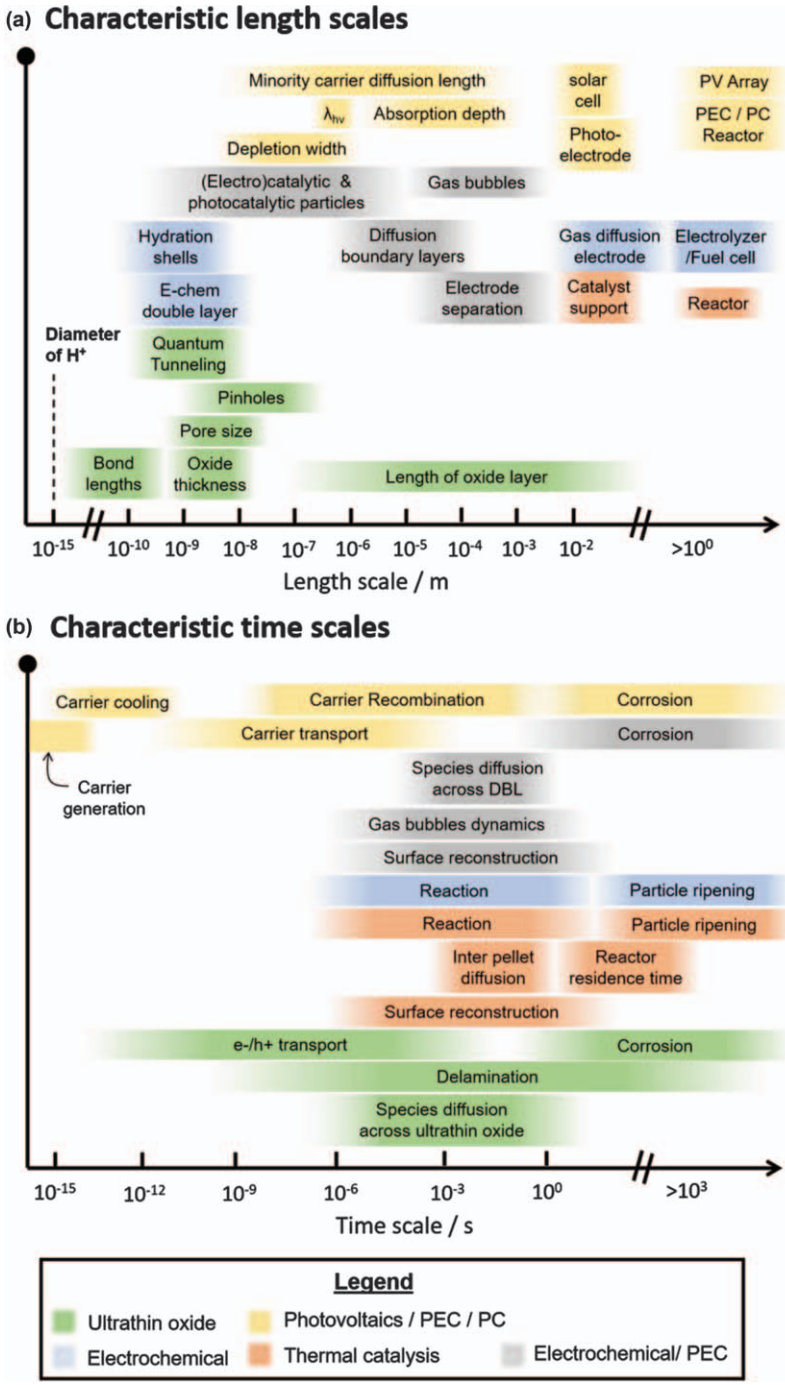
(a) Characteristic length scales
Minority carrier diffusion length
λhν
Absorption depth
Depletion width
(Electro)catalytic & photocatalytic particles
Gas bubbles
solar cell
Photo-electrode
PV Array
PEC / PC Reactor
Hydration shells
Diffusion boundary layers
Gas diffusion electrode
Electrolyzer /Fuel cell
E-chem double layer
Electrode separation
Catalyst support
Reactor
Diameter of H+
Quantum Tunneling
Pinholes
Pore size
Bond lengths
Oxide thickness
Length of oxide layer
10-15 10-10 10-9 10-8 10-7 10-6 10-5 10-4 10-3 10-2 >100
Length scale / m
(b) Characteristic time scales
Carrier cooling
Carrier Recombination
Corrosion
Carrier transport
Corrosion
Carrier generation
Species diffusion across DBL
Gas bubbles dynamics
Surface reconstruction
Reaction
Particle ripening
Reaction
Particle ripening
Inter pellet diffusion
Reactor residence time
Surface reconstruction
e-/h+ transport
Corrosion
Delamination
Species diffusion across ultrathin oxide
10-15 10-12 10-9 10-6 10-3 100 >103
Time scale / s
Legend
Ultrathin oxide
Photovoltaics / PEC / PC
Electrochemical
Thermal catalysis
Electrochemical/ PEC

behind that for crystalline oxides. One approach to increase throughput is to study well-defined crystalline oxide structures as surrogates for their amorphous or defective counterparts.[7–9] In cases where the local environments within the amorphous and crystalline materials are similar, this approximation may allow substantially higher throughput. However, this approach may not always be sufficient, especially if the properties or processes of interest are highly sensitive to atomic- or nanoscale variations in bond lengths, interstitial voids, and composition. Coupled with the fact that interfacial properties are inherently important for ultrathin oxides, and require modeling of not only the oxide but also at least one other solid-state component, high-throughput atomistic simulations of the properties and structure of ultrathin oxides at buried interfaces and/or in contact with an explicit solvent are especially daunting. Therefore, further refinement of the methods used to generate simulated oxides *in silico* and apply statistical methods that can accurately and efficiently describe the probability distributions of their bulk and interfacial structures and properties is desperately needed. The use of machine learning approaches to help generate DFT-trained interatomic potentials is a promising approach to increase the throughput of atomistic simulations of amorphous or disordered materials, but significant challenges relating to computational infrastructure (*e.g.* standardization across different software packages/programs, standardization of training and testing protocols, advances in centralized repositories) and technical barriers related to the ''combinatorial explosion'' of high-dimensional spaces remain to be addressed.[10]

Although the previous paragraph focused on computational challenges at the atomic scale, a ''materials by design'' approach must also be able to accurately account for chemical and physical phenomena that occur across a wide range of length scales (see Figure 12.1a). Most of the ultrathin oxide layers described throughout this book were inherently multiscale in nature,

**Figure 12.1** Typical characteristic (a) length scales and (b) timescales associated with objects and phenomena, respectively, for solar, electrocatalytic, and thermal catalytic applications. Characteristic length ($L$) and time ($\tau$) scales are given as ranges that are typical of commonly studied materials and devices, but the limits of these ranges are often poorly defined and may be significantly different from the limits shown here for outlier materials and/or operating conditions. Timescales provided in (b) are generally consistent with those provided in other references for photovoltaic,[11] (electro)catalytic,[12] and photoelectrochemical[13] processes. For some transport processes, characteristic timescale ranges were estimated based on characteristic length scales ($L$) from part (a) and known ranges of species permeabilities or effective diffusivities ($D_{e,i}$) based on the relationship $\tau = L^2/D_{e,i}$. Applications are color coded according to the legend, where PEC = photoelectrochemical and PC = photocatalytic. Green coloring denotes length and/or timescales that are specifically associated with ultrathin oxides used in one or more of these applications. $\lambda_{h\nu}$ is the wavelength of visible light relevant to solar energy conversion, and DBL is the diffusion boundary layer.

and in all of the energy conversion applications discussed, a variety of physical processes are present that are described by a wide range of characteristic length scales. Whereas the ''ultrathin'' oxide layer itself is characterized by nanoscale thicknesses, the lateral distance of an oxide coating can span up to meter length scales (*e.g.* in photovoltaic panels), and the other components with which an oxide interfaces can likewise span from nano- to macroscopic dimensions. Such disparate length scales often require different computational methods to capture and describe accurately key physical and chemical phenomena that underlie energy conversion and degradation processes.[5] Therefore, atomistic simulation tools such as DFT and molecular dynamics (MD) must be supplemented by coarse-grained and/or continuum-level approaches and methods such as finite element methods that can accurately describe key processes that occur at larger characteristic length scales. At larger length scales, the system complexity also tends to increase owing to the need to include multiple materials components and theories that span multiple fields of physics in order to describe accurately the couplings between these processes and components. For example, photoelectrochemical and photocatalytic systems will in many cases require theory and modeling approaches rooted in optics, mechanics, chemical physics, and condensed matter physics.

The multiscale challenge is not limited to the spatial dimension, but also includes the temporal realm.[11–13] As illustrated in Figure 12.1b, the fundamental processes that underlie many of the solar and (electro)catalytic technologies covered in this book tend to be characterized by characteristic timescales ($\tau$) that span many orders of magnitude. Considering an ultrathin oxide layer used as a coating on a photoelectrode or photocatalyst particle, the oxide layer itself could be directly involved with carrier transport ($10^{-12}$ s$<\tau<10^{-3}$ s), carrier recombination ($10^{-9}$ s$<\tau<10^{-1}$ s), electrochemical charge-transfer events ($10^{-7}$ s$<\tau<10^{0}$ s), and corrosion processes ($10^{0}$ s$<\tau<10^{8}$ s). To accurately predict dynamic processes across such a wide range of timescales, multiple computational methodologies are necessary, just as multiple methodologies are needed to describe processes that occur at different characteristic length scales. Commonly employed atomistic simulation methods such as DFT and classical MD are suitable for studying many fundamental processes that occur at short timescales (typically up to $\sim10^{-10}$ s for DFT and up to $\sim10^{-6}$ s for MD), but the computational cost required to extend these methods to many transport and kinetic processes at longer timescales generally places them out of reach for high-throughput computational studies.[13] Modeling efforts based on coarse-grained models and/or kinetic Monte Carlo (kMC) methodologies have proven useful for describing the dynamics of a variety of processes that occur across much larger length and/or timescales, but rely strongly on a detailed understanding of well-defined elementary processes for the system of interest, and also high-quality inputs from *ab initio* methods such as DFT and quantum Monte Carlo (QMC) methods.[13] Moving forward, advances in scale-bridging computational methodologies that are tailored to ultrathin

oxides and able to seamlessly interface with atomistic simulation methods can be expected to be invaluable in enabling a holistic ''materials by design'' framework.

Even when all of the individual computational methods have been successfully integrated to form a multiscale, multiphysics modeling framework, additional challenges may still remain. Within our ''materials by design'' simulator, it will also be necessary to apply post-processing methods that can make sense of the massive quantities of data—both computational and experimental—that span large dimensional design spaces. Even for leading experts, the outputs from a ''materials by design'' simulator will need to be condensed down to a manageable set of instructions or guidelines that can easily be reduced to practice. Towards this end, modern data science and statistical methods can be expected to be of great value in helping to reduce the dimensionality of the design problem by identifying ''descriptor'' parameters for oxide layers that correlate strongly with key properties or performance metrics.[14–19] Some of these descriptors are likely to be bulk properties of the oxide, such as a dielectric constant or band gap energy, which in many cases can be readily accessed from existing data hubs. However, the inherently nanoscale nature of ultrathin oxide layers often gives extra importance to their interfacial properties, which will also be highly dependent on the material(s) or electrolytes that form the other side of the interface, in addition to the chosen operating conditions. Far less attention has been paid to descriptors that are inherently interfacial in nature, but such interfacial descriptors can be expected to be of great value in establishing rational design rules for energy conversion technologies based on ultrathin oxides. With methods to rapidly identify and rank both bulk and interfacial descriptors for ultrathin oxides in hand, simulation tools not only can be expected to rapidly accelerate the selection of the composition and structure of candidate oxide layers, but may also be used to suggest optimal experimental conditions, to explore device-level performance limits, and to test the validity of proposed mechanisms and rate-limiting steps.

Accurate and efficient high-throughput computation-driven design and discovery of ultrathin oxide overlayers and composite structures are an exciting prospect, but it must be emphasized that the challenges to making this vision a reality are not purely computational in nature. Concurrent advances in experimental techniques – especially those capable of atomic- or nanoscale characterization of ultrathin oxides and their interfaces – are also very important thanks to their ability to provide valuable input needed to set up models, validate computational predictions, and provide data sets against which mechanistic hypotheses can be tested. For electrochemical and photoelectrochemical applications, the ability to probe changes in interfacial structures under reactive environments with high spatial and/or temporal resolution becomes even more valuable. Recognizing the value that experimental advances in these areas could bring, the remainder of this chapter discusses (i) experimental opportunities related to the spectroscopic characterization of buried interfaces between ultrathin oxides and a second

solid-state component (Section 12.3), and (ii) the need to apply these and other methods to study ultrathin oxides across a wide range of timescales (Section 12.4).

## 12.3 Spectroscopic Tools for Probing Buried Interfaces

As highlighted throughout this book, the structure and properties of buried interfaces involving ultrathin overlayers very often have huge impacts on the performance of solar and (electro)catalytic technologies. However, buried interfaces are inherently challenging to study because physical probes cannot interact directly with them and the signal intensity of many forms of electromagnetic radiation used to interrogate their properties is easily attenuated when passing through the solid-state overlayer. Fortunately, there are several classes of existing experimental methods and new emerging methods that are especially valuable in their ability to probe the atomic-level structure of buried interfaces. Towards the top of this list are vibrational spectroscopic techniques that can be used to measure the vibrational frequencies of interfacial bonds, which can produce unique, molecular structure-specific signatures compared with the bonds of the two disparate materials on either side of the buried interface and/or reactive intermediates located there. Several infrared techniques are currently practiced or are under development. Infrared–visible sum frequency generation spectroscopy (SFG) is an interface-specific method since infrared modes are active only for molecules in an environment that breaks the inversion symmetry.[20] Importantly, when run in total internal reflection configuration, one can selectively probe individual interfaces in multilayered systems because the SFG signal is enhanced up to 100-fold when the incident angles of the infrared and visible laser beams are near the critical angle for total internal reflection.[21] Examples are the elucidation of the molecular structure at a silica nanolayer/silicon solid/solid interface,[22] or at the buried interface of a polymer film on solid oxide.[21] The method is not suitable for samples featuring a strongly infrared light-absorbing layer that would significantly attenuate the intensity of the infrared beam before it reaches the buried interface(s) of interest. For this case, a fourth-order non-linear Raman spectroscopic technique was developed that employs visible or near-infrared instead of mid-infrared light.[23] The selection of fourth-order non-linear Raman spectroscopy is based on the fact that the non-linear susceptibility is non-zero only at the interface and vanishes in the bulk, thus introducing interface sensitivity. Note that stimulated Raman scattering, which plays a prominent role in mechanistic studies of heterogeneous catalysis, does not exhibit such interface selectivity because it is a third-order non-linear Raman spectroscopic technique.

FT-IRRAS (Fourier transform infrared reflection absorption spectroscopy) is another IR-based vibrational spectroscopic technique that is especially

valuable for studying buried interfaces if the metal oxide, or a stack of metal oxide layers, is supported by a metal. As illustrated by examples in Chapter 11 for monitoring the buried Co oxide/silica and the Pt metal/silica interfaces, FT-IRRAS is able to achieve high sensitivity to interfacial bonds thanks to the strong enhancement of p-polarized infrared light at metal surfaces. Various configurations of ATR (attenuated total reflection) FT-IR spectroscopy are employed for probing buried interfaces. The evanescent wave probes both the interior of a multilayer stack and its interfaces, and the method is not interface sensitive as such. However, the penetration depth of the wave can be tuned by adjusting the incident angle of the infrared beam that enters the ATR crystal. By comparing spectra probed at different depths, information about a buried interface can be extracted.[24] For the specific case of metals coated with an oxide nanolayer, the ATR FT-IR Kretschmann configuration has proven powerful for monitoring the buried metal/oxide nanolayer interface.[25] Here, the metal nanolayer is deposited on the ATR element followed by deposition of the ultrathin overcoat. As a side note, the metal nanolayer may serve as an electrical contact and working electrode to permit *in situ* FT-IR measurements for electrochemical applications. The electric field associated with the evanescent infrared beam can pass through the thin metal film and provides a spectral signal of the buried interface that is substantially enhanced compared with the interior of the oxide nanolayer.[26] When using a metal such as Au that provides local plasmon resonance enhancement of the evanescent field at the roughened surface, further enhancement of the infrared spectrum at the buried interface can be achieved.[27,28]

A rapidly expanding infrared technique that provides high spatial resolution in addition to resolving vibrational modes at buried interfaces is atomic force microscopy (AFM)-based infrared spectroscopy. The technique uses a tip of an AFM cantilever that responds to the thermal expansion when a rapidly pulsed infrared laser beam is absorbed by species at a buried interface beneath the ultrathin layer. As the infrared laser is tuned across the spectral region, the magnitude of the oscillation amplitude of the cantilever (monitored by a red light position laser) in contact with the layer changes according to the amount of light absorbed. Therefore, the red position laser amplitude reports the infrared bands of the absorbing species at the buried interface (Figure 12.2a,b).[29] As shown in Figure 12.2c, the AFM-IR measurement allows the detection of the carboxylate moiety of the poly(acrylic acid) (PAA) formed at the buried interface with $Al_2O_3$ at 1602 $cm^{-1}$. This band vanishes as the polymer thickness is increased, confirming that it originates from carboxylate moieties located at the buried interface.[30] Although AFM-IR spectroscopy has thus far been primarily used to study buried polymer/metal oxide interfaces, the high spatial resolution afforded by this technique also makes it interesting for studying inorganic ultrathin oxide layers that possess sample heterogeneity at the scale of nanometers.[31]

Although vibrational spectroscopic techniques have proved invaluable in the study of buried interfaces involving ultrathin oxides, they are not able to provide a complete atomic-level description of the structure and composition of a

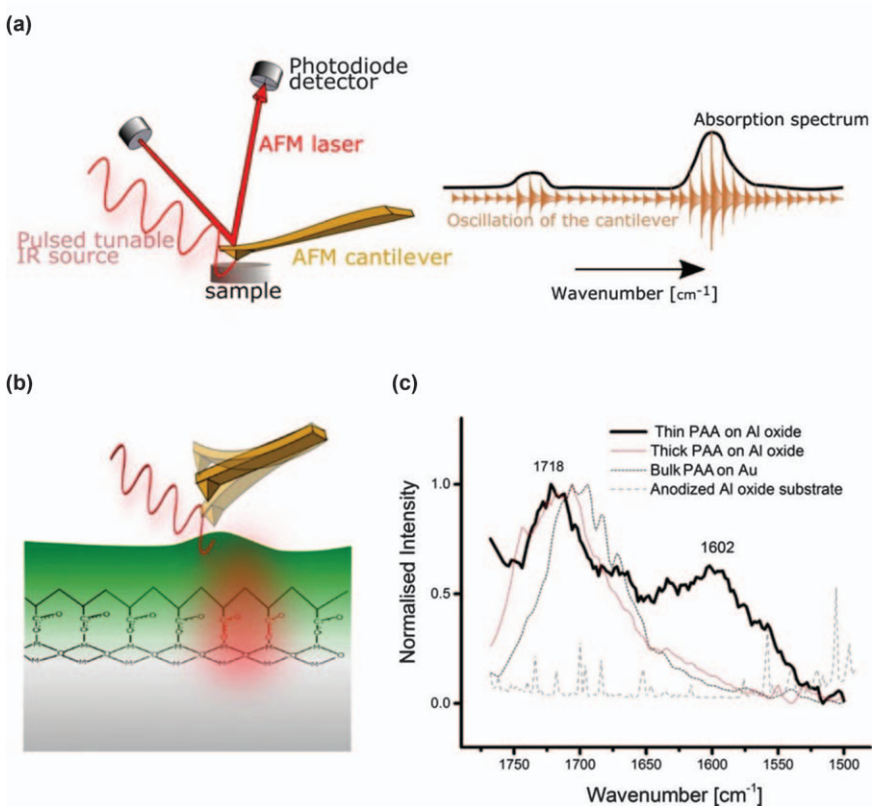


**Figure 12.2** (a) Concept of the AFM-IR spectroscopic method showing pulsed tunable infrared probe light penetrating to a buried interface while measuring the AFM cantilever oscillation amplitude as a function of IR wavelength. (b) Infrared probe light absorbed by interfacial species results in thermal expansion. (c) AFM-IR spectrum of a thin (20 nm) layer of poly(acrylic acid) (PAA) on $Al_2O_3$ (black trace) and of a thick (50 nm) PAA layer (red trace). Control spectra of alumina and neat PAA are also shown. Reproduced from ref. 30 with permission from American Chemical Society, Copyright 2019.

buried interface by themselves. Fortunately, various X-ray-based techniques, in particular emission, absorption, and photoemission spectroscopic methods, can provide highly complementary insights into the structure and composition of species at buried interfaces.[32] A prominent method is grazing incidence X-ray spectroscopy, which provides information on multiple structural parameters of the buried interface, such as elemental composition, phase (crystallographic or amorphous), or electronic structure.[33] X-ray standing-wave angle-resolved photoemission measurements allow local enhancement of regions at buried inorganic solid/solid interfaces by varying the angle of the incident X-ray beam that tunes the standing wave, thereby probing the electronic structure of the interface.[34] Similarly, high-resolution X-ray

photoelectron spectroscopy (XPS) depth profiling was shown to reveal detailed compositional information on multiple buried interfaces of inorganic layer stacks with layer thicknesses as small as a few nanometers.[35] These X-ray techniques will experience a big boost from the coherent nature of X-ray beams available at emerging X-ray free-electron laser (XFEL) facilities[36] that should permit the imaging of buried interfaces at atomic resolution.

Given the highly complementary nature of the spectroscopic methods discussed here, from X-ray, optical, infrared, and Raman to electron-based spectroscopy and imaging, there is often a need to apply them to the same sample in an identical environment. Capabilities for performing multimodal spectroscopy and imaging are emerging at major X-ray research facilities around the world. Another emerging priority is the need to accelerate the development of experimental approaches for *in situ* and time-resolved spectroscopic monitoring of interfacial phenomena under reaction conditions.

## 12.4 Temporally Resolved Dynamics of Processes at Interfaces

Expanding infrared, Raman, and X-ray spectroscopy of processes at interfaces into the time domain increases substantially the ability to uncover mechanisms and identify kinetic bottlenecks that limit the efficiency of charge and species transport, or the product selectivity of catalytic transformations. This is a rapidly growing research direction that will accelerate the development of new applications of ultrathin oxide layers in electrocatalytic systems for energy and for the manufacture of environmentally sustainable chemicals. Efforts will be further boosted by emerging vibrational and X-ray spectroscopic techniques that offer greatly enhanced temporal resolution and spectral sensitivity. Proof of concept for expanding scanning electron microscopic imaging of functionalized surfaces to the ultrafast time regime has also been reported.[37]

High time resolution of the infrared spectroscopy of electrocatalytic processes at buried or exposed interfaces under simultaneous potential control can be realized with an ATR configuration, as recently demonstrated for $H_2O$ oxidation at $SrTiO_3$ surfaces.[38] In this experiment, a femtosecond light pulse excites the band gap of the photocatalyst kept at an applied potential that is below the onset of electrocatalytic $H_2O$ oxidation, while a femtosecond infrared pulse, variably delayed, probes the $SrTiO_3$/aqueous interface, revealing the rise and reaction of the primary titanyl surface intermediate. The Fano lineshape of the infrared absorption band revealed the coupling of the titanyl surface intermediate with the $SrTiO_3$ excited electronic states responsible for its formation, demonstrating the unprecedented level of insight into interfacial charge-transfer dynamics enabled by time-resolved spectroscopic monitoring. The electronic charge dynamics could also be independently monitored by ultrafast optical pump–probe spectroscopy.[38]

The ability to precisely control the initiation and duration of charge delivery at a buried or exposed interface by using pulses of light, while freely

selecting the applied potential at the same time, opens up a wealth of spectroscopic investigations with infrared, Raman, UV–visible, and X-ray methods. Studies reported to date typically utilized some but not all of these capabilities and were focused mainly on the dynamics of charge transfer and chemical change at the metal oxide/aqueous interface, although these methods are equally applicable to buried interfaces. The recent discovery of intermediates by ATR FT-IR spectroscopy established the distinct molecular nature of multistep electrocatalytic pathways on oxide surfaces. For example, $Co^{IV}$ oxo and superoxide intermediates were detected by millisecond ATR FT-IR monitoring upon photosensitized charge transfer at the $Co_3O_4$/aqueous interface.[39] Steady-state FT-IR spectroscopy under band gap illumination of a potential-controlled $Fe_2O_3$ photocatalyst revealed $Fe^{IV}$ oxo[40] and superoxo intermediates.[41] *In situ* X-ray absorption spectroscopy of $H_2O$ oxidation at an Ir oxide surface initiated by an applied voltage pulse indicates that (dark) electrocatalytic processes are, likewise, driven by redox reactions of the surface metal sites rather than by changes of the interfacial electric field.[42] The growing number of surface intermediates of key energy conversion reactions such as $O_2$ evolution and $CO_2$ reduction identified in the past few years,[28,39–47] and the accompanying interfacial charge dynamics uncovered by metal K-edge and O K-edge X-ray absorption spectroscopy,[48] clearly show that a mechanistic understanding of interfacial processes is feasible at the level of detail thus far encountered only for pure molecular systems.

Several novel spectroscopic and imaging tools that have emerged recently will open up experiments for probing the kinetic behavior of interfacial processes at basically any timescale relevant for the system at hand. Specifically, monitoring processes with infrared light will benefit from newly developed quantum cascade lasers (QCLs). This novel broadband infrared tool extends the time resolution from 10 ns for existing continuous-wave methods to the sub-picosecond regime.[49] If employed in the field-resolved spectroscopy mode, the method introduces unprecedented molecule specificity.[50] Used as a pulsed excitation–continuous probe technique in any of the experimental setups described in the previous section, the QCL beam will probe full infrared spectra and reveal the dynamics of interfacial moieties or catalytic intermediates prompted by photoexcitation of the semiconductor band gap. Importantly, monitoring of processes at metal surfaces or metal/metal oxide buried interfaces is equally feasible, namely by supporting the metal catalyst on a semiconductor film (*e.g.* GaP) that allows the generation of light-triggered voltage jumps for synchronizing electro-driven processes on the metal surface on any timescale from ultrafast to seconds.

For elucidating the electronic structure dynamics of metal centers at interfaces, the advent of femtosecond X-ray pulses in the hard and soft X-ray regions at XFEL facilities being commissioned around the world is revolutionary.[36] For example, this new tool will allow researchers to follow the charge migration at interfaces by monitoring the depolarization of X-ray absorption on the femto- and picosecond timescales, or resolve the

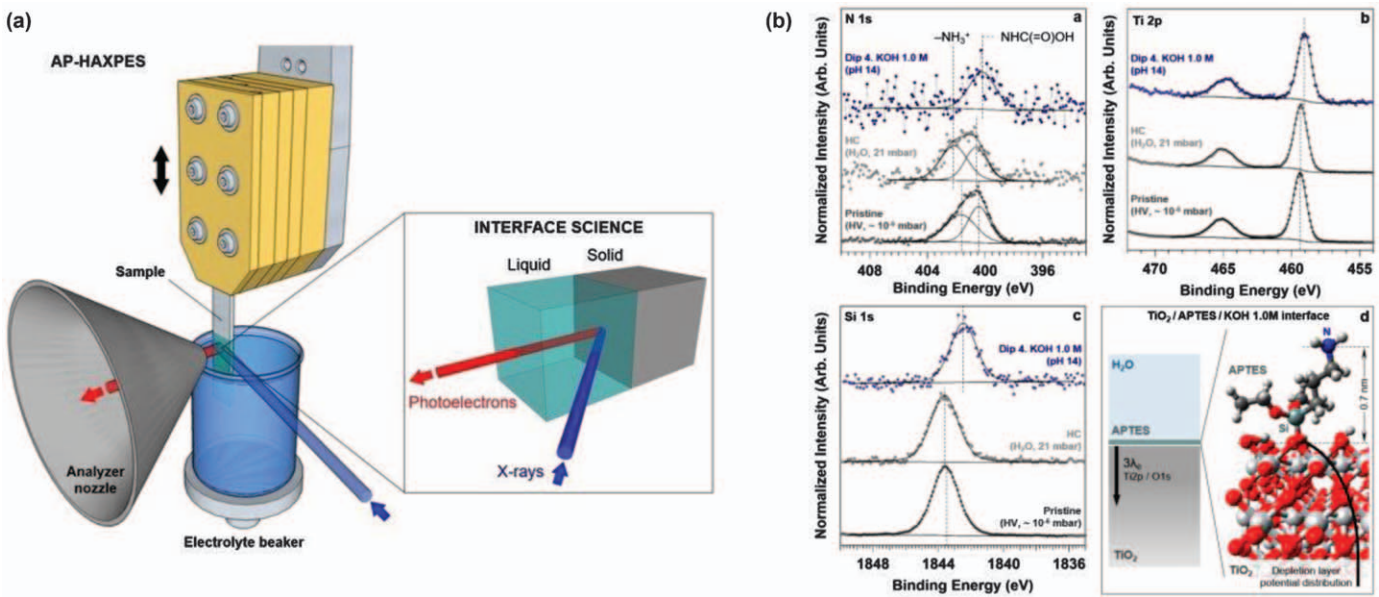


**Figure 12.3** (a) Schematic of the ''dip and pull'' technique for XPS monitoring. (b) The N 1s, Ti 2p and Si 1s core-level spectra acquired at the pristine conditions of $TiO_2$ surface covered with one monolayer of attached APTES (bottom), hydrated conditions (HC) (middle), and after dipping the sample in 1.0 M KOH solution (pH 14) (top). Bottom right: the structure obtained from molecular dynamics simulation of the adsorption of one APTES molecule on a rutile $TiO_2$ (110) surface through the formation of one Ti–O–Si bond (white, titanium; light gray, hydrogen; dark grey, carbon; light green, silicon; red, oxygen; blue, nitrogen). Reproduced from ref. 54, https://doi.org/10.3390/surfaces2010008, under the terms of a CC BY 4.0 license https://creativecommons.org/licenses/by/4.0/.

dynamics of chemical bond formation such as the O–O bond during $H_2O$ oxidation by O K-edge soft X-ray absorption spectroscopy at any timescale. The feasibility of detecting bond-forming steps on metal oxide catalysts by ultrafast XFEL spectroscopy was recently demonstrated for C–O bond formation of CO molecules with O atoms on an Ru catalyst surface.[51,52] A prominent example that demonstrates the extraordinary power of XFEL spectroscopy and diffractometry for elucidating mechanisms of multi-electron bond-breaking/forming processes of metal oxide moieties is the water oxidation catalysis of natural photosynthesis.[53]

Yet another recent development in the field of X-ray spectroscopy is ambient pressure XPS using high-energy (''tender'') X-rays in the range 2–10 keV. At the heart of this development is the ''dip and pull'' technique, which allows *in situ* monitoring of electrocatalysis under an applied potential at the solid/liquid interface, as illustrated in Figure 12.3a.[54,55] The aqueous layer is thin enough for probing the solid/liquid interface by photoelectron spectroscopy. Figure 12.3b shows N 1s, Ti 2p, and Si 1s core-level spectra of a $TiO_2$ surface covered with a monolayer of 3-aminopropyltriethoxysilane (APTES) covalently anchored *via* TiOSi linkages in high vacuum (HV, bottom trace), hydrated conditions [HC (21 mbar), middle], and liquid water film after dip and pull (Dip, top trace).[54] In addition to revealing the chemical bonding configuration of APTES on the $TiO_2$ surface, detailed insight into the nature of the solid/aqueous interface such as quantitative information on the electrical depletion layer is obtained by the analysis of the XPS measurements. An extraordinary resolution of 1 nm for the spatial arrangement of chemical species towards the bulk along the direction perpendicular to the interface is achieved when combining the AP XPS method with standing-wave photoemission spectroscopy.[56] However, the ''dip and pull'' technique also presents significant operational challenges that currently limit its broad application across materials and electrolytes of interest. Further innovations in cell design that can permit the application of these measurements to a wide range of ultrathin oxides and liquid electrolytes would greatly accelerate the knowledge gained from *operando* AP XPS and other powerful X-ray spectroscopic–scattering techniques.

## Acknowledgements

This work was supported by the Director, Office of Science, Office of Basic Energy Sciences, Division of Chemical, Geological and Biosciences of the US Department of Energy under Contract No. DE-AC02-05CH11231 (H.F.), and by the US National Science Foundation (NSF) (Award No. CBET-1752340) (D.V.E.). Any opinions, findings, and conclusions or recommendations expressed in this material are those of the author(s) and do not necessarily reflect the views of the US NSF. D.V.E. also thanks Aleksandra Vojvodic and Fikret Aydin for helpful discussions related to Section 12.2.

## References


1. G. B. Olson, in *Handbook of Materials Modeling: Methods*, ed. S. Yip, Springer Netherlands, Dordrecht, 2005, pp. 2667–2669, DOI: 10.1007/978-1-4020-3286-8_145.
2. W. Xiong and G. B. Olson, *npj Comput. Mater.*, 2016, **2**, 15009.
3. A. Zunger, *Nat. Rev. Chem.*, 2018, **2**, 0121.
4. J. Strand, M. Kaviani, D. Gao, A. El-Sayed, V. V. Afanas'ev and A. L. Shluger, *J. Phys.: Condens. Matter*, 2018, **30**, 21.
5. S. H. Garofalini, J. Lentz and M. Homann, *J. Am. Ceram. Soc.*, 2020, **103**, 2421–2431.
6. S. A. Khan, C. A. Vandervelden, S. L. Scott and B. Peters, *React. Chem. Eng.*, 2020, **5**, 66–76.
7. L. Lin and J. Robertson, *J. Appl. Phys.*, 2011, **109**, 094502.
8. M. Choi, A. Janotti and C. G. Van de Walle, *J. Appl. Phys.*, 2013, **113**, 044501.
9. J. Qu and A. Urban, *ACS Appl. Mater. Interfaces*, 2020, **12**, 52125–52135.
10. N. Artrith, *J. Phys.: Energy*, 2019, **1**, 032002.
11. M. Bernardi and J. C. Grossman, *Energy Environ. Sci.*, 2016, **9**, 2197–2218.
12. K. F. Kalz, R. Kraehnert, M. Dvoyashkin, R. Dittmeyer, R. Gläser, U. Krewer, K. Reuter and J.-D. Grunwaldt, *ChemCatChem*, 2017, **9**, 17–29.
13. D. V. Esposito, J. B. Baxter, J. John, N. S. Lewis, T. P. Moffat, T. Ogitsu, G. D. O'Neil, T. A. Pham, A. A. Talin, J. M. Velazquez and B. C. Wood, *Energy Environ. Sci.*, 2015, **8**, 2863–2885.
14. Z. Li, S. Wang, W. S. Chin, L. E. Achenie and H. Xin, *J. Mater. Chem. A*, 2017, **5**, 24131–24138.
15. Z. W. Ulissi, M. T. Tang, J. Xiao, X. Liu, D. A. Torelli, M. Karamad, K. Cummins, C. Hahn, N. S. Lewis, T. F. Jaramillo, K. Chan and J. K. Nørskov, *ACS Catal.*, 2017, **7**, 6600–6608.
16. P. Schlexer Lamoureux, K. T. Winther, J. A. Garrido Torres, V. Streibel, M. Zhao, M. Bajdich, F. Abild-Pedersen and T. Bligaard, *ChemCatChem*, 2019, **11**, 3581–3601.
17. D. Morgan and G. Ceder, in *Handbook of Materials Modeling: Methods*, ed. S. Yip, Springer Netherlands, Dordrecht, 2005, pp. 395–421, DOI: 10.1007/978-1-4020-3286-8_19.
18. W. T. Hong, R. E. Welsch and Y. Shao-Horn, *J. Phys. Chem. C*, 2016, **120**, 78–86.
19. A. J. Medford, M. R. Kunz, S. M. Ewing, T. Borders and R. Fushimi, *ACS Catal.*, 2018, **8**, 7403–7429.
20. Y. R. Shen and V. Ostroverkhov, *Chem. Rev.*, 2006, **106**, 1140–1154.
21. J. Zhou, E. Anim-Danso, Y. Zhang, Y. Zhou and A. Dhinojwala, *Langmuir*, 2015, **31**, 12401–12407.
22. J. N. Myers, X. Zhang, J. Bielefeld, Q. Lin and Z. Chen, *J. Phys. Chem. B*, 2015, **119**, 1736–1746.
23. S. Yamaguchi and T. Tahara, *Laser Photonics Rev.*, 2008, **2**, 74–82.
24. T. Frosch, K. L. A. Chan, H. Cheng-Wong, J. T. Cabral and S. G Kazarian, *Langmuir*, 2010, **26**, 19027–19032.

25. M. Oehman and D. Persson, *Electrochim. Acta*, 2007, **52**, 5159–5171.
26. G. T. Merklin and P. G. Griffith, *Langmuir*, 1997, **13**, 6159–6163.
27. K. Ataka, T. Yotsuyanagi and M. Osawa, *J. Phys. Chem.*, 1996, **100**, 10664–10672.
28. C. Lang, J. Li, K. R. Yang, Y. Wang, S. He, J. E. Thorne, S. Croslow, Q. Dong, Y. Zhao, G. Prostko, G. W. Brudvig, V. S. Batista, M. Waegele and D. Wang, *Chem*, 2021, **7**, 2101–2117.
29. A. Dazzi, R. Prazeres, F. Glotin and J. M. Ortega, *Opt. Lett.*, 2005, **30**, 2388–2390.
30. F. Cavezza, S. Pletincx, R. I. Revilla, J. Weaytens, M. Boehm, H. Terryn and T. Hauffman, *J. Phys. Chem. C*, 2019, **123**, 26178–26184.
31. S. Morsch, S. Lyon, S. Edmondson and S. Gibbon, *Anal. Chem.*, 2020, **92**, 8117–8124.
32. K. Stoev and K. Sakurai, *Anal. Sci.*, 2020, **36**, 901–922.
33. B. Pollakowski, B. Beckhoff, F. Reinhardt, S. Braun and P. Gawlitza, *Phys. Rev. B*, 2008, **77**, 235408.
34. D. Eiteneer, G. K. Palsson, S. Nemsak and A. X. Gray, *et al.*, *J. Electron Spectrosc. Relat. Phenom.*, 2016, **211**, 70–81.
35. J. Rubio-Zuazo, E. Martinez, P. Batude, L. Clavelier, A. Chabli and G. R. Castro, *Appl. Surf. Sci.*, 2011, **257**, 3007–3013.
36. *X-ray Free Electron Lasers*, ed. U. Bergmann, V. K. Yachandra and J. Yano, Energy Environment Series, RSC, Cambridge, UK, 2018.
37. D. S. Yang, O. F. Mohammed and A. H. Zewail, *Proc. Natl. Acad. Sci. U. S. A.*, 2010, **107**, 14993–14998.
38. D. M. Herlihy, M. M. Waegele, X. Chen, C. D. Pemmaraju, D. Prendergast and T. Cuk, *Nat. Chem.*, 2016, **8**, 549–555.
39. M. Zhang, M. de Respinis and H. Frei, *Nat. Chem.*, 2014, **6**, 362–367.
40. O. Zandi and T. W. Hamann, *Nat. Chem.*, 2016, **8**, 778–783.
41. Y. Zhang, H. Zhang, A. Liu, C. Chen, W. Song and J. Jiao, *J. Am. Chem. Soc.*, 2018, **140**, 3264–3269.
42. H. N. Nong, L. J. Falling, A. Bergmann and M. Klingenhof, *et al.*, *Nature*, 2020, **587**, 408–414.
43. O. Diaz-Morales, D. Ferrus-Suspedra and M. T. M. Koper, *Chem. Sci.*, 2016, **7**, 2639–2645.
44. I. V. Chernyshova, P. Somasundaran and S. Ponnurangam, *Proc. Natl. Acad. Sci. U. S. A.*, 2018, **115**, E9261–E9270.
45. H. Sheng, M. H. Oh, W. T. Osowiecki, W. Kim, A. P. Alivisatos and H. Frei, *J. Am. Chem. Soc.*, 2018, **140**, 4363–4371.
46. E. Perez-Gallent, M. C. Figueiredo, F. Calle-Vallejo and M. T. M. Koper, *Angew. Chem. Int. Ed.*, 2017, **56**, 3621–3624.
47. M. Favaro, H. Xiao, T. Cheng, W. A. Goddard III, J. Yano and E. J. Crumlin, *Proc. Natl. Acad. Sci. U. S. A.*, 2017, **114**, 6706–6711.
48. V. Pfeifer, T. E. Jones, J. J. Velasco-Velez, R. Arrigo, S. Piccinin, M. Haevecker, A. Knop-Gericke and R. Schloegl, *Chem. Sci.*, 2017, **8**, 2143–2149.
49. J. L. Klocke, M. Mangold, P. Allmendinger, A. Hugi, M. Geiser, P. Jouy, J. Faist and T. Kottke, *Anal. Chem.*, 2018, **90**, 10494–10500.

50. I. Pupeza, M. Huber, M. Trubetskov and W. Schweinberger, *et al.*, *Nature*, 2020, **577**, 52–59.
51. H. Oestroem, H. Oeberg and H. Xin, *Science*, 2015, **347**, 978–982.
52. M. Wagstaffe, L. Wenthaus, A. Dominguez-Castro and S. Chung, *et al.*, *ACS Catal.*, 2020, **10**, 13650–13658.
53. J. Kern, *et al.*, Structure of the intermediates of Kok's photosynthetic water oxidation clock, *Nature*, 2018, **563**, 421–425.
54. M. Favaro, F. F. Abdi, E. J. Crumlin, Z. Liu, R. van de Krol and D. E. Starr, *Surfaces*, 2019, **2**, 78–99.
55. M. Favaro, J. Yang, S. Nappini, E. Magnano, F. M. Toma, E. J. Crumlin, J. Yano and I. D. Sharp, *J. Am. Chem. Soc.*, 2017, **139**, 8960–8970.
56. S. Nemsak, A. Shavorskiy, O. Karslioglu, I. Zegkinoglou, A. Rattanachata, C. S Conlon, A. Keqi, P. K. Greene, E. C. Burks, F. Salmassi, E. M. Gullikson, S. H. Yang, H. Bluhm and C. S. Fadley, *Nat. Commun.*, 2014, **5**, 5441.

# *Subject Index*